Magma Storage, Evolution and Transport at Villarrica volcano, Chile

Felix Oliver Boschetty

Submitted in accordance with the requirements for the degree of
Doctor of Philosophy

The University of Leeds
School of Earth and Environment

March 2024

Abstract

Villarrica volcano is one of Chile's most active volcanoes with over one hundred eruptions since 1558. Moreover, eruptions at Villarrica have a large range in eruption intensity and magnitude, from mafic-ignimbrite-forming eruptions to intense lava fountaining, but this diversity is not reflected in its dominantly basaltic to basaltic andesite erupted products. In this thesis, I use two different methodologies to investigate if this homogeneity is merely a reflection of 'chemical averaging' of whole-rock analysis, focusing on complete and transparent error propagation to support its findings. First, I consider the variable compositions of erupted crystal cargoes at Villarrica, utilising unsupervised machine learning techniques to group mineral compositions and relate their complexity to eruptive behaviour using thermodynamic modelling. Mixing between evolved and primitive melts is identified as the driving force for Villarrica's most explosive eruptions. Then I examine the assumption that melt inclusion saturation pressures have low uncertainties compared to traditional mineral-based barometers. Volatile-saturation pressures require multiple analytical techniques and complex processing to account for CO_2 in both the melt inclusion glass and vapour bubble, making error propagation non-trivial. Errors in melt inclusion volumes estimated using 2D techniques dominate the total error, leading to comparable errors to classic mineral and mineral-melt barometers. With additional constraints on volume from micro-x-ray tomography or strategic polishing, the errors are several times lower. Finally, I investigate the major-, trace- and volatile-element contents of melt inclusions from four eruptions of Villarrica. Volatile saturation pressures demonstrate that Villarrica's magmatic system is vertically extensive. Trace elements show substantial variety despite homogeneous major elements, but show no trends with eruption. In combination, this strongly supports the application of the trans-crustal magmatic system model at Villarrica, whereby crystals from chemically distinct mushy reservoirs are assembled throughout the crust before their eruption.

Intellectual Property

I confirm that the work submitted is my own, except where work which has formed part of jointly authored publications has been included. My contribution and the other authors to this work has been explicitly indicated below. I confirm that appropriate credit has been given within the thesis where reference has been made to the work of others.

The following chapters are based on work from jointly-authored papers, with the Contributor Roles Taxonomy (CRediT) used to define authorship details:

- **Chapter 1**: *Insights Into Magma Storage Beneath a Frequently Erupting Arc Volcano (Villarrica, Chile) From Unsupervised Machine Learning Analysis of Mineral Compositions.* Felix O. Boschetty, David J. Ferguson, Joaquín A. Cortés, Eduardo Morgado, Susanna K. Ebmeier. Daniel J. Morgan, Jorge E. Romero, and Carolina Silva Parejas. Geochemistry, Geophysics, Geosystems, 23, e2022GC010333. `https://doi.org/10.1029/2022GC010333`. Published: 06 April 2022; originally submitted: 13 January 2022; resubmitted following review (minor corrections): 29 March 2022; accepted: 29 March 2022.
  - Felix O. Boschetty (first and corresponding author): conceptualisation, data curation, formal analysis, investigation, methodology, visualisation, writing - original draft, writing - review and editing.
  - David J. Ferguson: conceptualisation, methodology, writing - original draft, writing - review and editing
  - Joaquín A. Cortés: conceptualisation, data curation, methodology, writing - original draft, writing - review and editing
  - Eduardo Morgado: data curation, writing - original draft, writing - review and editing
  - Susanna K. Ebmeier: methodology, writing - original draft, writing - review and editing

- Daniel J. Morgan: supervision, writing - original draft, writing - review and editing
- Jorge E. Romero: data curation, writing - original draft, writing - review and editing
- Carolina Silva Parejas: data curation, writing - original draft, writing - review and editing

- **Chapter 2**: *Assessing the Impacts of Uncertainties for Volatile Saturation Pressures from Melt Inclusions.* Felix O. Boschetty, David J. Ferguson, Kevin Wong, Helen R. Thornhill, Penny E. Wieser, Margaret E. Hartley, and Nicholas D. Barber. To be submitted to Volcanica.
  - Felix O. Boschetty (first and corresponding author): conceptualisation, data curation, formal analysis, investigation, methodology, visualisation, writing - original draft, writing - review and editing.
  - David J. Ferguson: conceptualisation and writing - review and editing.
  - Kevin Wong: data curation, writing -original draft and writing - review and editing.
  - Helen R. Thornhill: writing - original draft and writing - review and editing.
  - Penny E. Wieser: data curation and writing - review and editing.
  - Margaret E. Hartley: data curation and writing - review and editing.
  - Nicholas D. Barber: data curation and writing - review and editing.

Acknowledgements

First I'd like to thank my supervisors. First Susi, for providing much needed pragmatism, for introducing me to remote sensing, and in the process pushing me outside of my comfort zone. Dan, for impromptu science meetings to discuss the nitty gritty: the ins and outs of diffusion, probe-data (and a lack of), and error propagation. As well as communist strategies for milk distribution, weird and wonderful rocks, and post-doc applications. Eduardo for making multiple trips to Chile possible and dealing with the endless bureaucracy and associated challenges. Not least, putting up with endless earnestly-delivered Spanglish without batting an eye, fearlessly sliding down glaciers, and introducing the concept of the thirst-quenching lunchtime fanshop. Finally, Dave for supporting me since day one, putting up with some very questionable driving, and entertaining far too many hair-brained science ideas that came to nothing.

A special thanks goes out to the numerous technical staff, whom without, I would be data-less and severely lacking essential research skills. Harri Wyn-Williams for painstakingly explaining all things sample prep, fostering a wide-reaching appreciation of Radio 2's pop-master, using the medium of excess epoxy to create abstract art, and trusting me to hit emergency stop on my way out. Richard Walshaw whose careful juggling of the SEM and Probe, ill-advised trust that I wouldn't do anything too stupid, and mopping up when I was overambitious with the scope of data collection, allowed gathering of the data that formed that backbone of this thesis. Dan Baker, for allowing me to cannibalise the Raman, sourcing stages at short notice by dismantling other carefully crafted setups, delving deep into engineering settings, and provided easy access to all things optical. Finally the team at the NERC Ion Probe Facility in Edinburgh, Cristina Talaveras-Rodrigues, Cees-Jan de Hoog, and John Craven, who answered never-ending questions about error propagation, and picked up late-night calls when I was panicking about sample-exchange.

Thank you to the original 7.182 gang: Edna, Eoin, Andrew, Jack, Kev, Steph, Claire, Sara, Fei and honorary member Maeve, who despite Covid and the resultant University-of-Leeds-management mandated

hellscape, made the last five years truly enjoyable. That we all made it is truly a tale for the ages.

Thank you Eoin and Sorcha. Without you I'm not sure how I would have made it through the pandemic: your support and company were vital, both during and beyond. I'm looking forward to future walking/coffee-tasting/brewery-sampling adventures.

Finally, I am extremely grateful to Grace for your belief, encouragement and for frequently convincing me to take very necessary breaks. This thesis marks the end of an almost five year adventure, and the start of our next.

Contents

List of Figures

List of Tables

Chapter 1

Introduction

This thesis seeks to improve our understanding of Villarrica volcano's magmatic architecture and relate this to eruptive behaviour. This chapter provides a brief introduction to the overall context of this project and synthesises recent developments in our understanding of the structure of magmatic systems. It also highlights some key questions that are addressed by the research presented in this thesis and outlines its overall structure.

1.1 Trans Crustal Magmatic Systems

Traditionally, magmatic systems have been conceptualised as shallow, liquid-dominated magma chambers connected to a deeper source region, where influxes of more primitive magma provide thermal energy to keep the system above the solidus temperature, and eruptions remove volatiles and evolved material (Cashman and Edmonds 2019; Cashman et al. 2017; Marsh 1989). However, as observations and models of magmatic systems improve, there is increasing evidence that long-lived, voluminous (>1.5 km^3) regions of melt do not exist within the upper crust (Annen et al. 2015). Modelling of magmatic systems suggests that a voluminous shallow region of melt will be unstable and prone to overturning (e.g. Dufek and Bachmann 2010), and therefore can only be ephemeral. Instead, seismic tomography studies suggest low proportions of melt in upper-crustal systems of 2–9 % distributed over large volumes (for example, 10,000 and 46,000 km^3 for an upper and lower crustal reservoir at Yellowstone, respectively, e.g., Huang et al. 2015). Finally, the large array of crystallisation pressures recorded by crystals in a single eruption (e.g. Mutch et al. 2019) and crustal contamination (Hildreth and Moorbath 1988) implies that magmas can be stored throughout the crust, rather than just in a shallow magma chamber.

The Trans-Crustal Magmatic System (TCMS) model was conceptualised around the turn of the 21st century in response to the questions: how do the volumes of evolved magma which are required to feed large silicic eruptions assemble, and how are plutonic and volcanic systems connected? To generate a large volume of evolved magma with a relatively low solidus temperature, it has been suggested that the majority of compositionally evolved magma is stored at temperatures just below the solidus as a crystal mush (Bachmann and Bergantz 2003; Marsh 2006). A mush is defined as a partially molten region comprising melt, crystals and volatiles, but where the crystalline phase(s) forms a continuous network (Marsh 1981). This definition is built upon the understanding that magmatic bodies undergo a large change in rheology when they reach crystallinities of around 50 % and above, becoming uneruptible (Marsh 1981). A region of mush can then be brought back above the solidus (e.g. Bachmann and Bergantz 2006; Cooper and Kent 2014) to produce a large volume of eruptible magma.

Concepts originally applied to large silicic systems have been applied in recent years to smaller, more mafic systems as the "mush model paradigm" has taken hold in the silicic community (e.g. Bergantz et al. 2015; Neave et al. 2014; Zellmer et al. 2016). This project will address whether the TCMS-based model is relevant to frequently erupting, mafic to intermediate, volcanic systems, such as Villarrica volcano, Chile. The invocation of a TCMS-based model at Villarrica initially seems compelling to explain the large range of crystallisation depths recorded by phenocrysts (Figure 1.2) and the large proportion of non-equilibrium crystals erupted throughout Villarrica's eruptive history. The work contained in this thesis will: further constrain crystallisation pressures beneath Villarrica, increase understanding of the different magmatic inputs to the volcanic system, and model magmatic processes occurring within crustal storage regions. The ultimate aim of this work is to produce a model of the magmatic architecture at Villarrica volcano, with potential application to arc volcanoes globally.

1.2 Geological Setting

Chile's Southern Volcanic Zone (SVZ) is one of four volcanic zones that make up the Andean Volcanic arc and is composed of a chain of volcanoes bordered by the Juan Fernandez Ridge in the north and the Chilean Rise in the south (Stern 2004). These lie parallel to the subduction margin formed by the subduction of the Nazca Plate beneath the South American Plate. The SVZ is divided into four segments by Stern (2004): the Northern, Transitional, Central and Southern SVZ. Villarrica lies in the Central SVZ (Figure 1.1). The SVZ also has a tectonic control, which is expressed as the Liquiñe-Ofqui Fault Zone (LOFZ). This ~1200 km long dextral strike-slip fault zone, trends NNE-SSW along the SVZ (Figure 1.1)

(Díaz et al. 2020). More locally, Villarrica forms part of a margin-oblique volcanic lineament (NW-SE) along with Quetrupillán and Lanín volcanoes, five deeply-eroded Pleistocene volcanoes and numerous small eruptive centres comprising cones and maars (Lara and Clavero 2004). This chain is thought to lie along an old regional tectonic boundary that is currently marked by the Mocha-Villarrica Fault Zone (MVFZ; Figure 1.1) (Pavez et al. 2020).

1.3 Villarrica Volcano

Villarrica or Rukapillan (39.5°S, 71.9°) is a Quaternary stratovolcano and is one of Chile's most active volcanoes with more than 100 eruptions since 1558 (Global Volcanism Program 2013). Post-glacial volcanic activity (14ka-present) at Villarrica has displayed a wide range in eruption intensity and magnitude. For example, the intense but low-magnitude March 2015 eruption, lasting just twenty minutes (Romero et al. 2018); the low magnitude and low-intensity eruptions forming the Los Nevados parasitic cones and lavas; and the high intensity and high magnitude Licán mafic ignimbrite forming eruption, with a volume of greater than 10 km^3 (Lohmar et al. 2012). Despite this variety in eruptive style, Villarrica's volcanic products have a limited range in major element composition compared to other nearby Chilean volcanoes and are typified by a significantly lower SiO_2 content (Figure 1.3). Additionally, at Villarrica, there is evidence for both vertically-extensive magma storage (thermobarometric estimates, Figure 1.2) and laterally-extensive storage (deformation modelling, (Delgado et al. 2017). These suggest that there might be multiple magma storage zones that are tapped by different eruptions. I will test if these theorised multiple storage zones are instead a vertically extensive, trans-crustal magmatic system, and whether the dynamics of the system can explain the variety of eruptive behaviour observed at Villarrica.

1.4 Objectives of this Thesis

Broadly speaking the objective of this thesis is to expand our understanding of the structure and dynamics of Villarrica's magmatic system. This can be broken down into several research questions:

- Can a TCMS be petrologically 'imaged' beneath an arc volcano using thermobarometry and melt-saturation pressures? If so, how does storage throughout these systems relate to: i) eruptive style, ii) the locations of subsurface stress changes constrained by geodetic studies, and iii) the conductivity structure of the lithosphere from magnetotellurics?
- How do changes in the primary melt supply, particularly volatile contents, affect magma-storage

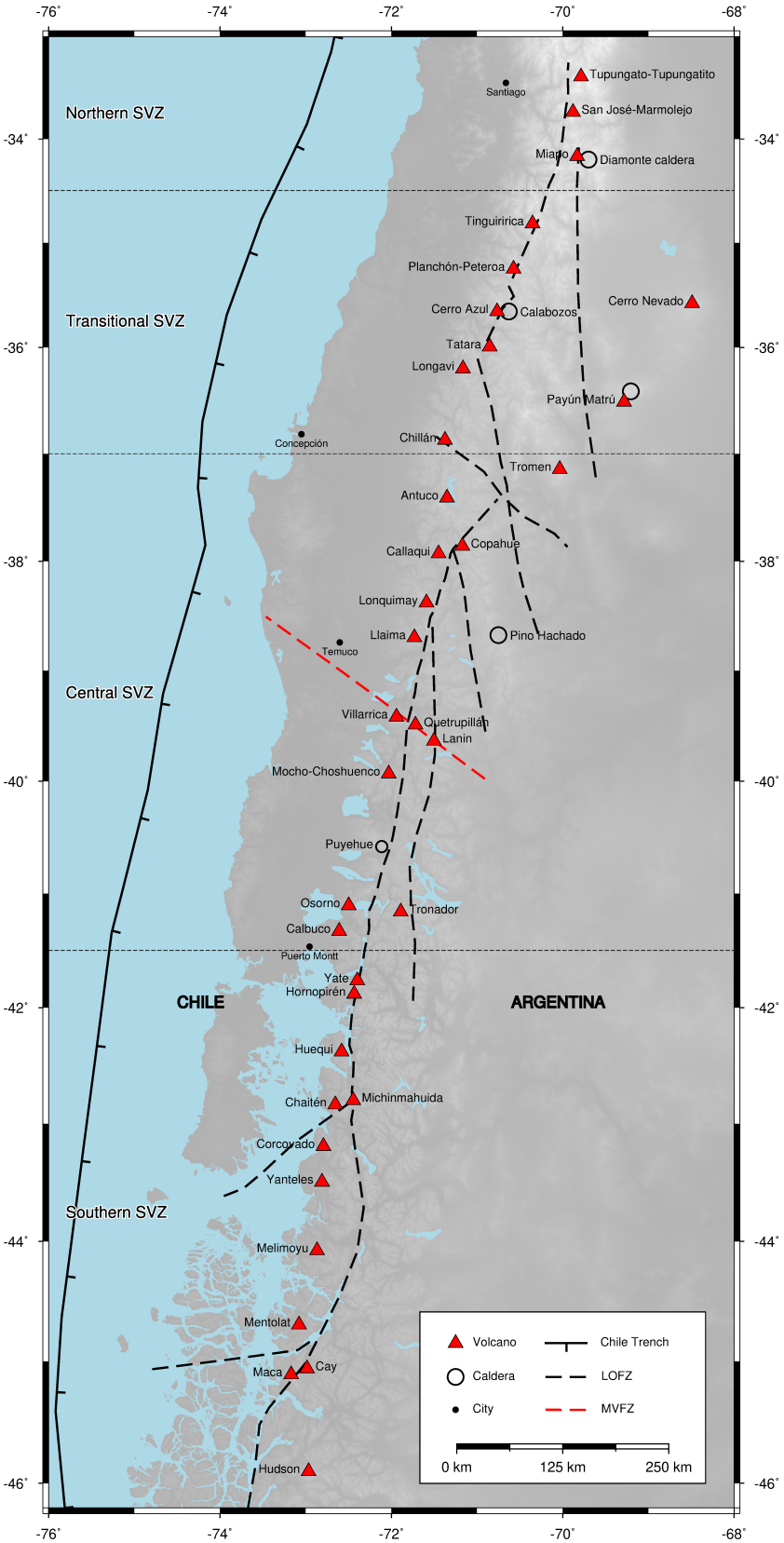

Figure 1.1: Map of the Southern Volcanic Zone divided into four zones as per Stern (2004) (thin black dashed). It shows the location of notable active volcanoes (red triangles), calderas (circles), the Chile Trench (black ticked), Liquiñe-Ofqui Fault Zone (LOFZ) (thick black dashed) and Mocha-Villarrica Fault Zone (MOFZ) (red dashed). The ASTER-GDEM was obtained via EarthExplorer, USGS (http://earthexplorer.usgs.gov).

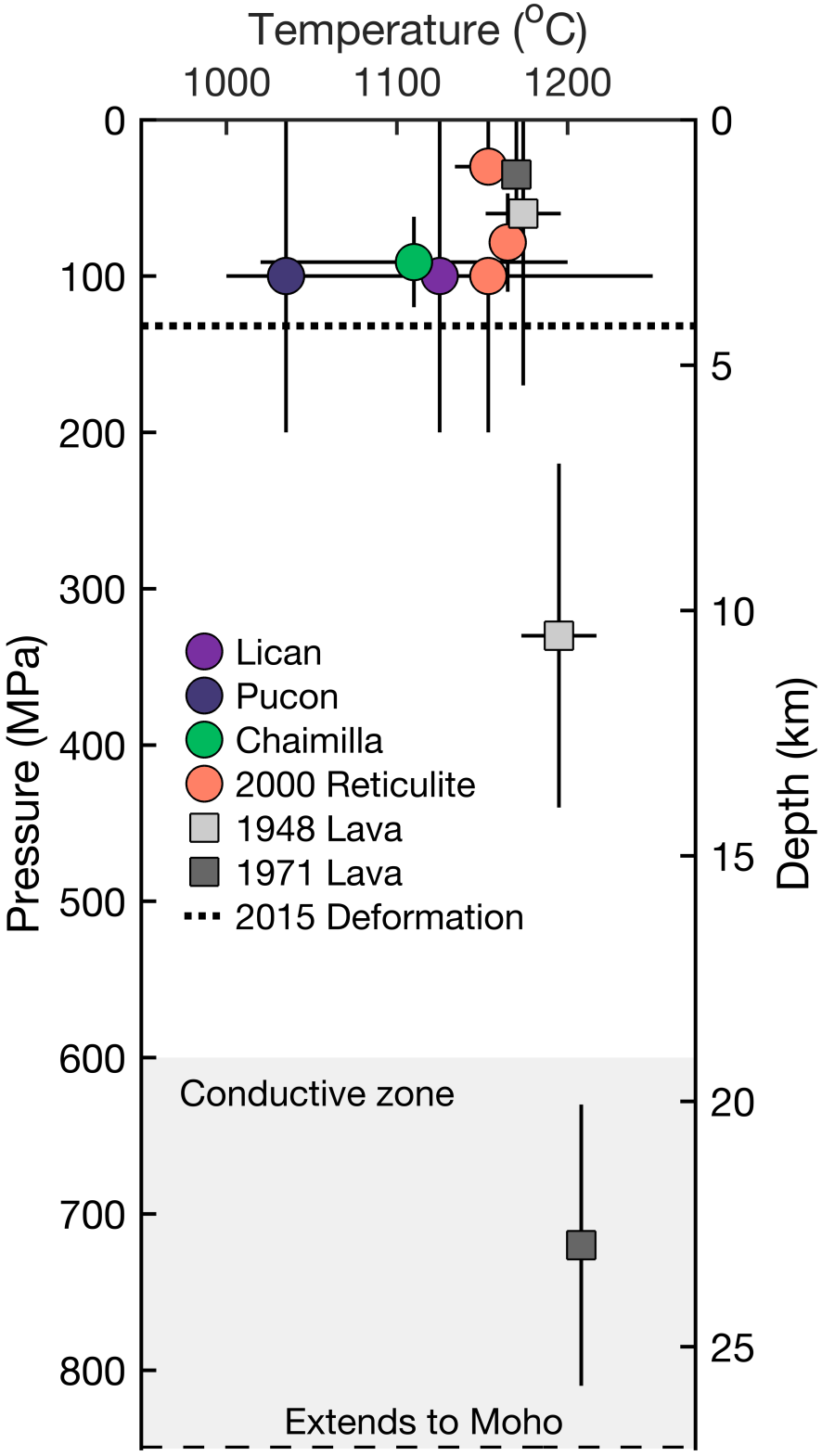

Figure 1.2: Pressure-temperature-depth plot of Villarrica products showing geothermobarometry results from past studies. The black dotted line shows the calculated depth (4.2 km) of the deformation source for the March 2015 eruption, about 5 km SE of the central vent (Delgado et al. 2017). The grey shading corresponds to an area of high conductivity (ca. 19–50 km) (Kapinos et al. 2016). The data imply at least two magma storage depths: a shallow source (<5 km) and a deeper source (>19 km) and therefore imply a vertically extensive magmatic system at Villarrica.

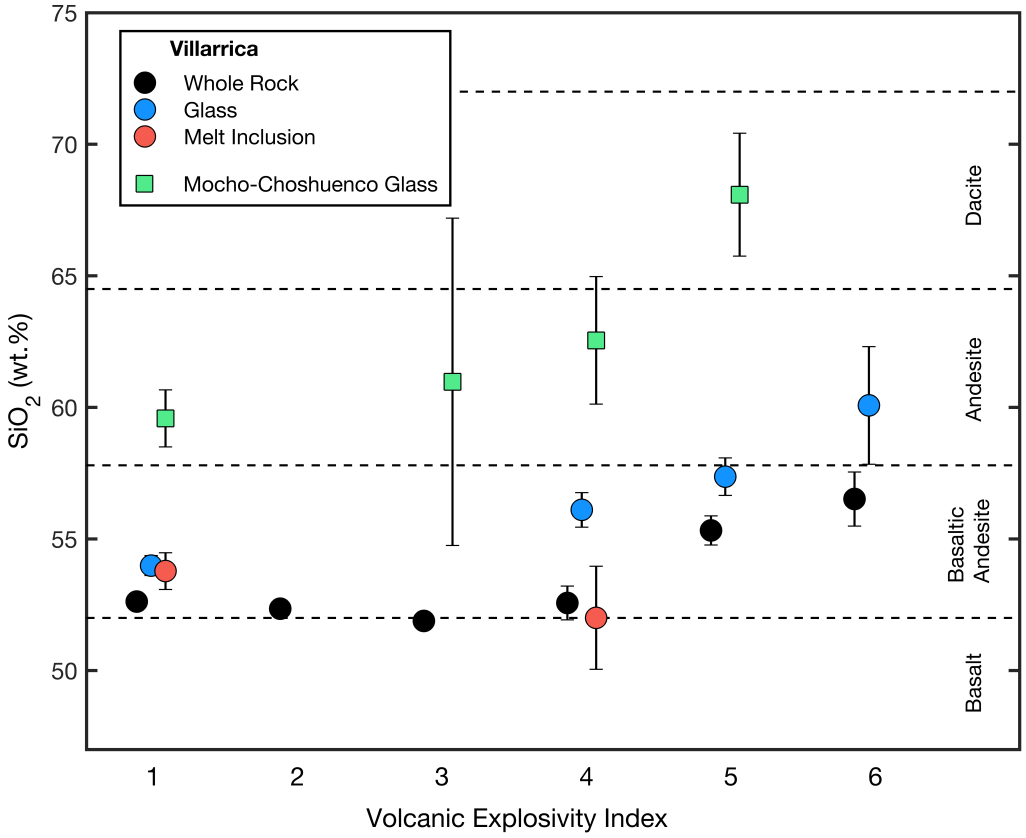

Figure 1.3: A plot of SiO_2 vs. Volcanic Explosivity Index (VEI) showing data from past studies of Villarrica and another Chilean SVZ volcano Mocho-Choshuenco (Rawson et al. 2015) for comparison. Villarrica VEI data is taken from the Global Volcanism Program (Global Volcanism Program 2013). Error bars represent ± 1 standard deviation. Villarrica data shows a small increase in SiO_2 with increasing VEI but its eruptions are substantially more mafic than similarly sized eruptions from Mocho-Choshuenco. Notably, the total range of SiO_2 for Villarrica is less than that for just VEI 3 eruptions at Mocho-Choshuenco.

dynamics and erupted mass?

- Can the potential source components for primary arc melts (such as the sub-arc mantle and subducted slab materials) be distinguished via trace element analysis and, if so, do they vary systematically by eruption?

1.5 Methods

In this thesis, I apply a range of analytical and data-processing techniques to characterise Villarrica's magmatic system. While each method's specifics are discussed in greater detail within their respective chapters, I present a brief conceptual overview of each here to provide context for the research methodology as a whole.

1.5.1 Analytical Techniques

1.5.1.1 Electron Probe Microanalysis (EPMA)

An electron microprobe uses wavelength-dispersive X-ray spectroscopy (WDS) to accurately quantify a sample's chemical composition at the micron scale. The technique requires extensive setup to produce compositional analyses of sufficient accuracy and precision, meeting the standards necessary for modern petrological studies. Preparation includes careful spectrometer tuning and rigorous analyses of both primary and secondary standards to mitigate instrument drift and ensure full quantification of analytical accuracy and precision. Collection parameters are tailored to maximise the accuracy and precision of the targeted major and/or trace elements. Achieving this balance involves optimising the number of elements measured and their count times against the total analysis time.

1.5.1.2 Micro-Raman Spectroscopy

Micro-Raman spectrometry is a non-destructive method used to analyse the constituent minerals, chemistry and in some cases the structure of samples. The method involves directing a monochromatic laser at the sample and recording the wavelength of Raman-scattered light that is emitted. This scattered light produces characteristic peaks in the spectrum, which can be used to identify and quantify specific chemical compounds within the sample. It has a high spatial resolution and can be used to create 3D maps of samples. The downside is that resultant image processing can be extremely time-consuming.

1.5.1.3 Secondary Ion Mass Spectrometry (SIMS)

Secondary Ion Mass Spectrometry (SIMS) is a highly sensitive analytical technique used to measure isotopic and elemental composition at the micron scale. In SIMS, a focused beam of ions (commonly O^- or Cs^+ coupled with an electron gun) bombards the sample's surface, causing secondary ions to be ejected. These ions are then analysed to determine the sample's composition. This technique is particularly valuable for in situ microanalysis, allowing for high-resolution spatial analysis of trace and volatile elements and isotopic ratios within individual mineral phases.

1.5.2 Uncertainty Propagation

1.5.2.1 Monte Carlo Modelling

Monte Carlo modelling is employed to quantify uncertainty by simulating a large number of random samples based on known parameters and probability distributions. In this study, Monte Carlo simulations are used to propagate uncertainties in analytical measurements, providing a probabilistic range for each result. This approach allows for robust quantification of confidence intervals in derived parameters, particularly for intensive variables that require many-dimensional inputs.

1.5.2.2 Linear Regression

Linear regression techniques are used to establish and quantify relationships between variables. In this thesis, they are used to establish relationships between measured quantities, e.g., count intensities, with the concentrations of standards. Linear regression aims to find a relationship that best explains the observations. In this thesis, I use a method that allows for robust error propagation when there are uncertainties in both the measured and known values.

1.5.3 Data Interrogation

1.5.3.1 Unsupervised Machine Learning Techniques

Unsupervised machine learning methods describe algorithms that analyse and interpret data without prior labels or explicit instructions about the output. These techniques aim to identify underlying patterns, structures, or relationships. Common approaches include clustering, where data points are grouped based on similarity (e.g., k-means or hierarchical clustering), and dimensionality reduction, which seeks to simplify high-dimensional data while preserving essential features (e.g., principal component analysis

or t-SNE). Both hierarchical clustering and dimensionality reduction are used to explore the composition of crystal cargoes erupted at Villarrica.

1.5.3.2 Thermodynamic Modelling

Thermodynamic models are used to simulate the physicochemical conditions of Villarrica's magmatic system. By inputting compositional data into established thermodynamic software, such as MELTS or Petrolog3, it is possible to predict phase stability, melting behaviour, and crystallisation sequences under varying pressure, temperature, and compositional conditions. By finding best-fit models to measured compositions, multiple thermodynamic models can be inverted to identify corresponding best-fit intensive variables.

1.5.3.3 Thermobarometry

Thermobarometry involves calculating the temperature and pressure conditions under which minerals crystallised, based on their chemical composition. By applying established thermobarometric equations and calibrations to the mineral compositions obtained from compositional data, it is possible to reconstruct the magmatic conditions present during mineral and/or melt formation. This method is commonly used to identify intensive conditions from measured mineral compositions and equilibrium melts.

1.6 Structure of this Thesis

1.6.1 Chapter 2

Chapter two utilises previously published compositional data of Villarrica's mineral phases to examine the composition of erupted crystal cargoes. It employs the idea that Villarrica's eruptions are sampling a common magmatic system that may be poorly represented by the products of any individual eruption but can be more fully characterised by combining the crystal cargoes from many eruptions.

To analyse the compiled compositional data I create and test a hierarchical clustering method, a form of unsupervised machine learning, that groups multi-variate data based on similarity. The developed method uses a mathematically consistent approach whereby a log-ratio transformation is first applied to the compositional data. This is necessary as compositional data are not normally distributed and are subjected to a non-negative constraint: both barriers to the application of standard statistical treatment. Unlike previous clustering methodologies, I also implement multivariate outlier detection by calculating

the Mahalanobis distance of identified clusters. The robustness of each cluster is also tested by repeatedly randomly sampling and performing the hierarchical clustering.

I find that the proportion of identified clusters for olivine, plagioclase and clinopyroxene compositions vary considerably despite consistent whole-rock compositions. Cluster compositions are then compared to over 1500 thermodynamic simulations of magma evolution in a simplified Villarrica-like system. I perform a grid search over a range of pressures, oxygen-fugacities and initial water contents to find the best-fitting simulations for each compositional analysis and calculate the best-fitting conditions for each identified cluster. The results suggest vertically extensive magmatic storage is the norm at Vilarrica.

Key differences between the crystal cargoes of historic, typically low-intensity and low-magnitude eruptions, and the largest of Villarrica's eruptions, i.e. those forming large-mafic ignimbrites, imply fundamental differences in magma dynamics between eruption types. I develop a working model for generating large explosive eruptions at Villarrica, whereby stalled, more evolved melts dampen eruption frequency, in turn increasing the volume of the mushy system. With sufficient primitive input, this mush is then remobilised and crystal compositions from both evolved and primitive magmas are preserved as mineral cores and rim compositions. In contrast, the feeder magmas for more recent historic eruptions appear able to pass through the mushy system relatively uninhibited, preserving their more primitive character and assembling populations of antecrysts before their eruption.

1.6.2 Chapter 3

Chapter three examines the assumption that volatile-saturation pressures calculated using the volatile and major element composition of melt inclusions are significantly more certain than those calculated from mineral and mineral-liquid thermobarometry. Recent technological developments have revealed that a significant proportion of CO_2 in melt inclusions can be hosted within vapour bubbles that have been traditionally ignored. The use of micro-Raman spectrometry allows glass and vapour bubble CO_2 to be combined leading to more accurately calculated volatile saturation pressures. However, the conversion of measured CO_2 densities in the bubble phase into a concentration by mass balance requires additional information, including melt inclusion glass densities, and vapour bubble and melt inclusion volumes.

To assess the effect of analytical uncertainty in each component of the analytical workflow I apply more sophisticated linear regression methods and Monte-Carlo methods to propagate uncertainties into the final calculated pressure. I have developed a Python-based workflow that utilises pre-existing scripts to calculate glass densities, perform post-entrapment modification corrections, and calculate the volatile

saturation pressure.

Using this new treatment of error propagation I then reprocess data for twenty melt inclusions from four previously published studies. A full reassessment of all sources of analytical error shows that errors for volatile saturation pressure have been systematically underestimated. The major contributor towards the final error is melt inclusion volume estimation when this is done using traditional two-dimensional methods. The uncertainty for high-pressure melt inclusions with volumes estimated using 2D methods approaches that of often used clinopyroxene-only and clinopyroxene-liquid barometers. Assessment of melt inclusions without vapour bubbles shows that they have non-negligible errors and that all analytical uncertainties must be propagated to fully assess the error in calculated volatile-saturation pressures.

1.6.3 Chapter 4

This chapter presents geochemical data for olivine, plagioclase and clinopyroxene-hosted melt inclusions to investigate the following: (1) at which pressures are magmas stored in Villarrica's magmatic system? (2) which of these magma storage regions are intersected before significant eruptions? (3) are there variations in the compositions of the primitive liquids that feed these storage regions?

I use a combination of micro-Raman spectroscopy, Secondary Ionisation Mass Spectrometry and Electron Microprobe Analysis to collect volatile, trace and major element compositions of melt inclusions from four eruptions of Villarrica. In addition, I use the composition of olivine-hosted melt, and spinel inclusions to estimate the oxygen fugacity at the time of inclusion entrapment, which is vital to accurately correct for post-entrapment modification of melt inclusions. The workflow created in Chapter Three is then implemented to correctly propagate errors in volatile saturation pressures.

I find that inclusions were entrapped over a range of pressures, supporting the presence of a trans-crustal magmatic system beneath Villarrica. I also find that melt inclusions from all eruptions present a range of trace-element ratios which are unaffected by bulk fractional crystallisation. This range of trace element ratios does not correlate with source eruption, suggesting the presence of multiple reservoirs formed from distinct batches of magma. These are intercepted before eruption by ascending melts forming cargoes of antecrysts that host melt inclusions.

1.7 Supplementary Data

The data presented in this thesis is supplied as an Electronic Appendix, along with PDFs of relevant published papers. This includes:

- EMPA data from past studies used in Chapter 2
- EMPA data from Chapter 4
- Images of all melt inclusions and vapour bubbles from Chapter 4
- A summary of all melt inclusion data from Chapter 4

References

Annen, C., J. D. Blundy, J. Leuthold, and R. S. J. Sparks (2015). "Construction and evolution of igneous bodies: Towards an integrated perspective of crustal magmatism". In: *Lithos* 230, pages 206–221. DOI: 10.1016/j.lithos.2015.05.008. URL: https://linkinghub.elsevier.com/retrieve/pii/S0024493715001759 (visited on 07/09/2020).

Bachmann, O. and G. W. Bergantz (2003). "Rejuvenation of the Fish Canyon magma body: A window into the evolution of large-volume silicic magma systems". In: *Geology* 31.9, page 789. DOI: 10.1130/G19764.1. URL: https://pubs.geoscienceworld.org/geology/article/31/9/789-792/29357 (visited on 06/22/2020).

– (2006). "Gas percolation in upper-crustal silicic crystal mushes as a mechanism for upward heat advection and rejuvenation of near-solidus magma bodies". In: *Journal of Volcanology and Geothermal Research* 149.1, pages 85–102. DOI: 10.1016/j.jvolgeores.2005.06.002. URL: https://linkinghub.elsevier.com/retrieve/pii/S0377027305002076 (visited on 06/22/2020).

Bergantz, G. W., J. M. Schleicher, and A. Burgisser (2015). "Open-system dynamics and mixing in magma mushes". In: *Nature Geoscience* 8.10, pages 793–796. DOI: 10.1038/ngeo2534. URL: http://www.nature.com/articles/ngeo2534 (visited on 07/09/2020).

Cashman, K. V. and M. Edmonds (2019). "Mafic glass compositions: a record of magma storage conditions, mixing and ascent". In: *Philosophical Transactions of the Royal Society A: Mathematical, Physical and Engineering Sciences* 377.2139, page 20180004. DOI: 10.1098/rsta.2018.0004. URL: https://royalsocietypublishing.org/doi/10.1098/rsta.2018.0004 (visited on 06/25/2020).

Cashman, K. V., R. S. J. Sparks, and J. D. Blundy (2017). "Vertically extensive and unstable magmatic systems: A unified view of igneous processes". In: *Science* 355.6331, eaag3055. DOI: 10.1126/science.aag3055. URL: https://www.sciencemag.org/lookup/doi/10.1126/science.aag3055 (visited on 06/25/2020).

Cooper, K. M. and A. J. R. Kent (2014). "Rapid remobilization of magmatic crystals kept in cold storage". In: *Nature* 506.7489, pages 480–483. DOI: 10.1038/nature12991. URL: https://www.nature.com/articles/nature12991 (visited on 06/25/2020).

Delgado, F., M. E. Pritchard, S. Ebmeier, P. González, and L. Lara (2017). "Recent unrest (2002–2015) imaged by space geodesy at the highest risk Chilean volcanoes: Villarrica, Llaima, and Calbuco (Southern Andes)". In: *Journal of Volcanology and Geothermal Research* 344, pages 270–288. DOI: 10.1016/j.jvolgeores.2017.05.020. URL: https://linkinghub.elsevier.com/retrieve/pii/S0377027317303086 (visited on 10/10/2019).

Díaz, D., F. Zúñiga, and A. Castruccio (2020). "The interaction between active crustal faults and volcanism: A case study of the Liquiñe-Ofqui Fault Zone and Osorno volcano, Southern Andes, using magnetotellurics". In: *Journal of Volcanology and Geothermal Research* 393, page 106806. DOI: 10.1016/j.jvolgeores.2020.

106806. URL: http://www.sciencedirect.com/science/article/pii/S0377027319304408 (visited on 06/25/2020).

Dufek, J. and O. Bachmann (2010). "Quantum magmatism: Magmatic compositional gaps generated by melt-crystal dynamics". In: *Geology* 38.8, pages 687–690. DOI: 10.1130/G30831.1. URL: http://pubs.geoscienceworld.org/geology/article/38/8/687/130302/Quantum-magmatism-Magmatic-compositional-gaps (visited on 03/11/2020).

Global Volcanism Program (2013). "Villarrica (357120)". In: *Volcanoes of the World*. v. 4.9.0 (04 June 2020). URL: https://volcano.si.edu/volcano.cfm?vn=357120 (visited on 06/30/2020).

Hildreth, W. and S. Moorbath (1988). "Crustal contributions to arc magmatism in the Andes of Central Chile". In: *Contributions to Mineralogy and Petrology* 98.4, pages 455–489. DOI: 10.1007/BF00372365. URL: https://doi.org/10.1007/BF00372365 (visited on 06/25/2020).

Huang, H.-H., F.-C. Lin, B. Schmandt, J. Farrell, R. B. Smith, and V. C. Tsai (2015). "The Yellowstone magmatic system from the mantle plume to the upper crust". In: *Science* 348.6236, pages 773–776. DOI: 10.1126/science.aaa5648. URL: https://science.sciencemag.org/content/348/6236/773 (visited on 06/25/2020).

Kapinos, G., M. Montahaei, N. Meqbel, and H. Brasse (2016). "Three-dimensional electrical resistivity image of the South-Central Chilean subduction zone". In: *Tectonophysics* 666, pages 76–89. DOI: 10.1016/j.tecto.2015.10.016. URL: http://www.sciencedirect.com/science/article/pii/S004019511500565X (visited on 06/24/2020).

Lara, L. E. and J. Clavero (2004). *Villarrica Volcano (39.5°S), Southern Andes, Chile*. Volume Bulletin 61.

Lohmar, S., M. Parada, F. Gutiérrez, C. Robin, and M. C. Gerbe (2012). "Mineralogical and numerical approaches to establish the pre-eruptive conditions of the mafic Licán Ignimbrite, Villarrica Volcano (Chilean Southern Andes)". In: *Journal of Volcanology and Geothermal Research* 235-236, pages 55–69. DOI: 10.1016/j.jvolgeores.2012.05.006. URL: https://linkinghub.elsevier.com/retrieve/pii/S0377027312001448 (visited on 10/10/2019).

Marsh, B. D. (1989). "Magma Chambers". In: *Annual Review of Earth and Planetary Sciences* 17.1, pages 439–472. DOI: 10.1146/annurev.ea.17.050189.002255. URL: http://www.annualreviews.org/doi/10.1146/annurev.ea.17.050189.002255 (visited on 06/25/2020).

– (1981). "On the crystallinity, probability of occurrence, and rheology of lava and magma". In: *Contributions to Mineralogy and Petrology* 78.1, pages 85–98. DOI: 10.1007/BF00371146. URL: http://link.springer.com/10.1007/BF00371146 (visited on 06/22/2020).

– (2006). "Dynamics of Magmatic Systems". In: *Elements* 2.5, pages 287–292. DOI: 10.2113/gselements.2.5.287. URL: https://pubs.geoscienceworld.org/elements/article/2/5/287-292/137715 (visited on 06/25/2020).

Mutch, E. J. F., J. Maclennan, O. Shorttle, M. Edmonds, and J. F. Rudge (2019). "Rapid transcrustal magma movement under Iceland". In: *Nature Geoscience* 12.7, pages 569–574. DOI: 10.1038/s41561-019-0376-9. URL: https://www.nature.com/articles/s41561-019-0376-9 (visited on 06/25/2020).

Neave, D. A., J. Maclennan, M. E. Hartley, M. Edmonds, and T. Thordarson (2014). "Crystal Storage and Transfer in Basaltic Systems: the Skuggafjöll Eruption, Iceland". In: *Journal of Petrology* 55.12, pages 2311–2346. DOI: 10.1093/petrology/egu058. URL: https://academic.oup.com/petrology/article-lookup/doi/10.1093/petrology/egu058 (visited on 07/09/2020).

Pavez, M., E. Schill, S. Held, D. Díaz, and T. Kohl (2020). "Visualizing preferential magmatic and geothermal fluid pathways via electric conductivity at Villarrica Volcano, S-Chile". In: *Journal of Volcanology and Geothermal Research* 400, page 106913. DOI: 10.1016/j.jvolgeores.2020.106913. URL: http://www.sciencedirect.com/science/article/pii/S0377027319305049 (visited on 06/25/2020).

Rawson, H., J. A. Naranjo, V. C. Smith, K. Fontijn, D. M. Pyle, T. A. Mather, and H. Moreno (2015). "The frequency and magnitude of post-glacial explosive eruptions at Volcán Mocho-Choshuenco, southern Chile". In: *Journal of Volcanology and Geothermal Research* 299, pages 103–129. DOI: 10.1016/j.jvolgeores.2015.04.003. URL: http://www.sciencedirect.com/science/article/pii/S0377027315001109 (visited on 06/24/2020).

Romero, J. E., F. Vera, M. Polacci, D. Morgavi, F. Arzilli, M. A. Alam, J. E. Bustillos, A. Guevara, J. B. Johnson, J. L. Palma, M. Burton, E. Cuenca, and W. Keller (2018). "Tephra From the 3 March 2015 Sustained Column Related to Explosive Lava Fountain Activity at Volcán Villarrica (Chile)". In: *Frontiers in Earth Science* 6, page 98. DOI: 10.3389/feart.2018.00098. URL: https://www.frontiersin.org/article/10.3389/feart.2018.00098/full (visited on 10/18/2019).

Stern, C. R. (2004). "Active Andean volcanism: its geologic and tectonic setting". In: *Revista geológica de Chile* 31.2. DOI: 10.4067/S0716-02082004000200001. URL: http://www.scielo.cl/scielo.php?script=sci_arttext&pid=S0716-02082004000200001&lng=en&nrm=iso&tlng=en (visited on 03/11/2020).

Zellmer, G. F., M. Pistone, Y. Iizuka, B. J. Andrews, A. GÃ³mez-Tuena, S. M. Straub, and E. Cottrell (2016). "Petrogenesis of antecryst-bearing arc basalts from the Trans-Mexican Volcanic Belt: Insights into along-arc variations in magma-mush ponding depths, H_2O contents, and surface heat flux". In: *American Mineralogist* 101.11, pages 2405–2422. DOI: 10.2138/am-2016-5701. URL: https://pubs.geoscienceworld.org/ammin/article/101/11/2405-2422/227011 (visited on 07/09/2020).

Chapter 2

Insights Into Magma Storage From Unsupervised Machine Learning Analysis of Mineral Compositions

2.1 Preamble

This chapter is based on a paper published in the journal Geochemistry, Geophysics, Geosystems (G^3) titled: *Insights Into Magma Storage Beneath a Frequently Erupting Arc Volcano (Villarrica, Chile) From Unsupervised Machine Learning Analysis of Mineral Compositions*. Minor edits have been made to correct grammatical mistakes, and the spelling changed to British English. The supplementary figures and text can be found in Appendix A. A spreadsheet containing all the data used for this study can be found at: `https://doi.org/10.5285/703acf75-8996-45a4-b4b3-42afca269a1c`.

2.2 Abstract

A key method to investigate magma dynamics is the analysis of the crystal cargoes carried by erupted magmas. These cargoes may comprise crystals that crystallise in different parts of the magmatic system (throughout the crust) and/or at different times. While an individual eruption likely provides a partial view of the sub-volcanic plumbing system, compiling data from multiple eruptions can build a picture of a whole magmatic system. In this study, we use machine learning techniques to analyse a large (2000)

compilation of mineral compositions from a highly active arc volcano: Villarrica, Chile. Villarrica's post-glacial eruptive activity (14 ka–present) displays large variation in eruptive style (mafic ignimbrites to Hawaiian-style effusive eruptions) yet its eruptive products have a near constant basalt-basaltic andesite bulk-rock composition. What, therefore, is driving explosive eruptions at Villarrica and can differences in storage dynamics be related to eruptive style? Here we use hierarchical cluster analysis to detect previously unseen structure in the composition of olivine, plagioclase and clinopyroxene crystals erupted at Villarrica, revealing the presence of compositionally distinct clusters within each crystal population. Using rhyolite-MELTS thermodynamic modelling we related these clusters to intensive magmatic variables: temperature, pressure, water content and oxygen fugacity. Our results provide evidence for the existence of multiple discrete (spatial and temporal) magma reservoirs beneath Villarrica where melts differentiate and mix with incoming more primitive magma. The compositional diversity within an erupted crystal cargo strongly correlates with eruptive intensity, and we postulate that mixing between primitive and differentiated magma drives explosive activity at Villarrica.

2.3 Plain Language Summary

Studies of volcanoes often focus on a single eruption. However, the magmatic systems beneath volcanoes are complex: magmas crystallise throughout the crust and the minerals erupted at the surface can be formed just prior to eruption, or thousands of years earlier. Here we use machine-learning methods to group mineral compositions from many eruptions of an active Chilean volcano (Villarrica) to build a picture of the magmatic system. By using the appropriate mathematical treatment, we find that there are distinct groups of mineral compositions that were not identified by past studies. These different compositions are used to demonstrate that different batches of magma have mixed throughout Villarrica's post-glacial history. This suggests that the mixing of different magmas drives explosive eruptions at Villarrica volcano.

2.4 Introduction

Arc volcanoes produce most of the Earth's subaerial volcanic activity and are responsible for some of the largest historical eruptions (Siebert et al. 2015). However, the structure of the magmatic systems that feed these volcanoes is still largely unknown. The traditional view that the magmas erupted from arc volcanoes reside within a melt-dominated sub-volcanic 'magma chamber' has been superseded in recent years by a more nuanced view of magma storage and supply, whereby melts ascend through a

vertically-extensive series of melt-rich zones, termed a 'trans-crustal magma system' (TCMS; Cashman et al. 2017). This conceptual model describes the complex processing of primary magmas throughout the entire crust by crystallisation, assimilation, and mixing (e.g., Annen et al. 2006; Annen et al. 2015). This combination of processes provides a theoretical framework to investigate the origins of the variety of mineral compositions and textures found in a single eruption's crystal cargo.

Another recent advance in understanding magmatic systems is that crystal cargoes can be rapidly assembled from different parts of a magmatic system after protracted storage (e.g., Bergantz et al. 2015; Cooper and Kent 2014; Mutch et al. 2019). Together with the TCMS model, they explain how a mineral assemblage erupted during a single event may contain: crystals formed from the carrier melt (autocrysts), crystals remobilised from other parts of the magmatic system (antecrysts), those from outside the magmatic system (xenocrysts), and crystals that form due to undercooling upon eruption (microlites) (Jerram and Martin 2008). Therefore the crystal cargo of an eruptive deposit can be thought of as a snapshot of the underlying magmatic system. While an individual eruption likely provides a partial view of the sub-volcanic plumbing, compiling data from multiple eruptions can be used to build up a picture of the whole system. Building this complete picture requires well-characterised magmatic products from as many closely-spaced eruptions as possible.

Here we use established unsupervised machine learning techniques to analyse a large (>2000) compilation of mineral compositions from a highly active arc volcano: Villarrica, Southern Andes, Chile. We reveal previously unidentified structure in erupted mineral compositions and identify trends throughout Villarrica's eruptive history related to crystal zoning and eruptive style. We utilise thermodynamic modelling to constrain the physical and chemical characteristics of Villarrica's magmatic system to assess the suitability of the TCMS model. Finally, we discuss the role of magma mixing in driving explosive behaviour at Villarrica volcano and the implications for future eruptions.

2.5 Unsupervised Machine Learning Applied to Geochemical Data

The term 'unsupervised machine learning' describes a class of algorithms that are designed to find patterns in multidimensional data. They are termed 'unsupervised' as they do not require any prior knowledge of the relationships between data. Unsupervised machine learning techniques can be used to gain insight into the structure of multivariate compositional data (data that describe quantity relative to a whole, i.e. close to a constant value such as 100%), which is common in geochemistry (e.g., Chiasera and Cortés 2011; Liu et al. 2020b; Templ et al. 2008). The main advantage of these methods is that they

allow the data to be interrogated in a multivariate sense and can highlight trends that otherwise would be difficult to identify using traditional Harker-style bi-variate plots (Cortés 2009). Cluster analysis is an unsupervised machine learning technique that attempts to group data by some measure of similarity. The most similar data points are iteratively combined, until all data points belong to a single cluster. Hierarchical cluster analysis describes the relationship of all the data points to each other during this process, producing a hierarchy of data clusters organised by their similarity.

The majority of past studies that utilise cluster analysis have used it to characterise the composition of volcanic products via analysis of whole-rock data sets, both for individual volcanoes (e.g., Mt Etna, Italy; Corsaro et al. 2013, Izu-Oshima, Japan; Kuritani et al. 2018) and regional volcanism (e.g., the Virunga Volcanic Province; Barette et al. 2017). Others have applied cluster analysis to individual phases from a single volcano e.g., silicate melt inclusions (Hamada et al. 2020); tephra glass (Liu et al. 2020a); and minerals (Caricchi et al. 2020; Cortés et al. 2007; Gleeson et al. 2021). Some, but not all, of these studies have recognised that compositional data require special mathematical treatment prior to analysis. In this study, we use a log-ratio approach (i.e., Aitchison 1986) to transform the compositional data into a compatible Euclidean geometry.

2.6 Geological Background

Villarrica (39.5°S, 71.9°W) is a Quaternary stratovolcano in the Andean volcanic arc, and part of the Chilean Central Southern Volcanic Zone (Figure 2.1a). The volcano is Chile's most active, with more than 50 recorded eruptions since the year 1558 (Petit-Breuilh Sepúlveda 2004), and is considered by the Chilean geological survey (SERNAGEOMIN), as the most hazardous of the 92 geologically active Chilean volcanoes (SERNAGEOMIN 2020). Villarrica's post-glacial (14 ka–present) eruptive activity displays a wide range in eruptive intensity and magnitude. This includes two major eruptive events, that generated the Licán (ca. 13.9 ka BP) and Pucón (ca. 3.7 ka BP) mafic ignimbrites, with estimated volumes of 10 km^3 and 5 km^3(non-DRE), respectively (Lohmar et al. 2012; Silva Parejas et al. 2010). In contrast, historic eruptions (1900–present) have ranged from Hawaiian to violent Strombolian and are dominated by effusive lava flows (Pizarro et al. 2019). However, the paroxysmal March 2015 eruption, which lasted just 20 minutes, was characterised by a 1.5 km high fire fountain (Romero et al. 2018) and is the most recent demonstration of Villarrica's explosive potential. Despite this variety in post-glacial eruptive style, Villarrica's volcanic products have a limited compositional range: 98% of the juvenile whole-rock compositions collated in this study have 52–57 wt.% SiO_2 (Figure 2.1c). However, whole-

rock data may not fully reflect the compositional variety of a magmatic system as heterogeneity may be present at a scale smaller than that of the whole-rock sample (Pichavant et al. 2007). Therefore in this study, we focus on the main mineral phases erupted at Villarrica, whose compositions give insight into magma dynamics and the physical conditions of the magmatic system.

Typical Villarrica lavas and tephras are porphyritic with 10–15 % modal crystals of mainly plagioclase feldspar and olivine, subordinate clinopyroxene, and small amounts of chromian spinel (Lohmar 2008; Lohmar et al. 2012; Morgado et al. 2015; Pioli et al. 2015; Pizarro et al. 2019). Olivine crystals are usually euhedral to subhedral, often with resorbed rims. Clinopyroxene usually occurs as an unzoned subhedral phase, while plagioclase typically occurs as subhedral, reverse-zoned crystals with oxide inclusions, or as subhedral and unzoned crystals lacking inclusions. Groundmasses range from highly vesicular to highly crystalline and are typically formed of plagioclase microlites and glass.

2.7 Materials and Methods

2.7.1 Database Compilation

We compiled a database of existing electron microprobe analyses of the most abundant mineral phases that are present in almost all of Villarrica's erupted products: olivine, plagioclase and clinopyroxene. These were sourced from published studies (Costantini et al. 2011; Morgado et al. 2015; Pioli et al. 2015; Pizarro et al. 2019; Wehrmann et al. 2014; Witter et al. 2004; Zajacz and Halter 2009), theses (Clavero-Ribes 1996; Lohmar 2008), and unpublished analyses. All data and their sources can be found in Appendix A.

To ensure that only phases relevant to the magmatic system were considered, any analyses labelled as xenolith or microlite by the original authors were removed from the data sets. The analyses were then manually screened for errors e.g., misclassified, mixed-phase and poor-quality analyses. Any analysis without an analytical total between 98 wt.% and 102 wt.% was removed. The cations per formula unit (cfu) were calculated for each mineral analysis based on stoichiometry, using 4, 32 and 6 oxygens for olivine, plagioclase and clinopyroxene, respectively. Total iron was assumed to be entirely FeO for plagioclase and olivine analyses. The method of Droop (1987) was used to calculate the proportion of Fe^{2+} to Fe^{3+} in clinopyroxene analyses. Clinopyroxene analyses with a total cfu outside 4.00 ± 0.02 were removed. After the screening, 2267 analyses (out of an initial 2611) were deemed suitable, these are broken down by eruption in Table 2.1.

Table 2.1: Breakdown of Villarrica microprobe analyses included in the compiled database by eruption. Eruption stages are shown in italics where relevant. Eruptions are ordered from oldest to youngest. Radiometric ages and their source are shown where known.

Deposit	Age (years BP)	Ol	Plag	Cpx
Dacitic Dome	95,000 ± 15,000[a]	11	20	8
Intraglacial Pyroclastic Deposit	40,000–14,000[a]	3	9	8
Licán Ignimbrite	14,500–13,500[b,c]			
Initial Fall Deposit		2	6	1
Main Eruption		19	85	48
Pucura Lava	>10,600[d]	8	10	5
Afunalhue Pyroclastic Flow	4090[d]	5	2	8
Pre-Pucón Surge		3	14	10
Pre-Pucón Lava		6	12	3
Pucón Ignimbrite	3510–3710[e]			
Initial Fall Deposit		6	8	4
Unit 1		27	31	32
Unit 2		27	56	33
Unspecified		25	56	40
Post-Pucón Lava		30	64	22
Chaimilla Fall Deposit	3180 ± 40[f]			
Lower		58	110	20
Upper		64	71	19
Unspecified		6	12	10
Los Nevados Cones	<2600 and >2600[a]	25	42	26
Chaillupén Cones	<3700 and >3700[a]	10	11	17
Historic Eruptions				
1921		42	91	54
1948		19	67	31
1963		4	0	0
1971		57	71	17
1984		16	54	0
1999		49	48	9
2000		43	81	0
March 2015		142	64	1
Post-March 2015		11	25	1
Unknown		6	0	0
	Totals	724	1120	423

BP, Before Present. Ol, Olivine. Plag, Plagioclase. Cpx, Clinopyroxene. [a]*Geología del volcán Villarrica, Regiones de La Araucanía y de Los Lagos.* (2006). [b]Moreno (1993). [c]Clavero-Ribes (1996). [d]Lara and Clavero (2004). [e]Silva Parejas et al. (2010). [f]Costantini et al. (2011).

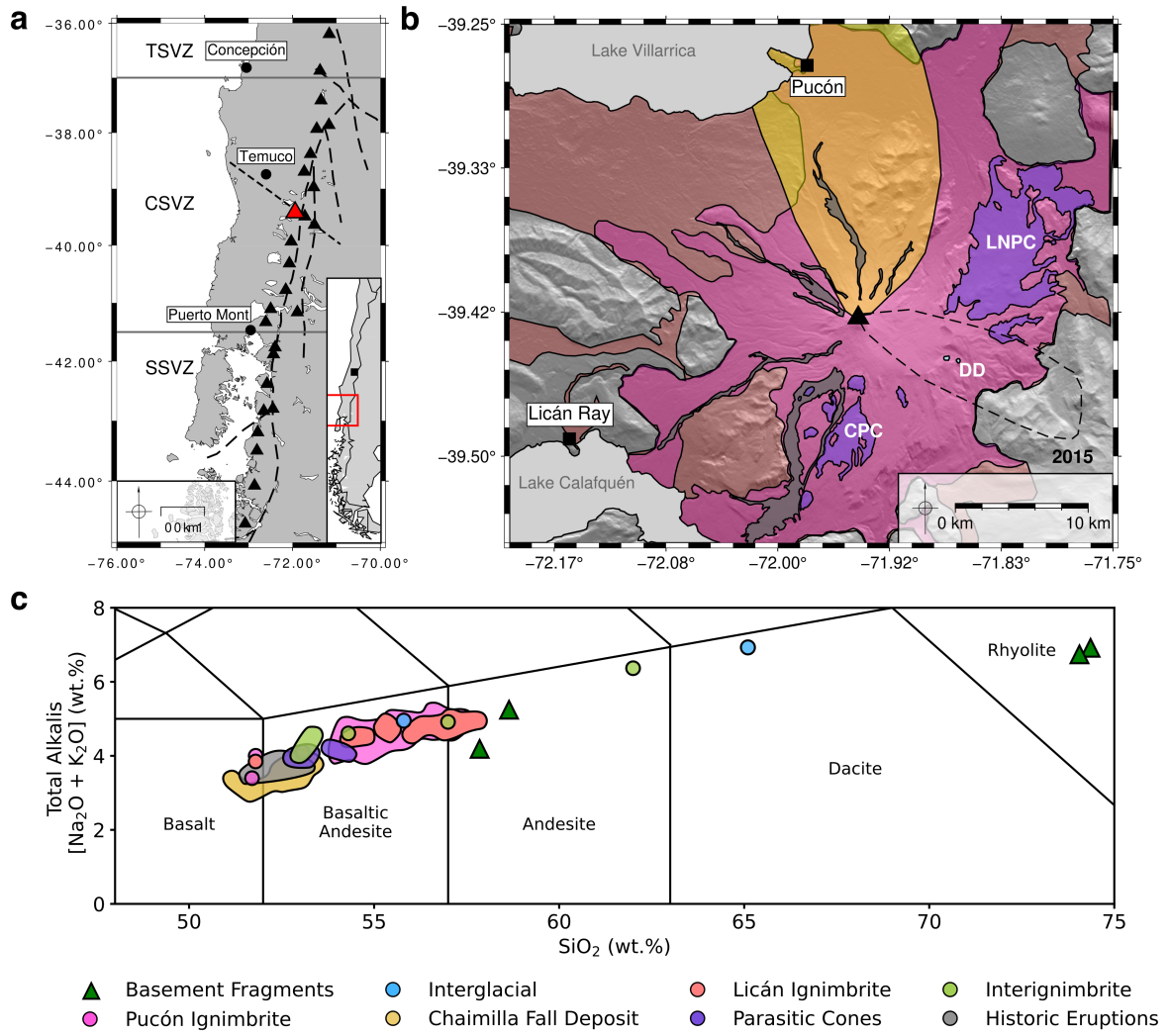

Figure 2.1: A) Map showing the location of Villarrica (red triangle) and other nearby active volcanoes (black triangles) in Chile's Southern Volcanic Zone (SVZ). The long-dashed black line is the Liquiñe-Ofqui Fault Zone, short-dashed black line is the Mocho-Villarrica Fault Zone (Cembrano and Lara 2009). TSVZ, Transitional South Volcanic Zone. CSVZ, Central South Volanic Zone. SSVZ, Southern South Volcanic Zone (Stern 2004). The inset shows the location of the CSVZ (red box) and the capital Santiago (black square). B) Simplified geological map (modified from *Geología del volcán Villarrica, Regiones de La Araucanía y de Los Lagos.* (2006)) showing the extent of key Villarrica eruptive deposits. The colour of each deposit corresponds to the legend in Figure 2.1c. LNPC, Los Nevados Parasitic Cones. CPC, Chaillupén Parasitic Cones. DD, Dacitic Domes. The location of the March 2015 tephra is shown by the black dashed line (Romero et al. 2018). C) Total-Alkali Silica (TAS; Le Bas et al. 1986) diagram showing the bulk rock compositions of Villarrica eruptions and basement rocks from past studies (Clavero-Ribes 1996; Hickey-Vargas et al. 2016; Hickey-Vargas et al. 1989; Lohmar 2008; McGee et al. 2017; Morgado et al. 2015; Pioli et al. 2015; Pizarro et al. 2019; Silva Parejas 2008; Wehrmann et al. 2014; Witter et al. 2004; Zajacz and Halter 2007). This shows the homogeneous nature of Villarrica eruptive products: the vast majority of the juvenile products (98%) have 52–57 wt.% SiO_2.

2.7.2 Data Quality and Limitations

The database used in this study contains a large (>2200) total number of analyses, but the number of analyses per eruption is much smaller: only the 2015 eruption has nearly 100 analyses for either of the

two most modally abundant minerals, olivine and plagioclase (Table 2.1). This has implications for relating compositions to textural features e.g., crystal zoning. Cheng et al. (2017) suggests that 100 or more analyses are required to characterise the compositional and textural features of a complexly zoned mineral population. However, we find no relationship between zoning and compositional clustering.

All eruptive deposits have not been sampled and analysed equally. Table 2.1 shows that there are a higher number of analyses of high-volume eruptions (the Licán and Pucón ignimbrites), historic eruptions, and those with easily accessible deposits. The main route up Villarrica, the Pucón Ski Center Road, cuts both the Pucón ignimbrite and the Chaimilla Fall Deposit and provides easy access to historic eruptions. Conversely, the Los Nevados and Chaillupén parasitic cones, and the Dacitic Domes are further from established roads and tracks. While this bias prevents us from commenting on individual eruptions that are poorly studied, a first-order understanding of Villarrica's magmatic system is still possible.

Finally, there are likely systematic errors related to the different analytical equipment in different labs, which are in turn calibrated with different standards. This results in different analytical uncertainties for each of the past studies complicating direct comparison. There is also little overlap between the eruptions sampled by different studies. Without this, there is no way to quantify these potential inter-lab biases. Despite this, over half the data was obtained from a single lab, which reduces the chance of this having an effect (Lohmar 2008). Furthermore, as discussed later in the paper, we find no systematic bias in the clustering that results from the source of the data.

2.7.3 Compositional Data Constraints and the Log-Ratio Transformation

Compositional data carry only relative information, subject to non-negative and constant-sum constraints (100 wt.% etc.). These constraints mean that often-used statistical methods that assume that data are normally distributed (i.e. unconstrained to a constant value and varying from $-\infty$ to $+\infty$), are not directly applicable. In his seminal work, Chayes (1971) established that it is the ratios between compositional data that measure variability rather than absolute differences. To circumvent this problem, Aitchison (1986) introduced several log-ratio transformations: linear transformations that map compositional data into an unconstrained Euclidean space.

There are several proposed log-ratio transformations: the additive log-ratio transformation (Aitchison 1986), the centred log-ratio transformation (Aitchison 1986) and the isometric log-ratio transformation (Egozcue et al. 2003). In this study, the mineral data sets were transformed using the isometric log-ratio (ilr) transformation (equation 2.1), implemented using the *Pyrolite* python library (Williams et al. 2020).

This transformation was chosen as it ensures the transformed data have a non-singular covariance matrix and preserves the geometric properties of the raw compositional data (Egozcue et al. 2003):

$$ilr(x) = \sqrt{\frac{i}{i+1}} \ln \left[\frac{g(x_1, \ldots, x_i)}{x_{i+1}} \right], \quad i = 1, 2, \ldots, D-1, \tag{2.1}$$

where x is a compositional analysis, i is a specific part, D is the number of parts (elements analysed), and $g(x_i)$ is the geometric mean of the parts of x:

$$g(x_i) = \left(\prod_{i=1}^{n} x_i \right)^{\frac{1}{n}}. \tag{2.2}$$

A requirement of using any log-ratio transformation is that the data cannot contain zeros (Cortés et al. 2007; Fry et al. 2000). Zeros in compositional data can be structural (e.g., K in clinopyroxene), below detection of the analytical technique, or simply not analysed (Fry et al. 2000). We removed structural zeros by only considering elements that reasonably exist in a mineral's structure. To deal with zeros resulting from detection limits, a detection limit of 0.05 wt.% was assumed for all elements. The detection limits were generalised because detection limits were not reported in all cases. Zeros resulting from detection limits were replaced using the Multiplicative Replacement method of Martín-Fernández et al. (2000) and Fry et al. (2000), which is equivalent to distributing a detection limit threshold evenly among the below detection zeros. Not all elements (especially minor elements) were analysed in every study. Elements that were measured for less than half of each of the mineral data sets were not used in our analysis. The elements used in cluster analysis for each of the mineral data sets are shown in table A.1.

Variables with low abundances but high relative variances (often minor and trace elements) have high log-ratio variances and therefore dominate any analysis of the complete log-ratio transformed data set (Baxter et al. 2005; Greenacre 2019; Greenacre and Lewi 2009). To prevent this, we normalised the log-transformed data set using the column (part) medians and standard deviations:

$$X' = x'_{ij} = \frac{x_{ij} - \tilde{x_i}}{\sigma_i} \tag{2.3}$$

where X' is the normalised data set, x_{ij} the i^{th} part of the j^{th} analysis, $\tilde{x_i}$ is the column median, and σ_i is the column standard deviation. The median was chosen over the arithmetic mean as the transformed data sets were non-normal: all four ilr-transformed data sets failed the Henze-Zirkler multivariate normality test with a specificity of 0.05 (Henze and Zirkler 1990). Relationships between the transformed

compositional data were then explored using hierarchical clustering methods over an Euclidean space.

2.7.4 Hierarchical Cluster Analysis

Hierarchical clustering algorithms attempt to group data into clusters by some measure of similarity. Agglomerative clustering methods start by grouping the two most similar data points into a cluster and then treating them as a single data point. The most similar data points or clusters are then iteratively combined until only a single cluster containing all the data remains. To cluster the data, a measure of dissimilarity (often called distance) must be chosen. A popular measure is the Euclidean distance which is the equivalent of Pythagoras's Theorem but over more than two dimensions:

$$d_E = \sqrt{\sum_{i=1}^{n} (x_i - y_i)^2} \tag{2.4}$$

where d_E is the Euclidean distance matrix, i is the number of parts, and x and y are the points considered.

Next, a linkage method must be chosen, i.e. a method describing how the distances between points and clusters are used to relate them. We used ward clustering (Ward 1963), which minimises the in-cluster variance, over alternatives such as single-linkage or average-linkage as it doesn't suffer from chaining (Williams and Lambert 1966; Wishart 1969). The hierarchical clustering algorithm was implemented using the scikit-learn python library (Pedregosa et al. 2011). Dendrograms depicting the resultant hierarchy were used to determine a suitable number of clusters independently for each mineral data set. Choosing the number of clusters that best represent the data set is a balance between showing global versus local variability: a small number of clusters will highlight the largest differences in the data at the cost of potentially obscuring more subtle differences, and vice versa for a large number of clusters. Figure 2.2 shows that the olivine and plagioclase data sets are well described by two clusters until almost half of their respective maximum distances. However, to maximise our ability to detect more subtle compositional changes between clusters we chose the next lowest number of clusters that well describe them. This was chosen by finding the maximum separation (second highest for olivine and plagioclase) between branches on the dendrogram. This results in three, five and four clusters for olivine, plagioclase and clinopyroxene, respectively.

We assessed the robustness of the identified clusters by repeatedly (1000×) resampling half of each mineral's data set and performing hierarchical clustering. the clusters from sub-sampled data were consistent with those identified in the complete data set, demonstrating that they are not strongly dependent on the

size of our complete database. Further details can be found in Appendix A, section A.2.

2.7.5 Multivariate Outlier Detection

Each cluster contained points normally distributed about its centre, therefore outliers are, according to the empirical rule for normal distributions, those values located at distances larger than three standard deviations from its centre. To identify potential outliers, the Mahalanobis distance, i.e. the distance of a given data point x and a distribution (Mahalanobis 1936), was calculated for each cluster:

$$D_M(\vec{x}) = \sqrt{(\vec{x} - \vec{\mu})^T C^{-1} (\vec{x} - \vec{\mu})} \tag{2.5}$$

where D_M is the Mahalanobis distance, $\vec{x}$ is a matrix of data points in each cluster, and $\vec{\mu}$ and C are the location and covariance estimators. The location and covariance estimators were robustly calculated using the Minimum Covariance Determinant estimator (MCD) (as in Filzmoser and Hron 2008), implemented using the FastMCD algorithm (Rousseeuw and Driessen 1999) available in the scikit-learn python package (Pedregosa et al. 2011). The Mahalanobis distances for each cluster can be approximated by a χ^2 distribution (Rousseeuw and Zomeren 1990). A critical Mahalanobis distance was determined for each cluster, above which a point is considered an outlier:

$$D_M > (\chi^2_{p,1-\alpha})^{1/2}, \tag{2.6}$$

which is the square root of the upper-α quartile of the χ^2 distribution with p degrees of freedom, which were 5, 7, and 10 for olivine, plagioclase and clinopyroxene, respectively. The typical choice for (1-α) 0.975 (Rousseeuw and Zomeren 1990) was used i.e., the outliers will be contained in the upper 2.5 % of the χ^2 distribution. Any identified outliers were removed from the data sets.

2.7.6 Estimating Cluster Centres

To characterise each of the identified clusters, a measure of central tendency is required. For compositional data, the best unbiased estimator of the expected value is defined by the closed geometric mean Cortés et al. 2007, and references within. To ensure that the centre of the cluster is a valid mineral composition, the closed geometric mean of each cluster was calculated, and the nearest (according to a Euclidean distance matrix) data point to each mean was used to represent each cluster.

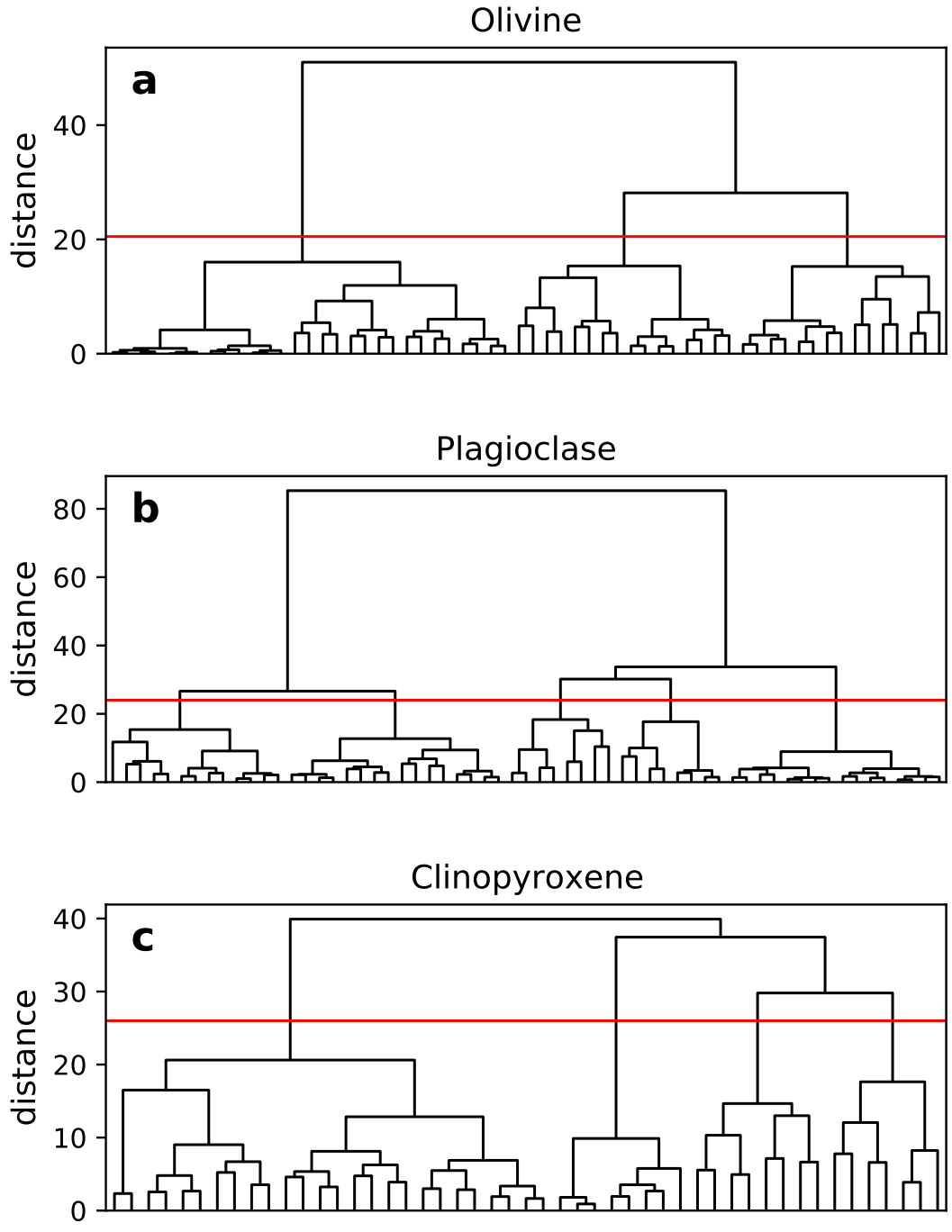

Figure 2.2: Dendrogram for each mineral data set, only the top five levels of each dendrogram are shown. The cutoff line which determines the number of clusters is shown by the red horizontal line.

2.7.7 Thermodynamic Modelling

The current consensus, especially in arc settings, is that the majority of erupted minerals are remobilised antecrysts from a mushy magmatic system (Edmonds et al. 2019). This means it is unlikely that an erupted mineral-phase is in equilibrium with its carrier liquid, making traditional mineral-liquid thermobarometry impossible. For the same reason, mineral-mineral thermobarometry (e.g., olivine-augite) may not be accurate, unless equilibrium is also strongly supported by textural evidence. To circumvent these issues we compare measured mineral compositions to many thermodynamic simulations of a simple Villarrica-like system, with a range of intensive variables. This avoids the need for mineral-liquid and mineral-mineral equilibrium.

Thermodynamic modelling was carried out to investigate the likely provenance of the identified mineral clusters with respect to the physical and chemical conditions of magma evolution at Villarrica. We used the rhyolite-MELTS v1.2.0. algorithm (Ghiorso and Gualda 2015; Gualda et al. 2012), via the alphaMELTS 2.0 (originally Adiabat_1ph; Smith and Asimow 2005) front end, to model crystal fractionation from a primitive input melt. The initial bulk composition of each model was estimated using the most primitive glass composition reported at Villarrica: a post-entrapment-crystallisation corrected, olivine-hosted melt inclusion (VL15B-ol5-inc1, Mg# 65 at QFM+1) from an upper unit of the Chaimilla Fall Deposit (Pioli et al. 2015). Isobaric fractional crystallisation models were performed with temperature decreasing in 1 °C increments from above the liquidus, at a range of pressures (25 MPa, 50 MPa, 75 MPa and 100 MPa and then increments of 100 MPa from 200–700 MPa), variable initial water contents (0.0–6.0 wt.% in increments of 0.5 wt.%, and oxygen fugacity buffers (fO_2) QFM−0.5 (0.5 log units below the Quartz-Fayalite-Magnetite buffer) to QFM+2.25, in increments of 0.25 log units. A total of 1560 rhyolite-MELTS simulations were performed, one for each pressure, H_2O and fO_2 permutation.

We identified the best-fit intensive variables by comparing the composition of minerals crystallised in each rhyolite-MELTS simulation to those in each identified cluster. We calculated the cfu, and then *ilr*-transformed the composition of olivine, plagioclase and clinopyroxene crystallised at each temperature step for all 1560 rhyolite-MELTS simulation by the same procedure as for the measured compositions. As detection limits are not defined sensu stricto in MELTS, any zeros in the simulated compositions were replaced with 0.0001 cfu. With both the simulated and measured compositions in the same Euclidean space, we used the Euclidean distance between each as a measure of similarity (equation 2.4). The best-fitting intensive variables were those that produce the 'closest' compositions to those measured: those that have the smallest distance.

To back out the best-fit intensive variables for each cluster, we calculate the weighted arithmetic mean and weighted standard deviation of the best-fitting T, P, fO_2, and H_2O from all measured compositions that comprise the cluster. The weights used were the inverse of the Euclidean distance: the measured compositions that were best reproduced by a simulation are given a higher weight. The weighted average and standard deviation for each mineral cluster are given in Table 2.3 and plotted in Figure 2.7.

We used a Monte-Carlo approach to estimate the effects of the analytical uncertainty in the initial bulk composition inputted into the Rhyolite-MELTS simulations and the analytical uncertainty in the clustered mineral compositions. Normal distributions of both the bulk composition and mineral compositions were randomly sampled according to their analytical uncertainties and the resultant simulations compared to the measured compositions, further details can be found in Appendix A. The maximum resultant uncertainties are comparable to those of mineral-liquid or mineral-mineral thermobarometric methods: ca. 50 °C, 200 MPa, 0.5 log units, and 1.5 wt.% H_2O. This is to be expected as both MELTS and thermobarometers are calibrated on experimental data sets from the Library of Experimental Phase Relations (LEPR; Hirschmann et al. 2008).

2.8 Results

The compositions of minerals erupted in Villarrica's crystal cargoes are diverse, especially in comparison to whole-rock compositions (Figure 2.1c). Olivine compositions range from Fo_{50-87}, plagioclase An_{50-96}, and clinopyroxene Mg_{57-92}. Despite this range in mineral compositions, hierarchical cluster analysis and outlier detection were performed successfully on the three mineral data sets. We identified 4, 94 and 15 outliers for olivine, plagioclase and clinopyroxene, which corresponds to 0.6 %, 8.4 % and 3.5 % of each respective data set. The representative compositions (centres) of each identified mineral cluster are shown in Table 2.2. The clusters are ordered from most primitive to most evolved (e.g., Ol_1 is the most primitive olivine). Violin and box-plot diagrams showing the compositional differences for each mineral's clusters are included in Appendix A. We compared the cluster designations with each composition's source study and found no obvious dependence. Cluster designations appear to be purely compositional.

To visualise the distribution of the identified clusters and verify that they were compositionally distinct, two techniques were chosen to reduce the dimensionality of the ilr-transformed data. First, principal component analysis (PCA) was performed and the resulting first and second principal components were plotted (Figure 2.3a-c). Then a t-distributed Stochastic Neighbour Embedding (t-SNE) algorithm (Van der Maaten and Hinton 2008) was implemented with a perplexity value of 40. 10,000 iterations were used to ensure that the projection was stable (Figure 2.3d-f). Both the PCA and t-SNE projections show that the clusters identified by hierarchical cluster analysis are well-defined and have good separation. The distribution of outliers implies that outlier detection was successful: outliers are evenly distributed among the identified clusters and do not form clusters of their own.

A major advantage of cluster analysis and the multivariate methods used in this study is that they allow patterns to be identified in multivariate space and reveal trends that are hard to detect using traditional bivariate plots. A good example of this is shown by the olivine data set. Figure 2.4 shows probability density functions (PDFs) for each of the mineral data sets and the identified clusters generated using Kernel Density Estimation (Silverman 1986). The molar forsterite content ($X_{\mathrm{Fo}} = 100 \cdot \mathrm{Mg}/[\mathrm{Mg}+\mathrm{Fe}^{2+}+\mathrm{Mn}]$), molar anorthite content ($X_{\mathrm{An}} = 100 \cdot \mathrm{Ca}/[\mathrm{Ca}+\mathrm{Na}+\mathrm{K}]$), and molar magnesium number ($\mathrm{Mg}_{\#} = 100 \cdot \mathrm{Mg}/[\mathrm{Mg}+\mathrm{Fe}^{2+}]$) were calculated, for olivine, plagioclase and clinopyroxene, respectively. The resulting PDFs were multiplied by the number of data points in each cluster, making them analogous to non-normalised histograms. The distribution of molar Fo for the complete olivine data set might suggest

the existence of two clusters with Fo_{76} and Fo_{84}. However, our clustering approach, which considers the concentration of multiple elements (including minor elements), detects three clusters which could not be identified by looking at the PDF of the complete data set alone. This demonstrates how cluster analysis can identify and reveal otherwise hidden structure in mineral composition data sets by detecting similarities in all elements analysed.

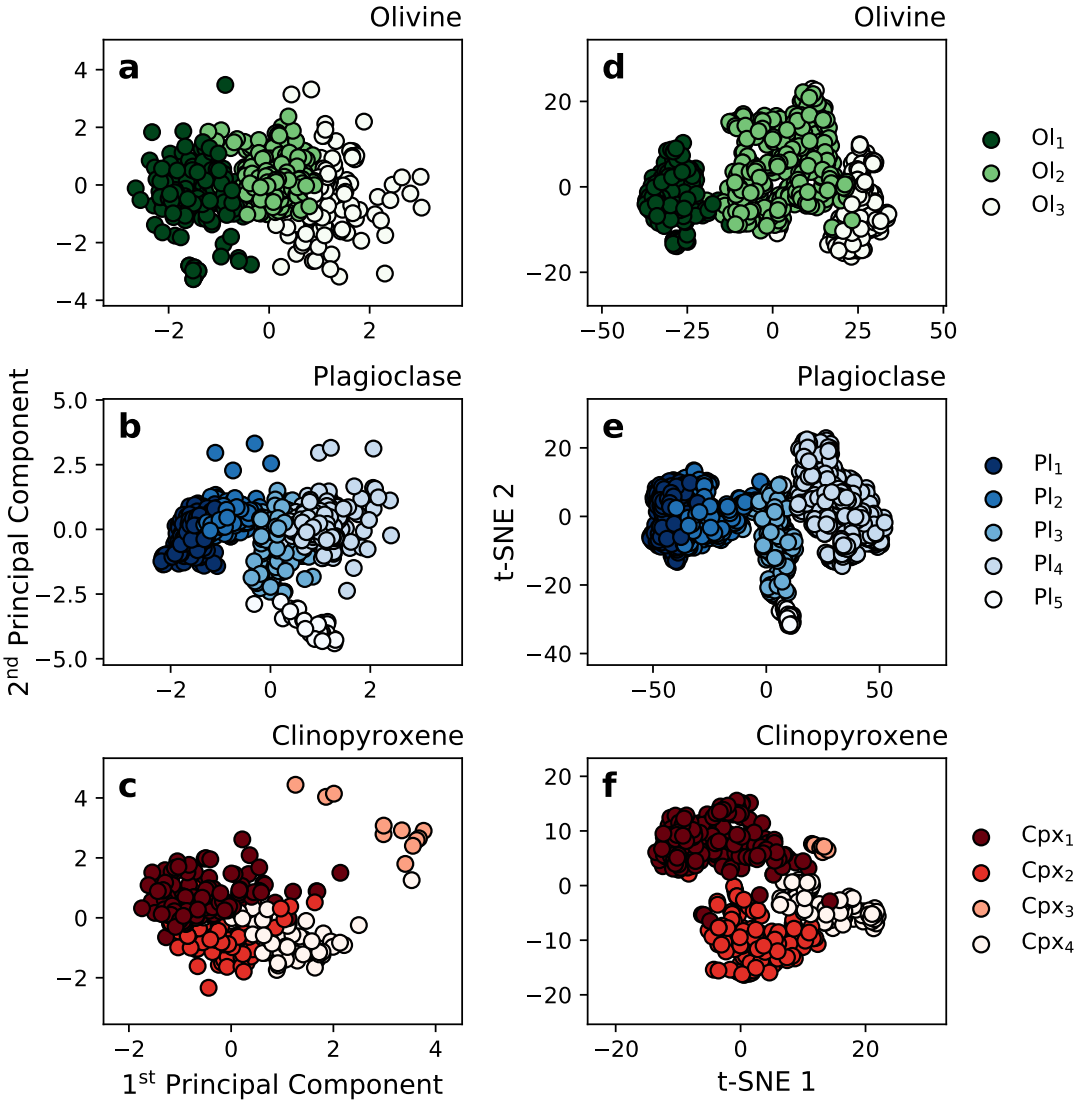

Figure 2.3: **(a-c)** Clustered data projected using the first and second principal components. **(d-f)** Clustered data projected using t-distributed stochastic neighbourhood embedding (t-SNE) axes. Both projections show that the clusters identified by hierarchical clustering are well-defined.

Table 2.2: Representative compositions of each identified mineral cluster, given in wt.% oxide and cations per formula unit. The concentration of FeO and Fe_2O_3 in clinopyroxene was calculated with the method of Droop (1987). Clusters are ordered from most to least primitive.

Mineral	Olivine			Plagioclase					Clinopyroxene			
Cluster	Ol_1	Ol_2	Ol_3	Pl_1	Pl_2	Pl_3	Pl_5	Pl_5	Cpx_1	Cpx_2	Cpx_3	Cpx_4
SiO_2 (*wt%*)	39.67	38.30	37.21	45.56	48.08	51.30	53.67	57.61	51.51	50.15	51.29	51.52
TiO_2									0.46	0.78	0.53	0.67
Al_2O_3				33.27	32.95	30.23	28.61	27.22	2.29	3.59	2.52	1.86
Cr_2O_3									0.49	0.09	0.10	b.d.
Fe_2O_3	-	-	-	-	-	-	-	-	1.57	2.09	0.00	1.86
FeO	15.57	21.40	26.56	0.49	0.64	0.79	0.87	0.43	6.16	6.97	8.91	9.85
MnO	0.24	0.35	0.44						0.20	0.23	0.22	0.45
MgO	45.21	39.80	34.86	0.08	0.12	0.12	0.18	b.d.	16.88	14.51	14.59	14.52
CaO	0.18	0.25	0.24	17.59	16.93	13.79	12.66	9.58	19.04	20.55	19.93	19.32
Na_2O				1.26	2.03	3.76	4.31	5.82	0.27	0.29	0.23	0.27
K_2O				b.d.	b.d.	0.10	0.18	0.19				
Si (*mol*)	0.991	0.992	0.997	10.375	10.601	11.184	11.500	12.060	1.958	1.934	1.968	1.958
Ti									0.013	0.023	0.015	0.019
Al				4.464	4.281	3.883	3.612	3.358	0.051	0.082	0.057	0.091
Cr									0.007	0.001	0.002	b.d.
Fe^{3+}	-	-	-	-	-	-	-	-	0.022	0.030	0.000	0.027
Fe^{2+}	0.325	0.464	0.595	0.093	0.118	0.144	0.156	0.075	0.193	0.222	0.281	0.314
Mn	0.012	0.008	0.010						0.007	0.008	0.007	0.014
Mg	1.683	1.537	1.393	0.027	0.039	0.039	0.058	0.016	0.956	0.834	0.835	0.823
Ca	0.005	0.007	0.007	4.291	3.999	3.221	2.907	2.149	0.775	0.849	0.819	0.787
Na				0.278	0.434	0.795	8.94	1.181	0.010	0.011	0.009	0.010
K					b.d.	b.d.	0.014	0.025	0.025			
Fo (*mol%*)	83.60	76.54	69.71									
An				93.76	90.07	79.93	75.98	64.04				
Mg#									83.19	78.94	74.83	72.40

Blank cells denote elements not used in cluster analysis. b.d., below detection limit. -, not calculated. Fo, molar forsterite content. An, molar anorthite content. Mg#, magnesium number.

Olivine compositions were grouped into three clusters, whose cfu contents show the expected proportionality with Fo (Table 2.2). Fe^{2+}, Si and Mn are all inversely proportional to Fo. However, Ca varies independently of Fo and the other elements, and therefore has the potential to give insight into differing parental magma minor-element compositions and/or differing H_2O-contents (Gavrilenko et al. 2016; Kamenetsky et al. 2006).

Plagioclase compositions were grouped into five clusters. These show expected trends with increasing An-content: increasing Ca and Al; and decreasing Si, Na and K (Table 2.2). However, Mg and Fe covary independently of the other elements and An-content. That they covary implies that the variations reflect one or more physical processes and are not due to the potentially high analytical uncertainties associated with Fe and Mg in plagioclase (Ginibre and Wörner 2007). Variations in Fe and Mg in plagioclase independent of other elements, have been attributed to changes in Fe and Mg in the parental melt (Ginibre and Wörner 2007; Singer et al. 1995), but might reflect melt-plagioclase disequilibrium caused by rapid growth (Ginibre and Wörner 2007; Mollo et al. 2011; Singer et al. 1995).

Clinopyroxene compositions were grouped into four clusters. However, the representative compositions show more complex trends than for plagioclase and olivine (Table 2.2). The identified clusters were characterised as follows: (1) high-Cr and high-Mg#, (2) high-Al and high-Ti, (3) low-Fe^{3+}, and (4) low-Al and low-Mg#. This might be the result of the higher complexity of the clinopyroxene mineral structure, compared to feldspar and olivine. However, the identified clusters still appear to show some expected correlations with Mg#, with the most primitive Cpx_1 having the lowest incompatible elements, e.g., Mn and Ti, and Cpx_4 having higher incompatible elements and Ca. Cpx_3 has much lower calculated Fe^{3+} content compared to the other three clusters which could reflect significantly different oxidation conditions during crystallisation.

2.8.1 Controls On Cluster Membership

2.8.1.1 Crystal Zoning

Original studies classified each mineral analysis as unzoned, zoned – cores, intermediates, or rims. However, this information was not reported for a significant number of analyses (olivine: 20%, plagioclase: 32%, clinopyroxene: 35%), and there is no way to judge the accuracy of the designations. Therefore it was assumed that each of the source studies categorised their analyses in the same manner. Figure 2.5 shows the proportion of crystal zones in each cluster for each category. There is no clear relationship between the cluster distribution and zoning for any of the three minerals.

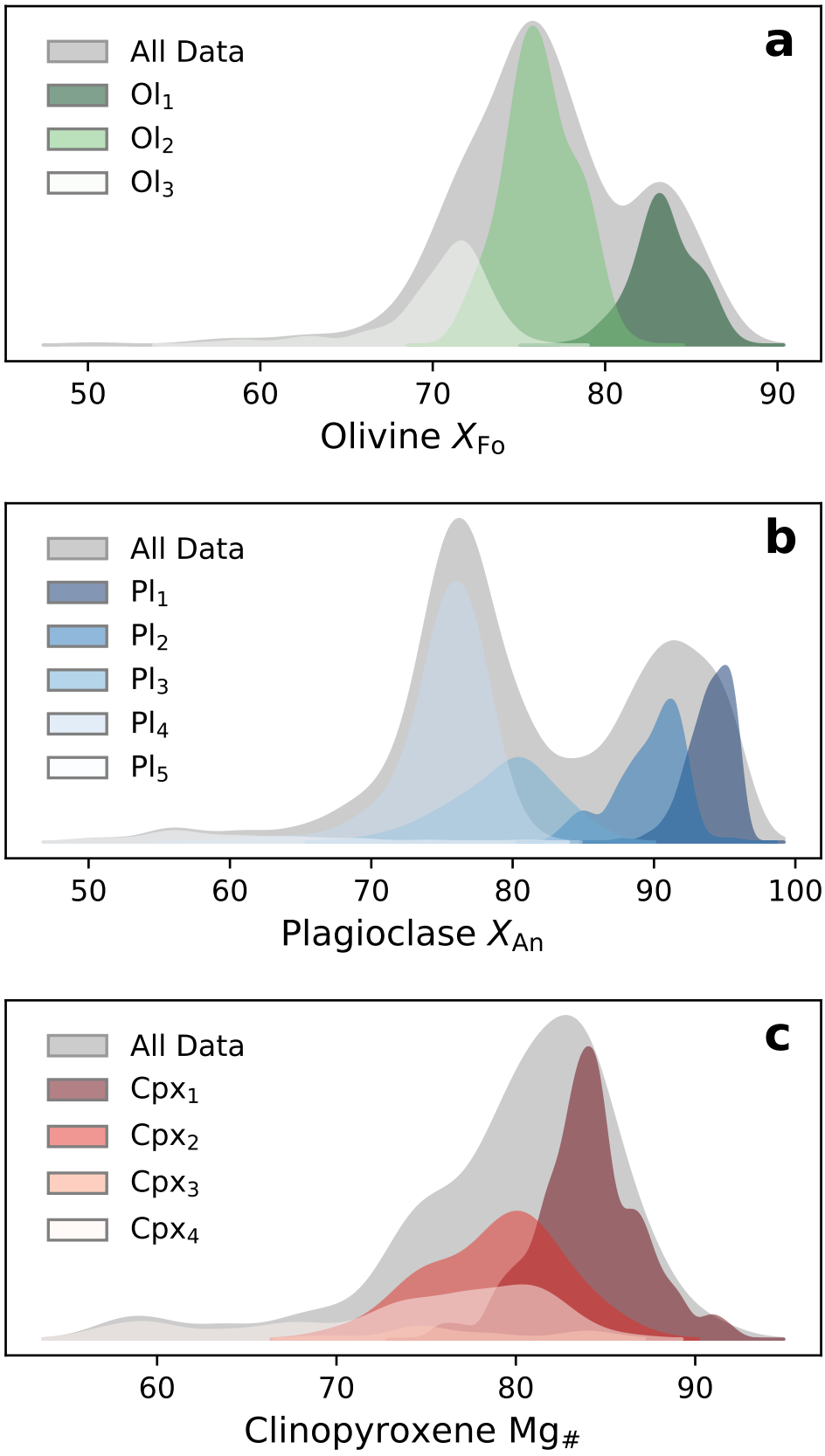

Figure 2.4: Plots of probability density functions (PDF) generated using Kernel Density Estimators (KDE) of each mineral subset and its clusters. Each PDF is scaled by the number of data points it was generated from, analogous to a histogram. Comparisons of the distribution of identified clusters with each respective complete data set highlights the ability of cluster analysis to identify otherwise hidden structure in mineral compositions.

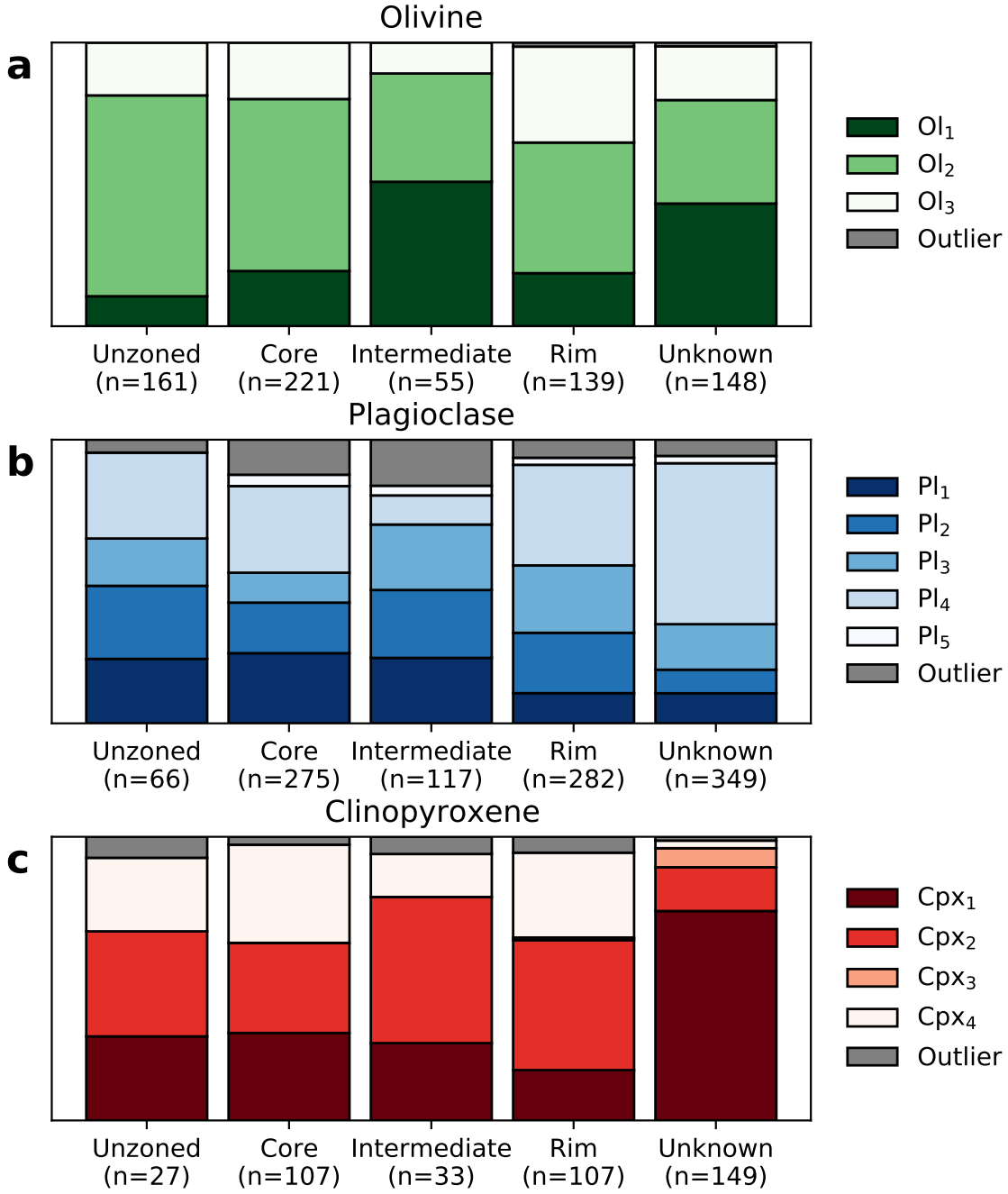

Figure 2.5: Stacked bar charts showing the effect of crystal zoning on cluster membership. The number of analyses in each category is shown in brackets. There is no clear pattern between cluster membership and crystal zoning.

2.8.1.2 Eruption Age

Figure 2.6 shows the proportion of phenocrysts from each cluster within individual eruptive deposits sorted by age. There is a stark contrast between the composition of crystal cargoes of historic eruptions (erupted in the last 100 years) and prehistoric eruptions (ca. 95–1.6 ka). Generally, the crystal cargoes of historic eruptions contain a smaller variety of crystal compositions. This is especially pronounced for feldspar and clinopyroxene compositions (Figure 2.6b,c). Both feldspar and clinopyroxene compositions become markedly more homogeneous through to the present day: erupted plagioclase compositions are dominated by Pl_4 and clinopyroxene compositions are dominated by Cpx_1. Generally, historic eruptions contain a higher proportion of Ol_2 than prehistoric eruptions, but olivine compositions are more variable than both plagioclase and clinopyroxene (Figure 2.6).

Of the three minerals considered in this study, olivine cluster proportions vary the most from eruption to eruption. For example, the Licán ignimbrite has a large proportion of primitive olivine (Ol_1) whereas the Pucón ignimbrite is made up almost entirely of more evolved olivine (Ol_3). The historic eruptions are dominated by more evolved olivine (Ol_2). However, the March 2015 eruption is distinct from the other historic eruptions, as it has a large proportion of all three olivine clusters. Therefore the olivine portion of the March 2015 eruption's crystal cargo is more similar to prehistoric crystal cargoes, than the other historic eruptions.

The proportion of plagioclase clusters varies widely between the historic and prehistoric eruptions. Generally, the prehistoric eruptions contain a greater variety of plagioclase compositions: the Dacitic Dome, Licán and Pucón ignimbrites are the only eruptions to contain all five plagioclase clusters. The most evolved plagioclase cluster (Pl_5) only occurs in the three oldest eruptions: the Dacitic Dome, and the Licán and Pucón ignimbrites. The most primitive plagioclase (Pl_1) is restricted almost entirely to prehistoric eruptions. In contrast, the crystal cargoes of the historic eruptions are dominated by the intermediate Pl_4, whose proportion increases through time from the 1921 eruption through to the March 2015 eruption.

Clinopyroxene cluster membership broadly corresponds to that of olivine and plagioclase: the greatest amount of variation is present in the oldest eruptions. Clinopyroxene becomes both more scarce and more compositionally homogeneous in later eruptions: cluster Cpx_2, Cpx_3 and Cpx_4 are most abundant in the prehistoric eruptions while Cpx_1 is noticeably more abundant in the historic eruptions. Very little clinopyroxene has erupted since the 1948 eruption.

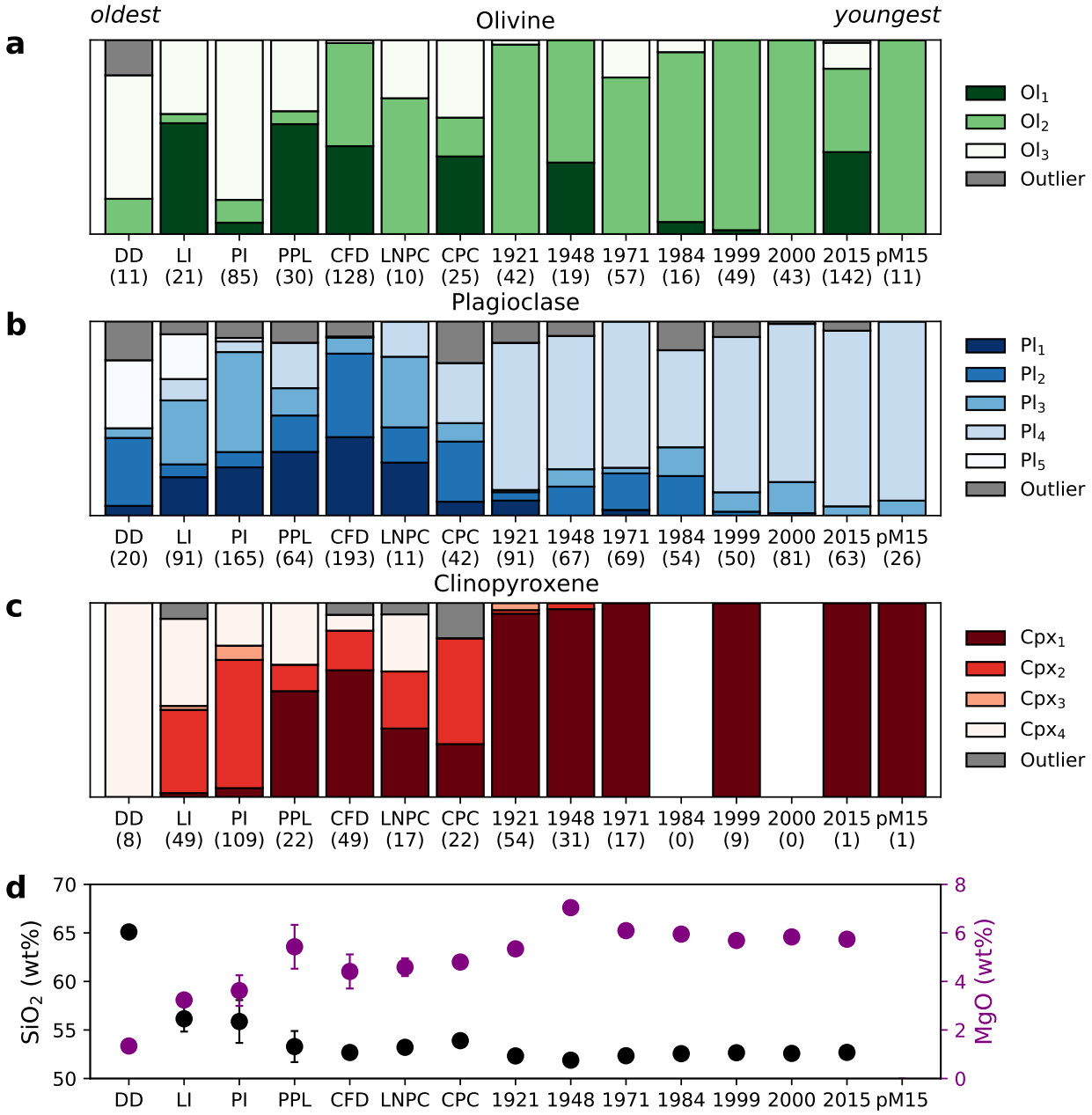

Figure 2.6: **(a-c)** Stacked bar charts showing the cluster membership of the different eruptions sorted by age. The number of analyses for each eruption is shown in brackets. Only those eruptions with more than 10 phenocryst compositions are shown. DD, Dacitic Dome. LI, Licán Ignimbrite. PI, Pucón Ignimbrite. PPL, Post-Pucón Lava. CFD, Chaimilla Fall Deposit. LNPC, Los Nevados Parasitic Cones. CPC, Chillupén Parasitic Cones pM15, post-March 2015. Historic eruptions are labelled by eruption year. **(d)** Plot of mean whole-rock SiO_2 and MgO contents. Error bars show ±1 standard deviation. There are no whole-rock analyses for the post-March 2015 samples. Whole-rock data sources are the same as in Figure 2.1.

2.8.1.3 Eruptive Center Location

Villarrica's flanks host over 30 parasitic or adventitious cones which form two groups: the Los Nevados group to the northeast and the Chaillupén group to the south (*Geología del volcán Villarrica, Regiones de La Araucanía y de Los Lagos.* 2006) (Figure 2.1b). Other than the scoria and lavas of these two groups of cones, all other eruptive deposits are thought to originate from Villarrica's main vent, although the location of this main vent has changed through time (*Geología del volcán Villarrica, Regiones de La Araucanía y de Los Lagos.* 2006). The cluster membership for the two groups of parasitic cones is shown in Figure 2.6 (labelled LNPC and CPC, respectively). The proportion of phenocrysts in each cluster for the two groups of cones is distinct. For example, the Chaillupén cones contain the most primitive olivine (Ol_1), and none of the most evolved clinopyroxene (Cpx_4), unlike the Los Nevados cones. This could be because the two sets of cones tap different parts of Villarrica's magmatic system, or they sample the system at different points in time. Compared to the eruptions from the central vent, the two sets of parasitic cones are more diverse than the historic eruptions, and most similar to the prehistoric eruptions. This is especially apparent when comparing the olivine and clinopyroxene cluster memberships. More detailed studies of the two groups of cones are needed to constrain their ages and their petrological differences to each other and products from the main vent (e.g., Robidoux et al. 2021).

2.8.1.4 Eruption Volume and Intensity

Villarrica's post-glacial eruptions show large variations in volume and intensity, most notable are the differences between the explosive high-volume mafic ignimbrites (Licán and Pucón) with the smaller-volume, comparatively effusive, historic eruptions. The large volume of the ignimbrites and their association with caldera collapse suggests that a larger portion of the magmatic system was evacuated during those eruptions. This might be expected to produce products with a higher compositional variety, e.g., both evolved and primitive compositions, especially if the magmatic system were to contain multiple somewhat isolated bodies that differentiated independently. This is indeed reflected in the cluster memberships of the historic versus older eruptions. Generally, the more explosive, older eruptions have a higher diversity in mineral compositions, especially the Licán and Pucón ignimbrites. Of the historic eruptions the intense March 2015 eruption, which produced a 1.5 km high fire fountain, erupted more diverse olivine compositions than any other historic eruption.

2.8.2 Thermodynamic Modelling

The representative compositions identified by hierarchical clustering were well reproduced by the relatively simple model set-up, shown by the low minimum distances (Table 2.3). However, the most primitive clusters (Ol_1 and Pl_1) have higher minimum distances than the other olivine and plagioclase clusters. This suggests that the initial bulk composition used, a primitive melt inclusion found at Villarrica, was not sufficiently primitive to reproduce exactly these compositions. However, the calculated distances are not so different as to suggest that the models do not provide a reasonable indication of the conditions of crystallisation.

The best-fitting pressure and temperature conditions from the rhyolite-MELTS simulations agree with the broad estimates available from previous thermobarometric studies (Figure 2.7). Pressures from both our simulations and past thermobarometry imply that polybaric crystallisation, extending to at least the mid to lower crust (ca. 600 MPa), is required to produce the variety of erupted mineral compositions at Villarrica. The predicted temperatures from rhyolite-MELTS (800–1000 °C) are less than those calculated by thermobarometry (1050–1250 °C). This discrepancy is likely due to the high (>2 wt.%) water contents of the majority of the best-fitting rhyolite-MELTS simulations as the olivine-augite geothermometer used by past studies was not calibrated on experiments with high water contents, and therefore likely overestimated temperatures (Loucks 1996).

Table 2.3: The weighted average of best fitting conditions for all compositions in each identified mineral cluster compared to rhyolite-MELTS thermodynamic models. One weighted standard deviation of the best-fitting conditions per cluster is shown. Oxygen fugacity offset (ΔfO_2) is shown in log units relative to the QMF buffer.

Mineral	Cluster	T (°C)	P (MPa)	ΔfO_2	H_2O (wt.%)	Min. Dist.
Ol	Ol_1	1090 ± 33	382 ± 147	0.73 ± 0.47	4.65 ± 0.84	0.042±0.068
	Ol_2	1048 ± 18	245 ± 89	0.05 ± 0.35	3.47 ± 0.70	0.024±0.018
	Ol_3	1018 ± 29	267 ± 109	−0.19 ± 0.29	3.54 ± 0.97	0.033±0.031
Pl	Pl_1	1010 ± 16	216 ± 46	−0.23 ± 0.56	5.24 ± 0.43	0.133±0.183
	Pl_2	1031 ± 42	185 ± 86	0.16 ± 0.70	4.14 ± 1.32	0.035±0.024
	Pl_3	1050 ± 70	232 ± 190	0.70 ± 0.90	2.67 ± 1.65	0.031±0.012
	Pl_4	1055 ± 81	311 ± 223	0.79 ± 0.86	2.36 ± 1.71	0.044±0.015
	Pl_5	978 ± 74	336 ± 245	0.98 ± 1.01	3.36 ± 1.69	0.025±0.012
Cpx	Cpx_1	1006 ± 68	57 ± 35	1.91 ± 0.41	0.79 ± 1.43	0.029±0.035
	Cpx_2	1010 ± 64	86 ± 74	0.92 ± 0.61	1.58 ± 1.72	0.017±0.018
	Cpx_3	926 ± 103	105 ± 108	1.10 ± 0.54	1.89 ± 2.49	0.083±0.074
	Cpx_4	985 ± 73	49 ± 27	1.40 ± 0.44	0.41 ± 1.12	0.037±0.065

T, temperature. P, pressure. Min. Dist., the minimum distance between *ilr*-transformed simulated and measured compositions.

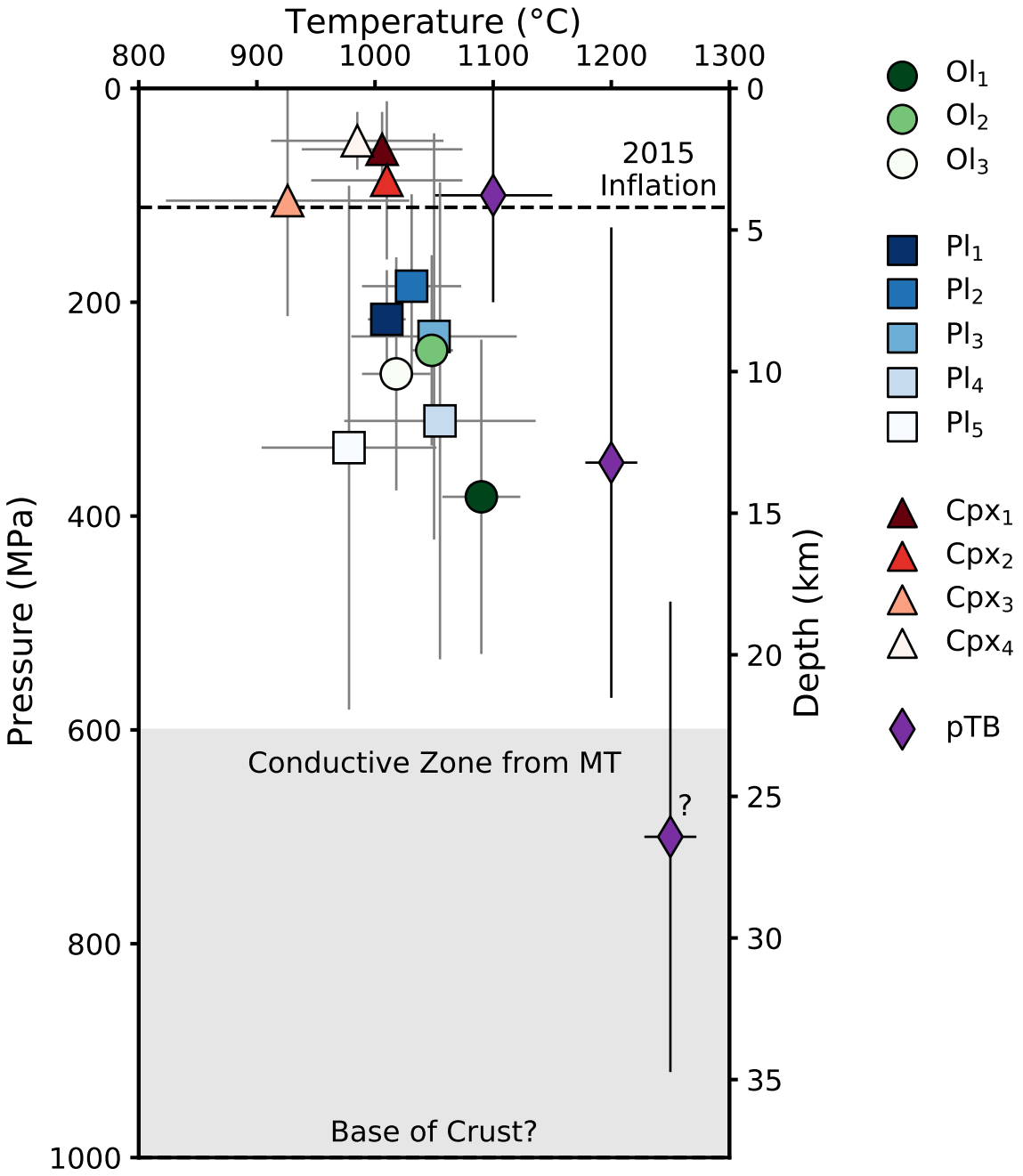

Figure 2.7: Weighted average of best fitting temperature and pressures from rhyolite-MELTS simulations for each of the identified mineral clusters. Grey error bars show ± one weighted standard deviation of best-fit pressures and temperatures per cluster. pTb, a compilation of past thermobarometry from past studies that correspond to a shallow, mid and deep-crustal storage (Lohmar 2008; Lohmar et al. 2012; Morgado et al. 2015; Pioli et al. 2015; Pizarro et al. 2019; Witter et al. 2004). The error bars correspond to the range of uncertainty for each result. The deep region is based on a single olivine-augite pair and therefore is less certain than the shallow and mid-crustal results. The corresponding depth is calculated assuming a constant density of 2.7 g·cm^{-3}. The black dashed line is the calculated depth (ca. 4.2 km) of re-inflation after the March 2015 eruption (Delgado et al. 2017). The grey shading corresponds to an area of high conductivity (ca. 19–50 km) (Kapinos et al. 2016).

The most primitive olivine (Ol_1) formed at relatively high temperatures and pressures (1093 °C, 382 MPa). Furthermore, Ol_1 has both the highest fO_2 and water content (QFM+0.73, 4.65 wt.%). This is in agreement with experimental and natural studies of olivine crystallisation from basaltic melts (Feig et al. 2010; Gavrilenko et al. 2016). This suggests that it formed from relatively primitive undegassed melts with a relatively low residence time in the crust prior to crystallisation. In contrast, the most evolved olivine cluster (Ol_4) formed at a lower temperature, pressure, fO_2, and water content. The two most primitive plagioclase clusters (Pl_1 and Pl_2) have high water contents (>4.0 wt.%) and relatively high temperatures (>1010 °C), as expected from experimental studies (Panjasawatwong et al. 1995; Takagi et al. 2005; Waters and Lange 2015). In contrast, the most evolved plagioclase (Pl_5) has a significantly lower crystallisation temperature (978 °C), and a notably higher pressure and fO_2 (336 MPa, QFM+0.98). All representative clinopyroxene compositions are best fit at lower pressures (50–100 MPa), and at a variety of temperatures (970–1041 °C) and water contents (0.0–0.2 wt.%).

2.9 Discussion

2.9.1 Vertically and Laterally Extensive Magma Processing

Several models of volcanic systems that integrate geophysical, geochemical, and petrological information have concluded that magma processing beneath arc volcanoes likely takes place throughout the crust in trans-crustal magma systems (Annen et al. 2006; Annen et al. 2015; Cashman et al. 2017; Hildreth and Moorbath 1988). Multiple lines of evidence suggest that this is the case at Villarrica volcano. We have compared representative mineral compositions identified via clustering, with thermodynamic fractional crystallisation models of a simple Villarrica-like system. The comparisons suggest that polybaric crystallisation, at pressures up to ca. 600 MPa, is required to produce the mineral compositions erupted at Villarrica (Figure 2.7). This is supported by thermobarometry from past studies that focused on individual eruptions (Figure 2.7). The majority of pressures calculated from thermobarometry are in the shallow crust (0–150 MPa), but pressures calculated from olivine-augite pairs erupted during historic eruptions extend to 700 MPa. Additionally, Kapinos et al. (2016) detected a low conductivity zone beneath Villarrica volcano that extends from 19–50 km, beyond the base of the crust (deeper than any of the crystallisation pressures identified in our study).

As well as vertical connectivity, there is also evidence of lateral connectivity within Villarrica's magmatic system (Ebmeier et al. 2018; Lerner et al. 2020). Nested calderas, kilometres in diameter, were produced during large eruptions at Villarrica and surround the current central vent: Caldera 1 (ca. 100 ka), Caldera

2 (ca. 14 ka), and Caldera 3 (ca. 3.7 ka) (*Geología del volcán Villarrica, Regiones de La Araucanía y de Los Lagos.* 2006). Calderas 1 and 2 cover an area of 6.5 km by 4.2 km (long axes), Caldera 3 is roughly circular and 2 km in diameter. Domes and sills erupted on caldera walls demonstrate lateral transport of magma during large eruptions (*Geología del volcán Villarrica, Regiones de La Araucanía y de Los Lagos.* 2006). After the March 2015 eruption, Delgado et al. (2017) detected re-inflation at depths of 4.2 km in part of Villarrica's magmatic system, ca. 5 km SE of the central vent near the edge of Calderas 1 and 2. Further afield still, are the two groups of parasitic cones on Villarrica's flanks. The Los Nevados group contain fissures and cones that extend to ca. 10 km to the NE and the Chaillupén group extend ca. 12 km to the south of the present central vent. Recently, Pavez et al. (2020) detected a low conductivity zone (ca. 4 km deep) associated with the Los Nevados group. Combined, all these lines of evidence demonstrate that Villarrica's magmatic system is spatially extensive and imply that different parts of the system are tapped to accumulate the crystal cargo of each eruption.

2.9.2 The Role of Magma Mixing

The mixing of compositionally distinct magmas has been suggested as the trigger for eruptions at many arc volcanoes globally (e.g., Bouvet de Maisonneuve et al. 2012; Cassidy et al. 2015; Kahl et al. 2011; Ruprecht et al. 2012), to the extent that it is considered ubiquitous (Cashman and Edmonds 2019). Here we define magma mixing as the physical interaction of magmas that have different chemical compositions and/or intensive variables. It doesn't imply total homogenisation of the two magmas.

The compositional variety observed within erupted crystal cargoes, combined with evidence for spatially extensive magma processing, suggest that Villarrica's magmatic system comprises multiple, variably evolved reservoirs distributed throughout the crust. This is supported by widely varying best-fitting intensive variables from rhyolite-MELTS thermodynamic simulations (Table 2.3). In addition to the range of best-fit pressures, there is a large range of best-fitting crystallisation temperatures that reproduce crystal compositions (850–1100 °C). There is also a large variation in best-fitting water contents from anhydrous to 5.5 wt.%. This implies that degassing plays a large role in driving crystallisation in Villarrica's magmatic system, as has been suggested for other arc volcanoes (e.g., Blundy et al. 2006; Bouvet de Maisonneuve et al. 2012). The large range of best fitting fO_2 values (−0.5–2.00 ΔQFM) suggests that crystallisation is occurring from melts that have undergone different amounts of degassing and fractional crystallisation (Carmichael 1991; Lindsley and Frost 1992; Sato 1978). The presence of minerals produced by different intensive variables in a single crystal cargo means there must be physical interaction between reservoirs in Villarrica's magmatic system. Reservoirs that are infrequently disturbed

by ascending primitive magma, can cool and differentiate via fractional crystallisation to produce evolved crystal compositions e.g., Pl_5 (An_{64}). Before eruption, ascending primitive melt interacts with multiple reservoirs, accumulating differing minerals. This mixing of magmas with different compositions produces new compositions which may be recorded in zoned crystals (Figure 2.5). These antecrysts are accumulated as melts ascend resulting in a variety of erupted mineral compositions in a single crystal cargo (Figure 2.6).

The important role of magma mixing at Villarrica is supported by our observation that the proportion of identified clusters does not show clear trends when they are compared to crystal zoning (Figure 2.5). If fractional crystallisation is the dominant process during magma processing in Villarrica's magmatic system, we would expect mineral cores to be dominated by primitive compositions and rims by more evolved compositions. However, both primitive and evolved clusters are present as cores, intermediate, and rim zones of all three of the commonly erupted minerals. This implies that magma mixing plays a role in assembling crystal cargoes at Villarrica (e.g., Ruprecht et al. 2012; Streck 2008)

Furthermore, textural evidence for magma mixing is present in almost all of Villarrica's eruptive deposits. The Dacitic Dome contains reverse and oscillatory-zoned plagioclase, olivine with fayalitic rims (Fo_{58}) and reverse-zoned clinopyroxene (Lohmar 2008). The Licán ignimbrite has both reverse and oscillatory-zoned plagioclase, reverse-zoned clinopyroxene, and orthopyroxene rims surrounding olivine crystals (Lohmar et al. 2012). A pre-Pucón surge deposit contains banded pumice, the pale bands have a bulk SiO_2 of 63 wt.% (Lohmar 2008; Moreno et al. 1994). The Pucón ignimbrite contains plagioclase crystals with resorbed cores and rims, sieve textures, and low-An microlites. Clinopyroxene is often reverse-zoned (Lohmar 2008). Additionally, what is thought to be a dacitic enclave in a basaltic scoria bomb of the Pucón ignimbrite has been observed (McCurry et al. 2004; McCurry and Schmidt 2001). The Chaimilla Fall Deposit contains complexly zoned plagioclase crystals with both reverse rims and widespread evidence of resorption (Pioli et al. 2015). Multiple historic eruptions also contain similar indicators: An-poor plagioclase is present as both rims of oscillatory-zoned crystals and crystals with resorption textures. Both olivine and clinopyroxene crystals display resorption textures (Morgado et al. 2015; Pizarro et al. 2019).

The ubiquity of evidence for magma mixing in Villarrica's eruptive products implies complex magma dynamics involving multiple variably-evolved reservoirs. These may be intermittently connected and tapped prior to eruption resulting in the variable crystal cargoes of eruptive deposits.

2.9.3 Linking Crystal Cargo and Whole-Rock Composition to Eruptive Behaviour

The complex temporal trends in the compositions of erupted crystal cargoes show strong correlations with both whole-rock composition and eruptive style. There is a stark contrast between the composition of crystal cargoes of historic eruptions and prehistoric eruptions (Figure 2.6). Generally, the crystal cargoes of historic eruptions contain a smaller variety of crystal compositions, this is especially pronounced for feldspar and clinopyroxene compositions. This disparity strongly correlates with whole-rock compositions (Figure 2.6d): historic eruptions have average bulk SiO_2 and MgO contents of 54 wt.% and 5 wt.%, respectively, whereas prehistoric eruptions range from 54–65 wt.% SiO_2 and 1–5 wt.% MgO. Both the composition of erupted crystal cargoes and whole-rock compositions strongly correlate with eruptive style: the most differentiated eruptive deposits contain the more variable crystal cargoes and are the most explosive and high-volume.

2.9.3.1 Dacitic Dome

The Dacitic Dome (c.a. 95 ka) is the most differentiated of Villarrica's products analysed to date, with substantially higher bulk SiO_2 content than any subsequent eruption (65 wt.% vs. ~55 wt.% Figure 2.1). However, the magma that formed the Dacitic Dome is almost certainly a mix of evolved and more primitive magmas (e.g., Eichelberger et al. 2006; Reubi and Blundy 2009), supported by textural observations described above (Lohmar 2008). The dacitic composition may have formed from mafic magmas ascending through evolved mushes (e.g., Reubi and Blundy 2009) or from differentiated melts ascending through mafic mushes (e.g., Kent et al. 2010). Of the three eruptions that contain it, the crystal cargo of the Dacitic Dome contains the highest proportion of An-poor plagioclase (Pl_5, Figure 2.6b), along with its high bulk-SiO_2 content.

2.9.3.2 The Licán and Pucón Mafic Ignimbrites

The Licán (ca. 14 ka) and Pucón (ca. 3.7 ka) mafic ignimbrites are deposits from the two most explosive, high-volume eruptions at Villarrica (Lohmar et al. 2012; Silva Parejas 2008). Both have high, but variable, bulk-SiO_2 contents (Figure 2.6d) compared to historic eruptions. They are also the last two eruptions whose crystal cargoes contain the evolved Pl_5. Their whole-rock chemistry correlates with the proportion of Pl_5 in their crystal cargoes: the Licán has lower MgO and slightly higher SiO_2 than the Pucón, and has a higher proportion of Pl_5 (Figure 2.6b,d).

Rhyolite-MELTS models show that Pl_5 likely crystallised from an evolved melt (ca. 60 wt.% SiO_2), after

substantial differentiation via crystal fractionation, resulting in a bulk crystal fraction of at least 50%. The eruption of a reservoir with such a high crystal fraction requires liberation via mush dis-aggregation to reduce its viscosity (Sparks and Marshall 1986). This may result from a combination of chemical or thermal mixing, and/or volatile fluxing from an incoming more primitive basaltic melt (e.g., Bachmann and Bergantz 2006; Bergantz et al. 2015; Bouvet de Maisonneuve et al. 2012; Pistone et al. 2017; Zellmer et al. 2016). Upon mixing with the primitive magma, plagioclase crystals from the evolved reservoir would become reversely zoned, with low-An cores and higher-An rims. In turn, primitive plagioclase carried by this primitive melt would grow low-An rims upon mixing (as suggested in Lohmar 2008; Lohmar et al. 2012). Therefore mixing between an evolved and primitive magma explains how Pl_5 can exist as cores, intermediates, and rims (Figure 2.5).

The correlation of whole-rock compositions with the proportion of low-An Pl_5 in erupted crystal cargoes, combined with textural data and thermodynamic modelling, supports the triggering of these mafic-ignimbrite generating eruptions via destabilisation of a differentiated (dacitic) mush by an influx of primitive magma.

2.9.3.3 The March 2015 Fire Fountain

In contrast to the ignimbrite-forming eruptions, historic eruptions have been dominated by effusive activity, punctuated by fire fountaining which appears to be related to lahar generation (e.g., 1908, 1948-49, 1963, 1964 1971 and 2015, (Lara and Clavero 2004)). The paroxysmal eruption of March 2015 is significant in that it was the most intense historic eruption at Villarrica, producing a fire fountain that was 1.5 km in height but lasted just thirty minutes (Romero et al. 2018). The composition of olivine erupted in 2015 is more varied than both all preceding historic eruptions, and in spatter erupted later that year (Figure 2.6). This is in stark contrast to the March 2015's otherwise homogeneous cargo, which consists of only intermediate plagioclase clusters Pl_3 and Pl_4 and few clinopyroxene crystals. This implies that the mafic portion of the March 2015's crystal cargo was accumulated by primitive melt as it ascended through Villarrica's magmatic system. Plagioclase may have formed in response to degassing upon ascent (as in Blundy et al. 2006) as with the other historic eruptions. The low-SiO_2 and high-MgO bulk composition of erupted spatter suggests that the intensity of the eruption is unlikely to be caused by the same mechanism as the mafic ignimbrites. Instead high primary volatile contents likely drove fast magma ascent, resulting in the vigorous fountaining behaviour (Allison et al. 2021; Barth et al. 2019; La Spina et al. 2021) and allowing it to punch through existing reservoirs and assemble its more varied crystal cargo.

2.9.4 A Model for Generating Explosive Eruptions at Villarrica Volcano

The eruption of the Dacitic Dome (ca. 95 ka) demonstrates that evolved portions of Villarrica's magmatic system existed prior to the most explosive post-glacial eruptions known at Villarrica, the Licán ignimbrite. Therefore portions of Villarrica's magmatic system were differentiated beyond the typical whole rock compositions of erupted historic products (Figure 2.1c). The existence of this evolved (dacitic) reservoir has implications for magma dynamics. It has been shown that felsic mushes are sufficiently viscous that they are non-eruptible (Marsh 2002; Sparks and Marshall 1986). In combination with their low relative density, they can act as a density filter, preventing more dense mafic melts from ascending to the surface (Kent et al. 2010). Therefore the establishment of a significant volume of evolved mush within the magmatic system could dampen the eruption of mafic magma and increase the overall volume of evolved melt until a sufficiently large volume of ascending primitive melt can destabilise it (Sparks and Marshall 1986).

The eruption of large-volume eruptive deposits, such as Licán and Pucón ignimbrites, requires significant volumes of mobile magma to exist within the magmatic system (Druitt and Sparks 1984). If the majority of Villarrica's magmatic system is composed of near-solidus mush (as implied by the TCMS model), this would require a large volume of magma to destabilise it (Marsh 2002; Sparks and Marshall 1986). The composition of minerals (Ol_1 and Pl_1, Table 2.2) and melt inclusions at Villarrica suggest primitive magmas were present within its system (Pioli et al. 2015). The best fitting conditions for the most evolved plagioclase (Pl_5) are in the middle crust, at low temperatures and after significant crystal fractionation (Figure 2.7). Therefore we propose that the trigger of the Licán and Pucón ignimbrites was a large influx of primitive magma, which mixed with an evolved reservoir (Figure 2.8a). The remnants of the mush that this primitive magma interacted with are shown by the presence of evolved plagioclase, Pl_5 in both ingimbrites' crystal cargo. In the case of the Licán ignimbrite, the trigger may have been facilitated by widespread deglaciation in the Southern Andes around 14 ka, altering the stress state of the crust to facilitate magma ascent (e.g., Jellinek et al. 2004; Rawson et al. 2016; Watt et al. 2013; Wilson and Russell 2020). After the eruption of the Licán ignimbrite, another evolved reservoir of similar composition likely accumulated over a period of ca. 10 ka. The existence of an evolved reservoir prior to the Pucón Ignimbrite (ca. 3.7 ka) is suggested by the mineralogy of a Pre-Pucón pyroclastic surge deposit Lohmar (2008), which contains a large proportion of evolved (63 wt.% SiO_2) pumice. The Pucón ignimbrite forming eruption may then have been triggered in a similar fashion to the Licán eruption, i.e. destabilisation of an evolved reservoir by an influx of primitive magma.

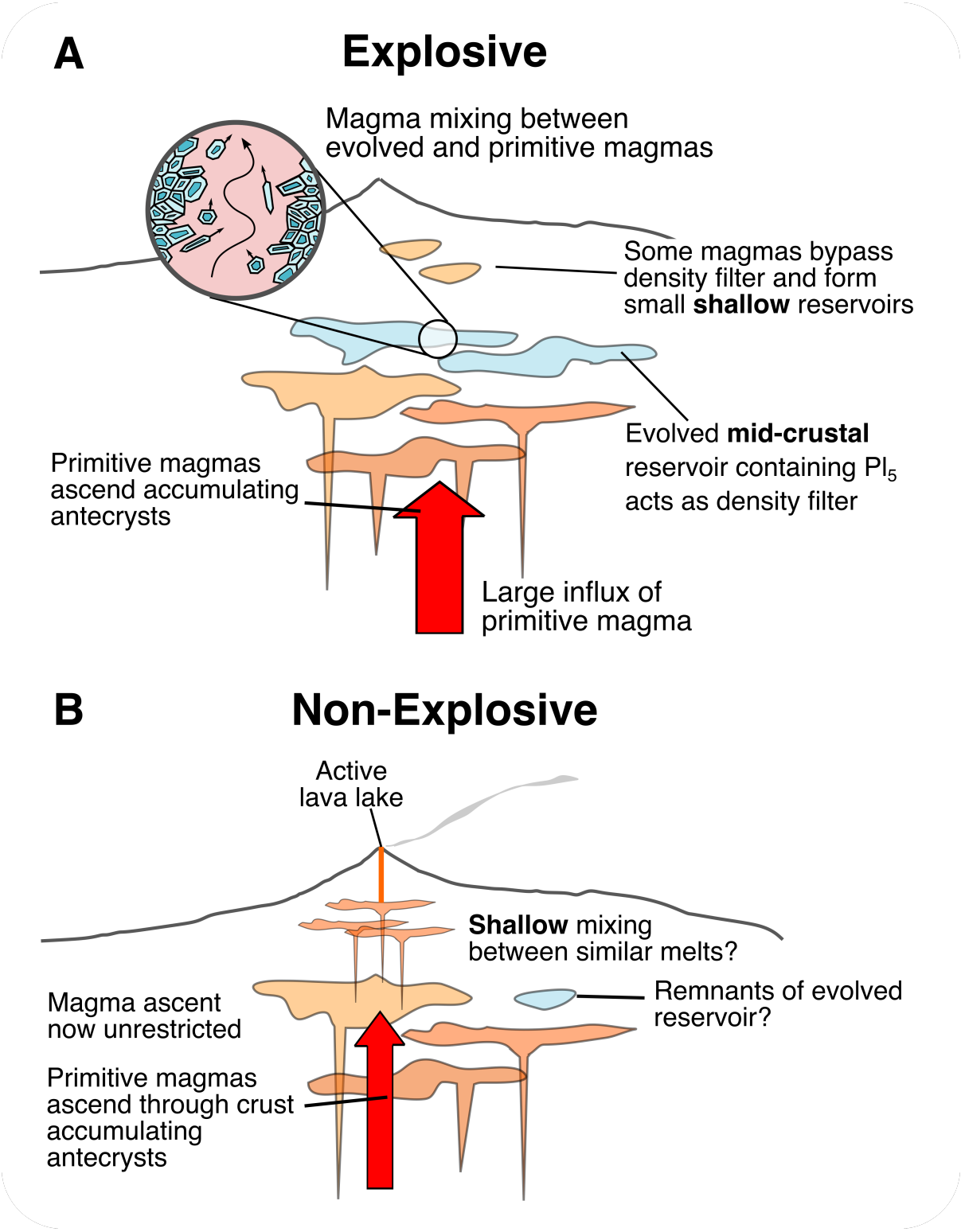

Figure 2.8: Conceptual model for Villarrica's magmatic system prior to (A) an explosive, ignimbrite-forming eruption and (B) a non-explosive historic eruption.

These evolved reservoirs were likely depleted by mixing with primitive magma prior to the ignimbrite-forming eruptions, as subsequently erupted crystal cargoes (3.7 ka to present) contain no trace of Pl_5 (Figure 2.6). Without the density filter provided by the evolved reservoirs, the most recently erupted magmas were able to ascend through Villarrica's magmatic system faster, perhaps only mixing in the shallowest parts, resulting in less differentiated erupted compositions (Figure 2.8b). The absence of mixing between highly differentiated and primitive compositions results in substantially lower explosivity. Instead recent lava fountaining is likely driven by rapid ascent, enabled by high volatile contents (e.g., the March 2015 eruption). The near-continuous activity at Villarrica's lava lake over the last ca. 40 years demonstrates the ability of magma to ascend relatively unhindered through the magmatic system. The absence of activity at the summit and/or the eruption of crystals in equilibrium with differentiated melt compositions (e.g., Pl_5) may signal the onset of evolved reservoir development, and signal an increased likelihood of high-volume explosive eruption occurring.

2.10 Conclusions

The use of multivariate cluster analysis has allowed us to identify previously unidentified structure in the composition of minerals erupted throughout Villarrica's eruptive history. Comparisons of identified representative compositions with >1500 Rhyolite-MELTS thermodynamic simulations show that magma processing at Villarrica takes place at a range of pressures, temperatures, water contents, and oxygen fugacities. These thermodynamic models strongly suggest that magma storage beneath the volcano is characterised by a series of ephemerally connected, variably-evolved mush-dominated sills. Prior to eruption, magma ascends through this trans-crustal magmatic system, accumulating different antecrysts which are erupted as variable crystal cargoes.

We have identified temporal trends in the composition of erupted crystal cargoes that correlate with trends in whole-rock composition and eruption style. We propose that prior to high-volume, ignimbrite-forming explosive mafic eruptions (the Licán and Pucón ignimbrites) much of Villarrica's magmatic system had differentiated by fractional crystallisation. These mid-crustal evolved reservoirs acted as density filters, suppressing the eruption of small volumes of primitive magma. Only when a sufficiently large influx of primitive magma entered the system was this evolved portion destabilised. Magma mixing ensued, producing the complex textures observed by past studies, and resulting in the relatively primitive, basaltic-andesite compositions of the two ignimbrites. The only remnants of the evolved reservoir are low-anorthite plagioclase which is present as both cores and rims of more primitive crystals.

The lack of evidence for an evolved reservoir after these high-volume explosive eruptions explains the homogeneous, more primitive, whole-rock compositions of subsequent eruptions. Without the density filter of the evolved reservoirs, more primitive melts ascend relatively uninhibited, mixing and degassing in the shallow subsurface before eruption. Further petrological work utilising melt inclusion compositions, trace-element data, and diffusion chronometry will allow further investigation of magma dynamics at Villarrica.

References

Aitchison, J. (1986). *The Statistical Analysis of Compositional Data*. Chapman and Hall. 416 pages.

Allison, C. M., K. Roggensack, and A. B. Clarke (2021). "Highly Explosive Basaltic Eruptions Driven by CO2 Exsolution". In: *Nature Communications* 12.1 (1), page 217. DOI: 10.1038/s41467-020-20354-2.

Annen, C., J. D. Blundy, and R. S. J. Sparks (2006). "The Genesis of Intermediate and Silicic Magmas in Deep Crustal Hot Zones". In: *Journal of Petrology* 47.3 (3), pages 505–539. DOI: 10.1093/petrology/egi084.

Annen, C., J. D. Blundy, J. Leuthold, and R. S. J. Sparks (2015). "Construction and Evolution of Igneous Bodies: Towards an Integrated Perspective of Crustal Magmatism". In: *Lithos* 230, pages 206–221. DOI: 10.1016/j.lithos.2015.05.008.

Bachmann, O. and G. W. Bergantz (2006). "Gas Percolation in Upper-Crustal Silicic Crystal Mushes as a Mechanism for Upward Heat Advection and Rejuvenation of near-Solidus Magma Bodies". In: *Journal of Volcanology and Geothermal Research* 149.1-2 (1-2), pages 85–102. DOI: 10.1016/j.jvolgeores.2005.06.002.

Barette, F., S. Poppe, B. Smets, M. Benbakkar, and M. Kervyn (2017). "Spatial Variation of Volcanic Rock Geochemistry in the Virunga Volcanic Province: Statistical Analysis of an Integrated Database". In: *Journal of African Earth Sciences* 134, pages 888–903. DOI: 10.1016/j.jafrearsci.2016.09.018.

Barth, A., M. Newcombe, T. Plank, H. Gonnermann, S. Hajimirza, G. J. Soto, A. Saballos, and E. Hauri (2019). "Magma Decompression Rate Correlates with Explosivity at Basaltic Volcanoes — Constraints from Water Diffusion in Olivine". In: *Journal of Volcanology and Geothermal Research* 387, page 106664. DOI: 10.1016/j.jvolgeores.2019.106664.

Baxter, M. J., C. C. Beardah, H. E. M. Cool, and C. M. Jackson (2005). "Compositional Data Analysis of Some Alkaline Glasses". In: *Mathematical Geology* 37.2 (2), pages 183–196. DOI: 10.1007/s11004-005-1308-3.

Bergantz, G. W., J. M. Schleicher, and A. Burgisser (2015). "Open-System Dynamics and Mixing in Magma Mushes". In: *Nature Geoscience* 8.10 (10), pages 793–796. DOI: 10.1038/ngeo2534.

Blundy, J., K. Cashman, and M. Humphreys (2006). "Magma Heating by Decompression-Driven Crystallization beneath Andesite Volcanoes". In: *Nature* 443.7107 (7107), pages 76–80. DOI: 10.1038/nature05100.

Bouvet de Maisonneuve, C., M. Dungan, O. Bachmann, and A. Burgisser (2012). "Insights into Shallow Magma Storage and Crystallization at Volcán Llaima (Andean Southern Volcanic Zone, Chile)". In: *Journal of Volcanology and Geothermal Research* 211–212, pages 76–91. DOI: 10.1016/j.jvolgeores.2011.09.010.

Caricchi, L., M. Petrelli, E. Bali, T. Sheldrake, L. Pioli, and G. Simpson (2020). "A Data Driven Approach to Investigate the Chemical Variability of Clinopyroxenes From the 2014–2015 Holuhraun–Bárdarbunga Eruption (Iceland)". In: *Frontiers in Earth Science* 8, page 18. DOI: 10.3389/feart.2020.00018.

Carmichael, I. S. E. (1991). "The Redox States of Basic and Silicic Magmas: A Reflection of Their Source Regions?" In: *Contributions to Mineralogy and Petrology* 106.2 (2), pages 129–141. DOI: 10.1007/BF00306429.

Cashman, K. V. and M. Edmonds (2019). "Mafic Glass Compositions: A Record of Magma Storage Conditions, Mixing and Ascent". In: *Philosophical Transactions of the Royal Society A: Mathematical, Physical and Engineering Sciences* 377.2139 (2139), page 20180004. DOI: 10.1098/rsta.2018.0004.

Cashman, K. V., R. S. J. Sparks, and J. D. Blundy (2017). "Vertically Extensive and Unstable Magmatic Systems: A Unified View of Igneous Processes". In: *Science* 355.6331 (6331), eaag3055. DOI: 10.1126/science.aag3055.

Cassidy, M., M. Edmonds, S. F. L. Watt, M. R. Palmer, and T. M. Gernon (2015). "Origin of Basalts by Hybridization in Andesite-dominated Arcs". In: *Journal of Petrology* 56.2 (2), pages 325–346. DOI: 10.1093/petrology/egv002.

Cembrano, J. and L. Lara (2009). "The Link between Volcanism and Tectonics in the Southern Volcanic Zone of the Chilean Andes: A Review". In: *Tectonophysics* 471.1-2 (1-2), pages 96–113. DOI: 10.1016/j.tecto.2009.02.038.

Chayes, F. (1971). *Ratio Correlation: A Manual for Students of Petrology and Geochemistry*. University of Chicago Press. 99 pages.

Cheng, L., F. Costa, and R. Carniel (2017). "Unraveling the Presence of Multiple Plagioclase Populations and Identification of Representative Two-Dimensional Sections Using a Statistical and Numerical Approach". In: *American Mineralogist* 102.9 (9), pages 1894–1905. DOI: 10.2138/am-2017-5929CCBYNCND.

Chiasera, B. and J. A. Cortés (2011). "Predictive Regions for Geochemical Compositional Data of Volcanic Systems". In: *Journal of Volcanology and Geothermal Research* 207.3-4 (3-4), pages 83–92. DOI: 10.1016/j.jvolgeores.2011.07.009.

Clavero-Ribes, J. E. (1996). "Ignimbritas Andesitico-Basalticas Postglaciales Del Volcán Villarrica, Andes Del Sur (39° 25'S)". Master's thesis. Universidad de Chile.

Cooper, K. M. and A. J. R. Kent (2014). "Rapid Remobilization of Magmatic Crystals Kept in Cold Storage". In: *Nature* 506.7489 (7489), pages 480–483. DOI: 10.1038/nature12991.

Corsaro, R. A., S. Falsaperla, and H. Langer (2013). "Geochemical Pattern Classification of Recent Volcanic Products from Mt. Etna, Italy, Based on Kohonen Maps and Fuzzy Clustering". In: *International Journal of Earth Sciences* 102.4 (4), pages 1151–1164. DOI: 10.1007/s00531-012-0851-7.

Cortés, J. A. (2009). "On the Harker Variation Diagrams; A Comment on "The Statistical Analysis of Compositional Data. Where Are We and Where Should We Be Heading?" By Aitchison and Egozcue (2005)". In: *Mathematical Geosciences* 41.7 (7), pages 817–828. DOI: 10.1007/s11004-009-9222-8.

Cortés, J. A., J. L. Palma, and M. Wilson (2007). "Deciphering Magma Mixing: The Application of Cluster Analysis to the Mineral Chemistry of Crystal Populations". In: *Journal of Volcanology and Geothermal Research* 165.3-4 (3-4), pages 163–188. DOI: 10.1016/j.jvolgeores.2007.05.018.

Costantini, L., L. Pioli, C. Bonadonna, J. Clavero, and C. Longchamp (2011). "A Late Holocene Explosive Mafic Eruption of Villarrica Volcano, Southern Andes: The Chaimilla Deposit". In: *Journal of Volcanology and Geothermal Research* 200.3-4 (3-4), pages 143–158. DOI: 10.1016/j.jvolgeores.2010.12.010.

Delgado, F., M. E. Pritchard, S. Ebmeier, P. González, and L. Lara (2017). "Recent Unrest (2002–2015) Imaged by Space Geodesy at the Highest Risk Chilean Volcanoes: Villarrica, Llaima, and Calbuco (Southern Andes)". In: *Journal of Volcanology and Geothermal Research* 344, pages 270–288. DOI: 10.1016/j.jvolgeores.2017.05.020.

Droop, G. T. R. (1987). "A General Equation for Estimating Fe3+ Concentrations in Ferromagnesian Silicates and Oxides from Microprobe Analyses, Using Stoichiometric Criteria". In: *Mineralogical Magazine* 51.361 (361), pages 431–435. DOI: 10.1180/minmag.1987.051.361.10.

Druitt, T. H. and R. S. J. Sparks (1984). "On the Formation of Calderas during Ignimbrite Eruptions". In: *Nature* 310.5979 (5979), pages 679–681. DOI: 10.1038/310679a0.

Ebmeier, S. K., B. J. Andrews, M. C. Araya, D. W. D. Arnold, J. Biggs, C. Cooper, E. Cottrell, M. Furtney, J. Hickey, J. Jay, R. Lloyd, A. L. Parker, M. E. Pritchard, E. Robertson, E. Venzke, and J. L. Williamson (2018). "Synthesis of Global Satellite Observations of Magmatic and Volcanic Deformation: Implications for Volcano Monitoring & the Lateral Extent of Magmatic Domains". In: *Journal of Applied Volcanology* 7.1 (1), page 2. DOI: 10.1186/s13617-018-0071-3.

Edmonds, M., K. V. Cashman, M. Holness, and M. Jackson (2019). "Architecture and Dynamics of Magma Reservoirs". In: *Philosophical Transactions of the Royal Society A: Mathematical, Physical and Engineering Sciences* 377.2139 (2139), page 20180298. DOI: 10.1098/rsta.2018.0298.

Egozcue, J. J., V. Pawlowsky-Glahn, G. Mateu-Figueras, and C. Barcelo-Vidal (2003). "Isometric Logratio Transformations for Compositional Data Analysis". In: *Mathematical Geology*, page 22.

Eichelberger, J. C., P. E. Izbekov, and B. L. Browne (2006). "Bulk Chemical Trends at Arc Volcanoes Are Not Liquid Lines of Descent". In: *Lithos* 87.1-2 (1-2), pages 135–154. DOI: 10.1016/j.lithos.2005.05.006.

Feig, S. T., J. Koepke, and J. E. Snow (2010). "Effect of Oxygen Fugacity and Water on Phase Equilibria of a Hydrous Tholeiitic Basalt". In: *Contributions to Mineralogy and Petrology* 160.4 (4), pages 551–568. DOI: 10.1007/s00410-010-0493-3.

Filzmoser, P. and K. Hron (2008). "Outlier Detection for Compositional Data Using Robust Methods". In: *Mathematical Geosciences* 40.3 (3), pages 233–248. DOI: 10.1007/s11004-007-9141-5.

Fry, J. M., T. R. L. Fry, and K. R. McLaren (2000). "Compositional Data Analysis and Zeros in Micro Data". In: *Applied Economics* 32.8 (8), pages 953–959. DOI: 10.1080/000368400322002.

Gavrilenko, M., C. Herzberg, C. Vidito, M. J. Carr, T. Tenner, and A. Ozerov (2016). "A Calcium-in-Olivine Geohygrometer and Its Application to Subduction Zone Magmatism". In: *Journal of Petrology* 57.9 (9), pages 1811–1832. DOI: 10.1093/petrology/egw062.

Geología del volcán Villarrica, Regiones de La Araucanía y de Los Lagos. (2006). In collaboration with H. Moreno and J. Clavero. Servicio Nacional de Geología y Minería.

Ghiorso, M. S. and G. A. R. Gualda (2015). "An H2O–CO2 Mixed Fluid Saturation Model Compatible with Rhyolite-MELTS". In: *Contributions to Mineralogy and Petrology* 169.6 (6), page 53. DOI: 10.1007/s00410-015-1141-8.

Ginibre, C. and G. Wörner (2007). "Variable Parent Magmas and Recharge Regimes of the Parinacota Magma System (N. Chile) Revealed by Fe, Mg and Sr Zoning in Plagioclase". In: *Lithos* 98.1-4 (1-4), pages 118–140. DOI: 10.1016/j.lithos.2007.03.004.

Gleeson, M. L. M., S. A. Gibson, and M. J. Stock (2021). "Upper Mantle Mush Zones beneath Low Melt Flux Ocean Island Volcanoes: Insights from Isla Floreana, Galápagos". In: *Journal of Petrology* 61.11-12 (11-12), egaa094. DOI: 10.1093/petrology/egaa094.

Greenacre, M. (2019). "Variable Selection in Compositional Data Analysis Using Pairwise Logratios". In: *Mathematical Geosciences* 51.5 (5), pages 649–682. DOI: 10.1007/s11004-018-9754-x.

Greenacre, M. and P. Lewi (2009). "Distributional Equivalence and Subcompositional Coherence in the Analysis of Compositional Data, Contingency Tables and Ratio-Scale Measurements". In: *Journal of Classification* 26.1 (1), pages 29–54. DOI: 10.1007/s00357-009-9027-y.

Gualda, G. A. R., M. S. Ghiorso, R. V. Lemons, and T. L. Carley (2012). "Rhyolite-MELTS: A Modified Calibration of MELTS Optimized for Silica-rich, Fluid-bearing Magmatic Systems". In: *Journal of Petrology* 53.5 (5), pages 875–890. DOI: 10.1093/petrology/egr080.

Hamada, M., H. Iwamori, P. A. Brandl, T. Ushikubo, K. Shimizu, M. Ito, H. Li, and I. P. Savov (2020). "Temporal Evolution of Proto-Izu–Bonin–Mariana Arc Volcanism over 10 Myr: Constraints from Statistical Analysis of Melt Inclusion Compositions". In: *Journal of Petrology* 61.1 (1), egaa022. DOI: 10.1093/petrology/egaa022.

Henze, N. and B. Zirkler (1990). "A Class of Invariant Consistent Tests for Multivariate Normality". In: *Communications in Statistics - Theory and Methods* 19.10, pages 3595–3617. DOI: 10.1080/03610929008830400.

Hickey-Vargas, R., M. Sun, and S. Holbik (2016). "Geochemistry of Basalts from Small Eruptive Centers near Villarrica Stratovolcano, Chile: Evidence for Lithospheric Mantle Components in Continental Arc Magmas". In: *Geochimica et Cosmochimica Acta* 185, pages 358–382. DOI: 10.1016/j.gca.2016.03.033.

Hickey-Vargas, R., H. M. Roa, L. L. Escobar, and F. A. Frey (1989). "Geochemical Variations in Andean Basaltic and Silicic Lavas from the Villarrica-Lanin Volcanic Chain (39.5 S): An Evaluation of Source Heterogeneity, Fractional Crystallization and Crustal Assimilation". In: *Contributions to Mineralogy and Petrology* 103.3 (3), pages 361–386. DOI: 10.1007/BF00402922.

Hildreth, W. and S. Moorbath (1988). "Crustal Contributions to Arc Magmatism in the Andes of Central Chile". In: *Contributions to Mineralogy and Petrology* 98.4 (4), pages 455–489. DOI: 10.1007/BF00372365.

Hirschmann, M. M., M. S. Ghiorso, F. A. Davis, S. M. Gordon, S. Mukherjee, T. L. Grove, M. Krawczynski, E. Medard, and C. B. Till (2008). "Library of Experimental Phase Relations (LEPR): A Database and Web Portal for Experimental Magmatic Phase Equilibria Data". In: *Geochemistry, Geophysics, Geosystems* 9.3, 2007GC001894. DOI: 10.1029/2007GC001894.

Jellinek, A. M., M. Manga, and M. O. Saar (2004). "Did Melting Glaciers Cause Volcanic Eruptions in Eastern California? Probing the Mechanics of Dike Formation". In: *Journal of Geophysical Research: Solid Earth* 109.B9, 2004JB002978. DOI: 10.1029/2004JB002978.

Jerram, D. A. and V. M. Martin (2008). "Understanding Crystal Populations and Their Significance through the Magma Plumbing System". In: *Geological Society, London, Special Publications* 304.1 (1), pages 133–148. DOI: 10.1144/SP304.7.

Kahl, M., S. Chakraborty, F. Costa, and M. Pompilio (2011). "Dynamic Plumbing System beneath Volcanoes Revealed by Kinetic Modeling, and the Connection to Monitoring Data: An Example from Mt. Etna". In: *Earth and Planetary Science Letters* 308.1-2 (1-2), pages 11–22. DOI: 10.1016/j.epsl.2011.05.008.

Kamenetsky, V. S., M. Elburg, R. Arculus, and R. Thomas (2006). "Magmatic Origin of Low-Ca Olivine in Subduction-Related Magmas: Co-existence of Contrasting Magmas". In: *Chemical Geology* 233.3-4 (3-4), pages 346–357. DOI: 10.1016/j.chemgeo.2006.03.010.

Kapinos, G., M. Montahaei, N. Meqbel, and H. Brasse (2016). "Three-Dimensional Electrical Resistivity Image of the South-Central Chilean Subduction Zone". In: *Tectonophysics* 666, pages 76–89. DOI: 10.1016/j.tecto.2015.10.016.

Kent, A. J. R., C. Darr, A. M. Koleszar, M. J. Salisbury, and K. M. Cooper (2010). "Preferential Eruption of Andesitic Magmas through Recharge Filtering". In: *Nature Geoscience* 3.9 (9), pages 631–636. DOI: 10.1038/ngeo924.

Kuritani, T., A. Yamaguchi, S. Fukumitsu, M. Nakagawa, A. Matsumoto, and T. Yokoyama (2018). "Magma Plumbing System at Izu-Oshima Volcano, Japan: Constraints From Petrological and Geochemical Analyses". In: *Frontiers in Earth Science* 6, page 178. DOI: 10.3389/feart.2018.00178.

La Spina, G., F. Arzilli, E. W. Llewellin, M. R. Burton, A. B. Clarke, M. de'Michieli Vitturi, M. Polacci, M. E. Hartley, D. Di Genova, and H. M. Mader (2021). "Explosivity of Basaltic Lava Fountains Is Controlled by Magma Rheology, Ascent Rate and Outgassing". In: *Earth and Planetary Science Letters* 553, page 116658. DOI: 10.1016/j.epsl.2020.116658.

Lara, L. E. and J. Clavero (2004). *Villarrica Volcano (39.5°S), Southern Andes, Chile*. 61. Servicio Nacional de Geología y Minería, page 75.

Le Bas, M. J., R. W. L. Maitre, A. Streckeisen, B. Zanettin, and IUGS Subcommission on the Systematics of Igneous Rocks (1986). "A Chemical Classification of Volcanic Rocks Based on the Total Alkali-Silica Diagram". In: *Journal of Petrology* 27.3 (3), pages 745–750. DOI: 10.1093/petrology/27.3.745.

Lerner, A. H., D. O'Hara, L. Karlstrom, S. K. Ebmeier, K. R. Anderson, and S. Hurwitz (2020). "The Prevalence and Significance of Offset Magma Reservoirs at Arc Volcanoes". In: *Geophysical Research Letters* 47.14 (14). DOI: 10.1029/2020GL087856.

Lindsley, D. H. and B. R. Frost (1992). "Equilibria among Fe-Ti Oxides, Pyroxenes, Olivine, and Quartz: Part I. Theory". In: *American Mineralogist* 77.9-10 (9-10), pages 987–1003.

Liu, E. J., K. V. Cashman, E. Miller, H. Moore, M. Edmonds, B. E. Kunz, F. Jenner, and G. Chigna (2020a). "Petrologic Monitoring at Volcán de Fuego, Guatemala". In: *Journal of Volcanology and Geothermal Research* 405, page 107044. DOI: 10.1016/j.jvolgeores.2020.107044.

Liu, X., W. Wang, Y. Pei, and P. Yu (2020b). "A Knowledge-Driven Way to Interpret the Isometric Log-Ratio Transformation and Mixture Distributions of Geochemical Data". In: *Journal of Geochemical Exploration* 210, page 106417. DOI: 10.1016/j.gexplo.2019.106417.

Lohmar, S. (2008). "Petrologia de Las Ignimbritas Licán y Pucón (Volcan Villarrica) y Curacautin (Volcan LLaima) En Los Andes Del Sur de Chile". Universidad de Chile.

Lohmar, S., M. Parada, F. Gutiérrez, C. Robin, and M. C. Gerbe (2012). "Mineralogical and Numerical Approaches to Establish the Pre-Eruptive Conditions of the Mafic Licán Ignimbrite, Villarrica Volcano (Chilean Southern Andes)". In: *Journal of Volcanology and Geothermal Research* 235–236, pages 55–69. DOI: 10.1016/j.jvolgeores.2012.05.006.

Loucks, R. R. (1996). "A Precise Olivine-Augite Mg-Fe-exchange Geothermometer". In: *Contributions to Mineralogy and Petrology* 125.2-3 (2-3), pages 140–150. DOI: 10.1007/s004100050211.

Mahalanobis, P. C. (1936). "On the Generalized Distance in Statistics". In: *Proceedings of the National Institute of Sciences from India*. Volume 2. National Institute of Science of India, pages 49–55.

Marsh, B. D. (2002). "On Bimodal Differentiation by Solidification Front Instability in Basaltic Magmas, Part 1: Basic Mechanics". In: *Geochimica et Cosmochimica Acta* 66.12 (12), pages 2211–2229. DOI: 10.1016/S0016-7037(02)00905-5.

Martín-Fernández, J. A., C. Barceló-Vidal, and V. Pawlowsky-Glahn (2000). "Zero Replacement in Compositional Data Sets". In: *Data Analysis, Classification, and Related Methods*. Redacted by H.-H. Bock, W. Gaul, and M. Schader, pages 155–160. DOI: 10.1007/978-3-642-59789-3_25.

McCurry, M., J. Chadwick, K. E. Wright, R. W. Smith, and M. T. Ford (2004). "Preliminary LA/ICP-MS and EPMA Examination of Dacite Enclaves and Melt Inclusions in Phenocrysts from Basaltic Andesite Pyroclasts from the Pucón Ignimbrite, Volcán Villarrica, Southern Andean Volcanic Zone: Implications for Mafic Ignimbrite Volcanism". In: *International Association of Volcanology and Chemistry of the Earth's Interior (IAVCEI) General Assembly, Puc{\'o}n, Chile*. International Association of Volcanology and Chemistry of the Earth's Interior (IAVCEI) General Assembly, Puc{\'o}n, Chile.

McCurry, M. and K. Schmidt (2001). "Petrology and Oxygen Isotope Geochemistry of the Pucón Ignimbrite - Southern Andean Volcanic Zone, Chile: Implications for Genesis of Mafic Ignimbrites". In: *South American Symposium on Isotope Geology*. Simposio Suda-mericano de Geología Isotópica (SSAGI), page 4.

McGee, L. E., R. Brahm, M. C. Rowe, H. K. Handley, E. Morgado, L. E. Lara, M. B. Turner, N. Vinet, M.-Á. Parada, and P. Valdivia (2017). "A Geochemical Approach to Distinguishing Competing Tectono-Magmatic Processes Preserved in Small Eruptive Centres". In: *Contributions to Mineralogy and Petrology* 172.6 (6), page 44. DOI: 10.1007/s00410-017-1360-2.

Mollo, S., K. Putirka, G. Iezzi, P. Del Gaudio, and P. Scarlato (2011). "Plagioclase–Melt (Dis)Equilibrium Due to Cooling Dynamics: Implications for Thermometry, Barometry and Hygrometry". In: *Lithos* 125.1-2 (1-2), pages 221–235. DOI: 10.1016/j.lithos.2011.02.008.

Moreno, H. (1993). "Volcán Villarrica, Geología y Evaluación Del Riesgo Volcánico, Regiones IX y x, 39 25 s". In: *Informe Final Proyecto FONDECYT* 1247, pages 1–112.

Moreno, H., J. Clavero, and L. Lara (1994). "Actividad Explosiva Postglacial del Volcan Villarrica, Andes del Sur (39o25'S)". In: *7th Congreso Geológico Chileno*. Volume 1, pages 329–333.

Morgado, E., M. Parada, C. Contreras, A. Castruccio, F. Gutiérrez, and L. McGee (2015). "Contrasting Records from Mantle to Surface of Holocene Lavas of Two Nearby Arc Volcanic Complexes: Caburgua-Huelemolle Small Eruptive Centers and Villarrica Volcano, Southern Chile". In: *Journal of Volcanology and Geothermal Research* 306, pages 1–16. DOI: 10.1016/j.jvolgeores.2015.09.023.

Mutch, E. J. F., J. Maclennan, O. Shorttle, M. Edmonds, and J. F. Rudge (2019). "Rapid Transcrustal Magma Movement under Iceland". In: *Nature Geoscience* 12.7 (7), pages 569–574. DOI: 10.1038/s41561-019-0376-9.

Panjasawatwong, Y., L. V. Danyushevsky, A. J. Crawford, and K. L. Harris (1995). "An Experimental Study of the Effects of Melt Composition on Plagioclase-Melt Equilibria at 5 and 10 Kbar: Implications for the Origin of Magmatic High-An Plagioclase". In: *Contributions to Mineralogy and Petrology* 118.4 (4), pages 420–432. DOI: 10.1007/s004100050024.

Pavez, M., E. Schill, S. Held, D. Díaz, and T. Kohl (2020). "Visualizing Preferential Magmatic and Geothermal Fluid Pathways via Electric Conductivity at Villarrica Volcano, S-Chile". In: *Journal of Volcanology and Geothermal Research* 400, page 106913. DOI: 10.1016/j.jvolgeores.2020.106913.

Pedregosa, F., G. Varoquaux, A. Gramfort, V. Michel, B. Thirion, O. Grisel, M. Blondel, P. Prettenhofer, R. Weiss, V. Dubourg, J. Vanderplas, A. Passos, D. Cournapeau, M. Brucher, M. Perrot, and É. Duchesnay (2011). "Scikit-Learn: Machine Learning in Python". In: *Journal of Machine Learning Research* 12.85 (85), pages 2825–2830. URL: http://jmlr.org/papers/v12/pedregosa11a.html.

Petit-Breuilh Sepúlveda, M. E. (2004). *La historia eruptiva de los volcanes hispanoamericanos (siglos XVI al XX): el modelo chileno*. Servicio de Publicaciones, Cabildo Insular de Lanzarote.

Pichavant, M., F. Costa, A. Burgisser, B. Scaillet, C. Martel, and S. Poussineau (2007). "Equilibration Scales in Silicic to Intermediate Magmas Implications for Experimental Studies". In: *Journal of Petrology* 48.10 (10), pages 1955–1972. DOI: 10.1093/petrology/egm045.

Pioli, L., L. Scalisi, L. Costantini, A. Di Muro, C. Bonadonna, and J. Clavero (2015). "Explosive Style, Magma Degassing and Evolution in the Chaimilla Eruption, Villarrica Volcano, Southern Andes". In: *Bulletin of Volcanology* 77.11 (11), page 93. DOI: 10.1007/s00445-015-0976-1.

Pistone, M., J. Blundy, and R. A. Brooker (2017). "Water Transfer during Magma Mixing Events: Insights into Crystal Mush Rejuvenation and Melt Extraction Processes". In: *American Mineralogist* 102.4 (4), pages 766–776. DOI: 10.2138/am-2017-5793.

Pizarro, C., M. A. Parada, C. Contreras, and E. Morgado (2019). "Cryptic Magma Recharge Associated with the Most Voluminous 20th Century Eruptions (1921, 1948 and 1971) at Villarrica Volcano". In: *Journal of Volcanology and Geothermal Research* 384, pages 48–63. DOI: 10.1016/j.jvolgeores.2019.07.001.

Rawson, H., D. M. Pyle, T. A. Mather, V. C. Smith, K. Fontijn, S. M. Lachowycz, and J. A. Naranjo (2016). "The Magmatic and Eruptive Response of Arc Volcanoes to Deglaciation: Insights from Southern Chile". In: *Geology* 44.4 (4), pages 251–254. DOI: 10.1130/G37504.1.

Reubi, O. and J. Blundy (2009). "A Dearth of Intermediate Melts at Subduction Zone Volcanoes and the Petrogenesis of Arc Andesites". In: *Nature* 461.7268 (7268), pages 1269–1273. DOI: 10.1038/nature08510.

Robidoux, P., D. Pastén, G. Levresse, G. Diaz, and D. Paredes (2021). "Volatile Content Implications of Increasing Explosivity of the Strombolian Eruptive Style along the Fracture Opening on the NE Villarrica Flank: Minor Eruptive Centers in the Los Nevados Group 2". In: *Geosciences* 11.8 (8). DOI: 10.3390/geosciences11080309.

Romero, J. E., F. Vera, M. Polacci, D. Morgavi, F. Arzilli, M. A. Alam, J. E. Bustillos, A. Guevara, J. B. Johnson, J. L. Palma, M. Burton, E. Cuenca, and W. Keller (2018). "Tephra From the 3 March 2015 Sustained Column Related to Explosive Lava Fountain Activity at Volcán Villarrica (Chile)". In: *Frontiers in Earth Science* 6, page 98. DOI: 10.3389/feart.2018.00098.

Rousseeuw, P. J. and B. C. V. Zomeren (1990). "Unmasking Multivariate Outliers and Leverage Points". In: *Journal of The American Statistical Association* 85.411 (411), pages 633–639. URL: Unmasking%20Multivariate%20Outliers%20and%20Leverage%20Points.

Rousseeuw, P. J. and K. V. Driessen (1999). "A Fast Algorithm for the Minimum Covariance Determinant Estimator". In: *Technometrics* 41.3 (3), pages 212–223. DOI: 10.1080/00401706.1999.10485670.

Ruprecht, P., G. W. Bergantz, K. M. Cooper, and W. Hildreth (2012). "The Crustal Magma Storage System of Volcán Quizapu, Chile, and the Effects of Magma Mixing on Magma Diversity". In: *Journal of Petrology* 53.4 (4), pages 801–840. DOI: 10.1093/petrology/egs002.

Sato, M. (1978). "Oxygen Fugacity of Basaltic Magmas and the Role of Gas-Forming Elements". In: *Geophysical Research Letters* 5.6 (6), pages 447–449. DOI: 10.1029/GL005i006p00447.

SERNAGEOMIN (2020). *Sernageomin da a conocer nuevo ranking de volcanes*. Nuevo Ranking de Riesgo Específico de Volcanes Activos en Chile. URL: https://www.sernageomin.cl/sernageomin-da-a-conocer-nuevo-ranking-de-volcanes/.

Siebert, L., E. Cottrell, E. Venzke, and B. Andrews (2015). "Chapter 12 - Earth's Volcanoes and Their Eruptions: An Overview". In: *The Encyclopedia of Volcanoes (Second Edition)*, pages 239–255. DOI: 10.1016/B978-0-12-385938-9.00012-2.

Silva Parejas, C. (2008). "Evolution and Dynamics of the 3.6 Ka BP Pucón Eruption of Villarrica Volcano, Chile". Universidad de Chile. 261 pages.

Silva Parejas, C., T. H. Druitt, C. Robin, H. Moreno, and J.-A. Naranjo (2010). "The Holocene Pucón Eruption of Volcán Villarrica, Chile: Deposit Architecture and Eruption Chronology". In: *Bulletin of Volcanology* 72.6 (6), pages 677–692. DOI: 10.1007/s00445-010-0348-9.

Silverman, B. W. (1986). *Density Estimation for Statistics and Data Analysis*. 26. Chapman & Hall/CRC. 175 pages.

Singer, B. S., M. A. Dungan, and G. D. Layne (1995). "Textures and Sr, Ba, Mg, Fe, K and Ti Compositional Profiles in Volcanic Plagioclase Clues to the Dynamics of Calc-Alkaline Magma Chambers". In: *American Mineralogist* 80.7-8 (7-8), pages 776–798. DOI: 10.2138/am-1995-7-815.

Smith, P. M. and P. D. Asimow (2005). "Adiabat_1ph: A New Public Front-End to the MELTS, pMELTS, and pHMELTS Models: ADIABAT_1PH FRONT-END". In: *Geochemistry, Geophysics, Geosystems* 6.2 (2). DOI: 10.1029/2004GC000816.

Sparks, R. and L. Marshall (1986). "Thermal and Mechanical Constraints on Mixing between Mafic and Silicic Magmas". In: *Journal of Volcanology and Geothermal Research* 29.1-4 (1-4), pages 99–124. DOI: 10.1016/0377-0273(86)90041-7.

Stern, C. R. (2004). "Active Andean Volcanism: Its Geologic and Tectonic Setting". In: *Revista geológica de Chile* 31.2 (2). DOI: 10.4067/S0716-02082004000200001.

Streck, M. J. (2008). "Mineral Textures and Zoning as Evidence for Open System Processes". In: *Reviews in Mineralogy and Geochemistry* 69.1 (1), pages 595–622. DOI: 10.2138/rmg.2008.69.15.

Takagi, D., H. Sato, and M. Nakagawa (2005). "Experimental Study of a Low-Alkali Tholeiite at 1–5 Kbar: Optimal Condition for the Crystallization of High-An Plagioclase in Hydrous Arc Tholeiite". In: *Contributions to Mineralogy and Petrology* 149.5 (5), pages 527–540. DOI: 10.1007/s00410-005-0666-7.

Templ, M., P. Filzmoser, and C. Reimann (2008). "Cluster Analysis Applied to Regional Geochemical Data: Problems and Possibilities". In: *Applied Geochemistry* 23.8 (8), pages 2198–2213. DOI: 10.1016/j.apgeochem.2008.03.004.

Van der Maaten, L. and G. Hinton (2008). "Visualizing Data Using T-SNE." In: *Journal of machine learning research* 9.11 (11).

Ward, J. H. (1963). "Hierarchical Grouping to Optimize an Objective Function". In: *Journal of The American Statistical Association* 58.301 (301), pages 236–244. URL: https://www.jstor.org/stable/2282967.

Waters, L. E. and R. A. Lange (2015). "An Updated Calibration of the Plagioclase-Liquid Hygrometer-Thermometer Applicable to Basalts through Rhyolites". In: *American Mineralogist* 100.10 (10), pages 2172–2184. DOI: 10.2138/am-2015-5232.

Watt, S. F., D. M. Pyle, and T. A. Mather (2013). "The Volcanic Response to Deglaciation: Evidence from Glaciated Arcs and a Reassessment of Global Eruption Records". In: *Earth-Science Reviews* 122, pages 77–102. DOI: 10.1016/j.earscirev.2013.03.007.

Wehrmann, H., K. Hoernle, G. Jacques, D. Garbe-Schönberg, K. Schumann, J. Mahlke, and L. E. Lara (2014). "Volatile (Sulphur and Chlorine), Major, and Trace Element Geochemistry of Mafic to Intermediate Tephras from the Chilean Southern Volcanic Zone (33–43°S)". In: *International Journal of Earth Sciences* 103.7 (7), pages 1945–1962. DOI: 10.1007/s00531-014-1006-9.

Williams, M., L. Schoneveld, Y. Mao, J. Klump, J. Gosses, H. Dalton, A. Bath, and S. Barnes (2020). "Pyrolite: Python for Geochemistry". In: *Journal of Open Source Software* 5.50 (50), page 2314. DOI: 10.21105/joss.02314.

Williams, W. T. and J. M. Lambert (1966). "Multivariate Methods in Plant Ecology: V. Similarity Analyses and Information-Analysis". In: *The Journal of Ecology* 54.2 (2), page 427. DOI: 10.2307/2257960.

Wilson, A. and J. Russell (2020). "Glacial Pumping of a Magma-Charged Lithosphere: A Model for Glaciovolcanic Causality in Magmatic Arcs". In: *Earth and Planetary Science Letters* 548, page 116500. DOI: 10.1016/j.epsl.2020.116500.

Wishart, D. (1969). "Numerical Classification Method for Deriving Natural Classes". In: *Nature* 221.5175 (5175), pages 97–98. DOI: 10.1038/221097a0.

Witter, J. B., V. C. Kress, P. Delmelle, and J. Stix (2004). "Volatile Degassing, Petrology, and Magma Dynamics of the Villarrica Lava Lake, Southern Chile". In: *Journal of Volcanology and Geothermal Research* 134.4 (4), pages 303–337. DOI: 10.1016/j.jvolgeores.2004.03.002.

Zajacz, Z. and W. Halter (2009). "Copper Transport by High Temperature, Sulfur-Rich Magmatic Vapor: Evidence from Silicate Melt and Vapor Inclusions in a Basaltic Andesite from the Villarrica Volcano (Chile)". In: *Earth and Planetary Science Letters* 282.1-4 (1-4), pages 115–121. DOI: 10.1016/j.epsl.2009.03.006.

Zajacz, Z. and W. Halter (2007). "LA-ICPMS Analyses of Silicate Melt Inclusions in Co-Precipitated Minerals: Quantification, Data Analysis and Mineral/Melt Partitioning". In: *Geochimica et Cosmochimica Acta* 71.4 (4), pages 1021–1040. DOI: 10.1016/j.gca.2006.11.001.

Zellmer, G. F., M. Pistone, Y. Iizuka, B. J. Andrews, A. Gómez-Tuena, S. M. Straub, and E. Cottrell (2016). "Petrogenesis of Antecryst-Bearing Arc Basalts from the Trans-Mexican Volcanic Belt: Insights into along-Arc Variations in Magma-Mush Ponding Depths, H_2O Contents, and Surface Heat Flux". In: *American Mineralogist* 101.11 (11), pages 2405–2422. DOI: 10.2138/am-2016-5701.

Chapter 3

Assessing Uncertainties in Volatile Saturation Pressures and Magma Storage Depths from Melt Inclusions

3.1 Preamble

This chapter is based on a paper to be submitted to the journal Volcanica titled: *Assessing Uncertainties in Volatile Saturation Pressures and Magma Storage Depths from Melt Inclusions*. The supplementary information has been directly incorporated into the text.

3.2 Abstract

Saturation pressures derived from melt and fluid inclusion volatile contents are frequently used to estimate magma storage pressures and pre-eruption processes. However, no consensus exists on how to estimate the uncertainties in these calculated pressures. Furthermore, multiple analytical techniques and data processing techniques are needed to determine total melt-inclusion volatile contents making uncertainty propagation complex. I present open-source Python scripts, which adapt existing models, to calculate volatile saturation pressures and estimate their uncertainties. I reprocess published data from past studies, showing that uncertainties in volatile saturation pressures are comparable to those of traditional mineral-based barometers when melt inclusion volumes are estimated using 2D methods. This chal-

lenges the assumption that melt inclusion-derived pressures are the 'gold standard' of thermobarometry. Additionally, I demonstrate that uncertainties are non-negligible for inclusions without vapour bubbles, highlighting the importance of propagating all sources of analytical uncertainty.

3.3 Introduction

Accurately determining the volatile element composition of magmas is essential for forecasting volcanic events (Fischer and Aiuppa 2020), understanding the Earth's deep volatile cycles (Hirschmann 2006; Kelemen and Manning 2015; Wong et al. 2019), and investigating the structure and behaviour of volcanic systems (Sides et al. 2014; Wieser et al. 2021; Wong et al. 2023). In the study of this latter case, the volatile elements CO_2 and H_2O, the most abundant volatiles in magmas, are commonly used to assess magmatic storage pressures and the processes leading to eruptions (e.g., Johnson et al. 2008; van Gerve et al. 2024).

The solubilities of CO_2 and H_2O are strongly dependent on pressure and magma composition (e.g., Allison et al. 2022; Dixon et al. 1995; Ghiorso and Gualda 2015; Shishkina et al. 2014). Comparatively, CO_2 is significantly less soluble than H_2O (e.g., Dixon et al. 1995), and will thus start degassing at deeper depths relative to H_2O. However, directly measuring CO_2 and H_2O concentrations in erupted magmas is nearly impossible due to low-pressure magmatic degassing before and during eruptions. Consequently, the concentrations of magmatic CO_2, H_2O and other volatile elements are often assessed through the study of melt inclusions (MIs), small pockets of magma trapped within growing crystals in subsurface magma reservoirs (Rose-Koga et al. 2021; Wallace et al. 2021).

While volatile element concentrations can be analysed from quenched MI glass, a secondary vapour bubble often forms within MIs. This is a by-product of changes in pressure, temperature, composition, and volume conditions in a dynamic magmatic system (e.g., Maclennan 2017; Moore et al. 2015). As the MI cools, it contracts relative to its host crystal, reducing internal pressure and causing exsolution of volatile elements, chiefly CO_2, to exsolve into a vapour bubble (Maclennan 2017). Additional post-entrapment modification (PEM) of MIs can drive further CO_2 into the bubble (Rasmussen et al. 2020) and modify the composition of the MI melt via crystallisation, melting and diffusive loss. Vapour bubbles can host a significant proportion, up to 90%, of the total MI CO_2 (Hartley et al. 2014; Moore et al. 2015). Therefore accurate determinations of MI CO_2 concentrations must account for CO_2 present in both the silicate melt and the vapour bubble.

A common workflow for determining CO_2 and H_2O concentrations from polyphase MIs (those containing both glass and a vapour bubble) involves multiple analytical methods and several stages of data processing (see Section 3.4). Each stage of this process introduces its uncertainties, which are compounded, ultimately contributing to the errors in the final calculated volatile saturation pressure.

In this chapter, I present a revised methodology for estimating and quantifying these uncertainties at each analytical stage, and for propagating them through the entire workflow. This new approach is applied to MI volatile data from several previous studies, that span a range of volatile contents and magmatic settings.

Furthermore, I describe an open-source Python 3 code designed to propagate uncertainties from MI data into the final calculation of volatile saturation pressures. The workflow, and the Python code, are implemented in the subsequent chapter (Chapter 4), where I apply it to melt inclusions from Villarrica's eruptive deposits. By doing so, I ensure that the calculated volatile saturation pressures reflect the full range of uncertainties in the analytical data, and models, they are based on. This allows the MI-derived pressures to be accurately compared to those calculated using MELTS in Chapter 2.

3.4 An Overview of the Melt Inclusion Analytical and Processing Workflow

The typical workflow to analyse total MI volatile contents (both glass and vapour phase) is summarised in Figure 3.1 and this section, and discussed in greater detail in the following sections. First MIs are identified within a target mineral phase (typically olivine, clinopyroxene, or plagioclase). Then MI and vapour bubble volumes are determined using optical photography alone or in conjunction with micro-X-ray computed tomography (micro-XCT). For inclusions that host vapour bubbles, the host mineral is then ablated via polishing to within ~30 µm of the bubble. Micro-Raman spectroscopy is then used to determine the density of CO_2 within the vapour bubble, which, when combined with measured MI volumes, allows for estimation of vapour bubble CO_2 concentrations via mass balance (e.g., Hartley et al. 2014):

$$[CO_2]_{vb} = 10^6 \cdot \frac{\rho_{CO_2} \cdot V_{vb}}{\rho_{melt} \cdot V_{melt}} \tag{3.1}$$

where V_{vb} is the vapour bubble volume, V_{melt} is the MI volume (total volume − V_{vb}), ρ_{vb} is the vapour bubble CO_2 density, and ρ_{melt} is the density of the MI glass.

MI glass CO_2 and H_2O concentrations are then determined either by Secondary Ion Mass Spectrometry (SIMS) or Fourier Transform Infrared spectroscopy (FTIR). Before SIMS analysis, the crystal is further

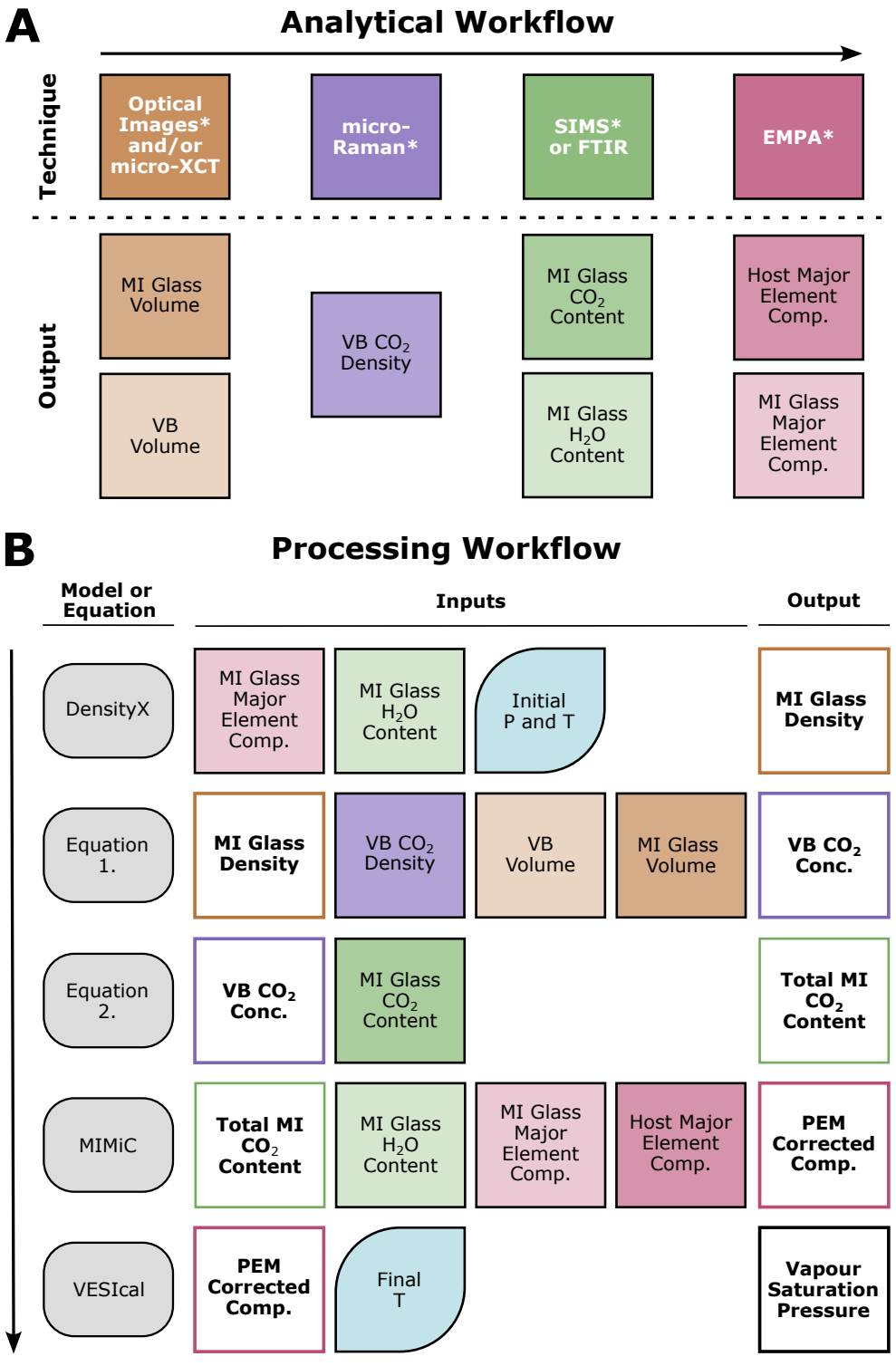

Figure 3.1: Schematics showing the (A) analytical and (B) processing workflows for calculating volatile saturation pressures from melt inclusions with vapour bubbles. *Techniques for which I have written Python code to process. Arrows show the order of the workflows. Abbreviations are as follows: Comp., Composition. Conc., Concentration. P, Pressure. T, Temperature. See text for additional definitions.

ablated by polishing to expose a sufficient analytical area (typical spot sizes are ~20 μm^2). For FTIR analysis a double-polished wafer must be produced, with a thickness of 200–600 μm. The concentrations of many non-volatile trace elements can also be measured during SIMS analysis or, if sufficient material remains, via an alternative in situ micro-analytical method (e.g., LA-ICP-MS).

The total MI CO_2 content is calculated by summing CO_2 concentrations in the glass and vapour bubble:

$$[CO_2]_{total} = [CO_2]_{vb} + [CO_2]_{melt} \tag{3.2}$$

To determine the major element composition of the MI and its host crystal, critical for PEM corrections, the sample is carbon-coated and subjected to electron probe micro-analysis (EPMA). EPMA should be performed last to avoid beam damage (Humphreys et al. 2006) and to prevent contamination from the carbon-coating (Lee et al. 2024). PEM corrections are then performed through iterative addition or subtraction of the equilibrium mineral composition, accounting for evolving equilibrium host mineral solid solution. These corrections may include post-entrapment crystallisation or dissolution corrections (e.g., Danyushevsky et al. 2002) and corrections for diffusive loss of cations from the MI (e.g., Fe-loss from olivine MIs, Danyushevsky et al. (2000)). The PEM-corrected composition of the MI is then fed into a volatile solubility model to calculate a minimum pressure of entrapment based on thermodynamic principles (e.g., Ghiorso and Gualda 2015) or empirical observations (e.g., Dixon et al. 1995; Newman and Lowenstern 2002; Shishkina et al. 2014).

3.5 Calibration Curve Statistics

A calibration curve, also called a working curve, converts measured (e.g., X-ray or ion counts) to derivative quantities (e.g., elemental concentrations). In a typical MI analytical workflow (Figure 3.1), calibration curves are required at most stages, including, but not limited to conversion of CO_2 diad separation into vapour bubble CO_2 density after Raman spectroscopy; conversion of co-correlating C-Si ion yields into CO_2 content from SIMS; and conversion of X-ray counts into mass proportions of oxides during EPMA (typically performed using integrated software; (e.g., Donovan 2021)).

Calibration curves are derived from repeat measurements of standards with known concentrations (e.g., from the GeoReM database; Jochum and Nohl 2008). These measurements are then interpolated (and sometimes extrapolated) using regression to obtain the calibration curve. This interpolation imparts an inherent uncertainty on values calculated using the resultant curve, which can be minimised by a) using

many calibration standards to create the curve, and b) performing multiple analyses on the standards. Furthermore, the composition of the standards should bracket the expected quantities of unknown analyses. This is because significant degrees of extrapolation, and to a lesser extent interpolation, will result in significant uncertainties (Miller 1991). This section summarises the primary regression methods used to obtain working curves from repeat analyses of standards.

3.5.1 Regression Methods

The regression method used to link measured values to derivative quantities introduces an additional uncertainty when the curve is applied to unknowns. Calibration typically uses a least-squares regression approach, which seeks to minimise the equation:

$$S = \sum w_i \, (Y_i - y_i)^2 \tag{3.3}$$

where Y_i is the calculated model value for the equivalent y_i (the measured value of the ith data point). The difference between the model and measured values ($Y_i - y_i$) is termed the residual. For Ordinary Least Squares regression (OLS), the weight applied to each data point (w_i) is 1, while for Weighted Least Squares regression (WLS), w_i is proportional to $1/\sigma_y^2$, where σ_y is the analytical uncertainty in y.

For heteroscedastic data (i.e., data with non-constant error), incorrect weighting leads to suboptimal estimates of best-fit parameter uncertainties (Tellinghuisen 2007). OLS assumes homoscedasticity (constant error), which is rarely the case for counts-based analytical methods (e.g., SIMS, EMPA, Raman), often dominated by proportional error at high intensities and systematic error at low intensities (Tellinghuisen 2019). Additionally, both OLS and WLS only consider the error or uncertainty in the y-variable, assuming the concentration of standards (on the x-axis) is perfectly known, or negligible compared to the analytical error on unknowns. However, this assumption is often incorrect; for example, the basaltic glasses of Shishkina et al. (2010), used as SIMS standards, have relative of ~8% CO_2 and ~20% H_2O.

Several alternatives have been proposed to address errors in both x and y (see Tellinghuisen (2020) for a review). One easy-to-code method incorporates the error in x into the weighting, creating an effective weight in y, allowing regular least-squares algorithms to be used (see Tellinghuisen 2018). This modified effective variance method (EV_2) uses partial derivatives of the response function to combine the errors (Williamson 1968):

$$w_i = \left[\left(\frac{\partial f}{\partial y} \right)^2 \cdot \sigma_{y_i}^2 + \left(\frac{\partial f}{\partial x} \right)^2 \cdot \sigma_{x_i}^2 \right]^{-1} \tag{3.4}$$

where $f(x)$ is the response function, $\partial f/\partial x$ and $\partial f/\partial y$ are its partial derivatives with respect to x and y, respectively, and σ_x and σ_y are the corresponding uncertainties.

For a straight line fit ($y = a + bx$), the $\mathbf{EV_2}$ method seeks to minimise:

$$S_{\mathrm{EV}_2} = \sum \frac{1}{\sigma_{y_i}^2 + b^2\sigma_{x_i}^2}(a + bx_i - y_i)^2 \tag{3.5}$$

By incorporating σ_x into the weight, this approach effectively treats x as error-free, meaning only the residual in y needs to be evaluated (Tellinghuisen 2010). A minor drawback is that some estimated parameters, the gradient b for a straight line, are included in the weight, requiring an iterative fitting process. However, 5–10 iterations are typically sufficient for convergence (Tellinghuisen 2010).

For straight lines, the $\mathbf{EV_2}$ method is equivalent to more complex total variance methods, that calculate the true errors in both variables (Tellinghuisen 2010; Williamson 1968). The $\mathbf{EV_2}$ approach can also be easily extended to higher-order polynomial and non-linear fits, performing comparably to more complex total variance methods (Tellinghuisen 2010).

3.5.2 Propagating Calibration Errors

Both the uncertainties in the regression parameter estimates and the uncertainty in the measured unknown can be propagated into the calculated concentration (Tellinghuisen 2019). Often-used 'classical' straight-line calibration equations do not include terms that account for correlations between regression parameters (e.g., Miller 1991). These must be accounted for to accurately propagate errors when using calibration curves (Tellinghuisen 2019). The propagated uncertainty for the calculated unknown using the calibration response function is given by:

$$\sigma_{x_0}^2 = \frac{\sigma_f^2(x_0) + \sigma_{y_0}^2}{(\mathrm{d}f/\mathrm{d}x)^2|_{x_0}} \tag{3.6}$$

where $\sigma_{x_0}^2$ is the variance in the calculated concentration, $\sigma_f^2(x_0)$ is the variance from the calibration response function at x_0, $\sigma_{y_0}^2$ is the uncertainty in the measured unknown, and $(\mathrm{d}f/\mathrm{d}x)^2|_{x_0}$ is the gradient of the response function at x_0.

The first term can be calculated by incorporating the new measured value (x_o) into the regression equation (re-centring) producing a new equation to solve (as in Tellinghuisen 2001, 2005, 2019). For a polynomial

response function of order n, this new equation becomes:

$$f(x) = a' + b'(x - x_0) + c'(x - x_0)^2 \cdots + z'(x - x_0)^n \tag{3.7}$$

At x_0, the function gives $f(x_0) = a'$, the measured unknown. This non-linear equation must be solved iteratively. As x_0 is now an adjustable parameter, the regression estimates its value and uncertainty while accounting for correlations between regression parameter estimates. The main disadvantage of this approach is that the equation must be refitted for each measured unknown. However, the fitting is not computationally expensive and can be readily performed in Excel (Salter and de Levie 2002). The second term is propagated by adding the variance in y ($\sigma^2_{y_0}$) divided by the gradient in quadrature with error from the regression (Salter and de Levie 2002).

By convention, calibration curves for SIMS and Raman are constructed with the measured value (H/Si or Δ_{CO_2}) on the x-axis and the calculated value (H_2O concentration or CO_2 density) on the y axis. This is known as an 'inverse' calibration in analytical chemistry and is preferred when the error structure of the known concentration is substantially larger than that of the measured value (Tellinghuisen 2000). The analytical and regression errors can be propagated for inverse calibration as described above, with minor adjustments to the re-centred equation. The x value is re-centred as described earlier to accommodate the measured unknown, and the y-intercept (a) is then the resultant y value with its associated uncertainty. The variance in the measured unknown is propagated through quadrature, as with regular calibration.

3.5.3 Measuring Goodness of Fit

The coefficient of determination (R^2) metric is commonly used to evaluate the quality of regressions, with values approaching 1.0 used to argue for good model choice:

$$R^2 = 1 - \frac{S}{\sum w_i (y_i - \bar{y}_w)^2} \tag{3.8}$$

However, for properly weighted fits, the theoretical value of R^2 will always be less than 1.0 (Tellinghuisen and Bolster 2011). Additionally, a significant amount of variability can be squeezed into the higher values, making it difficult to assess the suitability of multiple 'good' fits through R^2 values alone (Tellinghuisen and Bolster 2011). Furthermore, R^2 is only directly comparable for fits with the same number of data points and parameters, so it should not be used to compare the fits of the same data with different order polynomials.

Instead, the χ^2 parameter, or more exactly estimates of the χ^2 distribution from the regression equation, can be used to assess the goodness of fit:

$$\chi^2 \approx S = \sum w_i (Y_i - y_i)^2 \tag{3.9}$$

where χ^2 approaches the number of degrees of freedom of the fit ($\nu = n - p$, where n is the number of data points and p is the number of fit parameters) as n increases. As the χ^2 estimate tends to ν, the reduced chi-square ($\chi^2_\nu = \chi^2/\nu$), which tends to unity, is often used. Since both χ^2 and χ^2_ν account for the degrees of freedom, unlike R^2, they can be directly compared across different regression functions.

Deviations of χ^2_ν from unity may indicate poor regression function choice, insufficient or poorly chosen calibration data, or overly optimistic or pessimistic uncertainties in calibration. This is easier to attribute for regressions with a single set of errors, such as when using OLS or WLS. However, with effective or total variance regression methods for calibration data with errors in both x and y, identifying which (or if both) error sets are responsible is not straightforward without detailed Monte Carlo analysis (e.g., Milham et al. 2023).

3.5.4 Python Implementation

Python code provided with this paper uses the `LMFIT` library (Newville et al. 2014), to apply the EV_2 method for fitting calibration data with commonly used polynomial fits (orders 1–3), both with and without intercepts. The code uses the Levenberg-Marquardt Least Squares algorithm (Moré 1977) to fit the model equations. It also calculates various goodness of fit parameters, estimates the uncertainty in fit parameters, and propagates these uncertainties into concentrations derived from calibration curves.

Figure 3.2 compares OLS, WLS and EV_2 fits for a quadratic SIMS CO_2 calibration curve ($y = a+bx+cx^2$), showing the differences in calculated CO_2 concentrations and propagated errors for a measured unknown. Each regression method yields a different CO_2 concentration for a typical mid-range normalised intensity ratio of 0.050 ± 0.005. OLS produces the highest CO_2 concentration and the lowest error as it does not account for uncertainty in the calibration data. WLS skews towards lower concentrations at mid-to-high intensities due to low-y-uncertainties at low intensities, driven by proportional error in CO_2 content for the Shishkina et al. (2010) standards. EV_2, by considering uncertainties in both x and y, provides a more balanced fit and an uncertainty estimate that accurately reflects the calibration data.

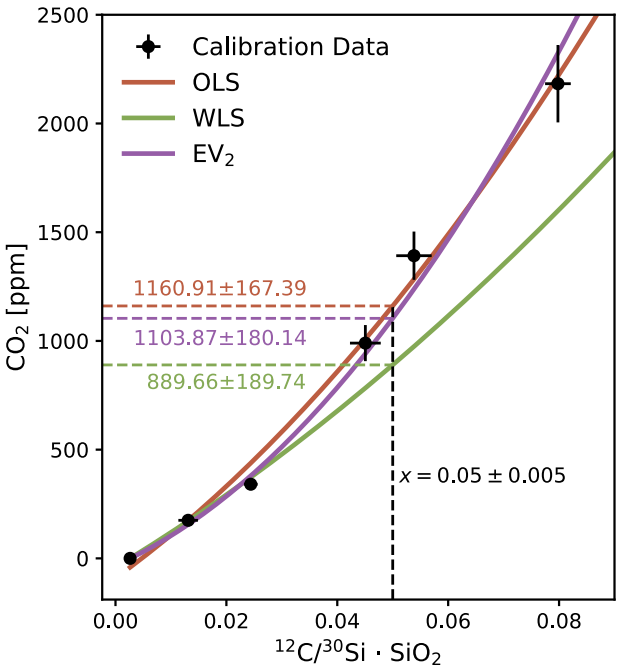

OLS: y = a + bx + cx²

	Value	Error
a	-90.8	85.9
b	1.85e+04	5.16e+03
c	1.31e+05	6.11e+04
χ^2_ν	8137.4319	
R^2	0.99308	

WLS: y = a + bx + cx²

	Value	Error
a	-41	4.47
b	1.537e+04	1.92e+03
c	6.479e+04	9.55e+04
χ^2_ν	0.0015	
R^2	-0.032536	

EV_2: y = a + bx + cx²

	Value	Error
a	-32.1	28.7
b	1.13e+04	3.17e+03
c	2.28e+05	5.53e+04
χ^2_ν	1.0887	
R^2	0.99009	

Figure 3.2: Comparison of OLS, WLS and EV_2 regressions for a SIMS CO_2 calibration curve of the form $y = a + bx + cx^2$. Dashed lines show the resultant differences in calculated CO_2 contents from an illustrative normalised SIMS measurement (0.050 ± 0.005) using each regression method. Tables show the regression parameter estimates, the parameter errors, the χ^2_ν, and R^2 values for each fit.

3.6 Melt Inclusion Glass Density

The density of a MI is commonly assumed to be around ~2.7 g·cm^{-3}, typical of basaltic glasses (Stolper and Walker 1980). However, it can be readily calculated from the major element composition of the MI itself (Iacovino and Till 2018). This allows for more accurate mass balance calculations between the vapour bubble and MI glass (Equation 3.1), using either individual MI densities (Barber et al. 2023; Wieser et al. 2021) or an average for the MI dataset (e.g., Wong et al. 2023).

A common method for determining MI densities is the Python library `DensityX` (Iacovino and Till 2018), which uses glass composition and water content (measured by EPMA and SIMS, respectively) and the thermodynamic model of Lange and Carmichael (1990). `DensityX` is calibrated for compositions from basalt to rhyolite, within the pressure range of 1–30 kbar, and temperatures up to 1627 °C. However, `DensityX` does not account for melt CO_2 content, which could lead to overestimates of MI density (Iacovino and Till 2018; Sakamaki et al. 2011). However, since a significant proportion (75–90 %) of the total MI CO_2 is often hosted in the vapour bubble, which is treated separately in the mass balance equation (Equation 3.1), CO_2 in MI glass is unlikely to have a strong effect on calculates MI glass densities.

Using `DensityX` effectively requires additional constraints on magmatic conditions. First, the temper-

ature of the melt can be determined using petrological thermometric methods (e.g., Helz and Thornber 1987; Putirka 2008; Zhang et al. 2023). As `DensityX` requires both FeO and Fe_2O_3, oxygen fugacity must be known. Either through thermodynamic relationships (e.g., Kress and Carmichael 1991) or additional analytical procedures (e.g., XANES; Cottrell et al. 2009). Finally, a pressure must also be provided, which can be chosen based on additional constraints (e.g., geophysical or petrological data). The use of a constant realistic pressure is recommended for all MI to prevent the overall process of estimating a volatile saturation pressure from becoming iterative.

A Monte Carlo approach can be used to assess uncertainty in the calculated glass density. The MI composition is sampled from a normal distribution (n=1000), with the mean equal to the measured composition for each element and the standard deviation from counting statistics (from EPMA and SIMS). The temperature for each simulated composition is determined using a liquid-only thermometer (e.g., Helz and Thornber 1987; Putirka 2008).

`DensityX` calculates both a density (Figure 3.3a) and its uncertainty (Figure 3.3b) which is derived from uncertainties in partial molar volumes, thermal expansivities and compressibilities (see Table 1 in Iacovino and Till (2018)). To combine this uncertainty with the distribution of densities from the Monte Carlo simulations, an additional 1000 values are drawn from a normal distribution with a mean of 0 and standard deviation equal to the `DensityX` uncertainty. These values are added to each calculated density, resulting in a total of 10^6 densities. The final distribution of densities is mainly influenced by the uncertainty in `DensityX` model parameters (Figure 3.3c). While the standard deviation resulting from Monte Carlo sampling of compositions is $\sim 10^{-3}$, the average model uncertainty calculated by `DensityX` is $\sim 5 \times 10^{-2}$, more than ten times higher.

3.7 Vapour Bubble CO_2 Contents from Raman Spectroscopy

The diagnostic feature in Raman spectra of gaseous CO_2 is the CO_2 diad, an artefact of Fermi resonance of the CO_2 molecule, featuring two peaks of similar intensity at $\sim 1388\,cm^{-1}$ and $\sim 1285\,cm^{-1}$ (Fermi 1931; Gordon and McCubbin 1966). The wavenumber separation between these two peaks, known as the peak splitting distance (Δ_{CO_2}), is a function of CO_2 density (Wang and Wright 1973). CO_2 densimeters use this relationship to determine CO_2 density in MI-hosted vapour bubbles and, in turn, derive CO_2 concentration (e.g., Lamadrid et al. 2017).

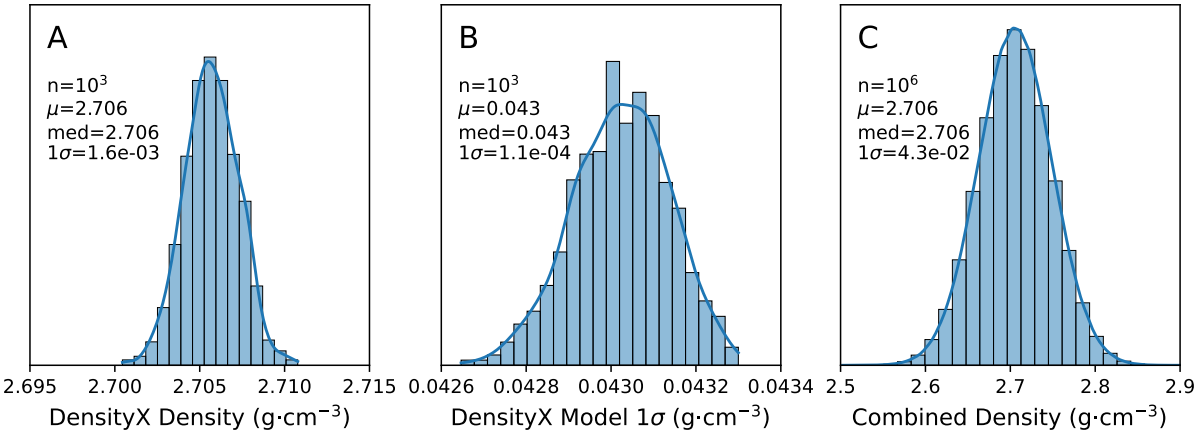

Figure 3.3: Distributions from Monte Carlo simulations of MI glass densities. n, number of simulations. μ, arithmetic mean. med, median. 1σ, one standard deviation. (A) Distribution of densities calculated using `DensityX`. (B) Distribution of `DensityX` model uncertainties, which are calculated from model value uncertainties. (C) Combined uncertainty, which is dominated by model uncertainties.

3.7.1 Diad Splitting Uncertainties

Uncertainty in measured diad splits from MI vapour bubbles depends on the spectral resolution of the Raman instrument, which determines the number of points defining each diad peak. After identifying peak and background regions of the spectra, the background is removed, and the two peaks are fit with a pseudo-Voigt function (a mix of Lorentzian andGaussian models), using a least squares fitting method to locate the peak centre (see Wieser and DeVitre 2023; Wieser et al. 2021). This fitting introduces uncertainty based on the quality of the peak fit.

`DiadFit`, an open-source Python library (Wieser and DeVitre 2023), processes Raman spectra by removing background, fitting peaks, assessing fits and calculating errors in calculated diad splits. This library fits a variety of non-linear models to Raman spectra. It calculates peak centres and their uncertainties directly from the covariance matrices of the fit results. The uncertainties in the position of each peak are then propagated through calculations for peak separation and drift correction and then through a CO_2 densimeter to calculate vapour bubble CO_2 density.

3.7.2 Correcting for Instrument Drift

To monitor drift during Raman spectra collection, the position of Ne spectral lines, or other well-established standard lines, are measured under the same analytical conditions as for CO_2 (e.g., Lamadrid et al. 2017; Wang et al. 2011),. Two spectral lines are chosen that bracket the position of the CO_2 diad, and their theoretical position in air (λ_1) are converted into Raman shifts (Δ_v, cm^{-1}) using the Raman laser's excitation

wavelength (λ_0, e.g., 532.05 nm; (Lin et al. 2007)):

$$\Delta_v = \frac{10^7}{\lambda_0} - \frac{10^7}{\lambda_1} \tag{3.10}$$

A linear correction factor is then generated for each Ne-line pair:

$$\text{Correction Factor} = \frac{\Delta_{\text{Ne}}^{\text{theoretical}}}{\Delta_{\text{Ne}}^{\text{measured}}} \tag{3.11}$$

This factor is applied to the measured CO_2 diad separation:

$$\Delta_{\text{CO}_2}^{\text{corrected}} = \text{Correction Factor} \times \Delta_{\text{CO}_2}^{\text{measured}} \tag{3.12}$$

Ne correction factors typically range from ca. 0.998,55–1.000,65 and significant affect diad-split replicability between analytical sessions (DeVitre et al. 2021; Lamadrid et al. 2017).

Alternatively, a correction factor can derived from repeat secondary standard measurements (e.g., MI vapour bubbles Barber et al. 2023; Wieser et al. 2021; Wong et al. 2023). Where CO_2 density is known from another method (e.g., high-pressure optical cell). The uncertainty in the correction factor is propagated in the same way as for the diad split, from the uncertainty in Ne-peak positions.

3.7.3 Constructing a CO_2 Densimeter Curve

A CO_2 densimeter is a calibration curve that defines the relationship between the CO_2 diad splitting measured via Raman-spectroscopy and CO_2 density. CO_2 densimeters can be derived by repeatedly measuring standards that span the expected density range of unknown samples, such as synthetic or natural fluid inclusions (Wieser et al. 2021). Another approach involves using high-pressure optical cells, where the pressure of CO_2 can be varied. An equation of state is then used to relate CO_2 pressure to density (e.g., DeVitre et al. 2021; Lamadrid et al. 2017; Lin et al. 2007; Span and Wagner 1996). Optical cells are particularly advantageous because they allow detailed examination across a wide density range which is important for medium (0.2–0.7 g·cm^{-3}) and high (>0.7 g·cm^{-3}) density inclusions, where densimeter relations are best represented by 2$^{\text{nd}}$ and 3$^{\text{rd}}$ order polynomial response functions, respectively (DeVitre et al. 2021).

It is important to note that Raman CO_2 densimeters must be specifically calibrated for each Raman spectrometer and analytical conditions. Analyses performed on optical-cell calibrated samples using different

micro-Raman spectrometers demonstrate that CO_2 peak splitting distance is dependent on instrumentation (e.g., optics, groove-density in gratings etc.), different collection parameters (e.g., laser power and wavelength, aperture and slit size), and other additional factors, such as ambient temperature (Lamadrid et al. 2017). Incorrect use of calibration curves can lead to significant differences in calculated CO_2 contents. Therefore, only densimeters calibrated on the same machine, under the same analytical conditions, should be used to process collected spectra (DeVitre et al. 2021; Lamadrid et al. 2017; Wieser et al. 2021).

Several regression methods have been used to construct CO_2 densimeters. OLS is the most common method for fitting various polynomials to calibration data. For lower CO_2 densities ($<0.2\,g{\cdot}cm^{-3}$), a straight-line fit is typically assumed to construct the calibration curve (DeVitre et al. 2021; Lamadrid et al. 2017; Mironov et al. 2020; Wieser et al. 2021). Above $0.2\,g{\cdot}cm^{-3}$, CO_2 no longer exists in the vapour bubble solely as a gas, and the densimeter relationship is best fit by higher-order polynomials (DeVitre et al. 2021; Lamadrid et al. 2017). Studies with vapour bubbles that span a significant range in density (0–$1.2\,g{\cdot}cm^{-3}$) use cubic or even higher-order polynomials (Fall et al. 2011; Kawakami et al. 2003; Song et al. 2009; Wang et al. 2019; Wang et al. 2011; Yamamoto and Kagi 2006). While higher-order polynomials will produce smaller residuals, they can lead to overfitting of the data (Shacham and Brauner 1997). Residuals analysis, and inspection of fit parameters and their errors, provide simple means to assess a suitable polynomial degree (e.g., DeVitre et al. 2021).

To my knowledge, Rosso and Bodnar (1995) is the only study to use WLS to construct a CO_2 densimeter. They applied WLS to fit a 1st-order polynomial to low-density data, with weights calculated as the inverse of propagated analytical and processing errors.

Similar to calibrations curves for SIMS data (Section 3.10.2), the best approach when constructing the densimeter is to use a method that accounts for errors in both the corrected CO_2 diad split (x) and the CO_2 density of standards (y). This approach ensures reliable estimates of the best-fit parameter uncertainties. This is the case for densimeters determined from either standards and HPOCs and for all CO_2 densities. The error in the unknowns can then be propagated through the densimeter as described in Section 3.5.

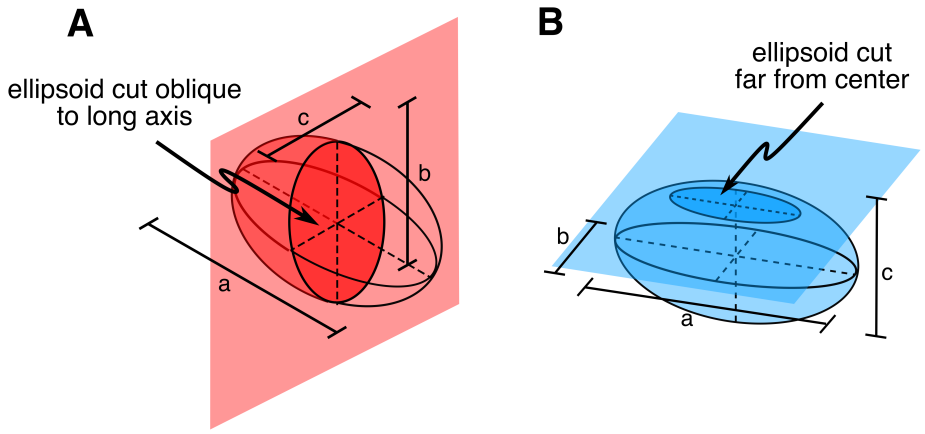

Figure 3.4: Bad intersection plane orientations for melt inclusion volume reconstruction from intersection ellipse geometry: (A) when the inclusion is cut perpendicular to its long axis, and (B) when the inclusion is cut far from its centre.

3.8 Melt Inclusion Volume

3.8.1 2D Methods - Optical Imagery

The most accessible method for reconstructing MI and vapour bubble volumes is the use of 2D imagery (optical or SEM images). The main disadvantage of this approach is that a single 2D image cannot provide a complete set of 3D information without making assumptions about the shape of the MI. Here, I consider the simple case where an MI can be represented by a triaxial ellipsoid with long axes $a \geq b \geq c$. Since 2D images only capture two axes, a and b, the third dimension, c, must be estimated using the geometry of the intersection ellipse between MI and a calibrated focused plane (Hartley et al. 2014; Tucker et al. 2019; Wieser et al. 2021; Wong et al. 2023). Common methods for estimating the third dimension include:

1. the arithmetic mean of the long and short axes ($c = [a + b]/2$) (Moore et al. 2015; Wieser et al. 2021; Wong et al. 2023),
2. the geometric mean of the long and short axes ($c = \sqrt{ab}$) (Ni et al. 2017), and
3. the shortest axis ($c = b$) (Hartley et al. 2014).

To estimate the uncertainties from these three methods, Tucker et al. (2019) use a Monte Carlo approach to simulate the intersection of polished planes with MIs. They simulate the intersection of randomly sized ellipsoids with randomly oriented planes to generate ellipses of intersection. In their model, the intersection plane always passes through the centre of the simulated ellipsoid. Tucker et al. (2019) determines that, while the arithmetic mean provides the best estimate of the true volume of the ellipsoid with

an asymmetrical 1σ error of -48% and 37%, all three methods routinely over- or underestimate the true volume (Figure 3.5a).

In practice, significant underestimations of MI volume occur for three main reasons. First, is when a strongly eccentric ellipsoid ($a \gg b \geq c$) is intersected at an extreme angle or even orthogonal to its long axis a (Figure 3.4a). This scenario is possible in Tucker et al. (2019)'s simulations but unlikely in reality, since, to maximise the area available for compositional analysis (e.g., the placement of a ~20 µm diameter SIMS spot), MIs are mounted parallel to their long axis. Secondly, the ellipsoid may be cut far from its centre, which is not accounted for in the simulations of Tucker et al. (2019) (Figure 3.4b). This scenario can be avoided if a well-focused optical photograph is taken before polishing and MI exposure, as opposed to a reflected light or backscatter electron image (e.g., Tucker et al. 2019). If the image is well-focused, it will capture the full extent of the MI. Finally, analysis of MIs with extreme aspect ratios is improbable, as pancake- or needle-shaped inclusions are unlikely to provide sufficient area for compositional analysis even when exposure is maximised.

To assess the changes that this a priori information makes to the effectiveness of volume reconstruction, I follow the approach of Tucker et al. (2019) in performing a series of Monte Carlo simulations. The key differences between my simulated approach and that of Tucker et al. (2019) are as follows:

1. Ellipsoid aspect ratios between axes are limited to <5 to reflect biases when selecting MI samples for analysis.

2. The orientation of the intersection plane is allowed to vary by a limited amount to mimic an oblique intersection with the MI. The dip direction of the intersection plane can change by ±10° relative to the horizontal and the strike of the plane by ±15° from the trend of the long axis.

Implementing these changes has three significant impacts on the results of Monte Carlo simulations, compared to those from Tucker et al. (2019) (Figure 3.5). First, the probability of obtaining the correct volume is increased for all three approaches (Figure 3.5c and d). The arithmetic mean predicts the correct volume more frequently than either the geometric mean or the shortest dimension. Second, by constraining the orientation of the intersection plane to be approximately parallel to the MI long axis, the probability of underestimating the MI volume using the arithmetic mean is approximately halved compared to the Tucker et al. (2019) simulations. However, this is balanced by a higher likelihood of overestimating MI volume (Figure 3.5c and d). All three methods produce non-normal error distributions for estimated MI volumes (Figure 3.5B). As a result, a Monte Carlo approach is required to propagate

volume uncertainty distributions when calculating vapour bubble CO_2 using mass balance (Equation 3.1) and other quantities dependent on MI volume (Figure 3.1).

Although the arithmetic mean and geometric mean are more likely to correctly predict the true volume of the MI (Figure 3.5), there are two practical reasons to select the shortest measured axis as the unknown third dimension. First, it is reasonable to suggest that the MI intersection ellipse exposing the two longest axes of the ellipsoids will be chosen before imaging to maximise the area for analysis. Using the most conservative length of the third dimension will then be most likely to accurately reconstruct the true MI volume, reducing the likelihood of overestimation. Second, both the arithmetic and geometric mean approaches produce highly non-normal error distributions with a significant divergence between their medians and modes (Figure 3.5D). This means that representative 1σ uncertainties in volumes cannot be approximated as normal distributions, thereby increasing the difficulty in determining the uncertainty in quantities dependent on the estimated volume.

To reduce the total number of simulations required to estimate the error in volatile saturation pressure, I suggest carrying only three volumes forward for the remainder of the processing workflow: the average volume and the average volume ± the asymmetric 1σ error estimated by the 16% and 84% percentiles. This ensures that the propagation of all uncertainties can be carried out using a reasonable number of Monte Carlo simulations.

3.8.2 3D Methods - Micro X-Ray Computed Tomography

The 2D volume reconstruction methods discussed above rely on a significant assumption: that MIs are well represented by triaxial ellipsoids. However, MIs frequently present negative crystal habits, which are not ellipsoids (Bennett et al. 2019; Lima 2000; Moore et al. 2015). Micro X-ray computed tomography (micro-XCT) is a non-destructive imaging technique that produces 3D maps of the internal structure of a sample. This technique has been applied to melt and fluid inclusion analysis for geometric analysis and imaging (Créon et al. 2018; Gaetani et al. 2015; Pamukcu et al. 2013, 2015; Richard et al. 2019) and to quantify olivine-hosted MI volume and therefore total MI CO_2 (e.g., DeVitre et al. 2023b; Hanyu et al. 2020; Miller et al. 2019; van Gerve et al. 2024).

Similar to a medical CT scan, X-ray attenuation contrasts are mapped around 360° and reconstructed to produce a 3D rendering of the internal density structure of the sample. The density contrasts between the vapour bubble, MI glass, and the host phenocryst are substantial enough to be imaged using this technique under appropriate analytical conditions. To obtain high spatial resolution (ca. 1–5 µm)

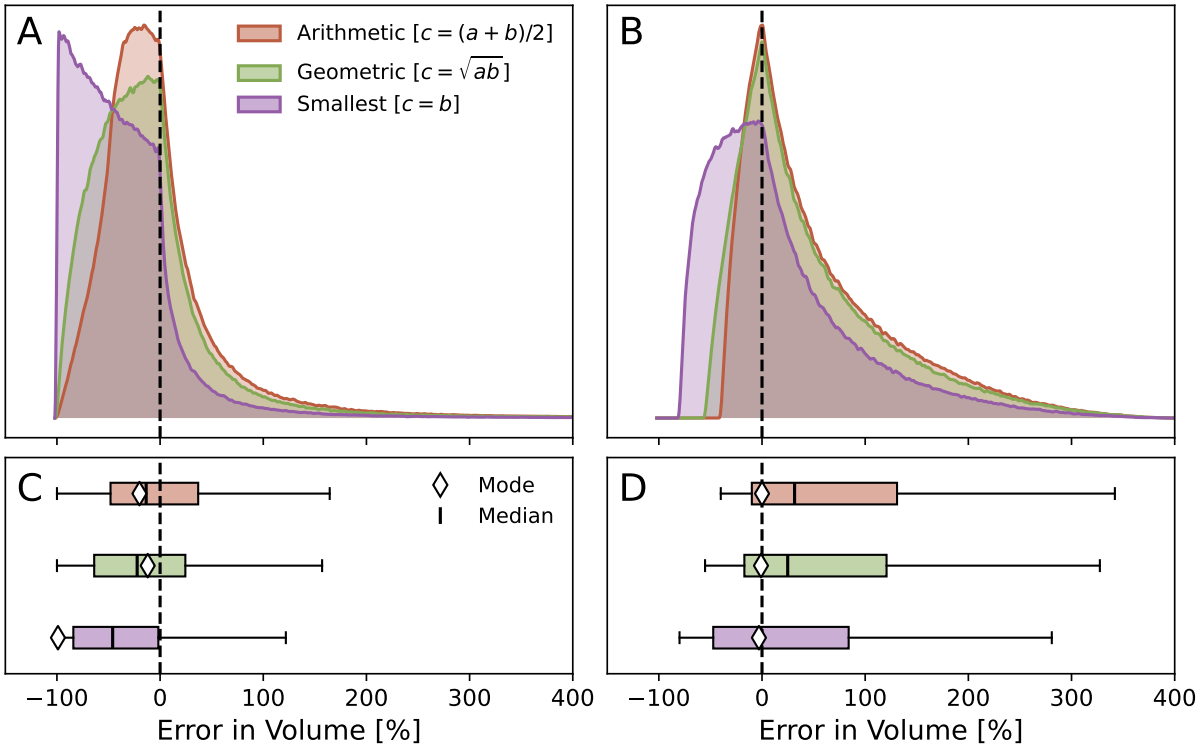

Figure 3.5: Comparison of plane-ellipsoid intersection models: (A) Tucker et al. (2019) with unconstrained melt inclusion dimensions and intersection orientations, and (B) realistic melt inclusion dimensions and intersection planes approximately parallel with melt inclusion long axes. The black dashed line marks the correct prediction of ellipsoid volume. (C) and (D) are box-whisker plots for each set of distributions. Note the edges of each box represent the 16% and 84% percentile of each distribution (the $\pm 1\sigma$ uncertainty), rather than the interquartile range. The white diamonds show the mode of each distribution.

and better radiographs (attenuation contrast), the detectors remain stationary while the sample is rotated slowly. 2D radiographs are collected contiguously at angles around 360°, and these are reconstructed using computational algorithms (e.g., Feldkamp et al. 1984) and back-projection to obtain a 3D data set.

Data is stored as 3D pixel cubes (voxels) which control the smallest volume element and therefore the spatial resolution of the scan. Voxel size is controlled by the resolution of the detectors and the sample size. Generally, scanning a smaller sample results in a smaller voxel size. Image processing techniques are used to extract quantitative information from the scans, and remove artefacts such as beam hardening and ring artefacts. This can be done in software such as `ImageJ` (Schneider et al. 2012), `Dragonfly ORS®` and `Avizo®`.

The uncertainty on calculated volumes comprises two parts (Lin et al. 2015). 1) the random error due to the partial volume effect, and 2) the systematic error due to the choice of thresholding algorithm. The partial volume effect occurs when the edges of an object do not perfectly align with the voxel grid. This means voxels will be partially filled, leading to over or underestimation of true volumes. This is assessed

by producing multiple scans at different relative orientations (Lin et al. 2015), or by scanning objects with known volumes comparable to the studied sample (Hanyu et al. 2020). Error resulting from the thresholding algorithm can be assessed by varying the thresholds for the different phases and calculating the effect on calculated volumes. Typical uncertainties for MI volumes measured using micro-XCT are ca. 10% relative (Hanyu et al. 2020; Lin et al. 2015).

3.8.3 Comparisons Between 2D and 3D Volume Methods

Several studies have compared 2D and 3D MI volume estimation methods. Mironov et al. (2020) compared MI volumes estimated using the 2D approach — assuming the unknown dimension was equal to the shortest measured — and 3D volumes calculated by directly measuring the third dimension through polishing the MI host orthogonally to the initial 2D measurement. They found an average absolute normalised difference of 23% between the volumes calculated using these two methods, with relative volume differences ranging from −22–100 %. (DeVitre et al. 2023b) compared volumes calculated from micro-XCT with those estimated from 2D methods and reported median absolute volume differences of ∼20–30 %. However, they also observed that 2D methods routinely over- or underestimated MI volume by up to 1.5 times, consistent with error distributions shown in Figure 3.5b. Hanyu et al. (2020) also compared volumes measured by micro-XCT with those estimated using 2D methods, assuming that the third unknown dimension was equal to the shorter of the two measured axes. Their results showed significant differences between the two methods, ranging from -5.36% to +203.52% relative, with an average absolute difference of ∼60%.

All three studies demonstrate that 2D methods frequently overestimate or underestimate MI volumes compared to 3D methods, even for MI which are approximately ellipsoidal. However, the relative differences in volume are well represented by the error distributions presented in Figure 3.5. As more 3D volume data for MI is collected, there is potential to refine ellipsoid axes ratio inputs and create error distributions that better reflect the uncertainties involved in estimating MI volume using 2D methods.

Additionally, DeVitre et al. (2023b) and Mironov et al. (2020) explored the benefits of measuring an additional dimension by polishing the host orthogonally to the primary surface. This approach allows for the direct measurement of the previously unknown depth of each MI, enabling more accurate estimates of MI volumes. This has the advantage of being more affordable and accessible than micro-XCT. DeVitre et al. (2023b) found that incorporating this additional constraint on the third dimension led to much more accurate estimates of MI volume. In most cases, MI volume differences were in the range of 10–20 %

compared to micro-XCT measurements, except when the MI were highly irregular and difficult to fit with an ellipsoid. Thus, orthogonal polishing therefore presents a viable low-cost alternative to micro-XCT.

3.9 Vapour Bubble Volume

Vapour bubble volumes (V_{vb}) are determined using the same methodologies as MIs. When using 2D imagery, spherical vapour bubbles are assumed, as a sphere minimises the surface area-to-volume ratio of a 3D shape. The uncertainty in vapour bubble volume ($\sigma_{V_{\mathrm{vb}}}$) can be estimated from the uncertainty in the bubble radius (σ_r) as follows:

$$\sigma_{V_{\mathrm{vb}}} = 4\pi r^2 \times \sigma_r \tag{3.13}$$

This approximation holds as long as σ_r (typically the image pixel size) is much less than the radius of the vapour bubble. This is the case for typical image resolutions: a 40× objective and 1080p sensor gives a pixel size of 0.16 µm. Applying Equation 3.13, this produces a 9.5% relative uncertainty in vapour bubble volume for a 5 µm radius bubble, decreasing to 2.5% for a 20 µm radius bubble.

There is also a systematic error in volume due to inaccuracies in measuring vapour bubble radii. To quantify this, I measured the radii of five vapour bubbles, from past studies reprocessed in this chapter, fifty times each and calculated a relative uncertainty from the standard deviation of the measurements. The bubbles measured were from the following inclusions: MHL-05_4_1 and MHL-07_19_2 (Hartley et al. 2014); LL8_626 (Wieser et al. 2021); and A_A5 and C_C4 (Wong et al. 2023). Their radii varied between ca. 5–25 µm, and I found relative errors of around 1% for the measured radii, corresponding to a relative volume error of approximately 3.3%. The uncertainty from image resolution and human error can be combined in quadrature for a single vapour bubble.

When using micro-XCT to calculate MI and vapour bubble volumes, the same approach can be applied to calculate volume uncertainties. However, vapour bubbles typically have volumes an order of magnitude smaller than their host MI, and the higher resolution of optical methods offers a significant advantage over micro-XCT. For instance, even with a voxel size of 3 µm, a typical vapour bubble would consist of fewer than ten voxels, leading to significant uncertainties in calculated volumes. Additionally, since vapour bubbles are generally spherical, their regularity diminishes the advantage that micro-XCT provides in accounting for irregular geometries.

3.10 Glass Volatile Contents from SIMS

3.10.1 Internal Precision

SIMS analyses for ^{12}C and ^{1}H are typically collected in batches of 10–20 cycles (Hauri et al. 2002). The first 7–10 cycles are discarded to remove the effects of surface contamination and to allow the signals for C and H_2O to stabilise. The mean and 2σ are then determined for each set of remaining cycles, with any that fall outside the 2σ error range identified as outliers and removed from further calculations. Finally, the internal precision, which reflects signal stability during an acquisition, is then calculated using the standard mean error. The internal precision from the analysis of standards is then considered during the calibration of a working curve. The internal precision for unknowns is propagated through the working curves to estimate errors in volatile concentrations.

3.10.2 Standard Working Curves

To convert elemental count intensities into concentrations, calibration curves are created using standard glasses with known volatile concentrations measured by other methods (e.g., near-IR and mid-IR, (Hauri et al. 2002; Moussallam et al. 2024)). Ideally, standards should be matrix-matched to avoid significant matrix effects, e.g., using basaltic standards when analysing basaltic glasses (Hauri et al. 2002; Hervig et al. 2003). CO_2 calibration curves are constructed from the ratio of $^{12}C/^{30}Si \times SiO_2$, where ^{12}C is the measured carbon intensity (in counts per second), against known CO_2 content (see Figure 3.2).Since H ion yields vary according to the SiO_2 of the glass (Shimizu and Gill 1997), ratios of elemental counts against Si are used ($^{1}H/^{30}Si$), without including a SiO_2 term.

Various methods have been used to generate SIMS calibration curves for volatile contents. However, in many studies, the calibration curves used are often not reported. If they are, it is often not clear how, or sometimes if, errors are propagated. Multiple studies use OLS and force the fit through the origin after background intensity subtraction (BS; Esposito et al. 2011, 2014; Hartley et al. 2014; Helo et al. 2011; Lloyd et al. 2014; Shimizu et al. 2009; Wieser et al. 2021; Wong et al. 2023).

Other studies use WLS but do not specify how the weights for each point were calculated (Blundy and Cashman 2005; Shimizu et al. 2017). In addition, some studies use methods that account for the errors in both x and y but do not perform as well as EV_2 (Tellinghuisen 2020). For example, Koga et al. (2003), Mosenfelder et al. (2011) and Shimizu et al. (2017) use the York method (York 1968), and Towbin et al. (2023) uses Orthogonal Distance Regression (Boggs et al. 1987).

3.10.3 Normalisation to an Internal Standard

After SIMS analysis, an internal standard, often ^{30}Si, is then measured using EMPA. As this is used to normalise the ^{30}Si counts per second, the analytical uncertainty on SiO_2 measured by the probe should also be propagated.

3.10.4 Presenting Results

When presenting SIMS data, authors should describe how calibration curves are derived, including the linear regression method, how weights are calculated, and how uncertainties from counting statistics are propagated into the final concentrations. In addition, publishing raw calibration data and unknowns, in addition to figures showing calibration curves, allows readers to assess how collection and processing methods influence final concentrations.

3.11 Water Contents from Host-MI Hygrometry

The diffusion of H^+ ions is accelerated when olivine crystals are held at high temperatures, either within the magmatic system or upon eruption in coarse tephra layers or lava flows (Lloyd et al. 2013). This can lead to dehydration or excess hydration of olivine-hosted MIs (Bucholz et al. 2013; Gaetani et al. 2012; Hartley et al. 2015). Gavrilenko et al. (2016) developed a Ca-exchange olivine-liquid hygrometer, which uses Ca as a proxy for water contents in subduction arc MIs. This is possible because Ca^{2+} diffuses much more slowly in olivine ($\sim 10^{-11}$ $m^2 \cdot s^{-1}$; Coogan et al. (2005)) compared to H^+ ($\sim 10^{-4}$ $m^2 \cdot s^{-1}$; Barth et al. (2019)) at magmatic temperatures. Therefore, original water concentrations in MI, even if affected by dehydration or hydration, can be reconstructed by considering proxy species like Ca in olivine (e.g., Brahm et al. 2022). For plagioclase-hosted MIs, a similar approach could be used utilising a plagioclase-liquid hygrometer (e.g., Cutler et al. 2024; Waters and Lange 2015), though no such corrections have been reported in the literature to my knowledge. Analytical uncertainties in both the host and MI compositions can be propagated using a Monte Carlo approach (e.g., as implemented in the open-source Python library `Thermobar`; Wieser et al. (2022c)).

3.12 Post-Entrapment Modification Corrections

Post-entrapment modification (PEM) refers to changes in MI composition after entrapment (e.g., Danyushevsky et al. 2000; Danyushevsky et al. 2002). Traditionally the software `Petrolog3` (Danyushevsky

and Plechov 2011) has been used to correct for PEM in olivine-hosted MIs. This software accounts for both post-entrapment crystallisation or dissolution (PEC/D) and diffusive Fe-loss from the MI (Danyushevsky and Plechov 2011). However, this software does not provide a means to readily propagate the analytical uncertainties of the MI and host major element compositions.

A more recent alternative is the open-source Python code Melt Inclusion Modification Corrections (`MIMiC`; Rasmussen et al. (2020)). `MIMiC` incorporates updated olivine-melt partitioning models (e.g., the olivine-liquid KdFe-Mg model of Toplis (2005)), and can model partitioning of CO_2 from the melt into the vapour bubble. Like `Petrolog3`, it accounts for both PEC/D and Fe-loss in the same manner, but it also propagates analytical uncertainties throughout PEM corrections using a Monte Carlo approach. `MIMiC` propagates for analytical uncertainties in both the MI and its host.

Both `Petrolog3` and `MIMiC` require an estimation of the original FeO of the MI before PEM (FeO*), to correct for Fe-loss. Fe-Mg re-equilibration during the post-entrapment growth of Fe-rich olivine around the MI leads to the diffusive loss of Fe through the olivine crystal into the surrounding melt. As the MI and its host do not record this process, the extent of Fe-loss is unknown and FeO* is unconstrained. To reconstruct FeO*, two approaches are commonly considered. The first utilises the average FeO of measured carrier melts from the magmatic system. This is used when it is clear that melt FeO is not significantly affected by olivine-only crystallisation and thus remains constant along the olivine liquid line of descent (Putirka 2005). A second approach must be taken if there is a clear correlation between olivine composition and carrier melt FeO (e.g. when another phase begins crystallising). Using whole-rock or glass composition, the equilibrium olivine compositions of carrier melts are determined using an olivine-liquid Fe-Mg exchange coefficient (e.g., $K_D = 0.30 \pm 0.03$ (Roeder and Emslie 1970)). The host olivine compositions of the MI suite are then matched to a corresponding FeO*, using the correlation between carrier melt FeO and equilibrium olivine. With either method, the uncertainty in calculated FeO* can be propagated via a Monte Carlo approach using `MIMiC`.

3.13 Volatile Solubility Models

Determining the CO_2 and H_2O concentrations of MIs, in combination with their major element compositions, form the basis of volatile saturation barometry. This approach estimates the pressure at which a melt becomes volatile-saturated. To calculate a pressure a model of volatile solubility is used. These relate the volatile and major element compositions of melts to the minimum pressure at which its constituent volatiles are soluble, for a given temperature.

Several volatile solubility models are available, covering a range of pressures, temperatures, and magma compositions. Wieser et al. (2022a) provides a comprehensive review and guidance on model selection. The uncertainty in a pressure calculated using these models depends on several factors: 1) the uncertainty in MI composition (post-PEM major and volatile elements), 2) the uncertainty in equilibration temperature, and 3) the inherent uncertainty derived from the calibration of the volatile solubility model.

`VESIcal` provides a single platform through which many volatile saturation models can be accessed, thereby allowing straightforward comparison of different models calibrated over a wide range of pressures, temperatures, and compositions (Iacovino et al. 2021). By repeated sampling from normal distributions defined by PEM compositions and their associated uncertainties (as determined by `MIMiC`), the impact of uncertainties in pressures derived from MI compositions can be propagated using a Monte Carlo approach (n=1000). This produces a distribution of calculated pressures that fully accounts for uncertainties in their constituent analytical data.

Table 3.1: Representative volatile contents, saturation pressures and details of past studies reassessed in this work.

Source	Location	Volcanic System	CO_2 Glass (ppm)	CO_2 VB (ppm)	H_2O (wt%)	P (kBar)
H2014[a,α]	Iceland	Laki	102 to 975	1,232 to 46,422	0.3 to 0.7	0.1 to >5
Wi2021[b]	Hawaii	Kīlauea	4 to 403	0 to 1,405	0.1 to 0.3	0.1 to 2.1
Wo2023[c]	Ethiopia	MER	35 to 5,770	0 to 1435	0.25 to 1.25	2.5 to 4.5
B2023[d,β]	Indonesia	Mt Slamet	0 to 8000	1800[γ]	0.0 to 4.0	0 to 4.0

[a]Hartley et al. (2014). [b]Wieser et al. (2021). [c]Wong et al. (2023). [d]Barber et al. (2023). [α]inclusions from tephra only. [β]olivine-hosted inclusions only. [γ]Only one VB produced a fermi diad. VB, VB. P, volatile saturation pressure. MER, Main Ethiopian Rift.

Table 3.2: Summary of methods used by past studies reprocessed in this work.

Source	**SIMS Cal**	**Densimeter**	**MI Vol**	**VB Vol**	**Vol Sat**	**MI Density** ($g \cdot cm^{-3}$)	**PEM**
H2014[a]	OLS, BS	OLS*	2D, Short	2D, Arith	VC, SE	Constant, 2.750	Pet3
Wi2021[b]	OLS, BS	OLS	2D, Arith	2D, Arith	MS	Variable, DX	Pet3
Wo2023[c]	OLS, BS	OLS	2D, Arith	2D, Arith	MS	Constant, 2.708	Pet3
B2023[d]	OLS, BS	OLS	2D, Short	2D, Arith	MS	Variable, DX	Pet3

[a]Hartley et al. (2014). [b]Wieser et al. (2021). [c]Wong et al. (2023). [d]Barber et al. (2023). *Used densimeter of Kawakami et al. (2003). MI, melt inclusion. VB, VB. Vol Sat, volatile saturation model. PEM, post-entrapment modification correction scheme. OLS, Ordinary Least Squares. BS, Background Subtracted. 2D, uses a 2D optical method. Short, assumed third axis was equal to the shortest measured. Arith, assumed third axis was equal to the mean of those measured. VC, (Newman and Lowenstern 2002). SE, (Witham et al. 2012). MS, (Ghiorso and Gualda 2015). DX, (Iacovino and Till 2018). Pet3, (Danyushevsky and Plechov 2011).

3.14 Application to Published Melt Inclusion Data

In this section, I reevaluate MI data from four key studies — Barber et al. (2023), Hartley et al. (2014), Wieser et al. (2021), and Wong et al. (2023) — using the methods developed in this chapter to reassess volatile saturation pressures and their uncertainties. All four use a combination of SIMS, micro-Raman, and EMPA to analyse the CO_2 and H_2O contents of MI glasses and vapour bubbles, along with the major element chemistry of the MI glass and host-olivine. These studies span a range of tectonic settings (rifts, ocean islands, subduction arcs), and feature MIs with varied compositions, ranging from basaltic to dacitic, and diverse CO_2 and H_2O contents. I selected five representative MIs from each study to capture the variability of their volatile contents, and these data are summarized in Table 3.1.

3.14.1 Previous Methods Used

All four studies used the same analytical methods to study MI: optical imagery for MI and vapour bubble volumes, micro-Raman spectroscopy for vapour bubble CO_2 contents, SIMS for MI glass volatile contents, and EMPA for MI glass and host major element compositions. However, the four studies used different approaches to calculate MI volatile contents and saturation pressures. These are summarised below and in Table 3.2.

3.14.1.1 MI Glass Density

Hartley et al. (2014) used a constant density of 2.750 g·cm^{-3}. Wong et al. (2023) also used a constant density of 2.708 g·cm^{-3}, representing the average density calculated by `DensityX` after post-entrapment modification correction. Wieser et al. (2021) and Barber et al. (2023) both calculated individual MI glass densities using `DensityX`. Wieser et al. (2021) calculated densities ranging from 2.69–2.79 g·cm^{-3}, while Barber et al. (2023) calculated densities between 2.42–2.99 g·cm^{-3}. None of the studies considered errors in the calculated or assumed densities.

3.14.1.2 MI and Vapour Bubble Volume

Hartley et al. (2014) calculated MI volume assuming that the third unknown dimension of the ellipsoid was equal to the minor axis of the measured intersection ellipse ($c = b$). The other three studies used the arithmetic mean of the two measured axes ($c = (a+b)/2$). All studies assumed that vapour bubbles were spherical, using the mean axes of best-fit ellipses to calculate their volume. Only Barber et al. (2023), Wieser et al. (2021), and Wong et al. (2023) accounted for uncertainties in MI volume, assuming an

uncertainty of −30–40 % after Tucker et al. (2019).

3.14.1.3 Vapour Bubble CO_2 Density

Hartley et al. (2014) used the CO_2 densimeter of Kawakami et al. (2003), which was constructed using OLS, and a cubic polynomial. Uncertainties from the average of three Raman spectra were propagated through the Kawakami et al. (2003) densimeter to calculate maximum and minimum CO_2 densities. In contrast, Barber et al. (2023), Wieser et al. (2021), and Wong et al. (2023) used the same straight-line, low-density densimeter constructed via measurement of calibrated standards first used in Wieser et al. (2021). Neither densimeters considered uncertainties in standard concentrations. Uncertainties on diad separations were estimated from three repeats and propagated through the densimeter equation. The quality of peak fitting was not considered.

3.14.1.4 MI Glass Volatile Contents

All studies used background-subtracted OLS to construct SIMS calibration curves, for both CO_2 and H_2O, using straight line fits forced through the origin ($y = bx$). Uncertainties in standard concentrations were not accounted for in the regression. Uncertainties estimated from counting statistics were carried forward into glass volatile concentrations.

3.14.1.5 PEM Correction

All studies used `Petrolog3` software (Danyushevsky and Plechov 2011) to correct MI major element compositions for post-entrapment modification. No uncertainties were propagated through the PEM correction, and `Petrolog3` does not account for the minor pressure dependence of olivine-liquid $Kd^{Fe\text{-}Mg}$. Wieser et al. (2021) used a constant FeO* of 11.33 wt.% for MI hosted in olivine with forsterite contents of greater than 79 mol.%. For lower forsterite contents a liquid line of descent calculated using MELTS (Gualda et al. 2012), was used giving 11.34–12.0 wt.% FeO*. Both Wong et al. (2023) and Barber et al. (2023) assumed an original FeO* using the mean of carrier glasses and oxygen fugacity of QFM, resulting in a FeO* of 12.9 wt.% and 11.0 wt.%, respectively.

3.14.1.6 Volatile Saturation Pressures

The four studies used different solubility models to calculate volatile saturation pressures. Hartley et al. (2014) compared results from both VolatileCalc (Newman and Lowenstern 2002) and SolEx (Witham et al. 2012). Wieser et al. (2021) compared results from VolatileCalc, MagmaSat (Ghiorso and Gualda

2015), and the models of Shishkina et al. (2014) and Iacono-Marziano et al. (2012). Maximum and minimum saturation pressures were calculated by inputting maximum and minimum CO_2 concentrations accounting for uncertainties from Raman and MI volume. Wong et al. (2023) used MagmaSat with a constant temperature of 1200 °C for all MI, inputting maximum and minimum CO_2 contents, as in Wieser et al. (2021), to derive maximum and minimum saturation pressures. Barber et al. (2023) used MagmaSat with a constant temperature of 1100 °C for all MI.

3.14.2 Reprocessing Volatile Saturation Pressures

3.14.2.1 SIMS Calibration Curves

For each set of H_2O and CO_2 calibration curves I employed a linear response function ($y = a + bx$), to match those used in the original studies. I used the same calibration standards but did not use background-corrected values, instead including an intercept in the response function. For consistency, all CO_2 calibration curves used $^{12}C/^{30}Si \times SiO_2$ against CO_2 (ppm). To propagate the uncertainties in standard compositions, measured ratios, and unknowns, I applied the EV_2 regression method. The reconstructed calibration curves are shown in Figure 3.7 (Hartley et al. 2014), Figure 3.8 (Wieser et al. 2021), Figure 3.9 (Wong et al. 2023), and Figure 3.10 (Barber et al. 2023).

To construct the calibration curves of Barber et al. (2023), Wieser et al. (2021), and Wong et al. (2023), I referenced published concentrations and 1σ values for the calibration standards of Shishkina et al. (2010) (see their Table 2). For the volatile-free standards (N72 and 519-4-1; Hauri et al. 2002) used these studies, I assigned an uncertainty of 3 ppm for CO_2 (the smallest error reported by Shishkina et al. (2010), corresponding to a concentration of 35 ppm) and an uncertainty of 0.11 wt.% for H_2O, the lowest reported uncertainty for glass standards in Shishkina et al. (2010). Since no uncertainties for SiO_2 are reported for these volatile-free standards, I assumed an uncertainty of 0.37 wt.%, representative of the SiO_2 uncertainty of the other standards used (Shishkina et al. 2010).

For Hartley et al. (2014), I used the published concentrations and 1σ values for the calibration standards of Shishkina et al. (2010) (St-1, St-2, St-3 and St-6; see Section 2.5 of Shishkina et al. 2010). Only the normalised starting composition from the average of fifty microprobe spots is given (50.17 wt.% SiO_2; Table 1 of Shishkina et al. 2010), without uncertainties. Therefore I used the average SiO_2 uncertainty for the other Shishkina et al. (2010) glasses used as standards by the other studies, 0.37 wt.%. For the H_2O calibration curve I used the published concentrations for KL2-G and NIST-SRM610 (0.015, 0.013 wt.%), and 1σ values of 5% relative (0.00075, 0.00065 wt.%), at the higher end of the suggested 2σ

range of 1–7 % relative (Jochum et al. 2006). It should be noted that these are very low, likely calculated assuming signal-proportionality and the true uncertainty is almost certainly much higher. For consistency with the other studies reprocessed, I used an uncertainty of 3 ppm CO_2 for the nominally volatile-free glass standards BCR-2G (Jochum et al. 2006) and 150-3 (Hall 1999) .

3.14.2.2 Melt Inclusion Glass Density

MI glass densities were recalculated with DensityX (Iacovino and Till 2018) across all studies. For relatively dry samples (Hartley et al. 2014; Wieser et al. 2021; Wong et al. 2023), I estimated temperature using the anhydrous liquid-only thermometer of Helz and Thornber (1987). For wetter samples (Barber et al. 2023) I used Equation 15 of Putirka (2008) which is dependent on both H_2O content and pressure. I used the following pressure estimates and oxygen fugacity buffers for density calculations: 0.5 kbar and QFM+0.7 (Hartley et al. 2014); 0.5 kbar and QFM+0.5 (Wieser et al. 2021); 2.0 kbar and QFM (Wong et al. 2023); and 1.0 kbar and QFM+1 (Barber et al. 2023).

Analytical uncertainties in major element compositions (measured by EPMA) and water concentrations (measured by SIMS) were propagated using a Monte-Carlo approach (n=1,000,000). Resulting densities were normally distributed, with the mean and standard deviation used as density and 1σ uncertainty estimates. A comparison of the density used in each study and recalculated densities are shown in Figure 3.11. Uncertainty in calculated density is non-negligible for all MI, ranging from 0.02–0.07 $g{\cdot}cm^{-3}$, with an average of 0.05 $g{\cdot}cm^{-3}$. It is largest for H_2O-rich MIs with higher uncertainties from SIMS as H_2O content has a significant effect on density.

3.14.2.3 Vapour Bubble CO_2 Density

Hartley et al. (2014) uses the Kawakami et al. (2003) Raman densimeter. There are no published uncertainties on either the standards used or measured diad separations for this densimeter. Therefore I used the densimeter as originally applied, without modification. Uncertainty in diad separation was propagated through the densimeter equation.

Barber et al. (2023), Wieser et al. (2021), and Wong et al. (2023) all use the same Raman densimeter derived by Wieser et al. (2021) from standards measured on a well-calibrated high-pressure optical cell at Virginia Tech (as described in Lamadrid et al. 2017). This densimeter was refit using the EV_2 approach using uncertainties in standard densities and error estimates from repeats and shown in Figure 3.6. As expected, the refitted densimeter equation ($\rho = 0.3230\Delta - 32.121$) is very similar to that calculated in

Wieser et al. (2021) ($\rho = 0.3217\Delta - 32.995$), but the parameter estimate uncertainties are lower: 0.015 and 1.629 versus 0.026 and 2.7 for the gradient and intercept, respectively. For each unknown, measured and drift-corrected diad separation and its uncertainty estimate from repeats was propagated through the new densimeter line to calculate the density and its associated error.

3.14.2.4 Vapour Bubble Volume

Vapour bubble volumes were calculated assuming that each vapour bubble is spherical. Where vapour bubbles were originally fitted with an ellipse, half the mean of the long and short measured axes was used as the radius. The uncertainty in vapour bubble volume was estimated by combining the systematic and random uncertainty described in section 3.9.

3.14.2.5 Melt Inclusion Volume

For each MI I estimated volume using the 16 and 84% percentiles from the Monte-Carlo simulations assuming that melt inclusions were oriented with their long axes oriented parallel to the intersection plane. I used the smallest of the two measured ellipse axes to estimate the third unknown axis, resulting in an asymmetric 1σ error envelope for each MI volume.

3.14.2.6 Total Melt Inclusion CO_2

The total MI CO_2 contents and uncertainties were estimated using a Monte Carlo approach. The normally distributed uncertainties in vapour bubble volume and vapour bubble CO_2 content and the asymmetric uncertainty in MI glass density and MI volume were sampled 1000 times and propagated through Equation 1, to calculate the CO_2 content of the vapour bubble and its uncertainty. These were then combined with the normally distributed uncertainty in MI glass CO_2 (measured by SIMS and also sampled 1000 times) using Equation 2.2 to calculate total MI CO_2 content.

3.14.2.7 Post Entrapment Modification Correction

PEM corrections for all MI compositions were performed using `MIMiC`. The significant asymmetric uncertainties in total MI CO_2 contents necessitated a Monte Carlo approach, drawing1000 CO_2 contents per MI. Uncertainties in major element composition (EPMA,) and H_2O contents (SIMS) were propagated using `MIMiC`'s built-in Monte-Carlo methods and the recommended fifty simulations for each MI (Rasmussen et al. 2020). This resulted in 50,000 simulations per MI. For consistency, I used the same FeO* content as the original study, with a conservative uncertainty of ±0.25 wt.%, and the original oxy-

gen fugacity. Fe^{2+}/Fe^{3+} ratios were calculated using the Kress and Carmichael (1991) model.. I used the default models in `MIMiC` to carry out the PEM-correction: the olivine-melt Kd model of Toplis (2005), the olivine-liquid thermometer of Putirka et al. (2007), and the MagmaSat volatile-saturation model (Ghiorso and Gualda 2015).

3.14.2.8 Volatile Saturation Pressure

To calculate volatile-saturation pressures I used the MagmaSat (Ghiorso and Gualda 2015) model, as it is calibrated on a broad range of MI compositions and is, therefore, the most universally applicable (Wieser et al. 2022a). I used the anhydrous liquid-only thermometer of Helz and Thornber (1987) for MI from Hartley et al. (2014), Wieser et al. (2021), and Wong et al. (2023) and the water-dependent Equation 15 of Putirka (2008) for MI from Barber et al. (2023). The same oxygen fugacities and pressures were used to calculate T, as when calculating density.

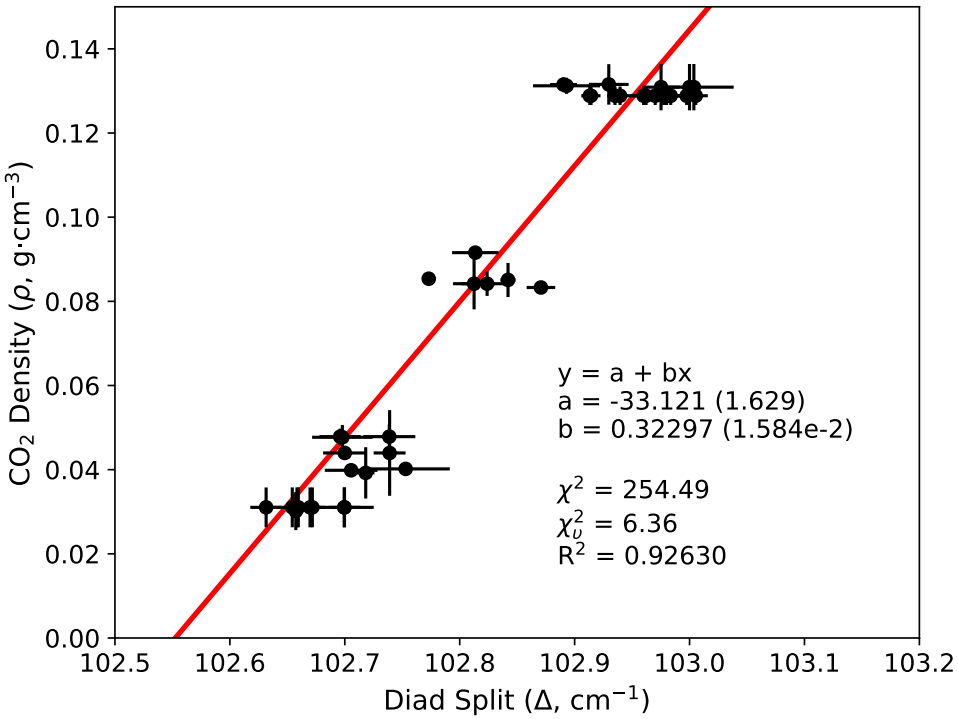

Figure 3.6: The Raman densimeter of Wieser et al. (2021) refit using the EV_2 method that accommodates uncertainties in both measured diad splits and the CO_2 density of standards used (error bars).

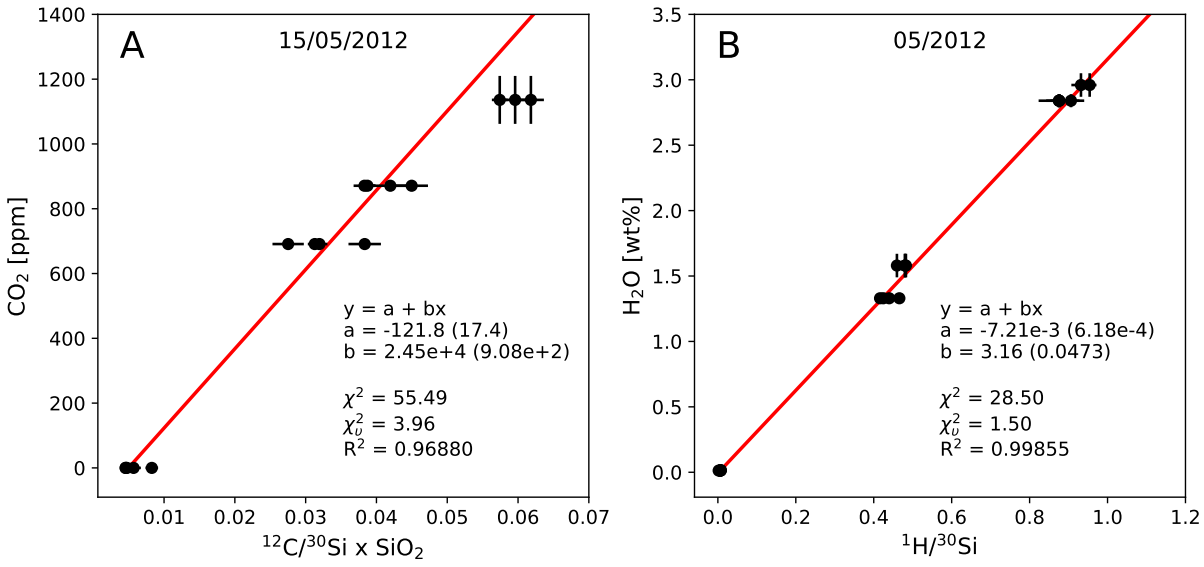

Figure 3.7: Reprocessed SIMS calibration curves and associated statistics for Hartley et al. (2014). A) CO_2 calibration curve. B) H_2O calibration curve. Calibration data and $\pm 1\sigma$ uncertainties, taken into account by regression, are shown by error bars. Parameter estimate 1σ uncertainties are shown in brackets. χ^2, chi-square statistic. χ^2_ν, reduced-chi-square statistic. R^2, coefficient of determination.

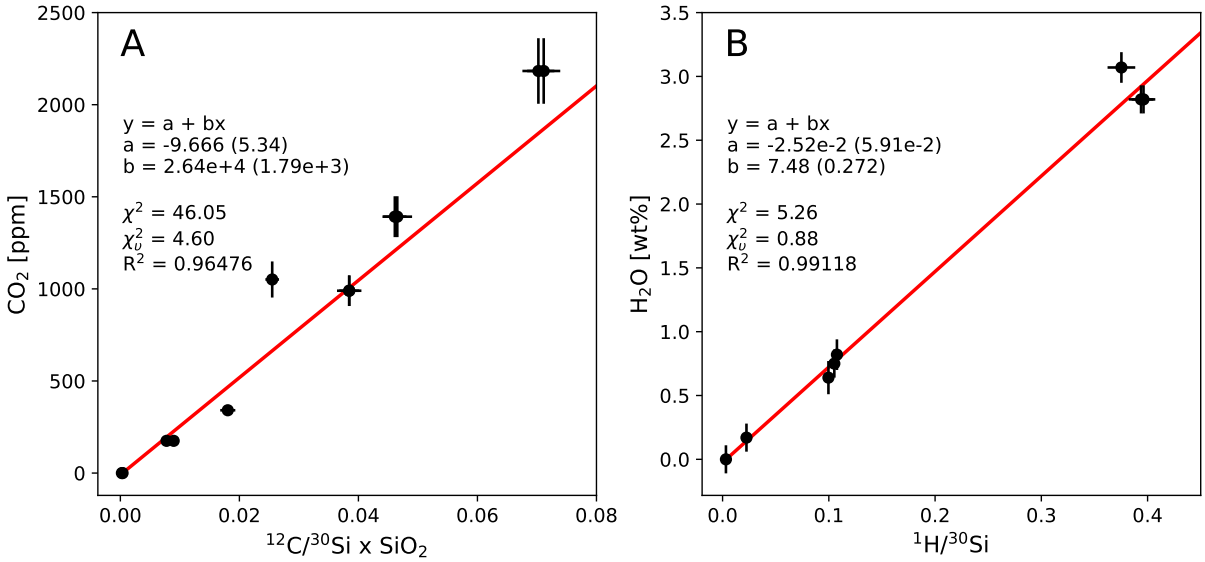

Figure 3.8: Reprocessed SIMS calibration curves and associated statistics for Wieser et al. (2021). A) CO_2 calibration curve. B) H_2O calibration curve. Calibration data and $\pm 1\sigma$ uncertainties, taken into account by regression, are shown by error bars. Parameter estimate 1σ uncertainties are shown in brackets. χ^2, chi-square statistic. χ^2_ν, reduced-chi-square statistics. R^2, coefficient of determination.

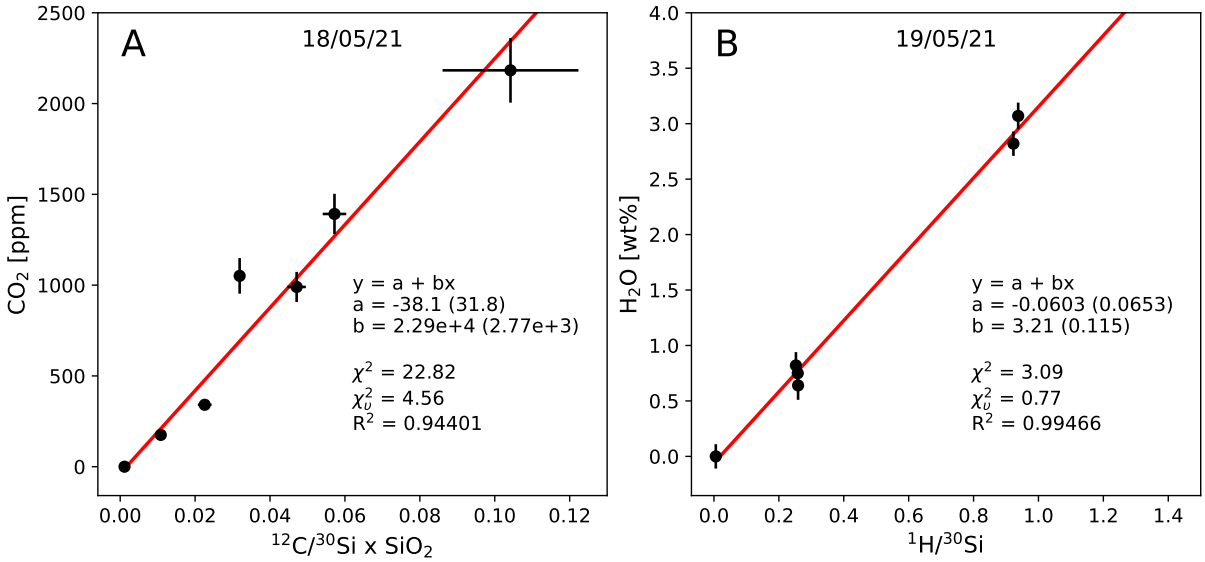

Figure 3.9: Reprocessed SIMS calibration curves and associated statistics for Wong et al. (2023). A) CO_2 calibration curve. B) H_2O calibration curve. Calibration data and $\pm 1\sigma$ uncertainties, taken into account by regression, are shown by error bars. Parameter estimate 1σ uncertainties are shown in brackets. χ^2, chi-square statistic. χ^2_ν, reduced-chi-square statistic. R^2, coefficient of determination.

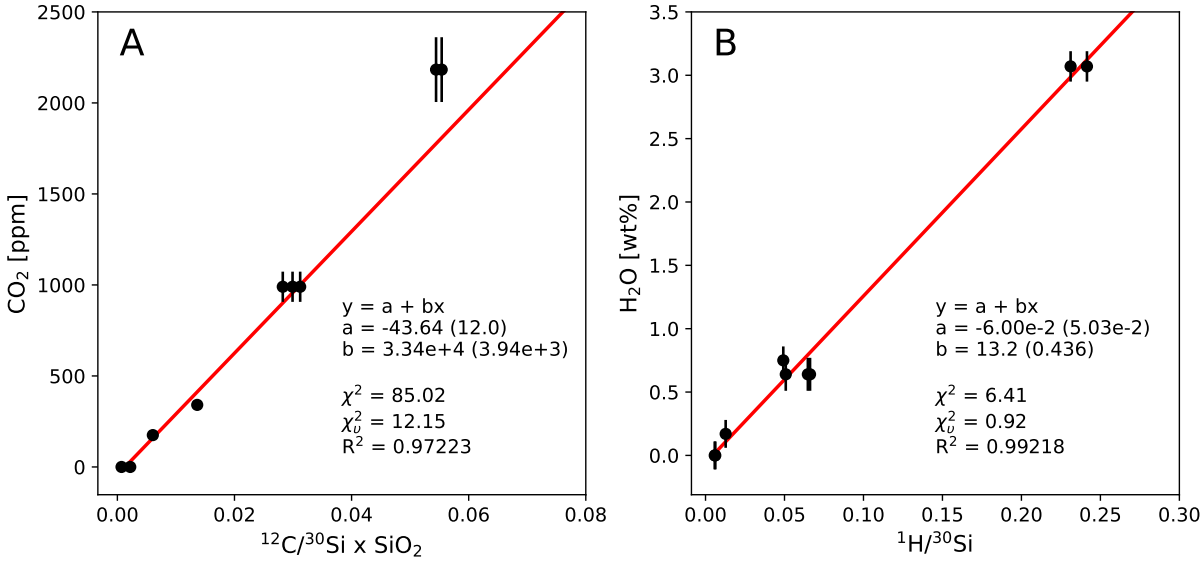

Figure 3.10: Reprocessed SIMS calibration curves and associated statistics for Barber et al. (2023). A) CO_2 calibration curve. B) H_2O calibration curve. Calibration data and $\pm 1\sigma$ uncertainties, taken into account by regression, are shown by error bars. Parameter estimate 1σ uncertainties are shown in brackets. χ^2, chi-square statistic. χ^2_ν, reduced-chi-square statistic. R^2, coefficient of determination.

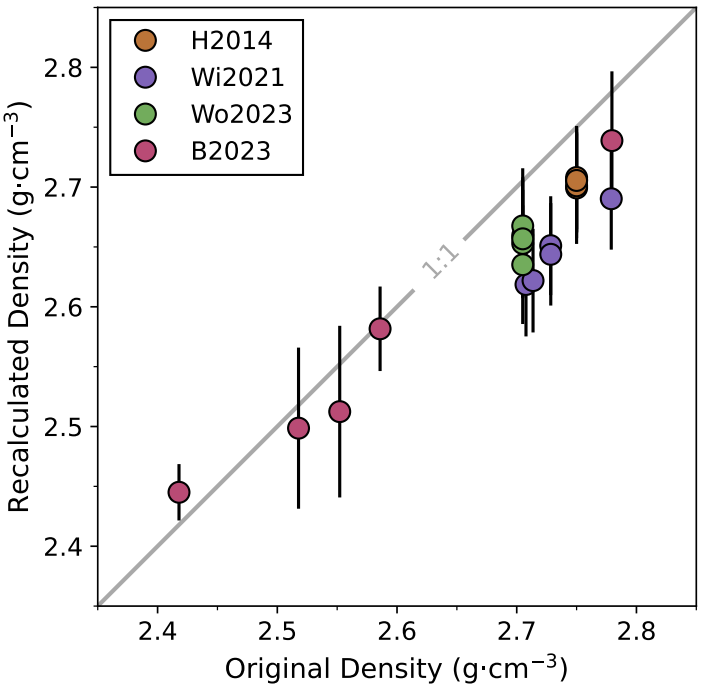

Figure 3.11: Comparison of original and recalculated densities. H2014, Hartley et al. (2014). Wi2021, Wieser et al. (2021). Wo2023, Wong et al. (2023). B2023, Barber et al. (2023). Uncertainty in calculated density is non-negligible for all MI. It is largest for H_2O-rich MI with higher uncertainties from SIMS as H_2O content has a significant effect on density.

3.15 Results

The reprocessed volatile saturation pressures show good agreement with those calculated in the original study (Figures 3.12, 3.13). For example, the Kīlauea MI from Wieser et al. (2021) have shallow pressures (<2 kbar), and Ethiopian MI from Wong et al. (2023) formed in the middle crust (~4 kbar). One of the five MI from Hartley et al. (2014) contained unrealistically high CO_2 concentrations (8.44(−4.01, +7.00) wt.%) and therefore resulted in a very high volatile-saturation pressure and corresponding uncertainty (26.5(−5.6, +6.6) kbar). This is likely due to the use of the Kawakami et al. (2003) densimeter, which was not calibrated for the micro-Raman spectrometer, and the analytical conditions used. The other four MI produced reasonable saturation pressures, consistent with those presented in Hartley et al. (2014).

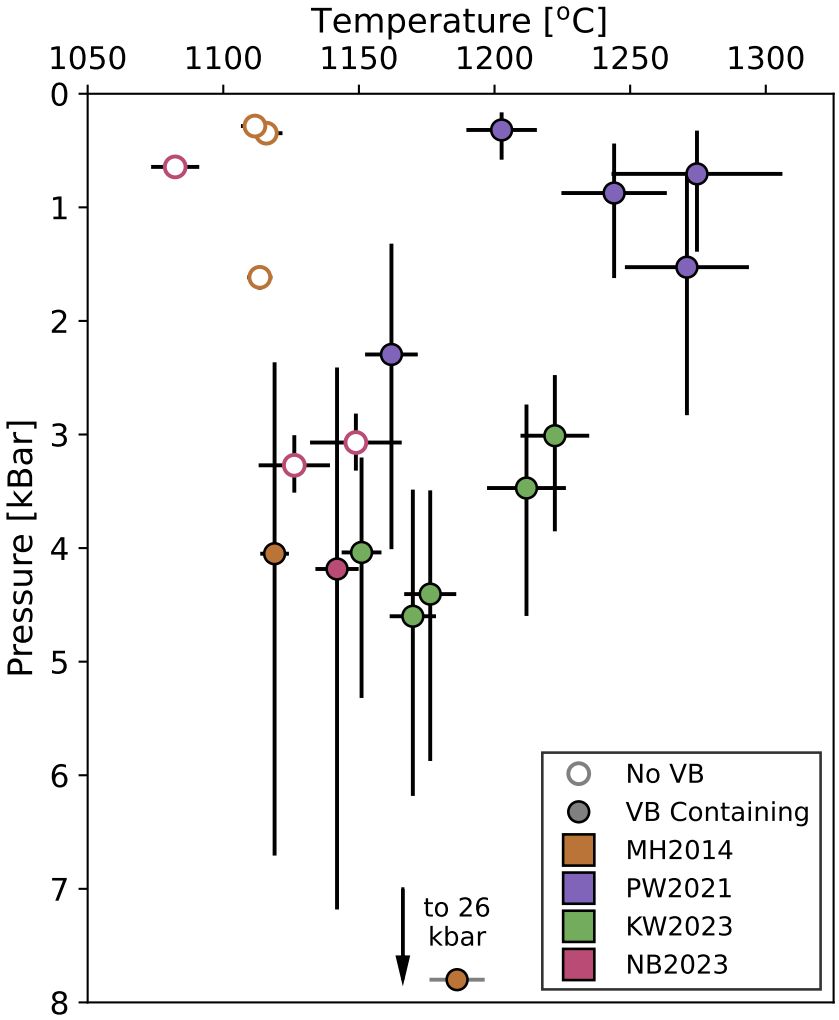

Figure 3.12: Reprocessed melt inclusion saturation pressures and temperatures with uncertainties (black error bars). MH2014, Hartley et al. (2014). PW2021, Wieser et al. (2021). KW2023, Wong et al. (2023). NB2023, Barber et al. (2023). There is a clear difference between melt inclusions with vapour bubbles (significant pressure uncertainties) and those without (y-bar smaller than marker).

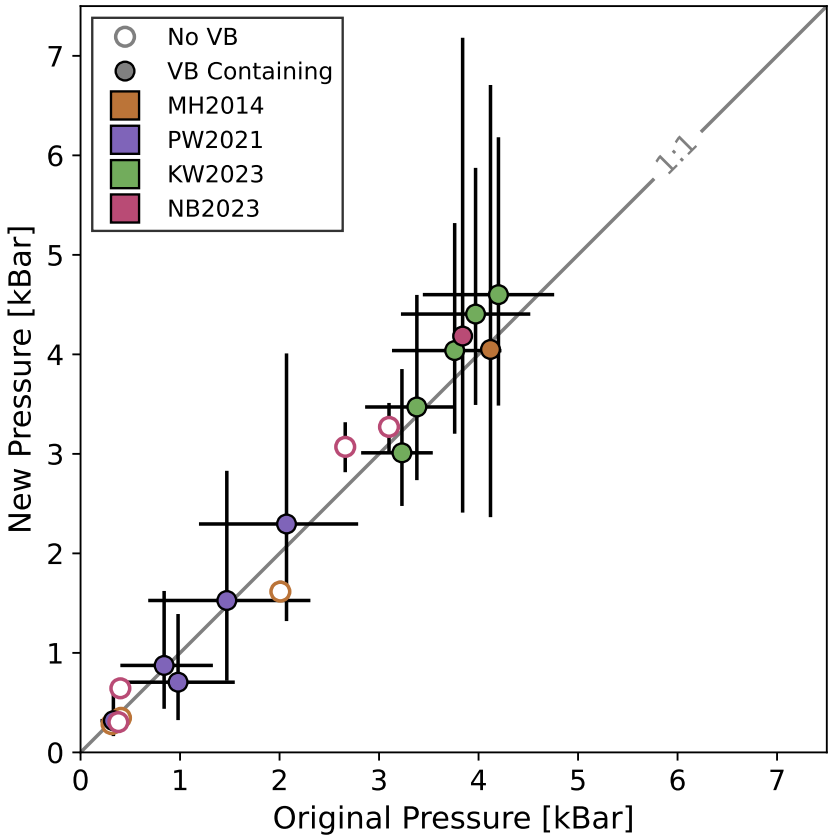

Figure 3.13: Comparison of original and recalculated volatile saturation pressures with uncertainties (black error bars). MH2014, Hartley et al. (2014). PW2021, Wieser et al. (2021). KW2023, Wong et al. (2023). NB2023, Barber et al. (2023). Results show good agreement with pressures from original studies but have substantially larger errors.

One of the five MI from Barber et al. (2023) repeatedly failed during PEM-correction with `MIMiC` and therefore was dropped from further calculations. Again the remaining four MI correspond well with the saturation pressures presented in the original study.

The errors for vapour bubble-hosting MI are substantial and asymmetric. Negative 1σ uncertainties range from 0.155–1.77 kbar with an average of 0.86 kbar (n=13). Positive 1σ uncertainties range from 0.26–3.00 kbar with an average of 1.39 kbar. In contrast, 1σ uncertainties for MI without vapour bubble, or detectable diads, are symmetric and much lower: ranging from ~0.04–0.27 % with an average of 0.13 % (n=6).

3.15.1 Error Budget

The impact of each analytical uncertainty on both the total MI CO_2 content and calculated volatile saturation pressure was assessed by isolating each source of uncertainty and comparing the resulting error with the total error. The average values across the twenty MIs reprocessed in this study are shown in

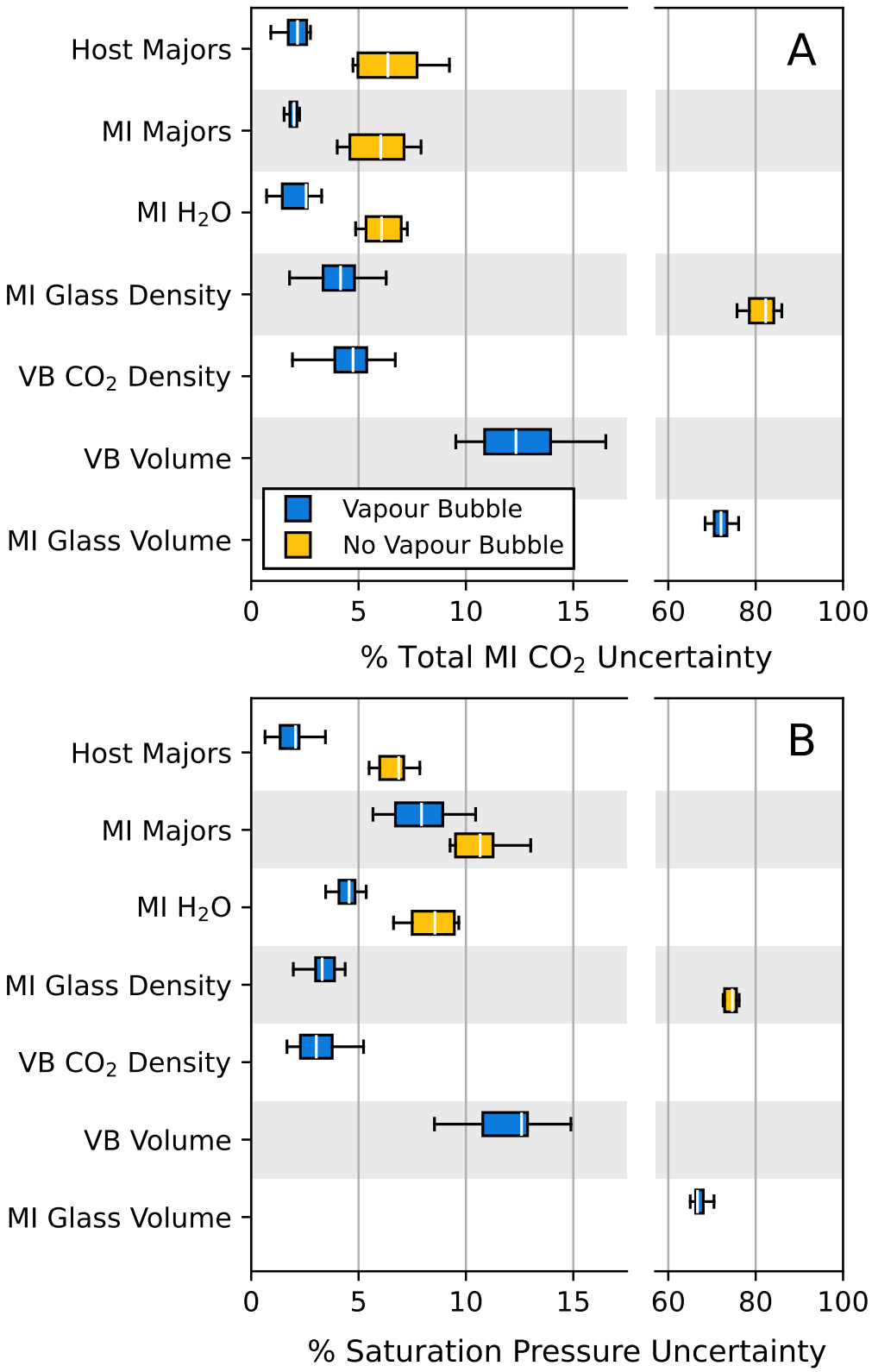

Figure 3.14: Boxplots showing the distribution of error contributions for each uncertainty source. Contributions for reprocessed MI with vapour bubbles are shown in blue and for MI without vapour bubbles in yellow. Note the break in the x-axis. White bars show the median. A) Error contributions for total MI CO_2. B) Error contributions for calculated saturation pressure.

Figure 3.14.

For MIs that contain a vapour bubble (VB), the largest contributor to the error in total MI CO_2 and saturation pressure is the MI glass volume, accounting for 73.5% of the total error. This is nearly six times larger than the next biggest contributor, which is the vapour bubble volume (12.3%). In contrast, for MI without vapour bubbles (No VB), the largest contributor is the MI glass CO_2 content, contributing 82.6% of the total error. This is significantly higher than the other sources, which each contribute roughly 6% or less. These error distributions are similar to the contributions to the overall error in saturation pressure (Figure 3.14).

3.16 Discussion and Conclusions

The results presented here highlight the significant uncertainties associated with calculating volatile saturation pressures from MIs, challenging the assumption that MI-based volatile saturation pressures are the gold standard for barometry. The 1σ errors calculated using the new approach are considerable, particularly for vapour bubble-bearing MIs, where errors reach up to 3.0 kbar, with an average uncertainty of 1.39 kbar. These uncertainties are comparable to those observed in recent reappraisals of mineral-only and mineral-melt barometers. For instance, Wieser et al. (2022b) reported similar error magnitudes for the best-performing thermobarometers for arc magmas. For example, the clinopyroxene-only barometer of Jorgenson et al. (2022) has an uncertainty of ~1.9 kbar. Similarly, the clinopyroxene-liquid barometer of Neave and Putirka (2017) also yields errors in the range of ~1.9 kbar, while the amphibole-liquid barometer of Ridolfi (2021), has an 18% relative error, which translates into ~2.2 kbar over its calibration range. These comparisons show that when all analytical uncertainties are taken into account, the uncertainties in MI volatile saturation pressures are substantial and need to be reduced to justify the complex analytical and data processing workflows they require.

That said, this study demonstrates that when all analytical uncertainties are well-characterised, volatile saturation pressures can be determined with much greater precision. For example, for MIs without vapour bubbles, uncertainties are much lower, indicating that precise volatile saturation pressures are achievable when key parameters, e.g., MI glass CO_2 content, are well constrained (Figures 3.12, 3.13). This highlights the importance of thorough uncertainty quantification for reliable barometric measurements and underscores the potential for achieving high-precision results when analytical inputs are accurately known.

While the results for non-vapour bubble-bearing MIs are promising, it is important to recognise that these MIs may have lost their vapour bubbles through decrepitation during sample extraction or analysis (e.g., Maclennan 2017). Therefore, the analysis of vapour bubble-bearing MIs should not be dismissed, as they still hold the potential for accurate volatile saturation pressure estimation with improved methods. The main contributor to uncertainty for vapour bubble-bearing MIs is the estimation of MI volume, which, for the MI reprocessed in this study, was obtained using standard two-dimensional methods. However, these methods are inherently limited, as a single two-dimensional image cannot accurately capture the three-dimensional volume of the MI, even in cases where the MI is ellipsoidal. To reduce uncertainties in volume estimation, future studies should employ either two perpendicular two-dimensional images (e.g., DeVitre et al. 2023a) or micro-XCT (DeVitre et al. 2023a; Hanyu et al. 2020; van Gerve et al. 2024). These 3D methods can reduce volume uncertainties to ~10-20%, improving the accuracy of the calculated volatile saturation pressures for vapour bubble-bearing MIs.

Finally, the Python code and uncertainty propagation methods presented in this study provide a robust tool for accurately assessing and propagating analytical uncertainties through to volatile saturation pressures. By incorporating all sources of error, this approach enables a more comprehensive understanding of the uncertainties associated with MI-based barometry, facilitating the development of more reliable methods for determining volatile saturation pressures in future studies.

References

Allison, C. M., K. Roggensack, and A. B. Clarke (2022). "MafiCH: A General Model for H_2O–CO_2 Solubility in Mafic Magmas". In: *Contributions to Mineralogy and Petrology* 177.3, page 40. DOI: 10.1007/s00410-022-01903-y.

Barber, N. D., S. L. Baldwin, M. Edmonds, F. O. Boschetty, H. E. Wibowo, and A. Harijoko (2023). "Monogenetic Volcanoes as Windows into Transcrustal Mush: A Case Study of Slamet and Loyang Volcanoes, Central Java". In: *Journal of Volcanology and Geothermal Research* 444, page 107945. DOI: 10.1016/j.jvolgeores.2023.107945.

Barth, A., M. Newcombe, T. Plank, H. Gonnermann, S. Hajimirza, G. J. Soto, A. Saballos, and E. Hauri (2019). "Magma Decompression Rate Correlates with Explosivity at Basaltic Volcanoes — Constraints from Water Diffusion in Olivine". In: *Journal of Volcanology and Geothermal Research* 387, page 106664. DOI: 10.1016/j.jvolgeores.2019.106664.

Bennett, E. N., F. E. Jenner, M.-A. Millet, K. V. Cashman, and C. J. Lissenberg (2019). "Deep Roots for Mid-Ocean-Ridge Volcanoes Revealed by Plagioclase-Hosted Melt Inclusions". In: *Nature* 572.7768 (7768), pages 235–239. DOI: 10.1038/s41586-019-1448-0.

Blundy, J. and K. Cashman (2005). "Rapid Decompression-Driven Crystallization Recorded by Melt Inclusions from Mount St. Helens Volcano". In: *Geology* 33.10, page 793. DOI: 10.1130/G21668.1.

Boggs, P. T., R. H. Byrd, and R. B. Schnabel (1987). "A Stable and Efficient Algorithm for Nonlinear Orthogonal Distance Regression". In: *SIAM Journal on Scientific and Statistical Computing* 8.6, pages 1052–1078. DOI: 10.1137/0908085.

Brahm, R., G. F. Zellmer, T. Kuritani, N. Sakamoto, H. Yurimoto, M. Nakagawa, and E. Sato (2022). "Olivine Melt Inclusion Constraints on Some Intensive Properties of Subvolcanic Crystal Mushes and Their Evolution through Boundary Layer Fractionation in Northern Japan". In: *Journal of Petrology* 63.3, egac016. DOI: 10.1093/petrology/egac016.

Bucholz, C. E., G. A. Gaetani, M. D. Behn, and N. Shimizu (2013). "Post-Entrapment Modification of Volatiles and Oxygen Fugacity in Olivine-Hosted Melt Inclusions". In: *Earth and Planetary Science Letters* 374, pages 145–155. DOI: 10.1016/j.epsl.2013.05.033.

Coogan, L., A. Hain, S. Stahl, and S. Chakraborty (2005). "Experimental Determination of the Diffusion Coefficient for Calcium in Olivine between 900°C and 1500°C". In: *Geochimica et Cosmochimica Acta* 69.14, pages 3683–3694. DOI: 10.1016/j.gca.2005.03.002.

Cottrell, E., K. A. Kelley, A. Lanzirotti, and R. A. Fischer (2009). "High-Precision Determination of Iron Oxidation State in Silicate Glasses Using XANES". In: *Chemical Geology* 268.3-4, pages 167–179. DOI: 10.1016/j.chemgeo.2009.08.008.

Créon, L., G. Levresse, L. Remusat, H. Bureau, and G. Carrasco-Núñez (2018). "New Method for Initial Composition Determination of Crystallized Silicate Melt Inclusions". In: *Chemical Geology* 483, pages 162–173. DOI: 10.1016/j.chemgeo.2018.02.038.

Cutler, K. S., M. Cassidy, and J. D. Blundy (2024). "Plagioclase-Saturated Melt Hygrothermobarometry and Plagioclase-Melt Equilibria Using Machine Learning". In: *Geochemistry, Geophysics, Geosystems* 25.4, e2023GC011357. DOI: 10.1029/2023GC011357.

Danyushevsky, L. V., F. N. Della-Pasqua, and S. Sokolov (2000). "Re-Equilibration of Melt Inclusions Trapped by Magnesian Olivine Phenocrysts from Subduction-Related Magmas: Petrological Implications". In: *Contributions to Mineralogy and Petrology* 138.1, pages 68–83. DOI: 10.1007/PL00007664.

Danyushevsky, L. V., A. W. McNeill, and A. V. Sobolev (2002). "Experimental and Petrological Studies of Melt Inclusions in Phenocrysts from Mantle-Derived Magmas: An Overview of Techniques, Advantages and Complications". In: *Chemical Geology* 183.1-4, pages 5–24. DOI: 10.1016/S0009-2541(01)00369-2.

Danyushevsky, L. V. and P. Plechov (2011). "Petrolog3: Integrated Software for Modeling Crystallization Processes". In: *Geochemistry, Geophysics, Geosystems* 12.7. DOI: 10.1029/2011GC003516.

DeVitre, C. L., C. M. Allison, and E. Gazel (2021). "A High-Precision CO_2 Densimeter for Raman Spectroscopy Using a Fluid Density Calibration Apparatus". In: *Chemical Geology* 584, page 19. DOI: 10.1016/j.chemgeo.2021.120522.

DeVitre, C. L., K. Dayton, E. Gazel, A. Pamukçu, G. Gaetani, and P. E. Wieser (2023a). "Laser Heating Effect on Raman Analysis of CO_2 Co-Existing as Liquid and Vapor in Olivine-Hosted Melt Inclusion Bubbles". In: *Volcanica* 6.2, pages 201–219. DOI: 10.30909/vol.06.02.201219.

DeVitre, C. L., E. Gazel, R. S. Ramalho, S. Venugopal, M. Steele-MacInnis, J. Hua, C. M. Allison, L. R. Moore, J. C. Carracedo, and B. Monteleone (2023b). "Oceanic Intraplate Explosive Eruptions Fed Directly from the Mantle". In: *Proceedings of the National Academy of Sciences* 120.33, e2302093120. DOI: 10.1073/pnas.2302093120.

Dixon, J. E., E. M. Stolper, and J. R. Holloway (1995). "An Experimental Study of Water and Carbon Dioxide Solubilities in Mid-Ocean Ridge Basaltic Liquids. Part I: Calibration and Solubility Models". In: *Journal of Petrology* 36.6, pages 1607–1631. DOI: 10.1093/oxfordjournals.petrology.a037267.

Donovan, J. J. (2021). *Probe for EPMA v. 13.0.5 User's Guide and Reference (Xtreme Edition)*.

Esposito, R., R. J. Bodnar, L. V. Danyushevsky, B. De Vivo, L. Fedele, J. Hunter, A. Lima, and N. Shimizu (2011). "Volatile Evolution of Magma Associated with the Solchiaro Eruption in the Phlegrean Volcanic District (Italy)". In: *Journal of Petrology* 52.12, pages 2431–2460. DOI: 10.1093/petrology/egr051.

Esposito, R., J. Hunter, J. D. Schiffbauer, N. Shimizu, and R. J. Bodnar (2014). "An Assessment of the Reliability of Melt Inclusions as Recorders of the Pre-Eruptive Volatile Content of Magmas". In: *American Mineralogist* 99.5-6, pages 976–998. DOI: 10.2138/am.2014.4574.

Fall, A., B. Tattitch, and R. J. Bodnar (2011). "Combined Microthermometric and Raman Spectroscopic Technique to Determine the Salinity of H_2O–CO_2–NaCl Fluid Inclusions Based on Clathrate Melting". In: *Geochimica et Cosmochimica Acta* 75.4, pages 951–964. DOI: 10.1016/j.gca.2010.11.021.

Feldkamp, L. A., L. C. Davis, and J. W. Kress (1984). "Practical Cone-Beam Algorithm". In: *Journal of the Optical Society of America A* 1.6, page 612. DOI: 10.1364/JOSAA.1.000612.

Fermi, E. (1931). "Über Den Ramaneffekt Des Kohlendioxyds". In: *Zeitschrift für Physik* 71.3, pages 250–259. DOI: 10.1007/BF01341712.

Fischer, T. P. and A. Aiuppa (2020). "AGU Centennial Grand Challenge: Volcanoes and Deep Carbon Global CO_2 Emissions From Subaerial Volcanism—Recent Progress and Future Challenges". In: *Geochemistry, Geophysics, Geosystems* 21.3, e2019GC008690. DOI: 10.1029/2019GC008690.

Gaetani, G. A., J. Maclennan, V. Le Roux, and F. Klein (2015). "Reconstructing Magma Storage Depths from Olivine-Hosted Melt Inclusions: Do Vapor Bubbles Matter?" In: *AGU Fall Meeting Abstracts*. Volume 2015, V13B–3124.

Gaetani, G. A., J. A. O'Leary, N. Shimizu, C. E. Bucholz, and M. Newville (2012). "Rapid Reequilibration of H_2O and Oxygen Fugacity in Olivine-Hosted Melt Inclusions". In: *Geology* 40.10, pages 915–918. DOI: 10.1130/G32992.1.

Gavrilenko, M., C. Herzberg, C. Vidito, M. J. Carr, T. Tenner, and A. Ozerov (2016). "A Calcium-in-Olivine Geohygrometer and Its Application to Subduction Zone Magmatism". In: *Journal of Petrology* 57.9, pages 1811–1832. DOI: 10.1093/petrology/egw062.

Ghiorso, M. S. and G. A. R. Gualda (2015). "An H_2O–CO_2 Mixed Fluid Saturation Model Compatible with Rhyolite-MELTS". In: *Contributions to Mineralogy and Petrology* 169.6, page 53. DOI: 10.1007/s00410-015-1141-8.

Gordon, H. R. and T. McCubbin (1966). "The 2.8-Micron Bands of CO_2". In: *Journal of Molecular Spectroscopy* 19.1-4, pages 137–154. DOI: 10.1016/0022-2852(66)90237-2.

Gualda, G. A. R., M. S. Ghiorso, R. V. Lemons, and T. L. Carley (2012). "Rhyolite-MELTS: A Modified Calibration of MELTS Optimized for Silica-rich, Fluid-bearing Magmatic Systems". In: *Journal of Petrology* 53.5 (5), pages 875–890. DOI: 10.1093/petrology/egr080.

Hall, L. (1999). "The Effect of Water on Mantle Melting". University of Bristol. 119 pages.

Hanyu, T., J. Yamamoto, K. Kimoto, K. Shimizu, and T. Ushikubo (2020). "Determination of Total CO_2 in Melt Inclusions with Shrinkage Bubbles". In: *Chemical Geology* 557, page 119855. DOI: 10.1016/j.chemgeo.2020.119855.

Hartley, M. E., J. Maclennan, M. Edmonds, and T. Thordarson (2014). "Reconstructing the Deep CO_2 Degassing Behaviour of Large Basaltic Fissure Eruptions". In: *Earth and Planetary Science Letters* 393, pages 120–131. DOI: 10.1016/j.epsl.2014.02.031.

Hartley, M. E., D. A. Neave, J. Maclennan, M. Edmonds, and T. Thordarson (2015). "Diffusive Over-Hydration of Olivine-Hosted Melt Inclusions". In: *Earth and Planetary Science Letters* 425, pages 168–178. DOI: 10.1016/j.epsl.2015.06.008.

Hauri, E., J. Wang, J. E. Dixon, P. L. King, C. Mandeville, and S. Newman (2002). "SIMS Analysis of Volatiles in Silicate Glasses 1. Calibration, Matrix Effects and Comparisons with FTIR". In: *Chemical Geology*. DOI: 10.1016/S0009-2541(01)00375-8.

Helo, C., M.-A. Longpré, N. Shimizu, D. A. Clague, and J. Stix (2011). "Explosive Eruptions at Mid-Ocean Ridges Driven by CO_2-rich Magmas". In: *Nature Geoscience* 4.4, pages 260–263. DOI: 10.1038/ngeo1104.

Helz, R. T. and C. R. Thornber (1987). "Geothermometry of Kilauea Iki Lava Lake, Hawaii". In: *Bulletin of Volcanology* 49.5, pages 651–668. DOI: 10.1007/BF01080357.

Hervig, R. L., F. K. Mazdab, G. Moore, and P. F. McMillan (2003). "Analyzing Hydrogen (H2O) in Silicate Glass by Secondary Ion Mass Spectrometry and Reflectance Fourier Transform Infrared Spectroscopy". In: *Melt Inclusions in Volcanic Systems Methods, Applications and Problems*. Volume 5, pages 83–103. DOI: 10.1016/S1871-644X(03)80025-6.

Hirschmann, M. M. (2006). "Water, Melting, and the Deep Earth H_2O Cycle". In: *Annual Review of Earth and Planetary Sciences* 34.1, pages 629–653. DOI: 10.1146/annurev.earth.34.031405.125211.

Humphreys, M. C., S. L. Kearns, and J. D. Blundy (2006). "SIMS Investigation of Electron-Beam Damage to Hydrous, Rhyolitic Glasses: Implications for Melt Inclusion Analysis". In: *American Mineralogist* 91.4, pages 667–679. DOI: 10.2138/am.2006.1936.

Iacono-Marziano, G., Y. Morizet, E. Le Trong, and F. Gaillard (2012). "New Experimental Data and Semi-Empirical Parameterization of H2O–CO2 Solubility in Mafic Melts". In: *Geochimica et Cosmochimica Acta* 97, pages 1–23. DOI: 10.1016/j.gca.2012.08.035.

Iacovino, K., S. Matthews, P. E. Wieser, G. M. Moore, and F. Bégué (2021). "VESIcal Part I: An Open-Source Thermodynamic Model Engine for Mixed Volatile (H_2O-CO_2) Solubility in Silicate Melts". In: *Earth and Space Science* 8.11. DOI: 10.1029/2020EA001584.

Iacovino, K. and C. Till (2018). "DensityX: A Program for Calculating the Densities of Hydrous Magmatic Liquids from 427–1,627 °C and up to 30 Kbar". In: *Volcanica* 2.1, pages 1–10. DOI: 10.30909/vol.02.01.0110.

Jochum, K. P. and U. Nohl (2008). "Reference Materials in Geochemistry and Environmental Research and the GeoReM Database". In: *Chemical Geology* 253.1-2, pages 50–53. DOI: 10.1016/j.chemgeo.2008.04.002.

Jochum, K. P., B. Stoll, K. Herwig, M. Willbold, A. W. Hofmann, M. Amini, S. Aarburg, W. Abouchami, E. Hellebrand, B. Mocek, I. Raczek, A. Stracke, O. Alard, C. Bouman, S. Becker, M. Dücking, H. Brätz, R. Klemd, D. de Bruin, D. Canil, D. Cornell, C.-J. de Hoog, C. Dalpé, L. Danyushevsky, A. Eisenhauer, Y. Gao, J. E. Snow, N. Groschopf, D. Günther, C. Latkoczy, M. Guillong, E. H. Hauri, H. E. Höfer, Y. Lahaye, K. Horz, D. E. Jacob, S. A. Kasemann, A. J. R. Kent, T. Ludwig, T. Zack, P. R. D. Mason, A. Meixner, M. Rosner, K. Misawa, B. P. Nash, J. Pfänder, W. R. Premo, W. D. Sun, M. Tiepolo, R. Vannucci, T. Vennemann, D. Wayne, and J. D. Woodhead (2006). "MPI-DING Reference Glasses for in Situ Microanalysis: New Reference Values for Element Concentrations and Isotope Ratios: MPI-DING REFERENCE GLASSES". In: *Geochemistry, Geophysics, Geosystems* 7.2 (2), page 44. DOI: 10.1029/2005GC001060.

Johnson, E. R., P. J. Wallace, K. V. Cashman, H. D. Granados, and A. J. Kent (2008). "Magmatic Volatile Contents and Degassing-Induced Crystallization at Volcán Jorullo, Mexico: Implications for Melt Evolution and the Plumbing Systems of Monogenetic Volcanoes". In: *Earth and Planetary Science Letters* 269.3-4, pages 478–487. DOI: 10.1016/j.epsl.2008.03.004.

Jorgenson, C., O. Higgins, M. Petrelli, F. Bégué, and L. Caricchi (2022). "A Machine Learning-Based Approach to Clinopyroxene Thermobarometry: Model Optimization and Distribution for Use in Earth Sciences". In: *Journal of Geophysical Research: Solid Earth* 127.4, e2021JB022904. DOI: 10.1029/2021JB022904.

Kawakami, Y., J. Yamamoto, and H. Kagi (2003). "Micro-Raman Densimeter for CO_2 Inclusions in Mantle-Derived Minerals". In: *Applied Spectroscopy* 57.11, pages 1333–1339. DOI: 10.1366/000370203322554473.

Kelemen, P. B. and C. E. Manning (2015). "Reevaluating Carbon Fluxes in Subduction Zones, What Goes down, Mostly Comes Up". In: *Proceedings of the National Academy of Sciences* 112.30. DOI: 10.1073/pnas.1507889112.

Koga, K., E. Hauri, M. Hirschmann, and D. Bell (2003). "Hydrogen Concentration Analyses Using SIMS and FTIR: Comparison and Calibration for Nominally Anhydrous Minerals". In: *Geochemistry, Geophysics, Geosystems* 4.2, 2002GC000378. DOI: 10.1029/2002GC000378.

Kress, V. C. and I. S. E. Carmichael (1991). "The Compressibility of Silicate Liquids Containing Fe_2O_3 and the Effect of Composition, Temperature, Oxygen Fugacity and Pressure on Their Redox States". In: *Contributions to Mineralogy and Petrology* 108.1-2, pages 82–92. DOI: 10.1007/BF00307328.

Lamadrid, H., L. Moore, D. Moncada, J. Rimstidt, R. Burruss, and R. Bodnar (2017). "Reassessment of the Raman CO_2 Densimeter". In: *Chemical Geology* 450, pages 210–222. DOI: 10.1016/j.chemgeo.2016.12.034.

Lange, R. L. and I. S. E. Carmichael (1990). "Thermodynamic Properties of Silicate Liquids with Emphasis on Density, Thermal Expansion and Compressibility". In: *Modern Methods of Igneous Petrology*. Volume 24, pages 25–64.

Lee, H., Y. Moussallam, E. F. Rose Koga, L. Piani, J. Villeneuve, N. Bouden, A. A. Gurenko, B. Monteleone, and G. A. Gaetani (2024). "High–Precision Determination of Carbon Stable Isotope in Silicate Glasses by Secondary Ion Mass Spectrometry: Evaluation of International Reference Materials". In: *Chemical Geology* 670, page 122428. DOI: 10.1016/j.chemgeo.2024.122428.

Lima, A. (2000). "Experimental Study on Silicate-Melt Inclusions in Clinopyroxene Phenocrysts from Roccamonfina Lavas (Italy)". In: *Mineralogy and Petrology* 70.3-4, pages 199–220. DOI: 10.1007/s007100070003.

Lin, F., R. Bodnar, and S. Becker (2007). "Experimental Determination of the Raman CH_4 Symmetric Stretching (ν_1) Band Position from 1–650 bar and 0.3–22°C: Application to Fluid Inclusion Studies". In: *Geochimica et Cosmochimica Acta* 71.15, pages 3746–3756. DOI: 10.1016/j.gca.2007.05.016.

Lin, Q., S. Neethling, K. Dobson, L. Courtois, and P. Lee (2015). "Quantifying and Minimising Systematic and Random Errors in X-ray Micro-Tomography Based Volume Measurements". In: *Computers & Geosciences* 77, pages 1–7. DOI: 10.1016/j.cageo.2014.12.008.

Lloyd, A. S., T. Plank, P. Ruprecht, E. H. Hauri, and W. Rose (2013). "Volatile Loss from Melt Inclusions in Pyroclasts of Differing Sizes". In: *Contributions to Mineralogy and Petrology* 165.1, pages 129–153. DOI: 10.1007/s00410-012-0800-2.

Lloyd, A. S., P. Ruprecht, E. H. Hauri, W. Rose, H. M. Gonnermann, and T. Plank (2014). "NanoSIMS Results from Olivine-Hosted Melt Embayments: Magma Ascent Rate during Explosive Basaltic Eruptions". In: *Journal of Volcanology and Geothermal Research* 283, pages 1–18. DOI: 10.1016/j.jvolgeores.2014.06.002.

Maclennan, J. (2017). "Bubble Formation and Decrepitation Control the CO_2 Content of Olivine-Hosted Melt Inclusions". In: *Geochemistry, Geophysics, Geosystems* 18.2, pages 597–616. DOI: 10.1002/2016GC006633.

Milham, P. J., J. Tellinghuisen, and P. Holford (2023). *Estimating Existing Sorbed Soil Phosphate from Its Effect on Subsequent Sorption: 2. Global Least-Squares Fitting of Phosphorus Soil Sorption Data with Weighting from Residuals Analysis*. Preprint. DOI: 10.2139/ssrn.4469534.

Miller, J. N. (1991). "Basic Statistical Methods for Analytical Chemistry. Part 2. Calibration and Regression Methods. A Review". In: *The Analyst* 116.1, page 3. DOI: 10.1039/an9911600003.

Miller, W. G., J. Maclennan, O. Shorttle, G. A. Gaetani, V. Le Roux, and F. Klein (2019). "Estimating the Carbon Content of the Deep Mantle with Icelandic Melt Inclusions". In: *Earth and Planetary Science Letters* 523, page 115699. DOI: 10.1016/j.epsl.2019.07.002.

Mironov, N., D. Tobelko, S. Smirnov, M. Portnyagin, and S. Krasheninnikov (2020). "Estimation of CO_2 Content in the Gas Phase of Melt Inclusions Using Raman Spectroscopy: Case Study of Inclusions in Olivine from the Karymsky Volcano (Kamchatka)". In: *Russian Geology and Geophysics* 61.5-6, pages 600–610. DOI: 10.15372/RGG2019169.

Moore, L. R., E. Gazel, R. Tuohy, A. S. Lloyd, R. Esposito, M. Steele-MacInnis, E. H. Hauri, P. J. Wallace, T. Plank, and R. J. Bodnar (2015). "Bubbles Matter: An Assessment of the Contribution of Vapor Bubbles to Melt Inclusion Volatile Budgets". In: *American Mineralogist* 100.4, pages 806–823. DOI: 10.2138/am-2015-5036.

Moré, J. J. (1977). "The Levenberg-Marquardt Algorithm: Implementation and Theory". In: *Numerical Analysis*. Volume 630, pages 105–116. DOI: 10.1007/BFb0067700.

Mosenfelder, J. L., M. Le Voyer, G. R. Rossman, Y. Guan, D. R. Bell, P. D. Asimow, and J. M. Eiler (2011). "Analysis of Hydrogen in Olivine by SIMS: Evaluation of Standards and Protocol". In: *American Mineralogist* 96.11-12, pages 1725–1741. DOI: 10.2138/am.2011.3810.

Moussallam, Y., W. H. Towbin, T. Plank, H. Bureau, H. Khodja, Y. Guan, C. Ma, M. B. Baker, E. M. Stolper, F. U. Naab, B. D. Monteleone, G. A. Gaetani, K. Shimizu, T. Ushikubo, H. J. Lee, S. Ding, S. Shi, and E. F. Rose-Koga (2024). "ND70 Series Basaltic Glass Reference Materials for Volatile Element (H_2O , CO_2 , S, Cl, F) Measurement and the C Ionisation Efficiency Suppression Effect of Water in Silicate Glasses in SIMS". In: *Geostandards and Geoanalytical Research* 48.3, pages 637–660. DOI: 10.1111/ggr.12572.

Neave, D. A. and K. D. Putirka (2017). "A New Clinopyroxene-Liquid Barometer, and Implications for Magma Storage Pressures under Icelandic Rift Zones". In: *American Mineralogist* 102.4 (4), pages 777–794. DOI: 10.2138/am-2017-5968.

Newman, S. and J. B. Lowenstern (2002). "VolatileCalc: A Silicate Melt–H_2O–CO_2 Solution Model Written in Visual Basic for Excel". In: *Computers & Geosciences* 28.5, pages 597–604. DOI: 10.1016/S0098-3004(01)00081-4.

Newville, M., T. Stensitzki, D. B. Allen, and A. Ingargiola (2014). *LMFIT: Non-Linear Least-Square Minimization and Curve-Fitting for Python*. Zenodo. DOI: 10.5281/ZENODO.11813.

Ni, P., Y. Zhang, and Y. Guan (2017). "Volatile Loss during Homogenization of Lunar Melt Inclusions". In: *Earth and Planetary Science Letters* 478, pages 214–224. DOI: 10.1016/j.epsl.2017.09.010.

Pamukcu, A. S., T. L. Carley, G. A. R. Gualda, C. F. Miller, and C. A. Ferguson (2013). "The Evolution of the Peach Spring Giant Magma Body: Evidence from Accessory Mineral Textures and Compositions, Bulk Pumice and Glass Geochemistry, and Rhyolite-MELTS Modeling". In: *Journal of Petrology* 54.6, pages 1109–1148. DOI: 10.1093/petrology/egt007.

Pamukcu, A. S., G. A. Gualda, F. Bégué, and D. M. Gravley (2015). "Melt Inclusion Shapes: Timekeepers of Short-Lived Giant Magma Bodies". In: *Geology* 43.11, pages 947–950. DOI: 10.1130/G37021.1.

Putirka, K. D. (2008). "Thermometers and Barometers for Volcanic Systems". In: *Reviews in Mineralogy and Geochemistry* 69.1, pages 61–120. DOI: 10.2138/rmg.2008.69.3.

Putirka, K. D. (2005). "Mantle Potential Temperatures at Hawaii, Iceland, and the Mid-ocean Ridge System, as Inferred from Olivine Phenocrysts: Evidence for Thermally Driven Mantle Plumes". In: *Geochemistry, Geophysics, Geosystems* 6.5, 2005GC000915. DOI: 10.1029/2005GC000915.

Putirka, K. D., M. Perfit, F. Ryerson, and M. G. Jackson (2007). "Ambient and Excess Mantle Temperatures, Olivine Thermometry, and Active vs. Passive Upwelling". In: *Chemical Geology* 241.3-4, pages 177–206. DOI: 10.1016/j.chemgeo.2007.01.014.

Rasmussen, D. J., T. A. Plank, P. J. Wallace, M. E. Newcombe, and J. B. Lowenstern (2020). "Vapor-Bubble Growth in Olivine-Hosted Melt Inclusions". In: *American Mineralogist* 105.12, pages 1898–1919. DOI: 10.2138/am-2020-7377.

Richard, A., C. Morlot, L. Créon, N. Beaudoin, V. S. Balistky, S. Pentelei, V. Dyja-Person, G. Giuliani, I. Pignatelli, H. Legros, J. Sterpenich, and J. Pironon (2019). "Advances in 3D Imaging and Volumetric Reconstruction of Fluid and Melt Inclusions by High Resolution X-ray Computed Tomography". In: *Chemical Geology* 508, pages 3–14. DOI: 10.1016/j.chemgeo.2018.06.012.

Ridolfi, F. (2021). "Amp-TB2: An Updated Model for Calcic Amphibole Thermobarometry". In: *Minerals* 11.3 (3), page 324. DOI: 10.3390/min11030324.

Roeder, P. L. and R. F. Emslie (1970). "Olivine-Liquid Equilibrium". In: *Contributions to Mineralogy and Petrology* 29.4, pages 275–289. DOI: 10.1007/BF00371276.

Rose-Koga, E., A.-S. Bouvier, G. Gaetani, P. Wallace, C. Allison, J. Andrys, C. Angeles de la Torre, A. Barth, R. Bodnar, A. Bracco Gartner, D. Butters, A. Castillejo, B. Chilson-Parks, B. Choudhary, N. Cluzel, M. Cole, E. Cottrell, A. Daly, L. Danyushevsky, C. DeVitre, M. Drignon, L. France, M. Gaborieau, M. Garcia, E. Gatti, F. Genske, M. Hartley, E. Hughes, A. Iveson, E. Johnson, M. Jones, T. Kagoshima, Y. Katzir, M. Kawaguchi,

T. Kawamoto, K. Kelley, J. Koornneef, M. Kurz, M. Laubier, G. Layne, A. Lerner, K.-Y. Lin, P.-P. Liu, A. Lorenzo-Merino, N. Luciani, N. Magalhães, H. Marschall, P. Michael, B. Monteleone, L. Moore, Y. Moussallam, M. Muth, M. Myers, D. Narváez, O. Navon, M. Newcombe, A. Nichols, R. Nielsen, A. Pamukcu, T. Plank, D. Rasmussen, J. Roberge, F. Schiavi, D. Schwartz, K. Shimizu, K. Shimizu, N. Shimizu, J. Thomas, G. Thompson, J. Tucker, G. Ustunisik, C. Waelkens, Y. Zhang, and T. Zhou (2021). "Silicate Melt Inclusions in the New Millennium: A Review of Recommended Practices for Preparation, Analysis, and Data Presentation". In: *Chemical Geology* 570.120522, page 120145. DOI: 10.1016/j.chemgeo.2021.120145.

Rosso, K. and R. Bodnar (1995). "Microthermometric and Raman Spectroscopic Detection Limits of CO_2 in Fluid Inclusions and the Raman Spectroscopic Characterization of CO_2". In: *Geochimica et Cosmochimica Acta* 59.19, pages 3961–3975. DOI: 10.1016/0016-7037(95)94441-H.

Sakamaki, T., E. Ohtani, S. Urakawa, H. Terasaki, and Y. Katayama (2011). "Density of Carbonated Peridotite Magma at High Pressure Using an X-ray Absorption Method". In: *American Mineralogist* 96.4, pages 553–557. DOI: 10.2138/am.2011.3577.

Salter, C. and R. de Levie (2002). "Nonlinear Fits of Standard Curves: A Simple Route to Uncertainties in Unknowns". In: *Journal of Chemical Education* 79.2, page 268. DOI: 10.1021/ed079p268.

Schneider, C. A., W. S. Rasband, and K. W. Eliceiri (2012). "NIH Image to ImageJ: 25 Years of Image Analysis". In: *Nature Methods* 9.7, pages 671–675. DOI: 10.1038/nmeth.2089.

Shacham, M. and N. Brauner (1997). "Minimizing the Effects of Collinearity in Polynomial Regression". In: *Industrial & Engineering Chemistry Research* 36.10, pages 4405–4412. DOI: 10.1021/ie970236k.

Shimizu, K., N. Shimizu, T. Komiya, K. Suzuki, S. Maruyama, and Y. Tatsumi (2009). "CO_2-rich Komatiitic Melt Inclusions in Cr-spinels within Beach Sand from Gorgona Island, Colombia". In: *Earth and Planetary Science Letters* 288.1-2, pages 33–43. DOI: 10.1016/j.epsl.2009.09.005.

Shimizu, K., T. Ushikubo, M. Hamada, S. Itoh, Y. Higashi, E. Takahashi, and M. Ito (2017). "H_2O, CO_2, F, S, Cl, and P_2O_5 Analyses of Silicate Glasses Using SIMS: Report of Volatile Standard Glasses". In: *GEOCHEMICAL JOURNAL* 51.4, pages 299–313. DOI: 10.2343/geochemj.2.0470.

Shimizu, N. and J. Gill (1997). "Principles of SIMS and Modern Ion Microprobes". In: *Modern Analytical Geochemistry: An Introduction to Quantitative Chemical Analysis Techniques for Earth, Environmental and Materials Scientists*, pages 235–242.

Shishkina, T., R. Botcharnikov, F. Holtz, R. Almeev, and M. Portnyagin (2010). "Solubility of H_2O- and CO_2-bearing Fluids in Tholeiitic Basalts at Pressures up to 500MPa". In: *Chemical Geology* 277.1-2, pages 115–125. DOI: 10.1016/j.chemgeo.2010.07.014.

Shishkina, T. A., R. E. Botcharnikov, F. Holtz, R. R. Almeev, A. M. Jazwa, and A. A. Jakubiak (2014). "Compositional and Pressure Effects on the Solubility of H_2O and CO_2 in Mafic Melts". In: *Chemical Geology* 388, pages 112–129. DOI: 10.1016/j.chemgeo.2014.09.001.

Sides, I. R., M. Edmonds, J. Maclennan, D. A. Swanson, and B. F. Houghton (2014). "Eruption Style at Kīlauea Volcano in Hawai'i Linked to Primary Melt Composition". In: *Nature Geoscience* 7.6, pages 464–469. DOI: 10.1038/ngeo2140.

Song, Y., I. Chou, W. Hu, B. Robert, and W. Lu (2009). "CO_2 Density-Raman Shift Relation Derived from Synthetic Inclusions in Fused Silica Capillaries and Its Application". In: *Acta Geologica Sinica - English Edition* 83.5, pages 932–938. DOI: 10.1111/j.1755-6724.2009.00090.x.

Span, R. and W. Wagner (1996). "A New Equation of State for Carbon Dioxide Covering the Fluid Region from the Triple-Point Temperature to 1100 K at Pressures up to 800 MPa". In: *Journal of Physical and Chemical Reference Data* 25.6, pages 1509–1596. DOI: 10.1063/1.555991.

Stolper, E. and D. Walker (1980). "Melt Density and the Average Composition of Basalt". In: *Contributions to Mineralogy and Petrology* 74.1, pages 7–12. DOI: 10.1007/BF00375484.

Tellinghuisen, J. (2000). "Inverse vs. Classical Calibration for Small Data Sets". In: *Fresenius' Journal of Analytical Chemistry* 368.6, pages 585–588. DOI: 10.1007/s002160000556.

– (2001). "Statistical Error Propagation". In: *The Journal of Physical Chemistry A* 105.15, pages 3917–3921. DOI: 10.1021/jp003484u.

– (2005). "Simple Algorithms for Nonlinear Calibration by the Classical and Standard Additions Methods". In: *The Analyst* 130.3, page 370. DOI: 10.1039/b411054d.

– (2007). "Weighted Least-Squares in Calibration: What Difference Does It Make?" In: *The Analyst* 132.6, page 536. DOI: 10.1039/b701696d.

– (2010). "Least-Squares Analysis of Data with Uncertainty in x and y: A Monte Carlo Methods Comparison". In: *Chemometrics and Intelligent Laboratory Systems* 103.2, pages 160–169. DOI: 10.1016/j.chemolab.2010.07.003.

– (2018). "Least-Squares Analysis of Data with Uncertainty in *y* and *x* : Algorithms in Excel and KaleidaGraph". In: *Journal of Chemical Education* 95.6, pages 970–977. DOI: 10.1021/acs.jchemed.8b00069.

– (2019). "Calibration: Detection, Quantification, and Confidence Limits Are (Almost) Exact When the Data Variance Function Is Known". In: *Analytical Chemistry* 91.14, pages 8715–8722. DOI: 10.1021/acs.analchem.9b00119.

– (2020). "Least Squares Methods for Treating Problems with Uncertainty in *x* and *y*". In: *Analytical Chemistry* 92.16, pages 10863–10871. DOI: 10.1021/acs.analchem.0c02178.

Tellinghuisen, J. and C. H. Bolster (2011). "Using R^2 to Compare Least-Squares Fit Models: When It Must Fail". In: *Chemometrics and Intelligent Laboratory Systems* 105.2, pages 220–222. DOI: 10.1016/j.chemolab.2011.01.004.

Toplis, M. J. (2005). "The Thermodynamics of Iron and Magnesium Partitioning between Olivine and Liquid: Criteria for Assessing and Predicting Equilibrium in Natural and Experimental Systems". In: *Contributions to Mineralogy and Petrology* 149.1, pages 22–39. DOI: 10.1007/s00410-004-0629-4.

Towbin, W. H., T. Plank, E. Klein, and E. Hauri (2023). "Measuring H_2O Concentrations in Olivine by Secondary Ion Mass Spectrometry: Challenges and Paths Forward". In: *American Mineralogist: Journal of Earth and Planetary Materials* 108.5, pages 928–940. DOI: 10.2138/am-2022-8247.

Tucker, J. M., E. H. Hauri, A. J. Pietruszka, M. O. Garcia, J. P. Marske, and F. A. Trusdell (2019). "A High Carbon Content of the Hawaiian Mantle from Olivine-Hosted Melt Inclusions". In: *Geochimica et Cosmochimica Acta* 254, pages 156–172. DOI: 10.1016/j.gca.2019.04.001.

Van Gerve, T. D., D. A. Neave, P. Wieser, H. Lamadrid, N. Hulsbosch, and O. Namur (2024). "The Origin and Differentiation of CO2-rich Primary Melts in Ocean Island Volcanoes: Integrating 3D X-ray Tomography with Chemical Microanalysis of Olivine-Hosted Melt Inclusions from Pico (Azores)". In: *Journal of Petrology*, egae006. DOI: 10.1093/petrology/egae006.

Wallace, P. J., T. Plank, R. J. Bodnar, G. A. Gaetani, and T. Shea (2021). "Olivine-Hosted Melt Inclusions: A Microscopic Perspective on a Complex Magmatic World". In: *Annual Review of Earth and Planetary Sciences* 49.1, pages 465–494. DOI: 10.1146/annurev-earth-082420-060506.

Wang, C. and R. Wright (1973). "Raman Studies of the Effect of Density of the Fermi Resonance in CO_2". In: *Chemical Physics Letters* 23.2, pages 241–246. DOI: 10.1016/0009-2614(73)80261-1.

Wang, W., M.-C. Caumon, A. Tarantola, J. Pironon, W. Lu, and Y. Huang (2019). "Raman Spectroscopic Densimeter for Pure CO_2 and CO_2-H_2O-NaCl Fluid Systems over a Wide P-T Range up to 360 °C and 50 MPa". In: *Chemical Geology* 528, page 119281. DOI: 10.1016/j.chemgeo.2019.119281.

Wang, X., I.-M. Chou, W. Hu, R. C. Burruss, Q. Sun, and Y. Song (2011). "Raman Spectroscopic Measurements of CO_2 Density: Experimental Calibration with High-Pressure Optical Cell (HPOC) and Fused Silica Capillary Capsule (FSCC) with Application to Fluid Inclusion Observations". In: *Geochimica et Cosmochimica Acta* 75.14, pages 4080–4093. DOI: 10.1016/j.gca.2011.04.028.

Waters, L. E. and R. A. Lange (2015). "An Updated Calibration of the Plagioclase-Liquid Hygrometer-Thermometer Applicable to Basalts through Rhyolites". In: *American Mineralogist* 100.10, pages 2172–2184. DOI: 10.2138/am-2015-5232.

Wieser, P. E., K. Iacovino, S. Matthews, G. Moore, and C. M. Allison (2022a). "VESIcal: 2. A Critical Approach to Volatile Solubility Modeling Using an Open-Source Python3 Engine". In: *Earth and Space Science* 9.2. DOI: 10.1029/2021EA001932.

Wieser, P. and C. DeVitre (2023). *DiadFit: An Open-Source Python3 Tool for Peak Fitting of Raman Data from Silicate Melts and CO2 Fluids*. Preprint. Earth Sciences. DOI: 10.31223/X5CQ1F.

Wieser, P., A. Kent, and C. Till (2022b). *Barometers Behaving Badly II: A Critical Evaluation of Cpx-only and Cpx-Liq Thermobarometry in Variably-Hydrous Arc Magmas*. Preprint. Earth Sciences. DOI: 10.31223/X59655.

Wieser, P., M. Petrelli, J. Lubbers, E. Wieser, S. Ozaydin, A. Kent, and C. Till (2022c). "Thermobar: An Open-Source Python3 Tool for Thermobarometry and Hygrometry". In: *Volcanica* 5.2, pages 349–384. DOI: 10.30909/vol.05.02.349384.

Wieser, P. E., H. Lamadrid, J. Maclennan, M. Edmonds, S. Matthews, K. Iacovino, F. E. Jenner, C. Gansecki, F. Trusdell, R. Lee, and E. Ilyinskaya (2021). "Reconstructing Magma Storage Depths for the 2018 Kīlauean Eruption From Melt Inclusion CO_2 Contents: The Importance of Vapor Bubbles". In: *Geochemistry, Geophysics, Geosystems* 22.2. DOI: 10.1029/2020GC009364.

Williamson, J. H. (1968). "Least-Squares Fitting of a Straight Line". In: *Canadian Journal of Physics* 46.16, pages 1845–1847. DOI: 10.1139/p68-523.

Witham, F., J. Blundy, S. C. Kohn, P. Lesne, J. Dixon, S. V. Churakov, and R. Botcharnikov (2012). "SolEx: A Model for Mixed COHSCl-volatile Solubilities and Exsolved Gas Compositions in Basalt". In: *Computers & Geosciences* 45, pages 87–97. DOI: 10.1016/j.cageo.2011.09.021.

Wong, K., D. Ferguson, P. Wieser, D. Morgan, M. Edmonds, A. Z. Tadesse, G. Yirgu, J. Harvey, and S. Hammond (2023). "Focused Mid-Crustal Magma Intrusion During Continental Break-Up in Ethiopia". In: *Geophysical Research Letters* 50.11, e2023GL103257. DOI: 10.1029/2023GL103257.

Wong, K., E. Mason, S. Brune, M. East, M. Edmonds, and S. Zahirovic (2019). "Deep Carbon Cycling Over the Past 200 Million Years: A Review of Fluxes in Different Tectonic Settings". In: *Frontiers in Earth Science* 7, page 263. DOI: 10.3389/feart.2019.00263.

Yamamoto, J. and H. Kagi (2006). "Extended Micro-Raman Densimeter for CO_2 Applicable to Mantle-originated Fluid Inclusions". In: *Chemistry Letters* 35.6, pages 610–611. DOI: 10.1246/cl.2006.610.

York, D. (1968). "Least Squares Fitting of a Straight Line with Correlated Errors". In: *Earth and Planetary Science Letters* 5, pages 320–324. DOI: 10.1016/S0012-821X(68)80059-7.

Zhang, Y., O. Namur, W. Li, O. Shorttle, E. Gazel, E. Jennings, P. Thy, T. L. Grove, and B. Charlier (2023). "An Extended Calibration of the Olivine–Spinel Aluminum Exchange Thermometer: Application to the Melting Conditions and Mantle Lithologies of Large Igneous Provinces". In: *Journal of Petrology* 64.11, egad077. DOI: 10.1093/petrology/egad077.

Chapter 4

Petrological constraints on Villarrica's Magmatic System from Melt Inclusion Compositions

4.1 Abstract

In this chapter, I characterise Villarrica's magmatic system by analyzing melt inclusions (MI) from four distinct eruptions using micro-Raman spectroscopy, secondary ion mass spectrometry, and electron microprobe analysis. Notably, the volatile, trace, and major element compositions of olivine, plagioclase, and clinopyroxene-hosted MIs were characterized to investigate the relationships between magma composition and the diverse eruptive behaviours observed at Villarrica. Volatile contents, H_2O and CO_2, were used to estimate magma storage pressures, revealing a vertically extensive magmatic system with storage zones extending from the surface to depths of over 30 km. However, calculated H_2O and CO_2 contents have been modified by post-entrapment processes. Ol-liq Ca-exchange hygrometry demonstrates that measured H_2O contents have been reduced by dehydration or re-equilibration. A lack of detectable CO_2 diads in the majority of MI-hosted vapour bubbles suggests that substantial CO_2 may be contained within carbonates and therefore is not accounted for. Trace element data show that multiple reservoirs with distinct mantle sources and/or degrees of melting are assembled before their eruption. The range of storage pressures and compositions of Villarrica MI strongly support the existence of a trans-crustal magmatic system at Villarrica volcano, that has persisted for at least the last 3000 years.

4.2 Introduction

Villarrica volcano (Rukapillan; 39.5°S, 71.9°W) is a Quaternary stratovolcano and one of Chile's most active volcanoes, having experienced over 100 eruptions since 1558 (Petit-Breuilh Sepúlveda 2004). Its post-glacial volcanic activity, spanning from 14,000 years ago to the present, has displayed a wide range of eruption intensities and magnitudes. For example, the March 2015 fire fountain was intense but low-magnitude, lasting only twenty minutes (Romero et al. 2018). In contrast, the Los Nevados parasitic cones and their lavas were formed by low-magnitude and low-intensity eruptions; as well as the high-intensity and high-magnitude Licán mafic ignimbrite forming eruption, producing deposits with a volume of greater than 10 km^3 (Lohmar et al. 2012). Despite this variety in eruptive style, Villarrica's volcanic products have a limited range of major element composition compared to other nearby Chilean volcanoes.

Chapter 2 used a machine-learning approach to interrogate a compiled dataset of Villarrica crystal cargoes, which are more compositionally diverse than their whole-rock compositions would suggest. MELTS-based thermobarometry provided evidence for vertically extensive magma storage, extending to at least the middle crust (~20 km depth). Additionally, the variation in crystal cargo compositions suggests that multiple distinct reservoirs are tapped before their eruption. However, as the chapter only investigated major element compositions, more subtle distinctions between these reservoirs that may indicate different mantle sources could not be discerned.

4.2.1 Aims and Objectives

To further investigate magmatic storage and evolution at Villarrica in this Chapter I use melt inclusion (MI) compositions analysed by multiple analytical techniques. A combination of micro-Raman spectroscopy, secondary ion mass spectrometry, and electron microprobe analysis was used to measure the volatile, trace and major element composition of olivine, plagioclase and clinopyroxene-hosted melt inclusions from four eruptions of Villarrica. The primary aim of this analysis was to test whether the use of a TCMS model for magma storage at Villarrica is also supported by MI compositions. I targeted primitive MI hosts, which have the highest probability of preserving deep-crustal signatures, and the potential to extend recorded magma storage depths beyond those estimated in Chapter 2. Trace elements are used to constrain magma sources, and to infer whether measured volatile contents are representative of primary mantle values or were already modified by volatile loss before MI entrapment. Proper treatment of errors, as described in Chapter 3, allows a complete assessment of errors in volatile contents and calculated saturation pressures. These saturation pressures will allow me to assess the range of pressures over

which melt inclusions form, as a proxy for magma storage, and assess the suitability of the trans-crustal magmatic system model to describe the magmatic architecture at Villarrica volcano.

4.3 Sample Collection

During a field campaign to Villarrica in January 2020, a wide range of eruptive deposits were sampled. These included materials from most eruptions discussed in Chapter 2: such as the March 2015 eruption, the two large mafic ignimbrites (Licán and Pucón), the Chaimilla Fall deposit, and samples from both groups of parasitic cones, the Los Nevados, and Chaillupén groups. The primary goal of the campaign was to sample deposits from eruptions with varying eruptive styles throughout Villarrica's post-glacial eruptive history. To minimise the potential of post-eruption volatile diffusion, loose crystals and fine tephra were preferentially sampled over more crystalline products (lavas and bombs), as melt inclusions in the latter are more likely to have undergone significant volatile loss due to diffusion (Lloyd et al. 2013).

One of the major barriers to overcome was the typically low crystallinity (<10%) and the small size of crystals in Villarrica's eruptive deposits. This necessitated the collection of significant volumes of material (many hundreds of grams) to obtain a suitable number of crystals for analysis. However, only a small percentage of these crystals contained melt inclusions, most of which were too small for analysis.

Of all the deposits sampled, only samples from four eruptions consistently contained melt inclusions suitable for further investigation. In particular, rare olivine from the Licán mafic ignimbrite contained MIs that were invariably devitrified and cracked, making them unsuitable for analysis. Tephra from the Chaillupén parasitic cones was heavily oxidised and all crystals were coated in thick layers of glass, making it impossible to identify melt inclusions. After extensive preparation, only the following four eruptions contained MIs suitable for analysis: the Pucón Ignimbrite (Silva Parejas et al. 2010), the Chaimilla Fall Deposit (Costantini et al. 2011; Pioli et al. 2015), the Los Nevados Parasitic Cones (Robidoux et al. 2021) and the March 2015 eruption (Romero et al. 2018). The sample locations for these deposits are shown in Figure 4.1. Additionally, a spatter sample from the March 2015 eruption, collected shortly after the event by Hugo Moreno, was also analysed.

4.4 Sample Preparation

Coarser tephra was gently crushed using a ceramic pestle and mortar to liberate whole crystals. All samples were sieved into four size fractions (<600, 600–1000, 1000–2000 and >2000 µm). Olivine,

plagioclase and clinopyroxene crystals were then hand-picked using a binocular microscope and those containing silicate melt inclusions were identified. Inclusions were screened to exclude those that were devitrified or appeared to have undergone decrepitation. Glassy, intact MIs were then further categorised into MIs that contained a vapour bubble and those without.

All inclusion-bearing crystals were then mounted onto frosted glass slides using Crystalbond™, followed by hand lapping with15 µm and 9 µm aluminium oxide powder to form a polished surface parallel to the slide. Additional material was removed until vapour bubbles were within 30 µm of the surface. Inclusions without vapour bubbles were exposed for further analysis. The crystals were polished using increasingly fine diamond pastes until a 0.25 µm polish was achieved. Table 4.1 provides a summary of the eruptions, samples, host mineralogy and number of melt inclusions prepared and analysed. Photographs of each melt inclusion and vapour bubble can be found in the Appendix C.

Table 4.1: Breakdown of MIs studied by eruption and host-mineralogy.

Eruption	Host Mineral	No. MI
Pucón	Olivine	27
	Plagioclase	14
	Clinopyroxene	8
Chaimilla	Olivine	19
	Plagioclase	2
	Clinopyroxene	2
Los Nevados	Olivine	6
March 2015	Olivine	19
	Total	97

4.5 Studied Eruptive Deposits

4.5.1 The Pucón Large Mafic Ignimbrite

The Pucón Ignimbrite, dated at 3.7 ka B.P., is the second largest eruption in Villarrica's post-glacial history, with a non-dense-rock equivalent volume of 3 km^3. The deposits consist of dark grey to black scoriaceous tephra, comprised of scoria-rich, lithic-rich and surge units, which are distributed radially from the current central vent (Silva Parejas 2008; Silva Parejas et al. 2010). In areas where density currents were channelled by topography, the deposits exceed 10 m in thickness and consist of multiple flow units. These units are typically scoriaceous, lithic-rich and often overlain by a less dense surge deposit (Silva Parejas et al. 2010).

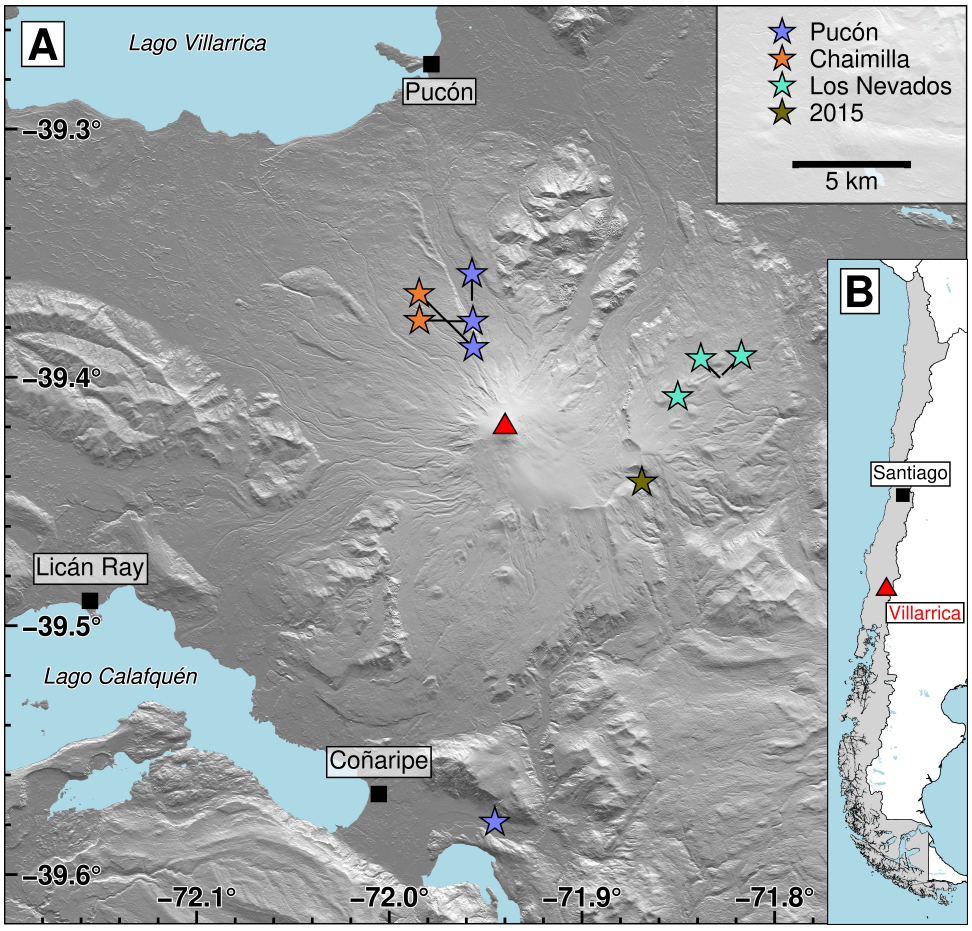

Figure 4.1: Map of Villarrica volcano and sampling locations. The digital elevation model is a Tandem-X 0.4″ DEM. Lake outlines are from the Biblioteca del Congreso Nacional de Chile. A) Stars show the location of the ten samples with melt inclusion-bearing crystals analysed in this study. The red triangle marks the summit of Villarrica. Black squares show the location of nearby towns. B) The inset shows the location of Villarrica volcano (red triangle) within Chile (grey shading). The black square shows the position of the capital city Santiago.

The bulk composition of the Pucón Ignimbrite is basaltic-andesite with a SiO_2 content ranging from 54–56 wt.%. (Lohmar 2008; Silva Parejas 2008; Silva Parejas et al. 2010)). Crystal cargoes are comprised of plagioclase (An_{52-93}), olivine (Fo_{64-88}), and clinopyroxene (Mg_{66-85}) phenocrysts and minor Fe-Ti oxides (Clavero-Ribes 1996; Lohmar 2008). Clavero-Ribes (1996) suggests that this eruption was triggered by the injection of basaltic magma into an andesitic chamber. This aligns with the conclusions of Chapter 2 which suggest the eruption was formed from an interaction between a mafic trigger magma and a more evolved crystalline reservoir.

4.5.2 The Chaimilla Fall Deposit

The Chaimilla fall deposit, dated at 3.2 ka B.P., is composed of a beige-orange tephra fall deposit, primarily located on the northern flank of Villarrica. The deposit contains several units, with compositions suggesting the interaction of two distinct magma batches triggered the eruption (Costantini et al. 2011). The deposit's bulk composition ranges from basaltic to basaltic-andesite (51–53 wt.% SiO_2; Costantini et al. 2011; Lohmar 2008; Pioli et al. 2015). Its crystal cargo is comprised of plagioclase (An_{70-94}), olivine (Fo_{75-85}) and clinopyroxene (Mg_{65-88}) phenocrysts and minor Cr-spinel found as inclusions in olivine (Lohmar 2008; Pioli et al. 2015).

Pioli et al. (2015) characterised several olivine-hosted and plagioclase-hosted melt inclusions which show a greater variety of major element compositions than both groundmass glasses and bulk compositions (49–58 wt.% SiO_2). They also display a range of H_2O contents (1.5–3.0 wt.%). However, only the MI glass volatile contents were measured, excluding vapour bubbles, likely leading to an underestimate of CO_2 contents (<400 ppm).

4.5.3 Los Nevados Parasitic Cones

The flanks of Villarrica host several parasitic or adventitious cones, which are categorised into two groups based on their position and orientation: the Chaillupén group on the southern flank, and the the Los Nevados group on the northeastern flank (*Geología del volcán Villarrica, Regiones de La Araucanía y de Los Lagos.* 2006). The Los Nevados group consists of a series of northeast-oriented scoria cones and lavas (Robidoux et al. 2021). These cones are presumed Holocene in age, as they are well preserved, and form two groups with relative ages of greater than2.6 ka and less than 2.6 ka (*Geología del volcán Villarrica, Regiones de La Araucanía y de Los Lagos.* 2006).

The cones vary in colour from oxidised red to black-grey and are composed of crystalline lavas as well as

crystal-poor scoria. Their bulk composition is basaltic-andesite with SiO_2 contents ranging frmo 54.5–55.2 wt.%. (Lohmar 2008; Robidoux et al. 2021)). Their crystal cargoescontain plagioclase (An_{60-90}), olivine (Fo_{57-86}) and minor clinopyroxene (Mg_{63-86}) (Lohmar 2008; Robidoux et al. 2021).

Robidoux et al. (2021) measured the volatile and major element composition of several olivine-hosted melt inclusions from these cones. However, like Pioli et al. (2015) they did not measure the CO_2 content of any vapour bubbles and therefore likely underestimated MI volatile contents and therefore saturation pressures. The authors relate volatile saturation depths to eruptive style, noting that earlier eruptions exhumed crystal-rich bombs from greater depths (ca. 9 km), while later, shallower activity (ca. 8 km) produced more vesicular bombs.

4.5.4 The March 2015 Fire Fountain

The 3rd of March 2015 fire fountain was an intense, short-lived eruption that ejected tephra and spatter over a ca. twenty-minute period on the morning of 03 March 2015 (Romero et al. 2018). The resultant spatter and tephra were primarily deposited on the eastern flank of the volcano, with some material transported up to 50 km away (Romero et al. 2018). The bulk composition is marginally basaltic-andesitic with a SiO_2 content of ca. 52.69 wt.%; (McGee et al. 2017). Various juvenile products contain olivine (Fo_{70-86}), plagioclase (An_{66-86}) and scarce clinopyroxene (Mg_{76}) crystals(Boschetty et al. 2022; Romero et al. 2022). The intense eruptive style of the fire fountain suggests rapid and efficient transport of phenocrysts by a volatile-rich magma (Romero et al. 2022).

4.6 Analytical Workflow

The analytical workflow used for analysing MI volatile contents follows the procedure described in Chapter 3, and Figure 3.1a, with some notable additions. In addition to volatile elements, additional light and heavy trace element contents were also measured using Secondary Ion Mass Spectrometry, and distinct post-entrapment modification corrections were applied to olivine-, plagioclase- and clinopyroxene-hosted MI.

Olivine-hosted spinel was also analysed to estimate oxygen fugacity for each eruption, which is required for post-entrapment modification corrections (see Section 4.7.1). Additionally, groundmass glasses were analysed for their major-element compositions, with a subset analysed via SIMS for their volatile and trace element contents. Further details are provided below by analytical technique.

4.6.1 Micro-Raman Spectroscopy

Micro-Raman spectroscopy was used to measure CO_2 contents of vapour bubbles within the majority of the studied melt inclusions. Following the methodology of Wieser et al. (2021), a densimeter was calibrated to relate the diad split (distance between the two dominant peaks found in Raman spectra of CO_2) to the density of CO_2 within the bubbles. The relationship between CO_2 density and diad split is linear at low densities (<0.2 g·cm^{-3}) commonly found in MI vapour bubbles (DeVitre et al. 2021; Lamadrid et al. 2017; Wieser et al. 2021). I calibrated a densimeter specifically for the micro-Raman spectrometer at Leeds, under specific operating conditions, using several synthetic pure-CO_2 fluid inclusions. The density of these standard fluid inclusions was previously determined using a well-calibrated micro-Raman system at Virginia-Tech (Lamadrid et al. 2017; Wieser et al. 2021).

CO_2 densities were converted into concentrations using the following equation:

$$[CO_2]_{\mathrm{VB}} = 10^6 \times \frac{\rho_{CO_2} \cdot V_{\mathrm{VB}}}{\rho_{\mathrm{melt}} \cdot V_{\mathrm{melt}}} \tag{4.1}$$

where ρ_{CO_2} is the vapour bubble CO_2 density V_{VB} is the vapour bubble volume, ρ_{melt} is the MI density, and V_{melt} is the MI volume. MI and vapour bubble volumes were estimated using optical imagery taken using a Leica DM750P optical microscope and a 40× objective. The volume of each vapour bubble was estimated assuming spherical geometry. The volume of each MI was estimated by measuring a best-fit ellipse for each inclusion and taking the third unknown axis as the shorter of the two measured axes. MI glass density was estimated by inputting the measured major element composition and H_2O content of the glass into DensityX (Iacovino and Till 2018). Total MI CO_2 concentration was calculated by summing the CO_2 content of the vapour bubble and MI glass. Details of densimeter calibration, peak fitting, standards, volume calculations and uncertainty propagation can be found in Appendix B.

4.6.2 Secondary Ionization Mass Spectroscopy

After micro-Raman spectroscopy, MI-bearing grains were carefully removed from glass slides by heating, and any remaining crystal bond was removed with acetone. The grains were then mounted in 25 mm diameter epoxy grain mounts and repolished using diamond pastes to 0.25 µm finish. The grain mounts were then sonicated in isopropanol and finally gold-coated for SIMS analysis. The mounts were held under vacuum for 48 h to minimise degassing of the epoxy and ensure a high vacuum for analysis.

Volatile and trace element concentrations were measured by secondary mass ion spectrometry (SIMS)

using the Cameca IMS 4f ion microprobe at the NERC microanalytical facility, University of Edinburgh. Additional details, including calibration standards, estimates of precision, calibration curves and operating conditions are provided in Appendix B.

Several adjustments were made to the 'standard' processing of SIMS raw intensity data. It has been the practice for many years for calibration curves for volatile elements, H_2O and CO_2 to be derived from straight-line calibration curves that pass through the origin, derived from background-subtracted normalised intensity ratios. These are usually calculated using an Ordinary Least Squares approach, which assumes homoscedastic intensity data, and perfectly known standards. To allow for effective error propagation (as described in Chapter 3), a different approach was used:

1. Non-background-subtracted normalised intensities were used and a constant was included in the response function, allowing direct assessment of background intensities.
2. Residuals analysis was conducted to identify the most suitable response function, which was a second-order polynomial ($y = a + bx + cx^2$) for CO_2 and a first-order polynomial ($y = a + bx$) for H_2O.
3. The Effective Variance regression method (EV_2; Tellinghuisen 2010, 2019) was applied to propagate uncertainties from counting statistics and the standards used, into derived volatile concentrations.

For further information, refer to Appendix B.

4.6.3 Electron Micro Probe Analysis

After SIMS analysis, the gold coating was removed with a potassium-iodide solution, and the mounts were re-polished with diamond pastes to remove SIMS pits, where necessary. A 10 nm carbon coat was then applied. Major element compositions were measured in melt inclusions, matrix and interstitial glasses, and host minerals using the JEOL JXA8230 Superprobe at the University of Leeds.

Analytical conditions were tailored for each phase to enhance analytical precision and accuracy dependent on their specific use:

- **Olivine:** Longer count times on Ca (140 s) were used to obtain the required precision for subsequent Olivine-Liquid Ca-exchange hygrometry (Gavrilenko et al. 2016).
- **Clinopyroxene:** Different beam conditions were used for major (20 nA) and minor (40 nA) ele-

ments, and extended count times for minor elements (60 s versus 20 s) to ensure sufficient precision for accurate clinopyroxene-only and clinopyroxene-liquid thermobarometry (Wieser et al. 2023b).

- **Spinel:** Additional, non-standard, minor elements (Ni, V, Co, Zn and Nb) were analysed to accurately derive Fe_2O_3 contents from stoichiometry (e.g., Wood and Virgo 1989).

Complete analytical details including analytes, count times, beam conditions, primary and secondary standards, and estimates of accuracy and precision can be found in Appendix B.

Multiple spots were analysed for each host mineral and MI to allow identification of mixed-phase or bad analyses, which were discarded, and duplicate analyses were averaged. Mineral analyses that deviated by more than 2 % relative to their ideal cations per formula unit (e.g., 3.000 ± 0.015 cfu. for olivine, or 4.00 ± 0.02 cfu. for clinopyroxene) were also excluded.

4.6.4 Back-Scattered Electron Imaging

Backscattered electron (BSE) imaging was conducted on select crystals for textural analysis. Images were taken using a FEI Quanta 650 FEG Scanning Electron Microscope (SEM) at LEMAS, University of Leeds. Imaging was performed using a 20 kV accelerating voltage, 30 nA beam current, and a Low-Voltage High-Contrast detector (vCD).

4.7 Processing Workflow

The processing workflow for MI analysis follows the structure outlined in Chapter 3, and Figure 3.1b, with the following important additions. Before estimating density and correcting for PEM, $fO_2$was estimated for each eruption, using the composition of olivine-hosted spinel and MI (Section 4.7.1). Liquid-only temperatures were estimated using equation 15 of Putirka (2008), assuming a pressure of 1 kbar. As olivine-, plagioclase- and clinopyroxene-hosted MI were measured, several different approaches to PEM-corrections are compared (Section 4.7.2). Ca-exchange Olivine-Liquid hygrometry is used to identify post-entrapment H^+ diffusion in olivine-hosted inclusions (Section 4.9.4.2).

4.7.1 Estimating Oxygen Fugacity from Olivine-Hosted Spinel and Melt Inclusions

4.7.1.1 Analytical Procedure

The composition of spinel inclusions hosted by olivine and coexisting MI were used to estimate the oxygen fugacity (fO_2) of olivine-crystallizing magmas. Only unzoned, spinel completely enclosed by olivine

was measured as spinel in olivine-rims was often zoned when in contact with adherent groundmass glass. The composition of 10 olivine-hosted spinel was measured from each of the four studied eruptions, 40 in total.

4.7.1.2 Data Processing

The method developed by Droop (1987) was used to partition the total iron (FeO_T, measured on the probe) between FeO and Fe_2O_3. Despite earlier concerns raised by some authors, Droop's method has been shown to be effective in calculating the FeO/Fe_2O_3 distribution in clinopyroxene, provided that sufficiently long count times are used for major and minor elements (Neave et al. 2024). I extended this approach to spinel analyses.

First, additional minor elements were measured to produce a complete analysis. The accuracy of partitioning FeO and Fe_2O_3 relies on all elements being measured (Wood and Virgo 1989). Second, count times were maximised to ensure high precision, which is as equally important for high-abundance elements (e.g. TiO_2 and FeO) and minor elements.

This approach assumes that the spinel is perfectly stoichiometric, although the stoichiometry of some subduction spinels has been debated (e.g., Kamperman et al. 1996). However, claims of non-stoichiometry were based on data of limited precision (Kamperman et al. 1996). Therefore the assumption of perfect stoichiometry in this study here is reasonable.

The cations per formula unit (cfu.) of each spinel were calculated on a four-anion-to-every-three-cation basis. The composition of each spinel was then compared to the compositional fields suggested by Kamenetsky et al. 2001 for arc-derived, magmatic spinel. These fields specify that spinels should have Al_2O_3 contents of less than 22 wt.%, and TiO_2 less than 2 wt.%. Some March 2015 spinel contained higher TiO_2 contents and were therefore treated with caution in subsequent calculations.

Spinel Mg# and host-olivine Fo contents were not compared as these are known to reflect subsequent re-equilibration, which occurs more rapidly for Fe-Mg than for trivalent cations in olivine (Kamenetsky et al. 2001).

Using the spinel-melt compositional relationships of Kamenetsky et al. (2001) and Maurel and Maurel (1982), the Al_2O_3 and TiO_2 contents of olivine-hosted spinel (ranging from 10–33 wt.% and 1.0–4.6 wt.%, respectively) were used to estimate that they crystallised from melts with Al_2O_3 contents of approximately 9–16 wt.% and TiO_2 contents of approximately 1.0–4.6 wt.%. The measured MI compo-

sitions fall within these compositional ranges, supporting the assumption of equilibrium, and validating the use of their coexisting compositions to estimate fO_2.

4.7.1.3 Calculation of Oxygen Fugacity

An updated version of the method of Danyushevsky and Sobolev (1996) was then applied to calculate an equilibrium melt Fe^{2+}/Fe^{3+} ratio, using the empirical relationship of Maurel and Maurel (1982):

$$\log_{10}\left(Fe^{2+}/Fe^{3+}\right)_{liq} = \left[\log_{10}\left(Fe^{2+}/Fe^{3+}\right)_{sp} + 0.343\right]/0.764 \tag{4.2}$$

Where "liq" and "sp" refer to the Fe^{2+}/Fe^{3+} ratios of the liquid and spinel, respectively. This relationship is calibrated for nominally basaltic melt and a range of equilibrium spinel compositions (Table 4.2 in Maurel and Maurel 1982) under the following intensive conditions: temperatures from 1080–1300 °C, fO_2 from 10^{-9} to 10^{-3}, and a pressure of one atmosphere.

To calculate melt fO_2, the empirical relationship of Borisov (2018) (Eq. 4, Model 4), which updates Borisov and Shapkin (1990) used in Danyushevsky and Sobolev (1996), was employed:

$$\begin{aligned}\log_{10}\left(X_{FeO_{1.5}}/X_{FeO}\right) = {} & 0.207 \cdot \log_{10} fO_2 + 4633.3/T \\ & - 0.445 \cdot X_{SiO_2} \\ & - 0.900 \cdot X_{TiO_2} + 1.532 \cdot X_{MgO} \\ & + 0.314 \cdot X_{CaO} + 2.030 \cdot X_{Na_2O} \\ & + 3.355 \cdot X_{K_2O} - 4.851 \cdot X_{P_2O_5} \\ & - 3.081 \cdot X_{SiO_2} \cdot X_{Al_2O_3} \\ & - 4.360 \cdot X_{SiO_2} \cdot X_{MgO} - 1.852\end{aligned} \tag{4.3}$$

where $X_{FeO_{1.5}}/X_{FeO}$ is the Fe^{3+}/Fe^{2+} ratio of the melt derived from spinel compositions and the relationship of Maurel and Maurel (1982), and X_{oxide} are the mole fractions for oxides in corresponding melt

Table 4.2: Compositional range of basaltic melts and equilibrium spinel from Maurel and Maurel (1982) given in wt.%.

	SiO_2	FeO_T	Al_2O_3	CaO	MgO	Na_2O	K_2O	TiO_2	Cr_2O_3
Liquid	50.3–55.6	3.8–11.6	7.9–14.9	9.5–12.8	6.6–13.3	1.6–3.4	0.3–0.7	1.3–2.3	<0.2
Spinel		13.6–61.7	4.7–20.7		11.6–19.1			0.6–2.5	8.1–56.8

inclusion compositions. The relationship of Borisov (2018) is calibrated under the following conditions: temperatures ranging from 1195–1636 °C, fO_2 from QFM−3.4 to +7.5, and is valid for melt SiO_2 contents of less than ~65 wt.%.

To calculate the temperature for both the initial oxygen fugacity calculation, and then to relate this oxygen fugacity to the QFM buffer (Frost 1991), the pressure- and water-dependent liquid-only thermometer of Putirka (2008) (Equation 15) was used, assuming a pressure of 1 kbar for all calculations.

Since only a few olivine hosted both spinel inclusions and MI, all olivine-hosted spinel compositions were compared to all MI compositions from the same eruption. This approach resulted in a range of calculated fO_2 for each eruption. However, where data are available, there is a strong overlap between the composition of MI-hosting olivine and spinel-hosting olivine (Figure 4.5). The MI and spinel therefore likely originated from the same magmatic environment.

4.7.1.4 Estimates of Uncertainty in Calculated Oxygen Fugacity

When using stoichiometric methods (e.g., Droop 1987) the calculated Fe_2O_3 content of the spinel is dependent on the uncertainty of all analysed cations (Wood and Virgo 1989). Therefore the analytical uncertainty of all measured oxides should be taken into account, not just FeO_T.

Maurel and Maurel (1982) does not provide a standard error for their regression, nor do they publish the data from which the relationship is established, so these errors cannot be directly accounted for. Borisov (2018) back-calculated the uncertainty in fO_2 from their Model 4, reporting a 1σ uncertainty of 0.38 log units. They also found that a temperature difference of 100 °C produced an uncertainty of less than 0.1 log units, relative to QFM, in the calculated fO_2. This suggests that temperature uncertainty has only a minor effect on the overall uncertainty in calculated fO_2.

To propagate the analytical uncertainties in both liquid and spinel compositions, a Monte Carlo approach was used. Oxide concentrations were repeatedly sampled (n=100) for each corresponding spinel and liquid analysis, resulting in 10,000 combinations per pair. The sampling followed normal distributions determined by the 1σ uncertainties from counting statistics (Tables B.12, B.9). These generated spinel-liquid pairs were then propagated through the relations of Droop (1987), Maurel and Maurel (1982) and Borisov (2018), as described above, to estimate uncertainties in the calculated fO_2. The median fO_2 are then used for each eruption along with their propagated standard errors.

This method does not account for correlations between elements measured, the uncertainties in the em-

pirical relations used, nor the errors on calculated liquid-only temperatures. However, it does provide a first-order estimate of the effect of analytical uncertainty on the calculated fO_2.

4.7.2 Correcting for Post-Entrapment Modification

4.7.2.1 Olivine-Hosted Melt Inclusions

For olivine-hosted MI a modified version of the Melt Inclusion Modification Correction (`MIMiC`) routine (Rasmussen et al. 2020) was used to correct for post-entrapment crystallisation and Fe-Mg exchange with external melt, commonly referred to as Fe-loss (e.g., Danyushevsky 2002, 2004). The routine was modified by incorporating the MagmaSat volatile saturation model (Ghiorso and Gualda 2015) using `VESIcal` (Iacovino et al. 2021). This modification was preferred as the default saturation model included in `MIMiC`, VolatileCalc (Newman and Lowenstern 2002), is only calibrated for MIs with SiO_2 contents of less than 52 wt.% and for a limited P-T range.

Melt inclusion $Fe^{3+}/\sum Fe$ were calculated using the estimated oxygen fugacity for each eruption and the model of Borisov (2018) (as described above). The following models were used in `MIMiC`: the olivine-melt equilibration model of Toplis (2005), and the olivine-liquid thermometer of Putirka et al. (2007). Initial FeO_T contents for inclusions per eruption were estimated by fitting a linear regression through whole-rock FeO_T contents against equilibrium olivine forsterite contents (Figure 4.2). The uncertainty in initial FeO_T was assumed to be 0.25 wt.%.

The error in Fe^{3+}/Fe^T was calculated using a Monte-Carlo approach for each MI, taking into account the uncertainty in fO_2 for each eruption. Uncertainties in the resulting PEM-corrected MI compositions were then calculated by propagating analytical uncertainties through the Monte-Carlo procedure, with 100 simulations per MI.

4.7.2.2 Plagioclase-Hosted Melt Inclusions

For plagioclase-hosted MIs, methods for correcting for PEC are less well-established than for olivine, and previous approaches vary greatly in terms of complexity. The simplest method involves incrementally adding equilibrium (or host) plagioclase back into the inclusion until its composition is in equilibrium with the host based on the $K_{D(Ca\text{-}Na)}^{plag\text{-}melt}$. The distribution coefficient is assumed to be either 0.11 ± 0.05 for temperatures less than 1050 °C or 0.27 ± 0.11 for temperatures >1050 °C, respectively (Putirka 2008)), or calculated for a given temperature and pressure using hydrous or anhydrous experimental data (e.g., Hamada and Fujii 2007; Namur et al. 2012).

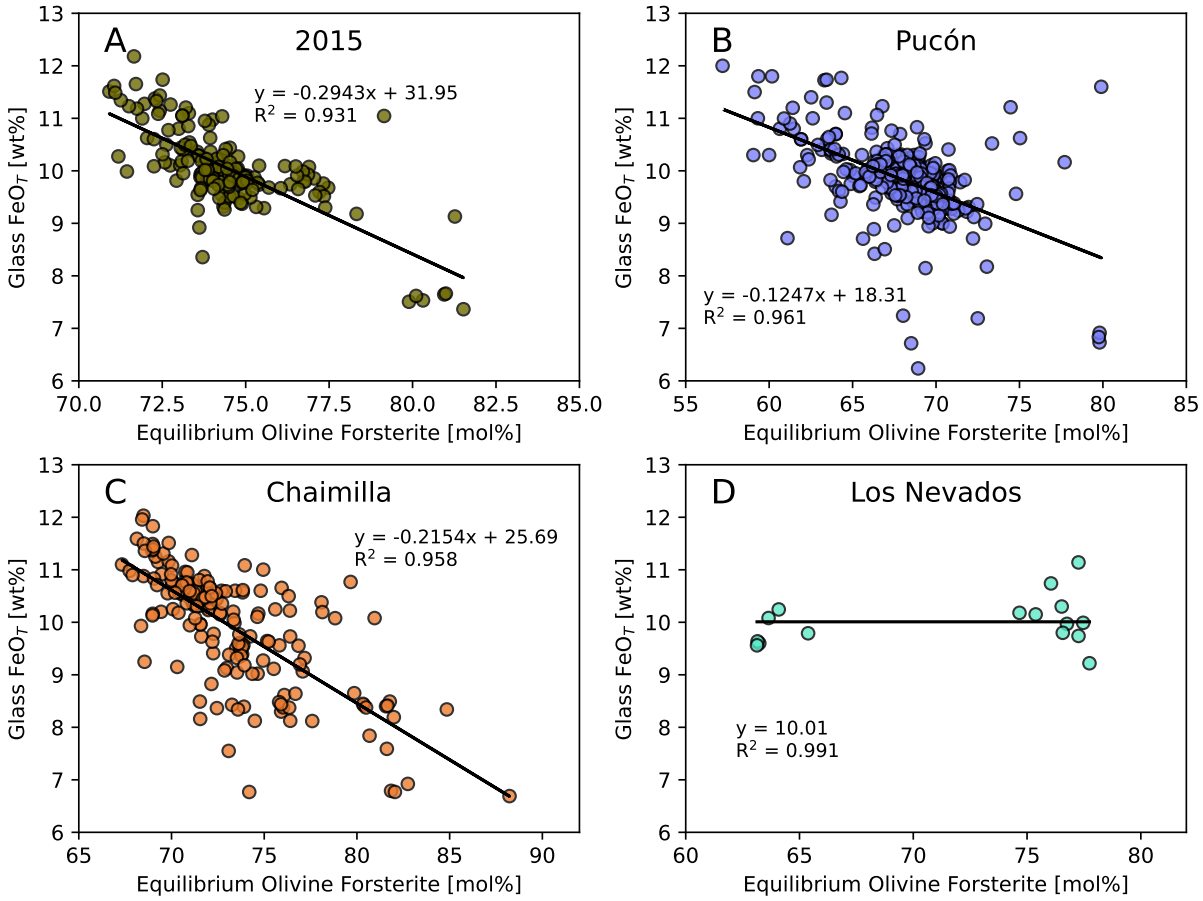

Figure 4.2: Regression curves used to correct PEC in olivine-hosted melt inclusions for the four studied eruptions: A) March 2015, B) Pucón Ignimbrite, C) Chaimilla Fall Deposit, and D) Los Nevados. Equilibrium forsterite content versus FeO_T of representative Villarrica groundmass glasses (this study; Boschetty et al. 2022; Clavero-Ribes 1996; Fontijn et al. 2016; Lohmar 2008; Pioli et al. 2015; Robidoux et al. 2021; Romero et al. 2022; Silva Parejas 2008). Equilibrium forsterite content was calculated using a K_D^{Fe-Mg} of 0.30 ± 0.03 (Roeder and Emslie 1970). The regression equations were used to estimate the original FeO_T of each olivine-hosted melt inclusion given the host forsterite content. Due to limited data for Los Nevados, the mean FeO_T was used.

Alternatively, Neave et al. (2017) added equilibrium plagioclase (calculated using the anhydrous model of Namur et al. (2012)) until the MI composition matched the MgO-Al_2O_3 systematics observed in Icelandic glass data. Similarly, Hartley et al. (2018) added host plagioclase composition until the MI matched the TiO_2-Al_2O_3 systematics of Icelandic glass data.

Bennett et al. (2019) found that the Neave et al. (2017) and Hartley et al. (2018) methods produced unrealistic MI compositions for their Gakkel Ridge data set. They proposed an alternative approach, which incrementally added host plagioclase to the MI composition until it intersected a pseudo-liquid line of descent, constructed from Mg#-Al_2O_3 regressions through both glass data and PEC-corrected olivine-hosted inclusions. Caracciolo et al. (2023) employed a similar method, adding host plagioclase back into the MI until the compositions aligned with Mg#-Al_2O_3 regressions through glass data and then

filtered the MIs with $K_{D(Ca\text{-}Na)}^{plag\text{-}melt}$ of 0.27±0.11 from Putirka (2008).

Kress and Ghiorso (2004) developed a PEC-correction scheme that utilises MELTS (note a version of MELTS that is not calibrated for a separate gas phase) to calculate equilibrium compositions for olivine-, plagioclase-, orthopyroxene-, and clinopyroxene-hosted inclusions, This method incrementally calculates the equilibrium host-phase, and then adds them back into the inclusion until they are in equilibrium with the measured host composition. This requires an initial estimate of pressure and fO_2, which are then adjusted to provide the best-fitting result, making the correction process iterative.

Using a PEC-correction method that iteratively adds equilibrium plagioclase, rather than host plagioclase, is preferable as this best represents an inverse of the PEC process. However, the approach of Neave and Putirka (2017) is only calibrated for anhydrous melts, and so is not suitable for Villarrica MI. Additionally, the glass systematics for Villarrica — both for TiO_2-Al_2O_3 and Al_2O_3-Mg# — do not display clear linear trends, which rules out the approach of Hartley et al. (2018) and Bennett et al. (2019). As a result, I used the approach of Kress and Ghiorso (2004), which, although based on an older version of MELTS, provides the advantage of giving additional constraints on entrapment pressure, temperature and fO_2 that can be compared to those calculated from volatile-saturation, liquid-only and olivine-spinel pairs. The method requires initial seed values for fO_2 and pressure, which were provided by the fO_2 calculated from spinel-MI pairs and pressure estimates from olivine-hosted MI.

4.7.2.3 Clinopyroxene-Hosted MIs

Traditionally, clinopyroxene-hosted MIs have been rehomogenised to counter potential post-entrapment crystallisation effects (e.g., Danyushevsky and Lima 2001; Schiano et al. 2004; Sobolev et al. 1996). However, this approach has several disadvantages: it carries the risk of decrepitation, drives H_2O-loss via diffusion, and is prone to over- or under-shooting the re-equilibration temperature. Some studies have instead tested for MI-clinopyroxene equilibrium, in the same way as clinopyroxene-liquid equilibrium is tested before thermobarometry (e.g., Neave and Putirka 2017), discarding MIs that are not in equilibrium with their hosts (e.g., Haddadi et al. 2017).

The MELTS-based method of Kress and Ghiorso (2004) is known to produce unrealistic PEC-corrected compositions for clinopyroxene-hosted MI (Kress and Ghiorso 2004). Similarly, I found that other MELTS-based correction schemes, such as those of Adams et al. (2021) and Barber et al. (2023), also produced unrealistic results for Villarrica-MI. Instead, I employed a simpler method, where host-clinopyroxene was added to each MI until it was in equilibrium with its host.

Olivine-liquid equilibrium was tested by comparing K_D(Fe-Mg) to the equilibrium value, 0.28 ± 0.08 from Putirka (2008), using Fe^{2+} in the liquid calculated using the equation of Borisov (2018), and Fe^{2+} in the clinopyroxene calculated using Droop (1987) after Neave et al. (2024). Additionally, equilibrium was assessed by comparing Enstatite-Ferrosilite and Diopside-Hedenbergite components, calculated using the method of Neave et al. (2024) for clinopyroxene, and the predicted values of Mollo et al. (2013) for melts after Wieser et al. (2023a).

Ideally, a method that iteratively adds equilibrium clinopyroxene, rather than host clinopyroxene, to correct MI would be used. However, no such methods are currently available. Future research into machine-learning approaches, like that developed in Cutler et al. (2024) for plagioclase-liquid equilibrium, may lead to suitable models.

4.7.3 Volatile Saturation Models

Measuring the volatile contents of MIs provides a major advantage, potentially offering much smaller uncertainties on thermobarometric estimates compared to commonly used clinopyroxene-liquid or amphibole-liquid barometers (e.g., Jorgenson et al. 2022; Ridolfi 2021). This is particularly relevant at Villarrica, where volcanic products contain no amphibole and historic eruptions contain little to no clinopyroxene (Boschetty et al. 2022).

The volatile saturation model MagmaSat (Ghiorso and Gualda 2015) accessed through the python library `VESIcal` (Iacovino et al. 2021) was used to calculate volatile-saturation pressures. MagmaSat was chosen as it is particularly suited to the basaltic, water-rich, MI compositions at Villarrica (Wieser et al. 2022a). Saturation pressures were determined iteratively using three different thermometers for olivine-, plagioclase- and clinopyroxene-hosted inclusions: equation 22 of Putirka (2008), Waters and Lange (2015), and Wang et al. (2021), respectively accessed via `Thermobar` (Wieser et al. 2022b). Initial temperature estimates were obtained using the liquid-only thermometer of Putirka (2008) (equation 15) for the first iteration. Iterations continued until the differences in saturation pressure were less than one bar.

4.7.4 Propagating Analytical Uncertainties

In addition to the methods for assessing uncertainties in calculated volatile saturated pressures outlined in Chapter 3, many calculated values rely on the measured values from the variety of techniques outlined in Section 4.6. Where possible, analytical uncertainties were propagated through to these calculated values (e.g., olivine forsterite contents, estimated temperatures and water contents). For simple calculated

ratios (e.g., forsterite and anorthite contents) uncertainties were combined in quadrature, assuming that errors were both small compared to their associated measurement and normally distributed. For more complex values derived from multi-dimensional analyses (e.g., olivine-liquid temperatures) Monte-Carlo simulations were used. For this approach, normal distributions defined by analytical results and their counting statistics were repeatedly sampled, and calculations were rerun for each variation. The results distributions of calculated values were checked for normality. For normal distributions, the mean and standard errors are reported. For non-normal distributions, the median, and the 16% and 84% percentiles are reported.

4.8 Results

4.8.1 Oxygen Fugacity

Oxygen fugacities (fO_2) for each eruption were estimated using olivine-hosted MI-spinel pairs. Using the method described above, the following fO_2 values were calculated relative to the Quartz-Fayalite-Magnetite (QFM) buffer (Frost 1991) for each eruption: Pucón -0.346 ± 0.078, Chaimilla -0.888 ± 0.057, Los Nevados -0.839 ± 0.041, and March 2015 1.785 ± 0.065. The range of estimated fO_2, as well as the assumed values for each eruption, are shown in (Figure 4.3).

4.8.2 Major Element Compositions

4.8.2.1 Olivine

Olivine was the most common MI host analysed. Olivine from the March 2015, Los Nevados, Chaimilla and Pucón eruptions were analysed. They show a range of compositions and a large degree of variability both within and between eruptions (Figure 4.5).

MI hosting olivine from the Pucón mafic ignimbrite has the highest forsterite content ($Fo = 100 \cdot Mg/[Mg + Fe^{2+}]$) ranging from approximately 82–88 Chaimilla olivine showed a similar range in Fo content 82–86 mol.% and comparable minor element concentrations This is again true for Los Nevados parasitic cones olivine (82–85 mol.%), with one outlier at 72 mol.%. Olivine hosts that erupted during the March 2015 eruption showed the largest range of Fo contents and the most evolved contents 75–83 mol.%.

The forsterite and minor element contents for all olivine hosts are consistent with non-mantle olivine (Figure 4.6), characterised by lower Fo contents, and high CaO contents compared to mantle olivine

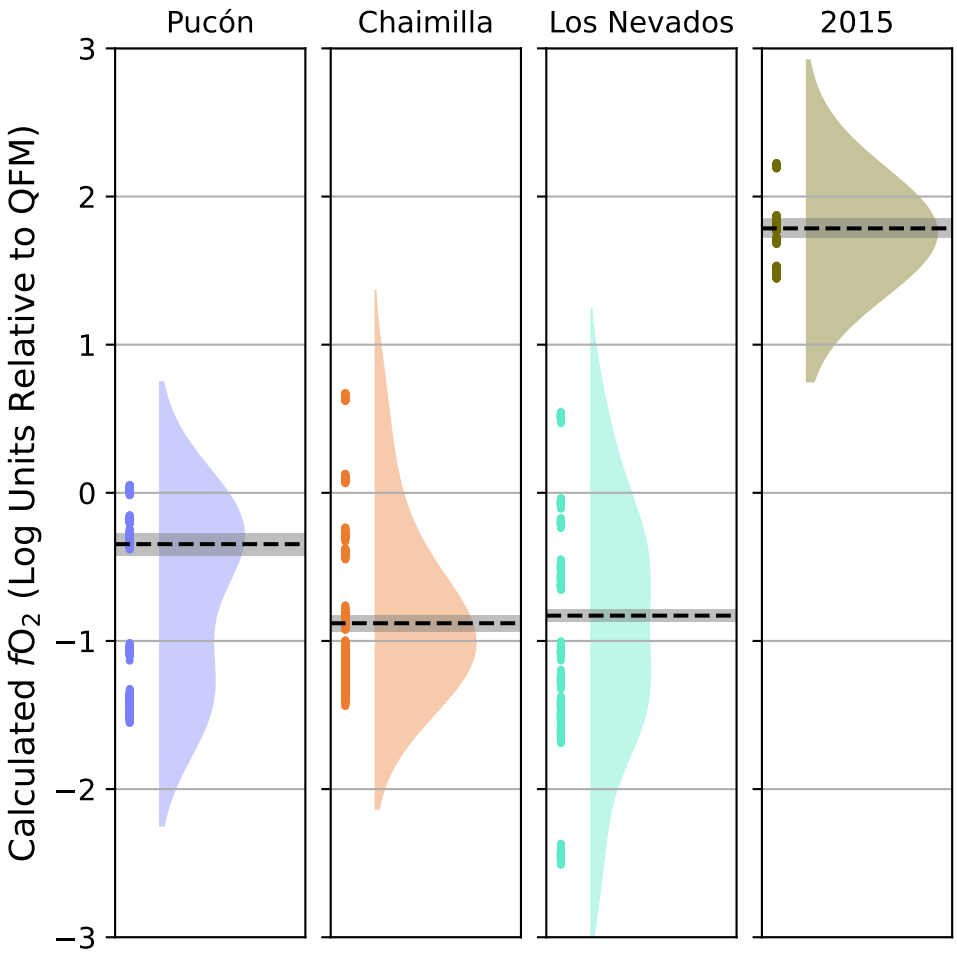

Figure 4.3: Calculated fO_2 for the four different eruptions using olivine-hosted spinel and melt inclusions, relative to the QFM buffer (Frost 1991). Coloured circles mark the mean spinel-liquid pairs and corresponding Kernel Density Estimates as coloured curves. Black dashed lines mark the median of the calculated oxygen fugacities with representative propagated analytical uncertainties shown as grey regions.

(Kamenetsky et al. 2006; Thompson and Gibson 2000).

Generally, the olivine hosts measured in this study have higher Fo-contents than most olivine reported in the literature (>Fo80; Figure 4.5. This is particularly true for Pucón, Chaimilla, and most of Los Nevados olivine. These primitive olivine-hosts most closely correspond to the Ol_1 cluster, the most primitive cluster identified in Chapter 2. As such, they represent some of the most primitive olivine found at Villarrica and are among the best candidates for sampling the most primitive melts at the volcano.

4.8.2.2 Plagioclase

MI-host plagioclase was measured from the Chaimilla (n=3) and Pucón (n=13) eruptions only, as plagioclase-hosted MI from the other eruptions appeared to be formed on resorption surfaces or were de-vitrified. The measured Chaimilla plagioclase MI-hosts were homogeneous Bytownite An89Ab11Or0, 0.54 wt.%

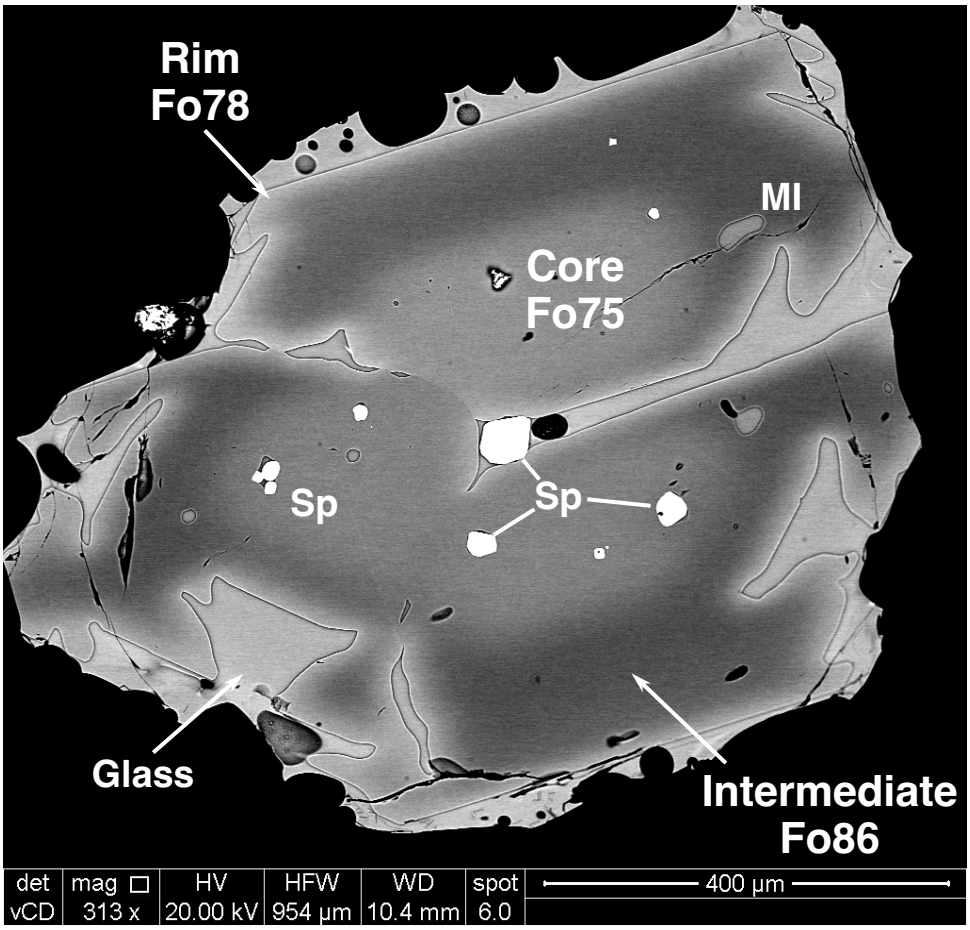

Figure 4.4: BSE image of a complex zoned olivine crystal clot from the March 2015 eruption. Cores remain relatively unaffected by primitive overgrowth (reversely zoned) and subsequent more evolved rims. Also contains multiple spinel-inclusions and melt inclusions.

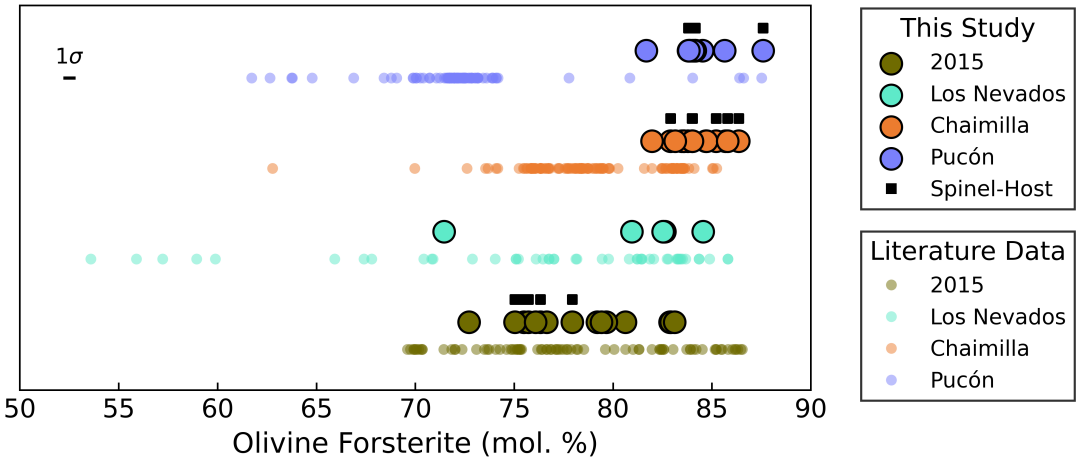

Figure 4.5: Host olivine forsterite contents measured adjacent to melt inclusions. The forsterite content of olivine spinel hosts is shown as black squares. Representative $\pm 1\sigma$ error shown by error bar for data collected in this study. Comparison of host-olivine forsterite content between eruptions and literature data. Literature data sources: Clavero-Ribes (1996), Cortes and Calder (2019), Lohmar (2008), Pioli et al. (2015), Robidoux et al. (2021), and Romero et al. (2022)

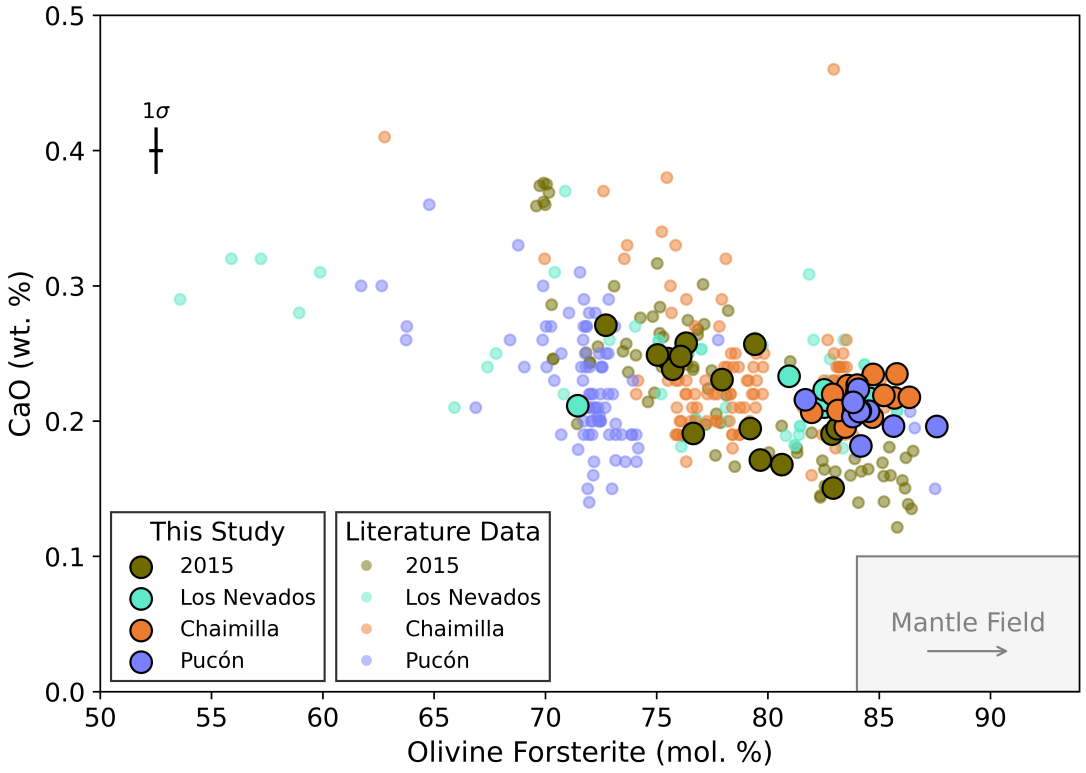

Figure 4.6: Olivine discrimination plot for host olivine compositions measured adjacent to melt inclusions. Mantle field, after Kamenetsky et al. (2006) and Thompson and Gibson (2000), extends to higher forsterite contents. Representative $\pm 1\sigma$ errors are shown by error bars for data collected in this study. Literature data sources same as Figure 4.5. Whilst some host olivines are relatively primitive, none have compositions that suggest they are primary, mantle-derived, melts.

FeO, 0.10 wt.% MgO and TiO_2 below the detection limit. Pucón plagioclase MI-hosts exhibited more variation, ranging from Labradorite–Anorthite: An75–92, Ab7–24, Or0.0–0.4, and have more variable minor element contents: 0.45–0.70 wt.% FeO, around 0.10 wt.% MgO, and 0.02–0.05 wt.% TiO_2. Neither eruption's hosts showed signs of Ab-rich halos typically formed by PEM around MIs. Ternary plagioclase components were calculated as: $An = 100 \cdot Ca/(Ca+Na+K)$, $Ab = 100 \cdot Na/(Ca+Na+K)$, and $Or = 100 \cdot K/(Ca+Na+K)$ where Ca, Na and K are atoms per formula unit. The results are plotted in Figure 4.8.

Additionally, large plagioclase crystals and glomerocrysts (>1 mm along the long axis) from the March 2015 eruption were BSE imaged and analysed on the probe. BSE images show consistent, homogeneous high-An cores (An70–80, light grey), mantled by an oscillatory-zoned MI-rich intermediate zone (An55–70, light and dark grey), and an oscillatory-zoned low-An rim (approximately An60, dark-grey) (Figures 4.7, 4.8).

The Chaimilla and Pucón plagioclase hosts measured in this study are among the more primitive, high-An compositions observed in eruptions at Villarrica. Previous studies of plagioclase phenocrysts from the

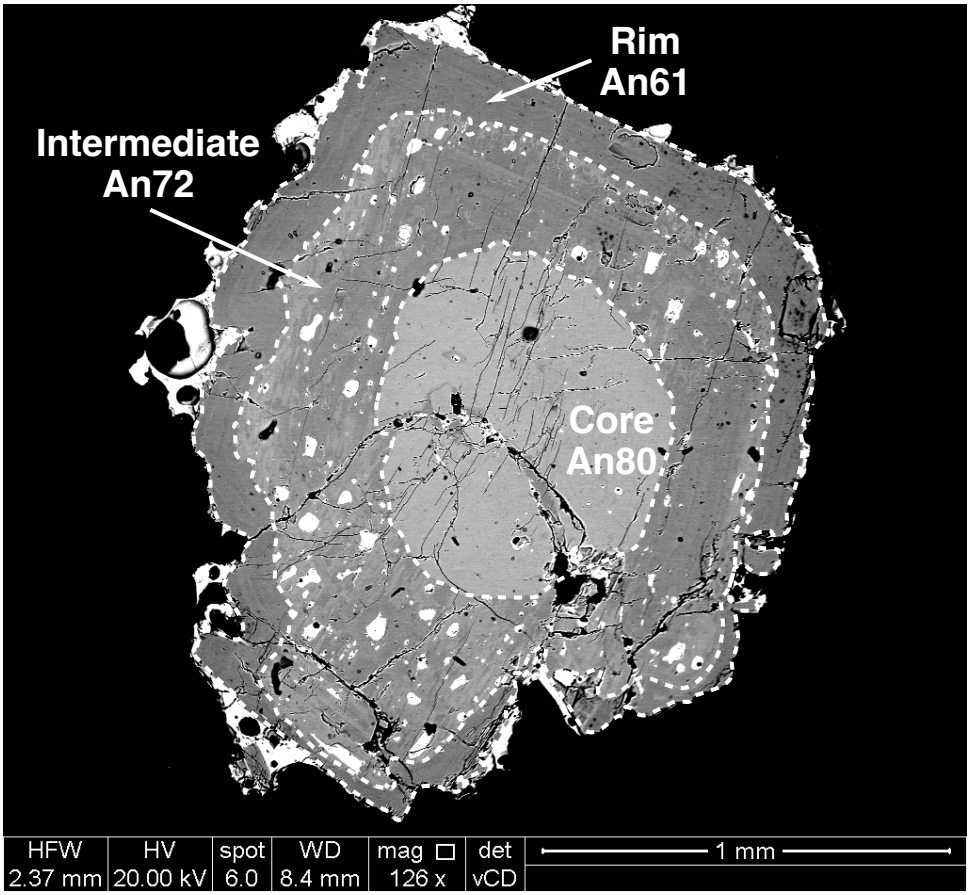

Figure 4.7: Representative complex-zoned plagioclase from the March 2015 eruption. The brightest parts are melt inclusions and adherent glass. MI from these crystals were not analysed as they appear to represent resorption surfaces. Zones depicted by white-dashed lines and designated as core, intermediate and rim.

Pucón, Chaimilla and March 2015 eruptions report compositions ranging from An52–94 mol.%, with the majority concentrated at An70–80 (Cortes and Calder (2019), Lohmar (2008), Pioli et al. (2015), and Romero et al. (2022); Figure 4.8). The measured primitive plagioclase hosts closely match the two most primitive plagioclase clusters identified in Chapter 2, Pl_1 and Pl_2. Similar to the olivine MI-hosts, this makes the plagioclase MI-hosts strong candidates for identifying primitive melt compositions at Villarrica.

4.8.2.3 Clinopyroxene

Host clinopyroxene compositions were only measured for the Chaimilla fall deposit (n=1) and Pucón mafic ignimbrite (n=6). The clinopyroxene MI-hosts are plotted alongside literature data on a pyroxene quadrilateral (Quad) plot (Figure 4.9) and QJ plot (Figure 4.10). Quad components (Morimoto 1988) are calculated as follows after (Neave et al. 2024): $En = 100 \cdot Mg/(Mg + \Sigma Fe^{*} + Ca)$, $Fs = 100 \cdot \Sigma Fe^{*}/(Mg + \Sigma Fe^{*} + Ca)$, and $Wo = 100 \cdot Ca/(Mg + \Sigma Fe^{*} + Ca)$, where, $\Sigma Fe^{*} = Fe^{2+} + Fe^{3+} + Mn$. Components for

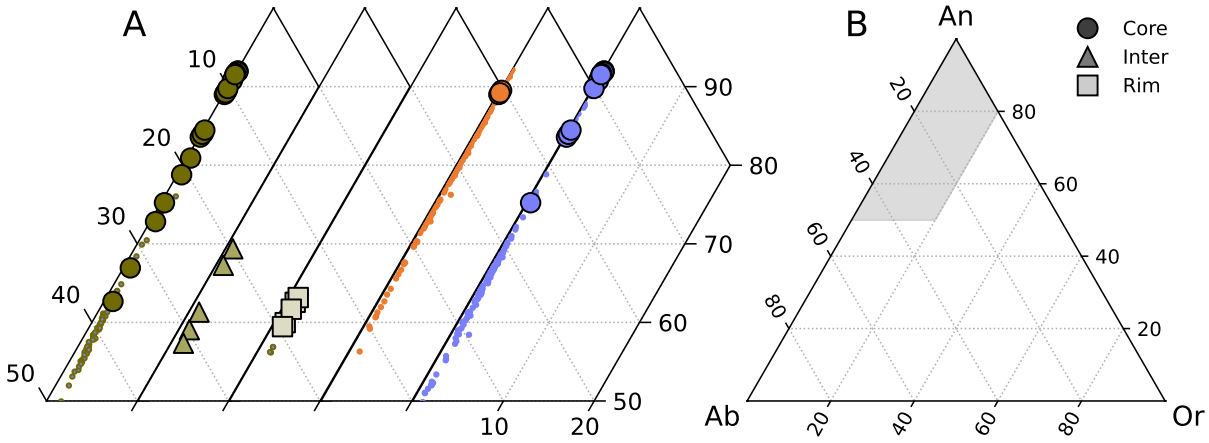

Figure 4.8: A) Truncated feldspar ternary diagrams comparing March 2015 complexly zoned feldspars (Figure 4.7), and Chaimilla and Pucón MI-hosts. Colours are the same as in Figure 4.5. B) Complete ternary showing the relative position of truncated ternaries in A. Inter, intermediate zone.

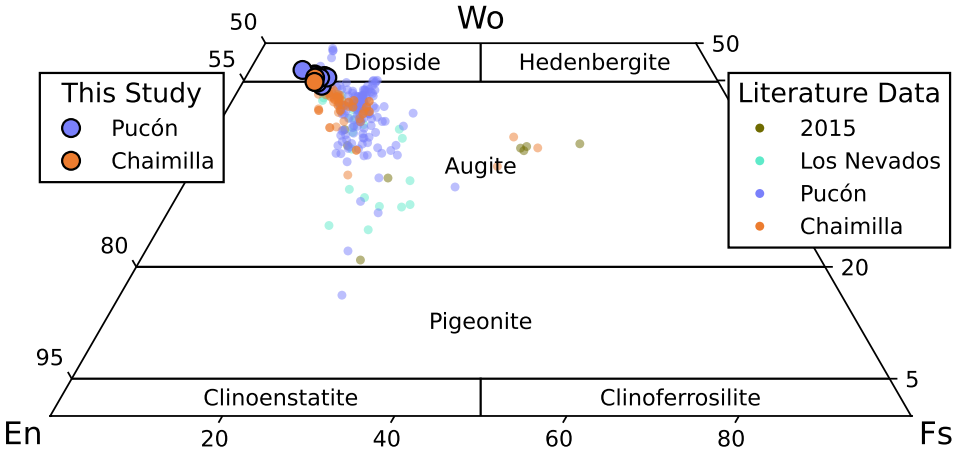

Figure 4.9: Pyroxene quadrilateral diagram comparing host clinopyroxene compositions, measured adjacent to melt inclusions, to literature data for the studied eruptions. Villarrica clinopyroxene mostly plots in the augite and diopside fields. Literature data from: Clavero-Ribes (1996), Cortes and Calder (2019), Lohmar (2008), Pioli et al. (2015), and Romero et al. (2022).

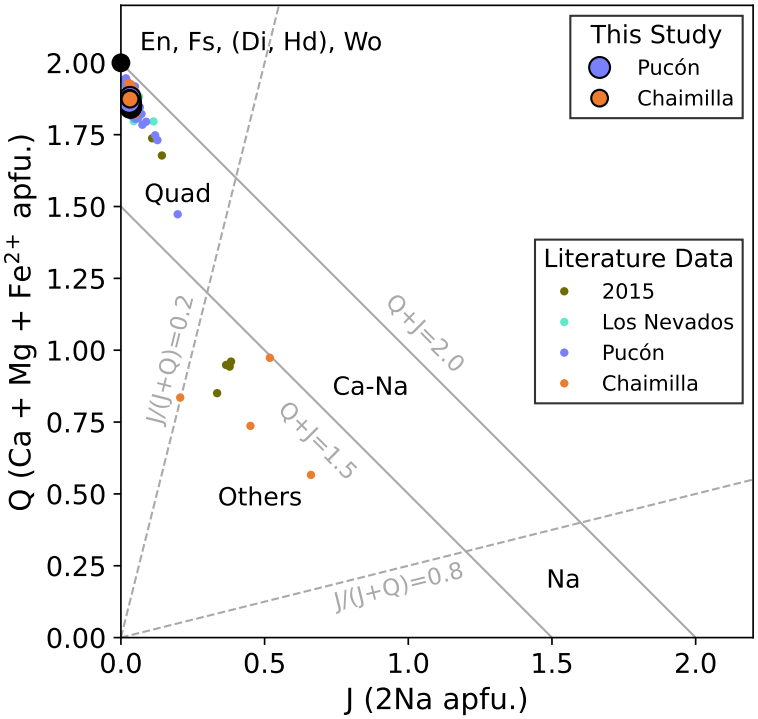

Figure 4.10: QJ plot (after Morimoto 1988) comparing host clinopyroxene compositions, measured adjacent to melt inclusions, and literature data for the studied eruptions. Nearly all Villarrica clinopyroxene plots in the Quad field. Literature data that plot in the Others field are likely mixed-phase analyses. Literature data sources are the same as in Figure 4.9.

the Q-J plot were calculated using elemental abundances as atoms per formula unit (afu) after Morimoto (1988): $Q = Ca + Mg + Fe^{2+}$ and $J = 2 \cdot Na$.

The measured clinopyroxene displays homogenous compositions: Mg# values of 88–93, Ca 0.85–-0.89 afu and Q+J values of 1.86-–1.88. They are classified as diopside-augite (Wo44–46, En45–47, Fs6–9). In contrast to literature data, the measured clinopyroxene is much more homogeneous, although this is based on a much smaller sample size (Figures 4.9 and 4.10. This comparatively greater homogeneity may partly be due to the use of non-ideal probe conditions in previously published analyses (e.g., Neave et al. 2024; Wieser et al. 2023a,b). As with the other MI-hosts, the measured clinopyroxene best corresponds with the most primitive clinopyroxene cluster, Cpx_1, identified in Chapter 2. This makes them strong candidates for sampling primitive Villarrica melts.

4.8.2.4 Olivine-Hosted Spinel Inclusions

Olivine-hosted spinel inclusions show compositional variation between eruptions (Figures 4.11 and 4.12). Spinel from the Los Nevados, Chaimilla and Pucón eruptions ranges from Cr-spinel to Cr-chromite, while March 2015 spinel consists of Fe-chromite and Cr-magnetite (Figure 4.11. The 2015 spinel ex-

hibits higher Fe^{3+}, Fe^{2+}, and lower Al, Cr, and Mg. This is reflected by the March 2015 olivine hosts, which generally have more evolved, lower-Fo contents (Figure 4.5). In contrast, measured Los Nevados, Chaimilla and Pucón spinel have higher Al, Cr, and Mg, and lower Fe^{3+}, Fe^{2+}, consistent with their more primitive olivine host compositions.

Compared to literature data, the 2015 spinel is most similar to the olivine-hosted spinel from spatter erupted at the crater rim in the year 2000 (Witter et al. 2004). Spinel from Los Nevados, Chaimilla and Pucón eruptions generally match reported literature compositions (Figure 4.11, 4.12). However, some high-Fe^{3+}, high-Ti and low-Mg spinel observed in these eruptions have more extreme compositions than those found in the March 2015 eruption (Figure 4.12). This suggests that the crystal cargoes of all measured eruptions contain olivine and spinel crystals that formed under similar conditions, supporting the conclusions from Chapter 2.

4.8.2.5 Post-Entrapment Modification Corrections

Uncorrected olivine-hosted MI have K_D values close to the expected 0.30 (-0.03, +0.05) for basaltic liquids (Matzen et al. 2011; Roeder and Emslie 1970; Toplis 2005) (Figure 4.13), indicating low levels of PEM for olivine-hosted MI. The range of olivine addition or subtraction for all MIs ranges from 13.5 wt.% to −3.98 wt.% with a median of −0.35 wt.%. The majority (93%) of olivine-hosted MI required less than 5% olivine addition or subtraction. There are eruption-specific trends: olivine-hosted MI from the March 2015 fire fountain and Chaimilla Fall deposit on average required ∼−1.5 wt.% addition, while the Pucòn ignimbrite MIs required ∼3.0 wt.% addition. This suggests different melt dynamics for the eruptions, with the Pucón olivine carried by cooler melt and the Chaimilla and 2015 by hotter melt. However, with the differences in correction magnitude relatively small, and limited sample size, this is a tentative conclusion.

In contrast, plagioclase-hosted MI have experienced significantly higher levels of PEM, with corrections ranging from 37–75 wt.%. The PEC scheme of Kress and Ghiorso (2004) also provided estimates of entrapment pressure, temperature, and fO_2. The estimated entrapment temperatures are generally higher for the Chaimilla than Pucón MI, ranging from 1245–1312 °C for Chaimilla and 1205–1263 °Cfor Pucón. Entrapment pressures are similar for both eruptions: 2.98–2.84 kbar and 3.01–3.76 kbar. Estimates of fO_2 are also comparable between the two, with values ranging from −0.04–0.08 and −0.07–0.15 log units relative to the QFM buffer, respectively.

Clinopyroxene-hosted MI also required substantial PEM corrections, ranging from 34–68 wt.% clinopy-

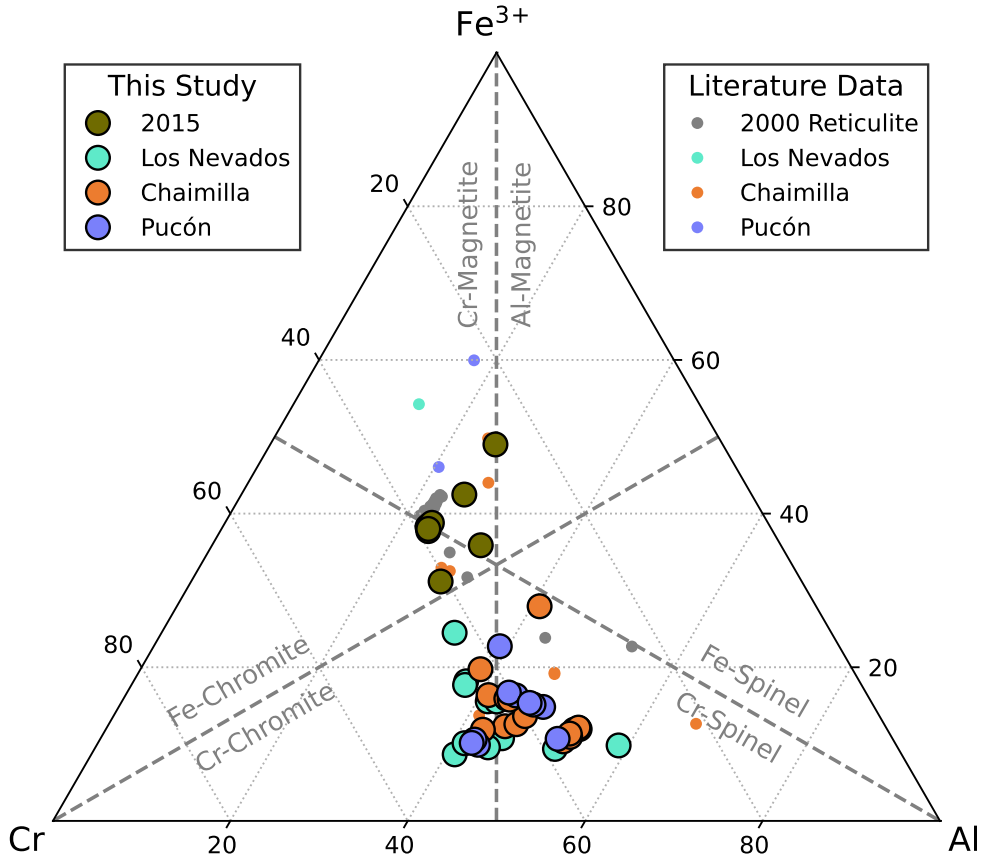

Figure 4.11: Spinel ternary plot showing the range in 3+ cations for olivine-hosted spinel in the four eruptions studied. Classification lines from Stevens (1944). The March 2015 spinel have substantially higher Fe^{3+} contents than those of the Chaimilla, Los Nevados, and Pucón, which are fairly consistent. Literature data from: Lohmar (2008), Pioli et al. (2015), and Witter et al. (2004).

roxene addition (Figure 4.15). Figure 4.15c shows deviation from the equilibrium field, suggesting that the simple PEM corrections employed may not fully account for PEM processes affecting clinopyroxene-hosted MIs. The movement of PEC-corrected compositions away from the equilibration line after the PEC-correction in Figures 4.15b and 4.15c could indicate that Fe-loss played a role after entrapment for clinopyroxene-hosted MI, or it may suggest that Mg# is not a reliable indicator of clinopyroxene-melt equilibrium (Putirka 2008; Wieser et al. 2022b).

4.8.2.6 PEM-Corrected Melt Inclusion Major Element Compositions

PEM-corrected MIs span a compositional range from basaltic to basaltic-andesite (Figure 4.16a) and from low-K to calc-alkaline (Figure 4.16b). Generally, clinopyroxene-hosted MI have lower alkalis than olivine- and plagioclase-hosted MI. The MI can be roughly divided into two groups based on their SiO_2

and alkali content (Figure 4.16), with the majority of March 2015 MI being more evolved than the other eruptions. This is reflected in their MI host compositions (Figure 4.5).

4.8.2.7 Groundmass Glass

In addition to the 97 MIs measured, over 200 analyses of adherent groundmass glass and interstitial glass were conducted. The composition of the groundmass glass broadly correlates with PEM-corrected MI contents but generally shows higher alkali contents and extends to higher SiO_2 contents (Figure 4.16). This trend is particularly noticeable for the Chaimilla, Pucón and Los Nevados glasses. The significant overlap between the March 2015 MIs and groundmass glass compositions suggests that the crystal cargo from the March 2015 eruption was comparatively unevolved, supporting the idea that the trigger magma was primitive and less mixed compared to other eruptions (Cortes and Calder 2019; Romero et al. 2022).

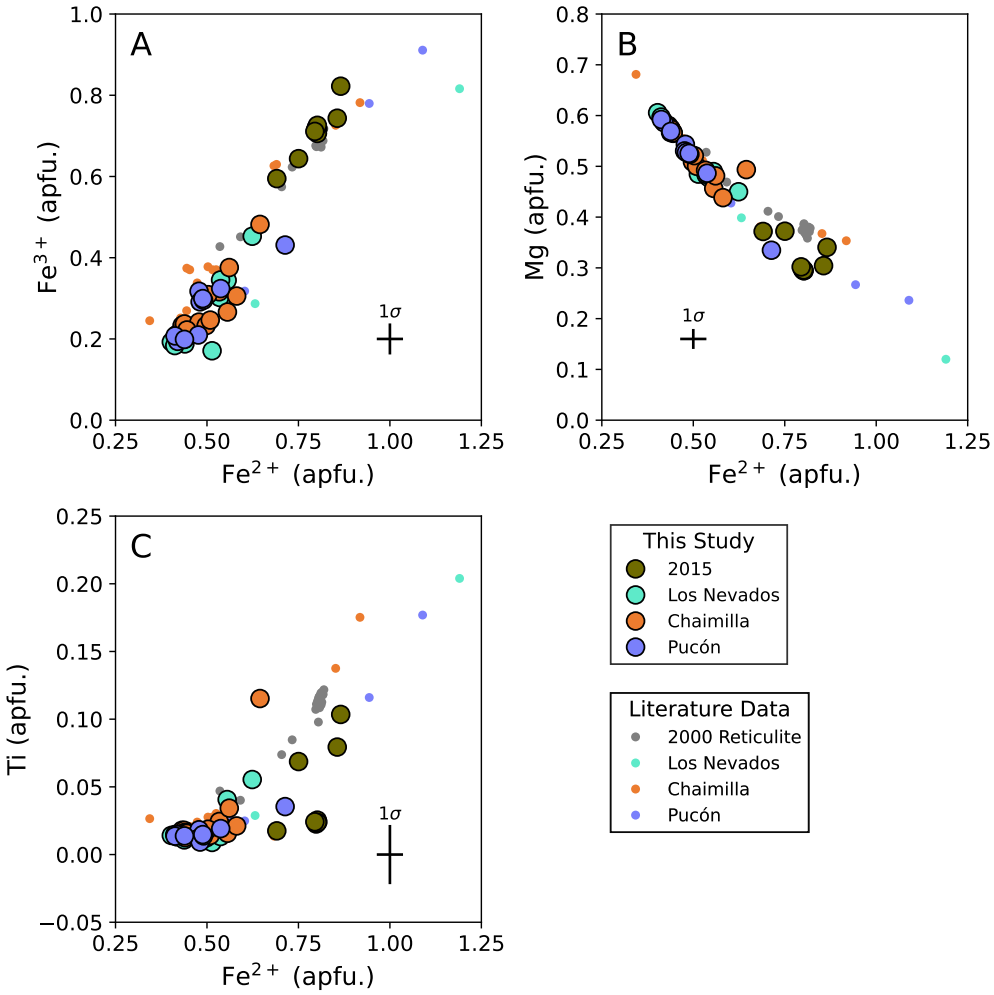

Figure 4.12: Spinel Bivariate plots showing the range of cations in olivine-hosted spinel. Representative $\pm 1\sigma$ errors are shown by error bars (data from this study only). Literature data sources the same as in Figure 4.11.

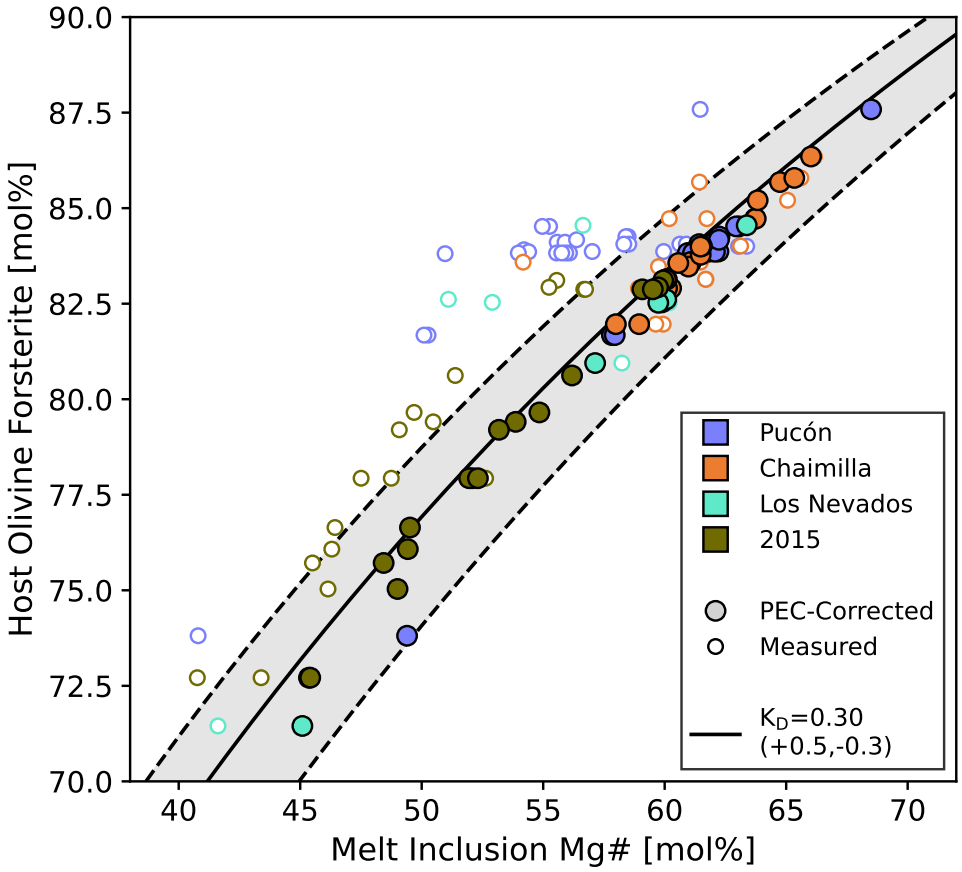

Figure 4.13: Olivine Rhodes plot after Dungan and Rhodes (1978) and Rhodes et al. (1979) showing both uncorrected and PEM-corrected MI compositions. As generally uncorrected MI lie close to the expected K_D of 0.3, most MI require less than 5% olivine addition or subtraction.

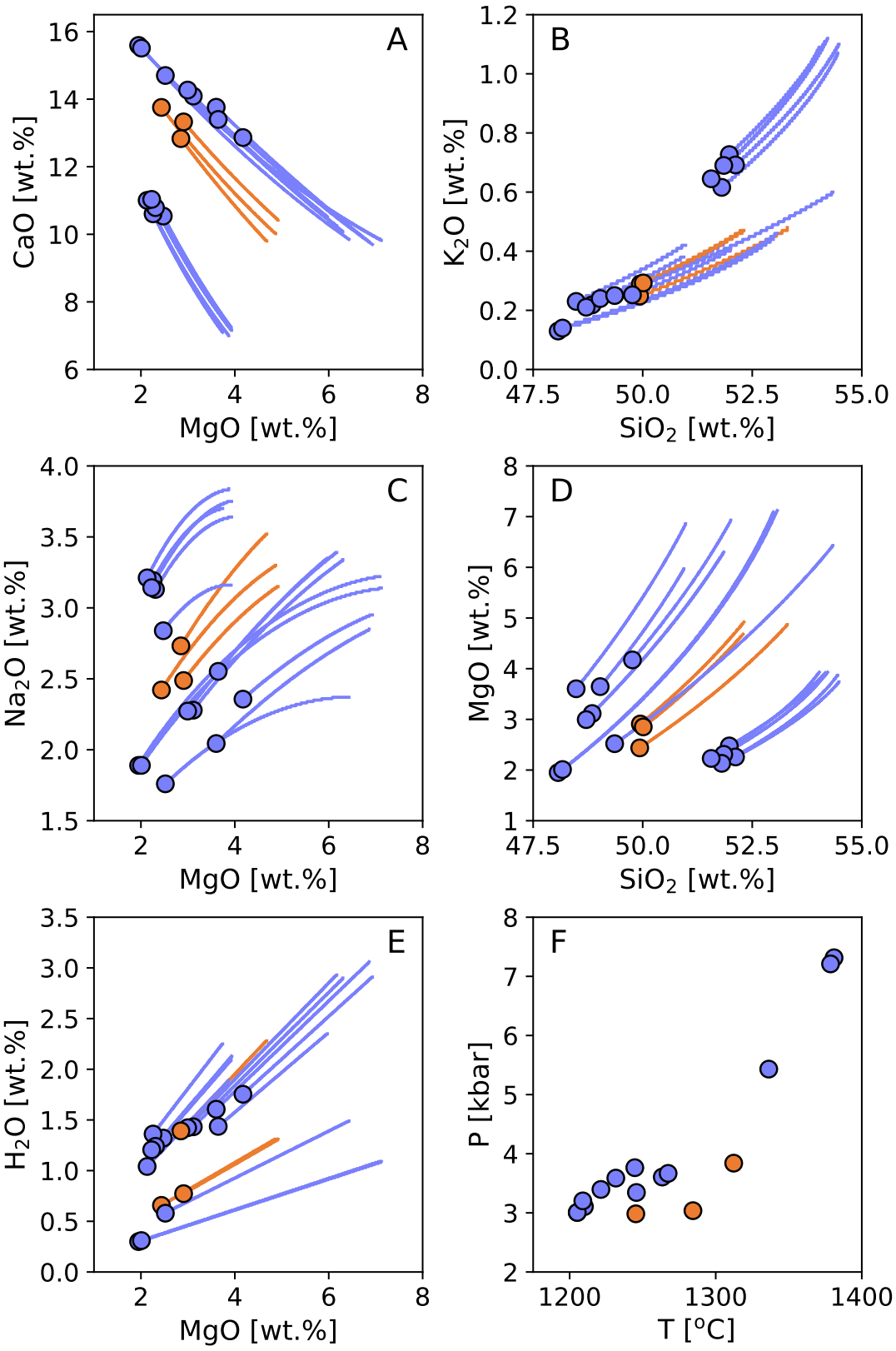

Figure 4.14: (A–E) Bivariate Harker plots showing the extent of post-entrapment crystallisation correction required for each plagioclase-hosted MI. Circle markers show the corrected composition. Plagioclase-hosted MI from the Pucón Mafic Ignimbrite are shown in purple, and MI from the Chaimilla Fall Deposit are shown in orange. (F) Estimated entrapment temperature and pressure from PEC-correction.

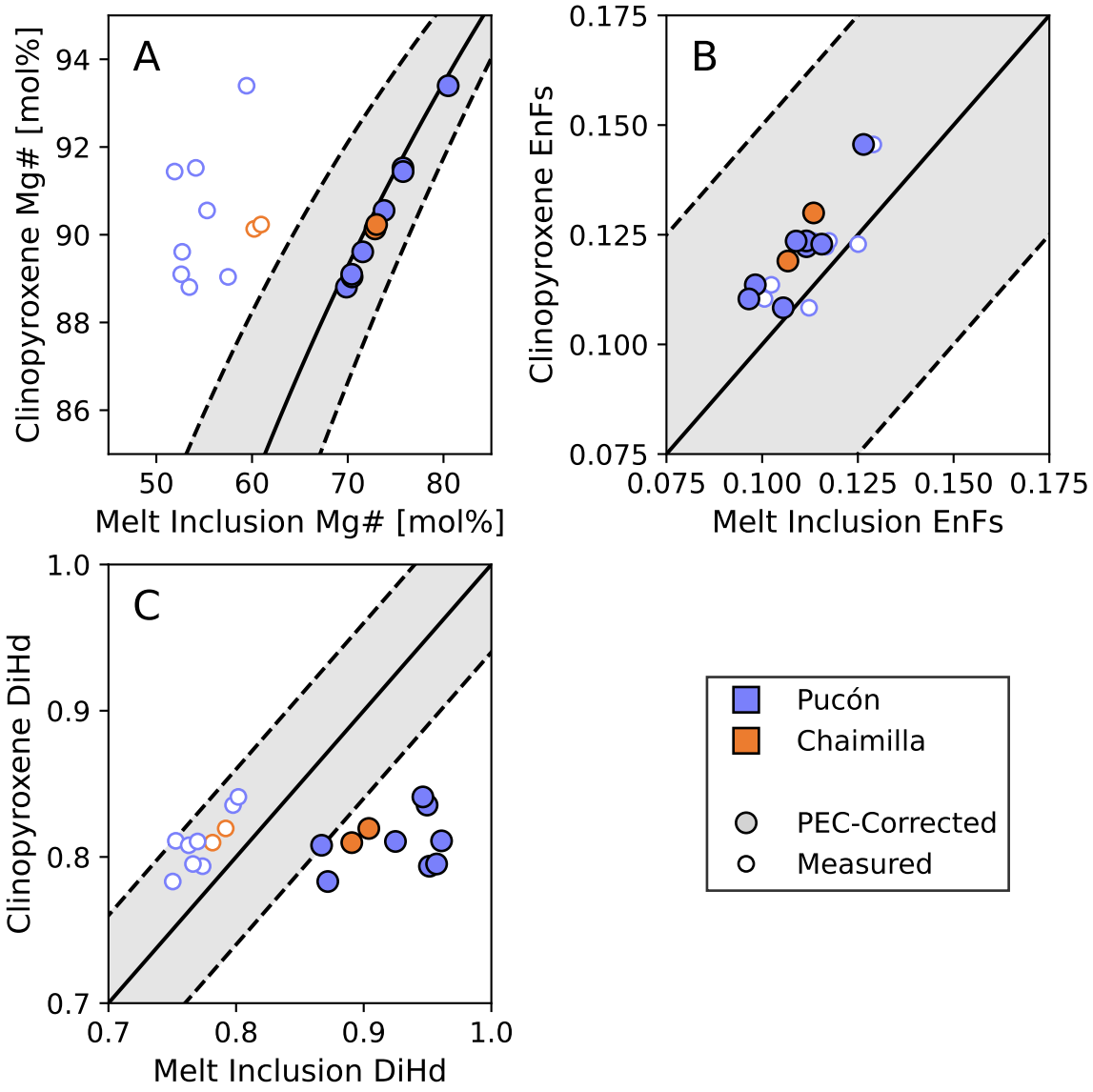

Figure 4.15: Clinopyroxene-liquid equilibrium plots showing the effects of PEC-corrections on clinopyroxene-hosted MI compositions. (A) Comparison of MI and host magnesium numbers. The solid line and field delineates a K_D of 0.27±0.08 after Putirka (2008). (B) Comparison of predicted MI and host EnFs contents. Solid line and field are a 1:1 line and 1σ uncertainty after Mollo et al. (2013). (C) Comparison of predicted MI and host DiHd contents. Solid line and field are a 1:1 line and 1σ uncertainty after Mollo et al. (2013).

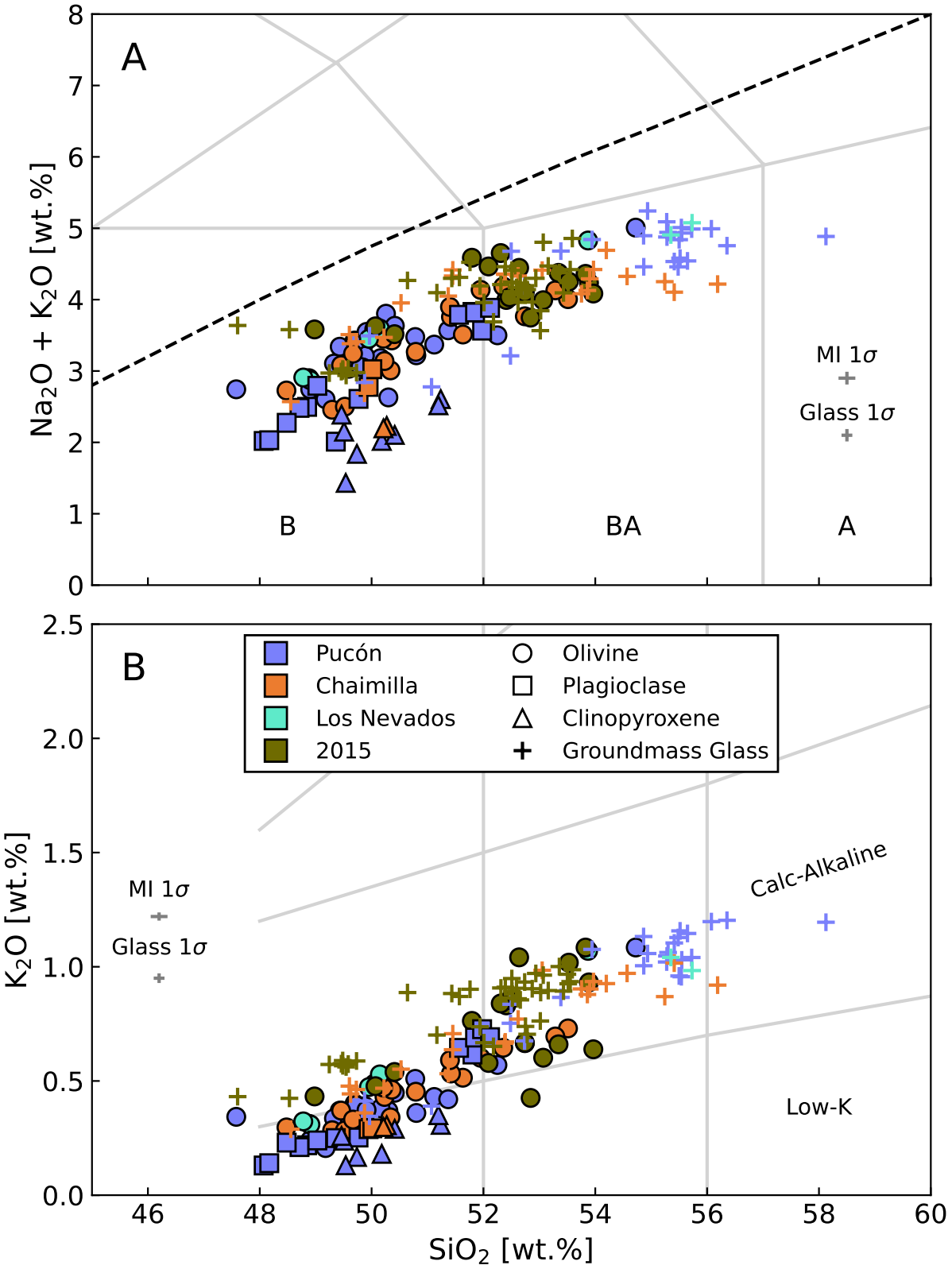

Figure 4.16: (A) Total-Alkali-Silica diagram, after Le Bas et al. (1986) and Le Maitre (1989) showing the composition of groundmass glass and post-entrapment-modification-corrected melt inclusion compositions. Separate error bars are shown for PEM-corrected melt inclusions and measured glass compositions. B, Basalt. BA, Basaltic-Andesite. A, Andesite. The dashed line separates sub-alkaline and alkaline fields from Irvine and Baragar (1971). (B) K_2O-SiO_2 diagram after Peccerillo and Taylor (1976).

4.8.3 Volatile Contents

The volatile contents of Villarrica melt inclusions and groundmass glasses show significant variability, ranging from completely degassed to 3.0 wt.% H_2O and >4500 ppm CO_2 (Figure 4.17). Plagioclase- and clinopyroxene-hosted MIs, which have undergone significant PEM, tend to have low volatile contents compared to olivine-hosted MIs. Uncertainties in total CO_2 contents are high due to high uncertainties on MI volumes, which impact the estimation of vapour bubble CO_2 contents. On average, Pucón and Los Nevados CO_2 contents are much lower than for the other studied eruptions, which is a result of a lack of detectable diads in these MI, rather than reflecting actual lower CO_2 contents.

A significant proportion of the total CO_2 of each MI is sequestered in the vapour bubble. For the 24 MIs with measurable diads, the vapour bubble accounts for 8.36–98.53 % of the total CO_2 with a median of 73 %. This is likely an underestimate, as this doesn't include carbon stored in carbonates within the bubbles. These proportions are similar to those found in other studies (Aster et al. 2016; Hartley et al. 2015; Moore et al. 2015), underscoring the importance of measuring the CO_2 sequestered in the bubble when calculating volatile saturation pressures for melt inclusions.

High CO_2 contents in olivine-hosted MI have been attributed to the co-entrapment of a fluid phase when the MI is formed (e.g., Aster et al. 2016). To identify this, past studies have used the relative volume of the bubble as an indicator that the MI contains a co-entrapped fluid. Aster et al. (2016) suggests that MI with vapour bubble volumes larger than 6–8% of MI volumes are likely to contain a co-entrapped fluid. In this study, thirteen out of ninety-seven Villarrica MIs have relative bubble volumes of greater than 6%, and three have bubble volumes exceeding 8% (Figure 4.18). However, this classification does not account for the large errors in MI volumes and significant errors in vapour bubble volumes (Chapter 3; Figure 4.18). Furthermore, none of the Villarrica MIs possess high enough CO_2 contents to suggest the presence of a co-entrapped fluid: CO_2 contents of up to 4500 ppm have been measured in MIs from other arc volcanoes in studies that accurately measure total CO_2 (Aster et al. 2016; Moore et al. 2015; Rasmussen et al. 2020; Robidoux et al. 2017).

4.8.4 Volatile Saturation Pressures and Temperatures

Temperatures were calculated using PEM-corrected MI compositions and their host minerals (see Section 4.7.3). The calculated mineral-liquid temperatures span the range ~1000–1225 °C (Figure 4.19a). Specifically, olivine-hosted MI have temperatures between 1075–1180 °C, plagioclase-hosted MI have lower temperatures between 1025–1080 °C, and clinopyroxene-hosted MI have higher temperatures 1170–

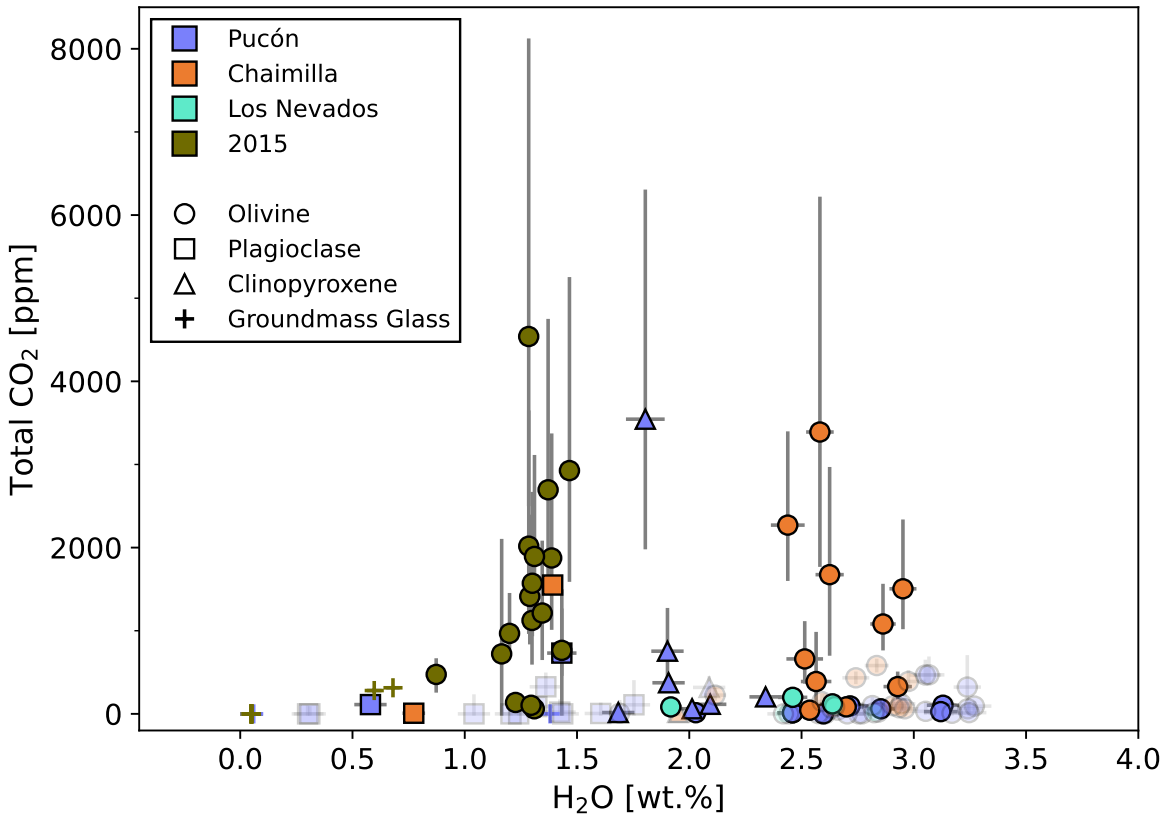

Figure 4.17: Comparison of volatile contents of Villarrica melt inclusions and groundmass glasses. CO_2 contents show large variability, in part due to a lack of detectable Raman diads, when estimating vapour bubble CO_2 contents. Those MI without detectable diads are shown as transparent symbols. However, for those with detectable diads (solid symbols), CO_2 contents are among the highest found at arc volcanoes.

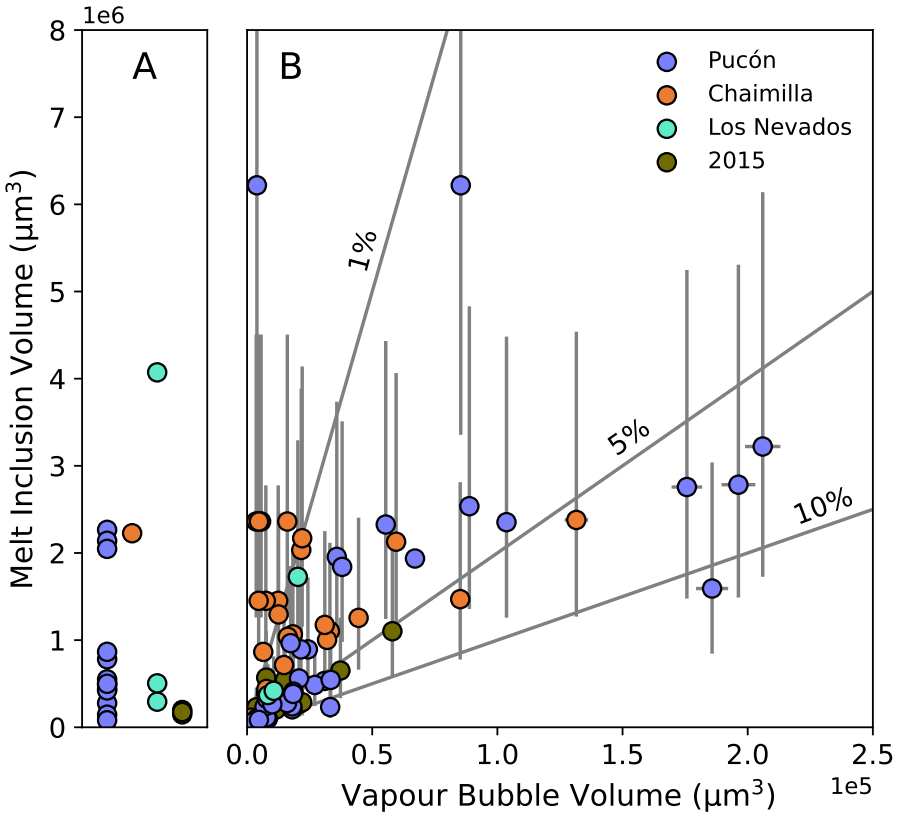

Figure 4.18: Comparison of melt inclusion and vapour bubble dimensions. A) volumes of melt inclusions without vapour bubble. B) volumes of melt inclusions and their host vapour bubbles. Grey lines mark lines of 1, 5 and 10% vapour bubble volume relative to MI volume.

1230 °C.

Saturation pressures were calculated with the MagmaSat (Ghiorso and Gualda 2015) volatile saturation model, utilising the temperatures derived above. These pressures range from 0–7.8 kbar, corresponding to depths of 0–28 km assuming a constant crustal density of 2.8 g·cm^{-3} (Figure 4.19). The pressures for each MI, form near-vertical arrays in temperature-pressure space and together define a vertically extensive magmatic system for Villarrica magmas.

For comparison, I also calculated pressures using the clinopyroxene-only barometer of Jorgenson et al. (2022), following the recommendation of Wieser et al. (2023a), using the python library Thermobar (Wieser et al. 2022b) (Figure 4.19b). These pressures were calculated for all clinopyroxene analyses available from the literature (as detailed in Chapter 2) after filtering for cation per formula unit totals between 3.98 and 4.02. This secondary pressure calculation offers a point of comparison for those derived from the MagmaSat model. Both methods yield consistent pressure estimates, suggesting that crystal cargoes sampled at Villarrica are sourced from a vertically extensive magmatic system beneath the volcano (Figure 4.19).

4.8.5 Trace Element Compositions

Villarrica MIs exhibit trace element compositions that are typical of arc volcanoes, characterised by relatively flat profiles and a distinct Nb anomaly (Figure 4.20). The range of compositions is similar to that observed in the whole-rock data from Villarrica (grey shaded region in Figure 4.20), which includes a wider range of compositions than the basaltic to basaltic-andesite compositions displayed by MI (Figure 2.1c from 2).

In general, the trace element compositions of MIs are most similar to those of enriched mid-ocean-ridge basalts (E-MORB), although they show significant deviations towards both oceanic-island basalts (OIB), and normal mid-ocean ridge basalt (N-MORB) compositions (Figure 4.20). These variations suggest that the melts at Villarrica are derived from multiple sources, consistent with the diverse nature of magmatic sources in subduction zone environments.

While the relatively few glass composition analyses performed by SIMS generally follow MI trends, one sample from the March 2015 eruption — from the reticulite collected by Hugo Moreno — shows a significant positive Nb anomaly. This anomaly may be the result of Fe-Ti oxide dissolution, which is known to contain significant amounts of Nb. This may reflect differing magma dynamics for the March 2015 eruption, whereby a hot trigger magma caused widespread dissolution and rapid growth of reverse

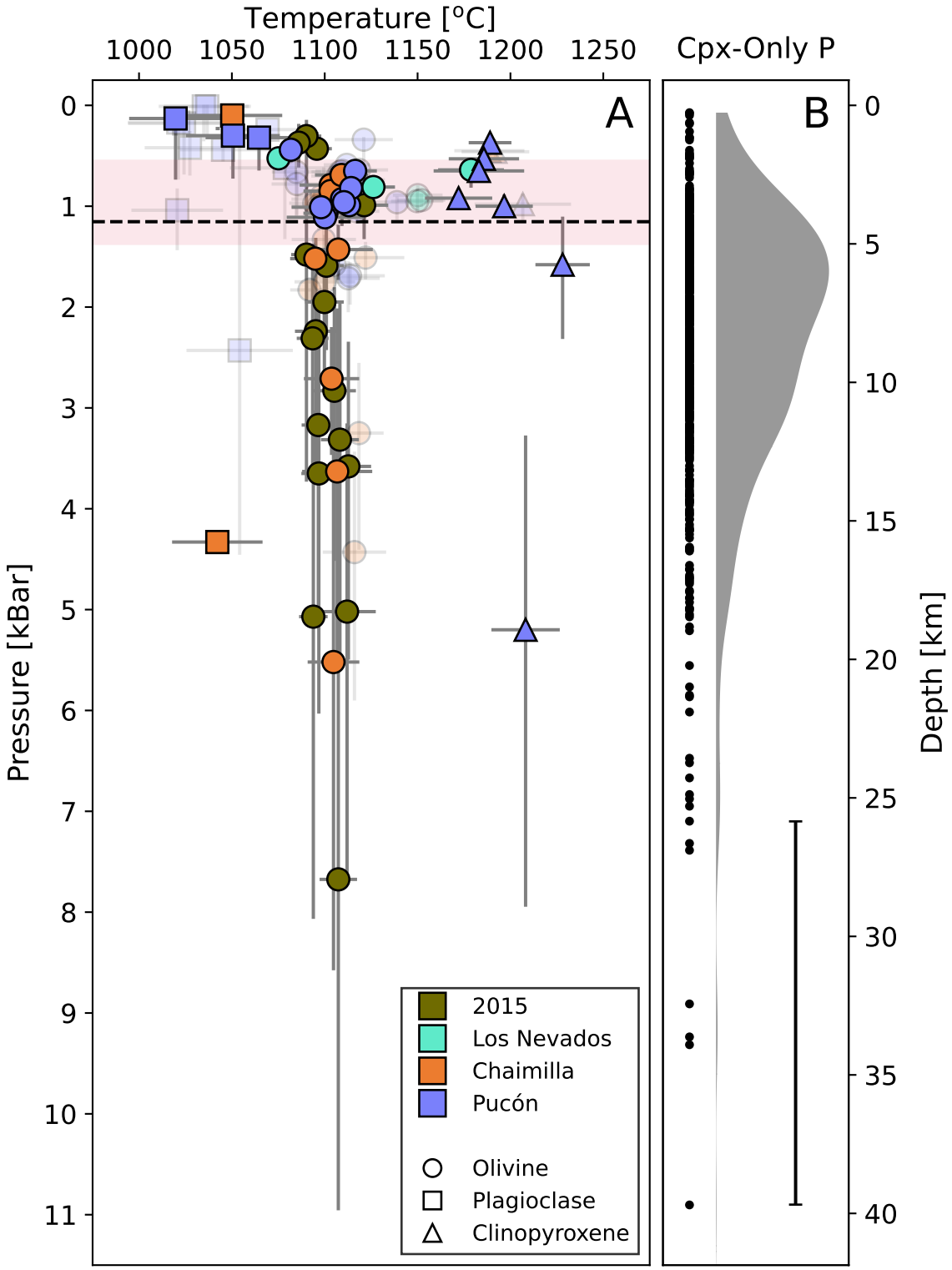

Figure 4.19: A) Mineral-liquid temperatures and volatile saturation pressures for Villarrica melt inclusions. Translucent symbols are MI without vapour bubbles or measurable diads. Solid symbols are those with reliable diad measurements. Uncertainties on T and P from Monte-Carlo propagation of analytical uncertainties shown by grey bars. The black dashed line shows the depth of the re-inflation signal after the March 2015 fire fountain from Delgado et al. (2017). The pink-shaded region shows the depth range of seismicity during the eruption of the March 2015 fire fountain from González-Vidal et al. (2022). B) Clinopyroxene-only pressures calculated using the barometer of Jorgenson et al. (2022) for all literature Villarrica clinopyroxene. A RMSE (±1.9 kbar after Wieser et al. (2023a)) for the barometer is plotted as the black error bar.

zones observed in BSE imagery (Figure 4.4).

4.9 Discussion

4.9.1 Oxygen Fugacity

The oxygen fugacity of Villarrica magmas has been the subject of several studies, with different values suggested, often depending on the eruption or methodology employed. The range of fO_2 calculated here is broadly consistent with those found in past studies, with some notable differences depending on the eruption studied.

Lohmar (2008) and Lohmar et al. (2012) calculated an fO_2 values of QFM (Quartz-Fayalite-Magnetie) and QFM-0.2 for the Licán Mafic Ignimbrite and a Dacitic Dome, respectively using Fe-Ti-oxide oximetry (Ghiorso and Evans 2008). These are relatively low fO_2, indicating more reducing conditions than might be expected for arc magmas. Similarly, Pizarro et al. (2019) assumed an oxygen fugacity of QFM for historic lavas. On the other hand,Witter et al. (2004) assumed an oxygen fugacity of NNO (Ni-NiO), which is equivalent to QFM+0.69 at 1 kbar and 1200 °C, when modelling spatter erupted in 2000. A more oxidised value of NNO+0.9±0.5 (equivalent to QFM+1.59±0.5 t 1 kbar and 1200 °C) was calculated by Zajacz and Halter (2009) for a late-Holocene (post-Pucón Ignimbrite) lava, using spinel-olivine relations (Ballhaus et al. 1991) and olivine-liquid V partitioning (Canil and Fedortchouk 2001).

In Chapter 2, I employed MELTS simulations (Ghiorso and Gualda 2015) and found that the best-fitting fO_2 range to be between QFM-0.2–2.0 to reproduce the range of observed mineral compositions at Villarrica. This large range is consistent with the compositional variability shown by mineral hosts, melt inclusion, and groundmass glasses indicating complex magma storage and evolution at Villarrica.

The calculated fO_2 for Villarrica magmas in this study are generally in agreement with these past results. The relatively high fO_2 calculated for the March 2015 eruption is not an outlier but aligns closely with the fO_2 calculated by Zajacz and Halter (2009) for a relatively recent historic lava, suggesting the 2015 eruption was more oxidised compared to the other eruptions studies here. This is reflected in the olivine-MI Rhodes diagram (Figure 4.13), where all measured inclusions plot near their host olivine compositions when differences in oxygen fugacity are accounted for.

However, it is important to note that the method used here may be sensitive to the re-equilibration of spinel with their host olivine, particularly for divalent cations such as Fe and Mg. This is a known limitation for popular olivine-spinel oxybarometers e.g., Ballhaus et al. (1991) and Nikolaev et al. (2018). Despite

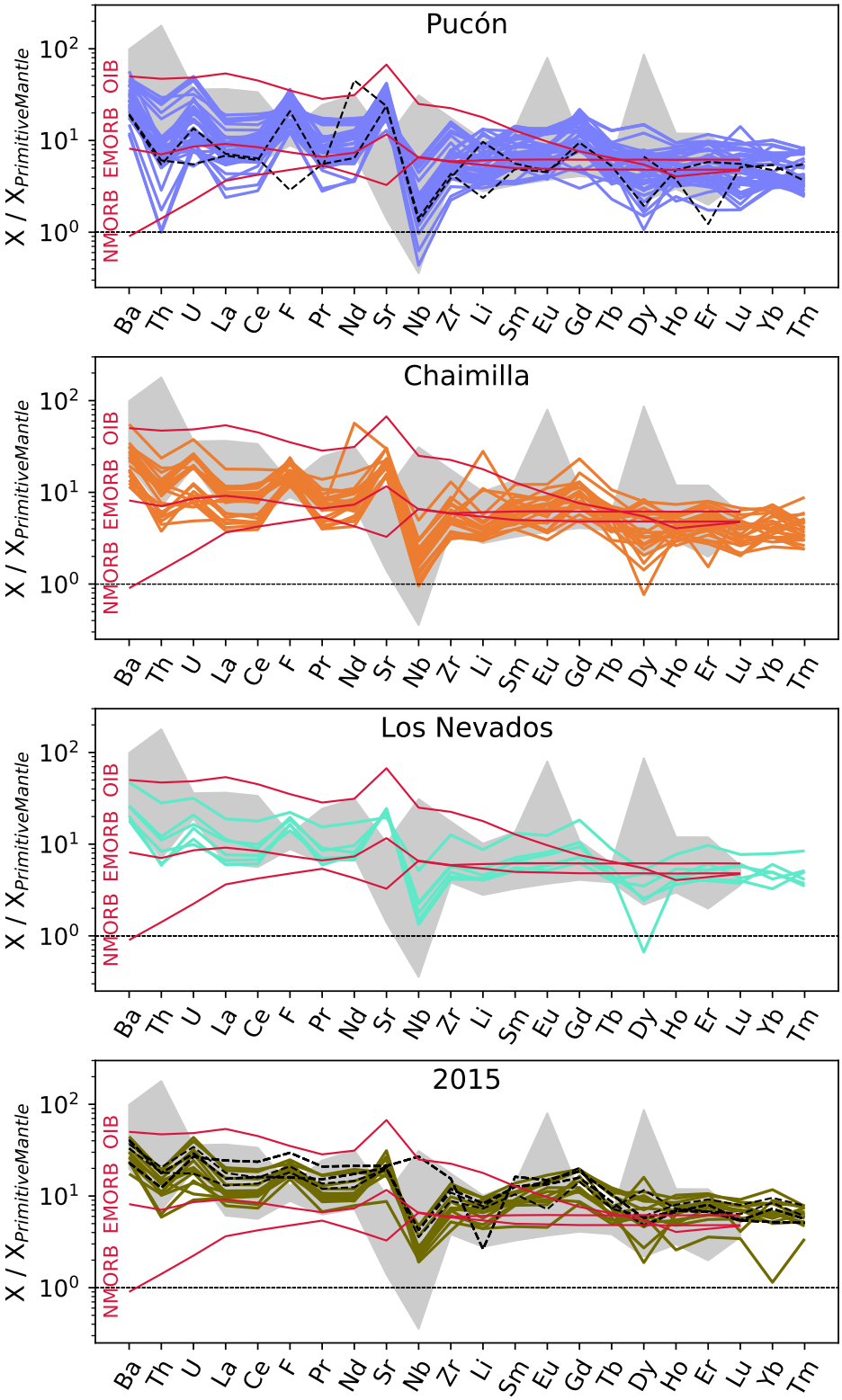

Figure 4.20: Trace-element spider diagrams, normalised to primitive mantle (Sun and McDonough 1989), showing the range of melt inclusion (coloured solid lines) and groundmass glass (black dashed lines) trace-element compositions measured by SIMS. Red lines show normalised trace elements of Normal Mid-Ocean-Ridge-Basalt (N-MORB), Enriched- Mid-Ocean-Ridge-Basalt (E-MORB), and Ocean-Island Basalt (OIB) all from Sun and McDonough (1989). Grey fields show the range of all whole-rock trace elements measured at Villarrica from the literature (Clavero-Ribes 1996; Hickey-Vargas et al. 2016; Hickey-Vargas et al. 1989; Lohmar 2008; McGee et al. 2017; Morgado et al. 2015; Pioli et al. 2015; Pizarro et al. 2019; Silva Parejas 2008; Wehrmann et al. 2014; Witter et al. 2004; Zajacz and Halter 2007).

this potential limitation, the method used should be robust to changes in oxidation state in the MI due to H^+ diffusion, unlike direct measurement of melt Fe^{2+}/Fe^{3+} (e.g., Botcharnikov et al. 2024).

A more robust alternative would be to use an olivine-liquid, vanadium-exchange oxybarometry (e.g., Shishkina et al. 2018), since vanadium is a relatively slow diffusing element, and its partition is less affected by re-equilibration than mobile divalent cations. However, since I did not measure V in either MIs or their olivine hosts, this approach was not feasible. Despite these limitations, the calculated oxygen fugacities have allowed for accurate PEM corrections for MIs and are valuable in understanding redox state variations between eruptions.

4.9.2 Volatile Contents

The volatile contents measured in this study provide new insights into the degassing and volatile evolution of Villarrica magmas. The CO_2 contents are notably high, reaching up to 4500 ppm. These are the highest measured at Villarrica to date, largely because both MI-glass and vapour bubble CO_2 contents were measured. Previous studies that only measured the CO_2 content of the MI glass, have likely largely underestimated their total CO_2 contents, and consequently the saturation pressures of Villarrica MI. For example, Witter et al. (2004) measured less than 100 ppm CO_2 in olivine-hosted MI glass from spatter erupted in 2000, Pioli et al. (2015) measured <300 ppm CO_2 in olivine-hosted MI glass from the Chaimilla fall deposit and Robidoux et al. (2021) reported <1500 ppm CO_2 olivine-hosted MI from the Los Nevados parasitic cones. Similarly, Cortes and Calder (2019) measured <500 ppm CO_2 contents for olivine-hosted MI from the March 2015 eruption, and other historic eruptions of Villarrica. In all cases where the same eruptions were analysed as in this study, the published CO_2 values agree with those from this study when only glass CO_2 contents are considered. As the majority of the total CO_2 of each MI is hosted in the vapour bubble, the findings of this chapter provide a significant step forward in understanding the true volatile budget of Villarrica magmas.

The CO_2 contents reported in this chapter are amongst the highest volatile contents measured for arc volcanoes globally. Few studies of arc volcanoes have measured total CO_2 (i.e., both in the MI-glass and vapour bubble). Notable exceptions include Aster et al. (2016), which reported up to 4200 ppm CO_2 contents for basaltic cinder cones near Mt. Lassen, USA; and the Jorullo and Parícutin cones in Mexico. Similarly, Robidoux et al. (2017) measured up to 1800 ppm CO_2 at San Cristobal volcano, Nicaragua, and Mironov et al. (2015) and Rasmussen et al. (2020) measured up to 3300 ppm CO_2 for Volcán Fuego, Guatemala.

The only other study to report similarly high CO_2 contents in MI from an arc stratovolcano is Feignon et al. (2022), which found ~4400 ppm for olivine-hosted MI erupted at Mocho Choschuenco, Chile, located about 50 km south of Villarrica. In their study, Feignon et al. (2022) also measured the carbon content of carbonates present in the vapour bubble using 3D-micro-Raman tomography and added this to their calculated vapour and glass CO_2 contents obtained via Raman CO_2 densimetry and SIMS, respectively. However, a significant flaw in their approach is the use of an uncalibrated CO_2 densimeter (from Lamadrid et al. (2017)), that was not specifically calibrated for their micro-Raman spectrometer and analytical setup. As shown by Lamadrid et al. (2017), micro-Raman densimeters are not universally transferable between different setups, and the lack of proper calibration could lead to large discrepancies in calculated CO_2 contents. Therefore, while the high CO_2 contents reported by Feignon et al. (2022) are consistent with those measured here, their methodology means their values should be treated with caution.

Water contents for Villarrica MI show considerable variability, ranging from ~0.25–3.4 wt.%. These values are similar to those reported by past studies (0.0–3.3 wt.% Cortes and Calder (2019), Pioli et al. (2015), Robidoux et al. (2021), and Witter et al. (2004)), but lower than the global average for arc volcanoes, approximately 4.0 wt.% (Plank et al. 2013). They are also far below maximum values measured at other arc volcanoes (up to 9.0 wt.% Plank et al. (2013)). The relatively low water contents measured here are likely the result of post-entrapment modification, as shown by the vertical array of H_2O vs CO_2 contents in Figure 4.17. This is also supported by the occurrence of vapour bubbles in the large majority of Villarrica MI, as dehydration is known to enhance vapour bubble formation (Aster et al. 2016).

In summary, this Chapter provides new, high-resolution volatile measurements for Villarrica magmas, with particularly high CO_2values that are among the highest recorded for arc volcanoes. These measurements reveal a more complex volatile budget than previously recognized, with significant amounts of CO_2 sequestered in vapour bubbles. This study also highlights the challenges of quantifying volatiles in arc magmas, especially in the context of post-entrapment modifications, and offers important implications for understanding volatile saturation and eruption dynamics at Villarrica and similar volcanoes.

4.9.3 Volatile Saturation Pressures

Volatile saturation pressures from Villarrica MI define a vertical array for olivine-, plagioclase-, and clinopyroxene-hosted MI (Figure 4.19a), ranging from the surface to 7.8 kbar, approximately 30 km deep. This is very comparable to clinopyroxene-only pressures calculated from literature clinopyroxene-compositions from Villarrica (Figure 4.19b). This is most apparent for MI from the March 2015 and

Chaimilla Fall deposit: olivine-hosted MI from the Pucón Ignimbrite are clustered at 1 kbar. However this is unlikely to be a reflection of different magma dynamics, instead, this is almost certainly due to a lack of vapour bubble CO_2 measurements for Pucón-hosted MI. Despite this, the calculated vapour saturation pressures are indicative of a trans-crustal magmatic system at Villarrica and agree well with pressure calculated from MELTS thermodynamic simulations in chapter 2 (Boschetty et al. 2022).

Overall there is no obvious trend with eruption, except most of the olivine-hosted MI erupted in the Los Nevados parasitic cone extend to higher temperatures at shallow pressures compared to the other olivine-hosted MI. However, once again this is likely a result of the lack of diads detected in Los Nevados vapour bubbles. Therefore I suggest that a trans-crustal magmatic system has existed at Villarrica at least since the Pucón Mafic Ignimbrite and that eruptions, regardless of intensity, sample olivine, plagioclase and clinopyroxene antecrysts from this mushy system. The range of saturation pressures, mineralogy and complex textures of mineral phases (Figures 4.7, 4.4) suggest complex interactions between carrier liquids and variably evolved mush that is remobilised before an eruption.

4.9.4 Post-Entrapment Modification of Volatile Contents

4.9.4.1 Bubble-Hosted Carbonate

Multiple lines of evidence strongly support the presence of carbonate in vapour bubbles hosted by Villarrica MIs. Optical images reveal that vapour bubbles often exhibit thick dark rims, which are more pronounced than expected from only a high-relief CO_2 gas phase. This suggests the presence of additional materials, such as carbonate, within the vapour bubble walls. Moreover, while CO_2 Fermi-diads were detectable in fewer than half of the analysed vapour bubbles, the presence or absence of a detectable diad follows a pattern. For example, almost all vapour bubbles hosted in March 2015 MI contained a detectable diad, whereas only one vapour bubble from the Pucòn Ignimbrite showed a detectable diad. This suggests that PEM differs between eruptions, controlling whether CO_2 is present as a gas or sequestered in solids.

Additionally, Raman spectra on vapour bubbles, both with and without detectable diads, frequently contained peaks indicative of carbonate minerals. A prominent peak associated with magnesite (magnesium carbonate, $MgCO_3$) was observed at $1050\,cm^{-1}$, alongside broad peaks that obscure the characteristic olivine peaks at around $900\,cm^{-1}$. These peaks are consistent with the presence of carbonate minerals in Villarrica MI vapour bubbles.

Two potential methods exist for quantifying carbon hosted in carbonates on vapour bubble walls. The first

method involves reheating or rehomogenisation of the MI, This can be done either at ambient pressure on a heated stage (e.g., Devitre et al. 2021; Hanyu et al. 2020), or at a higher pressure in either a piston cylinder (e.g., Buso et al. 2022; Rasmussen et al. 2020) or an internally heated pressure vessel (e.g., Mironov et al. 2015). However, reheating or rehomogenisation is known to drive dehydration of MI and often results in decrepitation (Schiavi et al. 2020). To avoid water loss, which would compromise the ability to calculate mixed-H_2O-CO_2 saturation pressures, or worse risk decrepitation, reheating or rehomogenisation was deemed unsuitable.

The second method utilises micro-Raman tomography, which constructs 3D hyper-spectral maps of phases present along the vapour bubble walls. This involves collecting Raman spectra for each voxel in the bubble, identifying the phase in each voxel using their characteristic Raman spectra, and then calculating the volume of each phase. The total carbon content for solid phases is then found by assuming a density for each identified carbon-hosting phase and their volumes are then converted into carbon contents (e.g., Feignon et al. 2022; Schiavi et al. 2020; Venugopal et al. 2020). While this method can be highly effective for quantifying carbonates in vapour bubbles, it has two significant drawbacks. First, it requires an accurate motorised x-y-z stage for 3D mapping which was not present on the micro-Raman spectrometer used in this study. Second, the process of collecting and processing of 3D hyper-spectral maps is extremely time-intensive, taking weeks to complete, making it impractical for this study.

As a result of these limitations, the carbonate content in Villarrica vapour bubbles could not be quantified directly. However, given the consistent presence of carbonate spectral signatures and the systematic patterns observed in the CO_2 diads, it is clear that carbonate plays an important role in the total carbon budget of Villarrica MI. Therefore, the CO_2 concentrations measured in this study should be considered underestimates, as they do not account for the carbon sequestered in carbonates within vapour bubbles, which could be substantial. While the methods presented in this study demonstrate a significant advancement over prior studies that focused solely on the MI-glass CO_2, such as those by Pioli et al. (2015), Robidoux et al. (2021), and Witter et al. (2004), additional work needed to fully quantify total MI CO_2. Future studies employing more advanced techniques, such as micro-Raman tomography or rehomogenisation, will be crucial for fully understanding the volatile and carbon fluxes of arc magmas.

4.9.4.2 Re-Equilibration with Low-H_2O Melts

The olivine-liquid Ca-exchange hygrometer of Gavrilenko et al. (2016) has been successfully used in multiple studies to assess MI water contents, particularly when dehydration is suspected to have altered

original water contents (Brahm et al. 2022; Ou et al. 2024). In particular, Brahm et al. (2022) modelled the compositional effects of PEM in a mushy system and found that recalculated water contents were consistent with the magnitude of changes due to Fe-Mg re-equilibration. While the use of the hygrometer provides valuable insights, it has large uncertainty relative to SIMS measurements, with a 1σ of 1.4 wt.% compared to the typical ~0.3 wt.% for SIMS-based analyses (Gavrilenko et al. 2016).

A comparison of the results of the hygrometer and H_2O contents measured using SIMS in Villarrica MI suggests that all MI at Villarrica have undergone re-equilibration with low-H_2O melts (Figure 4.21). However, there are distinct differences between eruptions that warrant further discussion.

First, when grouped by water contents estimated by the hygrometer of Gavrilenko et al. (2016), Villarrica

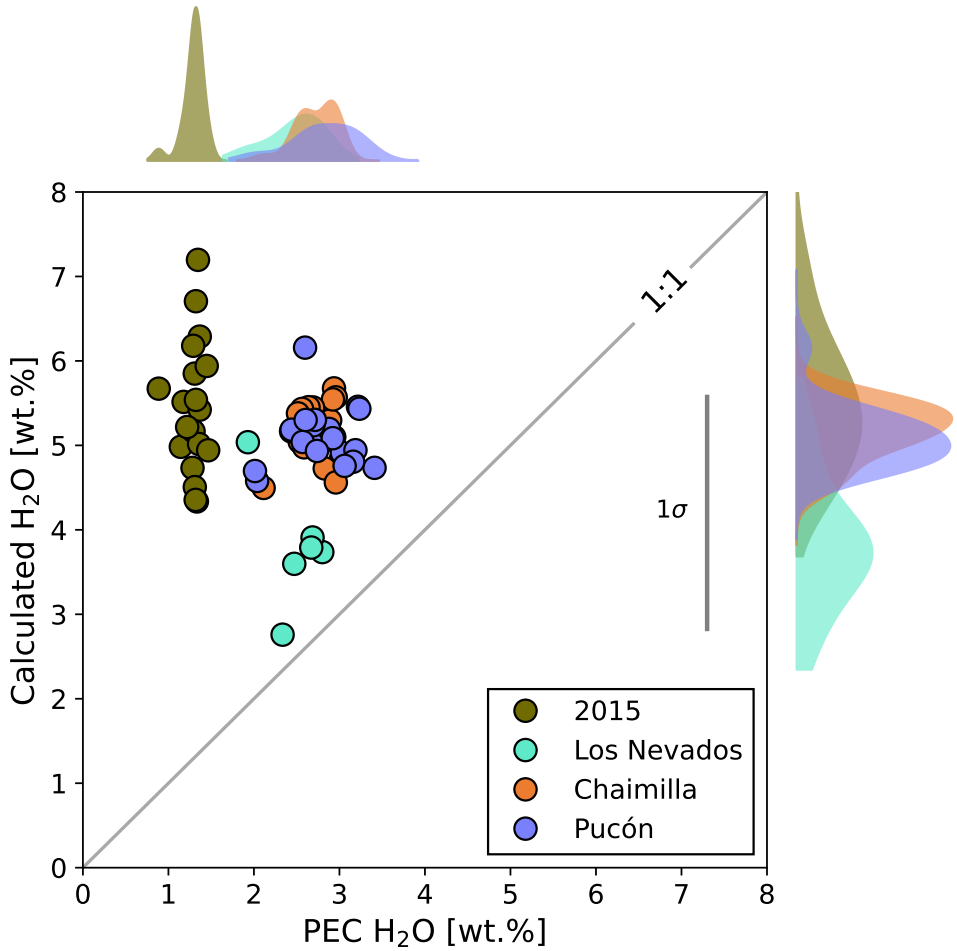

Figure 4.21: PEC-corrected melt inclusion water contents (measured by SIMS) versus water contents estimated by Ol-Liq Ca-exchange hygrometry using the equations of Gavrilenko et al. (2016). 1σ uncertainty from hygrometer shown as thick, vertical grey error bar. Propagated analytical uncertainties for both PEC-corrected water contents and those estimated by hygrometry are shown as grey error bars on each point. The distribution of all points to the top left of the 1:1 line suggests all MI have re-equilibrated with low-H_2O melts. MI-H_2O contents estimated from hygrometry show main-edifice eruptions originally had homogeneous water contents ~5 wt.%. Los Nevados MI had slightly lower ~3.5 wt.%

.

MIs can be divided into two main groups. The first group, encompassing MI from all studied main-edifice eruptions (March 2015, Chaimilla Fall Deposit, and Pucón Mafic Ignimbrite), shows relatively high water contents ranging from ~4.5–7 wt.%, higher than the global average (4.0 wt.%) for arc volcanoes (Plank et al. 2013). The second group, containing only MIs from the Los Nevados flank parasitic cones, has on average lower water contents, ~3.5 wt.%. Although, the difference between these two groups falls within the hygrometer's standard error (1σ 1.4 wt.%), the systematic variation between these groups suggests a genuine difference in water contents, which aligns with their difference in eruption intensities. The flank eruptions from Los Nevados, with lower water content, correspond to smaller eruption volumes and lower intensities, whereas the more water-rich MIs from the main edifice eruptions indicate more volatile-rich magmas that contributed to more explosive eruptions.

A second set of groupings emerges when considering the measured H_2O contents from SIMS, after correcting for PEM. Again water contents fall into two main groups: the first group, consisting of MI from the Los Nevados, Chaimilla Fall Deposit, and Pucón Mafic Ignimbrite, has water contents of ~3.3 wt.%, while the second group, comprising only of MI from the March 2015 eruption, has much lower water contents of ~1.5 wt.%. This discrepancy suggests that the two groups of MI re-equilibrated with melts with distinct water contents.

Notably only the most recent of the eruptions, the March 2015 fire fountain, displays substantially lower measured water contents. This phenomenon likely reflects modern changes in magma dynamics at Villarrica, which since 1983 has been characterised by its open vent and active lava lake (Calder et al. 2004; Moussallam et al. 2023; Witter et al. 2004). Witter et al. (2004) analysed spatter from the lava lake, collected in the year 2000, and found that olivine and plagioclase-hosted MI contained low volatile contents, in the range 0.6–1.4 wt.% H_2O. Additionally, unpublished water contents of olivine-hosted melt inclusions from a preliminary report (Cortes and Calder 2019) show a similar range for other modern Villarrica eruptions, both major eruptions (1971 and 1984) and background spatter (1999 and 2012). In combination, these results suggest that low water contents are a consistent feature of modern Villarrica eruptions.

Rapid degassing, facilitated by overturning and convection in open conduits, could explain this phenomenon (e.g., Allard et al. 2016; La Spina et al. 2024; Moussallam et al. 2016). I hypothesise that MIs from the March 2015 eruption re-equilibrated with degassed magmas in the open conduit system, whereas MIs from older eruptions re-equilibrated with more water-rich, less degassed magmas. This could have occurred in a part of the system isolated from the open conduit, likely for MIs erupted from

the Los Nevados parasitic cones, or there might have been no open conduit at Villarrica during the period spanning the Pucón and Chaimilla eruptions.

This difference in water content between the March 2015 eruption and previous eruptions may be tied to a modern shift in magma dynamics at Villarrica. It could suggest that open-vent behaviour may be a relatively new feature at Villarrica and did not occur before modern historic eruptions. Alternatively, this behaviour may not occur before large eruptive events. Testing whether Villarrica's open conduit system extends to significant depths or is voluminous enough to dampen large explosive events would require additional modelling of the influence of conduit parameters.

4.9.4.3 Effect on Volatile Saturation Pressures

The underestimation of both H_2O and CO_2 concentrations due to re-equilibration with low-H_2O melts and failure to account for carbonates in the vapour bubble means that calculated volatile saturation pressures are underestimates. Buso et al. (2022) found that a significant amount of carbon may be trapped as carbonate in vapour bubbles, with homogenised MIs containing up to 300% more CO_2 than non-homogenised MIs. Similarly, Devitre et al. (2021) showed that re-heating MI could result in a doubling of the total MI CO_2 content by releasing carbon from precipitated carbonates. Therefore, it is reasonable to assume that adding the carbon trapped in carbonates to Villarrica MI CO_2 totals could substantially increase the calculated volatile-saturation pressures.

On the other hand, the use of water contents calculated using the Gavrilenko et al. (2016) hygrometer, results in volatile-saturation pressures that are approximately 1.6 kbar higher than those obtained using PEM-corrected water contents. This relatively small difference is expected, as the solubility of H_2O is much less than that of CO_2 and therefore a much larger increase in H_2O content is required to produce the same effect on calculated pressure as an increase in CO_2 content (Dixon and Stolper 1995; Dixon et al. 1995; Ghiorso and Gualda 2015).

4.9.5 Magma Source Composition

To identify variations in mantle melting or enrichment/depletion of the mantle, the ratio of a light-rare-earth element (REE) against a heavy REE was used (Figures 4.22a and 4.22b). Villarrica MI shows a range of La/Yb ratios which are generally less than the range shown by Villarrica whole-rock compositions. However, two MIs from the March 2015 eruption show high La/Yb ratios up to ~9, suggesting low degrees of melting and/or melting of an enriched source.

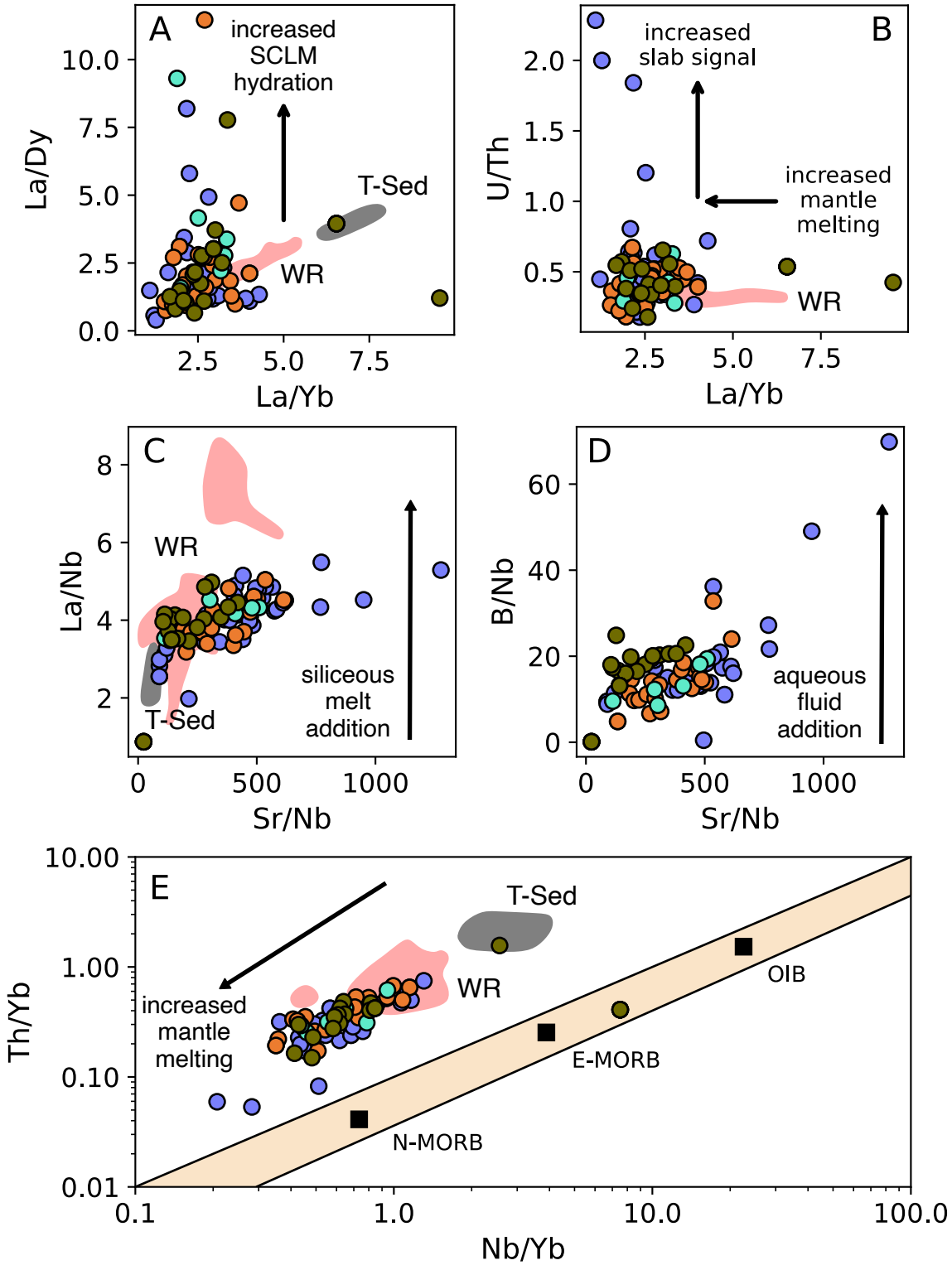

Figure 4.22: Trace element ratio plots for Villarrica melt inclusions, marker colours are the same as in all preceding plots. MI from all three host mineralogies are plotted. Grey field shows the compositional range of Chilean trench sediments (T-Sed) from Jacques et al. (2013) and Lucassen et al. (2010). The pink field shows the compositional range of published Villarrica whole-rock data (WR), data sources same as Figure 4.20. E) The yellow field shows the MORB-OIB mantle array of Pearce and Peate (1995), and representative N-MORB, E-MORB and OIB compositions from Pearce (2008).

MI La/Yb ratios were plotted against La/Dy ratios in Figure 4.22a. Here Dy, a middle REE, was used. This ratio is often employed to infer the amount of hydration or amphibole content of the sub-continental lithospheric mantle (SCLM). While no amphibole has erupted at Villarrica, unlike its nearby neighbour Mocho Choshuenco, the ratio was interpreted as corresponding to mantle hydration. Villarrica MI show a range of La/Dy ratios, extending to high values (~12), with the majority of MI sitting around the same ratio as whole-rock values.

Additionally, MI La/Yb ratios were also plotted against U/Th ratios in Figure 4.22b. The U/Th ratio is commonly used to indicate slab contribution, with higher values suggesting a greater contribution from the subducting slab. Almost all MI extend to higher values than Villarrica whole-rock data, with some Pucón MI reaching exceptionally high ratios (~2.5). The variations shown in Figures 4.22a and 4.22b suggest that MI have captured distinct melt compositions, derived from variable magmatic sources. As these ratios are not significantly affected by fractional crystallisation, the eruption of multiple source compositions within a single eruption implies that the MI hosts were sourced from multiple reservoirs, or lenses, formed from distinct batches of magma.

To ivestigate the nature of the slab component sourcing Villarrica melts, the ratios La/Nb and B/Nb were plotted against Sr/Nb (Figure 4.22c and 4.22d). These ratios were chosen because B indicates aqueous slab fluid contribution, while La suggests that the slab fluid is siliceous. Generally, both Villarrica whole-rock and MI La/Nb ratios are low (MI from Sangay, Ecuador have ratios that extend to 15 (Narváez et al. 2023)), with some Villarrica whole-rock values extending beyond MI (Figure 4.22c). In contrast, B/Nb are much higher (Figure 4.22d). For example, the highest B/Nb ratios at Sangay are around 25 (Narváez et al. 2023), similar to the highest B/Nb of the March 2015 MI, but some Pucón MI extend to ~70, suggesting they were sourced from melts with very high aqueous fluid contributions.

A plot of Th/Yb versus Nb/Yb is used to distinguish between Villarica MI and whole-rock data from the MORB-OIB mantle array of Pearce and Peate (1995) and Pearce (2008) (Figure 4.22e). As expected, all but one Villarrica MI plot above the array, indicating Th enrichment due to the addition of a slab component. The MIs form a diagonal array with enriched MIs plotting near the composition of trench sediments (resulting from low degrees of mantle melting), while more depleted MIs plot away from trench sediments, reflecting higher degrees of mantle melting. Villarrica MIs exhibit a greater degree of variation than Villarrica whole-rock data, even more so than the variation shown by all of the Chilean Central Southern Zone Volcano whole-rock data (Jacques et al. 2014).

Villarrica MI preserve greater variation in trace-element variation than whole-rock data, suggesting a

large variety in source-melt compositions with differing contributions from the subducting slab — including sediment, siliceous and aqueous fluids — and varying degrees of mantle melting. The relatively minor differences between eruptions suggest that multiple mushy reservoirs are intercepted by ascending magmas before their eruption, with antecrysts from these reservoirs sourced from the trans-crustal magmatic system that feeds Villarrica's eruptions.

4.9.6 Primary Volatile Contents

Despite the relatively high volatile contents measured in Villarrica MI, these are likely underestimates (discussed below) and do not reflect primary mantle volatile contents. Figure 4.23 shows H_2O-Ce, CO_2-Nb and CO_2-Ba systematics. Plots of CO_2-Ba-Nb systematics are very similar, suggesting similar behaviour of both Ba and Nb, as expected. Neither plots show signs of forming a horizontal plateau. This is to be expected given that CO_2 contents for Villarrica MI are almost certainly underestimates as vapour-bubble-hosted carbonate has not been accounted for.

In contrast, the dotted line in Figure 4.23c represents the apparent plateau in H_2O content if only PEC-corrected H_2O values are used to estimate primary H_2O contents. However, when the water content of olivine-hosted MIs estimated using the Ca-exchange hygrometer of Gavrilenko et al. (2016) is used, the H_2O contents and consequently, the H_2O/Ce ratios, extend to much higher values. This increase disrupts the apparent plateau, suggesting that no single plateau fits the data from all eruptions. Some MIs from the March 2015, Los Nevados and Pucón Ignimbrite eruptions appear to extend the trend to higher water contents, while others erupted in the Chaimilla, as well as some erupted in the Pucón and March 2015 appear to form a plateau.

If this plateau is real, it would suggest primary melt H_2O contents of just under 6.0 wt.%, which implies that Villarrica MI have degassed by a couple of wt.% before being erupted (Figure 4.21). The existence of multiple trends in H_2O-Ce space suggests that olivine-hosted MIs originate from different source magmas, but are later assembled into diverse crystal cargoes before their eruption.

4.10 Conclusions

The study of olivine-, plagioclase-, and clinopyroxene-hosted MIs erupted during different eruptions of Villarrica has revealed both similarities and clear differences. First PEM-corrected MI compositions from all hosts are remarkably similar to both glass and whole-rock compositions, at least for major elements. These MIs have basalt to basaltic-andesite compositions that follow the expected calc-alkaline

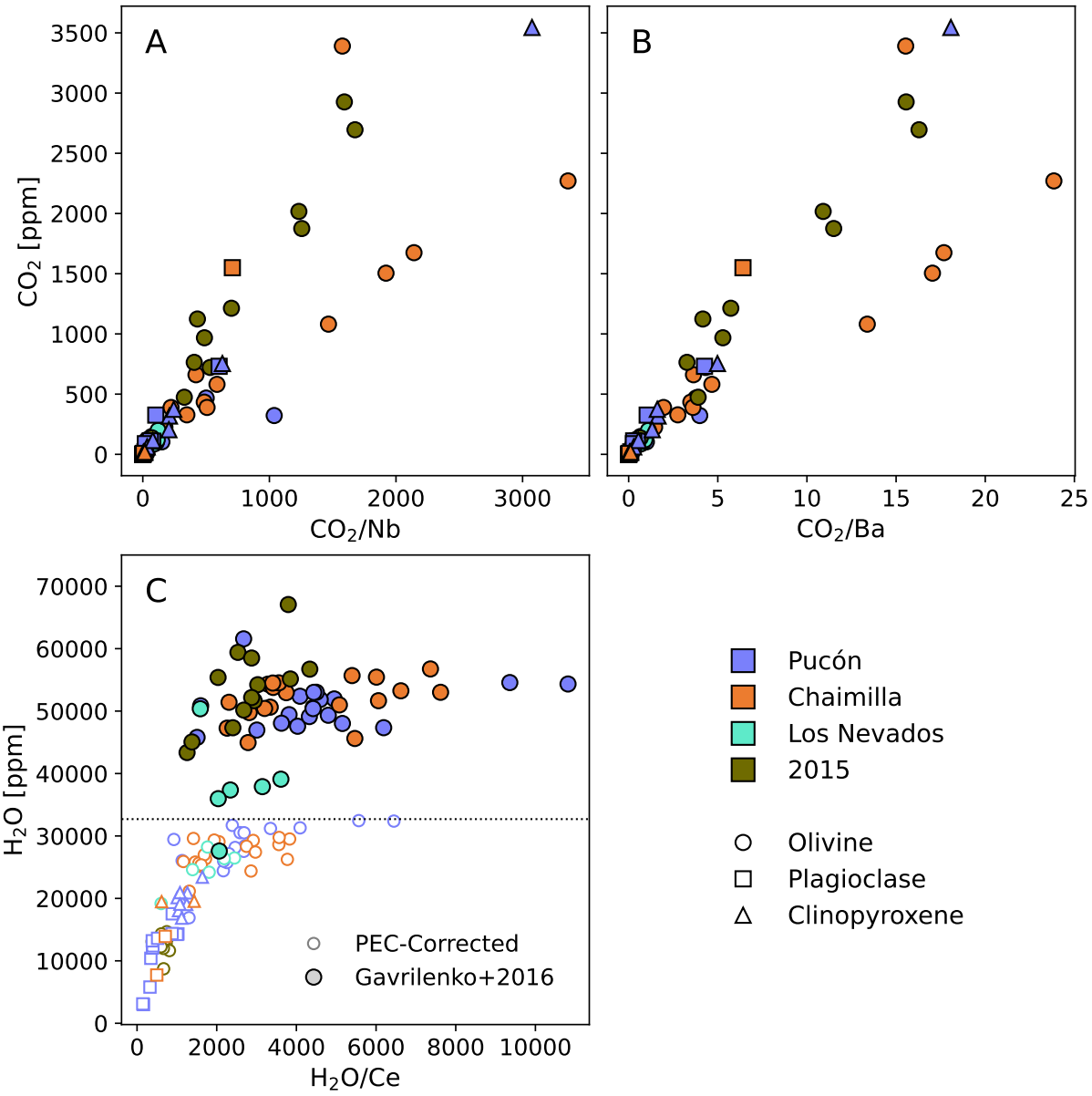

Figure 4.23: Volatile-trace-element systematics to assess primary volatile contents. A-B) CO_2-Ba and CO_2-Nb systematics. C) H_2O-Ce systematics of both PEC-corrected H_2O contents (empty symbols) and estimated original water contents calculated using the hygrometer of Gavrilenko et al. (2016). The dotted line shows the apparent plateau in H_2O contents if only PEC-corrected H_2O contents are used.

trend. Furthermore, MI from all hosts span a wide range of pressures from near the surface to a depth of ~30 km indicating that Villarrica has possessed a trans-crustal-type magmatic architecture since at least the eruption of the Pucón ignimbrite (3.7 ka). This is consistent with the findings of Chapter 2 and expands the extent of the magmatic system to higher pressures.

Measured volatile contents are the highest measured in Villarrica MI, primarily because they take into account gaseous CO_2 sequestered in vapour bubbles, which were found to host upwards of 75% of the total CO_2. These values are also among the highest measured at arc volcanoes globally. However, the reported CO_2 contents and calculated saturation pressures are almost certainly underestimated, as they do not capture water loss due to re-equilibration with low-H_2O melts, nor carbon trapped as carbonate within the vapour bubble. Future studies should employ techniques such as Raman tomography or re-homogenisation to better estimate true total CO_2 contents, which may be significantly higher. Concerns about water loss during re-homogenisation are less of an issue, given the evidence that substantial water loss has already occurred in olivine-hosted MI.

The MIs analysed show a broad range of absolute concentrations and trace-element ratios that do not vary systematically with eruption. This suggests that MI-hosts originate from multiple distinct batches of magma, likely separated in different reservoirs or lenses, which is also supported by the observation range in saturation pressures. This indicates that multiple mushy reservoirs are intercepted by trigger magma before an eruption, with antecrysts from these reservoirs assembled into diverse crystal cargoes. The contrasting slab signatures of some MIs that erupted during the oldest eruption studied, the Pucón Mafic Ignimbrite, compared with the most depleted signature of some of the MIs that erupted during the most recent March 2015 eruption, suggest either a temporal change in the magmatic source composition or magma dynamics. The latter possibility implies that smaller, more recent eruptions may fail to remobilise the same reservoirs as the older, larger eruptions. This again supports the findings of Chapter 2, that the dynamics of the different styles of eruption are a result of the magnitude of primitive magma injections.

Overall, Villarrica MIs provide strong evidence for complex magmatic storage, despite the basalt to basaltic-andesite whole-rock compositions. Future work, particularly focusing on the isotopic composition of MIs, could further clarify the diversity of magma source compositions at Villarrica. Additionally, a better understanding of the dynamics of magma storage and the timescales over which mushy reservoirs are remobilised will be crucial in understanding the controls on eruptive style, and the triggers of eruptions at Villarrica.

References

Adams, J. V., F. J. Spera, and M. G. Jackson (2021). "Trachytic Melt Inclusions Hosted in Clinopyroxene Offer a Glimpse Into Samoan EM2-Endmember Melts". In: *Geochemistry, Geophysics, Geosystems* 22.3 (3). DOI: 10.1029/2020GC009212.

Allard, P., M. Burton, G. Sawyer, and P. Bani (2016). "Degassing Dynamics of Basaltic Lava Lake at a Top-Ranking Volatile Emitter: Ambrym Volcano, Vanuatu Arc". In: *Earth and Planetary Science Letters* 448, pages 69–80. DOI: 10.1016/j.epsl.2016.05.014.

Aster, E. M., P. J. Wallace, L. R. Moore, J. Watkins, E. Gazel, and R. J. Bodnar (2016). "Reconstructing CO2 Concentrations in Basaltic Melt Inclusions Using Raman Analysis of Vapor Bubbles". In: *Journal of Volcanology and Geothermal Research* 323, pages 148–162. DOI: 10.1016/j.jvolgeores.2016.04.028.

Ballhaus, C., R. F. Berry, and D. H. Green (1991). "High Pressure Experimental Calibration of the Olivine-Orthopyroxene-Spinel Oxygen Geobarometer: Implications for the Oxidation State of the Upper Mantle". In: *Contributions to Mineralogy and Petrology* 107.1 (1), pages 27–40.

Barber, N. D., S. L. Baldwin, M. Edmonds, F. O. Boschetty, H. E. Wibowo, and A. Harijoko (2023). "Monogenetic Volcanoes as Windows into Transcrustal Mush: A Case Study of Slamet and Loyang Volcanoes, Central Java". In: *Journal of Volcanology and Geothermal Research* 444, page 107945. DOI: 10.1016/j.jvolgeores.2023.107945.

Bennett, E. N., F. E. Jenner, M.-A. Millet, K. V. Cashman, and C. J. Lissenberg (2019). "Deep Roots for Mid-Ocean-Ridge Volcanoes Revealed by Plagioclase-Hosted Melt Inclusions". In: *Nature* 572.7768 (7768), pages 235–239. DOI: 10.1038/s41586-019-1448-0.

Borisov, A. A. and A. I. Shapkin (1990). "A New Empirical Equation Rating Fe3+/Fe2+ in Magmas to Their Composition, Oxygen Fugacity, and Temperature". In: *Geochem. Int* 27.1 (1), pages 111–116.

Borisov, A. (2018). "Ferric/Ferrous Ratio in Silicate Melts: A New Model for 1 Atm Data with Special Emphasis on the Effects of Melt Composition". In: *Contributions to Mineralogy and Petrology*, page 15.

Boschetty, F. O., D. J. Ferguson, J. A. Cortés, E. Morgado, S. K. Ebmeier, D. J. Morgan, J. E. Romero, and C. Silva Parejas (2022). "Insights Into Magma Storage Beneath a Frequently Erupting Arc Volcano (Villarrica, Chile) From Unsupervised Machine Learning Analysis of Mineral Compositions". In: *Geochemistry, Geophysics, Geosystems* 23.4 (4). DOI: 10.1029/2022GC010333.

Botcharnikov, R., M. Wilke, J. Garrevoet, M. Portnyagin, K. Klimm, S. Buhre, S. Krasheninnikov, R. Almeev, S. Moune, and G. Falkenberg (2024). "Confocal μ -XANES as a Tool to Analyze Fe Oxidation State in Heterogeneous Samples: The Case of Melt Inclusions in Olivine from the Hekla Volcano". In: *European Journal of Mineralogy* 36.1, pages 195–208. DOI: 10.5194/ejm-36-195-2024.

Brahm, R., G. F. Zellmer, T. Kuritani, N. Sakamoto, H. Yurimoto, M. Nakagawa, and E. Sato (2022). "Olivine Melt Inclusion Constraints on Some Intensive Properties of Subvolcanic Crystal Mushes and Their Evolution

through Boundary Layer Fractionation in Northern Japan". In: *Journal of Petrology* 63.3, egac016. DOI: 10.1093/petrology/egac016.

Buso, R., D. Laporte, F. Schiavi, N. Cluzel, and C. Fonquernie (2022). "High-Pressure Homogenization of Olivine-Hosted CO₂-Rich Melt Inclusions in a Piston Cylinder: Insight into the Volatile Content of Primary Mantle Melts". In: *European Journal of Mineralogy* 34.3, pages 325–349. DOI: 10.5194/ejm-34-325-2022.

Calder, E. S., A. J. Harris, P. Peña, E. Pilger, L. P. Flynn, G. Fuentealba, and H. Moreno (2004). "Combined Thermal and Seismic Analysis of the Villarrica Volcano Lava Lake, Chile". In: *Revista geológica de Chile* 31.2 (2). DOI: 10.4067/S0716-02082004000200005.

Canil, D. and Y. Fedortchouk (2001). "Olivine-Liquid Partitioning of Vanadium and Other Trace Elements, with Applications to Modern and Ancient Picrites". In: *The Canadian Mineralogist* 39.2, pages 319–330. DOI: 10.2113/gscanmin.39.2.319.

Caracciolo, A., E. Bali, S. Halldórsson, G. Guðfinnsson, M. Kahl, I. Þórðardóttir, G. Pálmadóttir, and V. Silvestri (2023). "Magma Plumbing Architectures and Timescales of Magmatic Processes during Historical Magmatism on the Reykjanes Peninsula, Iceland". In: *Earth and Planetary Science Letters* 621, page 118378. DOI: 10.1016/j.epsl.2023.118378.

Clavero-Ribes, J. E. (1996). "Ignimbritas Andesitico-Basalticas Postglaciales Del Volcán Villarrica, Andes Del Sur (39° 25'S)". Master's thesis. Universidad de Chile.

Cortes, J. A. and E. Calder (2019). *Volatile Degassing Styles and the Triggering of an Eruptive Event in an Open, Persistently Degassing Volcanic System, Villarrica Volcano, Chile*. NERC IonProbe.

Costantini, L., L. Pioli, C. Bonadonna, J. Clavero, and C. Longchamp (2011). "A Late Holocene Explosive Mafic Eruption of Villarrica Volcano, Southern Andes: The Chaimilla Deposit". In: *Journal of Volcanology and Geothermal Research* 200.3-4 (3-4), pages 143–158. DOI: 10.1016/j.jvolgeores.2010.12.010.

Cutler, K. S., M. Cassidy, and J. D. Blundy (2024). "Plagioclase-Saturated Melt Hygrothermobarometry and Plagioclase-Melt Equilibria Using Machine Learning". In: *Geochemistry, Geophysics, Geosystems* 25.4, e2023GC011357. DOI: 10.1029/2023GC011357.

Danyushevsky, L. V. (2002). "Melt Inclusions in Olivine Phenocrysts: Using Diffusive Re-equilibration to Determine the Cooling History of a Crystal, with Implications for the Origin of Olivine-phyric Volcanic Rocks". In: *Journal of Petrology* 43.9 (9), pages 1651–1671. DOI: 10.1093/petrology/43.9.1651.

– (2004). "Melt Inclusions in Primitive Olivine Phenocrysts: The Role of Localized Reaction Processes in the Origin of Anomalous Compositions". In: *Journal of Petrology* 45.12 (12), pages 2531–2553. DOI: 10.1093/petrology/egh080.

Danyushevsky, L. V. and A. Lima (2001). "Relationships between Campi Flegrei and Mt. Somma Volcanism: Evidence from Melt Inclusions in Clinopyroxene Phenocrysts from Volcanic Breccia Xenoliths". In: *Mineralogy and Petrology* 73.1-3 (1-3), pages 107–119. DOI: 10.1007/s007100170013.

Danyushevsky, L. V. and A. V. Sobolev (1996). "Ferric-Ferrous Ratio and Oxygen Fugacity Calculations for Primitive Mantle-Derived Melts: Calibration of an Empirical Technique". In: *Mineralogy and Petrology* 57.3-4 (3-4), pages 229–241. DOI: 10.1007/BF01162360.

Delgado, F., M. E. Pritchard, S. Ebmeier, P. González, and L. Lara (2017). "Recent Unrest (2002–2015) Imaged by Space Geodesy at the Highest Risk Chilean Volcanoes: Villarrica, Llaima, and Calbuco (Southern Andes)". In: *Journal of Volcanology and Geothermal Research* 344, pages 270–288. DOI: 10.1016/j.jvolgeores.2017.05.020.

Devitre, C., A. Barth, E. Gazel, T. A. Plank, and R. Ramalho (2021). "Solving the Carbonate Problem in Melt Inclusion Bubbles". In: AGU Fall Meeting 2021. URL: https://agu.confex.com/agu/fm21/meetingapp.cgi/Paper/845682.

DeVitre, C. L., C. M. Allison, and E. Gazel (2021). "A High-Precision CO_2 Densimeter for Raman Spectroscopy Using a Fluid Density Calibration Apparatus". In: *Chemical Geology* 584, page 19. DOI: 10.1016/j.chemgeo.2021.120522.

Dixon, J. E. and E. M. Stolper (1995). "An Experimental Study of Water and Carbon Dioxide Solubilities in Mid-Ocean Ridge Basaltic Liquids. Part II: Applications to Degassing". In: *Journal of petrology* 36.6, pages 1633–1646. DOI: 10.1093/oxfordjournals.petrology.a037268.

Dixon, J. E., E. M. Stolper, and J. R. Holloway (1995). "An Experimental Study of Water and Carbon Dioxide Solubilities in Mid-Ocean Ridge Basaltic Liquids. Part I: Calibration and Solubility Models". In: *Journal of Petrology* 36.6, pages 1607–1631. DOI: 10.1093/oxfordjournals.petrology.a037267.

Droop, G. T. R. (1987). "A General Equation for Estimating Fe^{3+} Concentrations in Ferromagnesian Silicates and Oxides from Microprobe Analyses, Using Stoichiometric Criteria". In: *Mineralogical Magazine* 51.361 (361), pages 431–435. DOI: 10.1180/minmag.1987.051.361.10.

Dungan, M. A. and J. M. Rhodes (1978). "Residual Glasses and Melt Inclusions in Basalts from DSDP Legs 45 and 46: Evidence for Magma Mixing". In: *Contributions to Mineralogy and Petrology* 67.4 (4), pages 417–431. DOI: 10.1007/BF00383301.

Feignon, J.-G., N. Cluzel, F. Schiavi, S. Moune, O. Roche, J. Clavero, P. Schiano, and M. Auxerre (2022). "High CO2 Content in Magmas of the Explosive Andesitic Enco Eruption of Mocho-Choshuenco Volcano (Chile)". In: *Bulletin of Volcanology* 84.4, page 40. DOI: 10.1007/s00445-022-01550-y.

Fontijn, K., H. Rawson, M. Van Daele, J. Moernaut, A. M. Abarzúa, K. Heirman, S. Bertrand, D. M. Pyle, T. A. Mather, M. De Batist, J.-A. Naranjo, and H. Moreno (2016). "Synchronisation of Sedimentary Records Using Tephra: A Postglacial Tephrochronological Model for the Chilean Lake District". In: *Quaternary Science Reviews* 137, pages 234–254. DOI: 10.1016/j.quascirev.2016.02.015.

Frost, B. R. (1991). "Introduction to Oxygen Fugacity and Its Petrologic Importance". In: *Reviews in Mineralogy and Geochemistry* 25.1, pages 1–9.

Gavrilenko, M., C. Herzberg, C. Vidito, M. J. Carr, T. Tenner, and A. Ozerov (2016). "A Calcium-in-Olivine Geohygrometer and Its Application to Subduction Zone Magmatism". In: *Journal of Petrology* 57.9 (9), pages 1811–1832. DOI: 10.1093/petrology/egw062.

Geología del volcán Villarrica, Regiones de La Araucanía y de Los Lagos. (2006). Servicio Nacional de Geología y Minería.

Ghiorso, M. S. and B. W. Evans (2008). "Thermodynamics of Rhombohedral Oxide Solid Solutions and a Revision of the FE-TI Two-Oxide Geothermometer and Oxygen-Barometer". In: *American Journal of Science* 308.9 (9), pages 957–1039. DOI: 10.2475/09.2008.01.

Ghiorso, M. S. and G. A. R. Gualda (2015). "An H2O–CO2 Mixed Fluid Saturation Model Compatible with Rhyolite-MELTS". In: *Contributions to Mineralogy and Petrology* 169.6 (6), page 53. DOI: 10.1007/s00410-015-1141-8.

González-Vidal, D., C. Sens-Schönfelder, J. L. Palma, F. Quiero, L. Franco, M. Miller, D. Lange, G. Sielfeld, and J. Cembrano (2022). "The Hiccup of Villarrica Volcano (Chile) during the 2015 Eruption and Its Expression in LP Activity and VLP Ground Motion". In: *Geophysical Journal International* 231.2 (2), pages 1309–1323. DOI: 10.1093/gji/ggac253.

Haddadi, B., O. Sigmarsson, and G. Larsen (2017). "Magma Storage beneath Grímsvötn Volcano, Iceland, Constrained by Clinopyroxene-Melt Thermobarometry and Volatiles in Melt Inclusions and Groundmass Glass: Grímsvötn Magma Storage". In: *Journal of Geophysical Research: Solid Earth* 122.9 (9), pages 6984–6997. DOI: 10.1002/2017JB014067.

Hamada, M. and T. Fujii (2007). "H2O-rich Island Arc Low-K Tholeiite Magma Inferred from Ca-rich Plagioclase-Melt Inclusion Equilibria". In: *GEOCHEMICAL JOURNAL* 41.6 (6), pages 437–461. DOI: 10.2343/geochemj.41.437.

Hanyu, T., J. Yamamoto, K. Kimoto, K. Shimizu, and T. Ushikubo (2020). "Determination of Total CO2 in Melt Inclusions with Shrinkage Bubbles". In: *Chemical Geology* 557, page 119855. DOI: 10.1016/j.chemgeo.2020.119855.

Hartley, M. E., E. Bali, J. Maclennan, D. A. Neave, and S. A. Halldórsson (2018). "Melt Inclusion Constraints on Petrogenesis of the 2014–2015 Holuhraun Eruption, Iceland". In: *Contributions to Mineralogy and Petrology* 173.2 (2), page 10. DOI: 10.1007/s00410-017-1435-0.

Hartley, M. E., D. A. Neave, J. Maclennan, M. Edmonds, and T. Thordarson (2015). "Diffusive Over-Hydration of Olivine-Hosted Melt Inclusions". In: *Earth and Planetary Science Letters* 425, pages 168–178. DOI: 10.1016/j.epsl.2015.06.008.

Hickey-Vargas, R., M. Sun, and S. Holbik (2016). "Geochemistry of Basalts from Small Eruptive Centers near Villarrica Stratovolcano, Chile: Evidence for Lithospheric Mantle Components in Continental Arc Magmas". In: *Geochimica et Cosmochimica Acta* 185, pages 358–382. DOI: 10.1016/j.gca.2016.03.033.

Hickey-Vargas, R., H. M. Roa, L. L. Escobar, and F. A. Frey (1989). "Geochemical Variations in Andean Basaltic and Silicic Lavas from the Villarrica-Lanin Volcanic Chain (39.5 S): An Evaluation of Source Heterogeneity,

Fractional Crystallization and Crustal Assimilation". In: *Contributions to Mineralogy and Petrology* 103.3 (3), pages 361–386. DOI: 10.1007/BF00402922.

Iacovino, K., S. Matthews, P. E. Wieser, G. M. Moore, and F. Bégué (2021). "VESIcal Part I: An Open-Source Thermodynamic Model Engine for Mixed Volatile (H_2O-CO_2) Solubility in Silicate Melts". In: *Earth and Space Science* 8.11 (11). DOI: 10.1029/2020EA001584.

Iacovino, K. and C. Till (2018). "DensityX: A Program for Calculating the Densities of Hydrous Magmatic Liquids from 427-1,627 °C and up to 30 Kbar". In: *Volcanica* 2.1 (1), pages 1–10. DOI: 10.30909/vol.02.01.0110.

Irvine, T. N. and W. R. A. Baragar (1971). "A Guide to the Chemical Classification of the Common Volcanic Rocks". In: *Canadian Journal of Earth Sciences* 8.5, pages 523–548. DOI: 10.1139/e71-055.

Jacques, G., K. Hoernle, J. Gill, F. Hauff, H. Wehrmann, D. Garbe-Schönberg, P. Van Den Bogaard, I. Bindeman, and L. Lara (2013). "Across-Arc Geochemical Variations in the Southern Volcanic Zone, Chile (34.5–38.0°S): Constraints on Mantle Wedge and Slab Input Compositions". In: *Geochimica et Cosmochimica Acta* 123, pages 218–243. DOI: 10.1016/j.gca.2013.05.016.

Jacques, G., K. Hoernle, J. Gill, H. Wehrmann, I. Bindeman, and L. E. Lara (2014). "Geochemical Variations in the Central Southern Volcanic Zone, Chile (38–43°S): The Role of Fluids in Generating Arc Magmas". In: *Chemical Geology* 371, pages 27–45. DOI: 10.1016/j.chemgeo.2014.01.015.

Jorgenson, C., O. Higgins, M. Petrelli, F. Bégué, and L. Caricchi (2022). "A Machine Learning-Based Approach to Clinopyroxene Thermobarometry: Model Optimization and Distribution for Use in Earth Sciences". In: *Journal of Geophysical Research: Solid Earth* 127.4, e2021JB022904. DOI: 10.1029/2021JB022904.

Kamenetsky, V. S., A. J. Crawford, and S. Meffre (2001). "Factors Controlling Chemistry of Magmatic Spinel: An Empirical Study of Associated Olivine, Cr-spinel and Melt Inclusions from Primitive Rocks". In: *Journal of Petrology* 42.4 (4), pages 655–671.

Kamenetsky, V. S., M. Elburg, R. Arculus, and R. Thomas (2006). "Magmatic Origin of Low-Ca Olivine in Subduction-Related Magmas: Co-existence of Contrasting Magmas". In: *Chemical Geology* 233.3-4 (3-4), pages 346–357. DOI: 10.1016/j.chemgeo.2006.03.010.

Kamperman, M., L. V. Danyushevsky, W. R. Taylor, and W. Jablonski (1996). "Direct Oxygen Measurements of Cr-rich Spinel; Implications for Spinel Stoichiometry". In: *American Mineralogist* 81.9-10 (9-10), pages 1186–1194. DOI: 10.2138/am-1996-9-1017.

Kress, V. C. and M. S. Ghiorso (2004). "Thermodynamic Modeling of Post-Entrapment Crystallization in Igneous Phases". In: *Journal of Volcanology and Geothermal Research* 137.4 (4), pages 247–260. DOI: 10.1016/j.jvolgeores.2004.05.012.

La Spina, A., M. Burton, B. Houghton, A. Sutton, and B. Esse (2024). "Magmatic Degassing Dynamics at Halema'uma'u Crater, Kīlauea, Hawaii". In: *Earth and Planetary Science Letters* 648, page 119062. DOI: 10.1016/j.epsl.2024.119062.

Lamadrid, H., L. Moore, D. Moncada, J. Rimstidt, R. Burruss, and R. Bodnar (2017). "Reassessment of the Raman CO_2 Densimeter". In: *Chemical Geology* 450, pages 210–222. DOI: 10.1016/j.chemgeo.2016.12.034.

Le Bas, M. J., R. W. Le Maitre, A. Streckeisen, B. Zanettin, and IUGS Subcommission on the Systematics of Igneous Rocks (1986). "A Chemical Classification of Volcanic Rocks Based on the Total Alkali-Silica Diagram". In: *Journal of Petrology* 27.3, pages 745–750. DOI: 10.1093/petrology/27.3.745.

Le Maitre, R. W. (1989). "A Classification of Igneous Rocks and Glossary of Terms". In: *Recommendations of the international union of geological sciences subcommission on the systematics of igneous rocks*.

Lloyd, A. S., T. Plank, P. Ruprecht, E. H. Hauri, and W. Rose (2013). "Volatile Loss from Melt Inclusions in Pyroclasts of Differing Sizes". In: *Contributions to Mineralogy and Petrology* 165.1 (1), pages 129–153. DOI: 10.1007/s00410-012-0800-2.

Lohmar, S. (2008). "Petrologia de Las Ignimbritas Licán y Pucón (Volcan Villarrica) y Curacautin (Volcan LLaima) En Los Andes Del Sur de Chile". Universidad de Chile.

Lohmar, S., M. Parada, F. Gutiérrez, C. Robin, and M. C. Gerbe (2012). "Mineralogical and Numerical Approaches to Establish the Pre-Eruptive Conditions of the Mafic Licán Ignimbrite, Villarrica Volcano (Chilean Southern Andes)". In: *Journal of Volcanology and Geothermal Research* 235–236, pages 55–69. DOI: 10.1016/j.jvolgeores.2012.05.006.

Lucassen, F., M. Wiedicke, and G. Franz (2010). "Complete Recycling of a Magmatic Arc: Evidence from Chemical and Isotopic Composition of Quaternary Trench Sediments in Chile (36°–40°S)". In: *International Journal of Earth Sciences* 99.3, pages 687–701. DOI: 10.1007/s00531-008-0410-4.

Matzen, A. K., M. B. Baker, J. R. Beckett, and E. M. Stolper (2011). "Fe–Mg Partitioning between Olivine and High-magnesian Melts and the Nature of Hawaiian Parental Liquids". In: *Journal of Petrology* 52.7-8 (7-8), pages 1243–1263. DOI: 10.1093/petrology/egq089.

Maurel, C. and P. Maurel (1982). "Étude Expérimentale de l'équilibre Fe2+-Fe3+ Dans Les Spinelles Chromiferes et Les Liquides Silicatés Basiques Coexistants, a 1 Atm". In: *C. R. Acad. Sc. Paris, t* 295.2 (2), pages 209–215.

McGee, L. E., R. Brahm, M. C. Rowe, H. K. Handley, E. Morgado, L. E. Lara, M. B. Turner, N. Vinet, M.-Á. Parada, and P. Valdivia (2017). "A Geochemical Approach to Distinguishing Competing Tectono-Magmatic Processes Preserved in Small Eruptive Centres". In: *Contributions to Mineralogy and Petrology* 172.6 (6), page 44. DOI: 10.1007/s00410-017-1360-2.

Mironov, N., M. Portnyagin, R. Botcharnikov, A. Gurenko, K. Hoernle, and F. Holtz (2015). "Quantification of the CO 2 Budget and H 2 O–CO 2 Systematics in Subduction-Zone Magmas through the Experimental Hydration of Melt Inclusions in Olivine at High H 2 O Pressure". In: *Earth and Planetary Science Letters* 425, pages 1–11. DOI: 10.1016/j.epsl.2015.05.043.

Mollo, S., K. Putirka, V. Misiti, M. Soligo, and P. Scarlato (2013). "A New Test for Equilibrium Based on Clinopyroxene–Melt Pairs: Clues on the Solidification Temperatures of Etnean Alkaline Melts at Post-Eruptive Conditions". In: *Chemical Geology* 352, pages 92–100. DOI: 10.1016/j.chemgeo.2013.05.026.

Moore, L. R., E. Gazel, R. Tuohy, A. S. Lloyd, R. Esposito, M. Steele-MacInnis, E. H. Hauri, P. J. Wallace, T. Plank, and R. J. Bodnar (2015). "Bubbles Matter: An Assessment of the Contribution of Vapor Bubbles to Melt

Inclusion Volatile Budgets". In: *American Mineralogist* 100.4 (4), pages 806–823. DOI: 10.2138/am-2015-5036.

Morgado, E., M. Parada, C. Contreras, A. Castruccio, F. Gutiérrez, and L. McGee (2015). "Contrasting Records from Mantle to Surface of Holocene Lavas of Two Nearby Arc Volcanic Complexes: Caburgua-Huelemolle Small Eruptive Centers and Villarrica Volcano, Southern Chile". In: *Journal of Volcanology and Geothermal Research* 306, pages 1–16. DOI: 10.1016/j.jvolgeores.2015.09.023.

Morimoto, N. (1988). "Nomenclature of Pyroxenes". In: *Mineralogy and Petrology* 39.1 (1), pages 55–76. DOI: 10.1007/BF01226262.

Moussallam, Y., P. Bani, A. Curtis, T. Barnie, M. Moussallam, N. Peters, C. I. Schipper, A. Aiuppa, G. Giudice, Á. Amigo, G. Velasquez, and C. Cardona (2016). "Sustaining Persistent Lava Lakes: Observations from High-Resolution Gas Measurements at Villarrica Volcano, Chile". In: *Earth and Planetary Science Letters* 454, pages 237–247. DOI: 10.1016/j.epsl.2016.09.012.

Moussallam, Y., H. J. Lee, S. Ding, M. DeLessio, J. L. Everard, E. Spittle, G. Lu, J. Baur, E. Glazer, A. Peccia, et al. (2023). "Temperature of the Villarrica Lava Lake from 1963 to 2015 Constrained by Phase-Equilibrium and a New Glass Geothermometer for Basaltic Andesites". In: *Journal of Petrology*.

Namur, O., B. Charlier, M. J. Toplis, and J. Vander Auwera (2012). "Prediction of Plagioclase-Melt Equilibria in Anhydrous Silicate Melts at 1-Atm". In: *Contributions to Mineralogy and Petrology* 163.1, pages 133–150. DOI: 10.1007/s00410-011-0662-z.

Narváez, D., P. Samaniego, K. Koga, E. Rose-Koga, S. Hidalgo, and G. Ratzov (2023). "Two Types of Slab Components under Ecuadorian Volcanoes Supported by Primitive Olivine-Hosted Melt Inclusion Study". In: *Lithos* 442–443, page 107049. DOI: 10.1016/j.lithos.2023.107049.

Neave, D. A., M. E. Hartley, J. Maclennan, M. Edmonds, and T. Thordarson (2017). "Volatile and Light Lithophile Elements in High-Anorthite Plagioclase-Hosted Melt Inclusions from Iceland". In: *Geochimica et Cosmochimica Acta* 205, pages 100–118. DOI: 10.1016/j.gca.2017.02.009.

Neave, D. A. and K. D. Putirka (2017). "A New Clinopyroxene-Liquid Barometer, and Implications for Magma Storage Pressures under Icelandic Rift Zones". In: *American Mineralogist* 102.4 (4), pages 777–794. DOI: 10.2138/am-2017-5968.

Neave, D. A., A. G. Stewart, M. E. Hartley, and C. McCammon (2024). "Re-Evaluating Stoichiometric Estimates of Iron Valence in Magmatic Clinopyroxene Crystals". In: *Contributions to Mineralogy and Petrology* 179.1, page 5. DOI: 10.1007/s00410-023-02080-2.

Newman, S. and J. B. Lowenstern (2002). "VolatileCalc: A Silicate Melt–H2O–CO2 Solution Model Written in Visual Basic for Excel". In: *Computers & Geosciences* 28.5 (5), pages 597–604. DOI: 10.1016/S0098-3004(01)00081-4.

Nikolaev, G. S., A. A. Ariskin, and G. S. Barmina (2018). "SPINMELT-2.0: Simulation of Spinel–Melt Equilibrium in Basaltic Systems under Pressures up to 15 Kbar: I. Model Formulation, Calibration, and Tests". In: *Geochemistry International* 56.1 (1), pages 24–45. DOI: 10.1134/S0016702918010044.

Ou, Q., S.-P. Qian, K. Hoernle, B. B. Carvalho, F. Zi, K. Wang, L. Zhang, J.-Y. Liu, and J. Liao (2024). "Magmatic Processes within the Plumbing System of the Ultraslow-Spreading Southwest Indian Ridge: Constraints from Olivine, Plagioclase and Melt Inclusions". In: *Contributions to Mineralogy and Petrology* 179.3, page 20. DOI: 10.1007/s00410-024-02098-0.

Pearce, J. A. and D. W. Peate (1995). "Tectonic Implications of the Composition of Volcanic Arc Magmas". In: *Annual Review of Earth and Planetary Sciences* 23.1, pages 251–285. DOI: 10.1146/annurev.ea.23.050195.001343.

Pearce, J. A. (2008). "Geochemical Fingerprinting of Oceanic Basalts with Applications to Ophiolite Classification and the Search for Archean Oceanic Crust". In: *Lithos* 100.1-4, pages 14–48. DOI: 10.1016/j.lithos.2007.06.016.

Peccerillo, A. and S. R. Taylor (1976). "Geochemistry of Eocene Calc-Alkaline Volcanic Rocks from the Kastamonu Area, Northern Turkey". In: *Contributions to Mineralogy and Petrology* 58.1, pages 63–81. DOI: 10.1007/BF00384745.

Petit-Breuilh Sepúlveda, M. E. (2004). *La historia eruptiva de los volcanes hispanoamericanos (siglos XVI al XX): el modelo chileno*. Servicio de Publicaciones, Cabildo Insular de Lanzarote.

Pioli, L., L. Scalisi, L. Costantini, A. Di Muro, C. Bonadonna, and J. Clavero (2015). "Explosive Style, Magma Degassing and Evolution in the Chaimilla Eruption, Villarrica Volcano, Southern Andes". In: *Bulletin of Volcanology* 77.11 (11), page 93. DOI: 10.1007/s00445-015-0976-1.

Pizarro, C., M. A. Parada, C. Contreras, and E. Morgado (2019). "Cryptic Magma Recharge Associated with the Most Voluminous 20th Century Eruptions (1921, 1948 and 1971) at Villarrica Volcano". In: *Journal of Volcanology and Geothermal Research* 384, pages 48–63. DOI: 10.1016/j.jvolgeores.2019.07.001.

Plank, T., K. A. Kelley, M. M. Zimmer, E. H. Hauri, and P. J. Wallace (2013). "Why Do Mafic Arc Magmas Contain 4wt% Water on Average?" In: *Earth and Planetary Science Letters* 364, pages 168–179. DOI: 10.1016/j.epsl.2012.11.044.

Putirka, K. D. (2008). "Thermometers and Barometers for Volcanic Systems". In: *Reviews in Mineralogy and Geochemistry* 69.1 (1), pages 61–120. DOI: 10.2138/rmg.2008.69.3.

Putirka, K. D., M. Perfit, F. Ryerson, and M. G. Jackson (2007). "Ambient and Excess Mantle Temperatures, Olivine Thermometry, and Active vs. Passive Upwelling". In: *Chemical Geology* 241.3-4 (3-4), pages 177–206. DOI: 10.1016/j.chemgeo.2007.01.014.

Rasmussen, D. J., T. A. Plank, P. J. Wallace, M. E. Newcombe, and J. B. Lowenstern (2020). "Vapor-Bubble Growth in Olivine-Hosted Melt Inclusions". In: *American Mineralogist* 105.12 (12), pages 1898–1919. DOI: 10.2138/am-2020-7377.

Rhodes, J. M., M. A. Dungan, D. P. Blanchard, and P. E. Long (1979). "Magma Mixing at Mid-Ocean Ridges: Evidence from Basalts Drilled near 22° N on the Mid-Atlantic Ridge". In: *Tectonophysics* 55.1 (1), pages 35–61. DOI: 10.1016/0040-1951(79)90334-2.

Ridolfi, F. (2021). "Amp-TB2: An Updated Model for Calcic Amphibole Thermobarometry". In: *Minerals* 11.3 (3), page 324. DOI: 10.3390/min11030324.

Robidoux, P., A. Aiuppa, S. Rotolo, A. Rizzo, E. Hauri, and M. Frezzotti (2017). "Volatile Contents of Mafic-to-Intermediate Magmas at San Cristóbal Volcano in Nicaragua". In: *Lithos* 272–273, pages 147–163. DOI: 10.1016/j.lithos.2016.12.002.

Robidoux, P., D. Pastén, G. Levresse, G. Diaz, and D. Paredes (2021). "Volatile Content Implications of Increasing Explosivity of the Strombolian Eruptive Style along the Fracture Opening on the NE Villarrica Flank: Minor Eruptive Centers in the Los Nevados Group 2". In: *Geosciences* 11.8 (8). DOI: 10.3390/geosciences11080309.

Roeder, P. L. and R. F. Emslie (1970). "Olivine-Liquid Equilibrium". In: *Contributions to Mineralogy and Petrology* 29.4 (4), pages 275–289. DOI: 10.1007/BF00371276.

Romero, J. E., E. Morgado, A. Pisello, F. Boschetty, M. Petrelli, F. Cáceres, M. A. Alam, M. Polacci, J. L. Palma, F. Arzilli, F. Vera, R. Gutiérrez, and D. Morgavi (2022). "Pre-Eruptive Conditions of the 3 March 2015 Lava Fountain of Villarrica Volcano (Southern Andes)". In: *Bulletin of Volcanology* 85.1, page 2. DOI: 10.1007/s00445-022-01621-0.

Romero, J. E., F. Vera, M. Polacci, D. Morgavi, F. Arzilli, M. A. Alam, J. E. Bustillos, A. Guevara, J. B. Johnson, J. L. Palma, M. Burton, E. Cuenca, and W. Keller (2018). "Tephra From the 3 March 2015 Sustained Column Related to Explosive Lava Fountain Activity at Volcán Villarrica (Chile)". In: *Frontiers in Earth Science* 6, page 98. DOI: 10.3389/feart.2018.00098.

Schiano, P., R. Clocchiatti, P. Boivin, and E. Medard (2004). "The Nature of Melt Inclusions inside Minerals in an Ultramafic Cumulate from Adak Volcanic Center, Aleutian Arc: Implications for the Origin of High-Al Basalts". In: *Chemical Geology* 203.1-2 (1-2), pages 169–179. DOI: 10.1016/j.chemgeo.2003.10.001.

Schiavi, F., N. Bolfan-Casanova, R. Buso, M. Laumonier, D. Laporte, K. Medjoubi, S. Venugopal, A. Gómez-Ulla, N. Cluzel, and M. Hardiagon (2020). "Quantifying Magmatic Volatiles by Raman Microtomography of Glass Inclusion-Hosted Bubbles". In: *Geochemical Perspectives Letters* 16, pages 17–24. DOI: 10.7185/geochemlet.2038.

Shishkina, T. A., M. V. Portnyagin, R. E. Botcharnikov, R. R. Almeev, A. V. Simonyan, D. Garbe-Schönberg, S. Schuth, M. Oeser, and F. Holtz (2018). "Experimental Calibration and Implications of Olivine-Melt Vanadium Oxybarometry for Hydrous Basaltic Arc Magmas". In: *American Mineralogist* 103.3, pages 369–383. DOI: 10.2138/am-2018-6210.

Silva Parejas, C. (2008). "Evolution and Dynamics of the 3.6 Ka BP Pucón Eruption of Villarrica Volcano, Chile". Universidad de Chile. 261 pages.

Silva Parejas, C., T. H. Druitt, C. Robin, H. Moreno, and J.-A. Naranjo (2010). "The Holocene Pucón Eruption of Volcán Villarrica, Chile: Deposit Architecture and Eruption Chronology". In: *Bulletin of Volcanology* 72.6 (6), pages 677–692. DOI: 10.1007/s00445-010-0348-9.

Sobolev, A. V., A. A. Migdisov, and M. V. Portnyagin (1996). "Incompatible Element Partitioning between Clinopyroxene and Basalt Liquid Revealed by the Study of Melt Inclusions in Minerals from Troodos Lavas, Cyprus". In: 4.3 (3).

Stevens, R. E. (1944). "Composition of Some Chromites of the Western Hemisphere". In: *American Mineralogist* 29.1-2, pages 1–34.

Sun, S.-s. and W. F. McDonough (1989). "Chemical and Isotopic Systematics of Oceanic Basalts: Implications for Mantle Composition and Processes". In: *Geological Society, London, Special Publications* 42.1, pages 313–345. DOI: 10.1144/GSL.SP.1989.042.01.19.

Tellinghuisen, J. (2010). "Least-Squares Analysis of Data with Uncertainty in x and y: A Monte Carlo Methods Comparison". In: *Chemometrics and Intelligent Laboratory Systems* 103.2, pages 160–169. DOI: 10.1016/j.chemolab.2010.07.003.

– (2019). "Calibration: Detection, Quantification, and Confidence Limits Are (Almost) Exact When the Data Variance Function Is Known". In: *Analytical Chemistry* 91.14, pages 8715–8722. DOI: 10.1021/acs.analchem.9b00119.

Thompson, R. N. and S. A. Gibson (2000). "Transient High Temperatures in Mantle Plume Heads Inferred from Magnesian Olivines in Phanerozoic Picrites". In: *Nature* 407.6803 (6803), pages 502–506. DOI: 10.1038/35035058.

Toplis, M. J. (2005). "The Thermodynamics of Iron and Magnesium Partitioning between Olivine and Liquid: Criteria for Assessing and Predicting Equilibrium in Natural and Experimental Systems". In: *Contributions to Mineralogy and Petrology* 149.1 (1), pages 22–39. DOI: 10.1007/s00410-004-0629-4.

Venugopal, S., F. Schiavi, S. Moune, N. Bolfan-Casanova, T. Druitt, and G. Williams-Jones (2020). "Melt Inclusion Vapour Bubbles: The Hidden Reservoir for Major and Volatile Elements". In: *Scientific Reports* 10.1 (1), page 9034. DOI: 10.1038/s41598-020-65226-3.

Wang, X., T. Hou, M. Wang, C. Zhang, Z. Zhang, R. Pan, F. Marxer, and H. Zhang (2021). "A New Clinopyroxene Thermobarometer for Mafic to Intermediate Magmatic Systems". In: *European Journal of Mineralogy* 33.5 (5), pages 621–637. DOI: 10.5194/ejm-33-621-2021.

Waters, L. E. and R. A. Lange (2015). "An Updated Calibration of the Plagioclase-Liquid Hygrometer-Thermometer Applicable to Basalts through Rhyolites". In: *American Mineralogist* 100.10 (10), pages 2172–2184. DOI: 10.2138/am-2015-5232.

Wehrmann, H., K. Hoernle, G. Jacques, D. Garbe-Schönberg, K. Schumann, J. Mahlke, and L. E. Lara (2014). "Volatile (Sulphur and Chlorine), Major, and Trace Element Geochemistry of Mafic to Intermediate Tephras from the Chilean Southern Volcanic Zone (33–43°S)". In: *International Journal of Earth Sciences* 103.7 (7), pages 1945–1962. DOI: 10.1007/s00531-014-1006-9.

Wieser, P. E., K. Iacovino, S. Matthews, G. Moore, and C. M. Allison (2022a). "VESIcal: 2. A Critical Approach to Volatile Solubility Modeling Using an Open-Source Python3 Engine". In: *Earth and Space Science* 9.2 (2). DOI: 10.1029/2021EA001932.

Wieser, P., M. Petrelli, J. Lubbers, E. Wieser, S. Ozaydin, A. Kent, and C. Till (2022b). "Thermobar: An Open-Source Python3 Tool for Thermobarometry and Hygrometry". In: *Volcanica* 5.2 (2), pages 349–384. DOI: 10.30909/vol.05.02.349384.

Wieser, P. E., A. J. R. Kent, and C. B. Till (2023a). "Barometers Behaving Badly II: A Critical Evaluation of Cpx-Only and Cpx-Liq Thermobarometry in Variably-Hydrous Arc Magmas". In: *Journal of Petrology* 64.8, egad050. DOI: 10.1093/petrology/egad050.

Wieser, P. E., A. J. R. Kent, C. B. Till, J. Donovan, D. A. Neave, D. L. Blatter, and M. J. Krawczynski (2023b). "Barometers Behaving Badly I: Assessing the Influence of Analytical and Experimental Uncertainty on Clinopyroxene Thermobarometry Calculations at Crustal Conditions". In: *Journal of Petrology* 64.2 (2), egac126. DOI: 10.1093/petrology/egac126.

Wieser, P. E., H. Lamadrid, J. Maclennan, M. Edmonds, S. Matthews, K. Iacovino, F. E. Jenner, C. Gansecki, F. Trusdell, R. Lee, and E. Ilyinskaya (2021). "Reconstructing Magma Storage Depths for the 2018 Kīlauean Eruption From Melt Inclusion CO_2 Contents: The Importance of Vapor Bubbles". In: *Geochemistry, Geophysics, Geosystems* 22.2 (2). DOI: 10.1029/2020GC009364.

Witter, J. B., V. C. Kress, P. Delmelle, and J. Stix (2004). "Volatile Degassing, Petrology, and Magma Dynamics of the Villarrica Lava Lake, Southern Chile". In: *Journal of Volcanology and Geothermal Research* 134.4 (4), pages 303–337. DOI: 10.1016/j.jvolgeores.2004.03.002.

Wood, B. J. and D. Virgo (1989). "Upper Mantle Oxidation State: Ferric Iron Contents of Iherzolite Spinels by 57Fe Mössbauer Spectroscopy and Resultant Oxygen Fugacities". In: *Geochimica et Cosmochimica Acta* 53.6 (6), pages 1277–1291.

Zajacz, Z. and W. Halter (2009). "Copper Transport by High Temperature, Sulfur-Rich Magmatic Vapor: Evidence from Silicate Melt and Vapor Inclusions in a Basaltic Andesite from the Villarrica Volcano (Chile)". In: *Earth and Planetary Science Letters* 282.1-4 (1-4), pages 115–121. DOI: 10.1016/j.epsl.2009.03.006.

Zajacz, Z. and W. Halter (2007). "LA-ICPMS Analyses of Silicate Melt Inclusions in Co-Precipitated Minerals: Quantification, Data Analysis and Mineral/Melt Partitioning". In: *Geochimica et Cosmochimica Acta* 71.4 (4), pages 1021–1040. DOI: 10.1016/j.gca.2006.11.001.

Chapter 5

Conclusions

This work uses two techniques to investigate the complexity of magma storage, evolution and transport at Villarrica volcano. Chapter 2 utilises previously published mineral compositions to investigate variations in the crystal cargoes of successive eruptions, finding that the proportion of identified compositional clusters for olivine, plagioclase and clinopyroxene vary considerably over the 21 eruptions studied. This implies that magma processing is significantly more complex than the relatively restricted basaltic to basaltic-andesite range in whole-rock compositions would imply. As most crystals erupted at Villarrica are likely antecrystic, I compared measured compositions with over 1500 thermodynamic simulations of magma evolution in a simplified Villarrica-like system. I find the best-fitting simulations for each compositional analysis from a grid search over a range of pressures, oxygen-fugacities and initial water contents. The results imply magmas are stored and mixed in the middle-upper crust, in agreement with past thermobarometry. Notably, despite clusters overlapping in T-P space, each eruption carries crystals that are in equilibrium with a broad range of melt compositions. This implies that they were assembled from isolated batches of magma before eruption.

Key differences between the crystal cargoes of historic, typically low-intensity and low-magnitude eruptions, and the largest of Villarrica's eruptions, i.e. large-mafic ignimbrite forming events, imply fundamental differences in magma dynamics between the eruptive different styles. Plagioclase crystals that are in equilibrium with very evolved melts are only erupted before, and during, the two largest eruptions in Villarrica's post-glacial history. That these compositions exist as both cores and rims, in conjunction with more primitive compositions, strongly suggests magma mixing between stalled evolved magmas and ascending primitive melts as the driving force for large ignimbrite-forming eruptions. In contrast,

the feeder magmas of more recent historic eruptions do not contain these evolved compositions, suggesting their feeder magmas pass relatively uninterrupted through the mushy system, accumulating antecrysts from variably-fractionated mushy reservoirs before their eruption.

In Chapter 3 I investigate the assumption that determining volatile-saturation pressures using the composition of melt inclusions provides more reliable results compared to traditional methods based on mineral and mineral-liquid thermobarometry. Recent advancements have shown that melt inclusion vapour bubble CO_2 must be measured to constrain total melt inclusion volatile contents. However, accurately converting measured CO_2 densities of the bubbles into concentrations using mass balance requires multiple additional pieces of information about each melt inclusion.

To assess the impact of analytical uncertainty in each component, advanced non-linear regression and Monte Carlo methods are applied to propagate uncertainty into the final pressure calculations. A Python-based workflow is developed, utilising existing scripts to calculate glass densities, perform post-entrapment modification corrections, and determine volatile saturation pressures.

Twenty melt inclusions, from four previously published studies, were reanalysed considering all sources of analytical error. It is revealed that errors in volatile saturation pressure are consistently underestimated, with the main contributor being the estimation of melt inclusion volumes using traditional two-dimensional methods. The uncertainty associated with high-pressure melt inclusions estimated using 2D methods approaches that of commonly used clinopyroxene-only, clinopyroxene-liquid, and amphibole-only barometers. Additionally, assessing melt inclusions without vapour bubbles demonstrates non-negligible errors, emphasising the need to propagate all analytical uncertainties to fully evaluate the error in calculated volatile-saturation pressures. These results have wide-reaching implications for MI-based studies of melt storage in all volcanic settings.

In Chapter 4 I analyse the major, trace and volatile contents of olivine-, plagioclase-, and clinopyroxene-hosted melt inclusions from four eruptions of Villarrica. Utilising the error propagation workflow developed in Chapter 4 I find that inclusions were entrapped over a range of pressures, from the upper to the lower crust. These are almost certainly minima as I did not account for carbon that may be sequestered in vapour bubble carbonates, which appear to be present in most, if not all Villarrica MI. The range of entrapment pressures agrees well with pressures calculated from thermodynamic models in Chapter 3 and extends magma storage pressures to near the base of the crust. The complexity of mineral zoning and variety in the composition of erupted crystal cargoes requires that individual batches of magma can cool with limited interaction before being assembled before eruption.

Further proof of this is presented by trace element compositions of the same melt inclusions. They preserve a range of trace-element ratios which are unaffected by bulk fractional crystallisation, which do not correlate with eruption. The ratios require different proportions of mantle source components e.g., slab fluids, variably enriched mantle compositions and/or different degrees of melting. The variation requires that multiple reservoirs in Villarrica's magmatic system formed from distinct batches of magma. These are intercepted by ascending melts, and antecrysts hosting melt inclusions are assembled before eruption, again a key tenet of the trans-crustal magmatic system model.

When combined, the use of machine-learning techniques to assess crystal cargo variability and volatile and trace element analyses of melt inclusions allow for a thorough assessment of magma storage, evolution and transport at active volcanoes.

5.1 Application to Other Arc Volcanoes

The findings from this work at Villarrica have important implications for understanding the magmatic processes at other arc volcanoes. For instance, the broad pressure range of MIs, extending to depths of approximately 30 km, is almost certainly common to other arc volcanoes with deep-seated magma reservoirs. This would indicate that these systems are not confined to shallow crustal magmas, but instead involve complex, deep-reaching magmatic plumbing networks that tap into different crustal levels, allowing for a variety of magmatic and eruptive styles.

The volatile contents observed in Villarrica MIs, particularly the high CO_2 contents, are among the highest measured in arc volcanoes globally. However, this is not because Villarrica is particularly CO_2 rich, but because my methods more accurately determine the CO_2 content of the vapour bubble through the use of a well calibrated micro-Raman densimeter. Recent analyses of ocean island basalts have demonstrated that primary CO_2 contents readily exceed 1 wt.% (Buso et al. 2022; van Gerve et al. 2024). Application of calibrated raman densimetry in combination with assessment of the carbon content of vapour-bubble carbonates will likely reveal similarly high CO_2 contents at arc volcanoes globally.

The application of machine-learning based methods as described in Chapter 3 to analyse large data sets of mineral compositions has the potential to expand our understanding of other arc volcanoes. I have applied the same methodology to data from an Indonesian stratovolcano and its parasitic cone (Barber et al. 2023). Moreover the methodology has been adopted at two other arc volcanoes, Vulcano and Etna, Italy (Costa et al. 2023; Musu et al. 2023). The method has been extended to use trace-elements as well

as major elements, and has proved invaluable in linking zoned minerals to magmatic processes.

5.2 Future Research Directions

This work has identified several avenues for future research that would enhance our understanding of volcanic processes at Villarrica and other arc volcanoes. First and foremost, future work should focus on improving estimates of total CO_2 content in melt inclusions. As noted, the presence of carbonates within vapor bubbles likely leads to underestimates of CO_2 content, a challenge that is common to most MIs. Employing techniques such as Raman tomography or re-homogenisation methods could provide more accurate assessments of CO_2 concentrations. These improvements could significantly change our understanding of volatile cycles, magma evolution, and eruption triggers at subduction zone volcanoes.

In addition to refining volatile content measurements, further investigation into the dynamics of magma reservoirs at Villarrica is needed. This work highlights the complexity of magmatic storage, but the processes by which magma is transferred between reservoirs, remobilized, and eventually erupts are still poorly understood. Future research could focus on the timescales over which different magma batches are mixed or remobilized, and how this influences eruption timing and style. High-resolution isotopic studies of melt inclusions would be particularly useful in unraveling the diversity of magma sources and the role of subducted material in shaping volcanic systems.

Finally, understanding how different eruption sizes and styles correlate with magma plumbing system dynamics will be critical. The contrasting signatures observed between the Pucón Mafic Ignimbrite and the March 2015 eruption at Villarrica suggest that smaller eruptions may not tap into the same deep-seated magma sources as larger eruptions. Investigating these differences in more detail through both field studies and experimental research could help elucidate the factors that govern the scale of eruptions, and improve eruption forecasting models for arc volcanoes.

References

Barber, N. D., S. L. Baldwin, M. Edmonds, F. O. Boschetty, H. E. Wibowo, and A. Harijoko (2023). "Monogenetic Volcanoes as Windows into Transcrustal Mush: A Case Study of Slamet and Loyang Volcanoes, Central Java". In: *Journal of Volcanology and Geothermal Research* 444, page 107945. DOI: 10.1016/j.jvolgeores.2023.107945.

Buso, R., D. Laporte, F. Schiavi, N. Cluzel, and C. Fonquernie (2022). "High-Pressure Homogenization of Olivine-Hosted CO₂-Rich Melt Inclusions in a Piston Cylinder: Insight into the Volatile Content of Primary Mantle Melts". In: *European Journal of Mineralogy* 34.3, pages 325–349. DOI: 10.5194/ejm-34-325-2022.

Costa, S., L. Caricchi, M. Pistolesi, A. Gioncada, M. Masotta, C. Bonadonna, and M. Rosi (2023). "A Data Driven Approach to Mineral Chemistry Unveils Magmatic Processes Associated with Long-Lasting, Low-Intensity Volcanic Activity". In: *Scientific Reports* 13.1, page 1314. DOI: 10.1038/s41598-023-28370-0.

Musu, A., R. A. Corsaro, O. Higgins, C. Jorgenson, M. Petrelli, and L. Caricchi (2023). "The Magmatic Evolution of South-East Crater (Mt. Etna) during the February–April 2021 Sequence of Lava Fountains from a Mineral Chemistry Perspective". In: *Bulletin of Volcanology* 85.5, page 33. DOI: 10.1007/s00445-023-01643-2.

Van Gerve, T. D., D. A. Neave, P. Wieser, H. Lamadrid, N. Hulsbosch, and O. Namur (2024). "The Origin and Differentiation of CO2-rich Primary Melts in Ocean Island Volcanoes: Integrating 3D X-ray Tomography with Chemical Microanalysis of Olivine-Hosted Melt Inclusions from Pico (Azores)". In: *Journal of Petrology*, egae006. DOI: 10.1093/petrology/egae006.

Appendix A

Supporting Information for "Insights into Magma Storage Beneath a Frequently Erupting Arc Volcano (Villarrica, Chile) from Unsupervised Machine Learning Analysis of Mineral Compositions"

Contents of this file

1. Text S1–S3
2. Tables S1–S3
3. Figures S1–S8

Additional Supporting Information (Files uploaded separately)

1. Caption for Data Set S1

A.1 Introduction

This supporting information describes the details of assessing our clustering method, our approach to compare clustered compositions with those from Rhyolite-MELTS simulations, and our approach for error propagation using a Monte Carlo method to assess this comparison. Furthermore we include a table showing input major oxides for clustering for each mineral, tables showing the compositions and uncertainties used for the Monte Carlo error propagation, Violin and Box-plots that show the compositional differences between our identified clusters, pair plots that show the relationships between best fitting intensive variables from MELTS Simulations, and a map showing the evidence for the lateral extent of Villarrica's magmatic system.

The document also refers to an excel spreadsheet that contains the compositional data from past studies that were used in this work. All data have a reference to their original study.

A.2 Assessing Cluster Robustness

The stability of each cluster was calculated by taking a subset of each *ilr*-transformed mineral data set, performing hierarchical clustering on the subset and comparing the output to that of the complete data set. One thousand random subsets containing half the data for each mineral were selected and hierarchical clustering applied, using the same approach as for each complete mineral data set. This subsetting approach was chosen over the traditional bootstrap method which uses replacement, whereby the same data point can be selected more than once, as multiple copies of the same point will be interpreted by the clustering algorithm as 'mini clusters' (Hennig 2007). The Rand Index (RI) was used to calculate the ability of each subset to reproduce the hierarchy of clusters calculated from each complete data set:

$$\mathrm{RI}(C, K) = \frac{a + b}{C_2^{n_{\mathrm{samples}}}} \tag{A.1}$$

Where C is the cluster assignment from the complete data set and K is the assignment in each of the 1000 subsamples. a is the number of pairs of elements that are the same in C and K, and b is the number that are different. $C_2^{n_{\mathrm{samples}}}$ is the total number of possible pairs. RI varies from 0, no matches, to 1, completely matching. The average RI for olivine, feldspar and clinopyroxene are 0.88 ± 0.05, 0.92 ± 0.04, and 0.85 ± 0.05, respectively. Uncertainties are one standard deviation. These high scores suggest that the clusters are stable and not dependent on a few individual data points.

A.3 Comparing Measured and Simulated Mineral Compositions

The weighted average of the intensive variables (Temperature (T), Pressure (P), Oxygen Fugacity (fO_2) and Water Content (H_2O) were calculated as follows:

$$\bar{x}_{\text{wtd}} = \frac{\sum_{i=1}^{n} w_i x_i}{\sum_{i=1}^{n} w_i} \tag{A.2}$$

where x_i is a measurement, w_i is its weight ($i = 1 \ldots n$), the overbar indicates an average, and wtd indicates that it is weighted. In this case the weights used are measures of reliability rather than frequency, therefore the equation for the weighted standard deviation $(s_x)_{\text{wtd}}$ was:

$$(s_x)_{\text{wtd}} = \left[\left(\frac{n_{\text{eff}}}{n_{\text{eff}} - 1} \right) \frac{\sum_{i=1}^{n} w_i (x_i - \bar{x}_{\text{wtd}})^2}{\sum_{i=1}^{n} w_i} \right]^{-\frac{1}{2}} \tag{A.3}$$

where n_{eff} is the effective number of measurements, used to the correct the bias of using reliability weights:

$$n_{\text{eff}} = \frac{\left(\sum_{i=1}^{n} w_i \right)^2}{\sum_{i=1}^{n} \left(w_i^2 \right)} \tag{A.4}$$

A.4 Propagating Analytical Uncertainties

There are three major uncertainties that affect our identification of the best fitting Rhyolite-MELTS simulations: 1) the analytical uncertainty of the initial bulk composition, 2) the analytical uncertainty of the measured mineral composition we compare to the simulations and 3) uncertainties inherent in the Rhyolite-MELTS algorithms. The latter can likely be disregarded as Rhyolite-MELTS is well calibrated for basaltic to basaltic-andesite magmas (Ghiorso and Gualda 2015; Ghiorso and Sack 1995). The first two uncertainties were estimated using a Monte-Carlo approach.

To estimate the error due to the analytical uncertainty on the bulk composition used, ten thousand Rhyolite-MELTS simulations were performed using initial bulk compositions randomly selected from a normal distribution defined by the measured composition of the melt inclusion and the standard deviation as the analytical uncertainty. The bulk composition and each analyte's uncertainty are given in Table A.2

(Pioli et al. 2015). Any negative values produced by sampling the normal distribution were replaced by zero. The Rhyolite-MELTS simulations were run at the following conditions: 100 MPa, QFM and 3 wt.% H_2O. We compared the resultant simulations with the representative compositions of each mineral cluster and calculated the weighted average and standard deviation of the Temperature and Minimum Distance. Again the inverse of the Euclidean distance is the weight. The results are shown in Table A.3.

To estimate the error caused by the analytical uncertainty of the measured mineral composition we again used a Monte-Carlo approach. We generated ten thousand mineral compositions by randomly selecting a composition from a normal distribution where the mean is the first representative composition from the clustered olivine, plagioclase and clinopyroxene data sets and the uncertainty is that reported in their original study. Any negative values were replaced by zeros. Each of the ten thousand mineral compositions was compared to the original 1560 Rhyolite-MELTS simulations with a range of intensive variables. Again we calculated weighted averages and standard deviations where the weights are the inverse of the distance. The results of these simulations are shown in Table A.4.

All Monte Carlo simulations produce weighted standard deviations of comparable magnitude to the errors as commonly used traditional thermobarometers, oxybarometers and hygrometers. When both the uncertainty on the initial bulk composition and uncertainty on the mineral compositions are taken into account we find that the errors are: ca. 50 °C, 200 MPa, 0.5 log units and 1.5 wt.% H_2O. The olivine-liquid thermometers of Beattie (1993) and Putirka et al. (2007) have standard estimates of errors (SEE) of 55 °C and 30 °C; the plagioclase-liquid thermometer of Putirka (2005) has a SEE of 40 °C; and the clinopyroxene-liquid thermometer of Putirka (2008) has a SEE of 23 °C. The plagioclase-liquid barometer of Putirka (2005) has a SEE of 300 MPa and the clinopyroxene-liquid barometer of Neave and Putirka (2017) has a SEE of 140 MPa. The plagioclase-liquid hygrometer of Waters and Lange (2015) has a SEE of 0.35 wt.%. Finally the titanomagnetite-ilmenite oxybarometer of Sauerzapf et al. (2008) has a SEE of 0.4 log units.

A.5 Geochemical Database

Dataset S1. ds01.xlsx A compilation of electron probe microanalyses (EPMA) of Villarrica olivine, plagioclase, clinopyroxene and glass phases. This can be found at: `https://doi.org/10.5285/703acf75-8996-45a4-b4b3-42afca269a1c`.

Table A.1: Major element oxides that were used for cluster analysis of olivine (Ol), plagioclase (Plag) and clinopyroxene (Cpx).

Oxide	Ol	Plag	Cpx
SiO_2	yes	yes	yes
TiO_2	no	no	yes
Al_2O_3	no	yes	yes
Cr_2O_3	no	no	yes
Fe_2O_3	no	no	yes
FeO	yes	yes	yes
MnO	yes	no	yes
MgO	yes	yes	yes
CaO	yes	yes	yes
Na_2O	no	yes	yes
K_2O	no	yes	no

Table A.2: Compositions and analytical uncertainties used in Monte Carlo simulations. Bulk composition and uncertainties are from Pioli et al. (2015).

	Bulk	Ol_1	Pl_1	Cpx_1
SiO_2	50.74 ± 1.01	39.67 ± 0.79	45.56 ± 0.91	51.51 ± 1.03
TiO_2	1.04 ± 0.10			
Al_2O_3	14.68 ± 0.29		33.27 ± 0.67	2.29 ± 0.05
Cr_2O_3	0.05 ± 0.02			
FeO	8.34 ± 0.25	15.57 ± 0.47		6.16 ± 0.18
MnO	0.19 ± 0.08	0.24 ± 0.10		
MgO	7.86 ± 0.24	45.21 ± 1.36		16.88 ± 0.51
CaO	9.19 ± 0.28	0.18 ± 0.01	17.59 ± 0.53	19.04 ± 0.57
Na_2O	3.46 ± 0.35		1.26 ± 0.13	
K_2O	0.05 ± 0.01			
P_2O_5	0.21 ± 0.08			

Table A.3: Results of Monte Carlo simulations on initial bulk composition. Weighted averages and standard deviations of Temperature and Minimum Distance.

	T (°C)	Min. Dist.
Ol_1	1120±17	0.494±0.028
Pl_1	1067±12	0.409±0.058
Cpx_1	945±12	0.658±0.038

Table A.4: Results of Monte Carlo simulations on measured mineral compositions. Weighted averages and standard deviations of best fit intensive variables.

	T (°C)	P (MPa)	fO_2	H_2O (wt.%)	Min. Dist.
Ol_1	1064 ± 55	418 ± 231	0.90 ± 0.44	5.0 ± 0.9	0.092±0.140
Pl_1	1016 ± 38	200 ± 89	−0.50 ± 0.32	5.0 ± 1.2	0.030±0.110
Cpx_1	1032 ± 51	82 ± 141	1.67 ± 0.53	0.9 ± 1.4	0.021±0.061

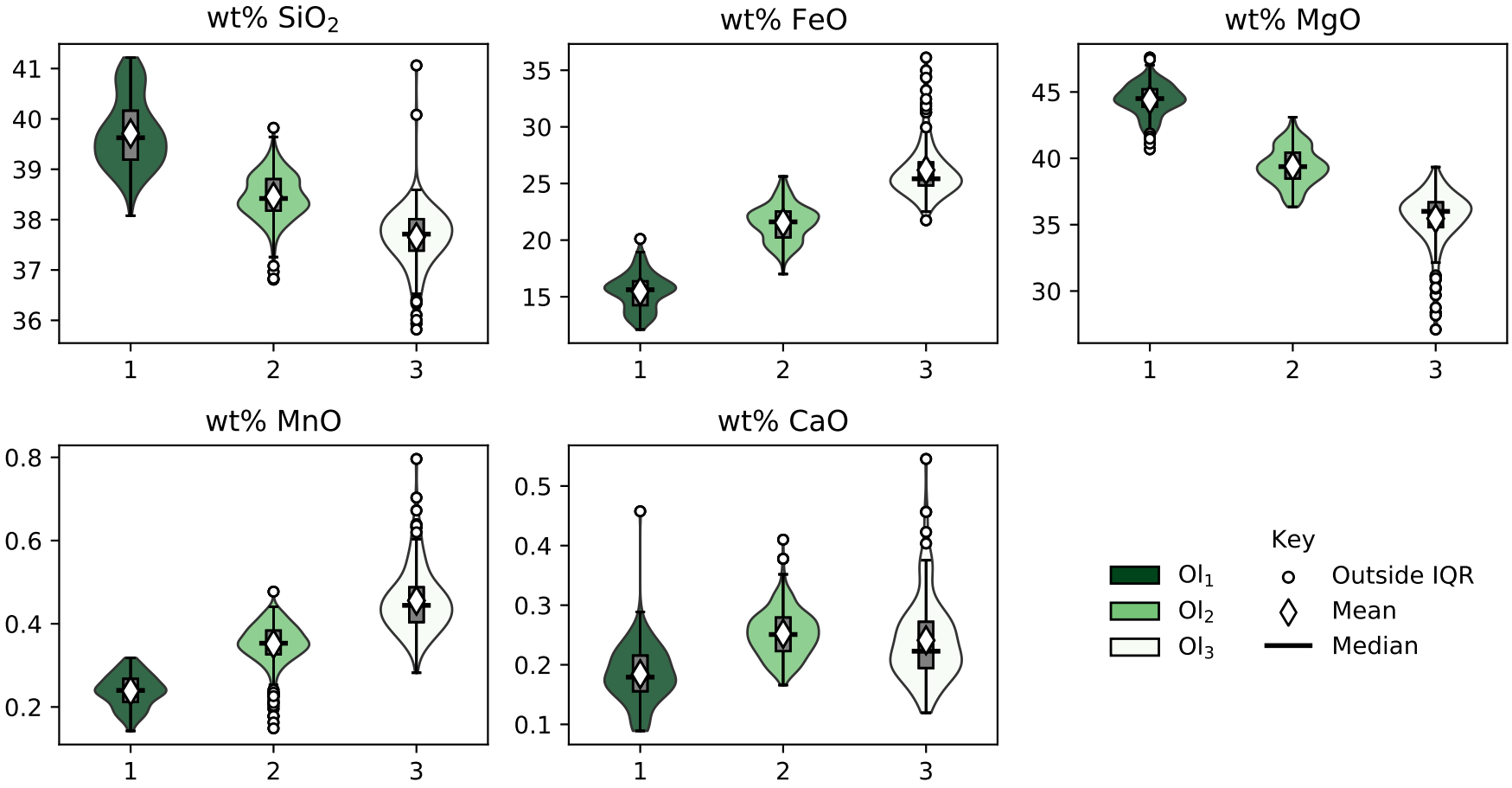

Figure A.1: Violin and box plots showing the compositional differences between each olivine cluster, shown in wt% oxide.

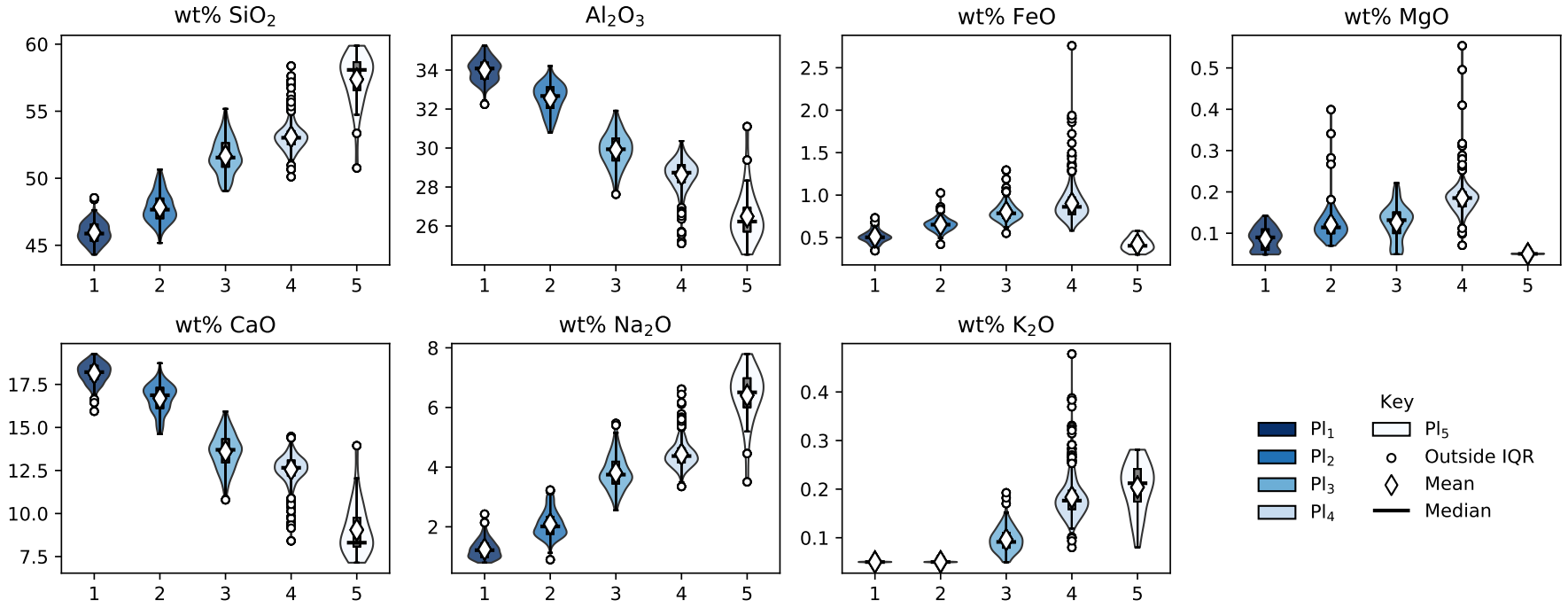

Figure A.2: Violin and box plots showing the compositional differences between each plagioclase cluster, shown in wt% oxide.

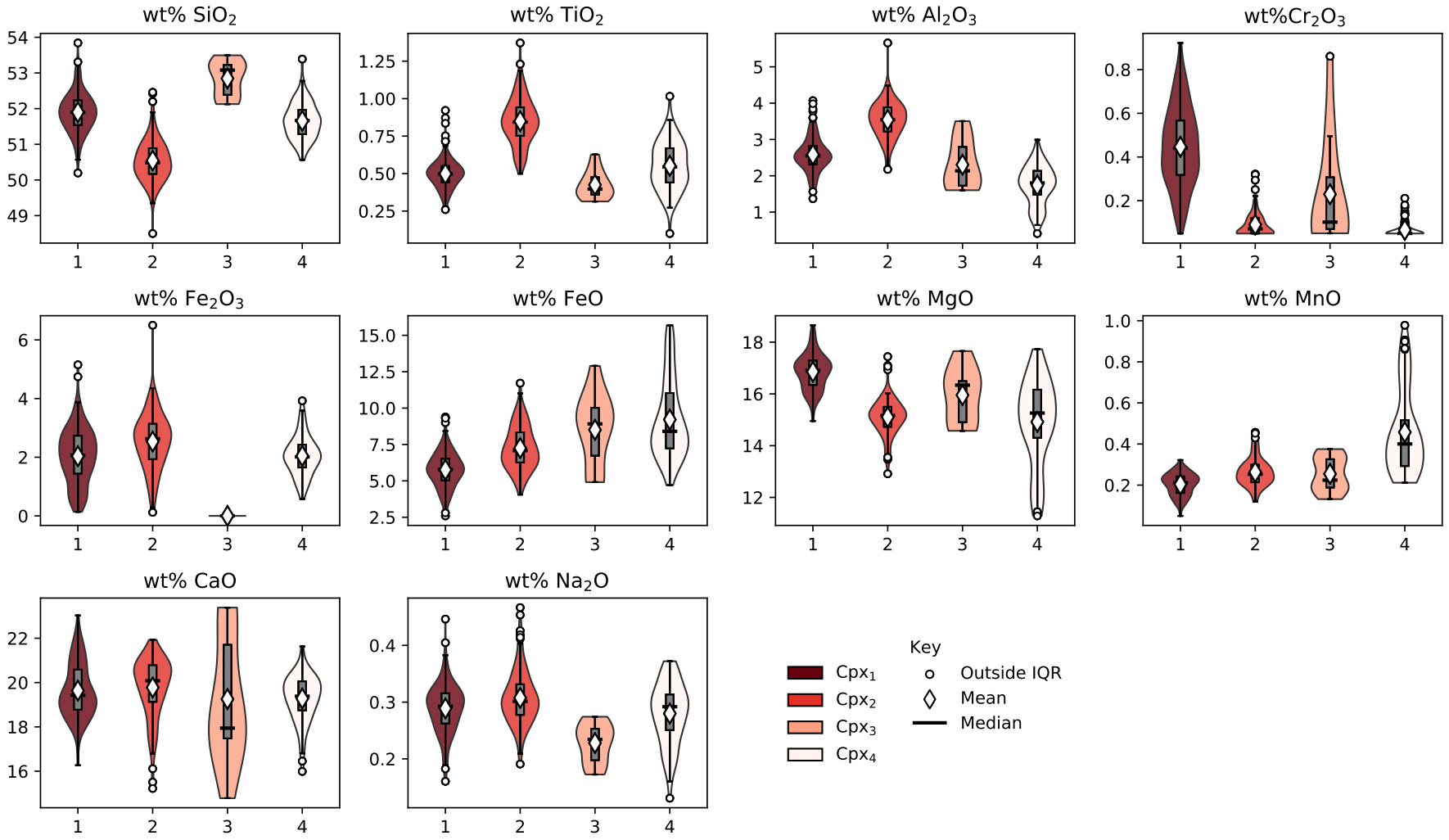

Figure A.3: Violin and box plots showing the compositional differences between each clinopyroxene cluster, shown in wt% oxide.

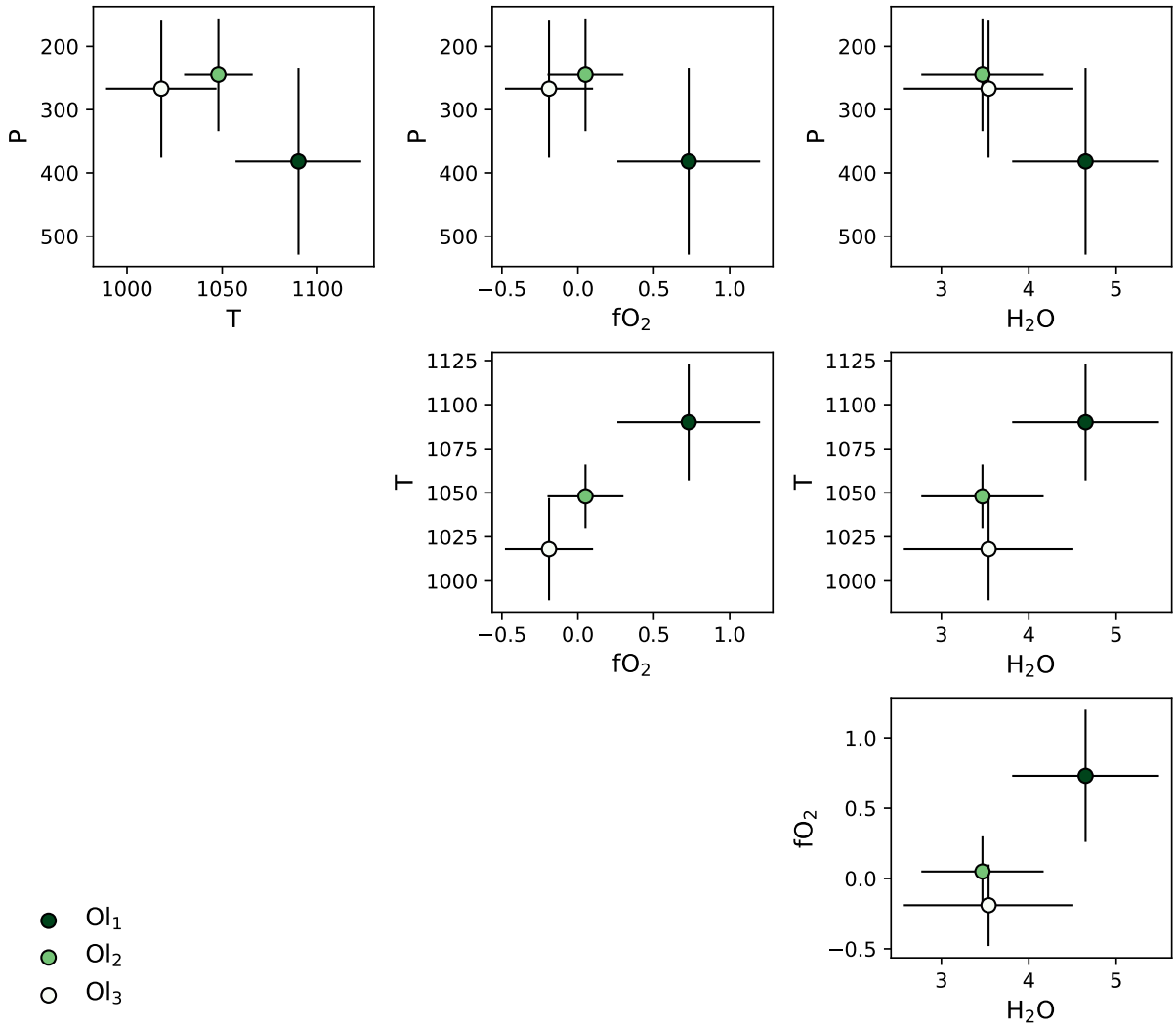

Figure A.1: Pair plots showing how the weighted average best fitting conditions for each olivine cluster covary.

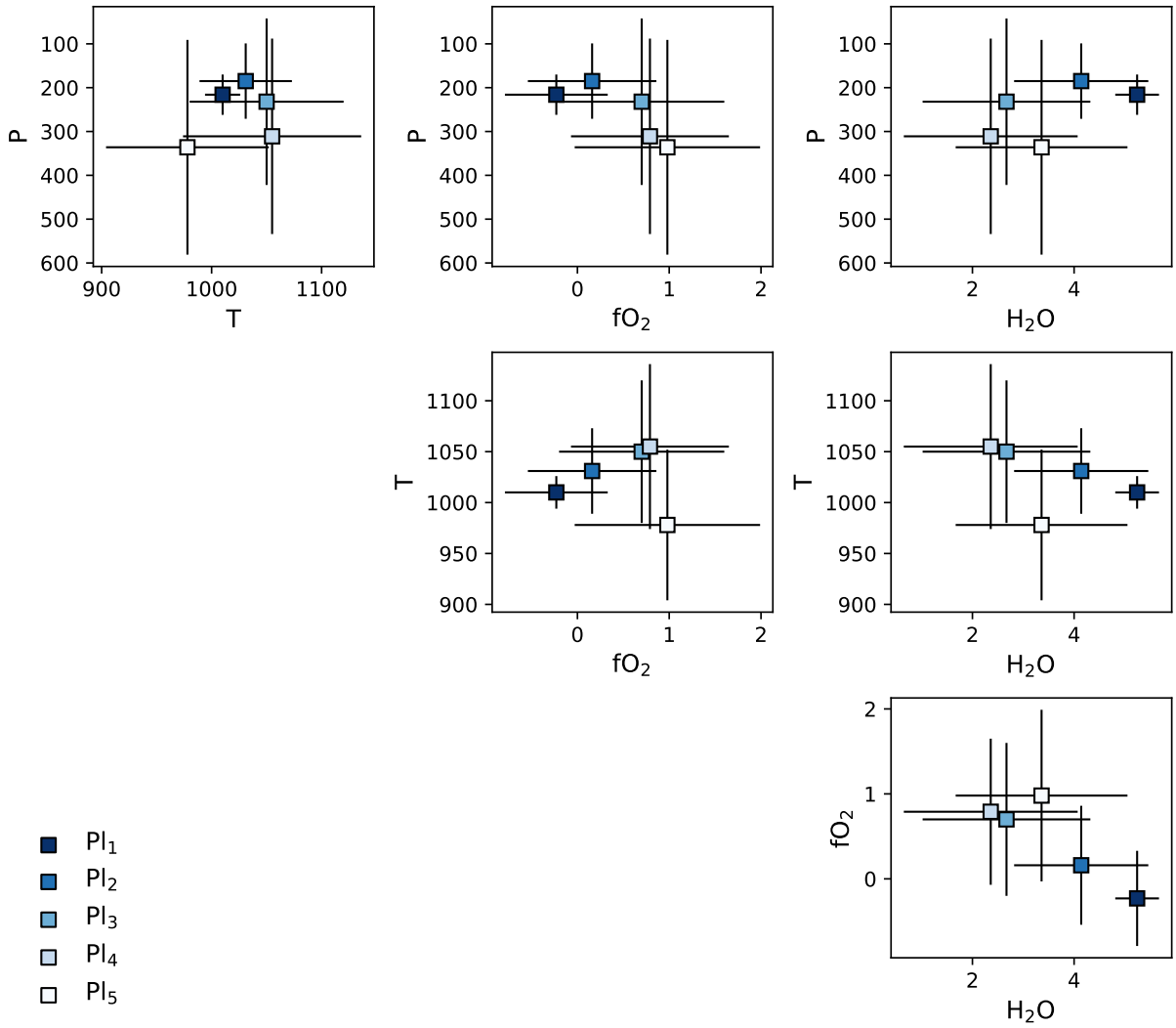

Figure A.2: Pair plots showing how the weighted average best fitting conditions for each plagioclase cluster covary.

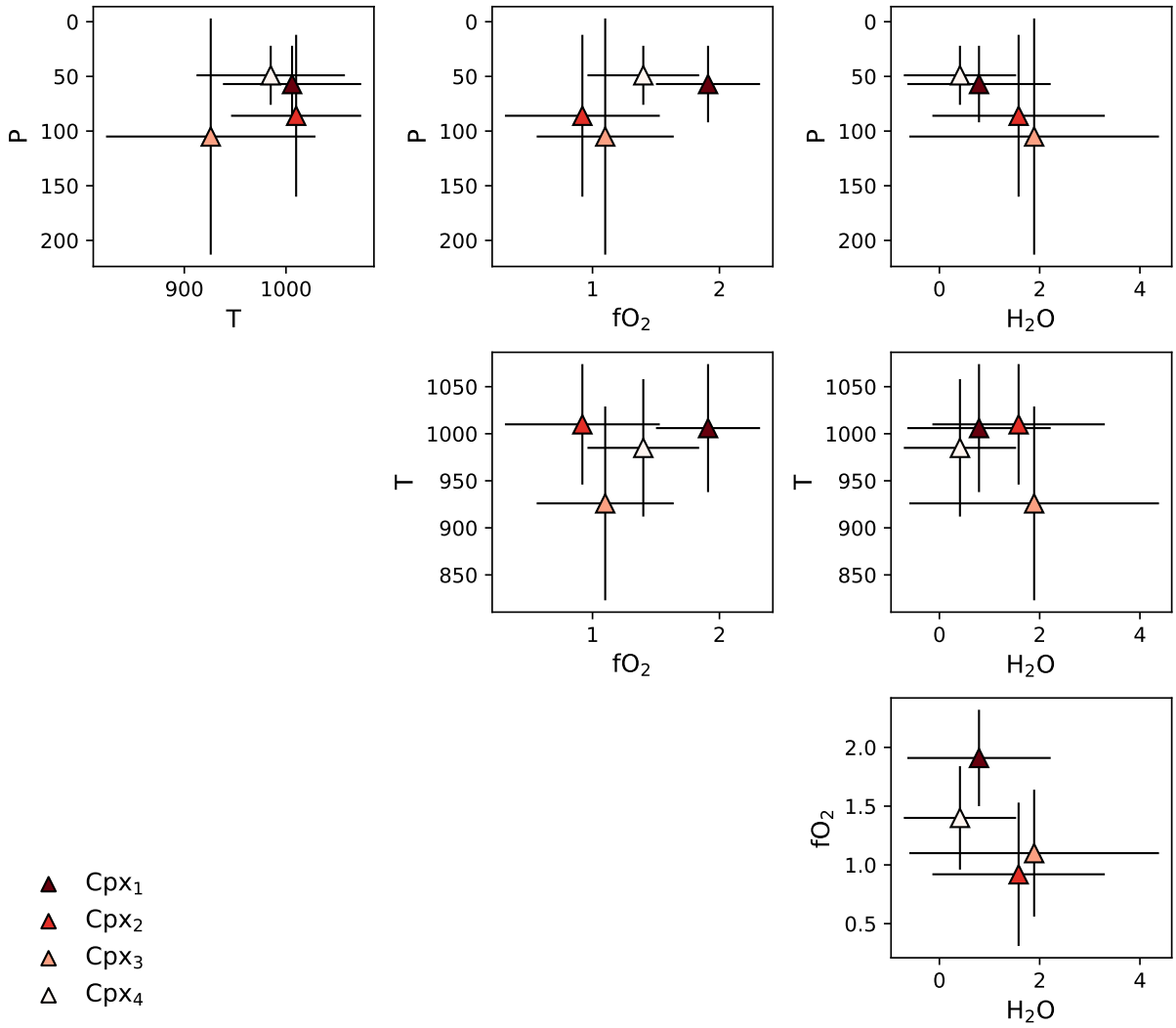

Figure A.3: Pair plots showing how the weighted average best fitting conditions for each clinopyroxene cluster covary.

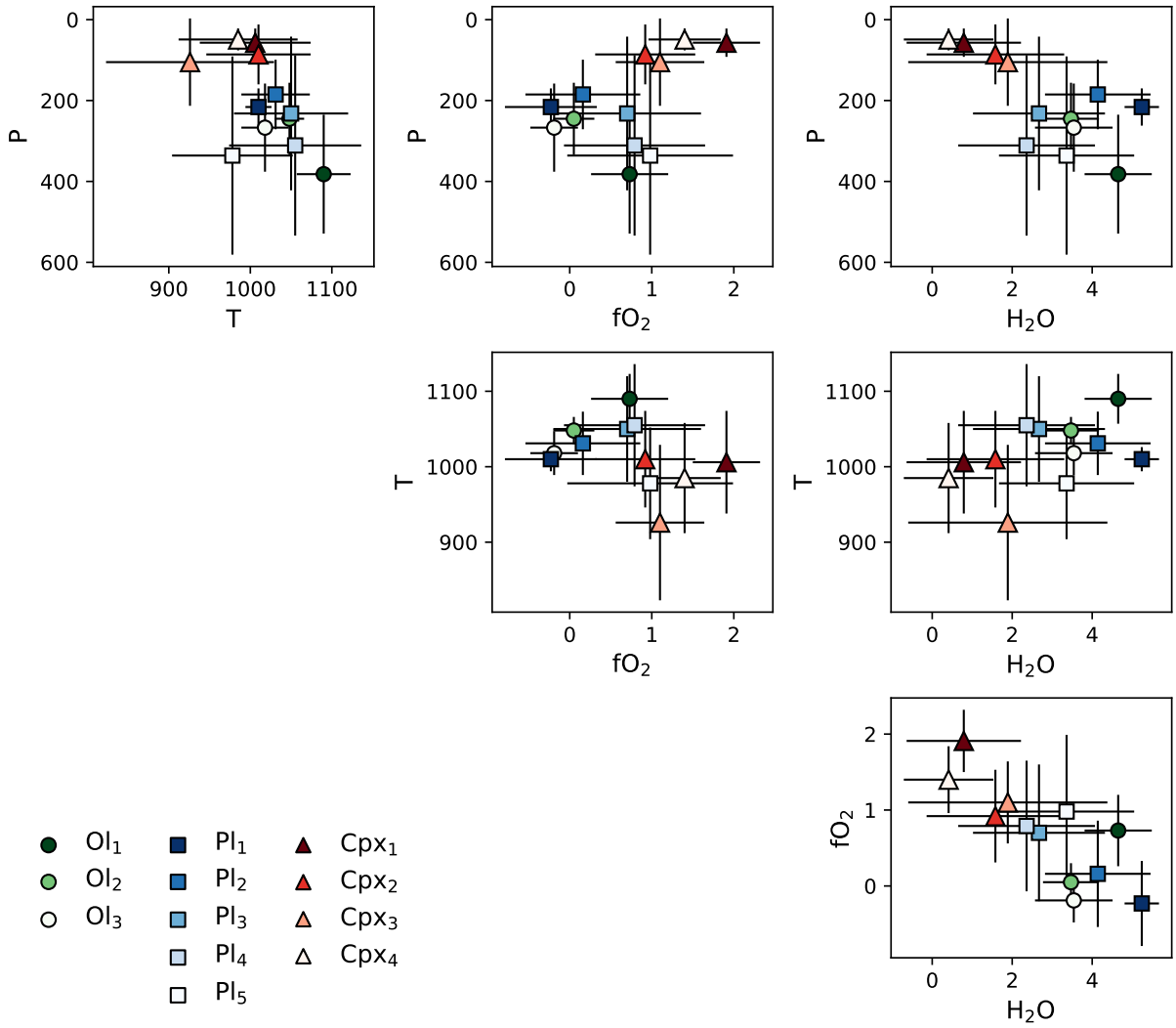

Figure A.4: Pair plots showing how the weighted average best fitting conditions for each cluster of all three minerals covary.

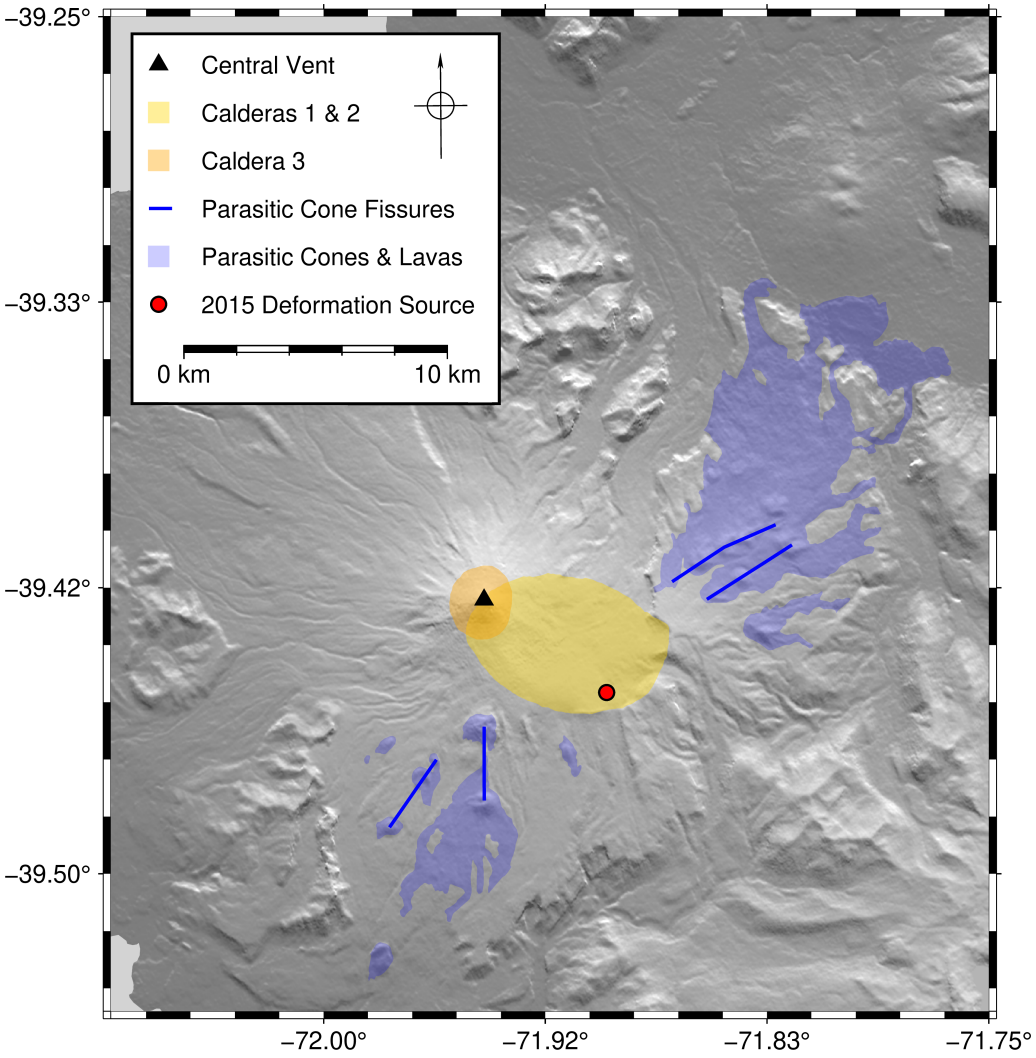

Figure A.5: Map showing location of features that imply laterally extensive magmatic processing at Villarrica volcano. The location of the central vent, calderas and parasitic cones, lavas and fissures are from *Geología del volcán Villarrica, Regiones de La Araucanía y de Los Lagos.* (2006). The location of the deformation source is from Delgado et al. (2017).

References

Beattie, P. (1993). "Olivine-Melt and Orthopyroxene-Melt Equilibria". In: *Contributions to Mineralogy and Petrology* 115.1 (1), pages 103–111. DOI: 10.1007/BF00712982.

Delgado, F., M. E. Pritchard, S. Ebmeier, P. González, and L. Lara (2017). "Recent Unrest (2002–2015) Imaged by Space Geodesy at the Highest Risk Chilean Volcanoes: Villarrica, Llaima, and Calbuco (Southern Andes)". In: *Journal of Volcanology and Geothermal Research* 344, pages 270–288. DOI: 10.1016/j.jvolgeores.2017.05.020.

Geología del volcán Villarrica, Regiones de La Araucanía y de Los Lagos. (2006). In collaboration with H. Moreno and J. Clavero. Servicio Nacional de Geología y Minería.

Ghiorso, M. S. and G. A. R. Gualda (2015). "An H2O–CO2 Mixed Fluid Saturation Model Compatible with Rhyolite-MELTS". In: *Contributions to Mineralogy and Petrology* 169.6 (6), page 53. DOI: 10.1007/s00410-015-1141-8.

Ghiorso, M. S. and R. O. Sack (1995). "Chemical Mass Transfer in Magmatic Processes IV. A Revised and Internally Consistent Thermodynamic Model for the Interpolation and Extrapolation of Liquid-Solid Equilibria in Magmatic Systems at Elevated Temperatures and Pressures". In: *Contributions to Mineralogy and Petrology* 119.2-3 (2-3), pages 197–212. DOI: 10.1007/BF00307281.

Hennig, C. (2007). "Cluster-Wise Assessment of Cluster Stability". In: *Computational Statistics & Data Analysis* 52.1 (1), pages 258–271. DOI: 10.1016/j.csda.2006.11.025.

Neave, D. A. and K. D. Putirka (2017). "A New Clinopyroxene-Liquid Barometer, and Implications for Magma Storage Pressures under Icelandic Rift Zones". In: *American Mineralogist* 102.4 (4), pages 777–794. DOI: 10.2138/am-2017-5968.

Pioli, L., L. Scalisi, L. Costantini, A. Di Muro, C. Bonadonna, and J. Clavero (2015). "Explosive Style, Magma Degassing and Evolution in the Chaimilla Eruption, Villarrica Volcano, Southern Andes". In: *Bulletin of Volcanology* 77.11 (11), page 93. DOI: 10.1007/s00445-015-0976-1.

Putirka, K. D. (2005). "Igneous Thermometers and Barometers Based on Plagioclase + Liquid Equilibria: Tests of Some Existing Models and New Calibrations". In: *American Mineralogist* 90.2-3 (2-3), pages 336–346. DOI: 10.2138/am.2005.1449.

– (2008). "Thermometers and Barometers for Volcanic Systems". In: *Reviews in Mineralogy and Geochemistry* 69.1 (1), pages 61–120. DOI: 10.2138/rmg.2008.69.3.

Putirka, K. D., M. Perfit, F. Ryerson, and M. G. Jackson (2007). "Ambient and Excess Mantle Temperatures, Olivine Thermometry, and Active vs. Passive Upwelling". In: *Chemical Geology* 241.3-4 (3-4), pages 177–206. DOI: 10.1016/j.chemgeo.2007.01.014.

Sauerzapf, U., D. Lattard, M. Burchard, and R. Engelmann (2008). "The Titanomagnetite–Ilmenite Equilibrium: New Experimental Data and Thermo-oxybarometric Application to the Crystallization of Basic to Intermediate Rocks†". In: *Journal of Petrology* 49.6 (6), pages 1161–1185. DOI: 10.1093/petrology/egn021.

Waters, L. E. and R. A. Lange (2015). “An Updated Calibration of the Plagioclase-Liquid Hygrometer-Thermometer Applicable to Basalts through Rhyolites”. In: *American Mineralogist* 100.10 (10), pages 2172–2184. DOI: 10.2138/am-2015-5232.

Appendix B

Analytical Methods

B.1 Micro-Raman Spectroscopy

B.1.1 Analytical Setup

The CO_2 density of melt-inclusion-hosted vapour bubbles was calculated from measurements made using micro-Raman Spectroscopy. Spectra were collected using a Renishaw InVia confocal micro-Raman spectrometer at the Bragg Centre, University of Leeds. This was equipped with a Renishaw 532 nm solid-state laser with a power of 50 mW, a Peltier-cooled CCD detector of 1040×256 pixels and a Leica DM 2700M optical microscope. A grating with 2400 lines·mm^{-1}, a 40 µm slit aperture, and a 50× microscope objective were used. Daily calibration was performed by measuring the offset from the known value of 520.7 cm^{-1} peak of Si (reference), and the laser line (532.5 nm). Raman spectra were collected using a single spectral window centred on 1250 cm^{-1}, and ranging from 439–1942 cm^{-1}. 5% laser power was selected from within the Renishaw software to limit the effects of laser heating (DeVitre et al. 2023). A laser intensity meter (ThorLabs S120C connected to a PM100D reader) was placed under the laser to measure the incidence intensity as power is reduced as the laser passes through the various parts of the machine. For a 50× objective and 5% laser power, an incidence power of 1.15 mW was measured.

The host crystals, mounted on glass slides, were placed on top of a Linkam PE120 Peltier-heated stage linked to a T96 Peltier LinkPad controller. The temperature was set to 37 °C to ensure inclusions were kept above the CO_2 supercritical point of 33.1 °C (DeVitre et al. 2021). The temperature of each crystal was measured with a temperature probe prior to each analysis to confirm it had equilibrated with the

Peltier stage. Additionally, the ambient air temperature was frequently measured to ensure stability, as the ambient temperature has been shown to have an impact on Raman peak locations (Lamadrid et al. 2017). The air temperature did not vary by more than ±0.5 °C over the analytical sessions.

B.1.2 Peak Fitting

Three acquisitions, each consisting of three 30–120 s accumulations, were taken to assess the reproducibility of the acquisitions. All peak fitting was performed using the Python library DiadFit (Wieser and DeVitre 2023). The spectral background was removed by fitting a 2nd order polynomial to regions outside the diad. Then, a pseudo-Voigt, a weighted sum of both a Lorentzian and a Gaussian model, the model was then fit to each peak in the CO_2 diad, using a least squares approach (Levenberg-Marguardt algorithm Moré 1977) directly estimating the peak centre and associated uncertainty. The difference between the peak centres of the two diads is then their separation ($\Delta^{\text{Measured}}_{CO_2}$).

B.1.3 Drift Correction

The position of Ne lines from a Neon lamp both before and after the CO_2 diad split was measured. This was done similarly as above for the diad separation. The Ne spectral lines at 1116.20 cm^{-1} and 1446.68 cm^{-1} were used as these have high intensities and bracket the CO_2 diad peaks. The background was removed by fitting a 2nd order polynomial to the region surrounding the peaks. Then a pseudo-Voigt, a weighted sum of both a Lorentzian and a Gaussian model, was fit for each peak, providing a peak centre and uncertainty from the regression. The separation of the Ne lines that bracket the CO_2 diad were used to correct for drift (e.g., Lamadrid et al. 2017; Lin et al. 2007; Wieser et al. 2021):

$$\Delta^{\text{Corrected}}_{CO_2} = \frac{\Delta^{\text{Theoretical}}_{\text{Ne}}}{\Delta^{\text{Measured}}_{\text{Ne}}} \times \Delta^{\text{Measured}}_{CO_2} \tag{B.1}$$

Where $\Delta^{\text{Theoretical}}_{Ne}$ is the Raman shift of Ne lines (cm^{-1}) from The National Institute of Standards and Technology (`https://physics.nist.gov/PhysRefData/ASD/lines_form.html`), which were converted from wavelength in air to Raman shift using the following equation (Lin et al. 2007):

$$\Delta_\nu = \left(\frac{10^7}{\lambda_0} - \frac{10^7}{\lambda_1}\right) \tag{B.2}$$

Where λ_0 is the theoretical Raman shift of Ne lines in nm, and λ_1 is the excitation wavelength of the laser, which was measured prior to, and after, each session and averaged 532.051 nm (1σ=0.003, n=12).

B.1.4 Low-Density CO_2 Densimeter

Below $0.20\,g{\cdot}cm^{-3}$ the relationship between the CO_2 diad split and the density of the CO_2 measured has been shown to be linear (DeVitre et al. 2021; Lamadrid et al. 2017). Therefore, I calibrated a densimeter for our spectrometer using repeated measurements of synthetic quartz-hosted pure-CO_2 inclusions whose density had been previously measured on a Raman spectrometer that had been fully calibrated using an optical cell (Lamadrid et al. 2017; Wieser et al. 2021). Each of the 15 standards were measured three times to allow reproducibility to be assessed. Any resultant fitted diads that had poorly defined peak centres or deviated significantly from other measurements of the same standard were discarded. 55 good analyses were then used to construct the densimeter line (Figure B.1a). This was done by accounting for both the uncertainties in standard densities, and the uncertainties propagated through the fitting and drift-correction processes. This was done by using the EV_2 regression method (Tellinghuisen 2020). Accounting for both x and y errors produces the best estimates of fit parameter uncertainties (Tellinghuisen 2020), which are then propagated when calculating unknown CO_2 densities. A comparison with other published densimeters (Figure B.1b) shows that the calculated densimeter lies fairly centrally supporting its validity.

B.1.5 Volume Estimation and CO_2 Mass

The volume of each vapour bubble and MI were calculated from optical photographs. For each VB and MI a best fit ellipse was found. To calculate the mass of CO_2 in each vapour bubble I estimated their volume by measuring the short and long axes of best-fit ellipses. Each image was focused to show the maximum diameter of the VB. I estimated the third dimension by taking the arithmetic mean of the two measured dimensions, as recommended in Tucker et al. (2019). I also measured melt inclusions in the same way. The maximum error in volume calculation occurs when the MI is cut obliquely to its long axis and at a depth far from its long axis (Figure?). In almost all cases I aligned the MIs with their long axes roughly perpendicular to the polished surface. Furthermore, I focused on each image to ensure that the maximum extent of MI could be ascertained from the image. This should reduce the uncertainty in volume estimation.

The resolution of the images taken through a 40× objective was $0.1\,\mu m{\cdot}pixel^{-1}$. This was taken to be the uncertainty on the measured diameters of both vapour bubbles and melt inclusions. Vapour bubble

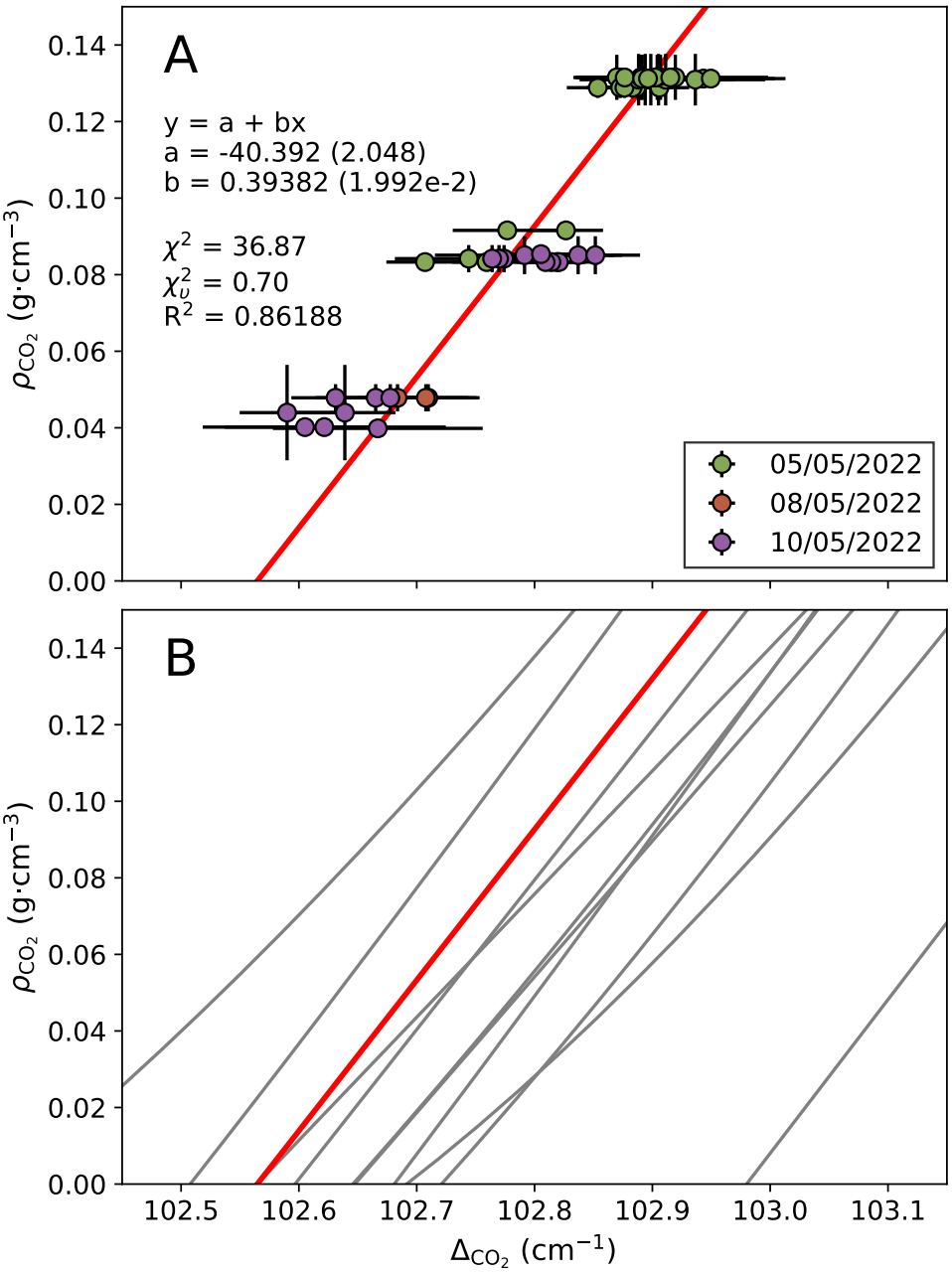

Figure B.1: A) Low-density CO_2 densimeter calculated from repeat analyses (n=55) of synthetic CO_2 inclusions with known densities. Calculated using the EV_2 regression method that takes into account both standard uncertainties and uncertainties in measured values (error bars). χ^2, chi-square statistic. χ^2_ν, reduced chi-square statistic. R^2, coefficient of determination. B) Comparison of densimeter developed in this study (red line) with literature densimeters (grey lines; DeVitre et al. 2021; Fall et al. 2011; Kawakami et al. 2003; Lamadrid et al. 2017; Rosso and Bodnar 1995; Song et al. 2009; Wang et al. 2019; Wang et al. 2011; Wieser et al. 2021; Yamamoto and Kagi 2006).

CO_2-densities were then converted into masses using the following equation:

$$[CO_2]^{VB} = 10^6 \times \frac{\rho_{CO_2} \cdot V_{VB}}{\rho_{Melt} \cdot V_{Melt}} \tag{B.3}$$

where V_{VB} is the vapour bubble volume and ρ_{CO_2} is the vapour bubble CO_2 density. ρ_{Melt} is the density of the PEC-corrected melt inclusion glass composition calculated using DensityX (Iacovino and Till 2018). The total CO_2 concentration of the MI is then calculated by summing the CO_2 of the vapour bubble and that of the silicate glass.

B.2 Secondary Ionisation Mass Spectrometry

B.2.1 Analytical Procedure

I measured concentrations of C, light (H, Li, F, Cl, B), and heavy trace elements in 100? melt inclusions using the Cameca IMS-7f-GEO at the NERC Edinburgh Ion Micro-Probe Facility (EIMF), over two sessions (26/09/22–29/09/22 and 31/10/22–03/11/22). Measurement of carbon, light and heavy trace element concentrations required three separate analytical setups to avoid magnet hysteresis, which are described in detail below. The electron gun was turned off for all analyses. Element concentrations and counting statistics were calculated using the in-house JCION software. Absolute intensities were calculated by normalising the intensities to Si (as measured using ^{30}Si) which was subsequently determined by electron microprobe analysis. Carbon, light and heavy trace element analyses were obtained on the same spots within melt inclusions.

B.2.2 Carbon Concentrations

A $^{16}O^{2-}$ primary ion beam generated by a Hyperion source with 5 nA current and an impact energy of 15 keV was used to sputter the sample surface by Kohler illumination, resulting in a spot size of 10 µm × 15 µm. Positive secondary ions were extracted at 4.5 kV, using energy filtering with an energy offset of 50 ± 20 eV to reduce transfer of ions into the secondary column. The image field (max. area) was 60 µm. Prior to each analysis, the secondary ion beam was centred in the field aperture, and the mass calibration was updated by determining the centre of the $^{28}Si^{2+}$ peak using an automated routine. During this period, the analytical area was sputtered for four minutes with a 15 µm raster using a primary beam current of 5.18 nA to remove surface contamination. For C analyses, the mass spectrometer was set to a mass resolution of 2997 (M/ΔM) to avoid interference of $^{24}Mg^{2+}$ on ^{12}C.

The first 7 cycles of each 15-cycle run were discarded to avoid the effects of surface contamination that survived the sputtering process. Count times for each analysed element can be found in Table B.1. The mean values of each run were compared to a calibration curve calculated daily from known standards (Figure B.2). The calibration curve was constructed by measuring M40-2, N72-2, M36-2, M5-2, M10-2, M47-2 glass standards with variable carbon contents (Hauri et al. 2002; Shishkina et al. 2010). The background C signal was determined through analysis of the nominally C-free N72-2 glass standard.

B.2.3 Water and Light Trace Element Concentrations

Water and light trace element concentrations were analysed using the same analytical conditions as above with the following differences. A different energy offset of 75 ± 25 eV was applied. The image field (max. area) was 100 µm. The mass spectrometer was set to a mass resolution of 399 (M/ΔM). The analytical area was sputtered for one minute with a 15 µm raster using a primary beam current of 5.07 nA to remove surface contamination. The first 5 cycles of each 10-cycle run were discarded. I measured the concentration of the following elements: $^{1}H^{+}$, $^{7}Li^{+}$, $^{11}B^{+}$, $^{19}F^{+}$, $^{24}Mg^{2+}$, $^{30}Si^{+}$, $^{35}Cl^{+}$ and $^{40}Ca^{2+}$. Count times for each analysed element can be found in Table B.2. For water, the mean values were compared to a calibration curve calculated daily from known standards (Figure B.3). Again, the calibration curve was constructed by measuring M40-2, N72-2, M36-2, M5-2, M10-2, M47-2 glass standards with variable water contents (Hauri et al. 2002; Shishkina et al. 2010). The background H signal was determined through analysis of the nominally H-free N72-2 glass standard. The concentration of other light elements were calculated relative to the T1G-2b glass standard (Jochum et al. 2006).

B.2.4 Heavy Trace Elements Concentrations

Heavy trace element concentrations were obtained using a secondary accelerating voltage of 4500 V with 75 eV offset and the image field (max. area) was 100 µm. The mass spectrometer was set to a mass resolution of 399 (M/ΔM). The analytical area was sputtered for one minute with a 15 µm raster using a primary beam current of 5.07 nA to remove surface contamination. I measured the concentration of the following elements: $^{30}Si^{+}$, $^{88}Si^{+}$, $^{90}Zr^{+}$, $^{93}Nb^{+}$, $^{138}Ba^{+}$, $^{139}La^{+}$, $^{140}Ce^{+}$ $^{141}Pr^{+}$, $^{143}Nd^{+}$, $^{149}Sm^{+}$, $^{153}Eu^{+}$, $^{157}Gd^{+}$, $^{159}Tb^{+}$, $^{161}Dy^{+}$, $^{162}Dy^{+}$, $^{165}Ho^{+}$, $^{166}Er^{+}$, $^{169}Tm^{+}$, $^{171}Yb^{+}$, $^{171}Lu^{+}$, $^{232}Th^{+}$ and $^{238}U^{+}$. Count times for each analysed element can be found in Table B.3. The heavy trace element concentrations were calculated relative to an MPI-DING glass standard, GSD-1 (Jochum et al. 2006).

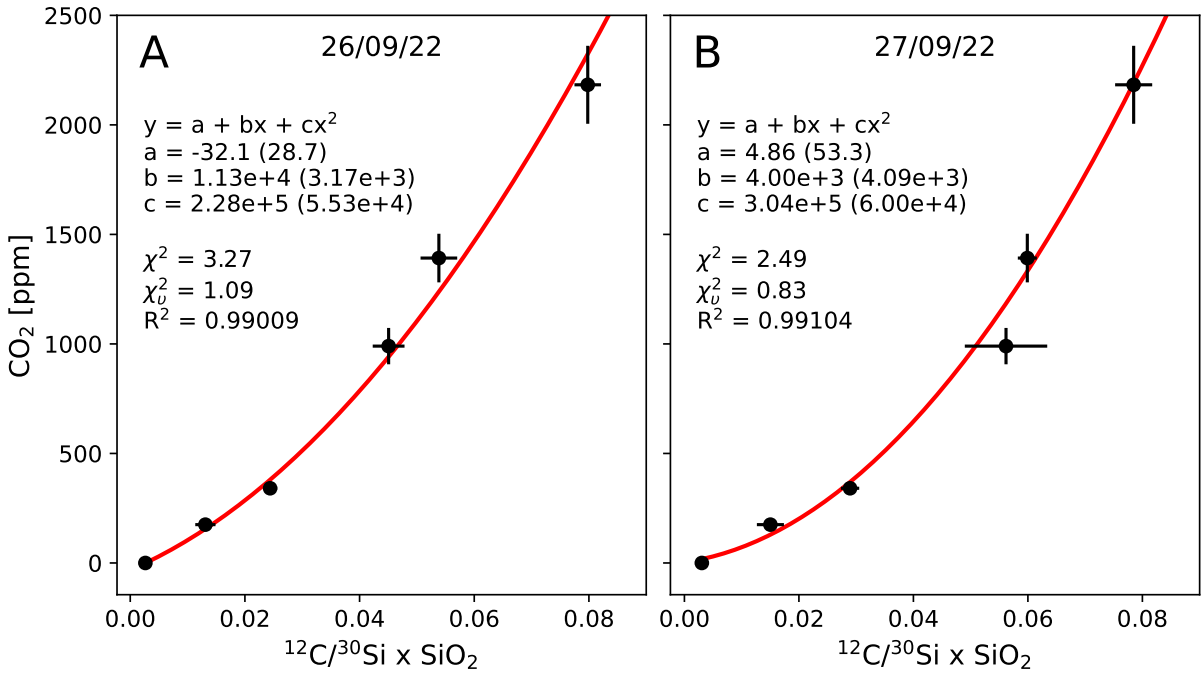

Figure B.2: Background-corrected calibration curves for basaltic glass standards (Hauri et al. 2002; Shishkina et al. 2010) used to convert normalised count ratios to CO_2 for sessions on (A) 26/09/2022, and (B) 27/09/2022. Error bars show propagated 1σ uncertainties. 1σ uncertainties in the best-fit parameter estimates shown in brackets. χ^2, chi-square estimate. χ^2_υ, reduced chi-square estimate. R^2, coefficient of determination.

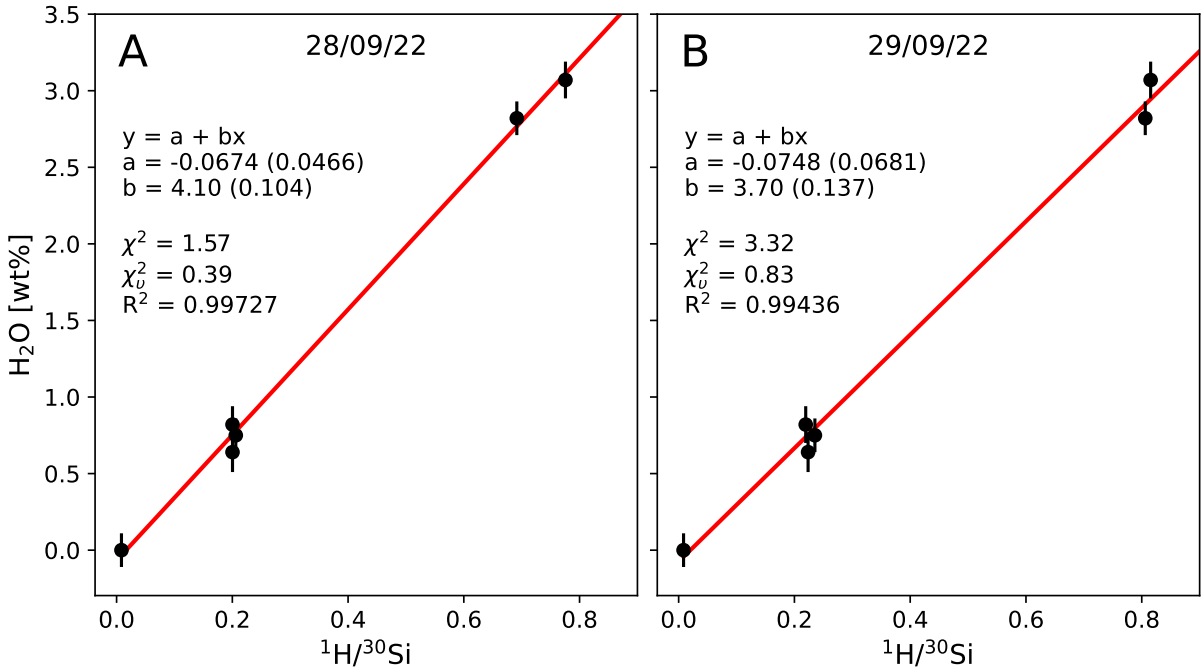

Figure B.3: Background-corrected calibration curves for basaltic glass standards (Hauri et al. 2002; Shishkina et al. 2010) used to convert normalised count ratios to H_2O for sessions on (A) 28/09/2022, and (B) 29/09/2022. Error bars show propagated 1σ uncertainties. 1σ uncertainties in the best-fit parameter estimates shown in brackets. χ^2, chi-square estimate. χ^2_υ, reduced chi-square estimate. R^2, coefficient of determination.

Table B.1: Carbon acquisition counting statistics, count and wait times for SIMS analysis.

Isotope	Mass/Q	2σ (µg·g^{-1})	Count Time (s)	Wait Time (s)
$^{24}Mg^{2+}$	11.99	22.28	4.96	0.96
$^{12}C^{+}$	12.00	1.51	10.00	0.56
$^{40}Ca^{2+}$	19.98	259	2.00	0.96
$^{30}Si^{+}$	29.97	287	2.00	0.96

Table B.2: Light trace element counting statistics, count and wait times for SIMS analysis.

Isotope	Mass/Q	2σ (µg·g^{-1})	Count Time (s)	Wait Time (s)
$^{1}H^{+}$	1.00	82.26	4.96	0.96
$^{7}Li^{+}$	7.01	0.26	2.96	0.48
$^{11}B^{+}$	11.01	0.66	4.96	0.24
$^{19}F^{+}$	18.99	28.23	10.00	0.24
$^{24}Mg^{2+}$	25.98	109	2.00	0.24
$^{30}Si^{+}$	29.97	798	2.00	0.24
$^{35}Cl^{+}$	34.96	37.51	4.96	0.24
$^{40}Ca^{2+}$	43.96	269	4.96	0.24

Table B.3: Heavy trace element counting statistics, count and wait times for SIMS analysis.

Isotope	Mass/Q	2σ (µg·g^{-1})	Count Time (s)	Wait Time (s)
$^{30}Si^{+}$	29.97377	1814	2.00	2.96
$^{88}Sr^{+}$	87.90563	6.66	2.00	0.64
$^{90}Zr^{+}$	89.90471	2.67	2.00	0.56
$^{93}Nb^{+}$	92.90638	0.26	4.96	0.56
$^{138}Ba^{+}$	137.9052	6.17	2.00	0.56
$^{139}La^{+}$	138.9064	0.80	2.00	0.56
$^{140}Ce^{+}$	139.9054	1.39	2.00	0.56
$^{141}Pr^{+}$	140.9077	0.29	4.96	0.56
$^{143}Nd^{+}$	142.9098	2.03	4.96	0.56
$^{149}Sm^{+}$	148.9172	0.73	8.00	0.56
$^{153}Eu^{+}$	152.9212	0.21	4.96	0.56
$^{157}Gd^{+}$	156.9240	1.19	4.96	0.56
$^{159}Tb^{+}$	158.9254	0.14	4.96	0.56
$^{161}Dy^{+}$	160.9269	0.69	4.96	0.56
$^{165}Ho^{+}$	164.9303	0.18	4.96	0.56
$^{166}Er^{+}$	165.9303	0.59	4.96	0.56
$^{169}Tm^{+}$	168.9342	0.11	4.96	0.56
$^{171}Yb^{+}$	170.9363	0.62	8.00	0.56
$^{175}Lu^{+}$	174.9408	0.10	8.00	0.56
$^{232}Th^{+}$	232.0381	0.26	8.00	0.56
$^{238}U^{+}$	238.0508	0.18	8.00	0.56

Table B.4: CO_2 abundances in basalt glass standards from SIMS and estimates of precision and accuracy based on repeat analyses.

Standard	R (µg·g^{-1})	$\bar{x}$ (µg·g^{-1})	2σ (µg·g^{-1})	$2\sigma_{\bar{x}}$ (µg·g^{-1})	%P	%A	n
M5[1]	990 (83)	1180	231	163	19.57	19.18	2
M10[1]	341 (27)	570	36	26	6.33	67.24	2
M36[1]	1392 (111)	1406	62	44	4.42	0.99	2
M40[1]	2183 (178)	1975	243	172	12.30	-9.51	2
M47[1]	175 (14)	261	12	8	4.58	49.17	2
N72[1]	0	0	0	0			2
GSD-1G	-	4	3	2			2
BCR2-G	-	-3	6	4			2
T1-G	-	-42	28	27			2

[1]Shishkina et al. (2010). R is the standard reference value, the 2σ value is given in brackets. $\bar{x}$ is the mean; 2σ the standard deviation; $2\sigma_{\bar{x}}$ the standard error of the mean; %P the percentage relative 2σ standard deviation; %A is the average percentage accuracy.

Table B.5: H_2O abundances in basalt glass standards from SIMS and estimates of precision and accuracy based on repeat analyses.

Standard	R (wt.%)	$\bar{x}$ (wt.%)	2σ (wt.%)	$2\sigma_{\bar{x}}$ (wt.%)	%P	%A	n
M5[1]	0.64 (0.13)	0.78	0.02	0.012	2.20	21.8	2
M10[1]	0.75 (0.11)	0.81	0.04	0.029	5.04	8.2	2
M36[1]	2.82 (0.11)	2.83	0.20	0.144	7.20	0.4	2
M40[1]	3.07 (0.12)	3.01	0.21	0.150	7.05	-1.8	2
M47[1]	0.82 (0.12)	0.77	0.00	0.003	0.54	-5.9	2
N72[1]	0.00	0.00	0.00	0.000			2
GSD-1G	-	0.01	0.01	0.010			2
BCR2-G	-	0.03	0.01	0.006			2
T1-G	-	0.00	0.04	0.025			2

[1]Shishkina et al. (2010). R is the standard reference value. $\bar{x}$ is the mean; 2σ the standard deviation; $2\sigma_{\bar{x}}$ the standard error of the mean; %P the percentage relative 2σ standard deviation; %A is the average percentage accuracy.

Table B.6: Light trace element abundances in basalt glass standards from SIMS and estimates of precision and accuracy based on repeat analyses.

Element	Standard	R (µg·g^{-1})	$\bar{x}$ (µg·g^{-1})	2σ (µg·g^{-1})	$2\sigma_{\bar{x}}$ (µg·g^{-1})	%P	%A	n
Li	GSD-1G[1]	44.7 (1.9)	40.49	1.34	0.950	3.32	-9.4	2
	BCR2-G[1]	9.4 (0.2)	8.19	0.26	0.183	3.16	-12.9	2
B	GSD-1G[2]	65 (0.6)	70.94	28.67	20.276	40.42	9.1	2
	BCR2-G	5.8 (n.a.)	6.12	3.40	2.401	55.49	5.5	2
F	GSD-1G[4]	19 (2)	48.59	2.41	1.705	4.96	155.8	2
	BCR2-G[3]	359 (6)	589.13	168.66	119.260	28.63	64.1	2
Cl	GSD-1G[5]	145 (4)	105.55	46.63	32.791	44.17	-27.2	2
	BCR2-G[5]	67 (2)	52.04	48.04	33.971	92.32	-22.3	2

[1]De Hoog and EIMF (2018). [2]Walowski et al. (2019). [3]Guggino and Hervig (2010). [4]Guggino and Hervig (2011). [5]Marks et al. (2017). R is the standard reference value. $\bar{x}$ is the mean; 2σ the standard deviation; $2\sigma_{\bar{x}}$ the standard error of the mean; %P the percentage relative 2σ standard deviation; %A is the average percentage accuracy.

Table B.7: Heavy trace element abundances in basalt glass standards from SIMS and estimates of precision and accuracy based on repeat analyses.

Element	Standard	R (μg·g⁻¹)	$\bar{x}$ (μg·g⁻¹)	2σ (μg·g⁻¹)	$2\sigma_{\bar{x}}$ (μg·g⁻¹)	%P	%A	n
Sr	BCR2-G	337.4 (6.7)	335.21	25.75	14.865	7.68	-0.65	3
	T1-G	284 (6)	288.85	17.84	10.301	6.18	1.71	3
Zr	BCR2-G	186.5 (1.5)	179.92	12.62	7.288	7.02	-3.53	3
	T1-G	155 (4)	145.18	14.12	8.150	9.72	0.82	3
Nb	BCR2-G	12.44 (0.2)	12.05	0.57	0.322	4.77	-3.14	3
	T1-G	8.87 (0.43)	8.37	0.15	0.084	1.74	-5.62	3
Ba	BCR2-G	683.9 (4.7)	660.03	93.42	53.937	14.15	-3.49	3
	T1-G	388 (12)	414.92	57.84	33.394	13.94	6.94	3
La	BCR2-G	25.08 (0.16)	22.92	1.84	1.060	8.01	-8.62	3
	T1-G	70.4 (2.4)	63.54	2.44	1.406	2.83	-9.75	3
Ce	BCR2-G	53.12 (0.33)	50.06	2.89	1.669	5.77	-5.75	3
	T1-G	127 (4)	117.22	4.69	2.710	4.00	-7.70	3
Pr	BCR2-G	6.827 (0.044)	6.27	0.29	0.169	4.66	-8.09	3
	T1-G	6.57 (0.14)	11.42	0.58	0.333	5.05	-7.93	3
Nd	BCR2-G	28.26 (0.37)	29.27	5.81	3.357	19.87	1.90	3
	T1-G	41.4 (1.2)	42.19	5.90	3.405	13.98	3.56	3
Sm	BCR2-G	6.457 (0.047)	5.94	0.60	0.344	10.01	-9.20	3
	T1-G	6.57 (0.14)	6.33	0.06	0.036	0.99	-3.72	3
Eu	BCR2-G	1.989 (0.024)	2.42	0.27	0.154	11.03	21.68	3
	T1-G	1.21 (0.04)	2.10	0.47	0.271	22.30	73.64	3
Gd	BCR2-G	6.811 (0.078)	10.86	3.60	2.077	33.14	59.38	3
	T1-G	5.31 (0.29)	13.21	0.51	0.295	3.87	148.71	3
Tb	BCR2-G	1.077 (0.026)	1.69	2.42	1.396	142.88	57.17	3
	T1-G	0.773 (0.029)	1.01	0.14	0.083	14.25	31.07	3
Dy	BCR2-G	6.424 (0.055)	6.16	1.54	0.886	24.91	-4.07	3
	T1-G	0.773 (0.029)	4.37	1.51	0.869	34.43	-2.85	3
Ho	BCR2-G	1.313 (0.011)	1.33	0.21	0.123	15.94	1.65	3
	T1-G	4.5 (0.12)	0.85	0.21	0.122	24.70	-0.59	3
Er	BCR2-G	3.67 (0.038)	4.45	0.21	0.123	4.77	21.25	3
	T1-G	2.49 (0.08)	3.56	0.08	0.046	2.21	43.04	3
Tm	BCR2-G	0.5341 (0.006)	0.53	0.10	0.058	18.92	0.14	3
	T1-G	0.354 (0.015)	0.38	0.15	0.088	39.91	8.34	3
Yb	BCR2-G	3.392 (0.036)	3.42	0.32	0.186	9.44	0.88	3
	T1-G	2.82 (0.08)	2.38	0.27	0.155	11.27	-0.03	3
Lu	BCR2-G	0.5049 (0.0078)	0.49	0.20	0.117	41.68	-3.61	3
	T1-G	0.354 (0.012)	0.36	0.12	0.068	33.03	0.43	3
Th	BCR2-G	5.828 (0.05)	4.45	0.46	0.268	10.44	-23.63	3
	T1-G	31.3 (1)	23.56	2.10	1.211	8.90	-24.73	3
U	BCR2-G	1.683 (0.017)	1.59	0.21	0.119	12.95	-5.29	3
	T1-G	1.71 (0.1)	1.63	0.19	0.112	11.91	-4.83	3

R is the standard reference value, 2σ shown in brackets. $\bar{x}$ is the mean; 2σ the standard deviation; $2\sigma_{\bar{x}}$ the standard error of the mean; %P the percentage relative 2σ standard deviation; %A is the average percentage accuracy.

B.3 Electron Probe Micro Analysis

Compositions of mineral and glass phases were acquired using wavelength-dispersive electron probe microanalysis using a JEOL SuperProbe JXA-8230 Electron Probe Microanalyser hosted at the Leeds Electron Microscopy and Analysis Suite (LEMAS), the University of Leeds. Internal data reduction was performed using the Phi-Rho-Z matrix correction algorithm of Armstrong/Love Scott implemented within the ProbeForEPMA software package (Donovan 2021).

B.3.1 Host Olivine

Spot analyses (n=162) of Si, Fe, Mg, Mn, Ca, Ni and Cr in a total of 48 olivine crystals were collected. Run conditions were 20 keV and current of 30 nA with a fully focused beam. The primary standards used for calibration, detection limits, relative errors, and count times can be found in Table B.8. Secondary standards of San Carlos Olivine (NMNH 111312/44; Jarosewich 2002) and an in-house Navajo Olivine were repeatedly measured to provide estimates of accuracy and precision. The olivine analyses were performed over two sessions. Estimates of accuracy and precision from repeat analyses of the secondary standards are given in Table B.13. Total oxides for olivine range between 99.35–101.88 wt.% with a mean value of 100.86 wt.%. Total cations per formula unit calculated on a four oxygen basis range between 2.999 and 3.012 with a mean of 3.007.

B.3.2 Host Plagioclase

Spot analyses (n=48) of Si, Ti, Al, Fe, Mg, Ca, Na, and K in a total of 10 plagioclase were collected. Run conditions were 20 keV and current of 30 nA with a fully focused beam. The primary standards used for calibration, detection limits, relative errors, and count times can be found in Table B.10. Secondary standards of in-house SKBy-1 Bytownite and SKL-1 Labradorite were repeatedly measured to provide estimates of accuracy and precision. All plagioclase analyses were run in a single session. Estimates of accuracy and precision from repeat analyses of the secondary standards are given in Table B.15. Total oxides for plagioclase range between 99.12–101.41 wt.% with a mean value of 99.84 wt.%. Total cations per formula unit calculated on a 32 oxygen basis range between 20.064 and 20.105 with a mean of 20.085.

B.3.3 Host Clinopyroxene

Spot analyses (n=36) of Si, Ti, Al, Cr, Fe, Mn, Mg, Ca and Na in a total of seven clinopyroxene crystals were collected. Run conditions were a beam potential of 20 keV and beam current of 30 nA with a fully

focused beam. The primary standards used for calibration, detection limits, relative errors, and count times can be found in Table B.11. All plagioclase analyses were run in a single session. Secondary standards of in-house NY Diopside (Jarosewich 2002, USNM 117733) and Geo2 Diopside were repeatedly measured to provide estimates of accuracy and precision. Estimates of accuracy and precision from repeat analyses of the secondary standards are given in Table B.16. Total oxides for clinopyroxene range between 99.05–101.24 wt.% with a mean value of 100.16 Total cations per formula unit calculated on a 6 oxygen basis do not differ from 4.00 until the fifth decimal place.

B.3.4 Melt Inclusions and Adherent Glass

Spot analyses of Si, Ti, Al, Fe, Mg, Mn, Ca, Na, K, P and S were measured in all sessions. Cr was only analysed in the final session. A total of 285 spot analyses of melt inclusions and 264 in adherent glass were collected. A dual-conditions run was performed. First a beam potential of 6 keV and a beam current of 30 nA was used to measure N and K. Second a beam potential of 15 keV and current of 30 nA was used for the remaining elements. A defocused, 10 µm, beam was used for all elements. Primary standards used for calibration, detection limits, and count times can be found in Table B.9. Secondary standards of ML3B-G and StHs-6/80-G (Jochum et al. 2006) were repeatedly measured to provide estimates of accuracy and precision. Estimates of accuracy and precision are given in Table B.14.

B.3.5 Olivine-hosted Spinel

Spot analyses (n=48) of Si, Ti, Al, Cr, Fe, Mn, Mg, Ca, Ni, Zn, V, Co and Nb in a total of 40 spinel inclusions were collected. Run conditions were an electron beam potential of 15 keV and a current of 30 nA with a fully focused beam. Primary standards used for calibration, detection limits, and count times can be found in Table B.12. Repeat measurements of USNM Chromite (USNM 117075; Jarosewich 2002) were used to determine estimates of precision and accuracy. Estimates of precision and accuracy are given in Table B.17. Total oxides, after calculation of Fe_2O_3 with Droop (1987), were between 96.04–104.43 wt.% with an average of 99.66. Total cations per formula unit calculated on a 4 oxygen basis were between 3.00–3.040 with a mean of 3.009.

Table B.8: Olivine EMPA collection parameters, primary standards and counting statistics. Spec., spectrometer number. d.l., detection limit. Peak, on-peak count time. Backgr., background count time.

Element	Spec.	Crystal	Standard	d.l. (ppm)	Peak (s)	Backgr. (s)
Si	1 & 5	TAP	Geo2 Almandine 7302[a]	49	40	40
Ti	2	LIFL	Geo2 Rutile 7320[b]	80	40	40
Cr	2	LIFL	Geo2 Cr_2O_3 7307[c]	94	60	60
Fe	4	LIFH	San Carlos Olivine 473[d]	85	40	40
Mn	4	LIFH	Geo2 Rhodonite 7319[e]	96	60	60
Mg	3	TAPH	Geo2 Periclase 7316[f]	56	40	40
Ca	1	PETJ	Geo2 Wollastonite 7323[g]	32	140	140
Ni	2	LIFL	Geo2 Ni-Metal 7317[h]	98	40	40

[a]Natural; Roxbury Connecticut, USA. [b]Synthetic; PI-KEM Ldt. UK. [c]Synthetic; Earth Jewelery Co. Japan. [d]USNM 111312/444 Jarosewich (2002). [e]Natural; Broken Hill, NSW Australia. [f]Synthetic. [g]Natural, Willsboro, New York, USA. [h]Batch W12918. Johnson Matthey, GmbH, Karlsrube Germany.

Table B.9: Glass EMPA collection parameters, primary standards and counting statistics. Spec., spectrometer number. d.l., detection limit. Peak, on-peak count time. Backgr., background count time.

Element	Spec.	Crystal	Standard	d.l. (ppm)	Peak (s)	Backgr. (s)
Si	1 & 5	TAP	Geo2 Almandine 7302[a]	104	20	20
Ti	4	PETH	Geo2 Rutile 7320[b]	164	20	20
Al	1 & 5	TAP	KL2-G Basalt 7511[c]	88	20	20
Cr	2	LIF	Geo2 Cr_2O_3 7307[d]	269	30	30
Fe	2	LIF	San Carlos Olivine 473[e]	353	20	20
Mn	2	LIF	Geo2 Rhodonite 7319[f]	349	20	20
Mg	1 & 5	TAP	Geo2 Periclase 7316[g]	94	20	20
Ca	4	PETH	KL2-G Basalt 7511[c]	76	40	40
Na	1	TAP	Geo2 Jadeite 7313[h]	332	20	20
K	3	PETH	Geo2 Orthoclase 7314[i]	141	20	20
P	3	PETH	Geo2 Apatite 7303[j]	174	20	20
S	3	PETJ	Geo2 Bartye 7304[k]	96	40	40

[a]Natural; Roxbury Connecticut, USA. [b]Synthetic; PI-KEM Ldt. UK. [c]Jochum et al. (2006). [d]Synthetic; Earth Jewelery Co. Japan. [e]USNM 111312/444 Jarosewich (2002). [f]Natural; Broken Hill, NSW Australia. [g]Synthetic. [h]Natural; Hweka+Mamon nr. Tawmaw, Myanmar. [i]Natural; Lucerne Switzerland. [j]Natural; Durango, Mexico. [k]Natural; Cow Green Mine, Harwood Fell, UK.

Table B.10: Plagioclase EMPA collection parameters, primary standards and counting statistics. Spec., spectrometer number. d.l., detection limit. Peak, on-peak count time. Backgr., background count time.

Element	Spec.	Crystal	Standard	d.l. (ppm)	Peak (s)	Backgr. (s)
Si	5	TAP	SPH Labradorite 7601[a]	146	10	10
Ti	2	LIFL	Geo2 Rutile 7320[b]	121	80	80
Al	1	TAP	SPH Labradorite 7601[a]	114	10	10
Fe	4	LIFH	GeO2 Almandine 7302[c]	49	80	80
Mg	3	TAPH	GeO2 Diopside 7308[d]	39	100	100
Ca	2	PETL	GeO2 Diopside 7308[d]	122	10	10
Na	3	TAPH	Geo2 Jadeite 7313[e]	326	10	10
K	2	PETL	Geo2 Orthoclase 7314[f]	115	10	10

[a]Natural; In-House Standard. [b]Synthetic; PL-KEM Ltd, UK. [c]Natural; Roxbury Connecticut, USA. [d]Natural; Dog Lake, Ontario, Canada. [e]Natural; Hweka+Mamon nr. Tawmaw U. Myanmar. [f]Natural; Lucerne Switzerland.

Table B.11: Clinopyroxene EMPA collection parameters, primary standards and counting statistics. Spec., spectrometer number. d.l., detection limit. Peak, on-peak count time. Backgr., background count time.

Element	Spec.	Crystal	Standard	d.l. (ppm)	Peak (s)	Backgr. (s)
Si	1 & 5	TAP	USNM Olivine 474[a]	97	20	20
Ti	4	LIFH	Geo2 Rutile 7320[b]	62	60	60
Al	5	TAP	GeO2 Al_2O_3 7301[c].	75	30	30
Cr	2	LIFL	Geo2 Cr_2O_3 7307[d].	91	60	60
Fe	4	LIFH	USNM Olivine 474[a]	150	20	20
Mn	2	LIFL	Geo2 Rhodonite 7319[e]	91	60	60
Mg	1 & 5	TAP	USNM Olivine 474[a]	99	20	20
Ca	3	PETH	Geo2 Wollastonite 7323[f]	113	20	20
Na	1	TAP	Geo2 Jadeite 7313[g]	108	60	60

[a]USNM Springwater Meteorite Olivine 2566. [b]Synthetic; PL-KEM Ltd, UK. [c]Synthetic; Corundum. [d] Synthetic; Earth Jewelery Co. Japan. [e]Natural; Broken Hill NSW, Australia. [f]Natural; Willsboro, New York, USA [g]Natural; Hweka+Mamon nr. Tawmaw U. Burma.

Table B.12: Spinel EMPA collection parameters, primary standards and representative counting statistics. Spec., spectrometer number. d.l., detection limit. Peak, on-peak count time. Backgr., background count time.

Element	Spec.	Crystal	Standard	d.l. (ppm)	Peak (s)	Backgr. (s)
Si	1 & 5	TAP	Geo2 Diopside 7308[a]	40	40	40
Ti	2	LIFL	Geo2 Rutile 7320[b]	228	40	40
Al	1 & 5	TAP	Geo2 Al_2O_3 7301[c]	43	40	40
Cr	2	LIFL	Geo2 Cr_2O_3 7307[d]	166	40	40
Fe	2	LIFL	Geo2 Haematite 7311[e]	189	40	40
Mn	4	LIFH	Geo2 Rhodonite 7319[f]	122	40	40
Mg	5	TAP	Geo2 Diopside 7308[a]	84	40	40
Ca	3	PETH	Geo2 Diopside 7308[a]	49	40	40
Ni	4	LIFH	Geo2 Ni Metal 7317[g]	176	40	40
Zn	4	LIFH	Geo2 ZnS 7325[h]	298	40	40
V	2	LIFL	Geo2 V Metal 7321[i]	169	40	40
Co	4	LIFH	Geo2 Co Metal 7306[j]	154	40	40
Nb	3	PETH	Nb Metal 7717[k]	223	40	40

[a]Natural; Dog Lake, Ontario, Canada. [b]Synthetic; PI-KEM Ldt, UK. [c]Synthetic; Corundum. [d]Synthetic; Earth Jewelery Co. Japan. [e]Natural Ferric Oxide; Bouse, La Paz, County Arizona, USA. [f]Natural; Broken Hill NSW, Australia. [g]Synthetic; Johnson Matthey, GmbH, Karlsruhe, Germany. Batch W12918. [h]Synthetic; Earth Jewelery Co. Japan. [i]Synthetic; Johnson Matthey. Batch 31310. [j]Synthetic; Johnson Matthey. Batch 08704. [k]Synthetic; KL Batch 8522h.

Table B.13: Major element composition of olivine secondary standards from EMPA and estimates of accuracy and precision from repeat analyses. Statistics calculated from 16 repeat analyses per standard for each session. n.a., not analysed. b.d. below detection limit.

Session		SiO_2	Cr_2O_3	FeO	MnO	MgO	CaO	NiO
	San Carlos[1]	40.46 (0.74)	0.015 (0.003)	9.65 (0.36)	0.144 (0.006)	49.12 (0.55)	0.093 (0.006)	0.379 (0.018)
01/12/22	$\bar{x}$	40.240	0.015	9.511	0.139	49.643	0.093	0.367
	2σ	0.575	0.011	0.061	0.016	0.416	0.003	0.015
	$2\sigma_{\bar{x}}$	0.144	0.003	0.015	0.004	0.104	0.001	0.004
	%P	1.43	68.70	0.64	11.47	0.84	3.70	4.01
	%A	-0.55	2.89	-1.46	-3.79	1.05	-0.15	-3.30
11/08/23	$\bar{x}$	39.939	0.19	9.676	0.139	49.195	0.095	0.367
	2σ	0.876	0.011	0.096	0.014	0.957	0.004	0.011
	$2\sigma_{\bar{x}}$	0.219	0.003	0.024	0.004	0.239	0.001	0.003
	%P	2.19	55.49	0.99	10.34	1.95	4.18	3.09
	%A	-1.30	21.52	0.27	-3.91	0.15	1.59	-3.23
	Navajo[2]	41.06 (0.37)	- -	9.51 (0.06)	0.134 (0.011)	50.09 (0.15)	- -	0.407 (0.021)
01/12/22	$\bar{x}$	40.903	0.017	8.816	0.132	50.916	0.073	0.386
	2σ	0.499	0.017	0.057	0.015	0.515	0.002	0.017
	$2\sigma_{\bar{x}}$	0.125	0.004	0.014	0.004	0.129	0.000	0.004
	%P	1.22	96.13	0.65	11.28	1.01	2.70	4.29
	%A	-0.38		-7.87	-1.26	1.62		-5.41
11/08/23	$\bar{x}$	40.773	0.020	9.380	0.130	50.176	0.073	0.371
	2σ	1.063	0.011	0.079	0.011	1.078	0.005	0.017
	$2\sigma_{\bar{x}}$	0.266	0.003	0.020	0.003	0.270	0.001	0.004
	%P	2.61	53.97	0.85	8.74	2.15	6.38	4.71
	%A	-0.71		-1.38	-3.18	0.17		-9.81

[1]Repeat analyses of USNM reference material from Lambart et al. (2022). [2]In-house olivine standard. The composition of each standard is given next to its name, 2σ is given in brackets. $\bar{x}$ is the mean; 2σ the standard deviation; $2\sigma_{\bar{x}}$ the standard error of the mean; %P the percentage relative 2σ standard deviation; %A is the average percentage accuracy.

Table B.14: Major element composition of glass secondary standards from EMPA and estimates of accuracy and precision from repeat analyses. Statistics calculated from 16 repeat analyses per standard for the sessions on 19/12/22 and 21/12/22, and 32 repeat analyses for the session on the 01/03/23. n.a., not analysed. b.d. below detection limit. -, not available.

Session		SiO_2	TiO_2	Al_2O_3	Cr_2O_3	FeO	MnO	MgO	CaO	Na_2O	K_2O	P_2O_5	SO_3
	ML3B-G[1]	51.4 (0.6)	2.13 (0.09)	13.6 (0.2)	0.05 (0.02)	10.9 (0.1)	0.170 (0.009)	6.59 (0.08)	10.5 (0.1)	2.40 (0.06)	0.385 (0.004)	0.230 (0.025)	0.0003 (-)
	$\bar{x}$	51.362	2.101	13.538	n.a.	10.851	0.160	6.324	10.440	2.310	0.389	0.240	b.d.
	2σ	0.38	0.07	0.24	n.a.	0.22	0.06	0.11	0.24	0.14	0.05	0.06	b.d.
19/12/22	$2\sigma_{\bar{x}}$	0.10	0.02	0.06	n.a.	0.06	0.02	0.03	0.06	0.04	0.01	0.02	b.d.
	%P	0.74	3.25	1.78	n.a.	2.03	38.15	1.75	2.26	6.15	11.77	25.17	b.d.
	%A	-0.07	-1.35	-0.46	n.a.	-0.45	-5.85	-4.04	-0.57	-3.75	36.65	4.56	b.d.
	$\bar{x}$	51.392	2.100	13.573	n.a.	10.701	0.169	6.324	10.562	2.460	0.391	0.242	b.d.
	2σ	0.784	0.063	0.209	n.a.	0.269	0.051	0.093	0.195	0.131	0.038	0.056	b.d.
21/12/22	$2\sigma_{\bar{x}}$	0.196	0.016	0.052	n.a.	0.067	0.013	0.023	0.049	0.033	0.010	0.014	b.d.
	%P	1.53	3.00	1.54	n.a.	2.51	30.02	1.47	1.85	5.32	9.82	23.27	b.d.
	%A	-0.02	-1.41	-0.20	n.a.	-1.83	-0.56	-4.03	0.59	2.52	37.19	5.37	b.d.
	$\bar{x}$	51.209	2.092	13.899	b.d.	10.885	0.167	6.570	10.412	2.355	0.389	0.238	b.d
	2σ	0.365	0.048	0.479	b.d.	0.251	0.048	0.116	0.073	0.155	0.029	0.053	b.d
01/03/23	$2\sigma_{\bar{x}}$	0.065	0.008	0.085	b.d.	0.044	0.008	0.020	0.013	0.027	0.005	0.009	b.d
	%P	0.71	2.28	3.45	b.d.	2.30	28.69	1.76	0.70	6.56	7.56	22.38	b.d
	%A	-0.37	-1.80	2.15	b.d.	-0.14	-1.56	-0.30	-0.84	-1.92	1.02	3.46	b.d
	StHs-6/80-G[1]	63.7 (0.5)	0.703 (0.021)	17.8 (0.2)	0.005 (0.001)	4.37 (0.07)	0.076 (0.004)	1.97 (0.04)	5.28 (0.09)	4.44 (0.14)	1.29 (0.02)	0.164 (0.018)	0.001 (-)
	$\bar{x}$	63.409	0.690	17.808	n.a.	4.278	0.059	1.932	5.304	4.424	1.294	0.189	b.d.
	2σ	0.325	0.061	0.182	n.a.	0.196	0.054	0.048	0.123	0.194	0.039	0.065	b.d.
19/12/22	$2\sigma_{\bar{x}}$	0.081	0.015	0.045	n.a.	0.049	0.014	0.012	0.031	0.048	0.010	0.016	b.d.
	%P	0.51	8.91	1.02	n.a.	4.58	92.27	2.49	2.31	4.38	3.03	34.14	b.d.
	%A	-0.46	-1.88	0.05	n.a.	-2.10	-22.63	-1.93	0.46	-0.37	0.31	15.41	b.d.
	$\bar{x}$	63.641	0.705	17.989	n.a.	4.296	0.066	1.949	5.368	4.576	1.291	0.183	b.d.
	2σ	0.956	0.033	0.271	n.a.	0.176	0.040	0.052	0.127	0.632	0.061	0.062	b.d.
21/12/22	$2\sigma_{\bar{x}}$	0.239	0.008	0.068	n.a.	0.044	0.010	0.013	0.032	0.158	0.015	0.016	b.d.
	%P	1.50	4.73	1.51	n.a.	4.11	60.92	2.66	2.37	13.82	4.71	34.04	b.d.
	%A	-0.09	0.24	1.06	n.a.	-1.69	-12.56	-1.07	1.66	3.06	0.11	11.38	b.d.
	$\bar{x}$	63.262	0.692	18.019	b.d.	4.387	0.080	2.021	5.340	4.473	1.279	0.183	b.d.
	2σ	0.250	0.031	0.446	b.d.	0.152	0.052	0.057	0.042	0.306	0.057	0.064	b.d.
01/03/23	$2\sigma_{\bar{x}}$	0.044	0.005	0.079	b.d.	0.027	0.009	0.010	0.007	0.054	0.010	0.011	b.d.
	%P	0.40	4.49	2.48	b.d.	3.46	64.54	2.83	0.79	6.85	4.42	35.18	b.d.
	%A	-0.69	-1.59	-1.22	b.d.	0.38	4.79	2.52	2.07	0.74	-0.87	10.43	b.d.

[1]USNM reference material (Jochum et al. 2006). The reference composition of each standard is given next to its name, 2σ is given in brackets. $\bar{x}$ is the mean; 2σ the standard deviation; $2\sigma_{\bar{x}}$ the standard error of the mean; %P the percentage relative 2σ standard deviation; %A is the average percentage accuracy.

Table B.15: Major element composition of feldspar secondary standards from EMPA and estimates of accuracy and precision from repeat analyses. Statistics calculated from 16 repeat analyses per standard for each session. n.a., not analysed. b.d. below detection limit.

Session		SiO_2	TiO_2	Al_2O_3	FeO	MgO	CaO	Na_2O	K_2O
	SKBy-1[1]	51.299	-	30.179	0.424	0.138	13.770	3.688	0.114
		-	-	-	-	-	-	-	-
	$\bar{x}$	51.129	0.038	30.526	0.412	0.136	13.817	3.832	0.117
	2σ	1.231	0.018	0.838	0.010	0.011	0.207	0.190	0.017
01/09/23	$2\sigma_{\bar{x}}$	0.290	0.004	0.197	0.002	0.002	0.049	0.045	0.004
	%P	2.41	47.38	2.74	2.41	7.78	1.50	4.96	14.90
	%A	-0.33	-	1.14	-2.88	-1.48	0.34	3.76	2.84
	SKL-1[1]	53.000	0.065	29.580	0.353	-	12.261	4.440	0.273
		-	-	-	-	-	-	-	-
	$\bar{x}$	53.024	0.083	29.553	0.452	0.089	12.266	4.550	0.344
	2σ	1.366	0.021	0.879	0.048	0.010	0.164	0.180	0.029
01/09/23	$2\sigma_{\bar{x}}$	0.322	0.005	0.207	0.011	0.002	0.039	0.043	0.007
	%P	2.58	24.81	2.97	10.56	10.90	1.34	3.97	8.46
	%A	0.04	21.59	-0.09	21.85	-	0.04	2.41	20.69

[1]In-house plagioclase standard. The composition of each standard is given next to its name, 2σ is given in brackets. $\bar{x}$ is the mean; 2σ the standard deviation; $2\sigma_{\bar{x}}$ the standard error of the mean; %P the percentage relative 2σ standard deviation; %A is the average percentage accuracy.

Table B.16: Major element composition of clinopyroxene secondary standards from EMPA and estimates of accuracy and precision from repeat analyses. Statistics calculated from 16 repeat analyses per standard for each session. n.a., not analysed. b.d. below detection limit.

Session		SiO_2	TiO_2	Al_2O_3	Cr_2O_3	FeO	MnO	MgO	CaO	Na_2O
	NY Diopside[1]	54.872	-	0.110	-	0.241	0.040	18.301	25.631	0.340
		-	-	-	-	-	-	-	-	-
	$\bar{x}$	55.661	0.016	0.010	0.070	0.200	18.369	0.031	26.174	0.082
	2σ	1.389	0.030	0.003	0.013	0.023	0.663	0.009	0.164	0.014
02/08/23	$2\sigma_{\bar{x}}$	0.347	0.009	0.002	0.003	0.006	0.166	0.002	0.041	0.004
	%P	2.50	182.66	30.96	18.93	11.27	3.61	30.58	0.63	17.71
	%A	1.42	-	-	-57.67	-20.32	0.37	-30.50	2.07	-315.47
	Geo2 Diopside[2]	55.360	-	-	-	0.900	-	18.130	25.720	-
		-	-	-	-	-	-	-	-	-
	$\bar{x}$	55.004	0.049	0.012	0.055	2.027	18.519	0.155	24.140	0.072
	2σ	1.625	0.061	0.006	0.181	10.019	1.973	0.601	12.130	0.034
02/08/23	$2\sigma_{\bar{x}}$	0.406	0.015	0.003	0.045	2.505	0.493	0.150	3.032	0.009
	%P	2,.95	123.19	53.47	329.94	494.15	10.65	388.61	50.25	47.63
	%A	-0.65	-	-	-	55.61	2.10	-	-6.54	-

[1]USNM reference material 117733 (Jarosewich 2002). [2]Natural; Dog Lake, Ontario, Canada. The composition of each standard is given next to its name, 2σ is given in brackets. $\bar{x}$ is the mean; 2σ the standard deviation; $2\sigma_{\bar{x}}$ the standard error of the mean; %P the percentage relative 2σ standard deviation; %A is the average percentage accuracy.

Table B.17: Major element composition of Fe-Ti oxide secondary standards from EMPA and estimates of accuracy and precision from repeat analyses. Statistics calculated from 12 repeat analyses per standard for each session. n.a., not analysed. b.d. below detection limit.

Session		SiO_2	TiO_2	Al_2O_3	Cr_2O_3	V_2O_3	Fe_2O_3	FeO	MnO	MgO	NiO	ZnO	CoO	Nb_2O_5
	Chromite	-	-	9.92	60.5	-	-	13.04	0.11	15.20	-	-	-	-
		-	-	-	-	-	-	-	-	-	-	-	-	-
	$\bar{x}$	0.035	0.109	9.823	60.487	0.079	-	13.072	0.252	14.454	0.165	0.073	0.043	b.d.
	2σ	0.130	0.036	0.263	1.173	0.028	-	0.130	0.029	0.679	0.021	0.034	0.018	b.d.
19/09/23	$2\sigma_{\bar{x}}$	0.022	0.006	0.044	0.195	0.005	-	0.022	0.005	0.113	0.003	0.006	0.03	b.d.
	%P	374.89	32.70	2.67	1.94	35.75	-	1.00	11.65	4.70	12.49	46.64	41.00	b.d.
	%A	-	-	-0.99	-0.02	-	-	0.24	56.38	-5.16	-	-	-	-
	$\bar{x}$	0.020	0.102	9.763	61.583	0.084	-	13.012	0.245	14.294	0.163	0.081	0.042	b.d.
	2σ	0.011	0.051	0.347	1.126	0.027	-	0.340	0.014	0.521	0.034	0.025	0.012	b.d.
10/01/24	$2\sigma_{\bar{x}}$	0.005	0.021	0.142	0.460	0.011	-	0.139	0.006	0.231	0.014	0.010	0.005	b.d.
	%P	55.56	49.54	3.54	1.83	32.14	-	2.61	5.66	3.65	20.76	31.19	29.63	b.d.
	%A	-	-	-1.61	1.76	-	-	-0.22	55.18	-6.34	-	-	-	b.d.
	$\bar{x}$	0.015	0.107	9.888	62.121	0.086	-	13.410	0.247	14.229	0.165	0.066	0.041	b.d.
	2σ	0.016	0.031	0.225	2.523	0.026	-	0.345	0.013	0.417	0.028	0.026	0.012	b.d.
11/01/24	$2\sigma_{\bar{x}}$	0.006	0.011	0.080	0.892	0.009	-	0.122	0.004	0.147	0.010	0.010	0.004	b.d.
	%P	102.97	28.96	2.28	4.06	30.11	-	2.57	5.11	2.93	16.89	40.10	28.80	b.d.
	%A	-	-	-0.33	2.61	-	-	2.76	55.47	-6.82	-	-	-	b.d.

The composition of each standard is given next to its name, 2σ is given in brackets. $\bar{x}$ is the mean; 2σ the standard deviation; $2\sigma_{\bar{x}}$ the standard error of the mean; %P the percentage relative 2σ standard deviation; %A is the average percentage accuracy.

References

De Hoog, J. C. M. and EIMF (2018). "Matrix Effects During SIMS Measurement of the Lithium Mass Fractions of Silicate Glasses: Correction Procedures and Updated Preferred Values of Reference Materials". In: *Geostandards and Geoanalytical Research* 42.4, pages 513–522. DOI: 10.1111/ggr.12237.

DeVitre, C. L., C. M. Allison, and E. Gazel (2021). "A High-Precision CO_2 Densimeter for Raman Spectroscopy Using a Fluid Density Calibration Apparatus". In: *Chemical Geology* 584, page 19. DOI: 10.1016/j.chemgeo.2021.120522.

DeVitre, C. L., K. Dayton, E. Gazel, A. Pamukçu, G. Gaetani, and P. E. Wieser (2023). "Laser Heating Effect on Raman Analysis of CO_2 Co-Existing as Liquid and Vapor in Olivine-Hosted Melt Inclusion Bubbles". In: *Volcanica* 6.2 (2), pages 201–219. DOI: 10.30909/vol.06.02.201219.

Donovan, J. J. (2021). *Probe for EPMA v. 13.0.5 User's Guide and Reference (Xtreme Edition)*. URL: https://probesoftware.com/download/PROBEWIN.pdf.

Droop, G. T. R. (1987). "A General Equation for Estimating Fe^{3+} Concentrations in Ferromagnesian Silicates and Oxides from Microprobe Analyses, Using Stoichiometric Criteria". In: *Mineralogical Magazine* 51.361 (361), pages 431–435. DOI: 10.1180/minmag.1987.051.361.10.

Fall, A., B. Tattitch, and R. J. Bodnar (2011). "Combined Microthermometric and Raman Spectroscopic Technique to Determine the Salinity of H_2O–CO_2–NaCl Fluid Inclusions Based on Clathrate Melting". In: *Geochimica et Cosmochimica Acta* 75.4 (4), pages 951–964. DOI: 10.1016/j.gca.2010.11.021.

Guggino, S. N. and R. L. Hervig (2010). "Determination of Fluorine in Fourteen Microanalytical Geologic Reference Materials Using SIMS, EPMA, and Proton Induced Gamma Ray Emission (PIGE) Analysis". In: 2010, pages V51C–2209. URL: https://ui.adsabs.harvard.edu/abs/2010AGUFM.V51C2209G.

– (2011). "Synthesis and Characterization of Five New F-bearing Basalt Reference Materials (Fba Glasses): Quantifying the Fluorine Content of the Basaltic Glass Standards BCR-2G, BHVO-2G. GSA-1G, GSC-1G, GSD-1G, GSE-1G, ML3B-G, KL2-G, and ALV-519-4". In: 2011, pages V31C–2535. URL: https://ui.adsabs.harvard.edu/abs/2011AGUFM.V31C2535G.

Hauri, E., J. Wang, J. E. Dixon, P. L. King, C. Mandeville, and S. Newman (2002). "SIMS Analysis of Volatiles in Silicate Glasses 1. Calibration, Matrix Effects and Comparisons with FTIR". In: *Chemical Geology*. DOI: 10.1016/S0009-2541(01)00375-8.

Iacovino, K. and C. Till (2018). "DensityX: A Program for Calculating the Densities of Hydrous Magmatic Liquids from 427-1,627 °C and up to 30 Kbar". In: *Volcanica* 2.1 (1), pages 1–10. DOI: 10.30909/vol.02.01.0110.

Jarosewich, E. (2002). "Smithsonian Microbeam Standards". In: *Journal of Research of the National Institute of Standards and Technology* 107.6 (6), page 681. DOI: 10.6028/jres.107.054.

Jochum, K. P., B. Stoll, K. Herwig, M. Willbold, A. W. Hofmann, M. Amini, S. Aarburg, W. Abouchami, E. Hellebrand, B. Mocek, I. Raczek, A. Stracke, O. Alard, C. Bouman, S. Becker, M. Dücking, H. Brätz, R. Klemd, D. de Bruin, D. Canil, D. Cornell, C.-J. de Hoog, C. Dalpé, L. Danyushevsky, A. Eisenhauer, Y. Gao, J. E. Snow,

N. Groschopf, D. Günther, C. Latkoczy, M. Guillong, E. H. Hauri, H. E. Höfer, Y. Lahaye, K. Horz, D. E. Jacob, S. A. Kasemann, A. J. R. Kent, T. Ludwig, T. Zack, P. R. D. Mason, A. Meixner, M. Rosner, K. Misawa, B. P. Nash, J. Pfänder, W. R. Premo, W. D. Sun, M. Tiepolo, R. Vannucci, T. Vennemann, D. Wayne, and J. D. Woodhead (2006). "MPI-DING Reference Glasses for in Situ Microanalysis: New Reference Values for Element Concentrations and Isotope Ratios: MPI-DING REFERENCE GLASSES". In: *Geochemistry, Geophysics, Geosystems* 7.2 (2), page 44. DOI: 10.1029/2005GC001060.

Kawakami, Y., J. Yamamoto, and H. Kagi (2003). "Micro-Raman Densimeter for CO_2 Inclusions in Mantle-Derived Minerals". In: *Applied Spectroscopy* 57.11 (11), pages 1333–1339. DOI: 10.1366/000370203322554473.

Lamadrid, H., L. Moore, D. Moncada, J. Rimstidt, R. Burruss, and R. Bodnar (2017). "Reassessment of the Raman CO_2 Densimeter". In: *Chemical Geology* 450, pages 210–222. DOI: 10.1016/j.chemgeo.2016.12.034.

Lambart, S., S. Hamilton, and O. I. Lang (2022). "Compositional Variability of San Carlos Olivine". In: *Chemical Geology* 605, page 120968. DOI: 10.1016/j.chemgeo.2022.120968.

Lin, F., A. K. Sum, and R. J. Bodnar (2007). "Correlation of Methane Raman N1 Band Position with Fluid Density and Interactions at the Molecular Level". In: *Journal of Raman Spectroscopy* 38.11 (11), pages 1510–1515. DOI: 10.1002/jrs.1804.

Marks, M. A. W., M. A. Kendrick, G. N. Eby, T. Zack, and T. Wenzel (2017). "The F, Cl, Br and I Contents of Reference Glasses BHVO -2G, BIR -1G, BCR -2G, GSD -1G, GSE -1G, NIST SRM 610 and NIST SRM 612". In: *Geostandards and Geoanalytical Research* 41.1, pages 107–122. DOI: 10.1111/ggr.12128.

Moré, J. J. (1977). "The Levenberg-Marquardt Algorithm: Implementation and Theory". In: *Numerical Analysis*. Volume 630, pages 105–116. DOI: 10.1007/BFb0067700.

Rosso, K. M. and R. J. Bodnar (1995). "Microthermometric and Raman Spectroscopic Detection Limits of CO2 in Fluid Inclusions and the Raman Spectroscopic Characterization of CO2". In: *Geochimica et Cosmochimica Acta* 59.19 (19), pages 3961–3975.

Shishkina, T., R. Botcharnikov, F. Holtz, R. Almeev, and M. Portnyagin (2010). "Solubility of H2O- and CO2-bearing Fluids in Tholeiitic Basalts at Pressures up to 500MPa". In: *Chemical Geology* 277.1-2 (1-2), pages 115–125. DOI: 10.1016/j.chemgeo.2010.07.014.

Song, Y., I. Chou, W. Hu, B. Robert, and W. Lu (2009). "CO_2 Density-Raman Shift Relation Derived from Synthetic Inclusions in Fused Silica Capillaries and Its Application". In: *Acta Geologica Sinica - English Edition* 83.5 (5), pages 932–938. DOI: 10.1111/j.1755-6724.2009.00090.x.

Tellinghuisen, J. (2020). "Least Squares Methods for Treating Problems with Uncertainty in *x* and *y*". In: *Analytical Chemistry* 92.16, pages 10863–10871. DOI: 10.1021/acs.analchem.0c02178.

Tucker, J. M., E. H. Hauri, A. J. Pietruszka, M. O. Garcia, J. P. Marske, and F. A. Trusdell (2019). "A High Carbon Content of the Hawaiian Mantle from Olivine-Hosted Melt Inclusions". In: *Geochimica et Cosmochimica Acta* 254, pages 156–172. DOI: 10.1016/j.gca.2019.04.001.

Walowski, K., L. Kirstein, J. De Hoog, T. Elliott, I. Savov, and R. Jones (2019). "Investigating Ocean Island Mantle Source Heterogeneity with Boron Isotopes in Melt Inclusions". In: *Earth and Planetary Science Letters* 508, pages 97–108. DOI: 10.1016/j.epsl.2018.12.005.

Wang, W., M.-C. Caumon, A. Tarantola, J. Pironon, W. Lu, and Y. Huang (2019). "Raman Spectroscopic Densimeter for Pure CO_2 and CO_2-H_2O-NaCl Fluid Systems over a Wide P-T Range up to 360 °C and 50 MPa". In: *Chemical Geology* 528, page 119281. DOI: 10.1016/j.chemgeo.2019.119281.

Wang, X., I.-M. Chou, W. Hu, R. C. Burruss, Q. Sun, and Y. Song (2011). "Raman Spectroscopic Measurements of CO_2 Density: Experimental Calibration with High-Pressure Optical Cell (HPOC) and Fused Silica Capillary Capsule (FSCC) with Application to Fluid Inclusion Observations". In: *Geochimica et Cosmochimica Acta* 75.14 (14), pages 4080–4093. DOI: 10.1016/j.gca.2011.04.028.

Wieser, P. and C. DeVitre (2023). *DiadFit: An Open-Source Python3 Tool for Peak Fitting of Raman Data from Silicate Melts and CO2 Fluids*. preprint. Earth Sciences. DOI: 10.31223/X5CQ1F.

Wieser, P. E., H. Lamadrid, J. Maclennan, M. Edmonds, S. Matthews, K. Iacovino, F. E. Jenner, C. Gansecki, F. Trusdell, R. Lee, and E. Ilyinskaya (2021). "Reconstructing Magma Storage Depths for the 2018 Kīlauean Eruption From Melt Inclusion CO_2 Contents: The Importance of Vapor Bubbles". In: *Geochemistry, Geophysics, Geosystems* 22.2 (2). DOI: 10.1029/2020GC009364.

Yamamoto, J. and H. Kagi (2006). "Extended Micro-Raman Densimeter for CO_2 Applicable to Mantle-originated Fluid Inclusions". In: *Chemistry Letters* 35.6 (6), pages 610–611. DOI: 10.1246/cl.2006.610.

Appendix C

Images of Studied Melt Inclusions and Vapour Bubbles

Images of each studied melt inclusion are presented below. They are organised into two columns, four melt inclusions per page. The left column are the images used to calculate melt inclusion volumes. The right column are images used to calculate vapour bubble volume.

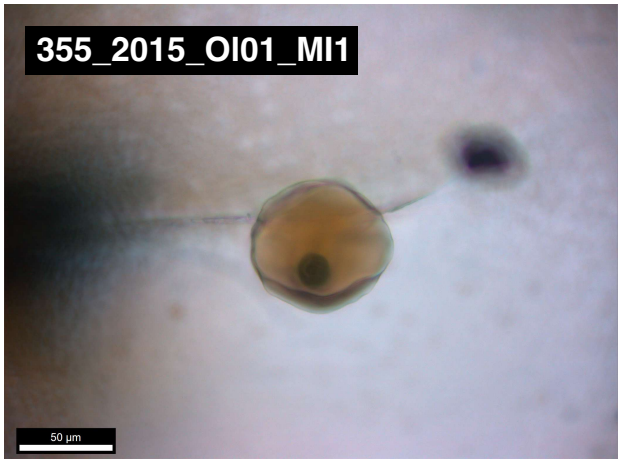
355_2015_OI01_MI1
50 µm

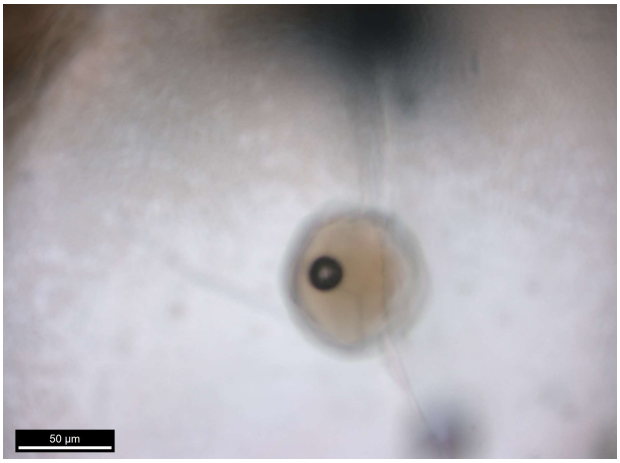
50 µm

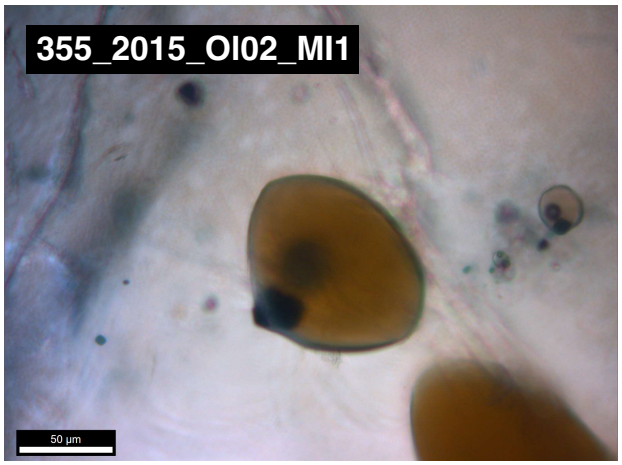
355_2015_OI02_MI1
50 µm

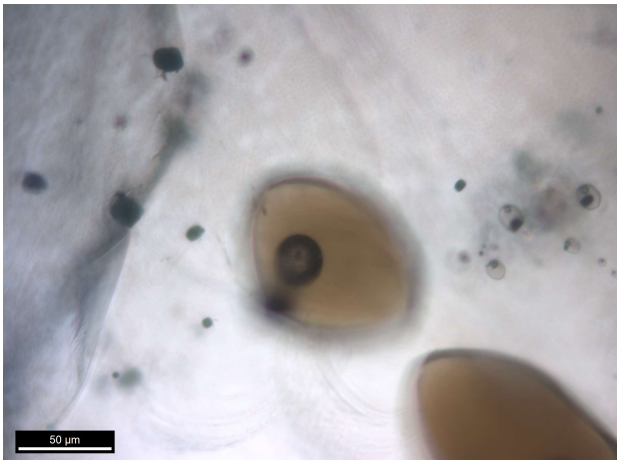
50 µm

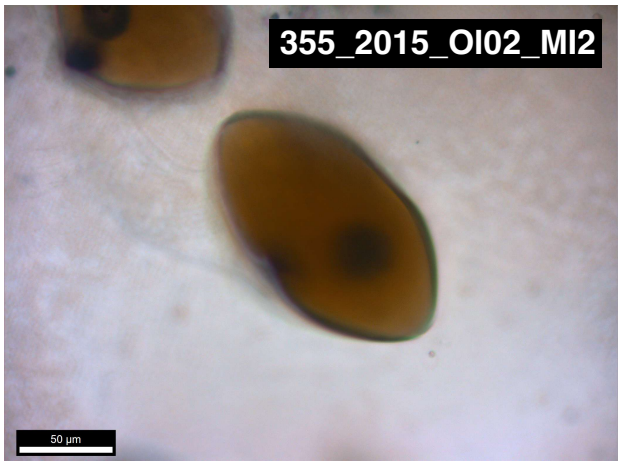
355_2015_OI02_MI2
50 µm

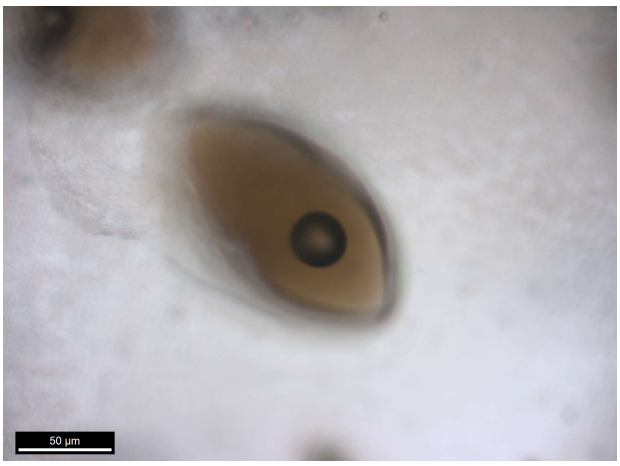
50 µm

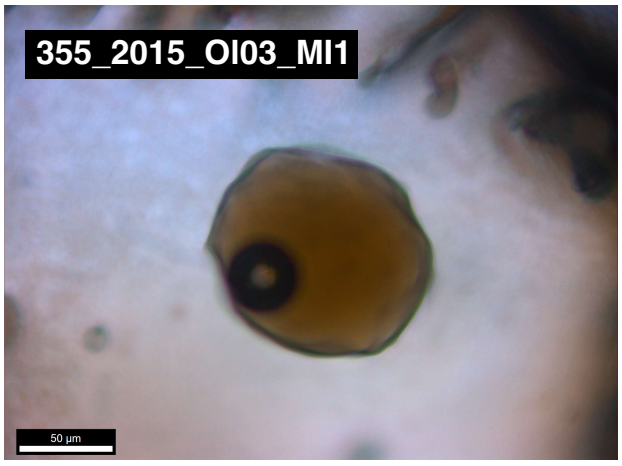
355_2015_OI03_MI1
50 µm

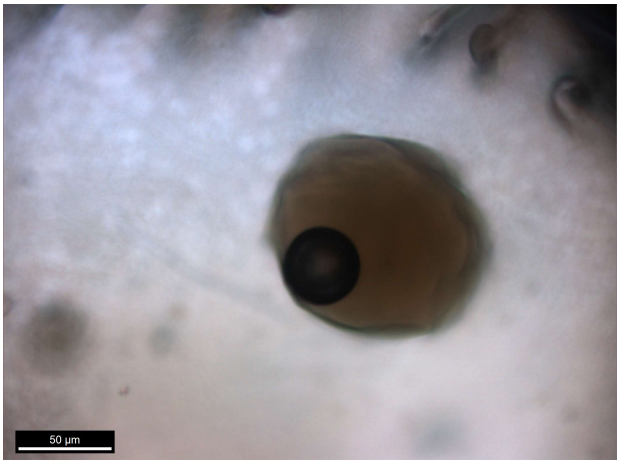
50 µm


355_2015_Ol04_MI1
50 µm

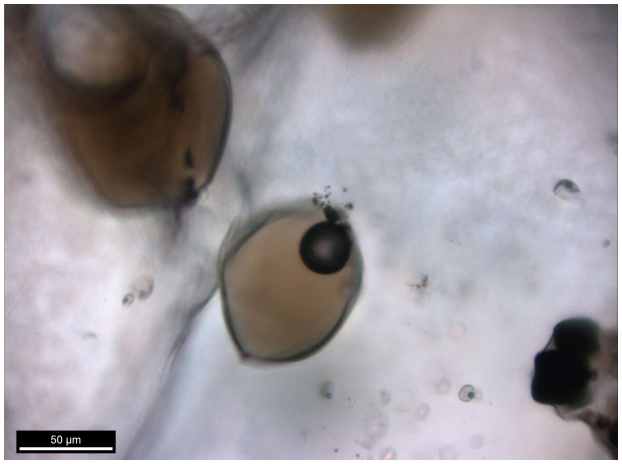
50 µm

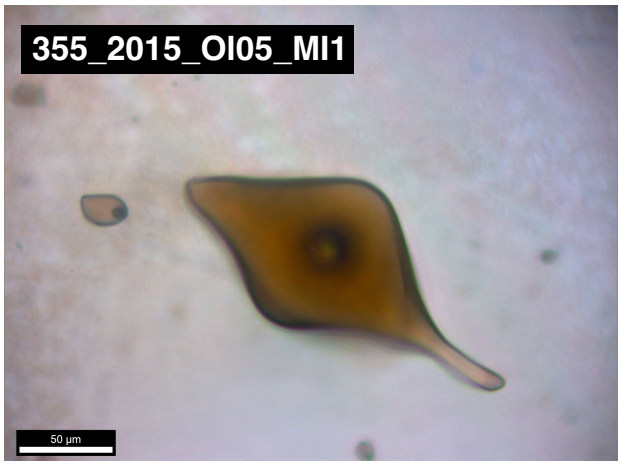
355_2015_Ol05_MI1
50 µm

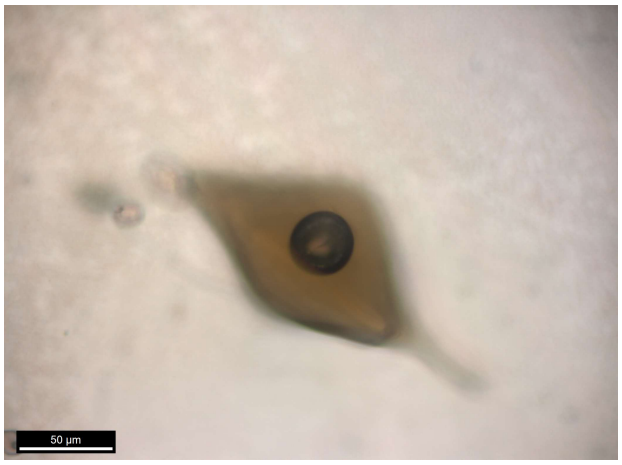
50 µm

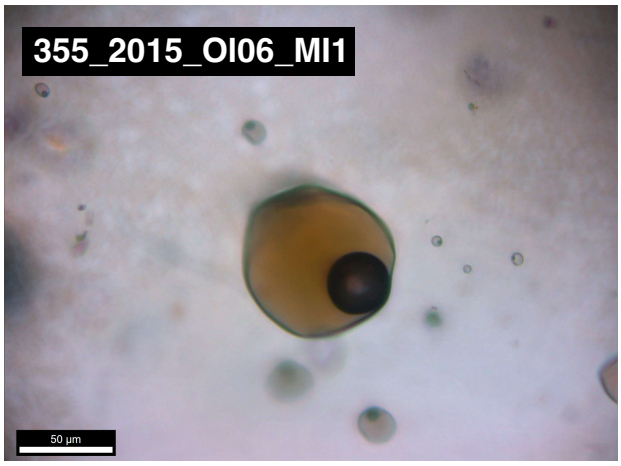
355_2015_Ol06_MI1
50 µm

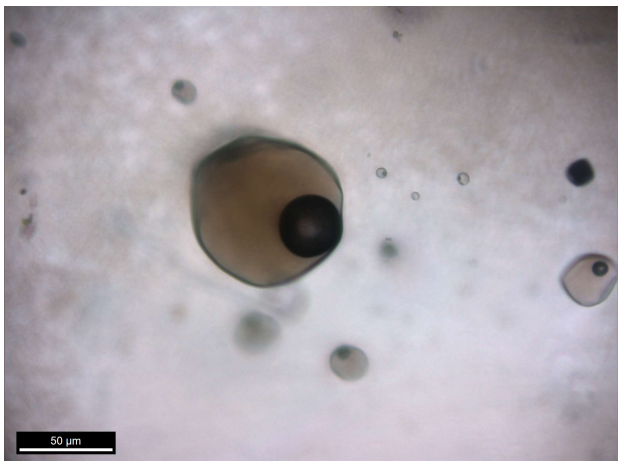
50 µm

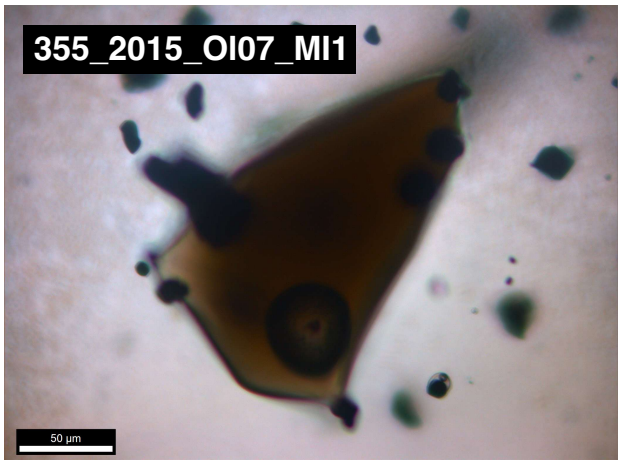
355_2015_Ol07_MI1
50 µm

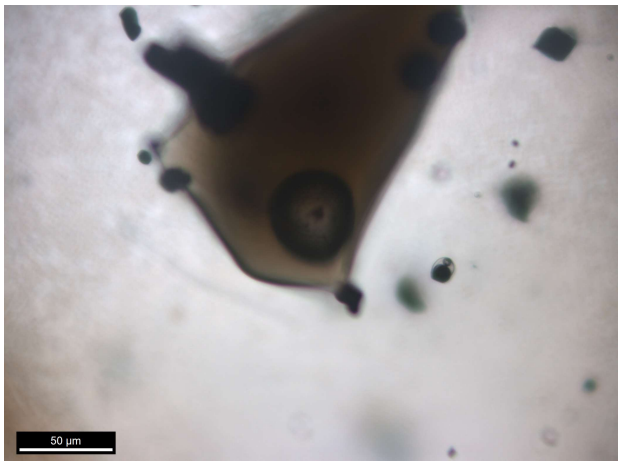
50 µm

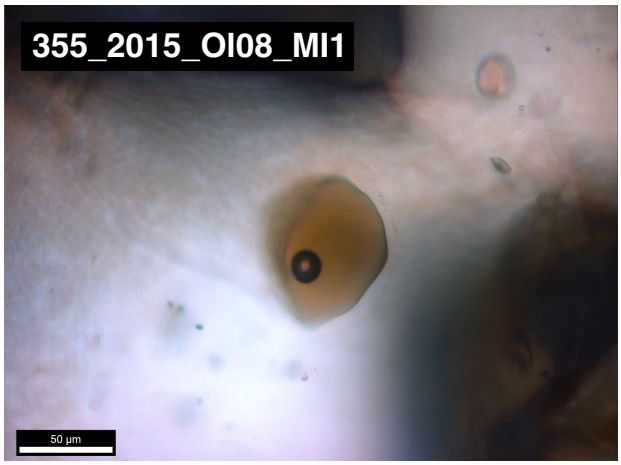
355_2015_OI08_MI1
50 µm

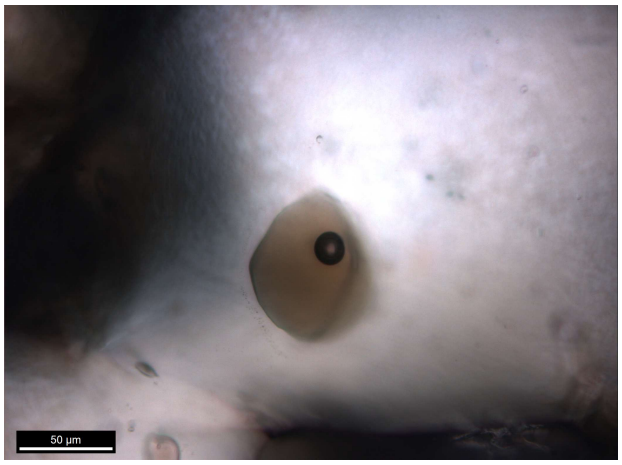
50 µm

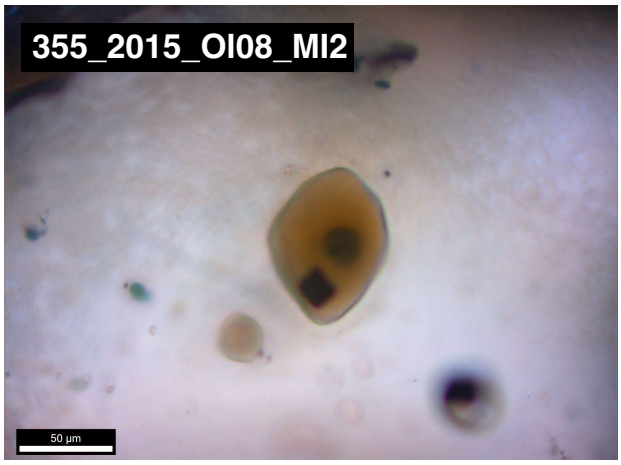
355_2015_OI08_MI2
50 µm


50 µm

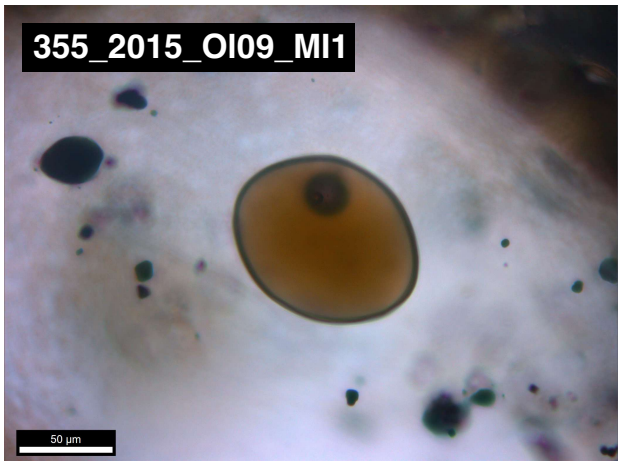
355_2015_OI09_MI1
50 µm

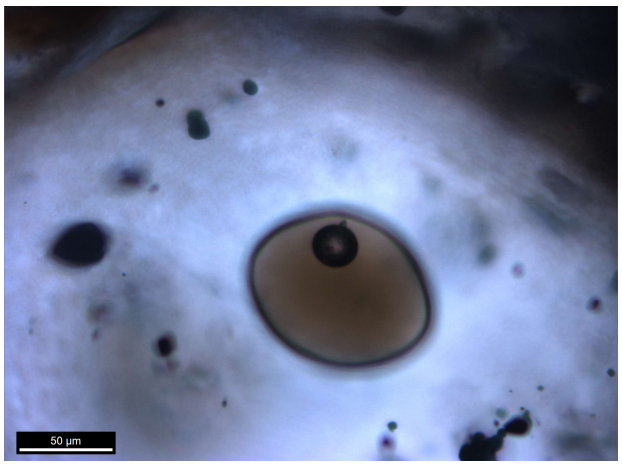
50 µm

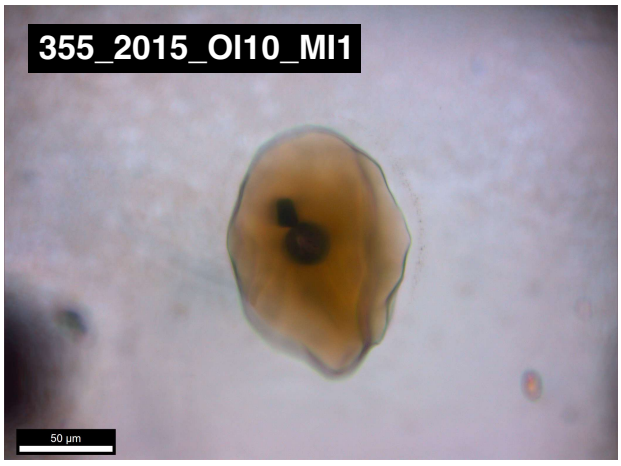
355_2015_OI10_MI1
50 µm

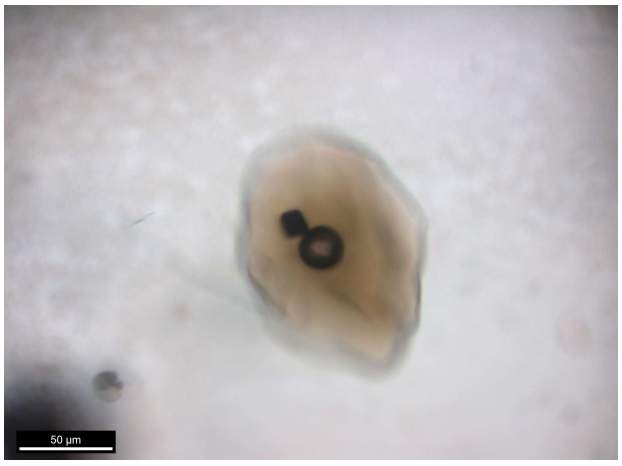
50 µm

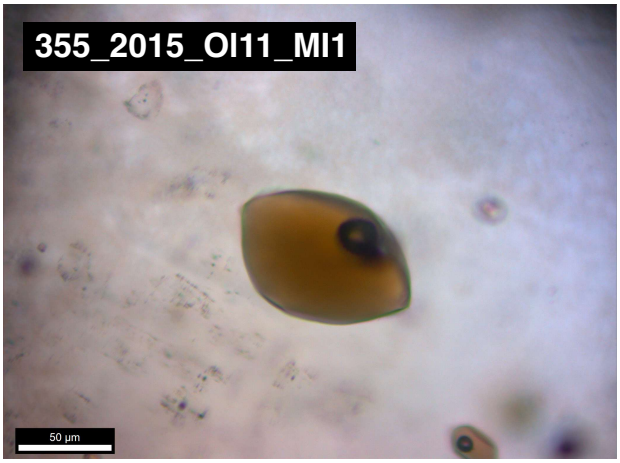
355_2015_Ol11_MI1
50 µm

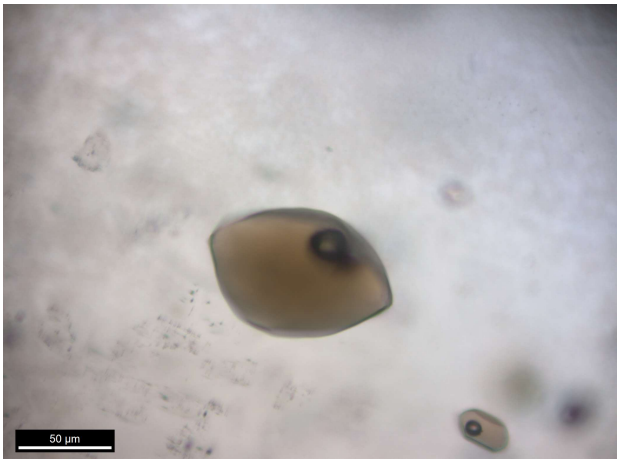
50 µm

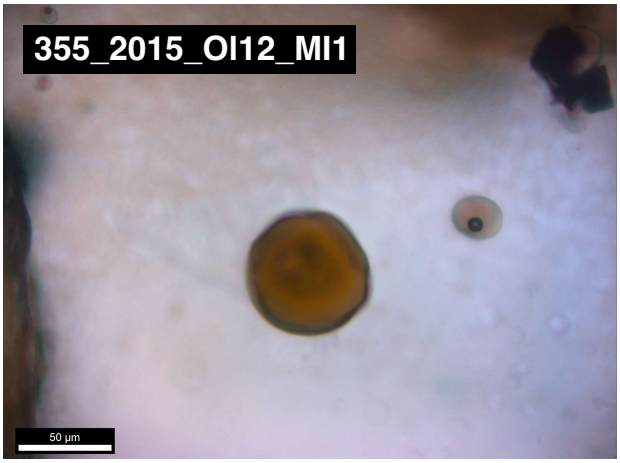
355_2015_Ol12_MI1
50 µm

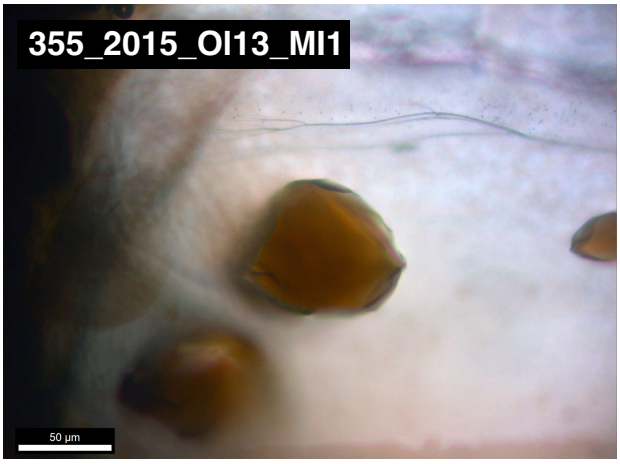
355_2015_Ol13_MI1
50 µm

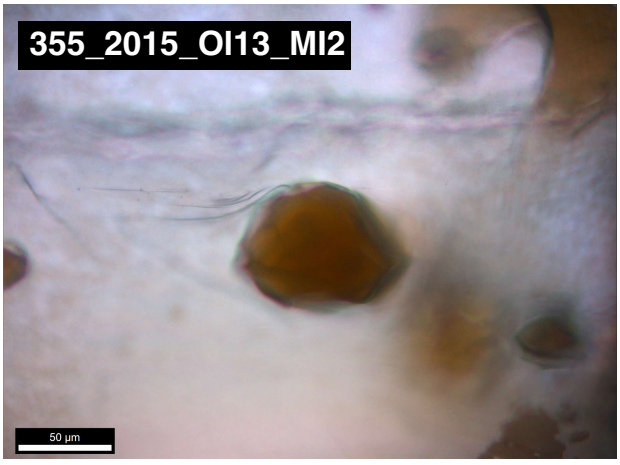
355_2015_Ol13_MI2
50 µm

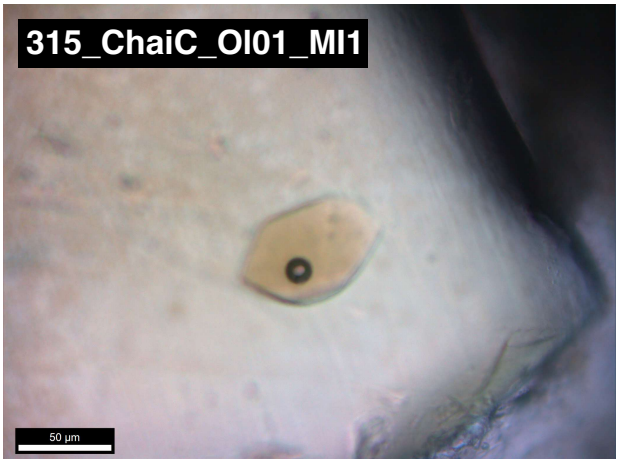
315_ChaiC_Ol01_MI1
50 µm

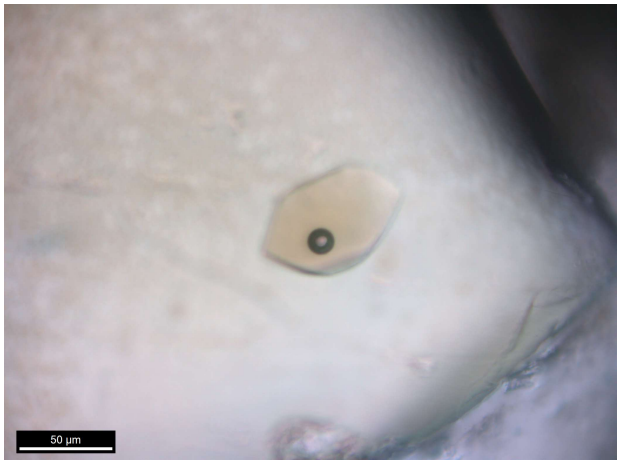
50 µm

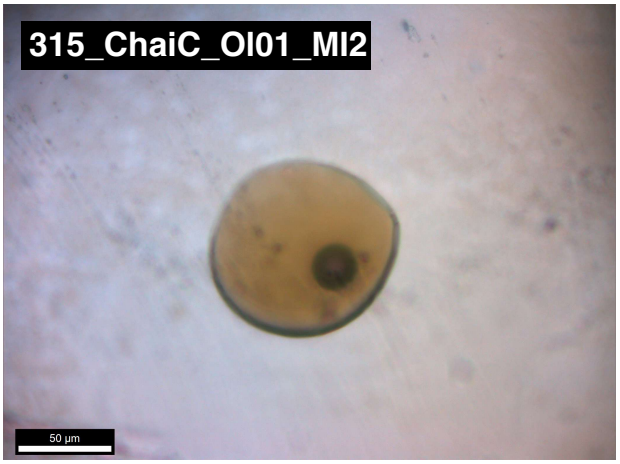
315_ChaiC_Ol01_MI2
50 µm

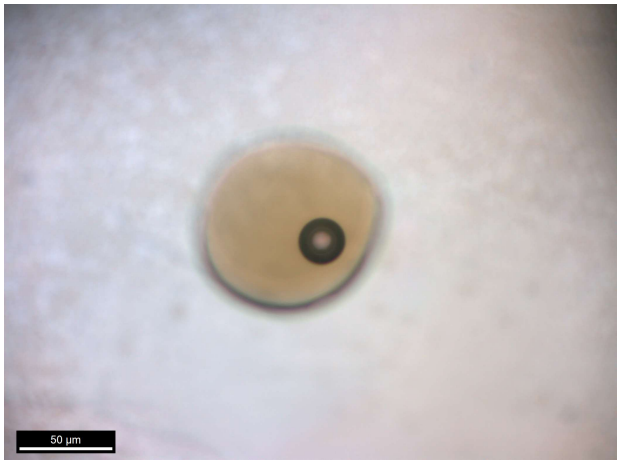
50 µm

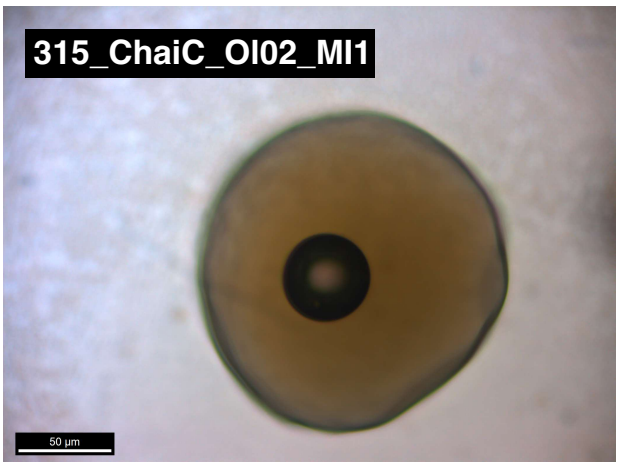
315_ChaiC_Ol02_MI1
50 µm

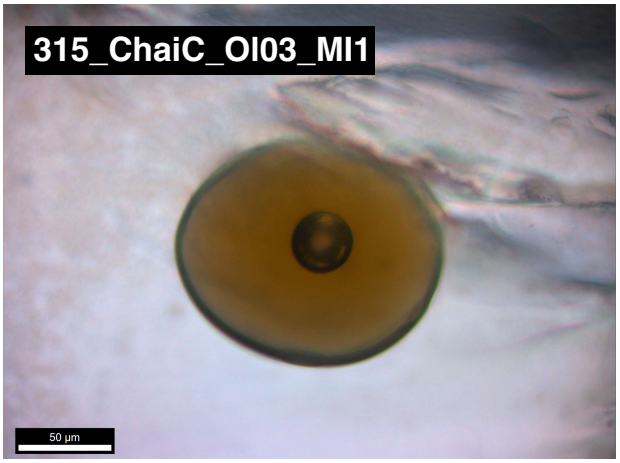
315_ChaiC_Ol03_MI1
50 µm

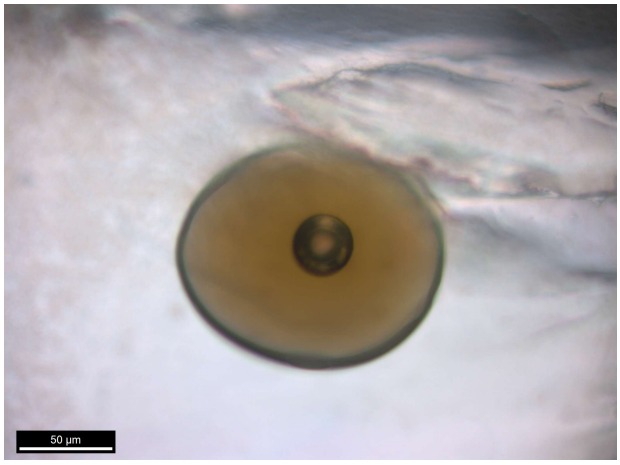
50 µm

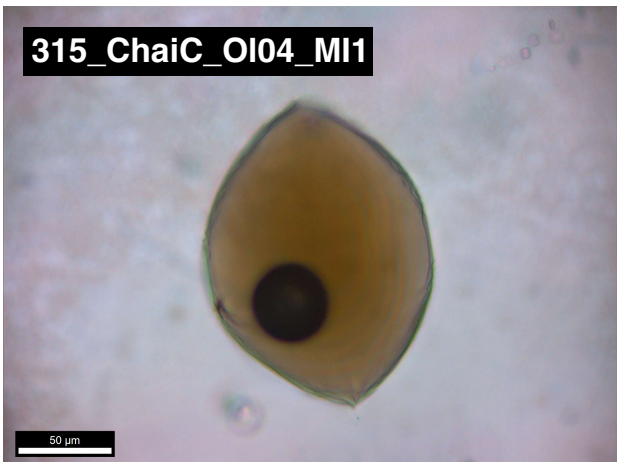
315_ChaiC_OI04_MI1
50 µm

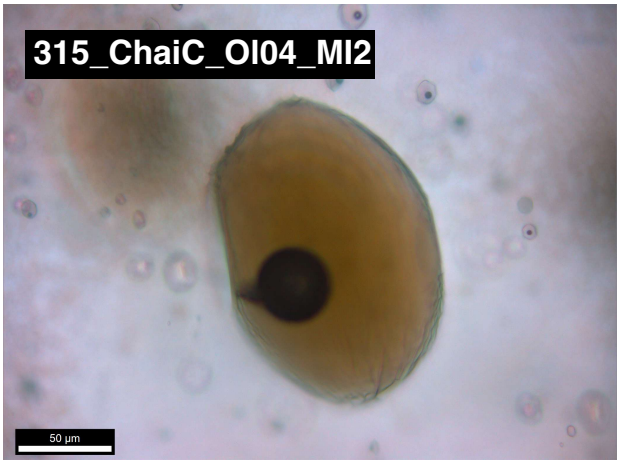
315_ChaiC_OI04_MI2
50 µm

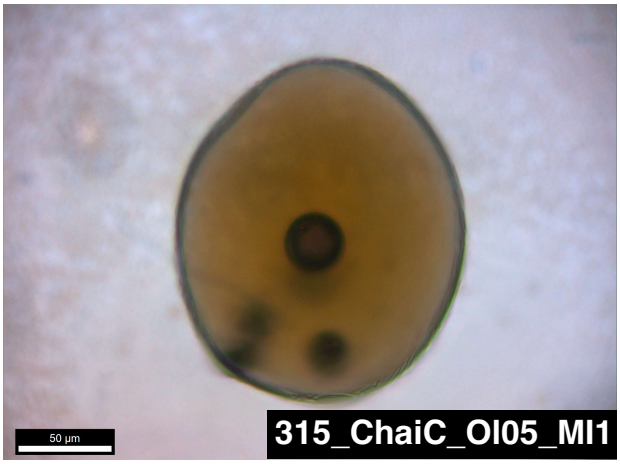
50 µm
315_ChaiC_OI05_MI1

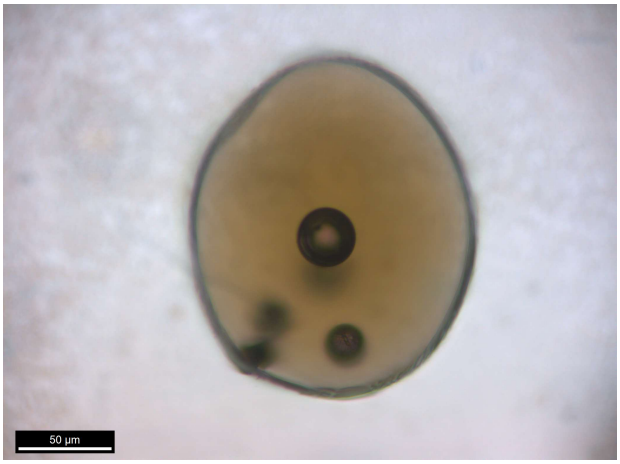
50 µm

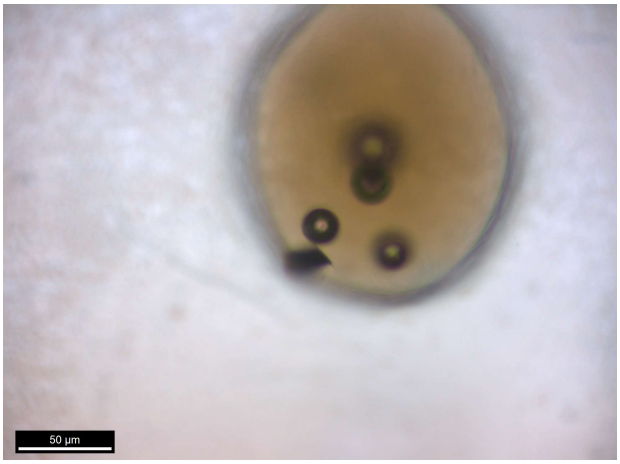
50 µm

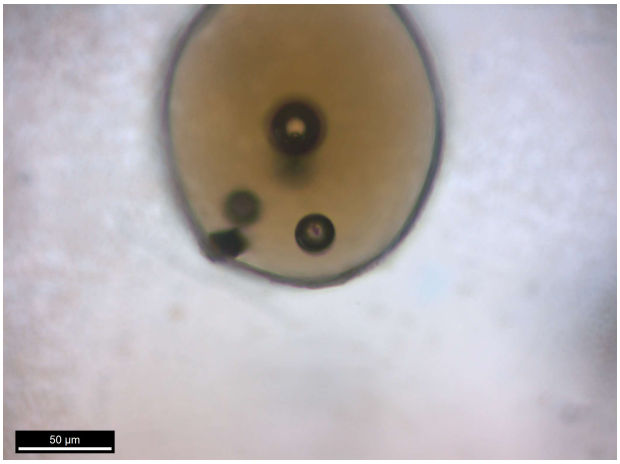
50 µm

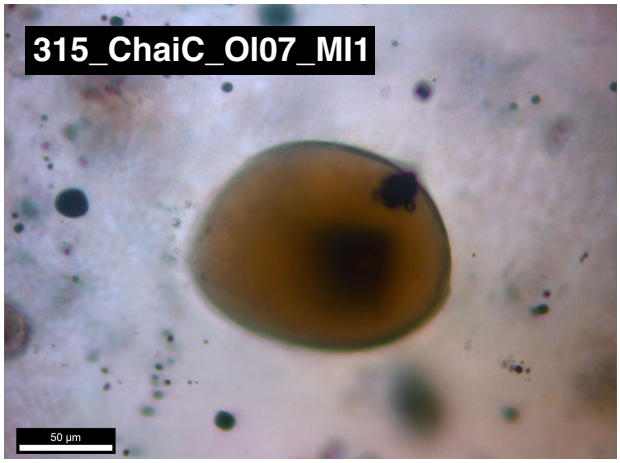
315_ChaiC_Ol07_MI1
50 µm

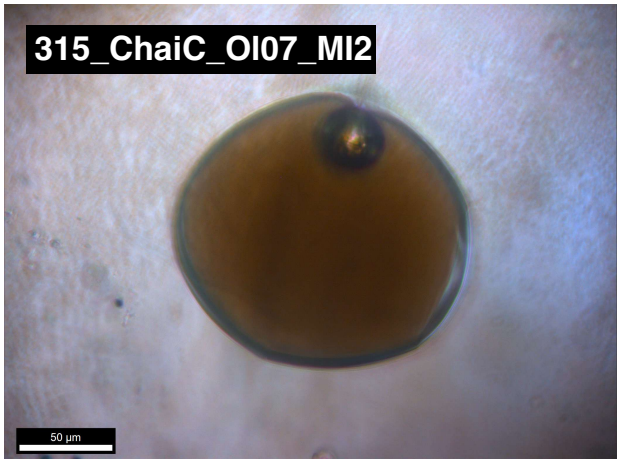
315_ChaiC_Ol07_MI2
50 µm

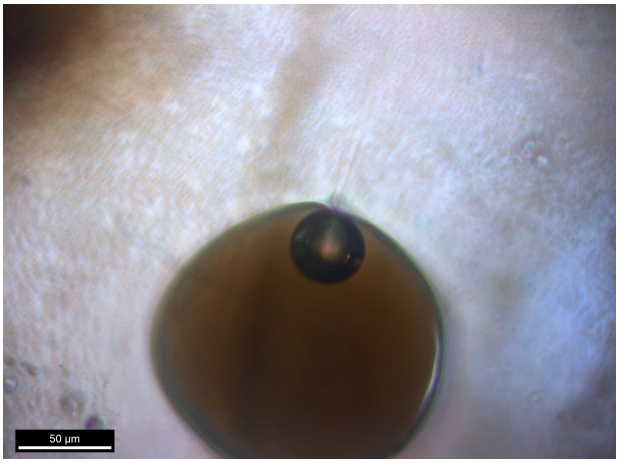
50 µm

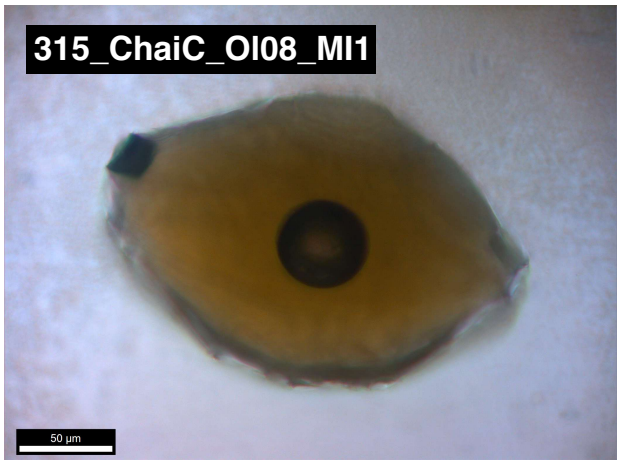
315_ChaiC_Ol08_MI1
50 µm

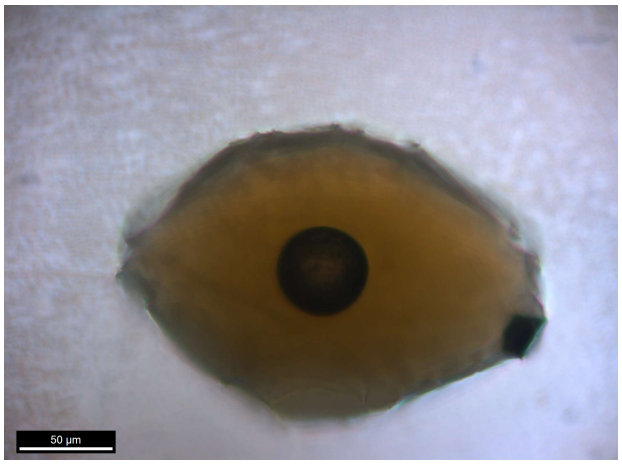
50 µm

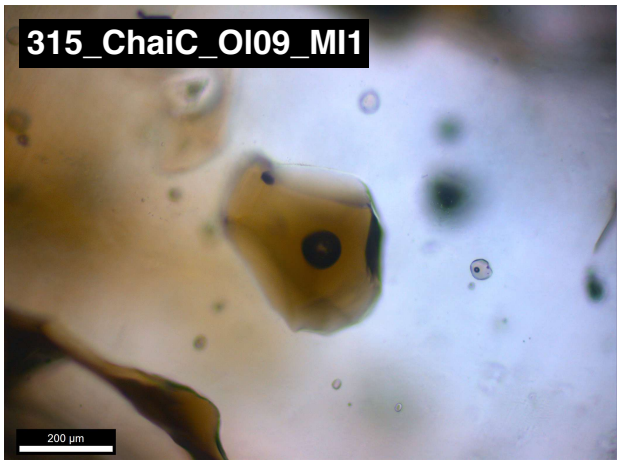
315_ChaiC_Ol09_MI1
200 µm


315_ChaiC_Plg01_MI1
50 µm

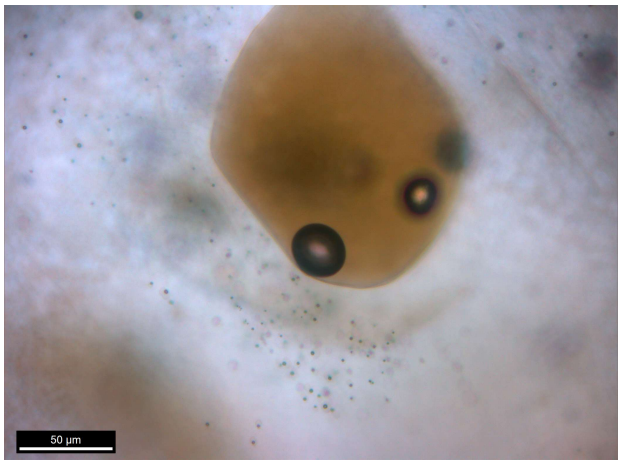
50 µm

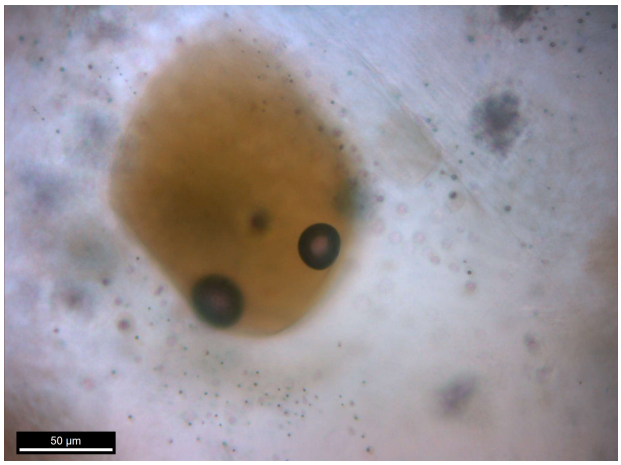
50 µm

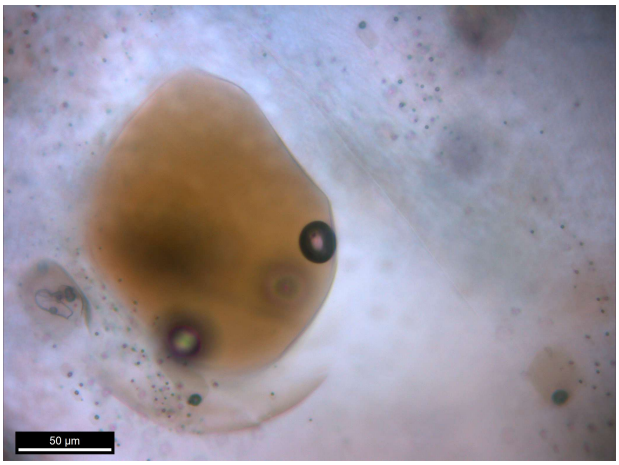
50 µm


315_ChaiC_Cpx01_MI1
50 µm

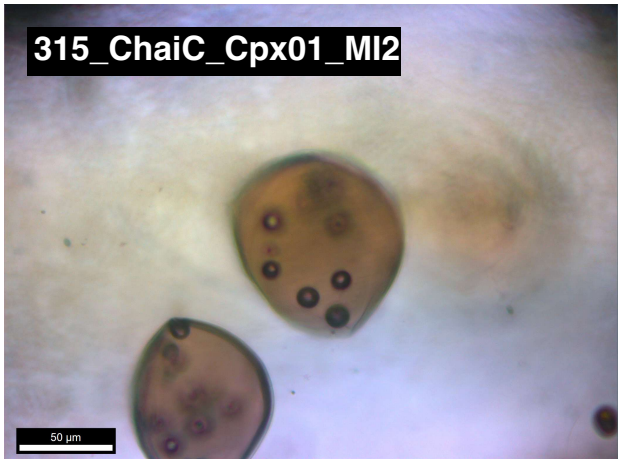
315_ChaiC_Cpx01_MI2
50 µm

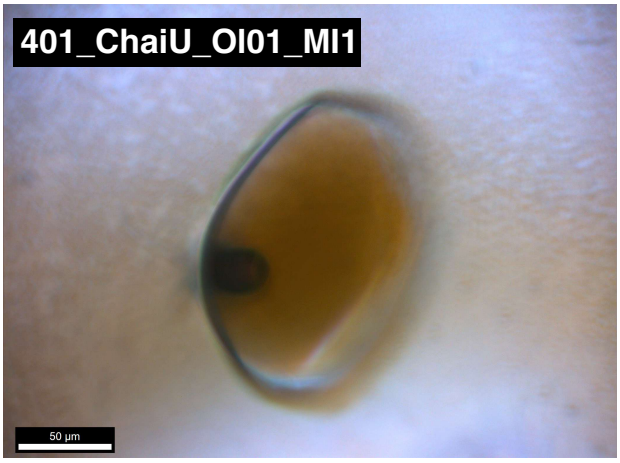
401_ChaiU_Ol01_MI1
50 µm

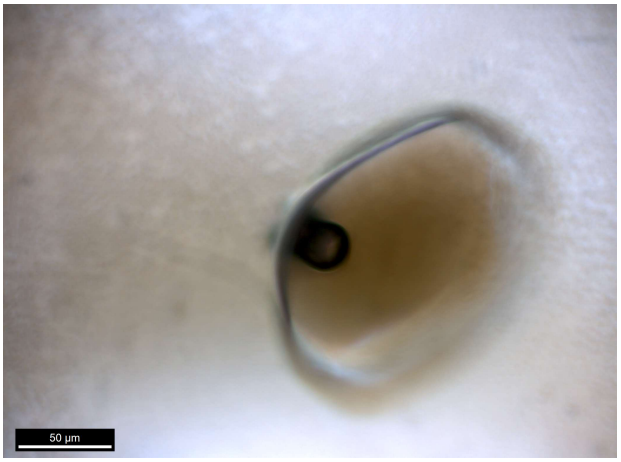
50 µm

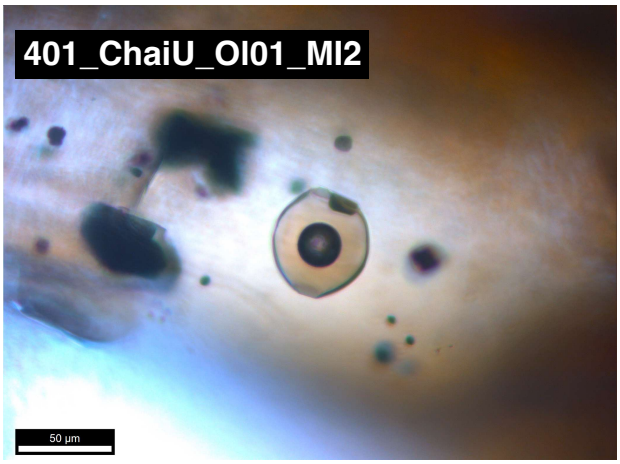
401_ChaiU_Ol01_MI2
50 µm

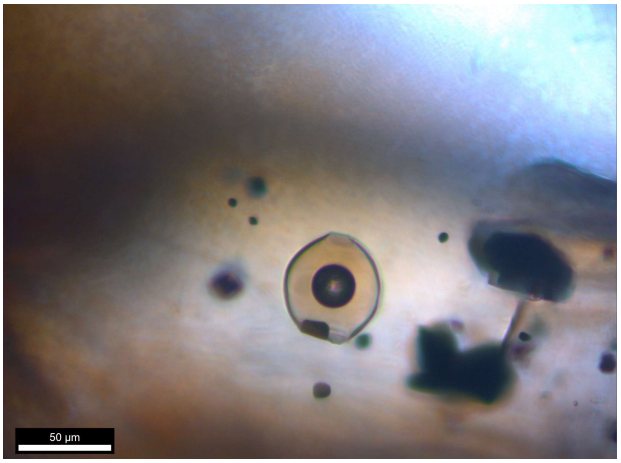
50 µm

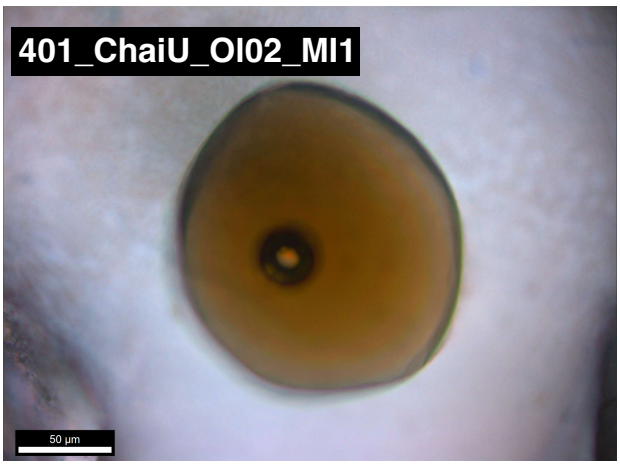
401_ChaiU_Ol02_MI1
50 µm

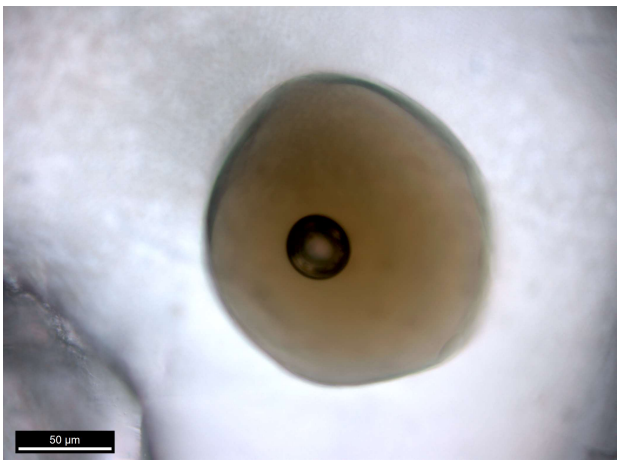
50 µm

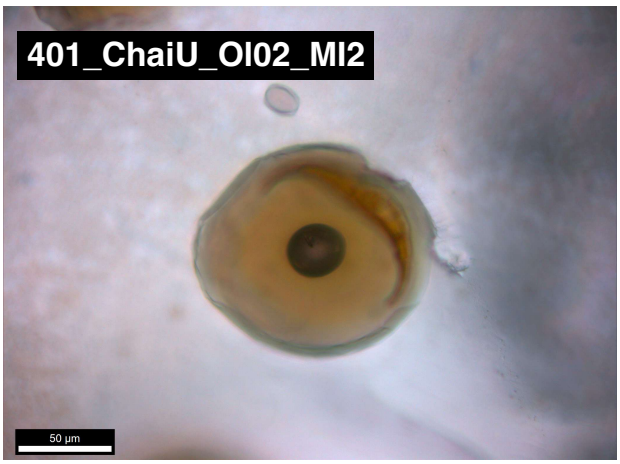
401_ChaiU_Ol02_MI2
50 µm

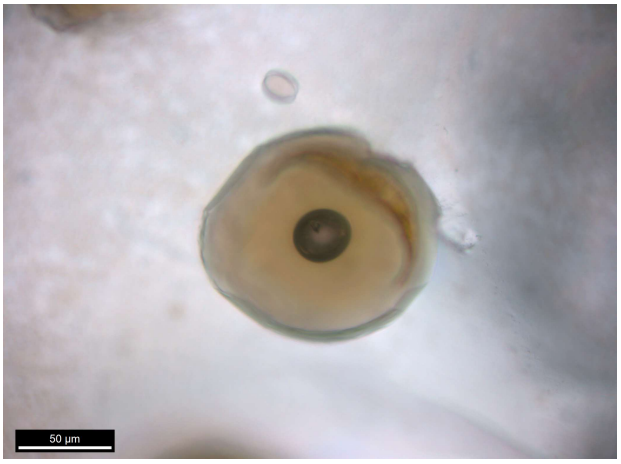
50 µm

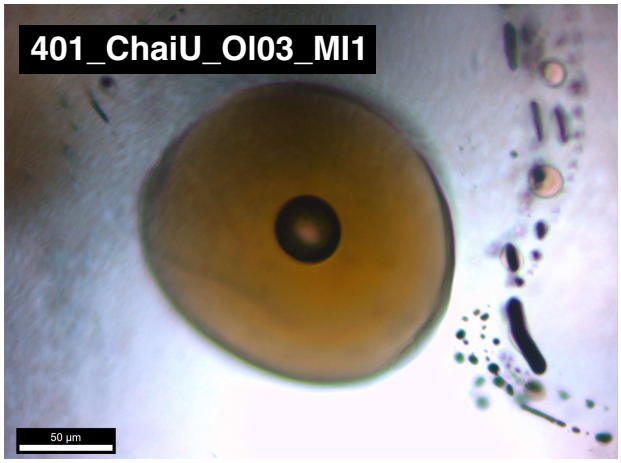
401_ChaiU_Ol03_MI1
50 µm

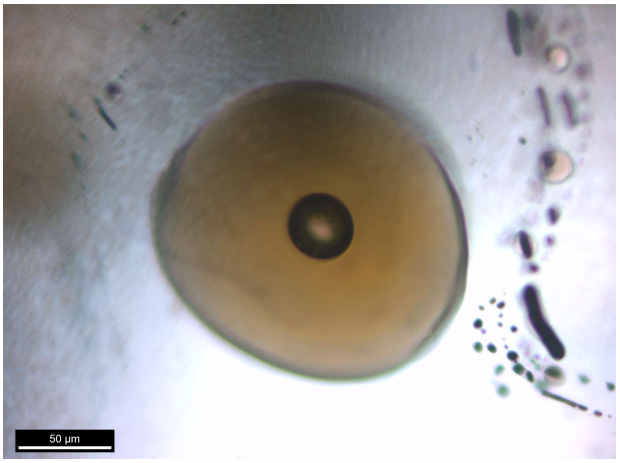
50 µm

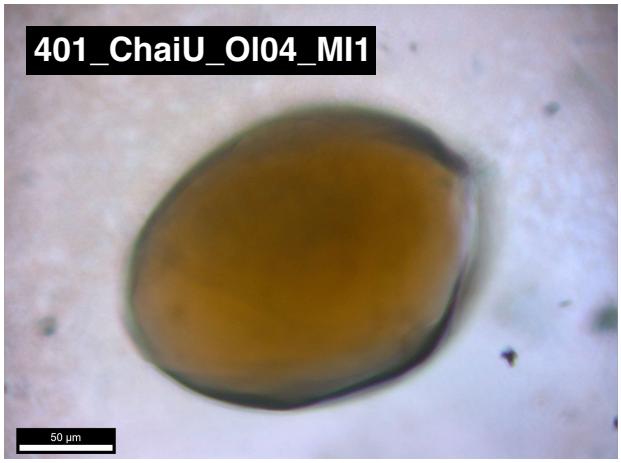
401_ChaiU_Ol04_MI1
50 µm

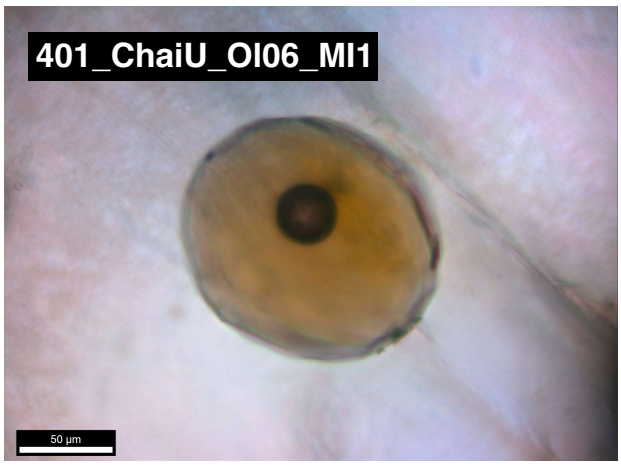
401_ChaiU_Ol06_MI1
50 µm

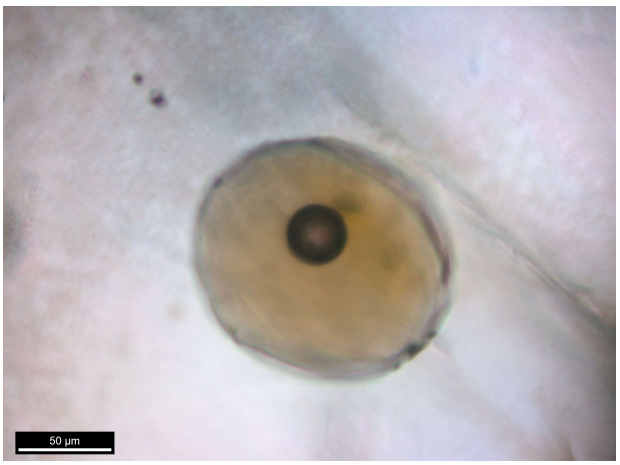
50 µm

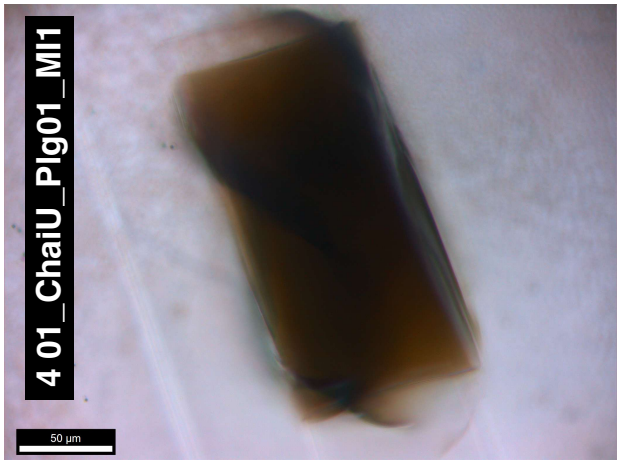
4 01_ChaiU_Plg01_MI1
50 µm

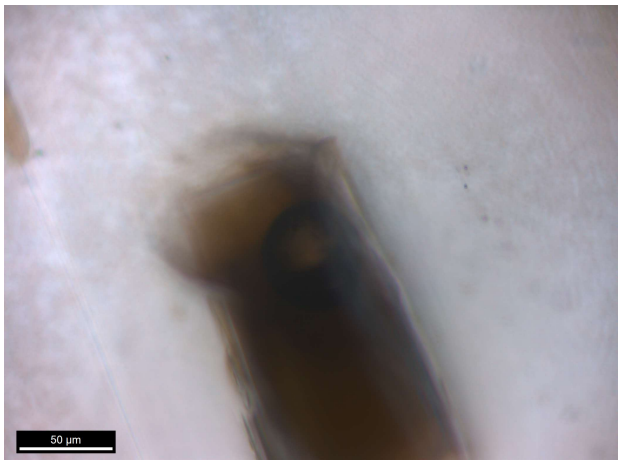
50 µm

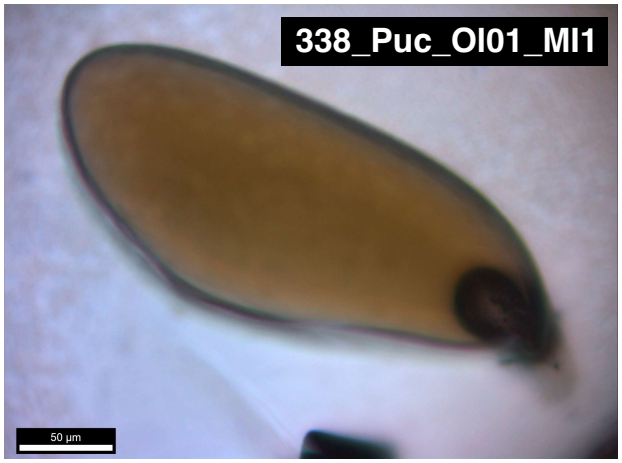
338_Puc_Ol01_MI1
50 µm

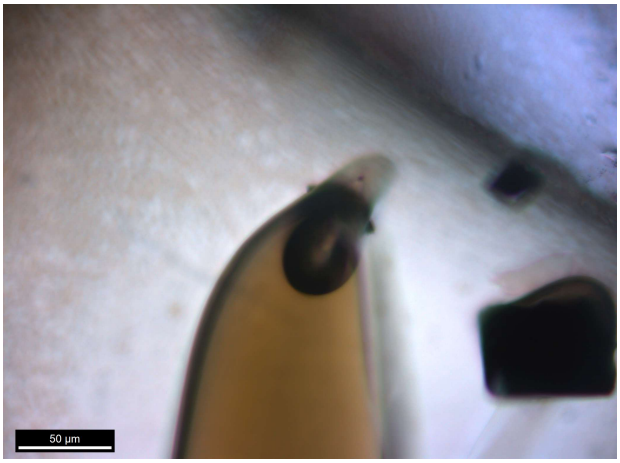
50 µm

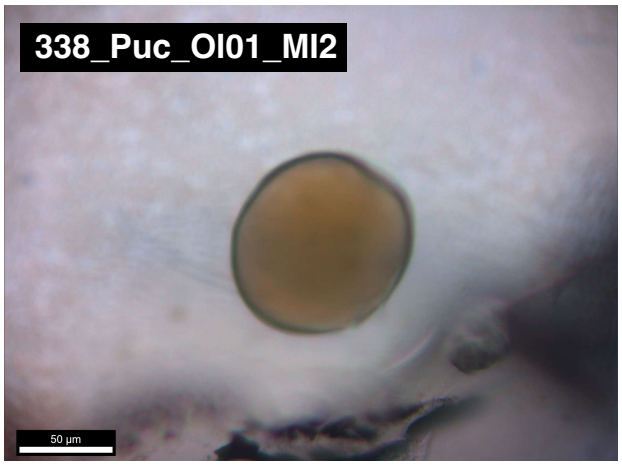
338_Puc_Ol01_MI2
50 µm

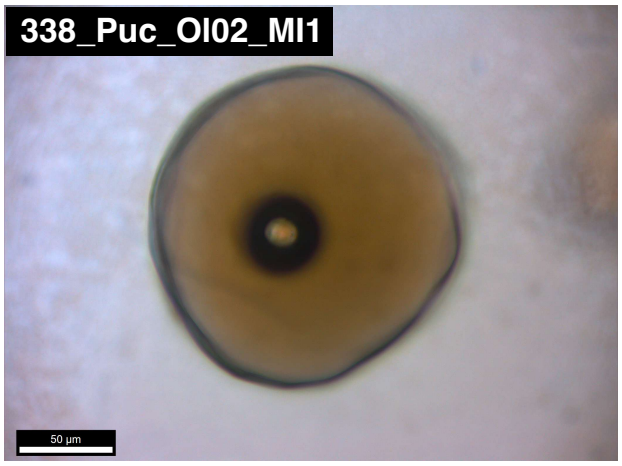
338_Puc_Ol02_MI1
50 µm

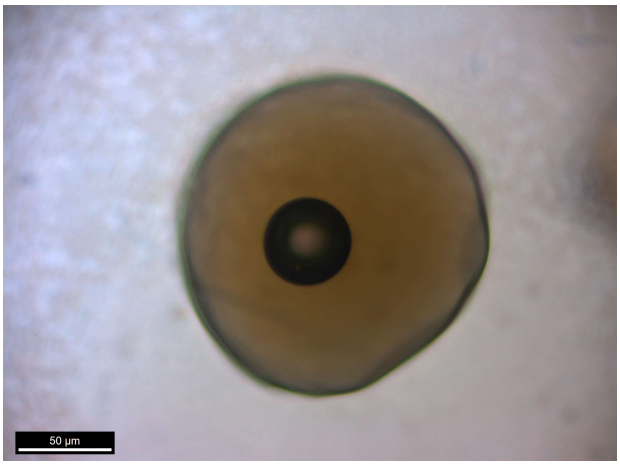
50 µm

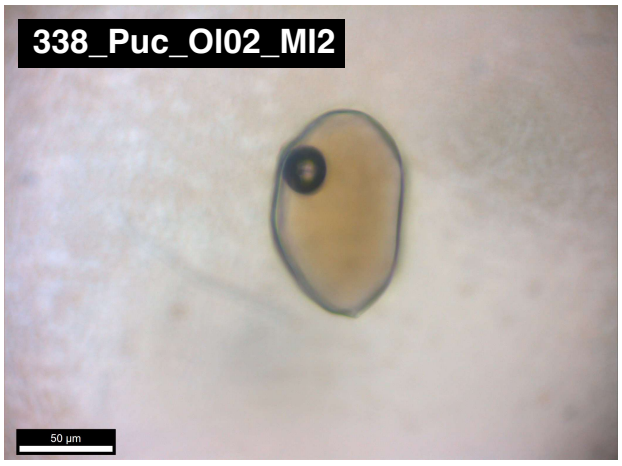
338_Puc_Ol02_MI2
50 µm

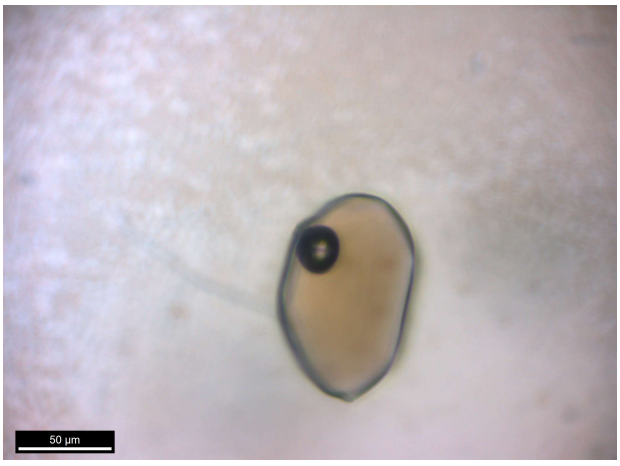
50 µm

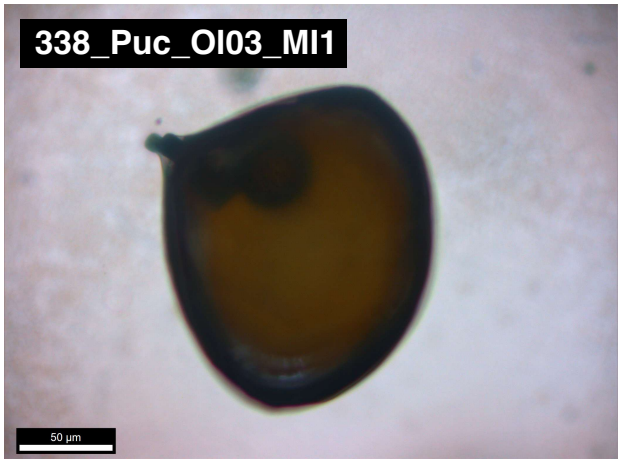
338_Puc_OI03_MI1
50 µm

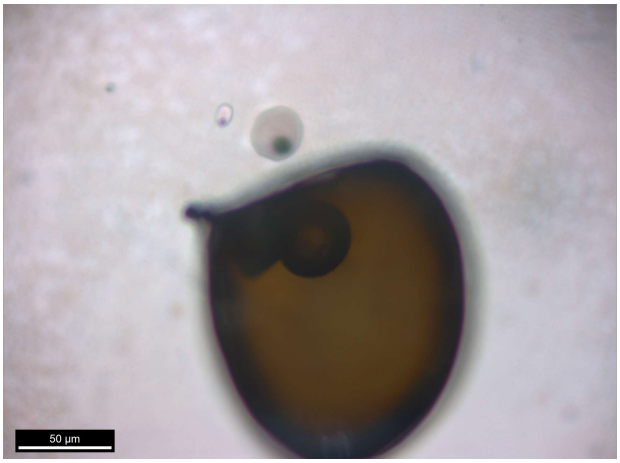
50 µm

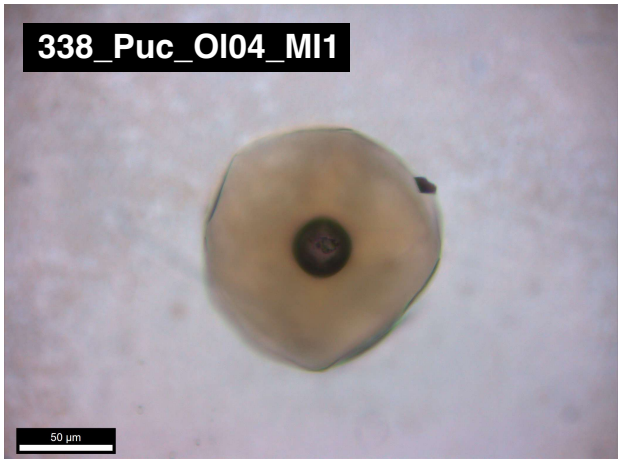
338_Puc_OI04_MI1
50 µm

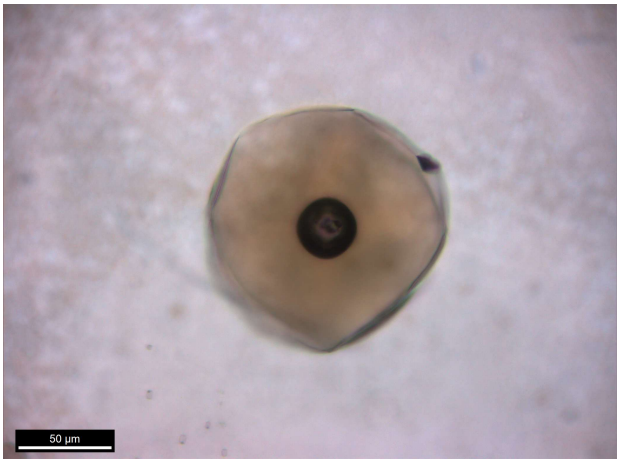
50 µm

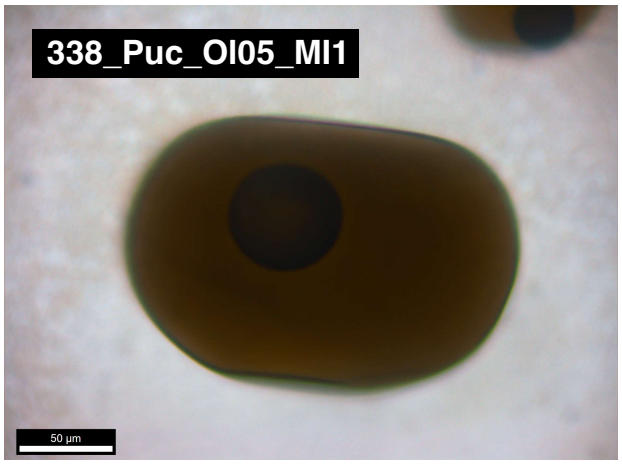
338_Puc_OI05_MI1
50 µm

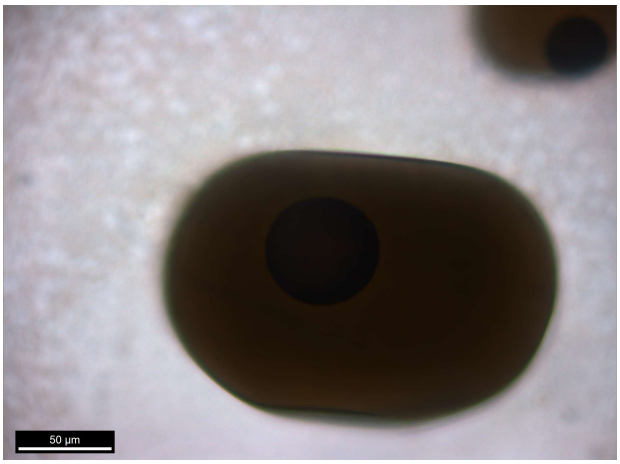
50 µm

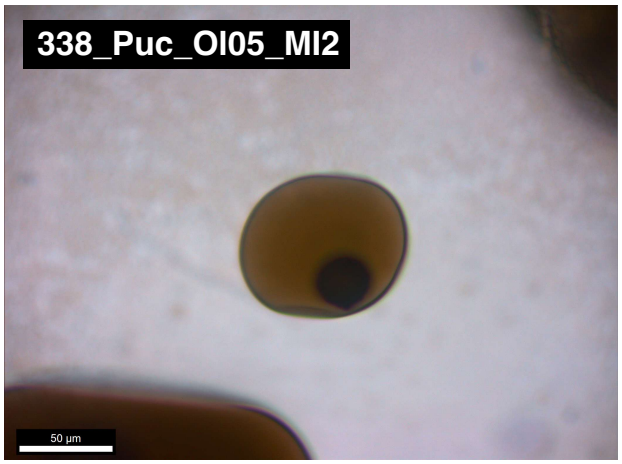
338_Puc_OI05_MI2
50 µm

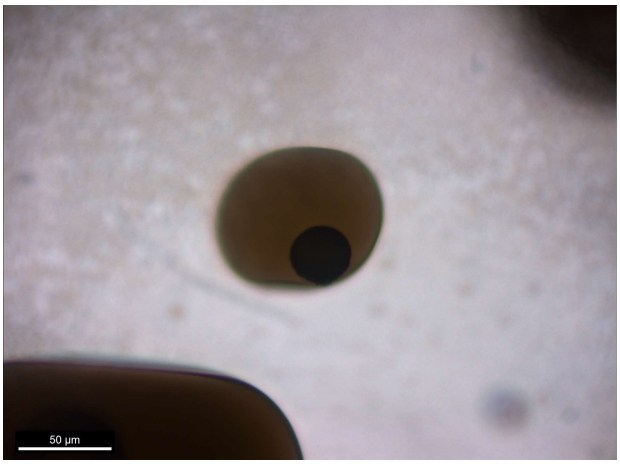
50 µm

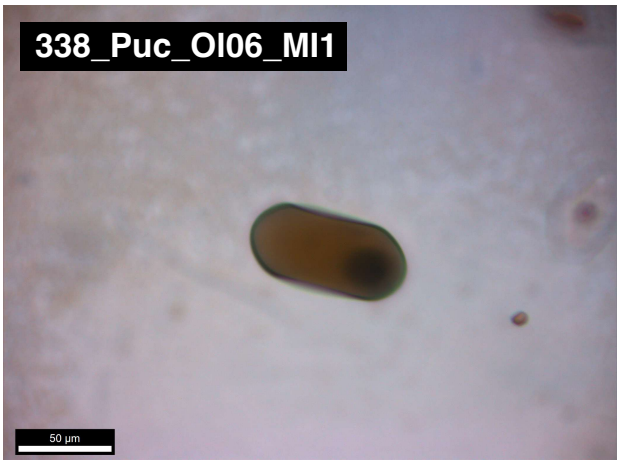
338_Puc_OI06_MI1
50 µm

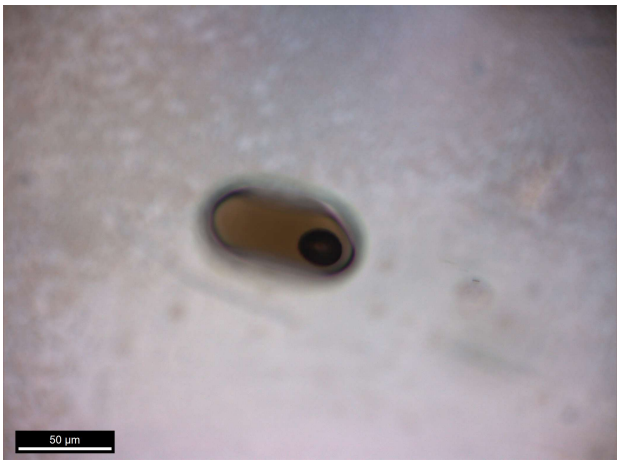
50 µm

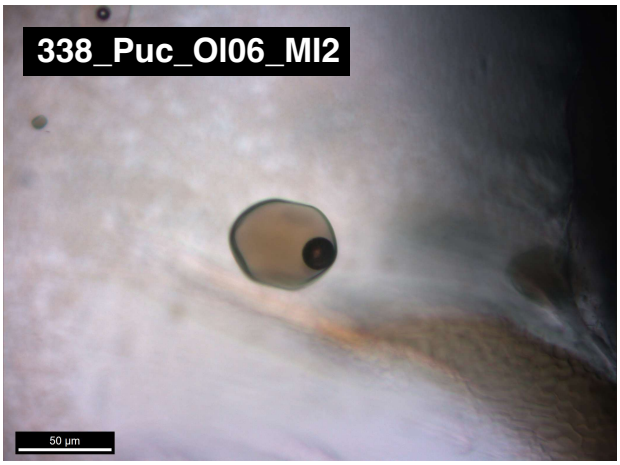
338_Puc_OI06_MI2
50 µm

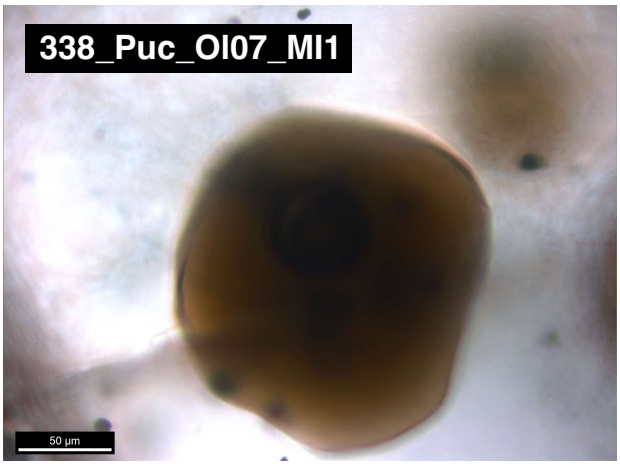
338_Puc_OI07_MI1
50 µm

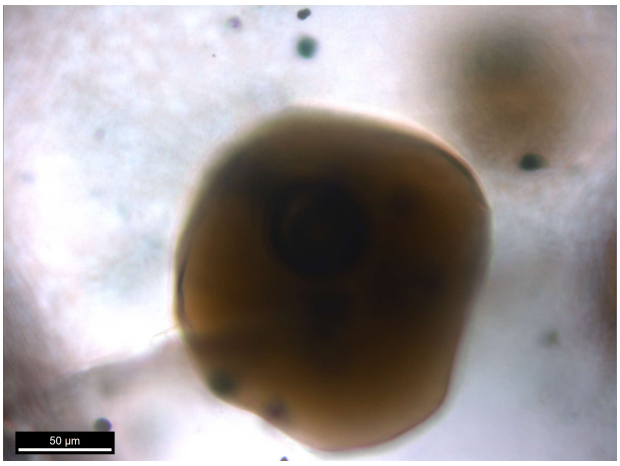
50 µm

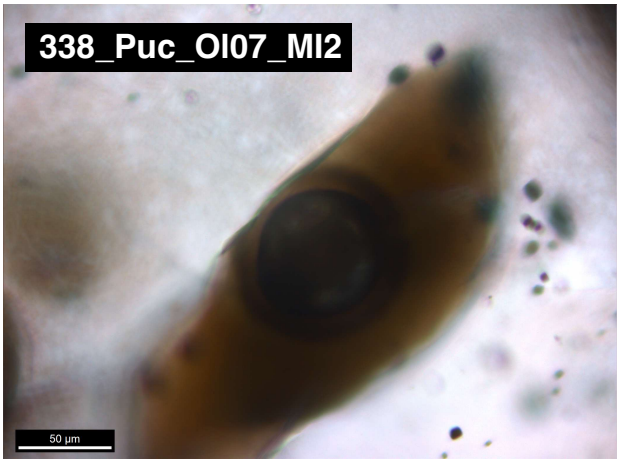
338_Puc_OI07_MI2
50 µm

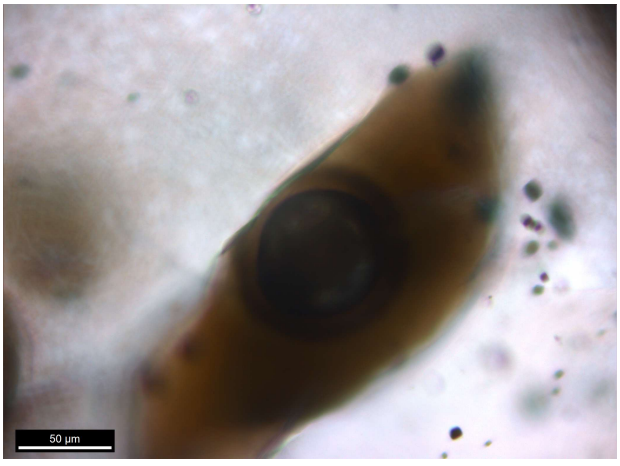
50 µm

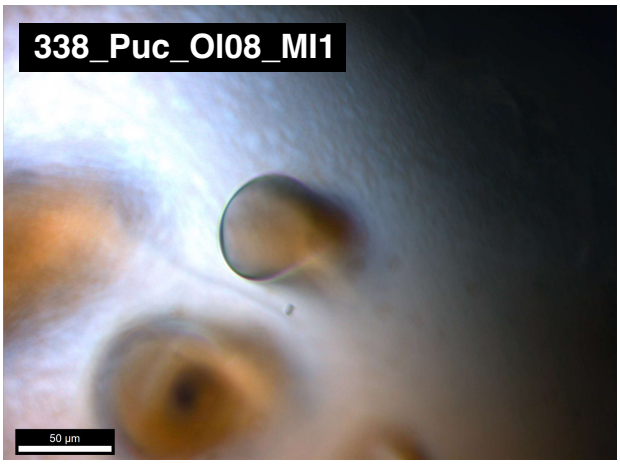
338_Puc_Ol08_MI1
50 µm

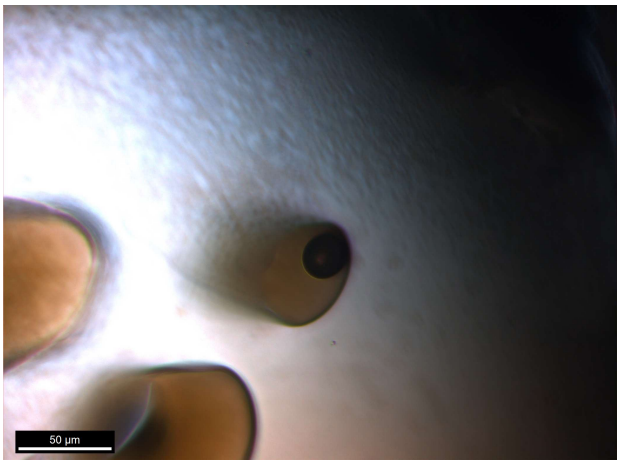
50 µm

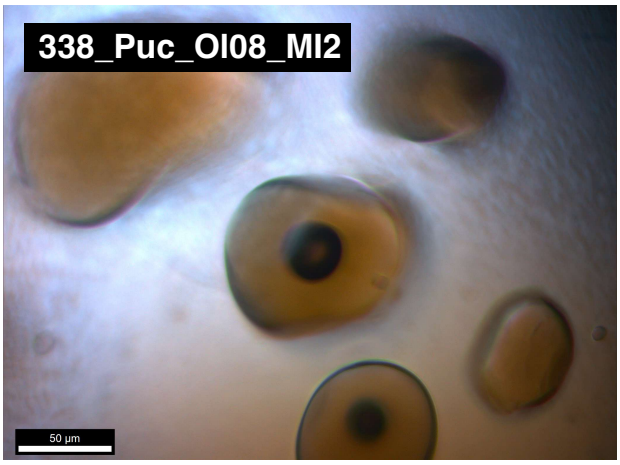
338_Puc_Ol08_MI2
50 µm

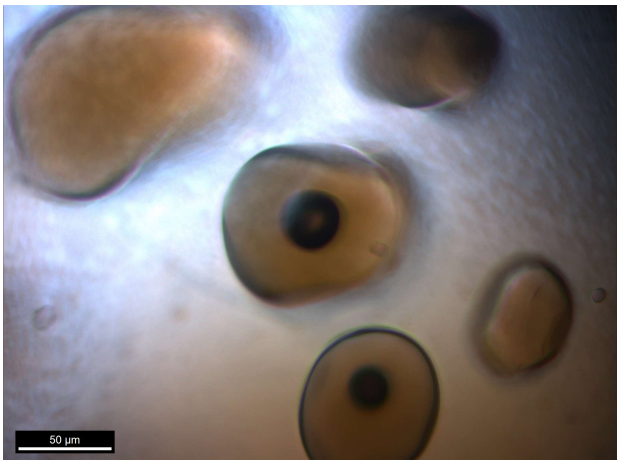
50 µm

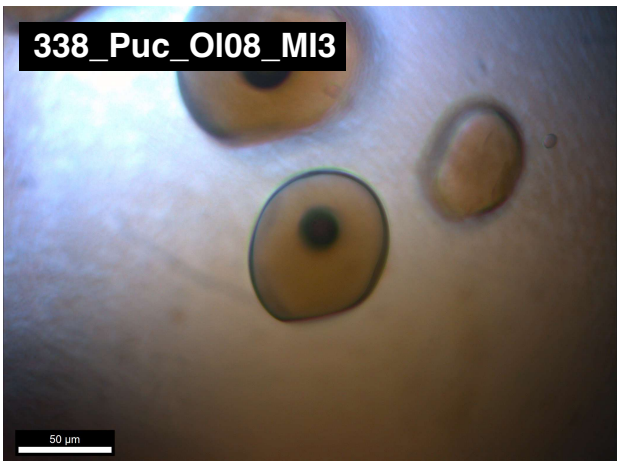
338_Puc_Ol08_MI3
50 µm

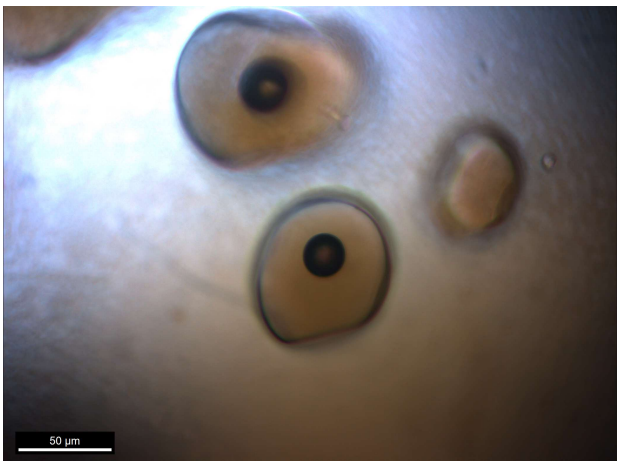
50 µm

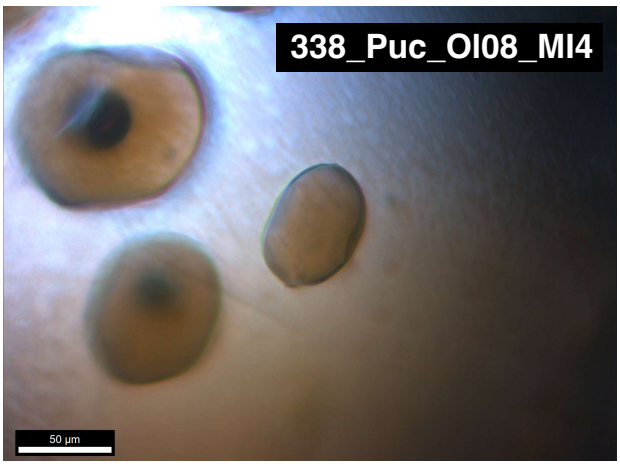
338_Puc_Ol08_MI4
50 µm

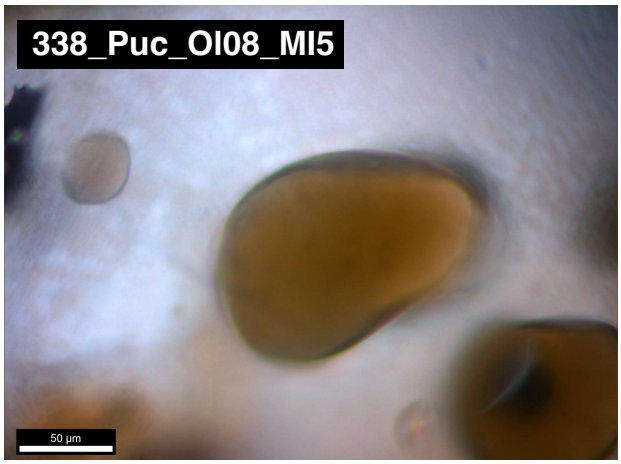
338_Puc_Ol08_MI5
50 µm

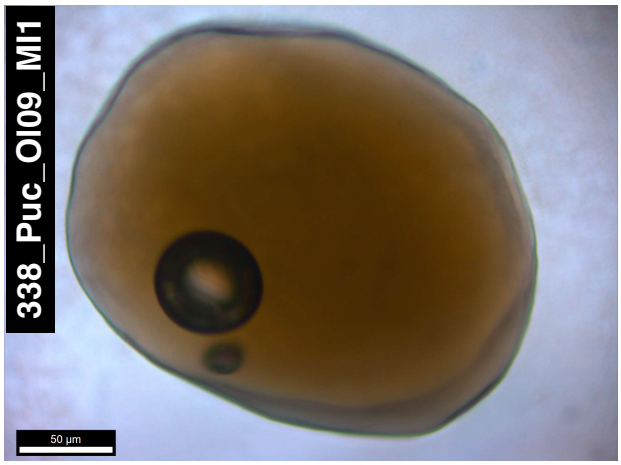
338_Puc_Ol09_MI1
50 µm

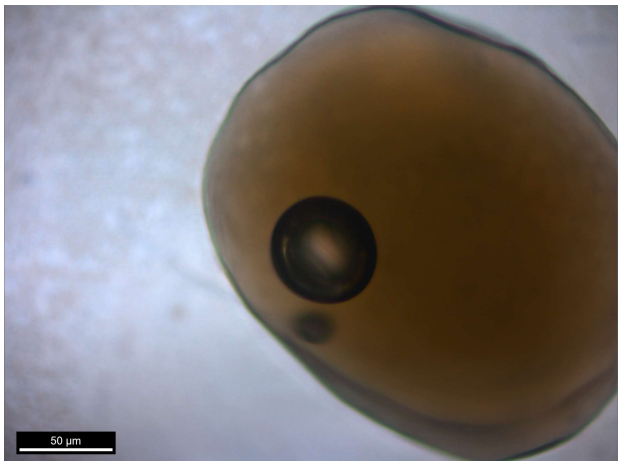
50 µm

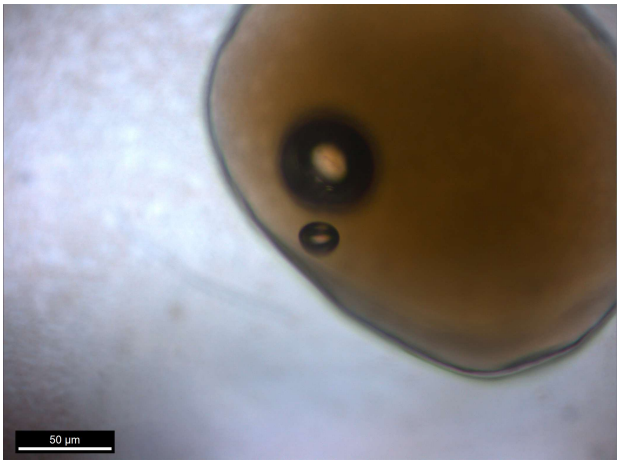
50 µm

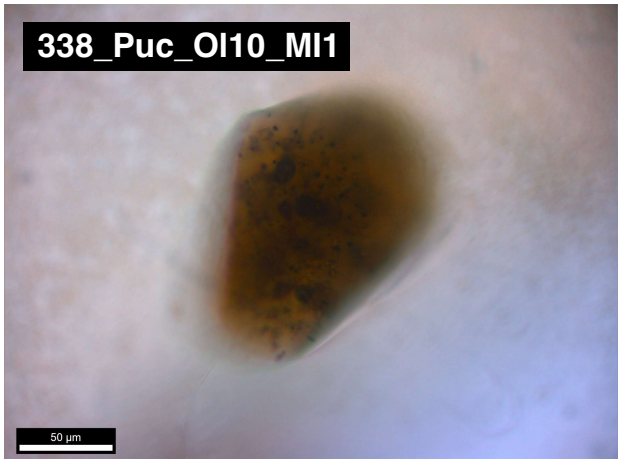
338_Puc_Ol10_MI1
50 µm

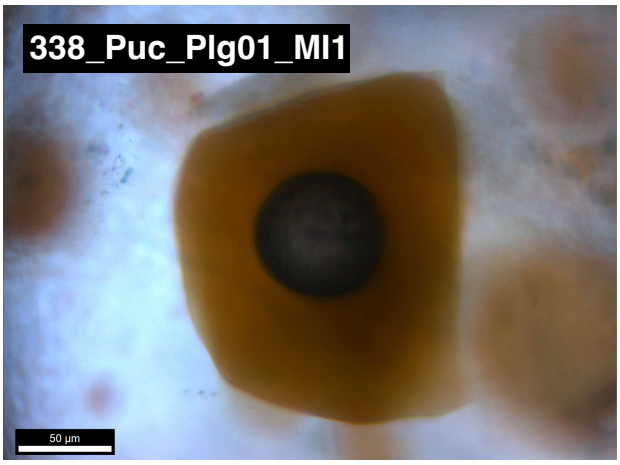
338_Puc_Plg01_MI1
50 µm

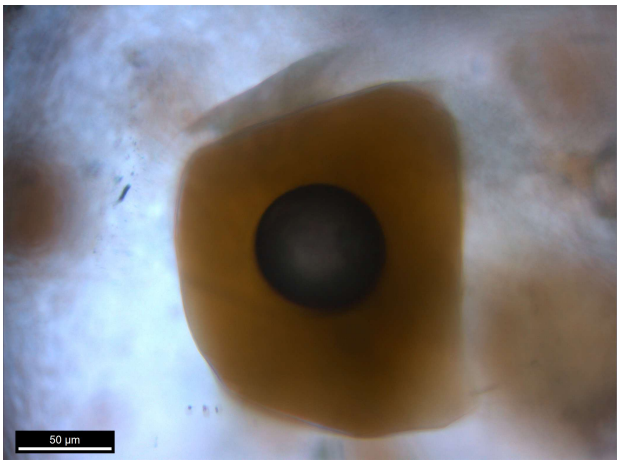
50 µm

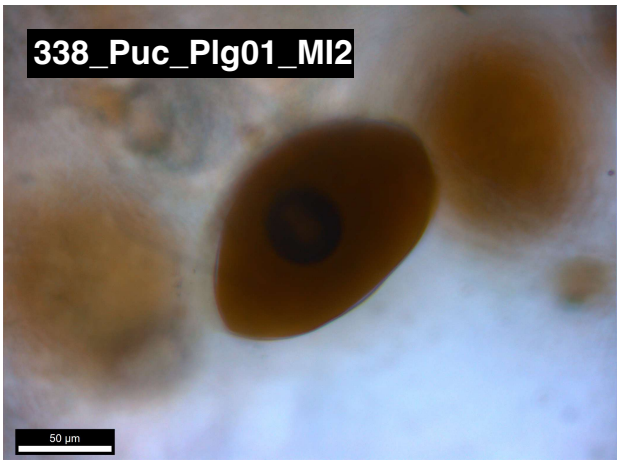
338_Puc_Plg01_MI2
50 µm

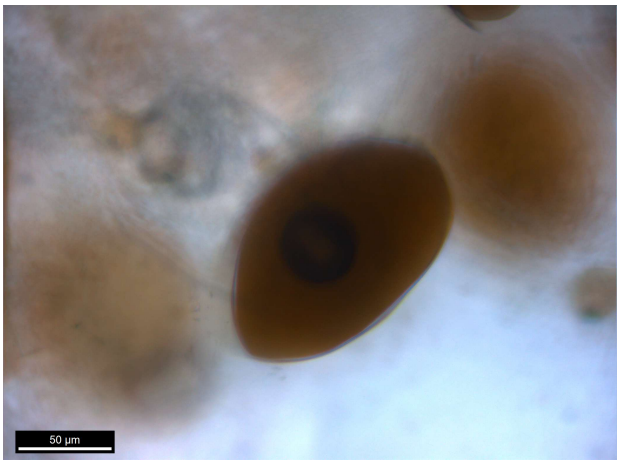
50 µm

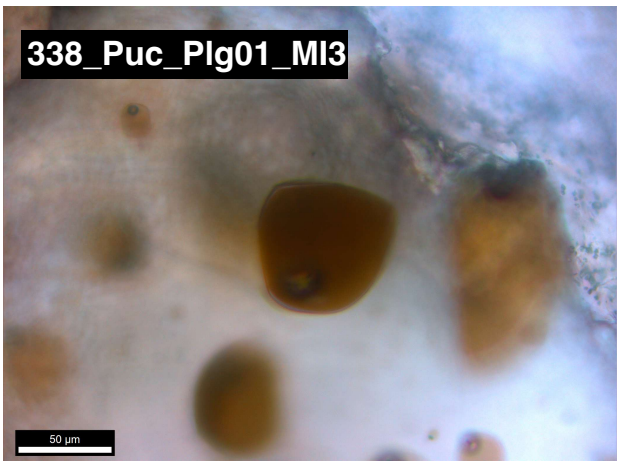
338_Puc_Plg01_MI3
50 µm

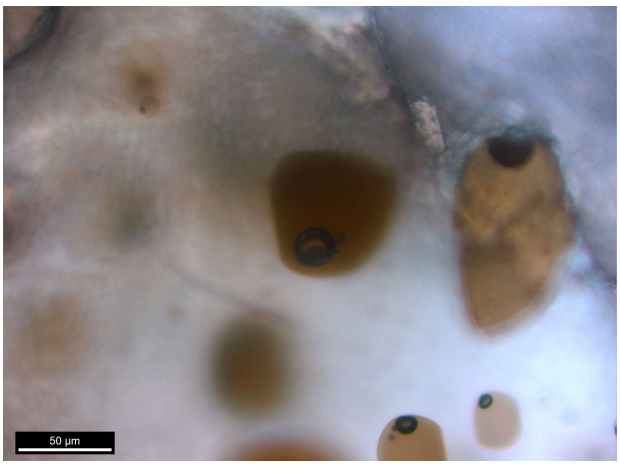
50 µm

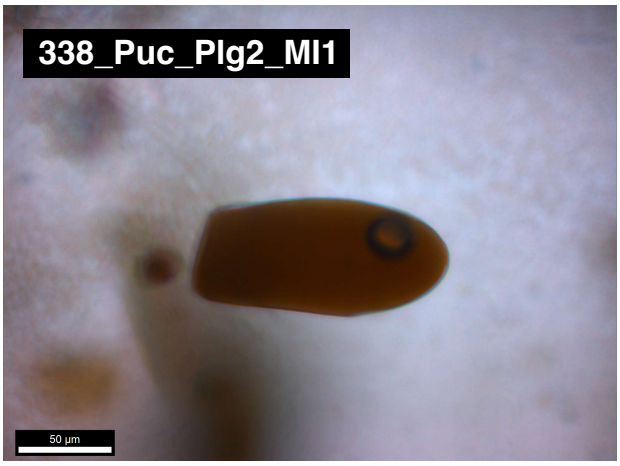
338_Puc_Plg2_MI1
50 µm

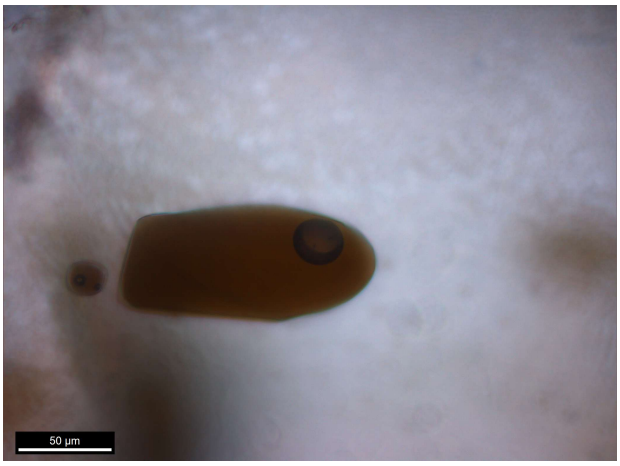
50 µm

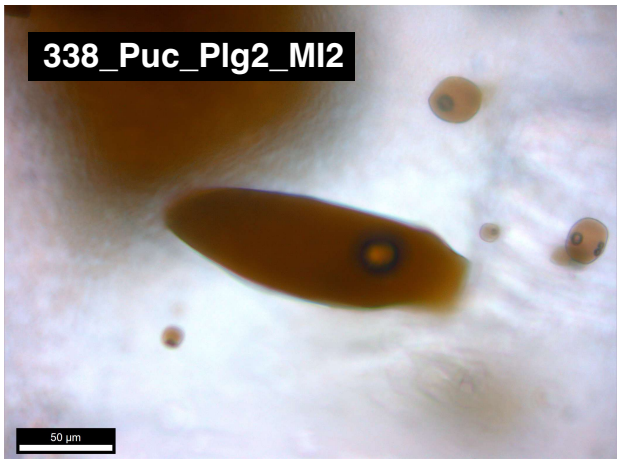
338_Puc_Plg2_MI2
50 µm

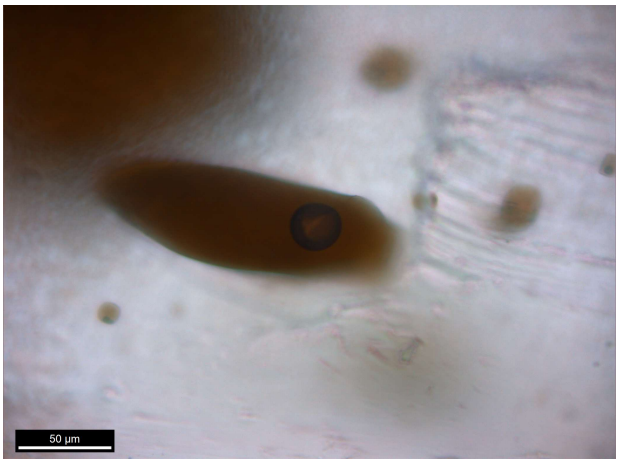
50 µm

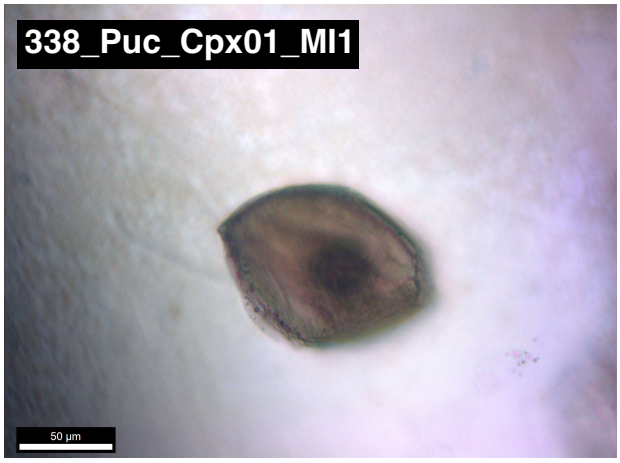
338_Puc_Cpx01_MI1
50 µm

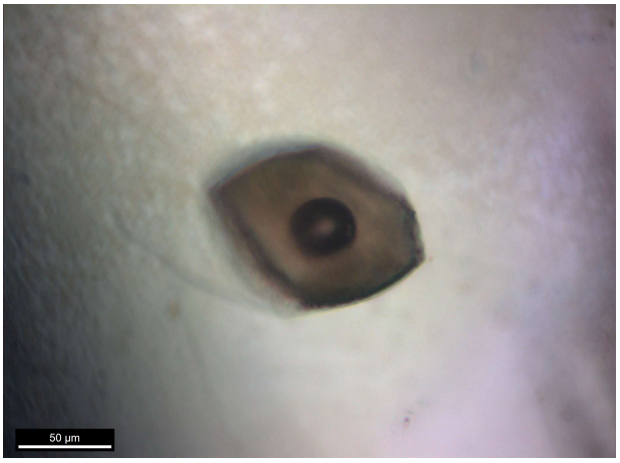
50 µm

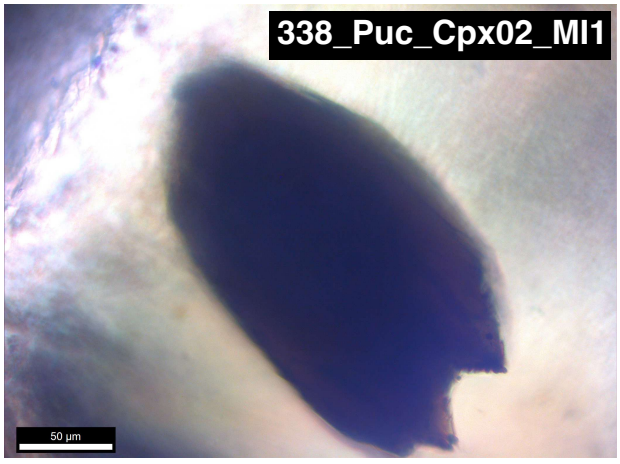
338_Puc_Cpx02_MI1
50 µm

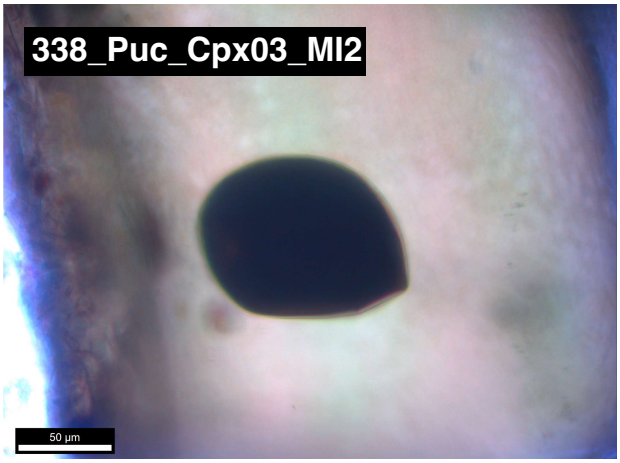
338_Puc_Cpx03_MI2
50 µm

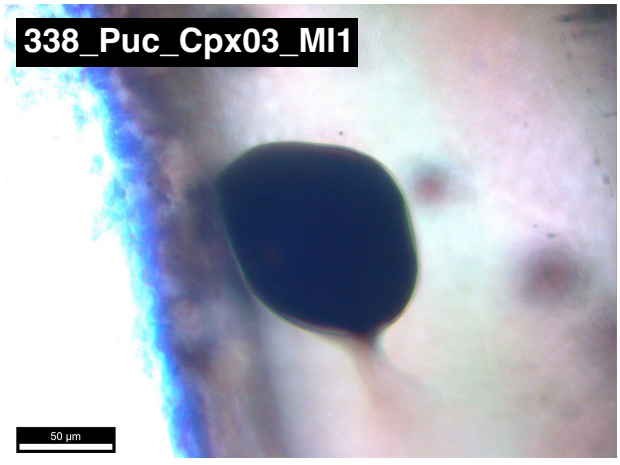
338_Puc_Cpx03_MI1
50 µm

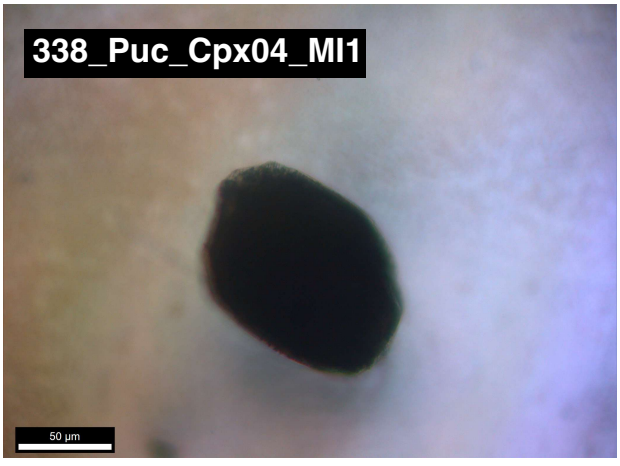
338_Puc_Cpx04_MI1
50 µm

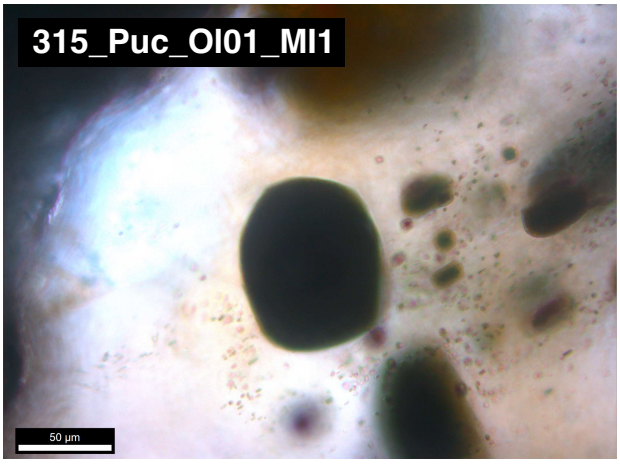
315_Puc_Ol01_MI1
50 µm

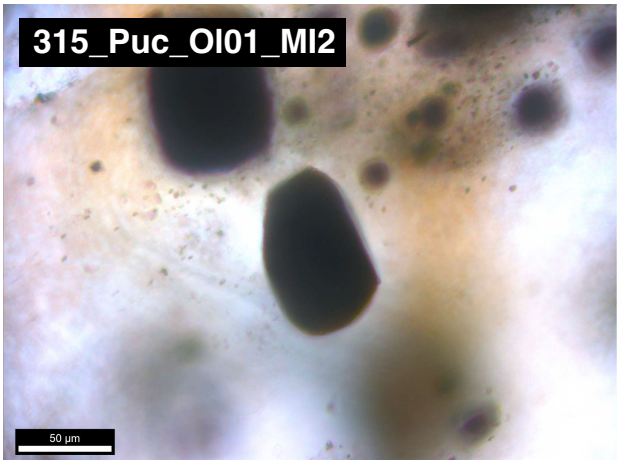
315_Puc_Ol01_MI2
50 µm

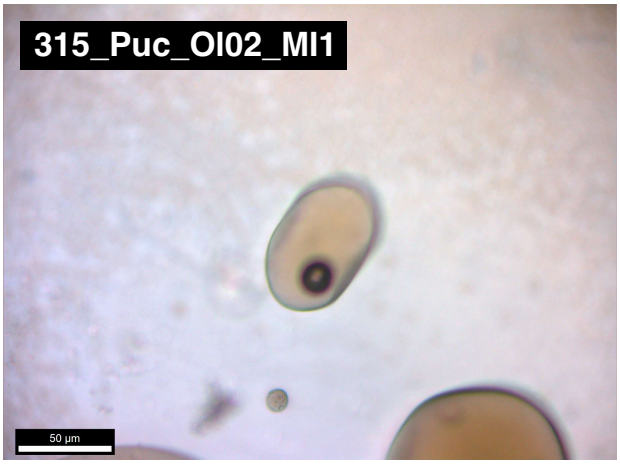
315_Puc_Ol02_MI1
50 µm

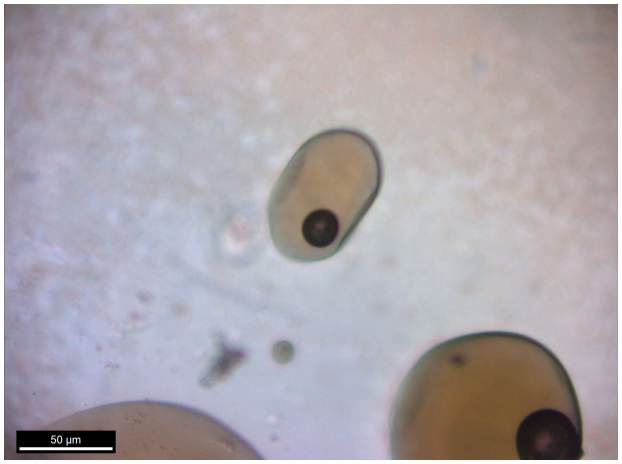
50 µm

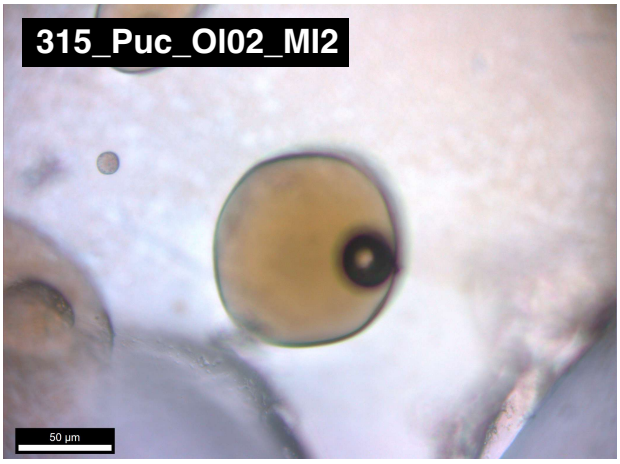
315_Puc_Ol02_MI2
50 µm

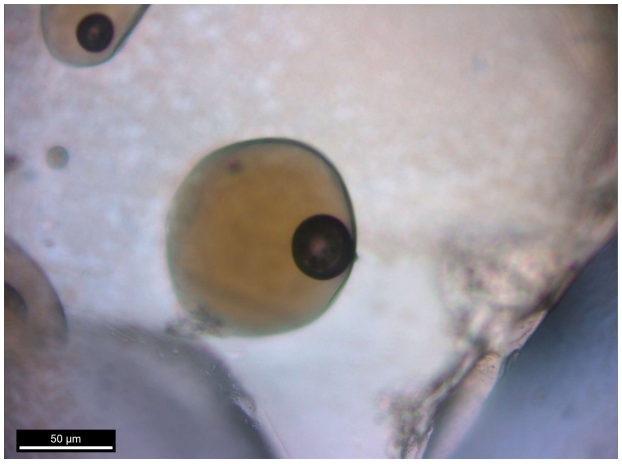
50 µm

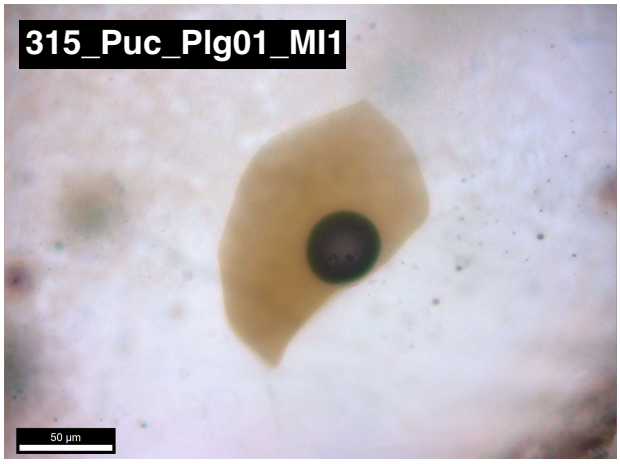
315_Puc_Plg01_MI1
50 µm

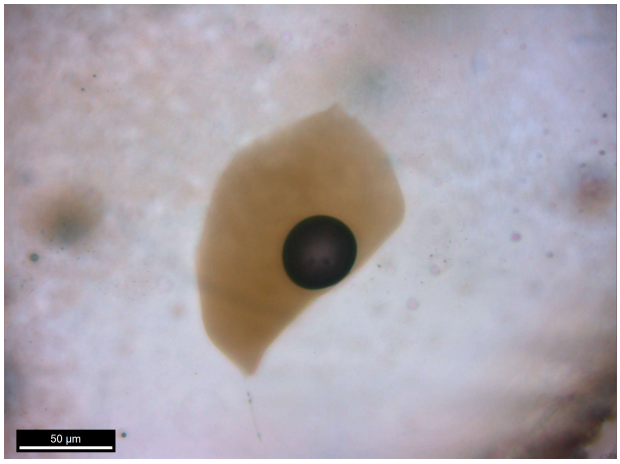
50 µm

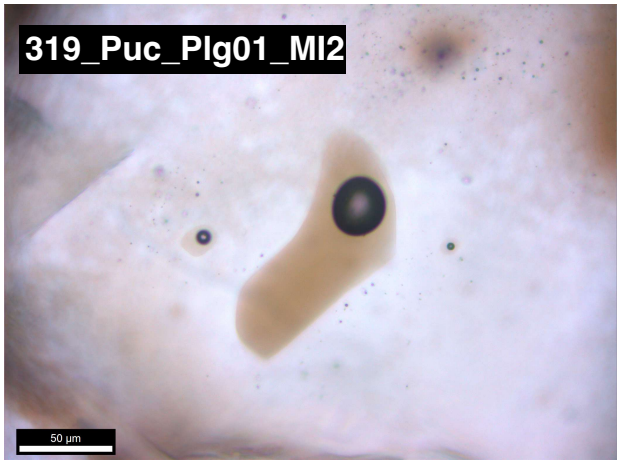
319_Puc_Plg01_MI2
50 µm


50 µm

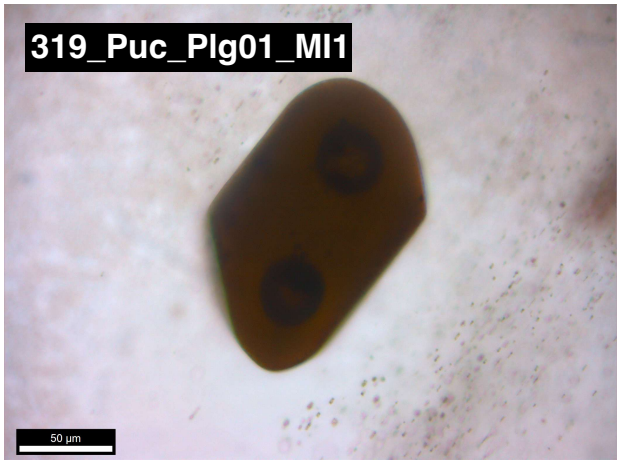
319_Puc_Plg01_MI1
50 µm

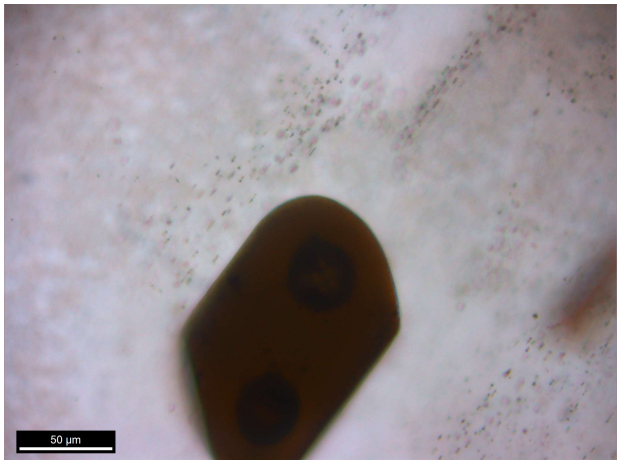
50 µm

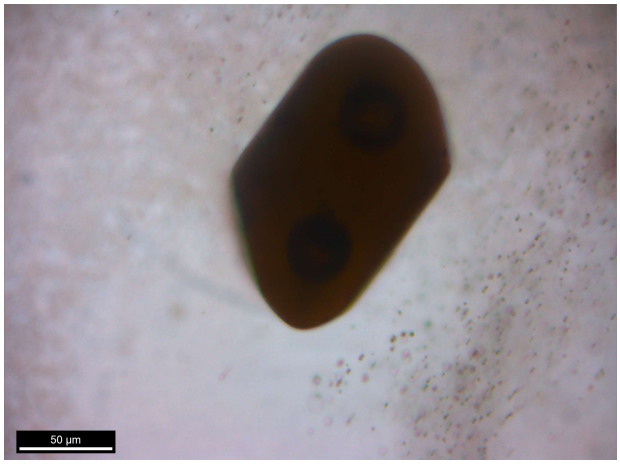
50 µm

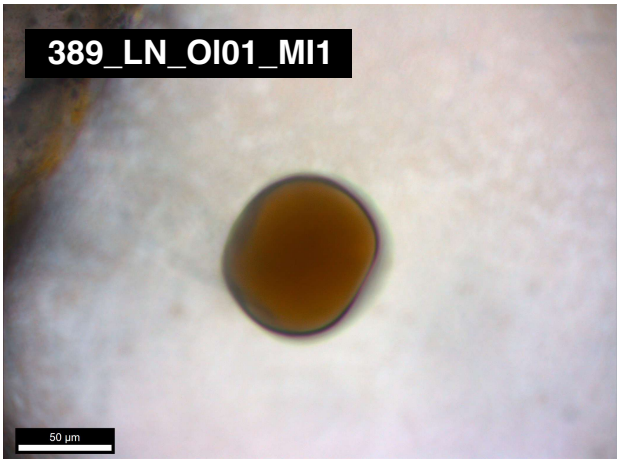
389_LN_OI01_MI1
50 µm

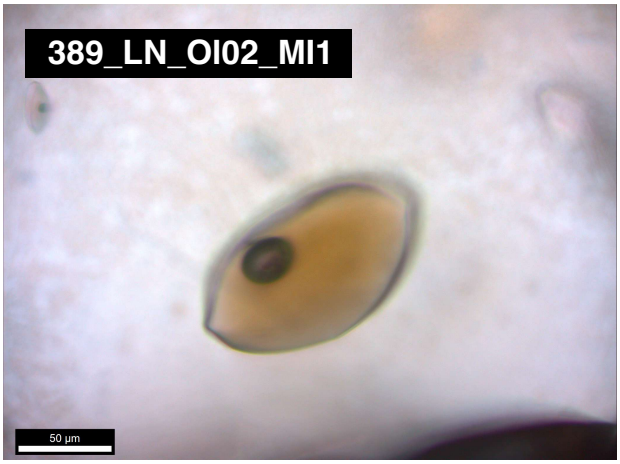
389_LN_OI02_MI1
50 µm

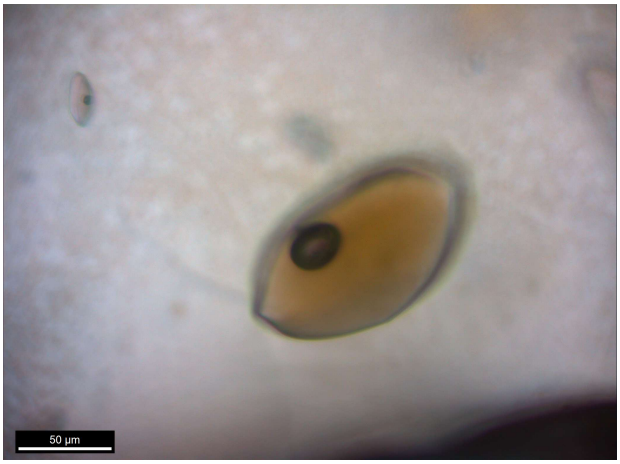
50 µm

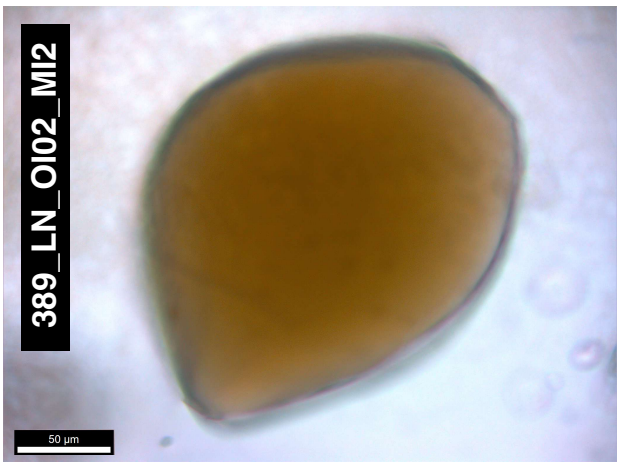
389_LN_OI02_MI2
50 µm

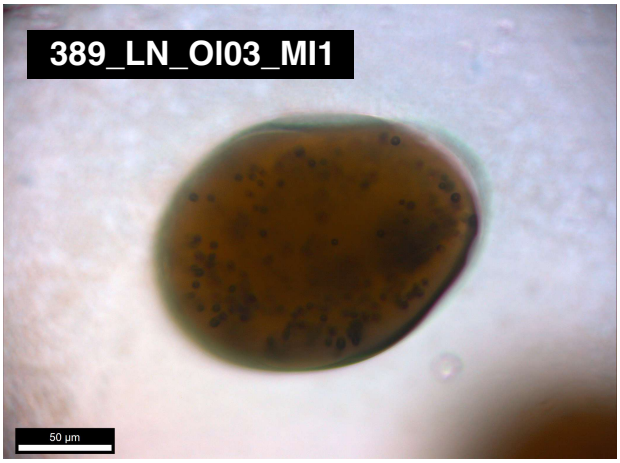
389_LN_OI03_MI1
50 µm

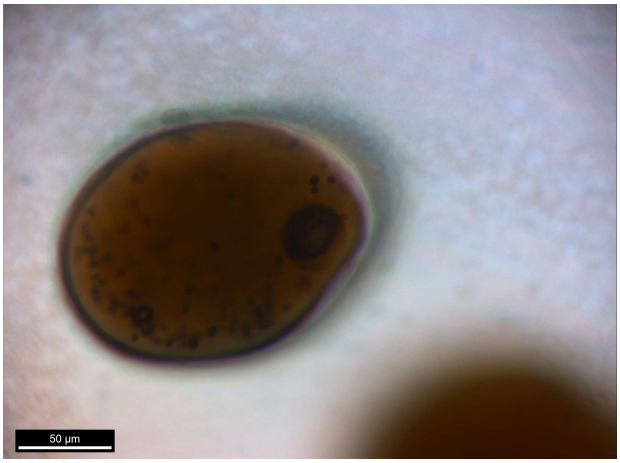
50 µm

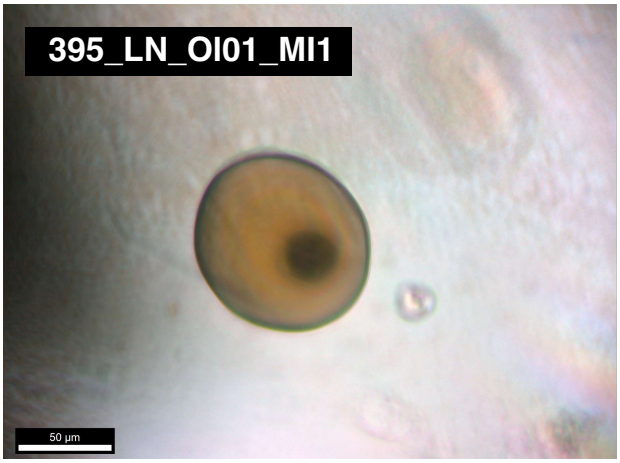
395_LN_OI01_MI1
50 µm

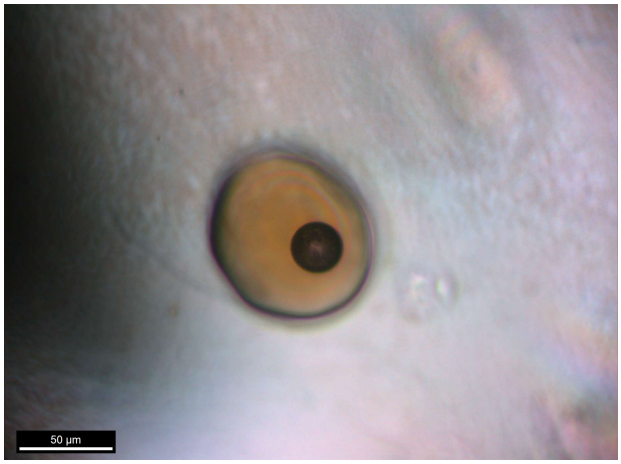
50 µm

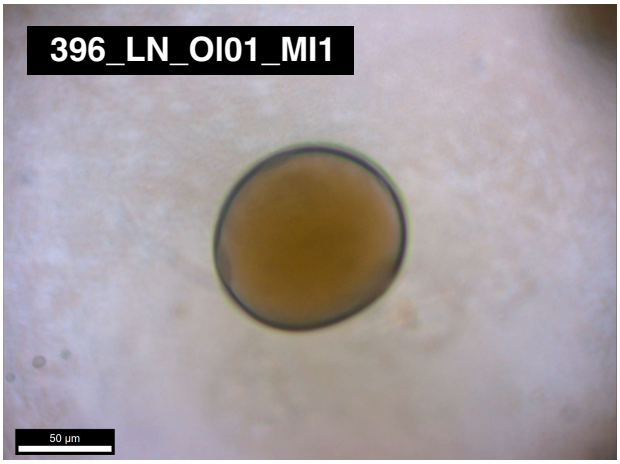
396_LN_OI01_MI1
50 µm

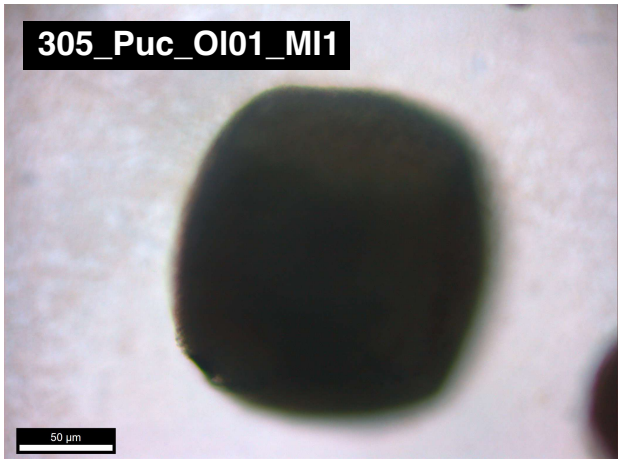
305_Puc_Ol01_MI1
50 µm

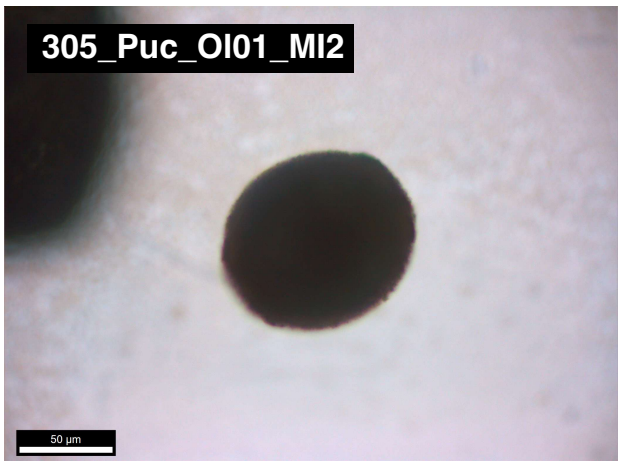
305_Puc_Ol01_MI2
50 µm

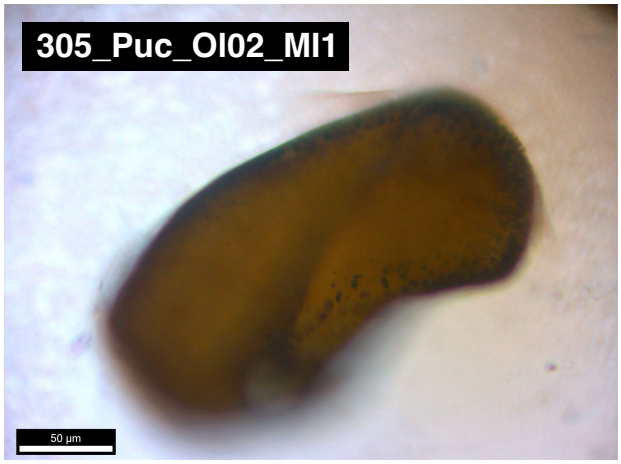
305_Puc_Ol02_MI1
50 µm

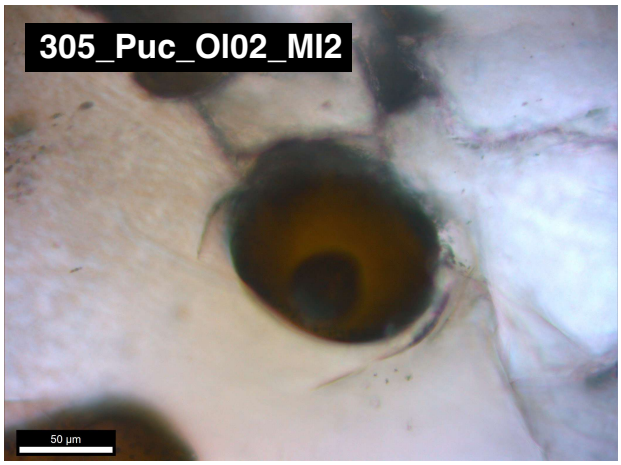
305_Puc_Ol02_MI2
50 µm

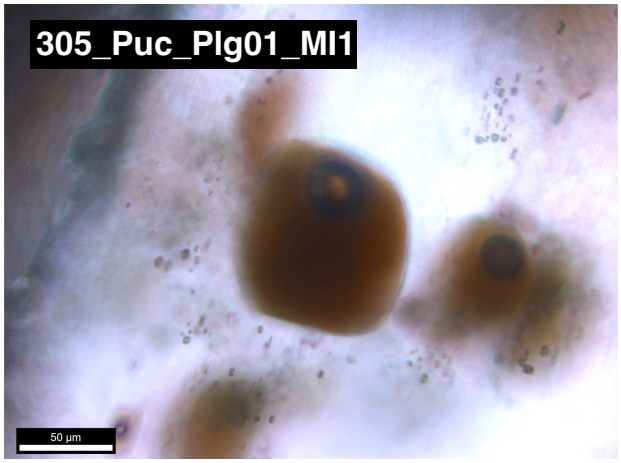
305_Puc_Plg01_MI1
50 µm

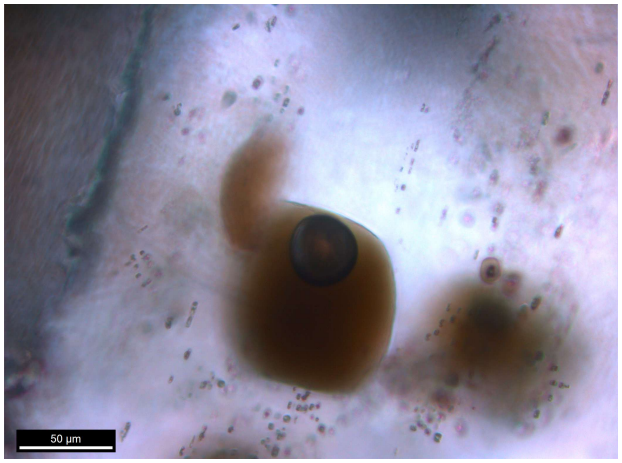
50 µm

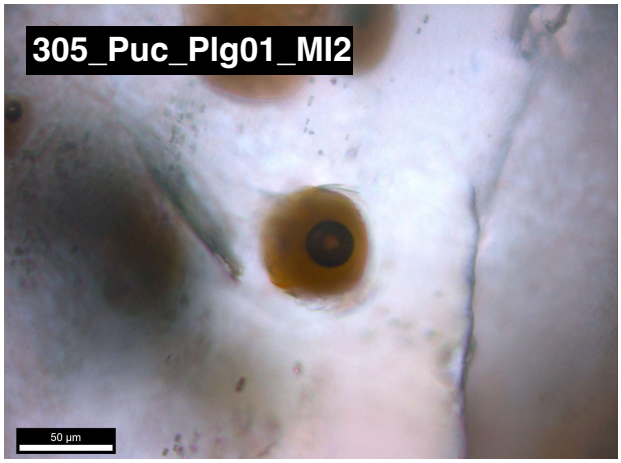
305_Puc_Plg01_MI2
50 µm

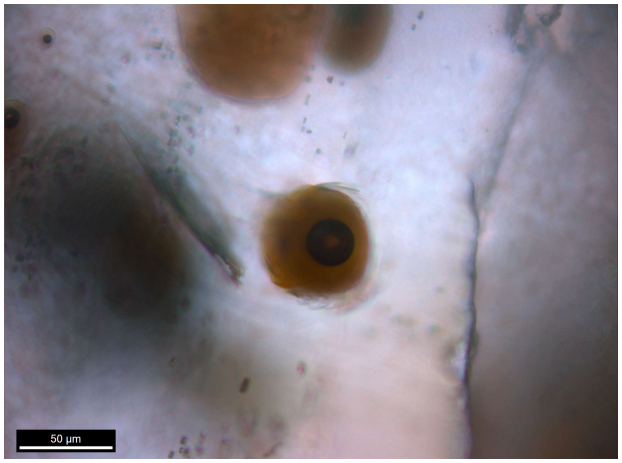
50 µm

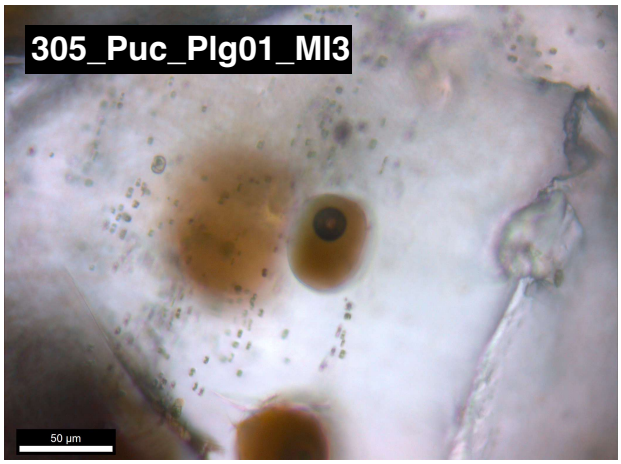
305_Puc_Plg01_MI3
50 µm

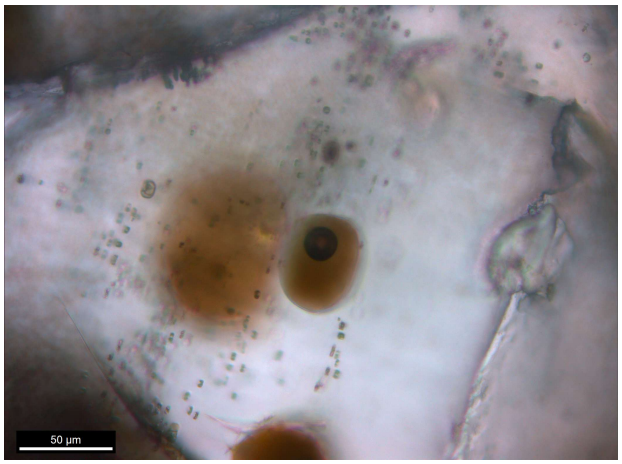
50 µm

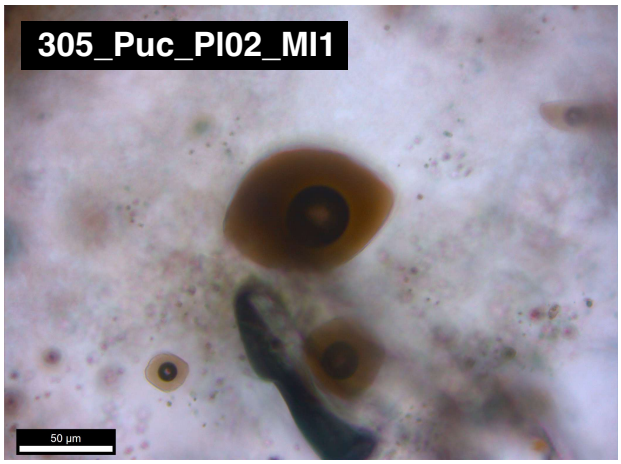
305_Puc_Pl02_MI1
50 µm

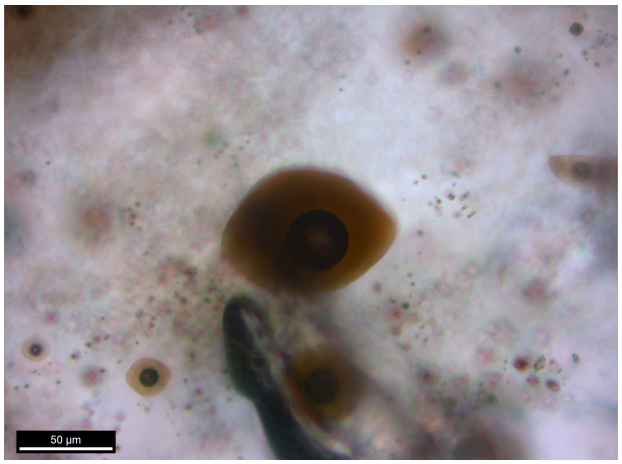
50 µm

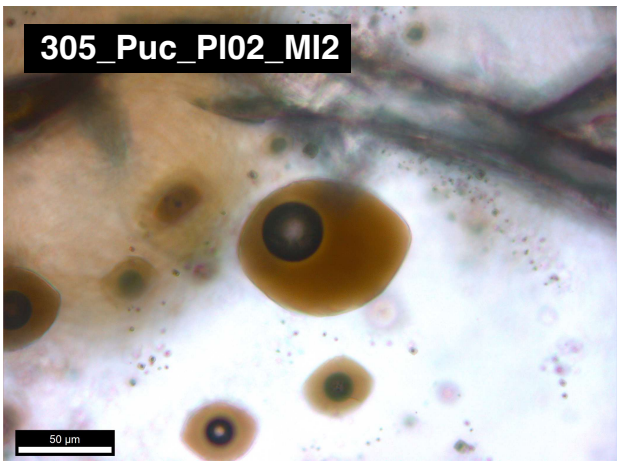
305_Puc_Pl02_Ml2
50 µm

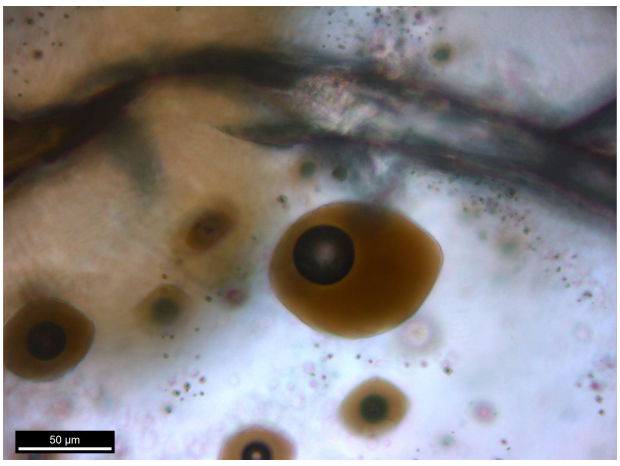
50 µm

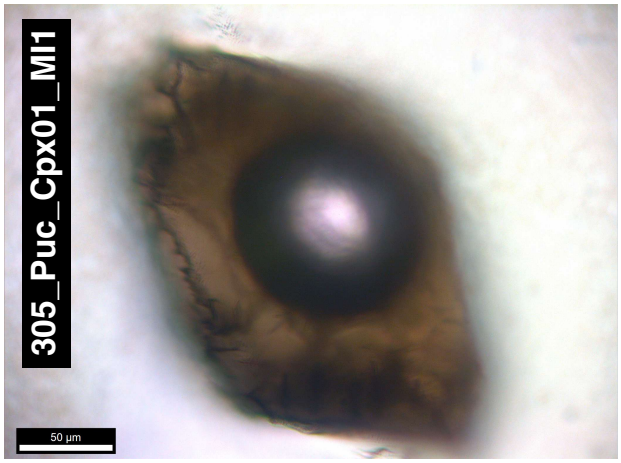
305_Puc_Cpx01_Ml1
50 µm

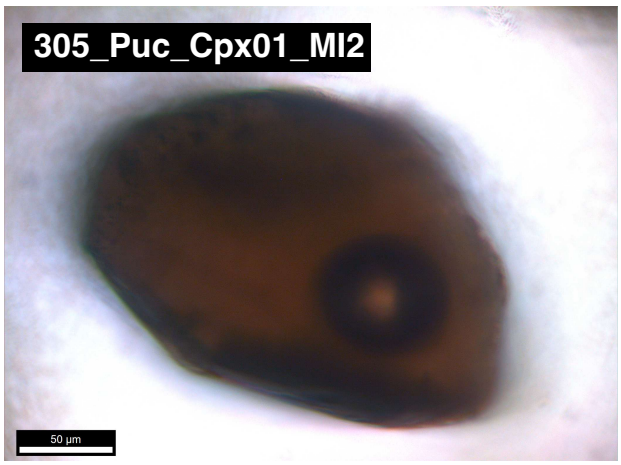
305_Puc_Cpx01_Ml2
50 µm

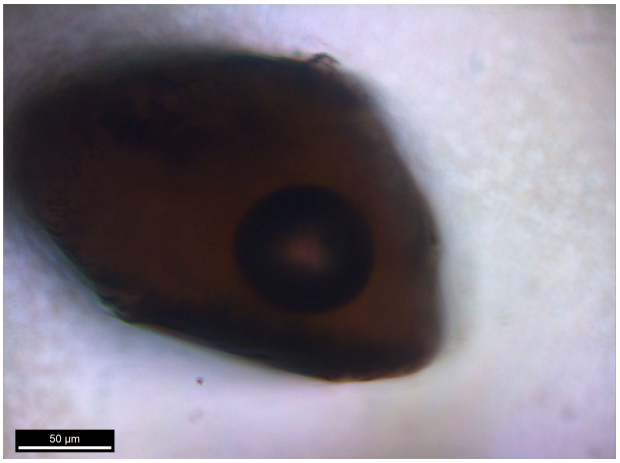
50 µm

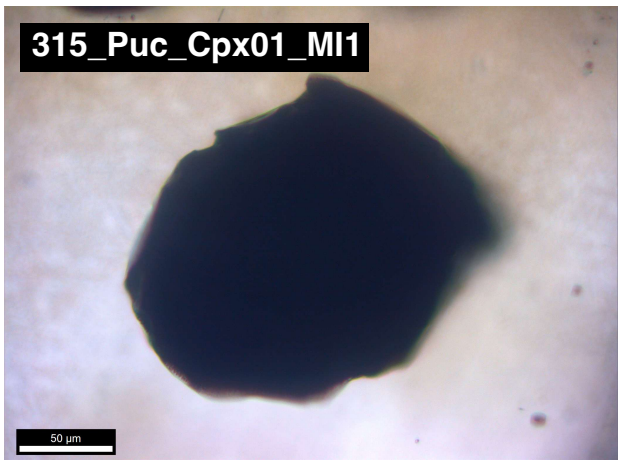
315_Puc_Cpx01_Ml1
50 µm

Appendix C

Images of Studied Melt Inclusions and Vapour Bubbles

Images of each studied melt inclusion are presented below. They are organised into two columns, four melt inclusions per page. The left column are the images used to calculate melt inclusion volumes. The right column are corresponding images used to calculate vapour bubble volume.

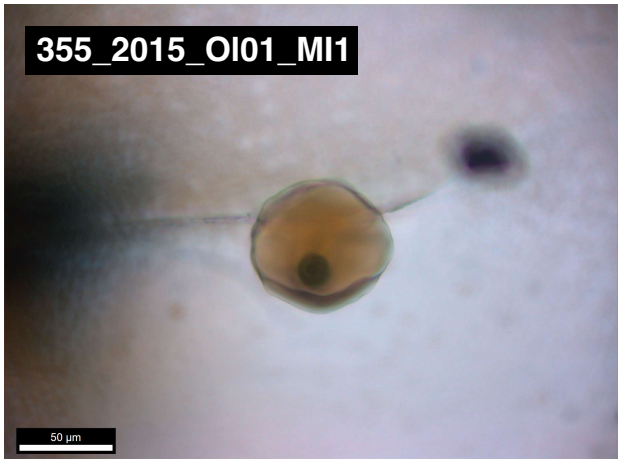
355_2015_OI01_MI1
50 µm

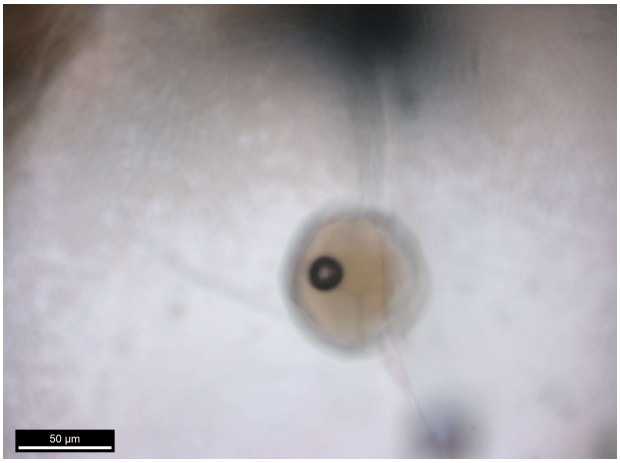
50 µm

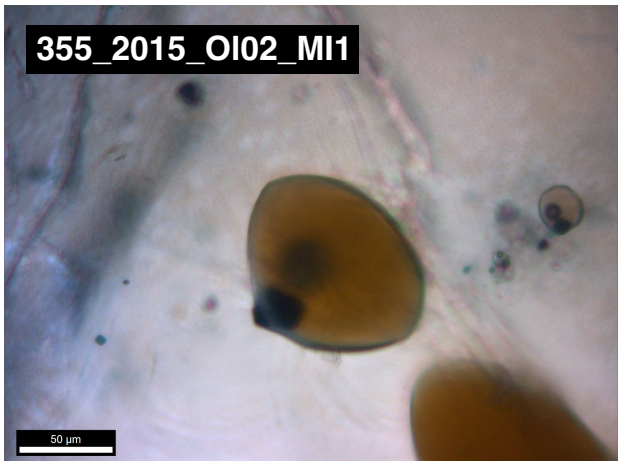
355_2015_OI02_MI1
50 µm

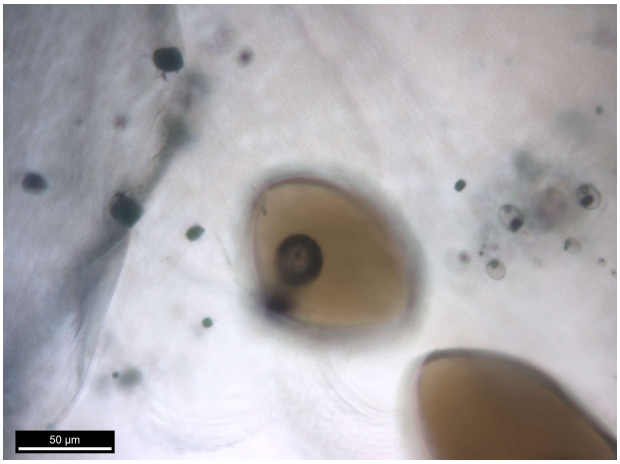
50 µm

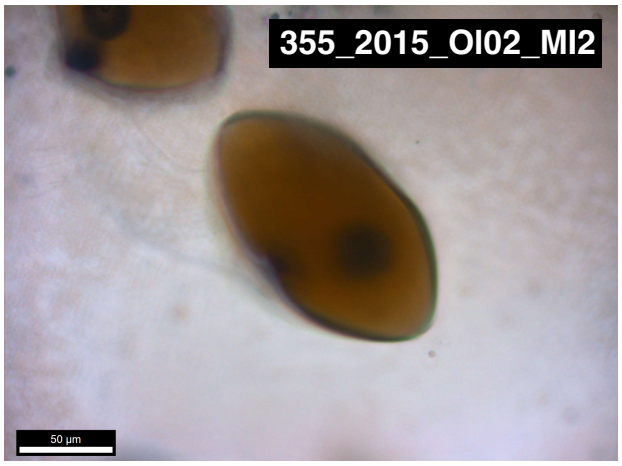
355_2015_OI02_MI2
50 µm

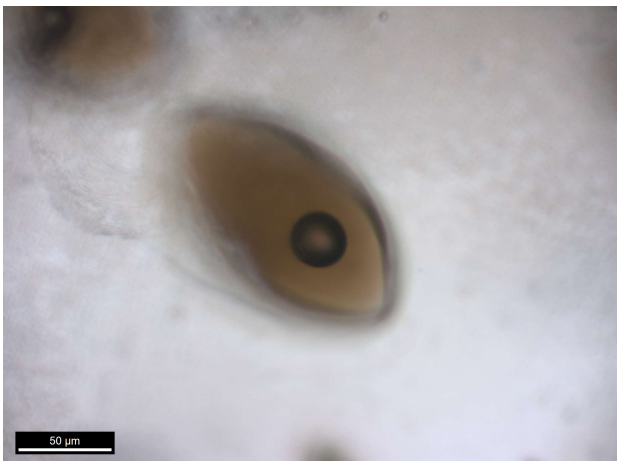
50 µm

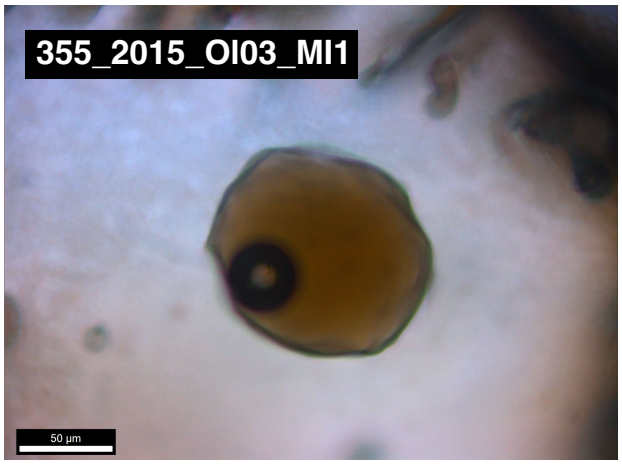
355_2015_OI03_MI1
50 µm

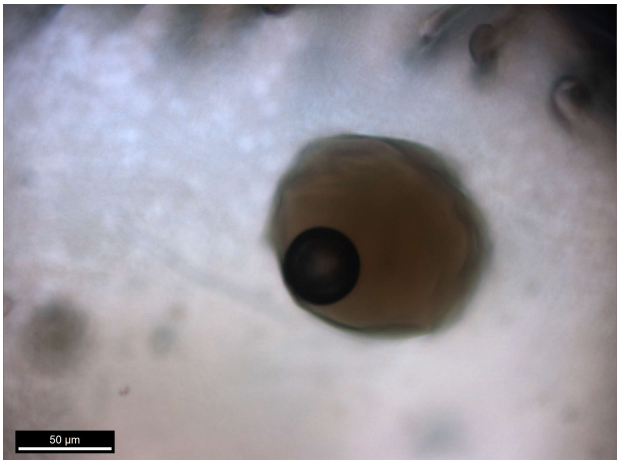
50 µm


355_2015_Ol04_MI1
50 µm

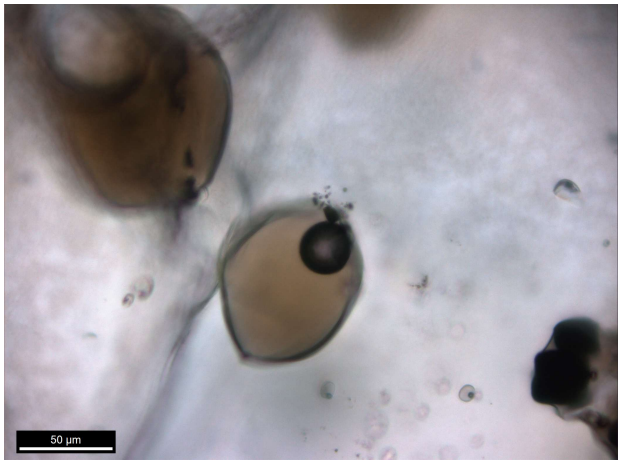
50 µm

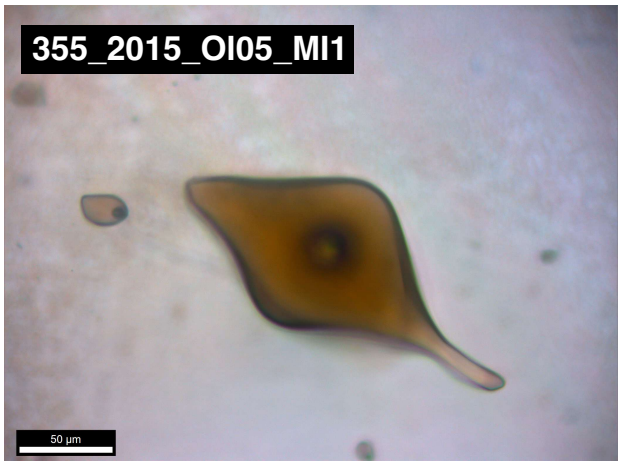
355_2015_Ol05_MI1
50 µm

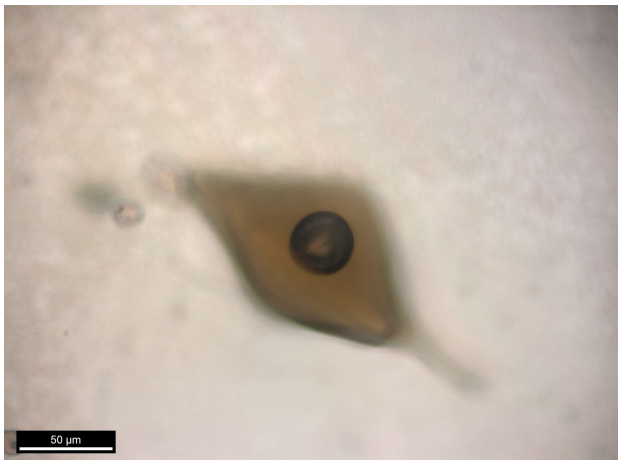
50 µm

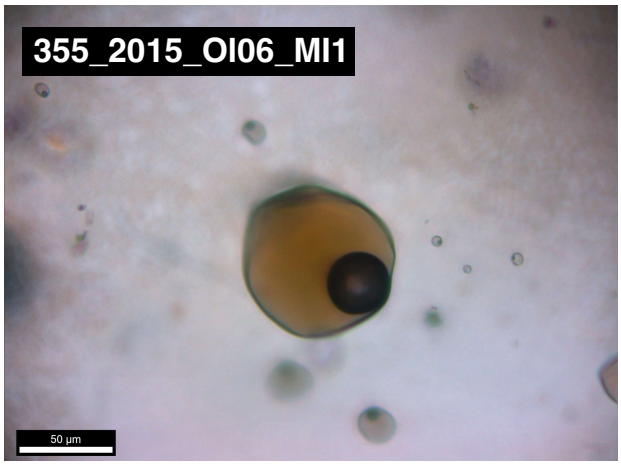
355_2015_Ol06_MI1
50 µm

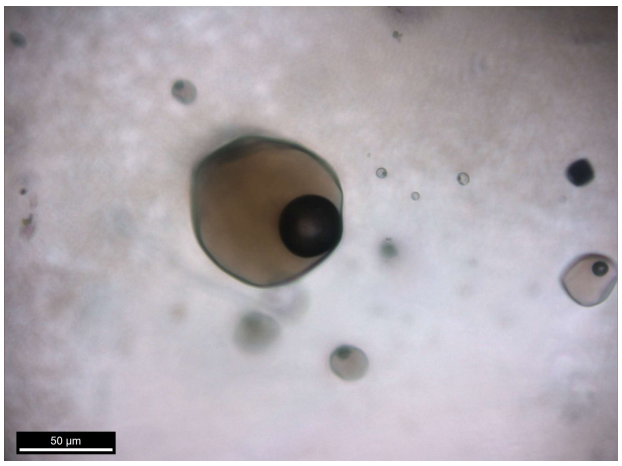
50 µm

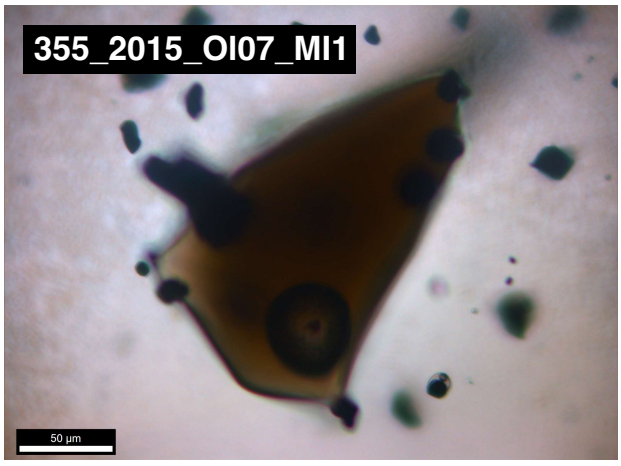
355_2015_Ol07_MI1
50 µm

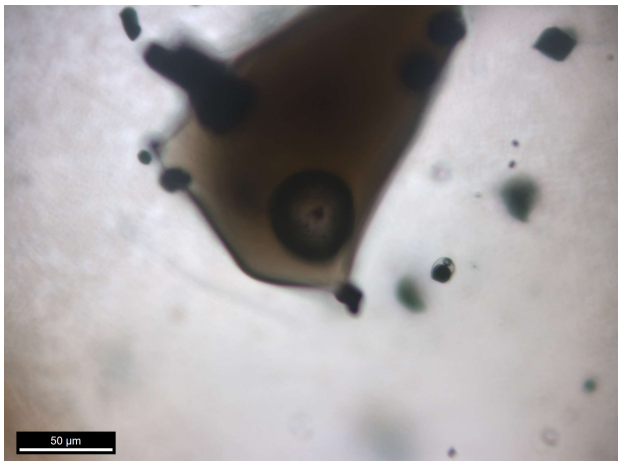
50 µm

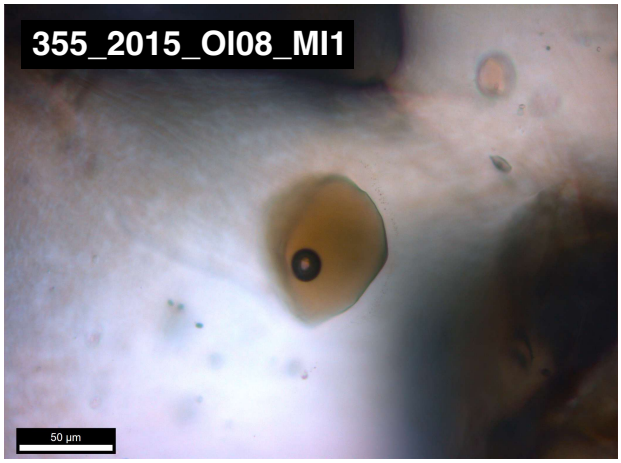
355_2015_OI08_MI1
50 µm

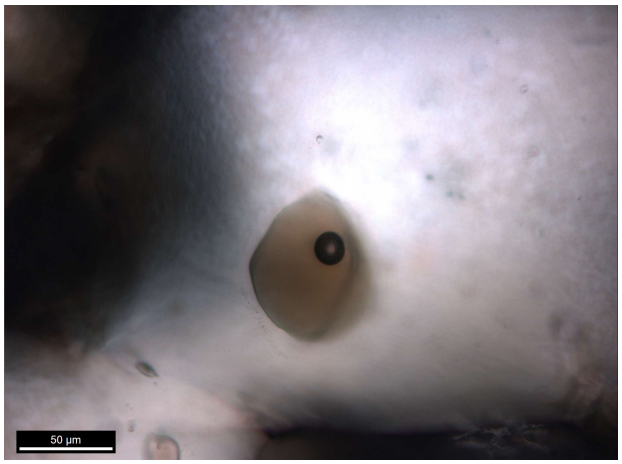
50 µm

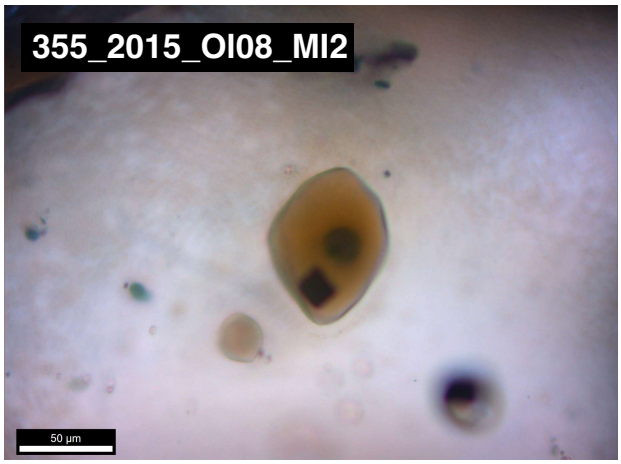
355_2015_OI08_MI2
50 µm

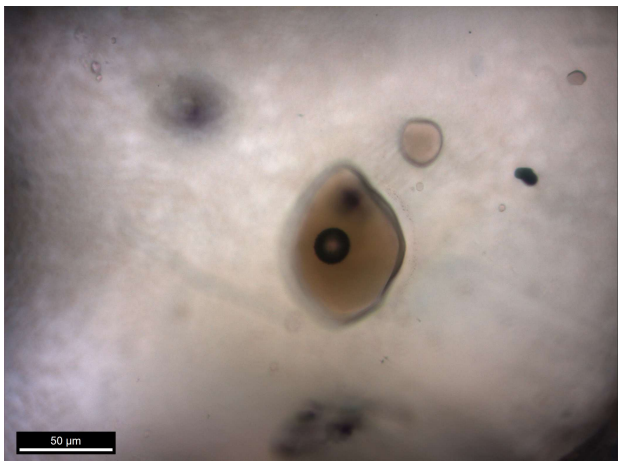
50 µm

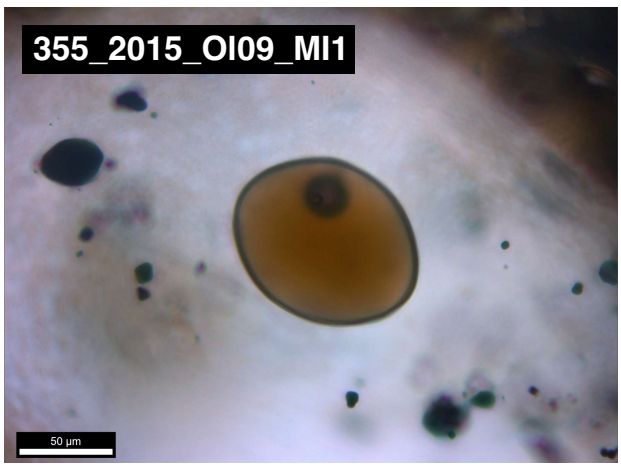
355_2015_OI09_MI1
50 µm

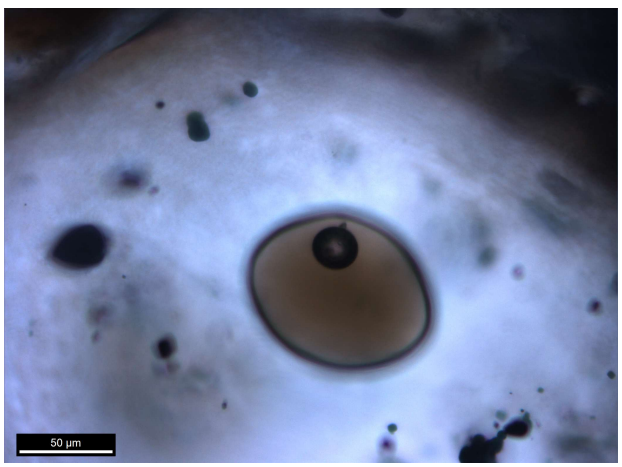
50 µm

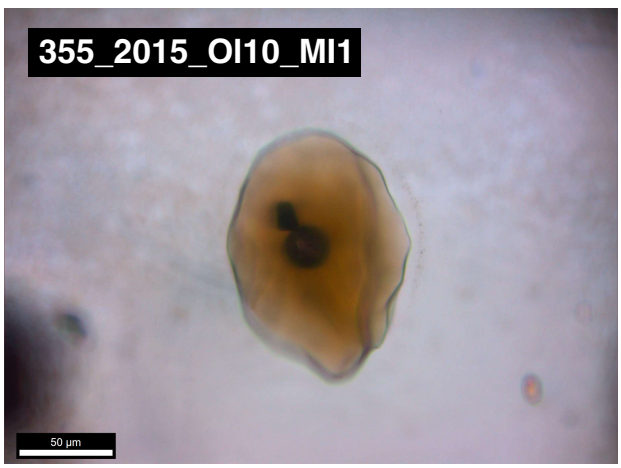
355_2015_OI10_MI1
50 µm

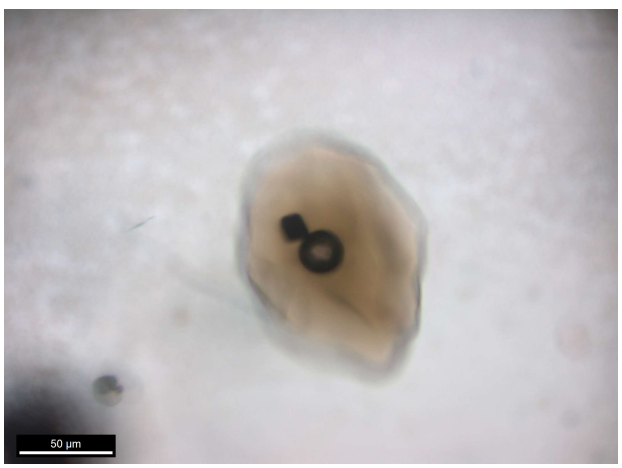
50 µm

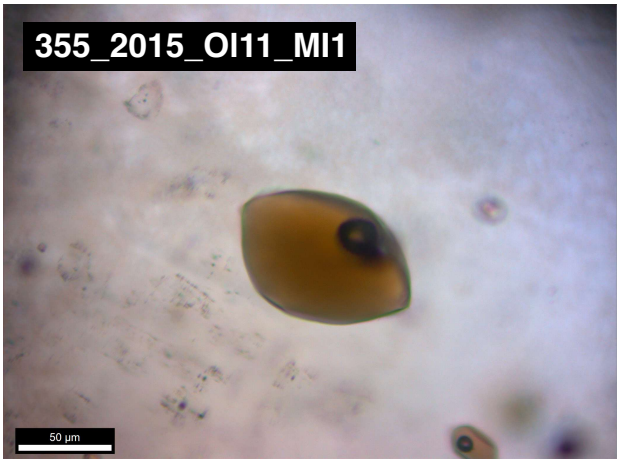
355_2015_Ol11_MI1
50 µm

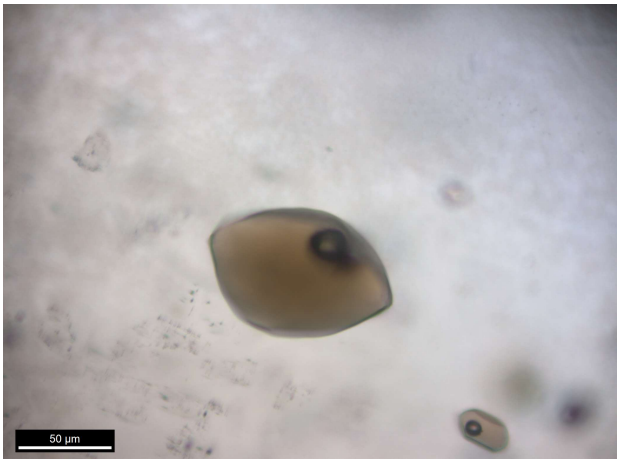
50 µm

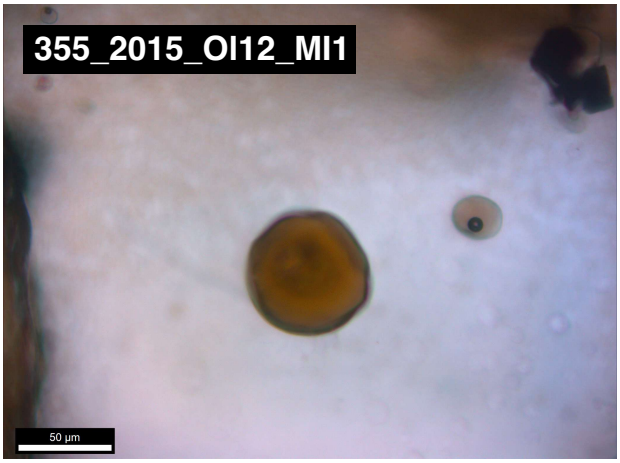
355_2015_Ol12_MI1
50 µm

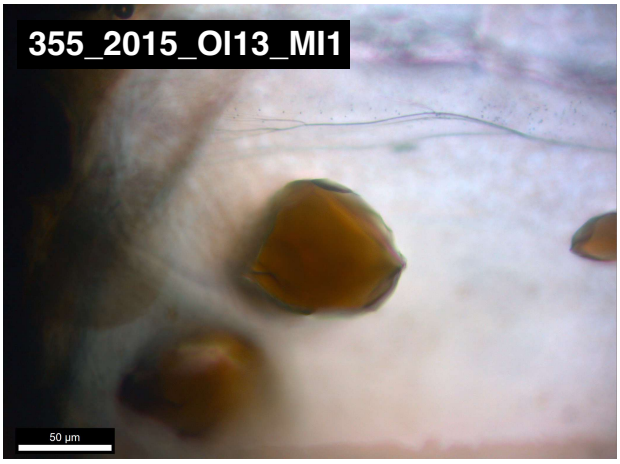
355_2015_Ol13_MI1
50 µm

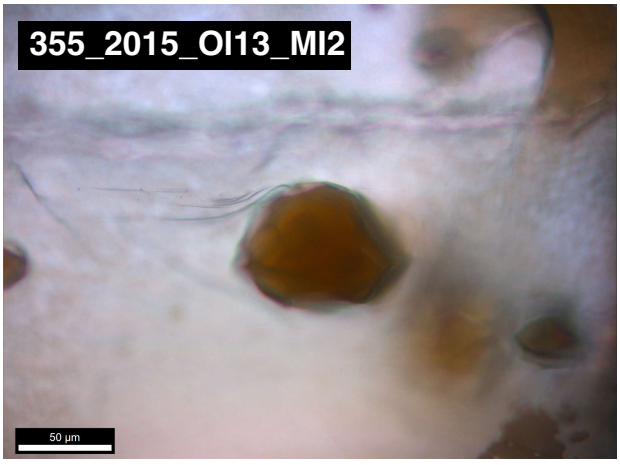
355_2015_Ol13_MI2
50 µm

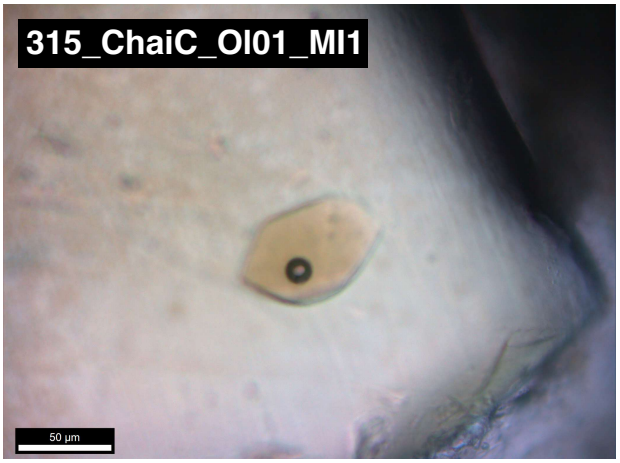
315_ChaiC_Ol01_MI1
50 µm

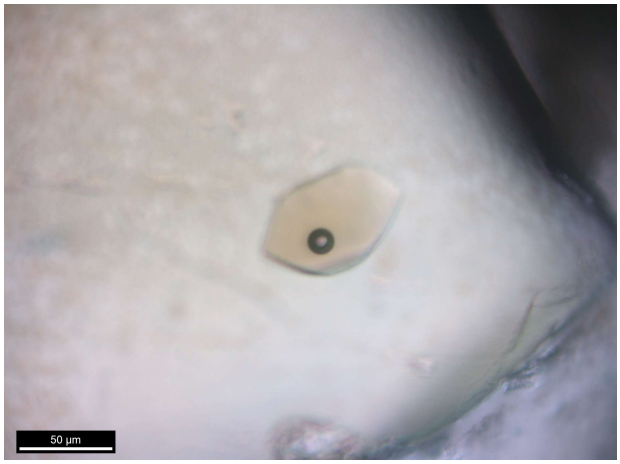
50 µm

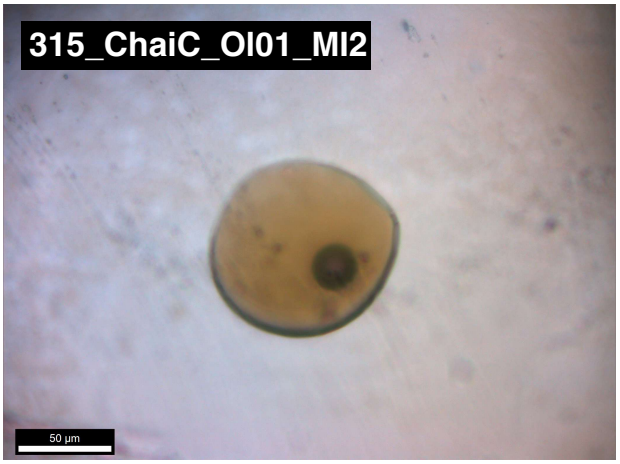
315_ChaiC_Ol01_MI2
50 µm

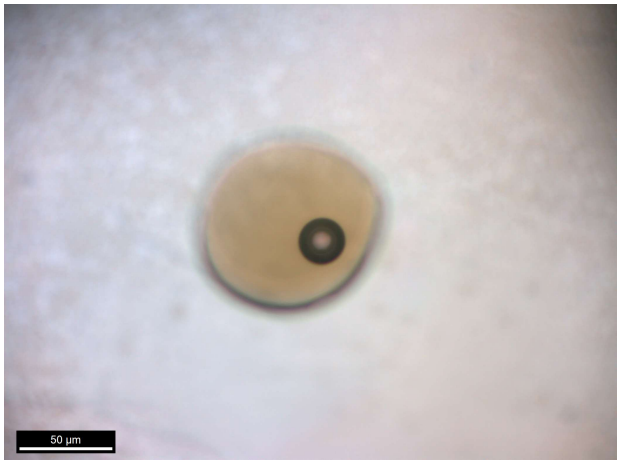
50 µm

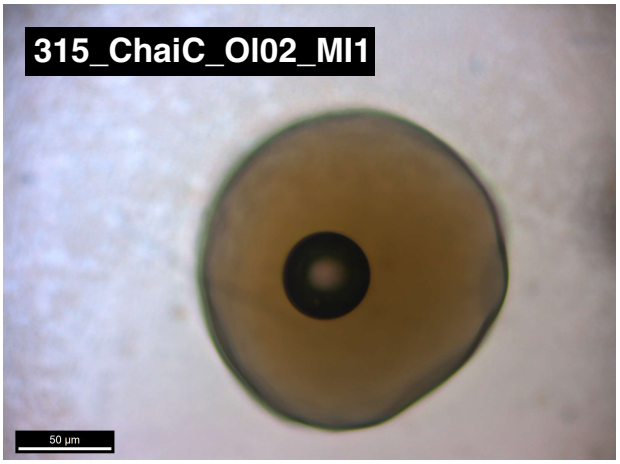
315_ChaiC_Ol02_MI1
50 µm

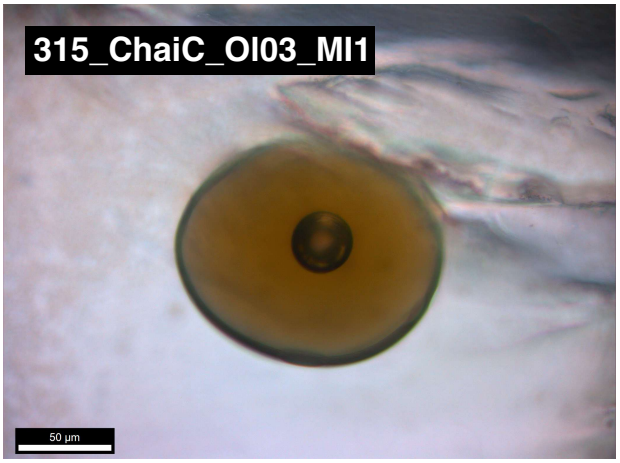
315_ChaiC_Ol03_MI1
50 µm

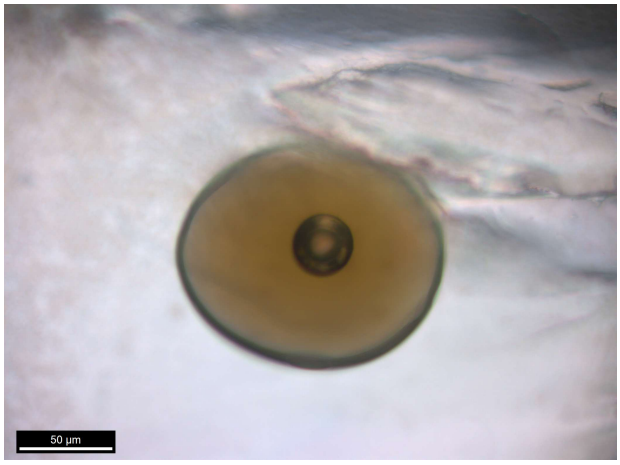
50 µm

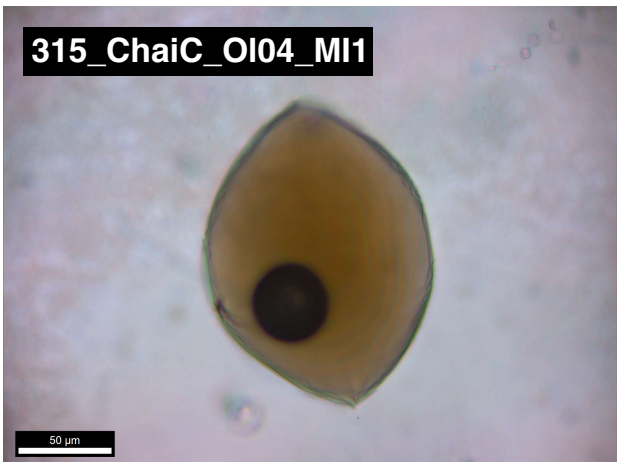
315_ChaiC_OI04_MI1
50 µm

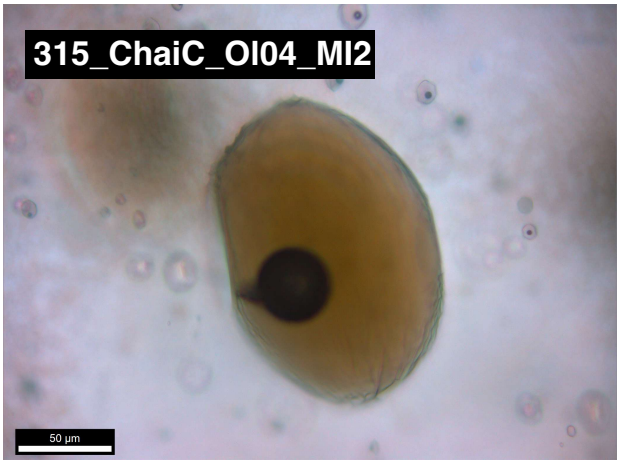
315_ChaiC_OI04_MI2
50 µm

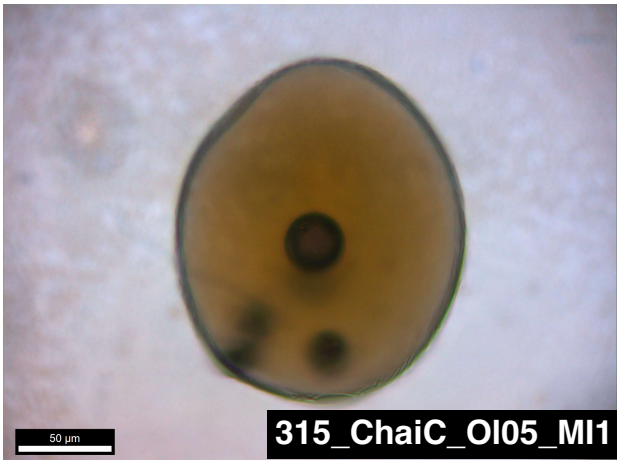
50 µm
315_ChaiC_OI05_MI1

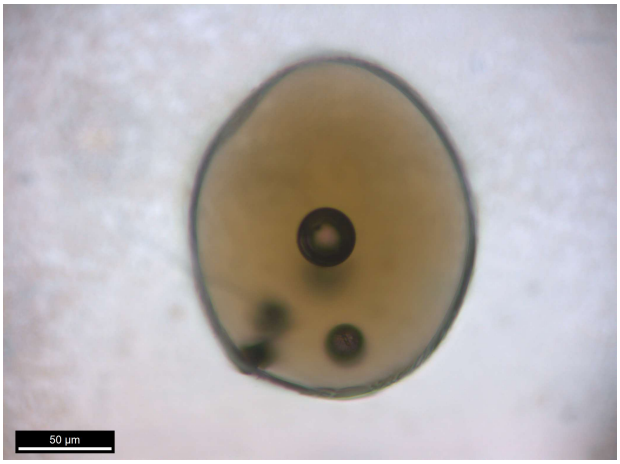
50 µm

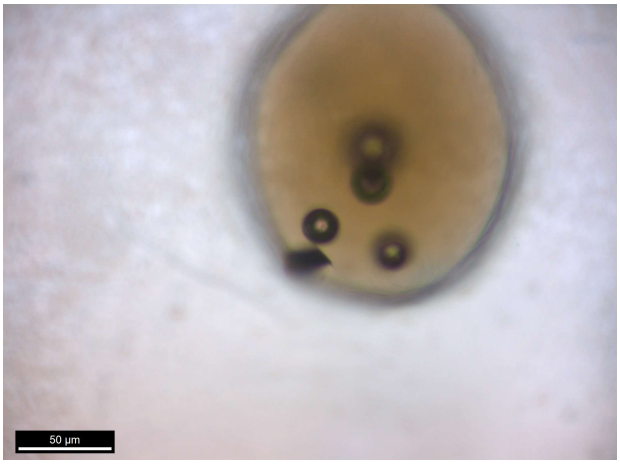
50 µm

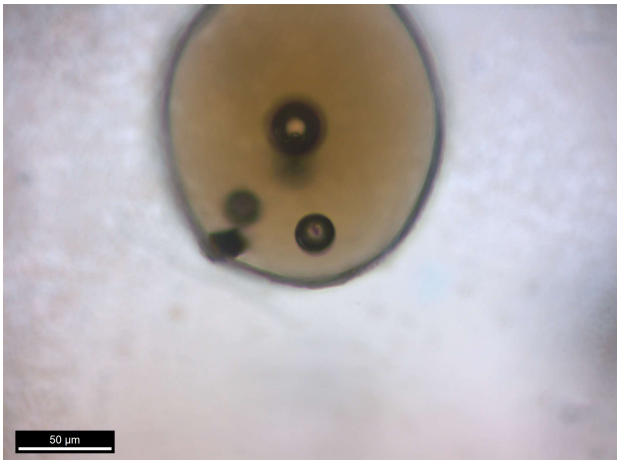
50 µm

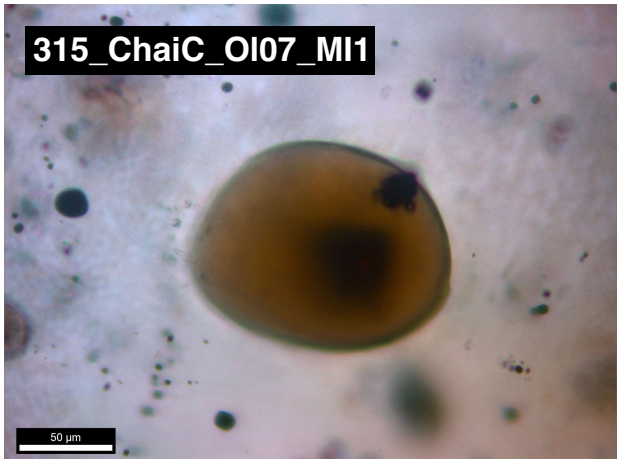
315_ChaiC_Ol07_MI1
50 µm

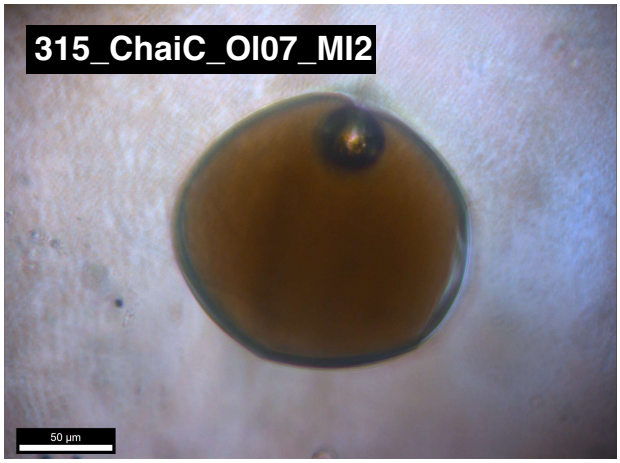
315_ChaiC_Ol07_MI2
50 µm

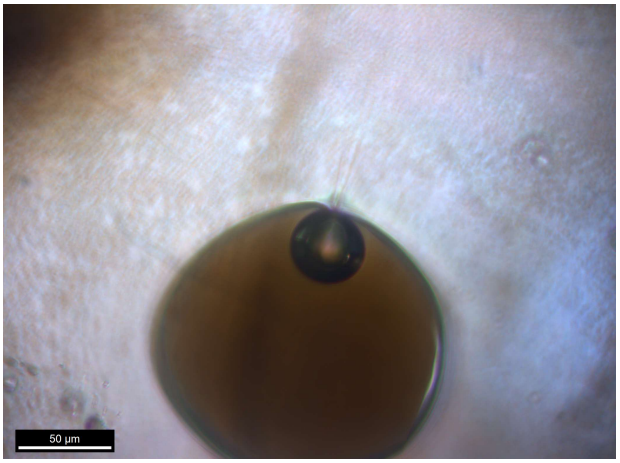
50 µm

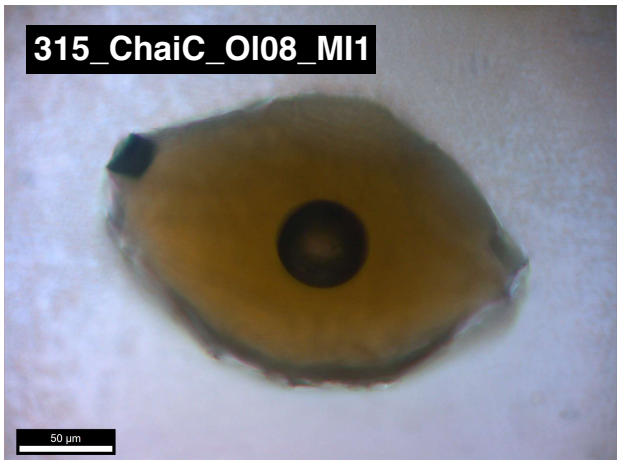
315_ChaiC_Ol08_MI1
50 µm

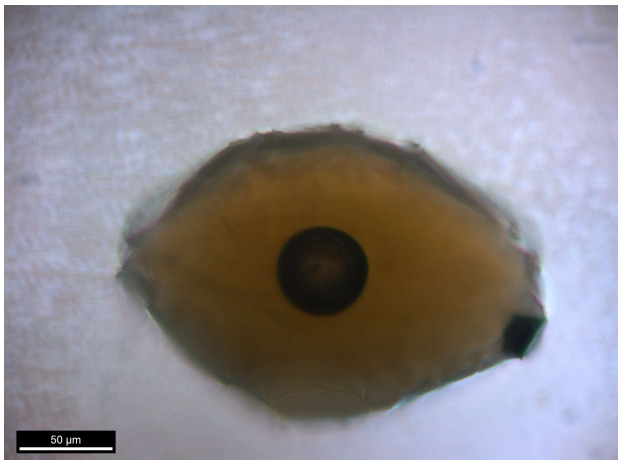
50 µm

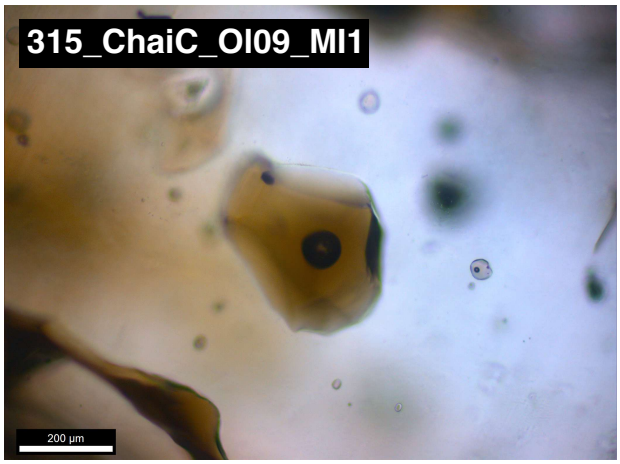
315_ChaiC_Ol09_MI1
200 µm


315_ChaiC_Plg01_MI1
50 µm

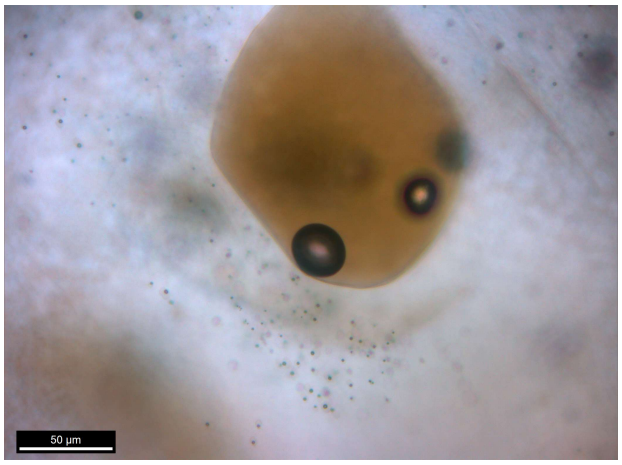
50 µm

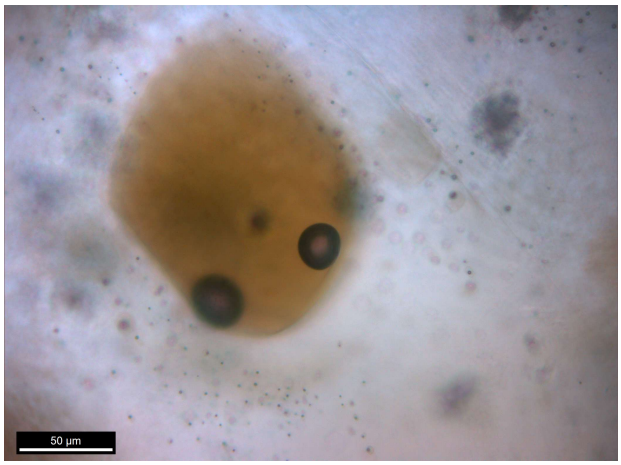
50 µm

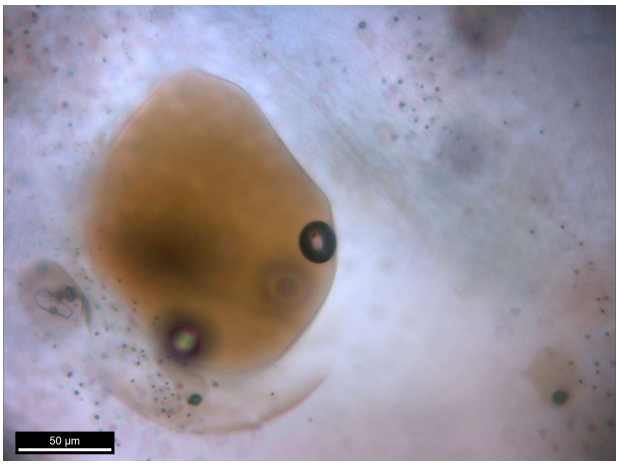
50 µm


315_ChaiC_Cpx01_MI1
50 µm

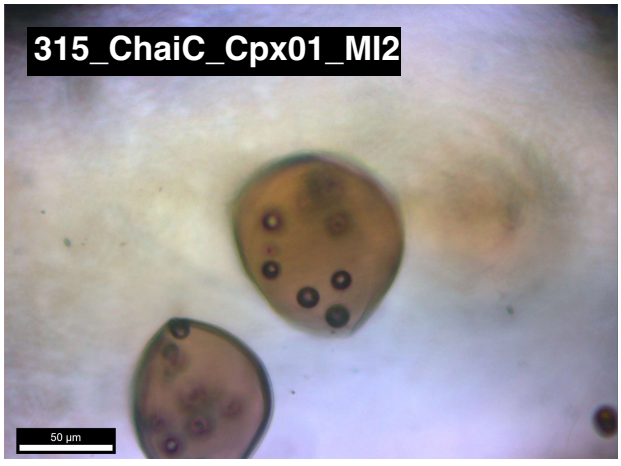
315_ChaiC_Cpx01_MI2
50 µm

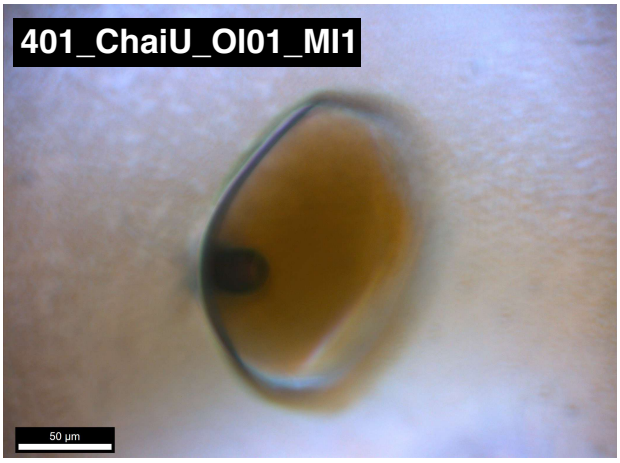
401_ChaiU_Ol01_MI1
50 µm

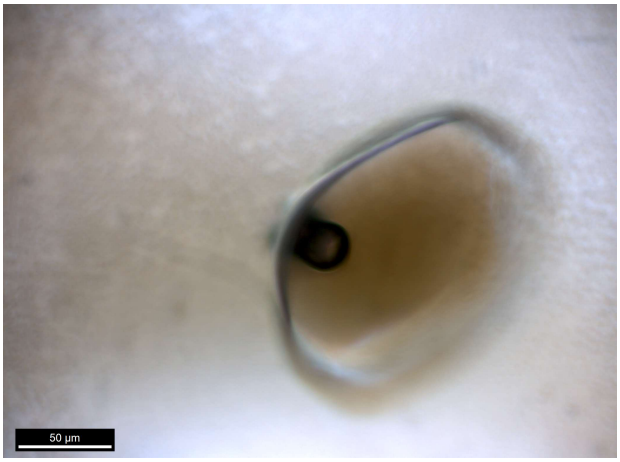
50 µm

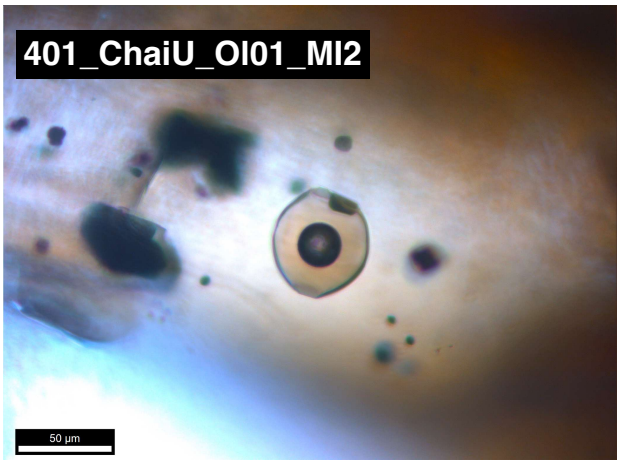
401_ChaiU_Ol01_MI2
50 µm

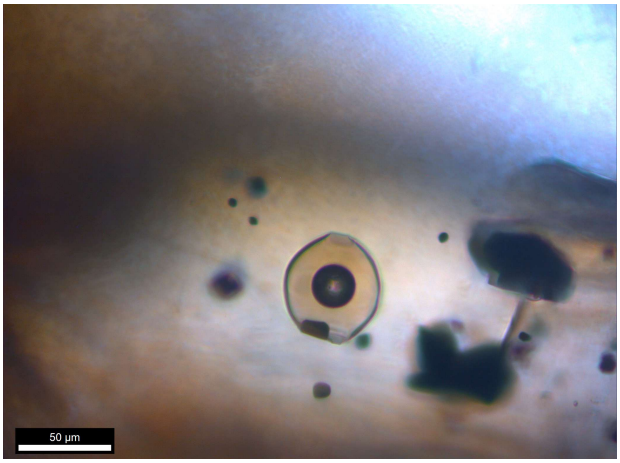
50 µm

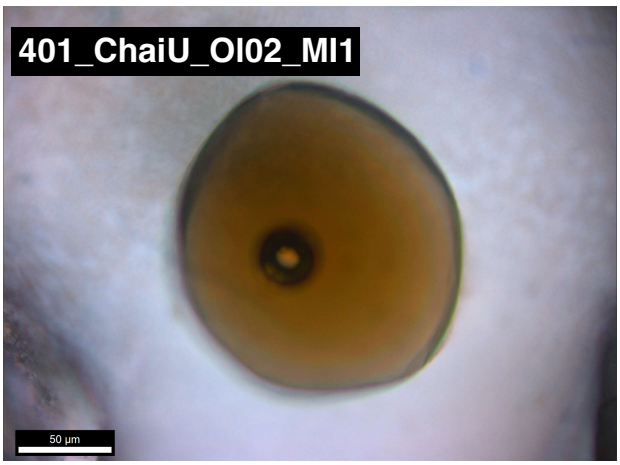
401_ChaiU_Ol02_MI1
50 µm

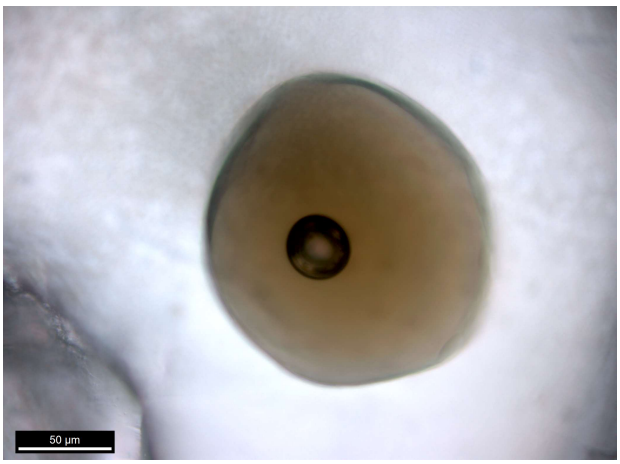
50 µm

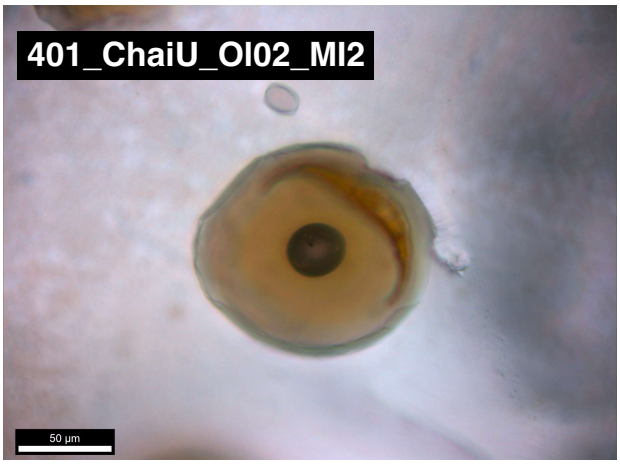
401_ChaiU_Ol02_MI2
50 µm

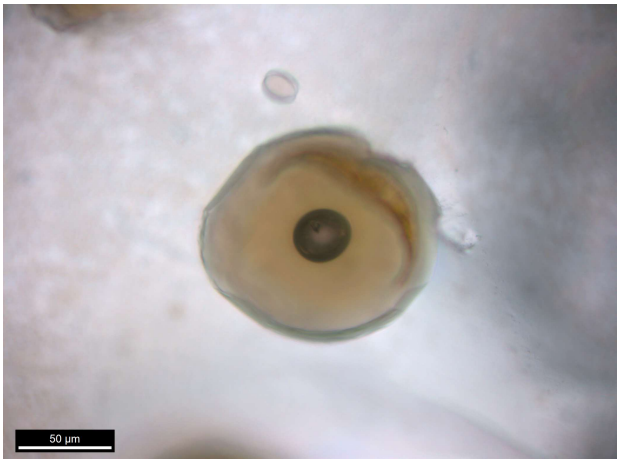
50 µm

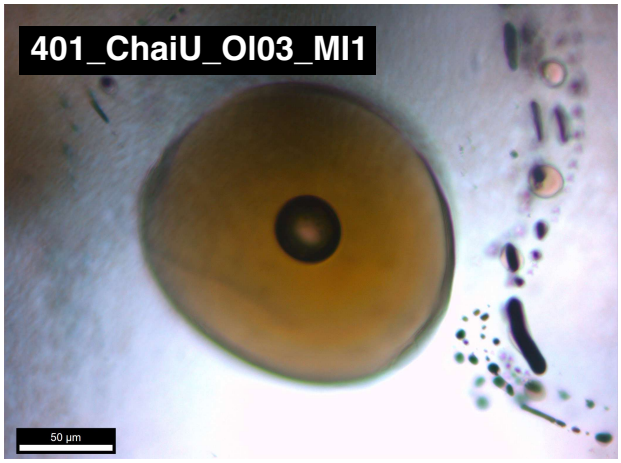
401_ChaiU_Ol03_MI1
50 µm

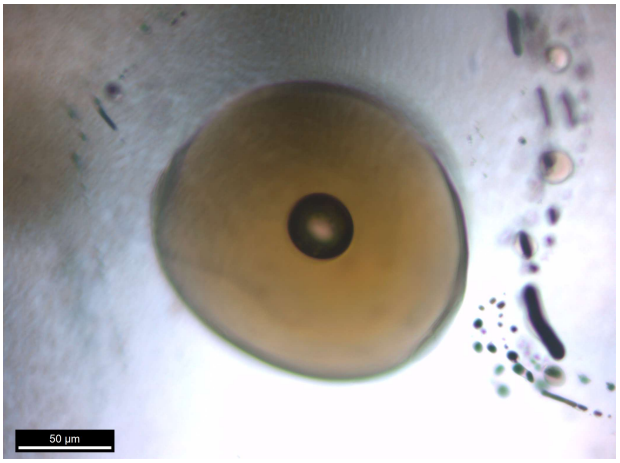
50 µm

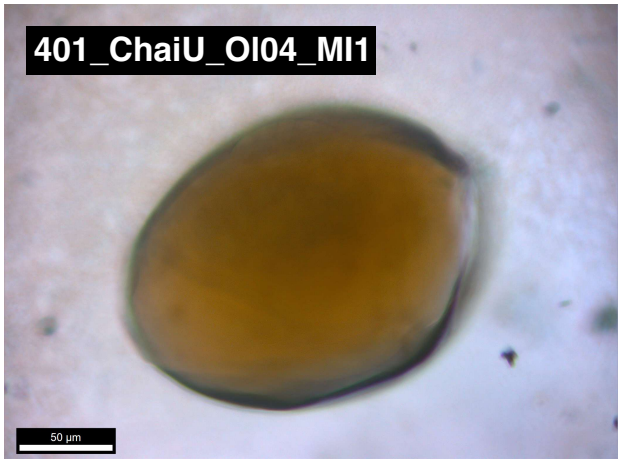
401_ChaiU_Ol04_MI1
50 µm

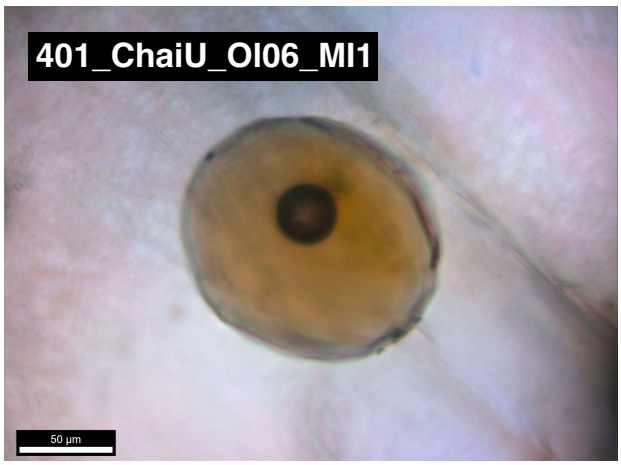
401_ChaiU_Ol06_MI1
50 µm

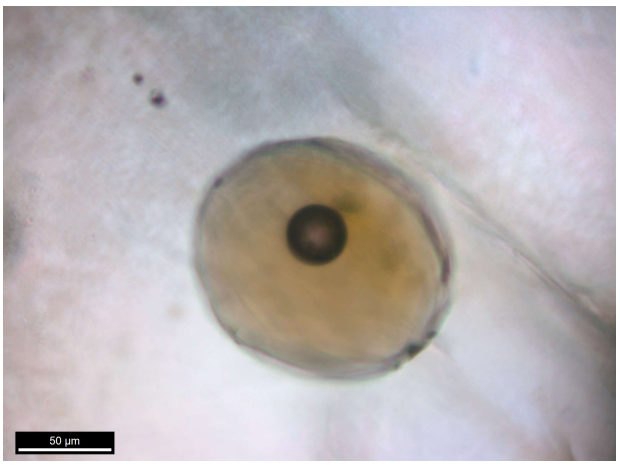
50 µm

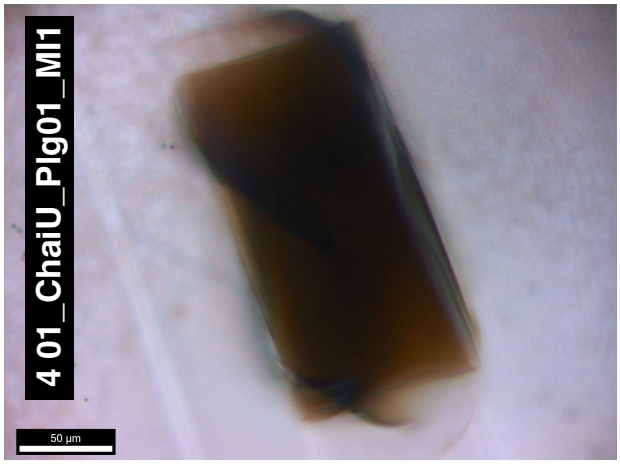
4 01_ChaiU_Plg01_MI1
50 µm

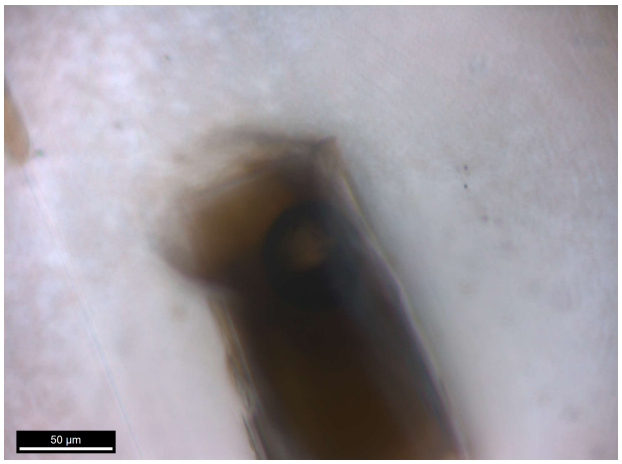
50 µm

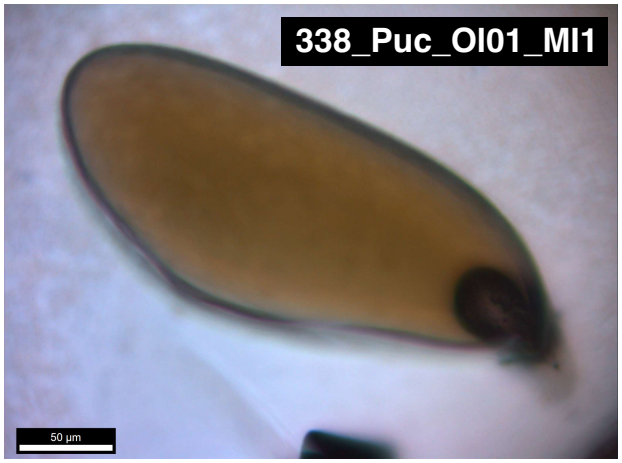
338_Puc_Ol01_MI1
50 µm

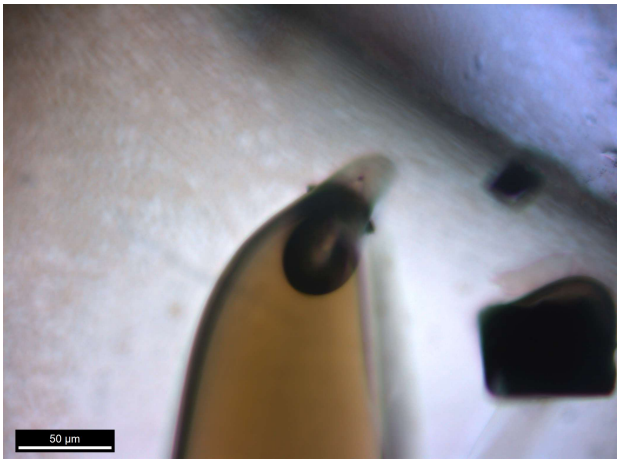
50 µm

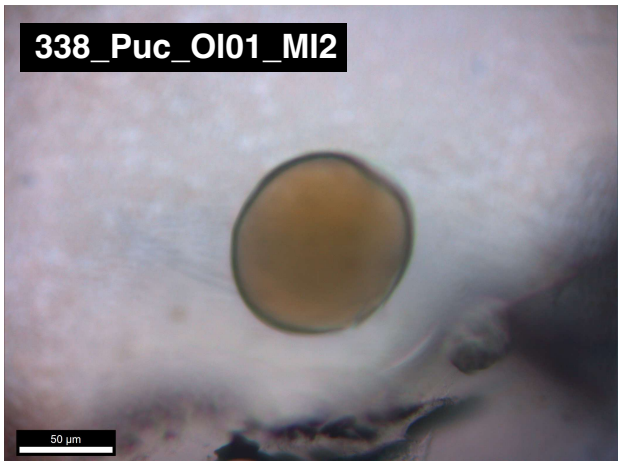
338_Puc_Ol01_MI2
50 µm

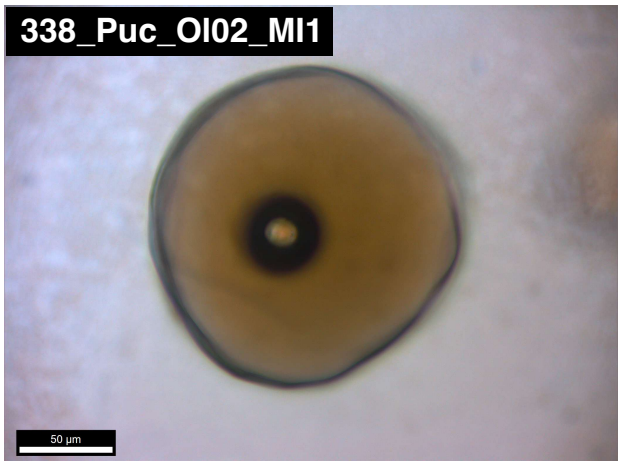
338_Puc_Ol02_MI1
50 µm

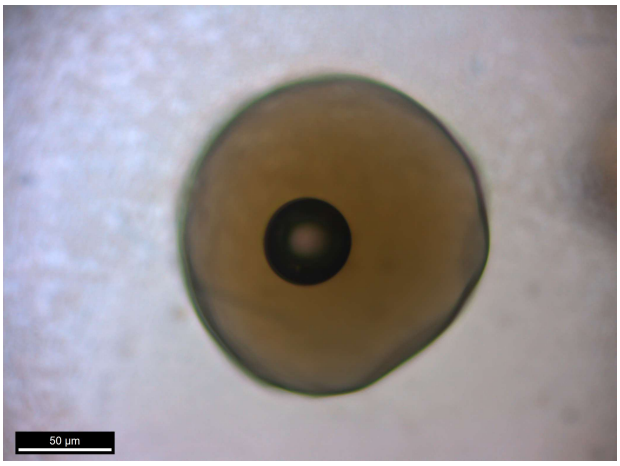
50 µm

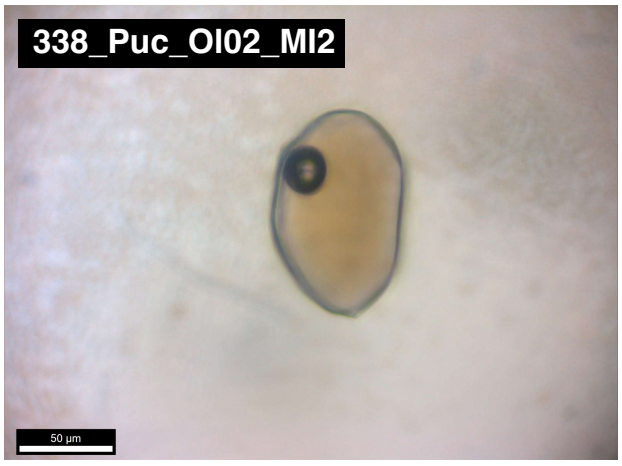
338_Puc_Ol02_MI2
50 µm

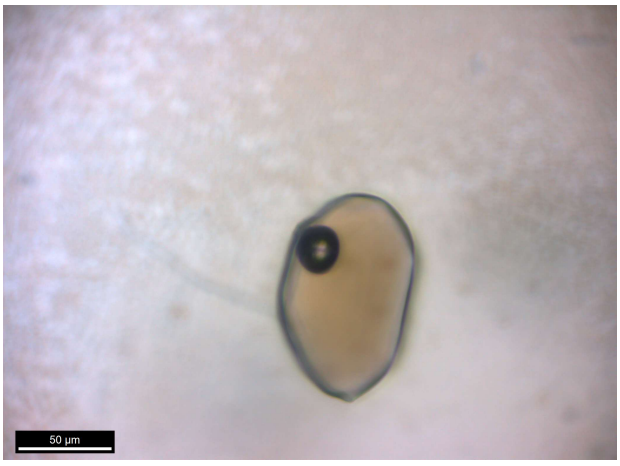
50 µm

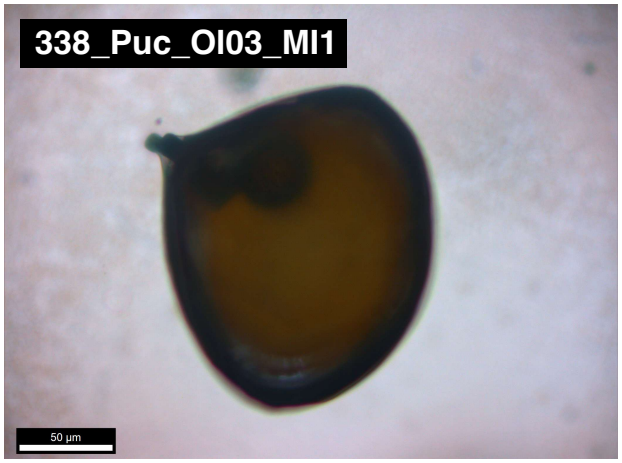
338_Puc_OI03_MI1
50 µm

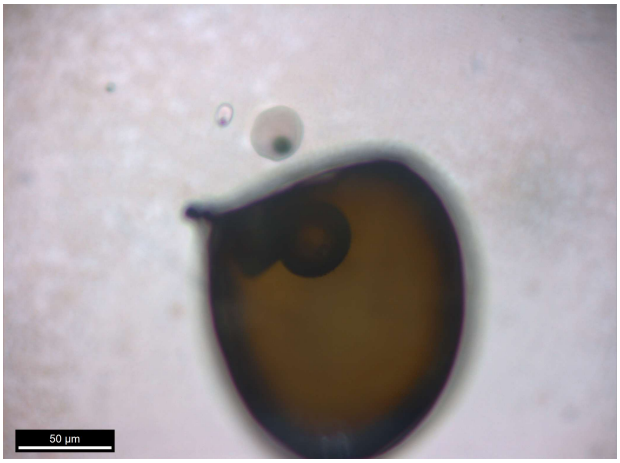
50 µm

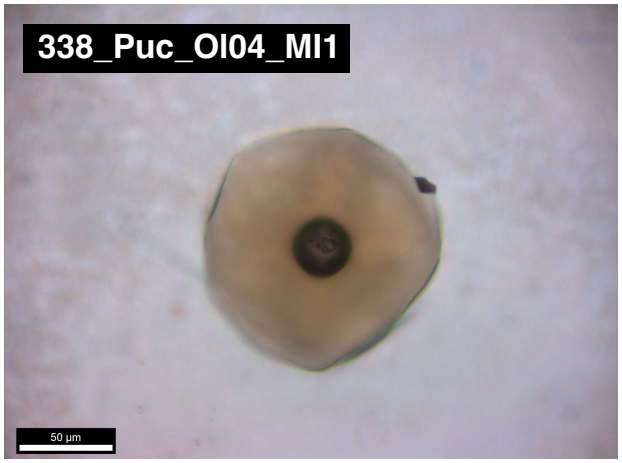
338_Puc_OI04_MI1
50 µm

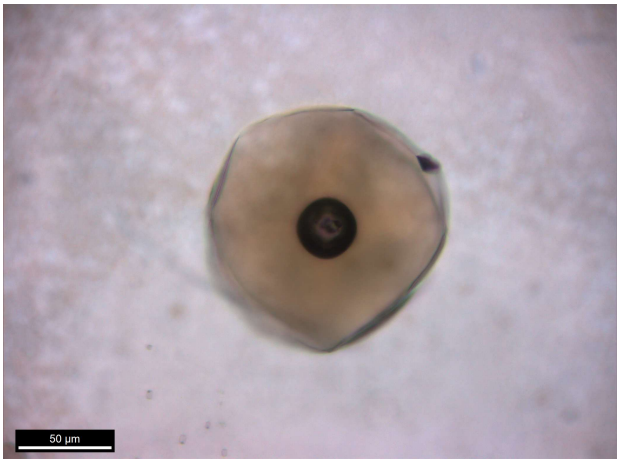
50 µm

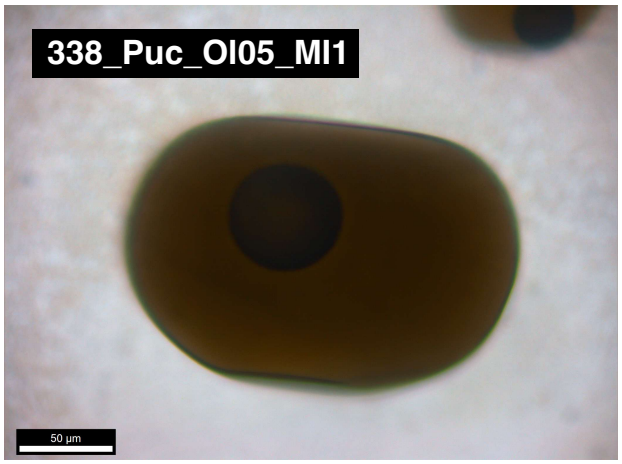
338_Puc_OI05_MI1
50 µm

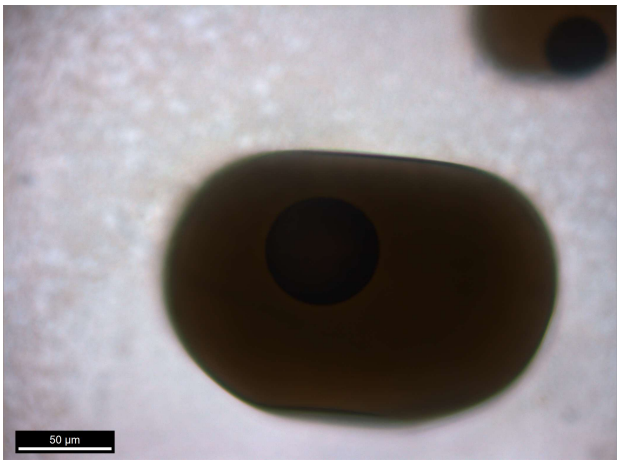
50 µm

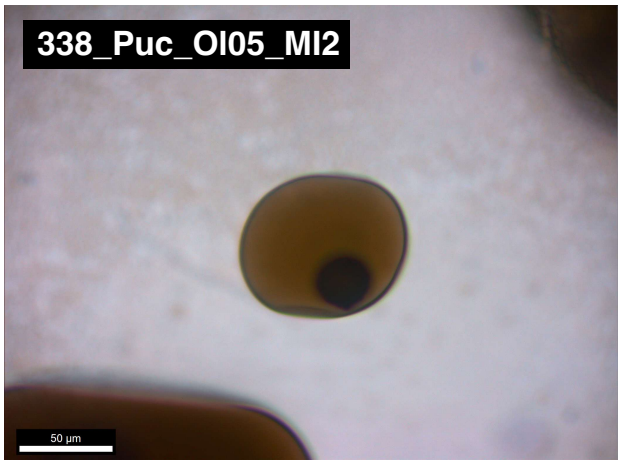
338_Puc_OI05_MI2
50 µm

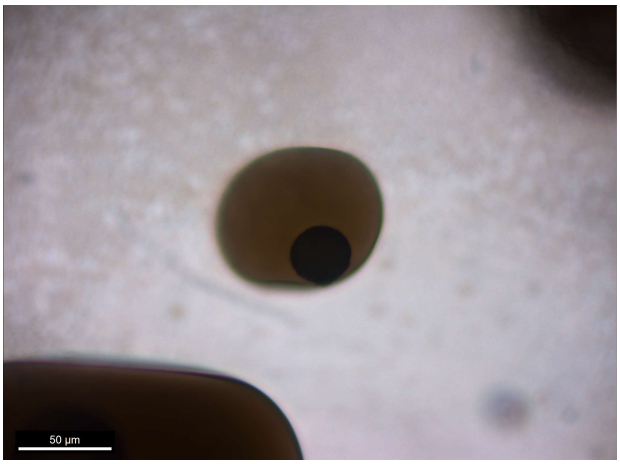
50 µm

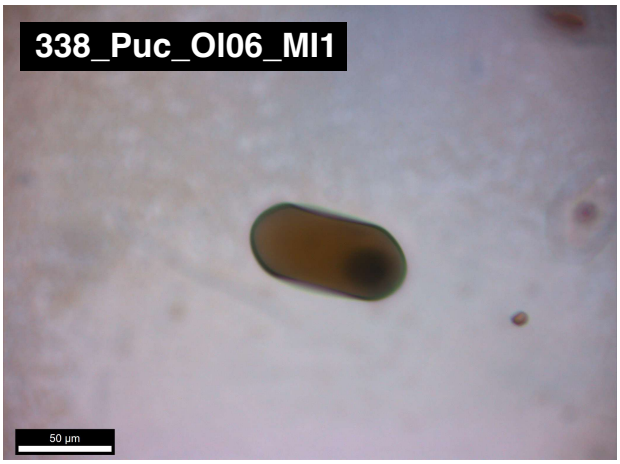
338_Puc_Ol06_MI1
50 µm

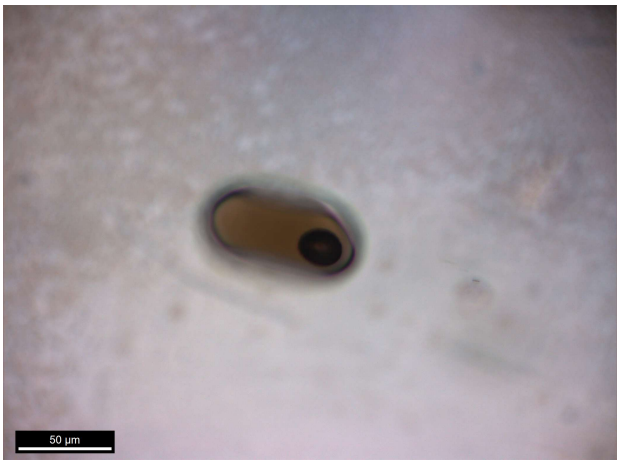
50 µm

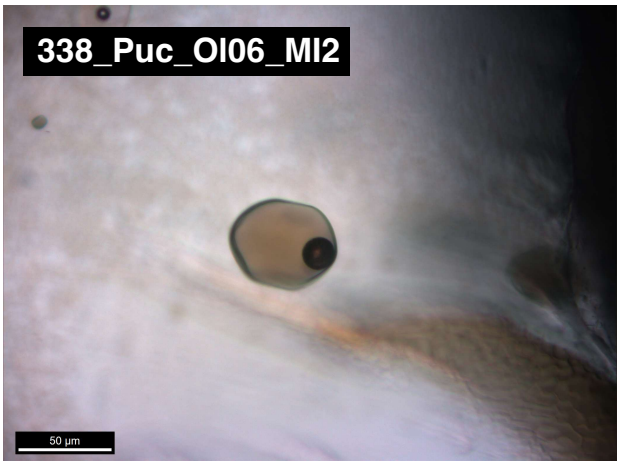
338_Puc_Ol06_MI2
50 µm

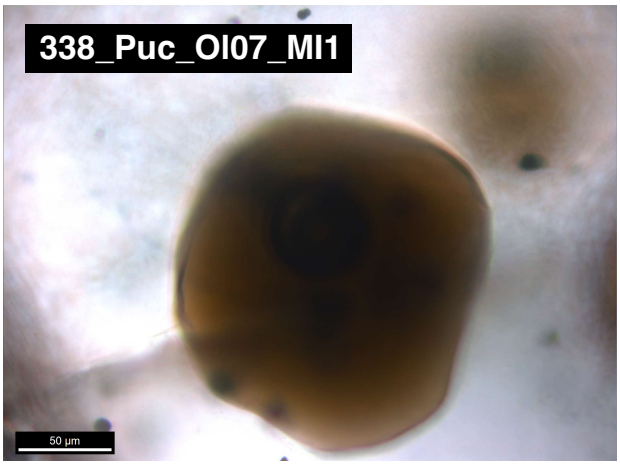
338_Puc_Ol07_MI1
50 µm

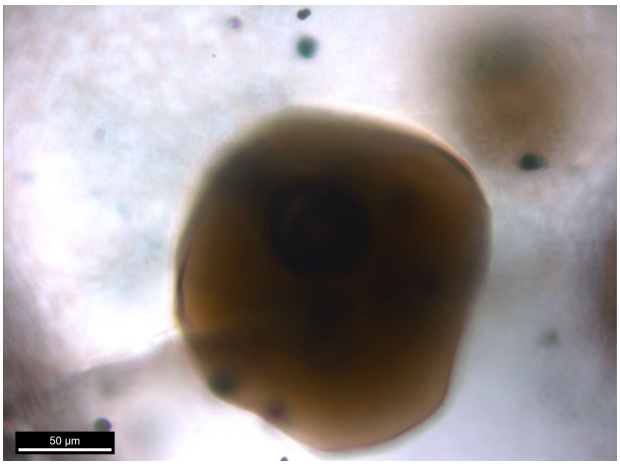
50 µm

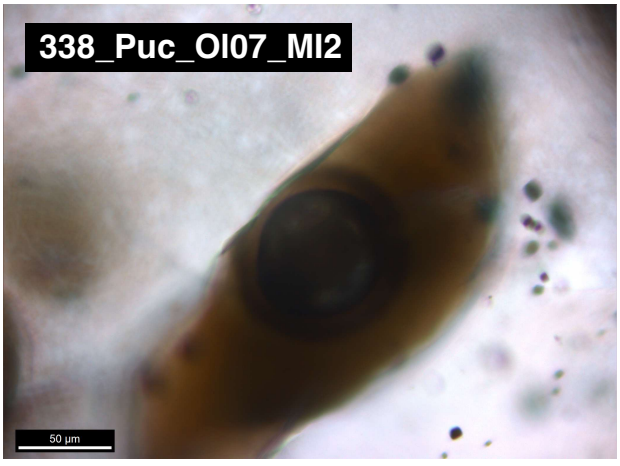
338_Puc_Ol07_MI2
50 µm

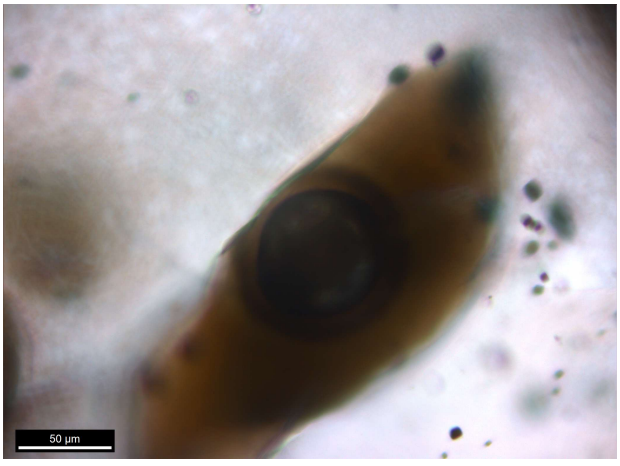
50 µm

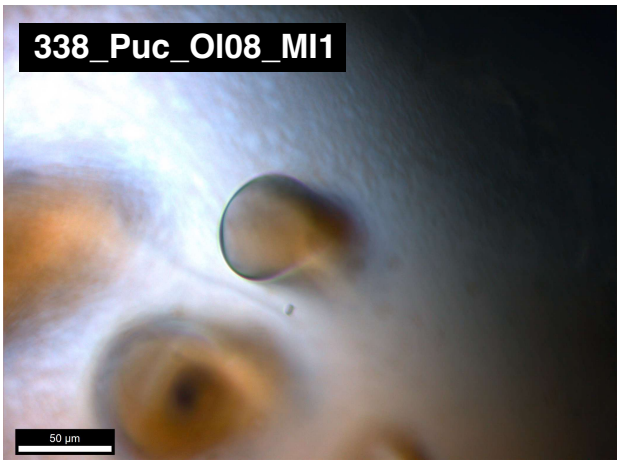
338_Puc_Ol08_MI1
50 µm

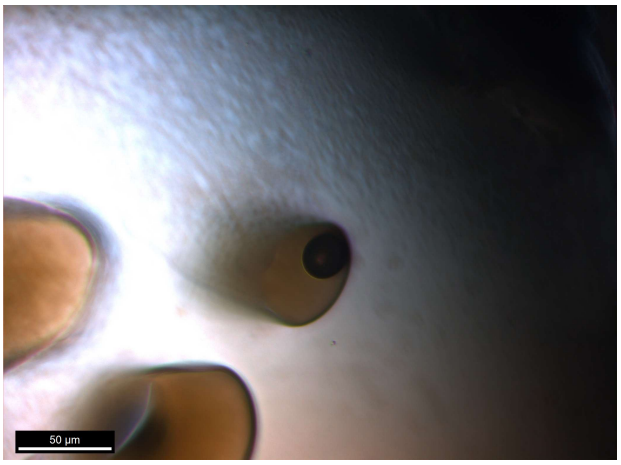
50 µm

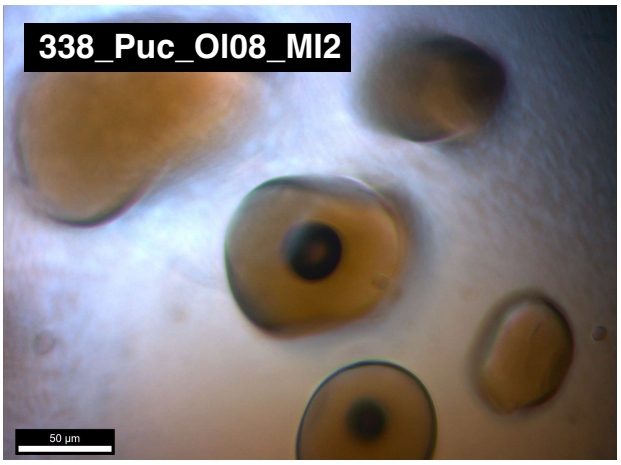
338_Puc_Ol08_MI2
50 µm

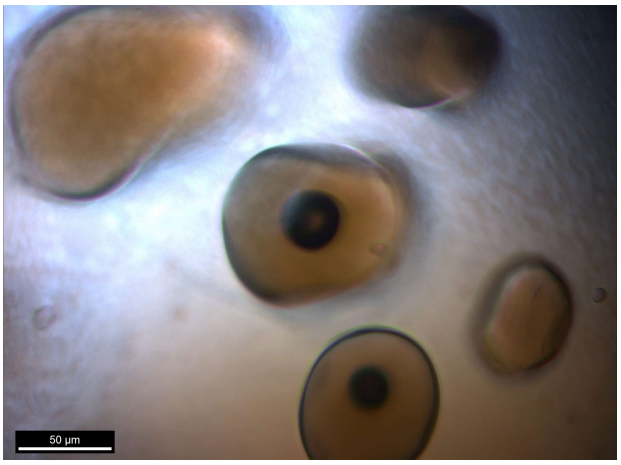
50 µm

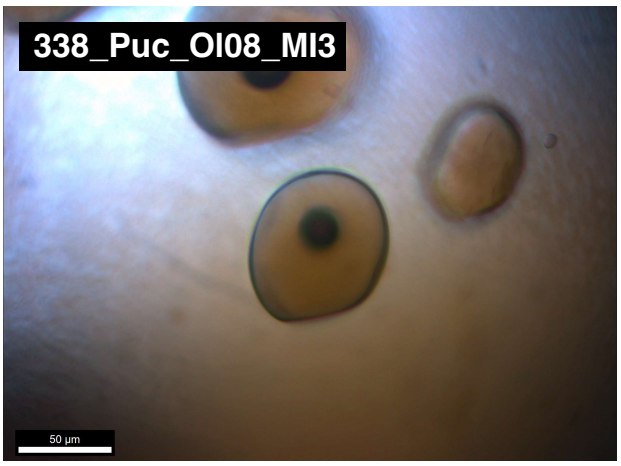
338_Puc_Ol08_MI3
50 µm

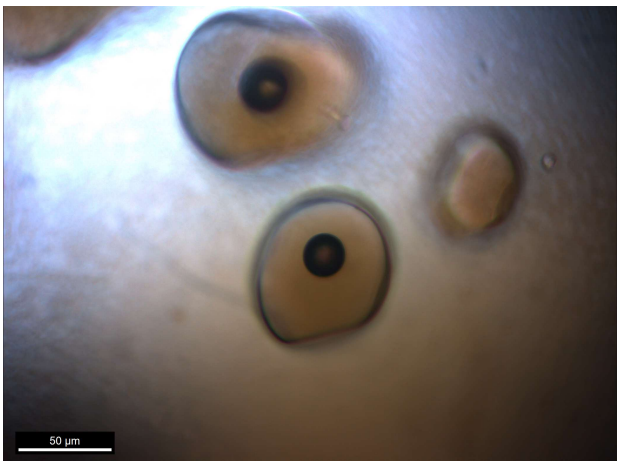
50 µm

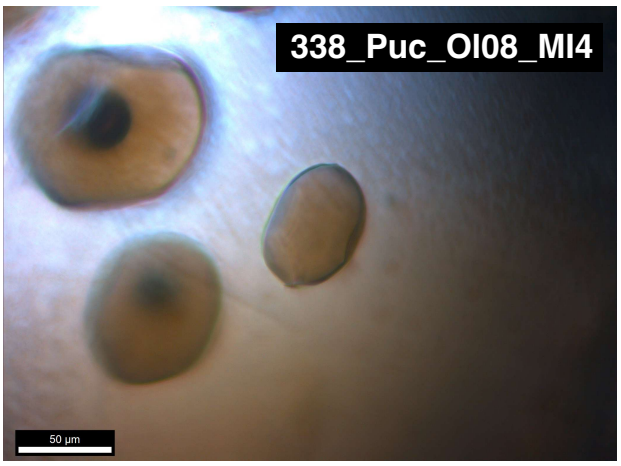
338_Puc_Ol08_MI4
50 µm

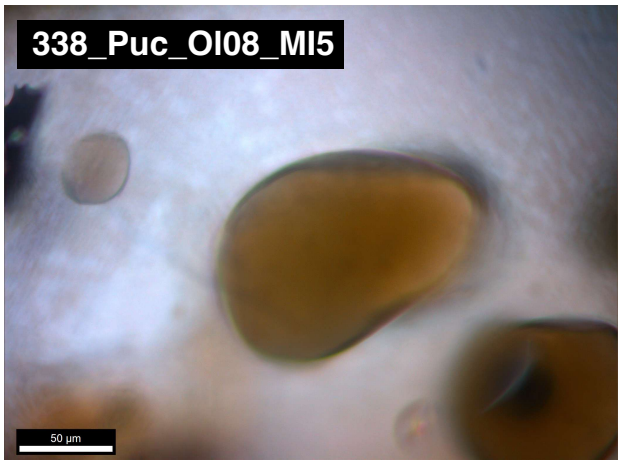
338_Puc_Ol08_MI5
50 µm

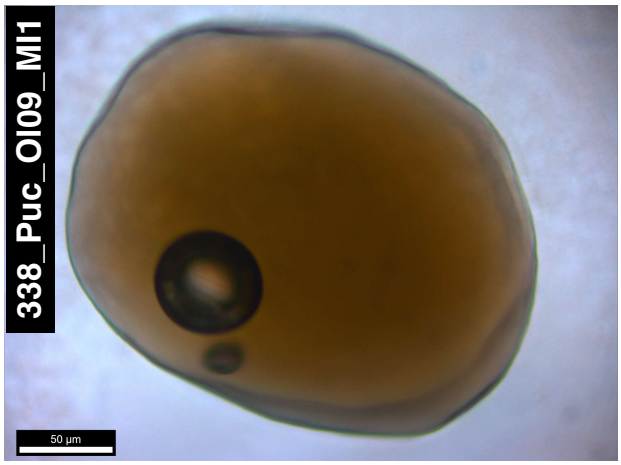
338_Puc_Ol09_MI1
50 µm

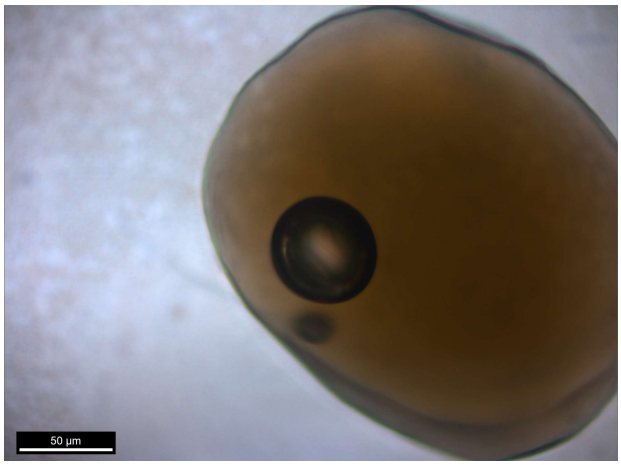
50 µm

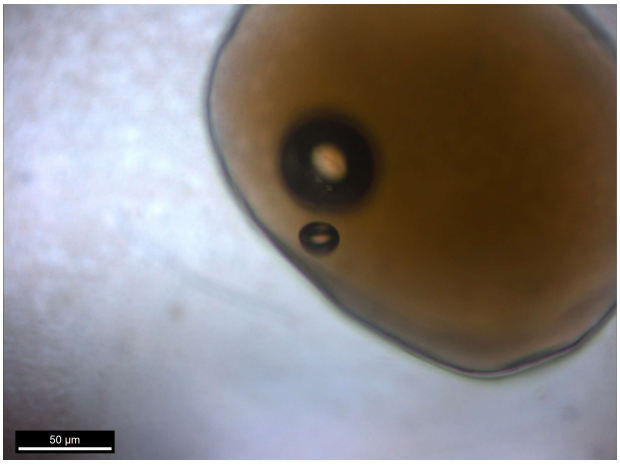
50 µm

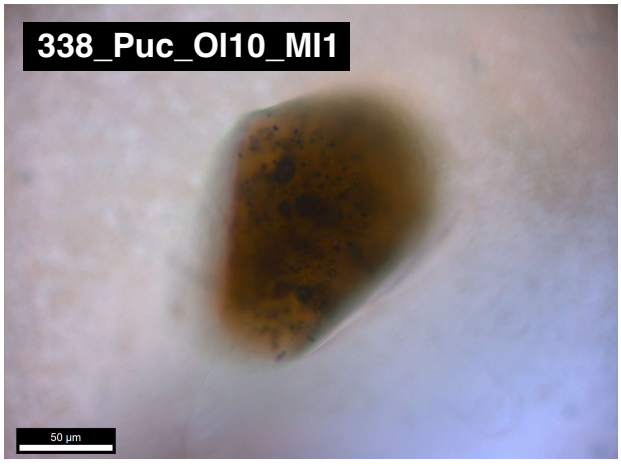
338_Puc_Ol10_MI1
50 µm

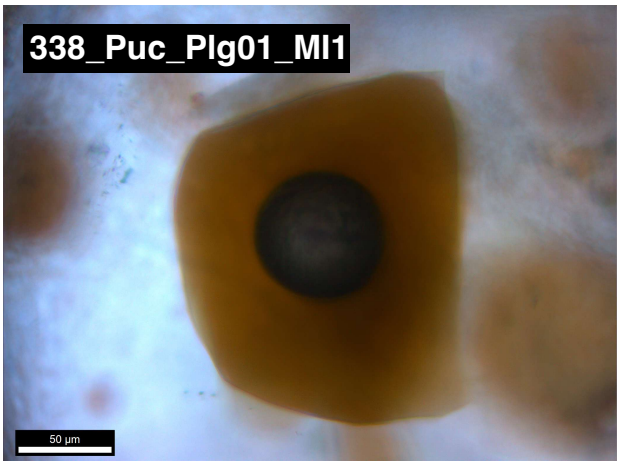
338_Puc_Plg01_MI1
50 µm

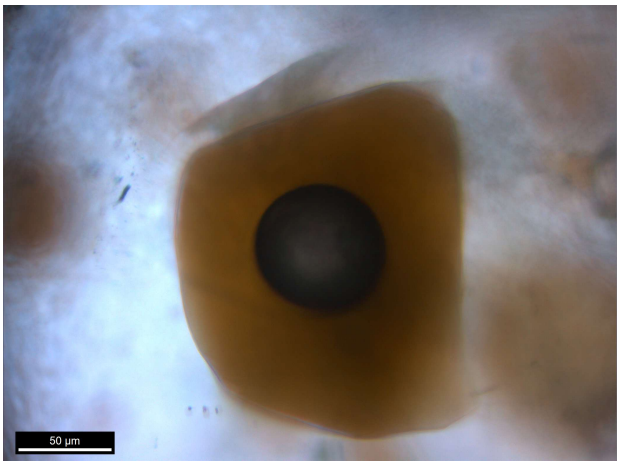
50 µm

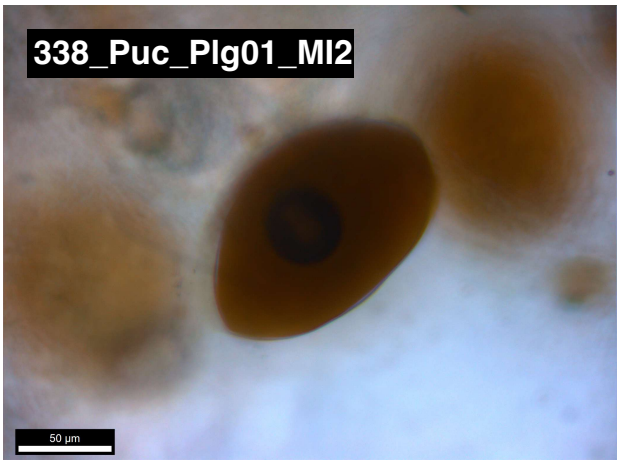
338_Puc_Plg01_MI2
50 µm

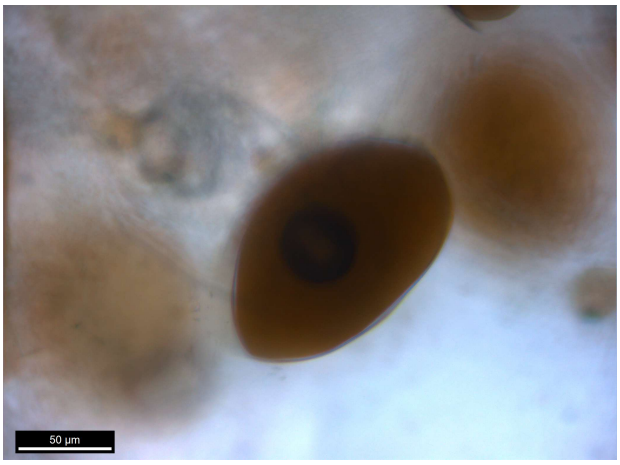
50 µm

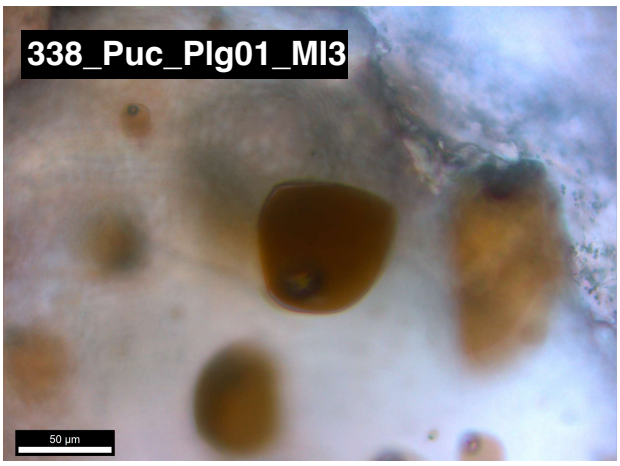
338_Puc_Plg01_MI3
50 µm

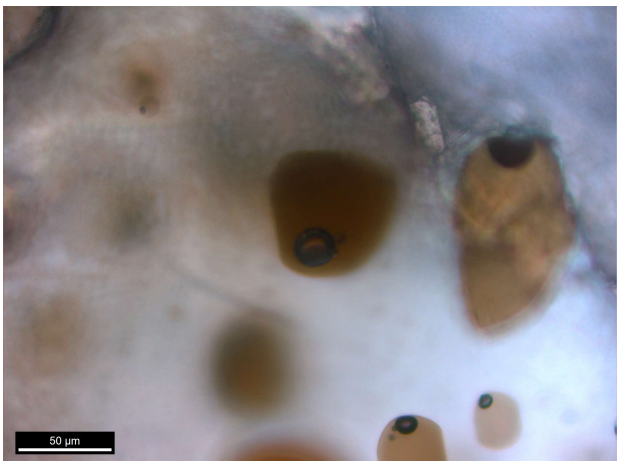
50 µm

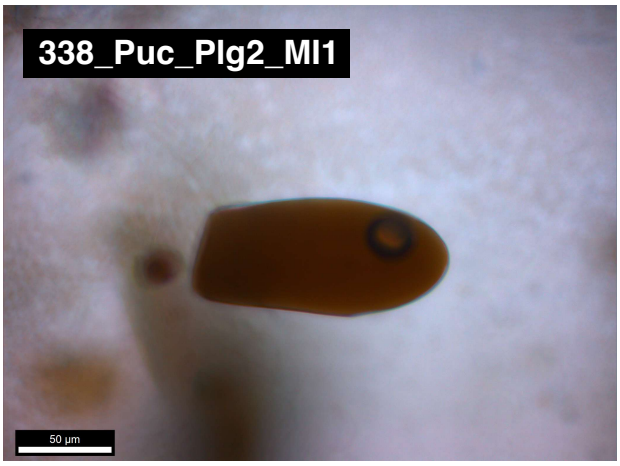
338_Puc_Plg2_MI1
50 µm

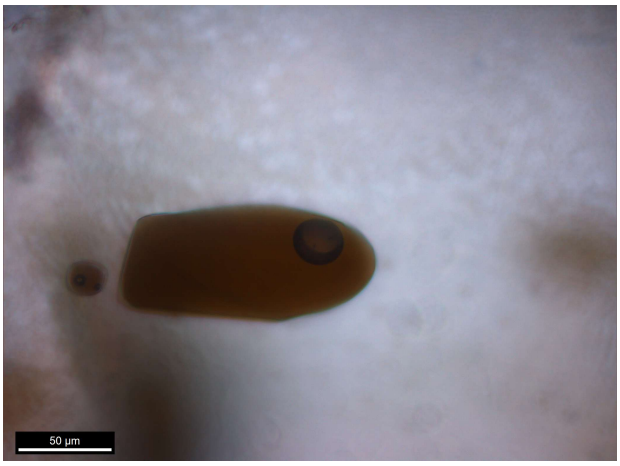
50 µm

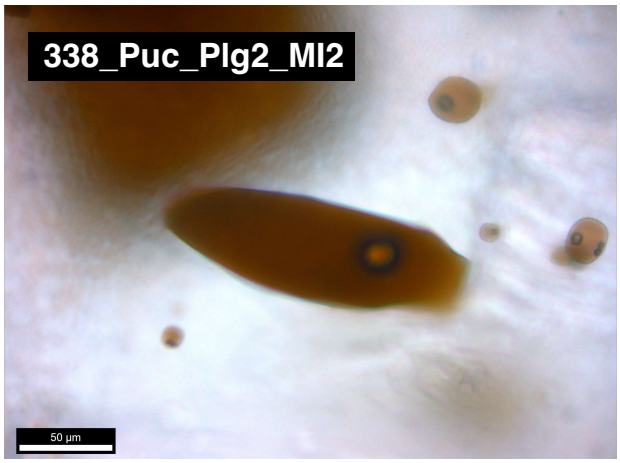
338_Puc_Plg2_MI2
50 µm

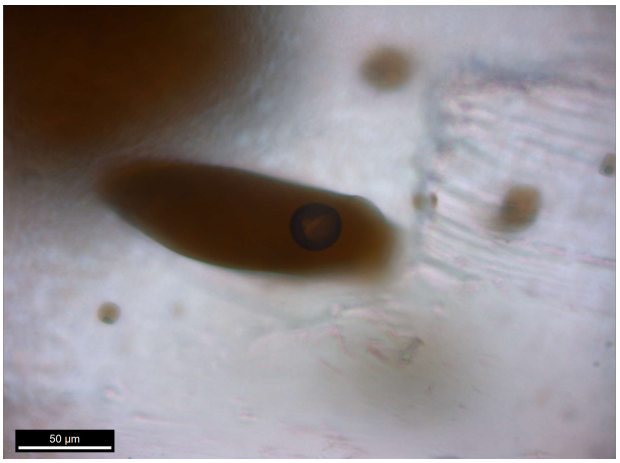
50 µm

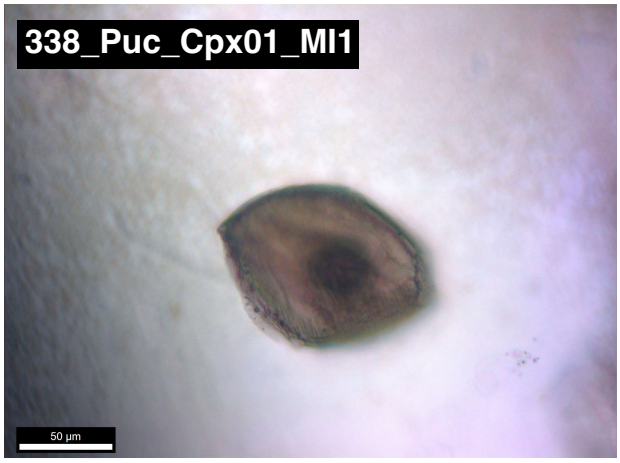
338_Puc_Cpx01_MI1
50 µm

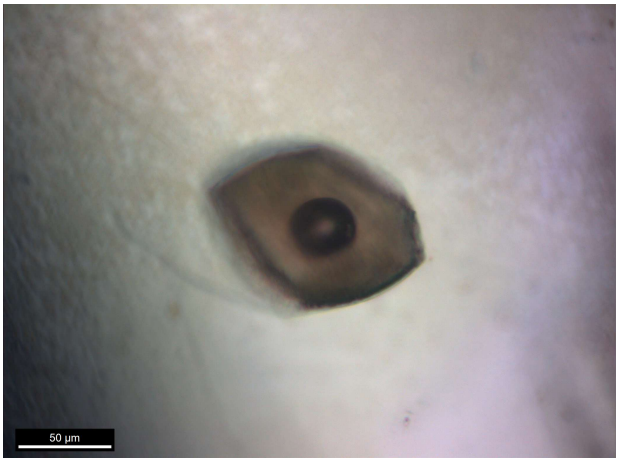
50 µm

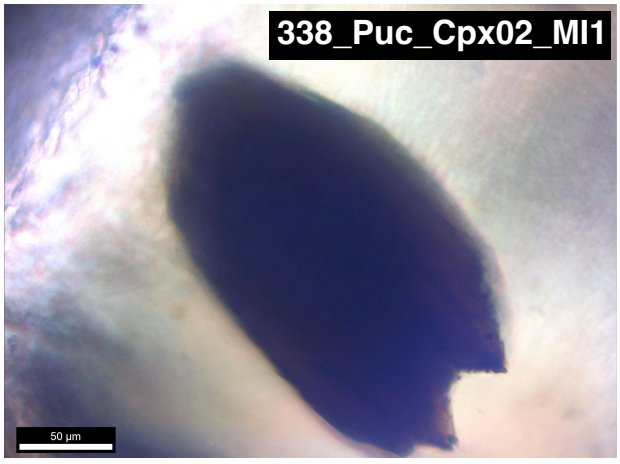
338_Puc_Cpx02_MI1
50 µm

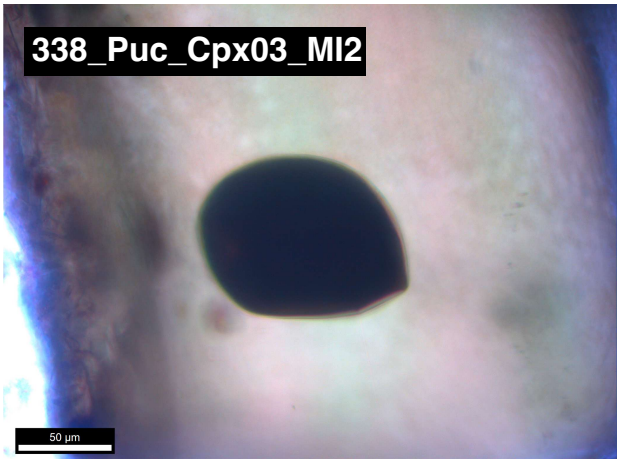
338_Puc_Cpx03_MI2
50 µm

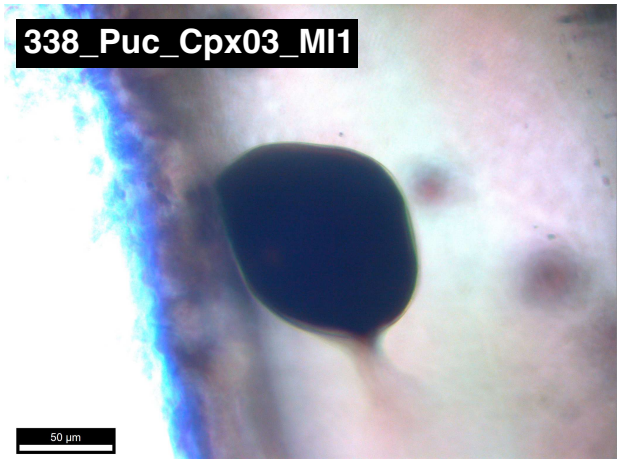
338_Puc_Cpx03_MI1
50 µm

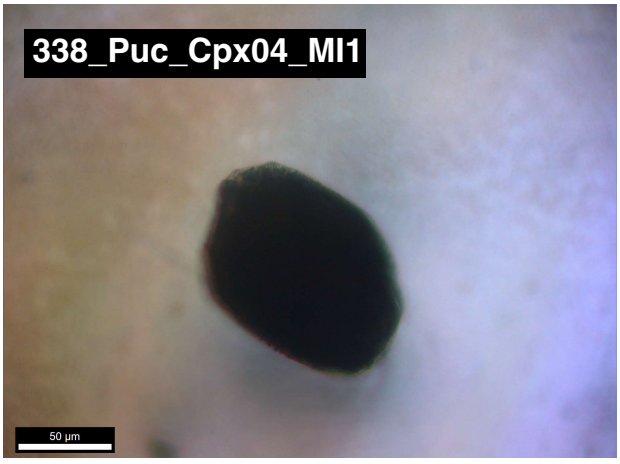
338_Puc_Cpx04_MI1
50 µm

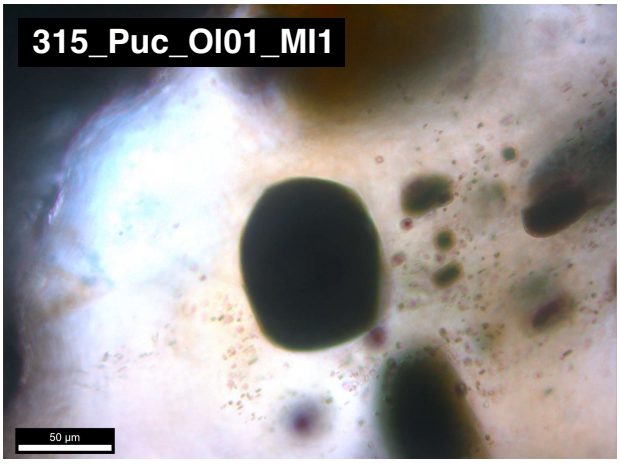
315_Puc_Ol01_MI1
50 µm

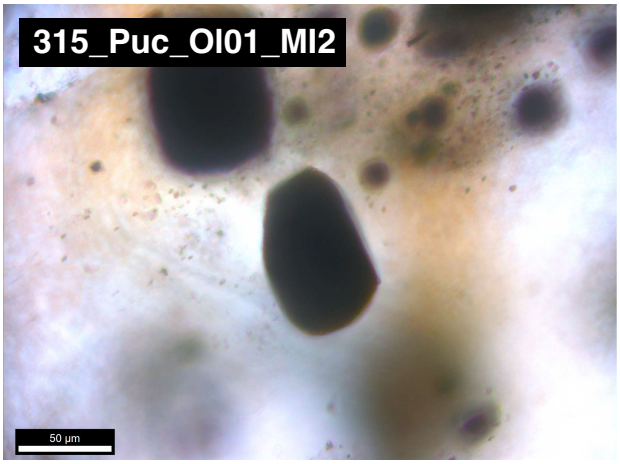
315_Puc_Ol01_MI2
50 µm

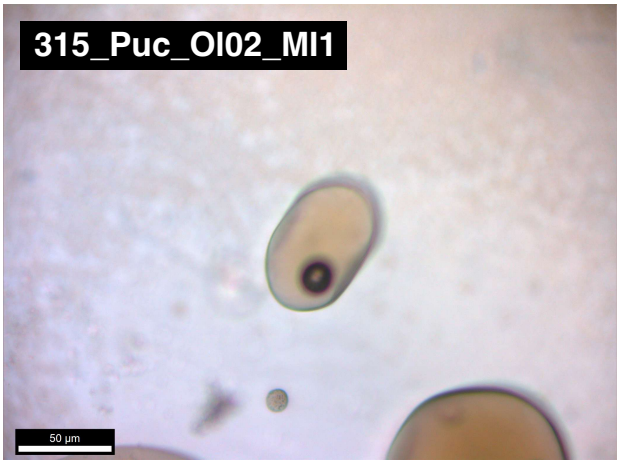
315_Puc_Ol02_MI1
50 µm

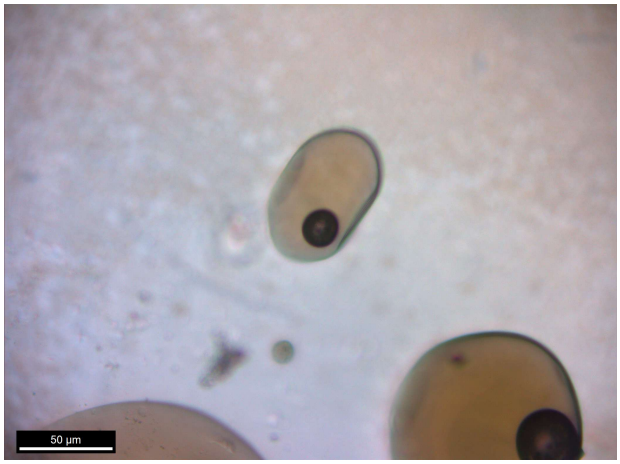
50 µm

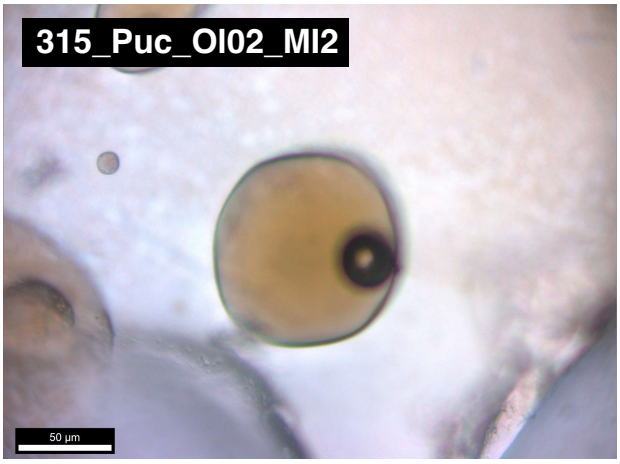
315_Puc_Ol02_MI2
50 µm

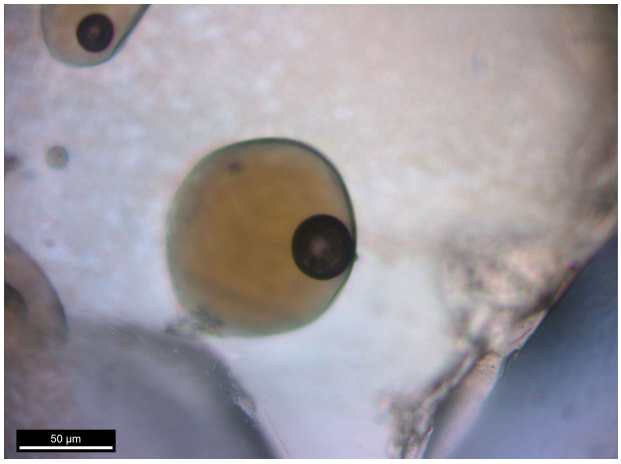
50 µm

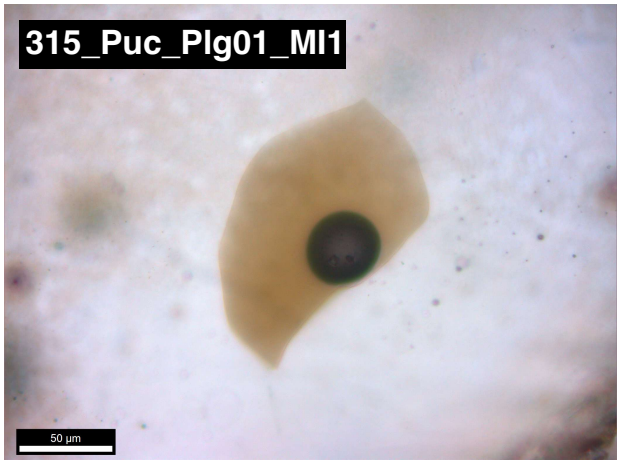
315_Puc_Plg01_MI1
50 µm

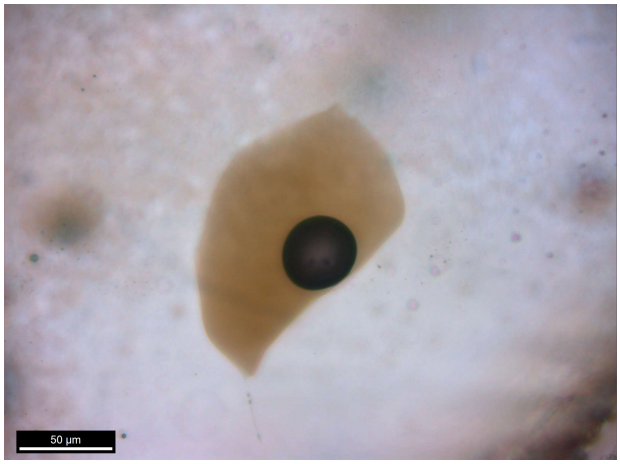
50 µm

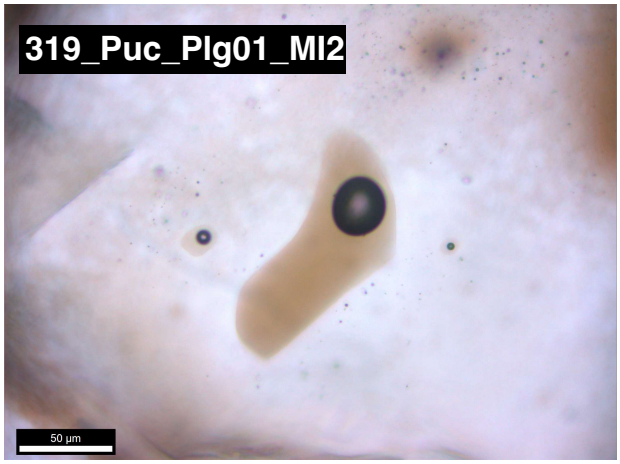
319_Puc_Plg01_MI2
50 µm


50 µm

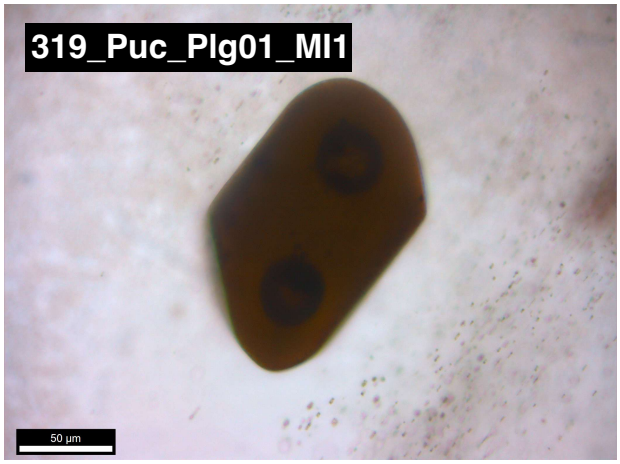
319_Puc_Plg01_MI1
50 µm

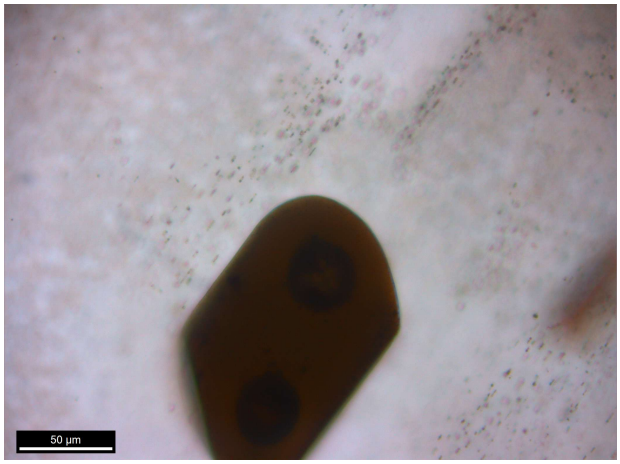
50 µm

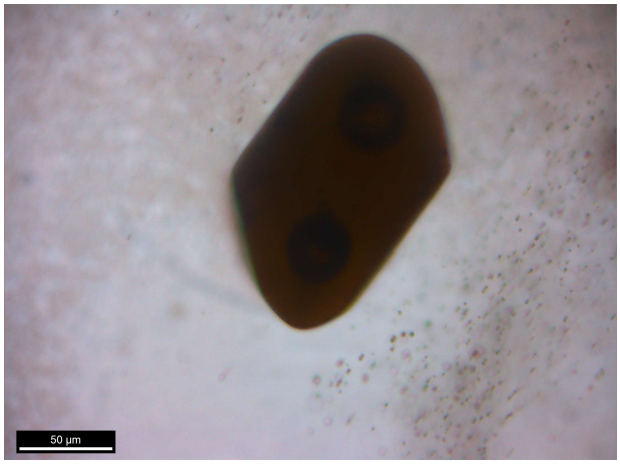
50 µm

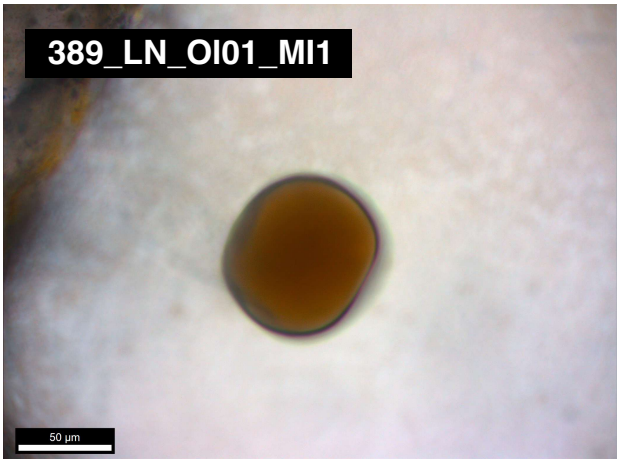
389_LN_OI01_MI1
50 µm

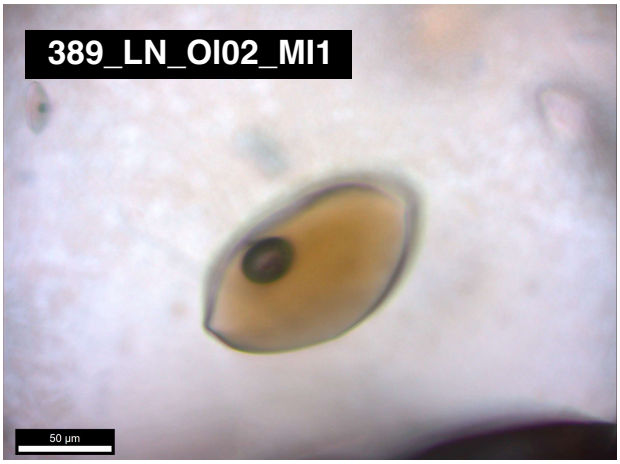
389_LN_OI02_MI1
50 µm

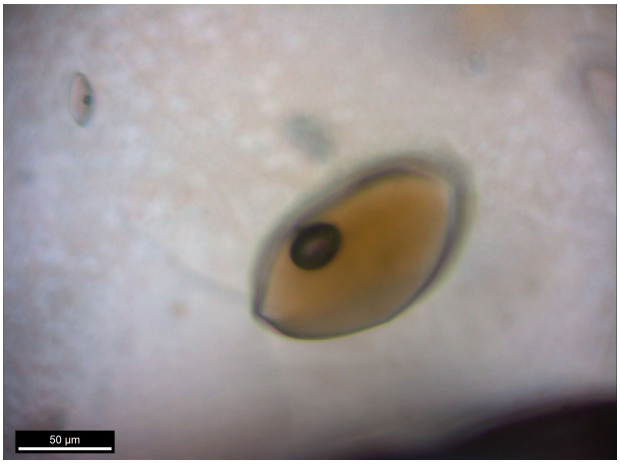
50 µm

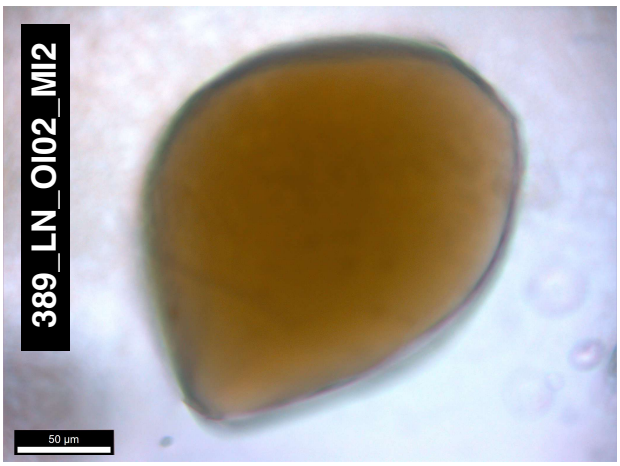
389_LN_OI02_MI2
50 µm

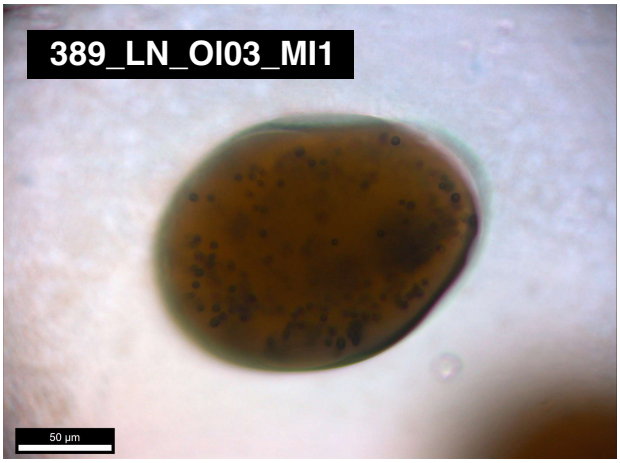
389_LN_OI03_MI1
50 µm

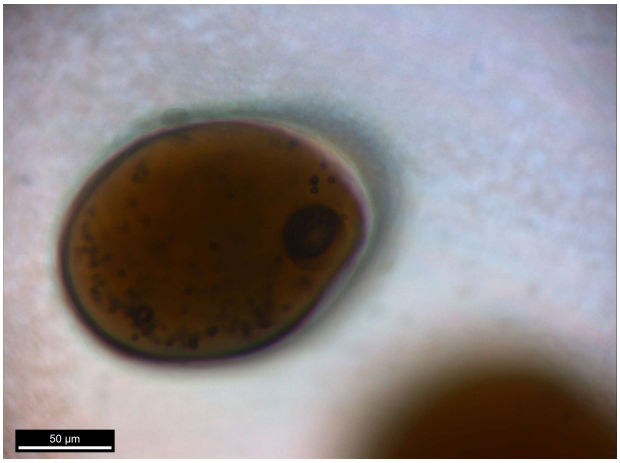
50 µm

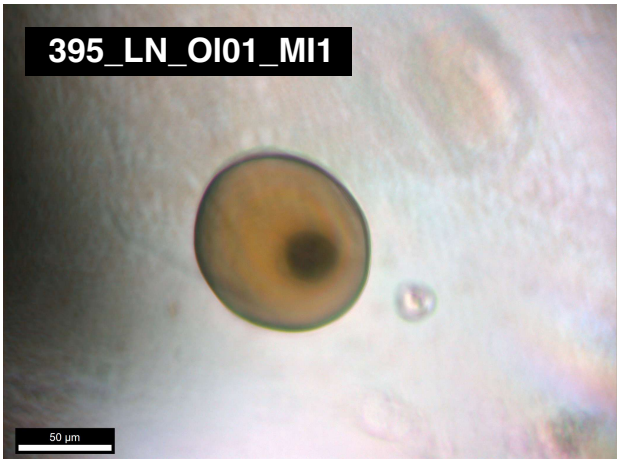
395_LN_OI01_MI1
50 µm

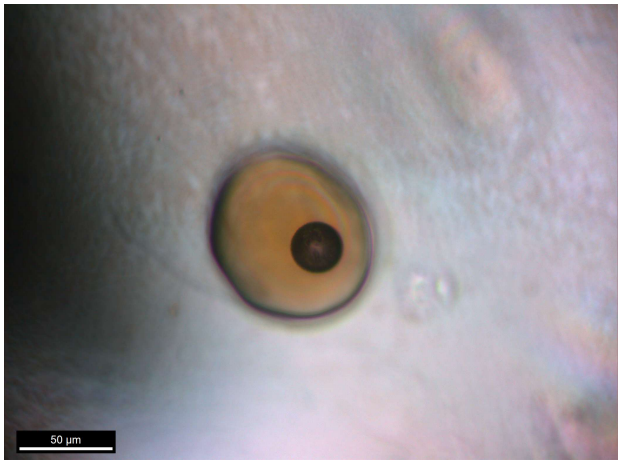
50 µm

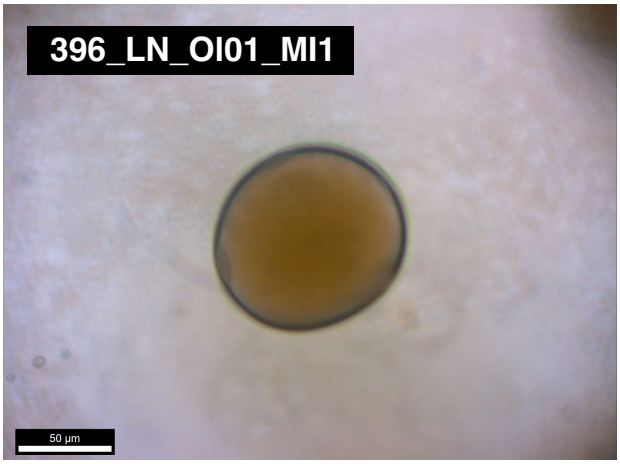
396_LN_OI01_MI1
50 µm

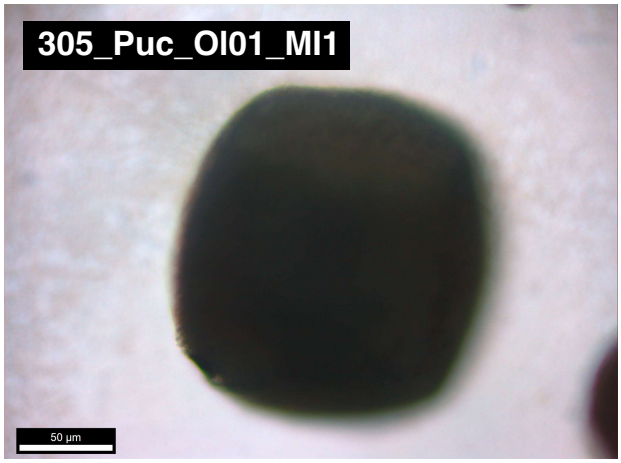
305_Puc_Ol01_MI1
50 µm

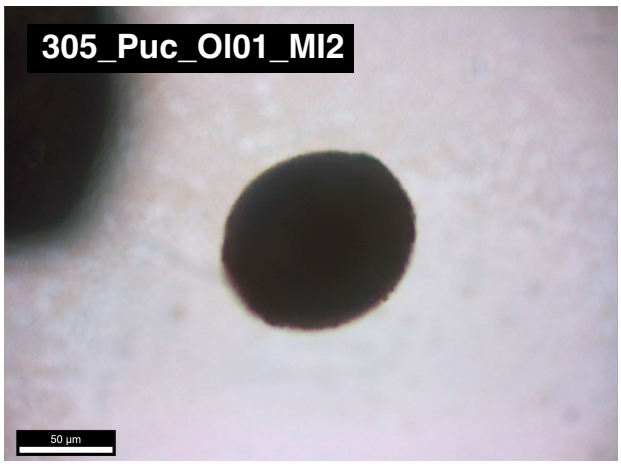
305_Puc_Ol01_MI2
50 µm

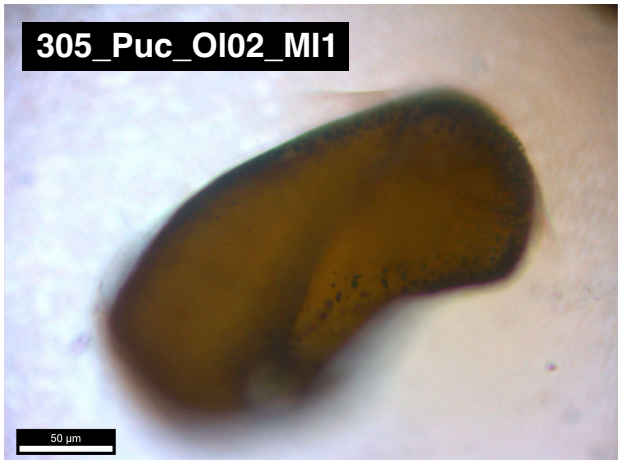
305_Puc_Ol02_MI1
50 µm

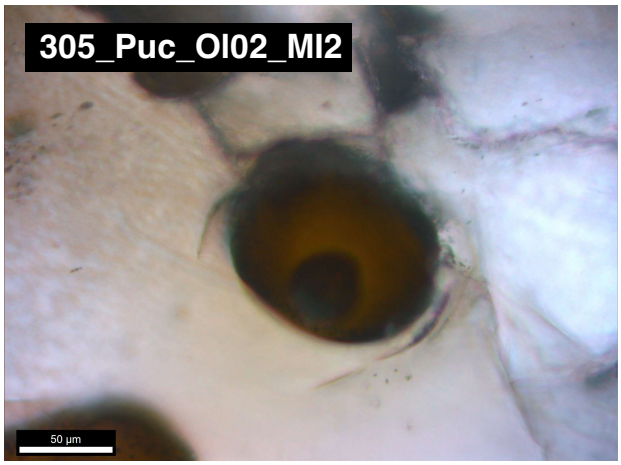
305_Puc_Ol02_MI2
50 µm

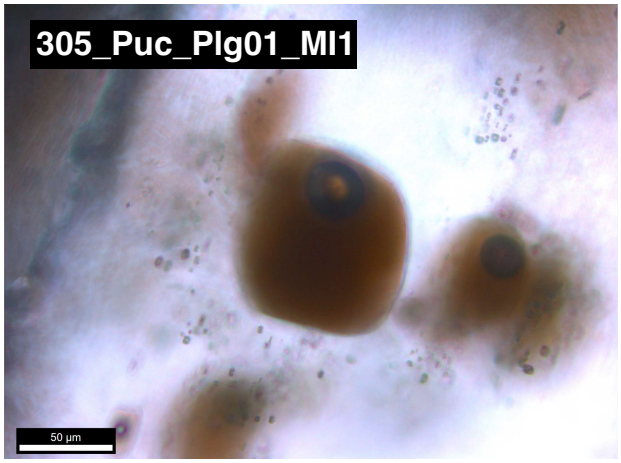
305_Puc_Plg01_MI1
50 µm

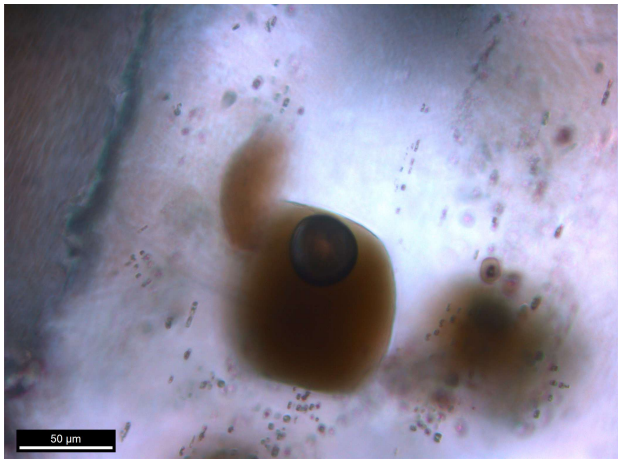
50 µm

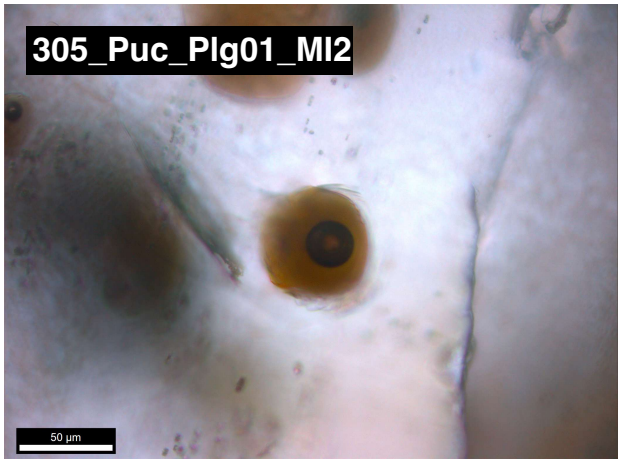
305_Puc_Plg01_MI2
50 µm

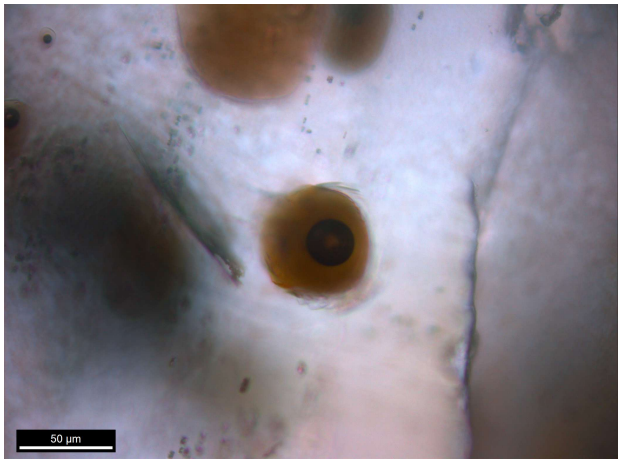
50 µm

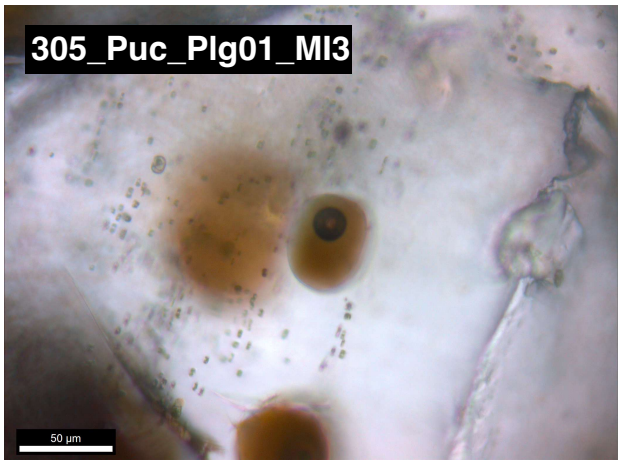
305_Puc_Plg01_MI3
50 µm

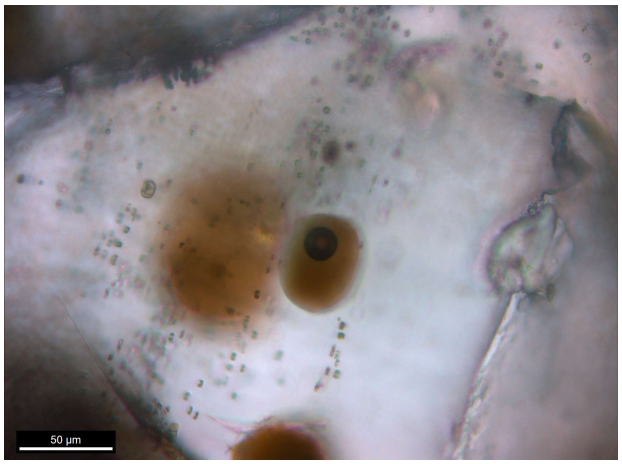
50 µm

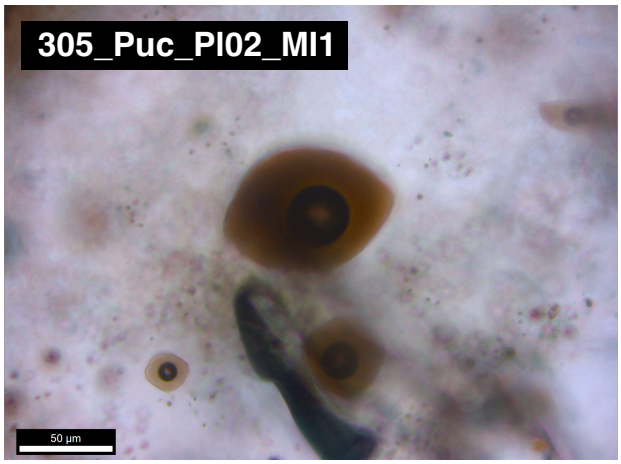
305_Puc_Pl02_MI1
50 µm

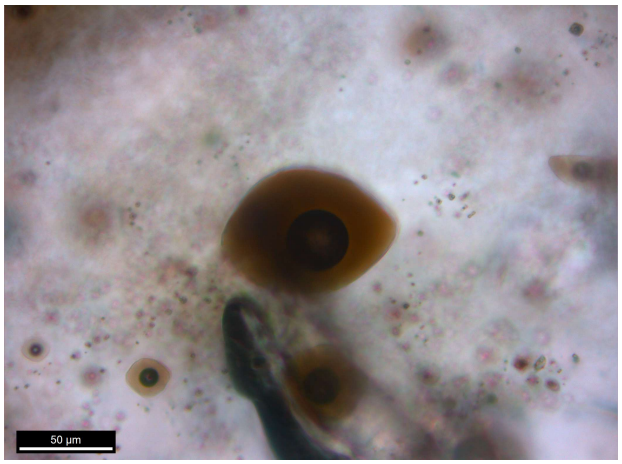
50 µm

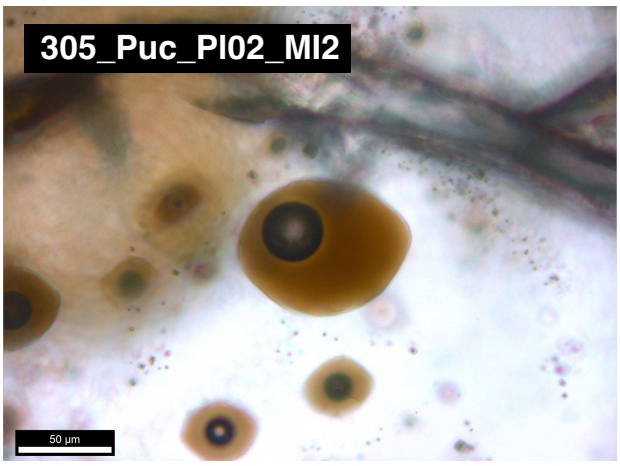
305_Puc_Pl02_Ml2
50 µm

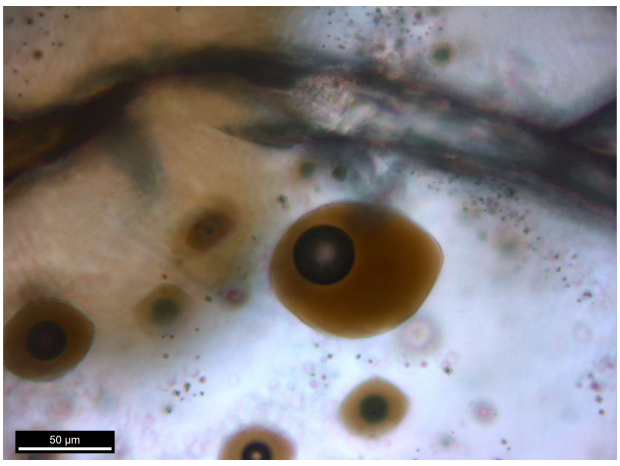
50 µm

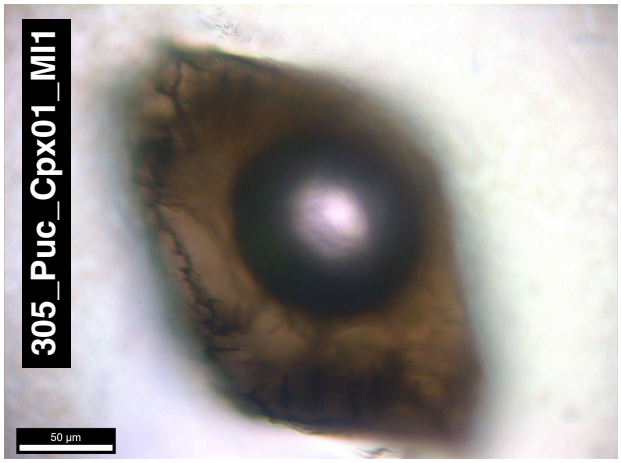
305_Puc_Cpx01_Ml1
50 µm

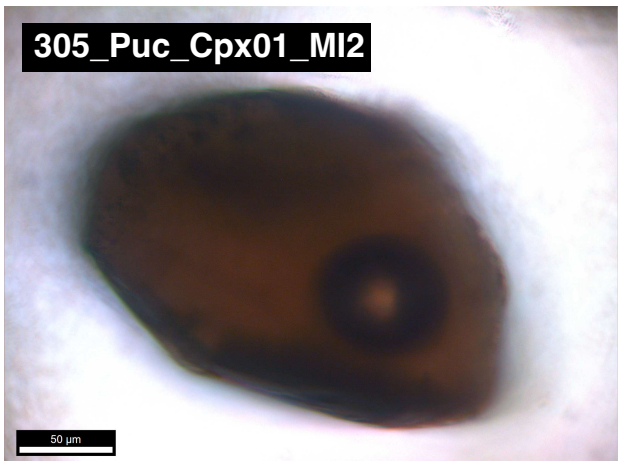
305_Puc_Cpx01_Ml2
50 µm

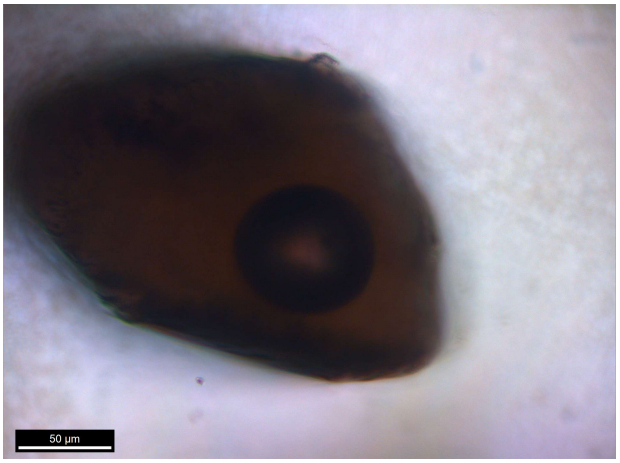
50 µm

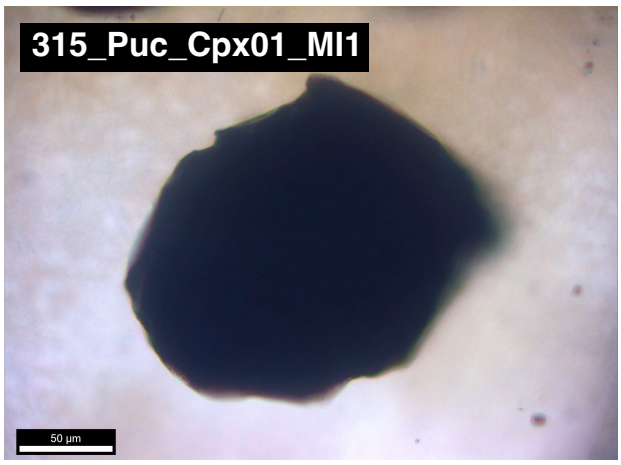
315_Puc_Cpx01_Ml1
50 µm